Yukon

Exploration & Geology

2025



Yukon Geological Survey Activities · Yukon Hardrock Mining, Development and Exploration
Yukon Placer Mining, Development and Exploration · Yukon Geological Research
Yukon Geoscience Publications

Yukon

Yukon Exploration & Geology 2025

Edited by

A. Stuart, L.H. Weston
and S.K. Schultz

Yukon Geological Survey
Energy, Mines and Resources
Government of Yukon

Published under the authority of the Department of Energy, Mines and Resources, Government of Yukon, https://yukon.ca.

Publié avec l'autorisation du Ministères de l'Énergie, des Mines et des Ressources du gouvernement du Yukon, https://yukon.ca.

©Department of Energy, Mines and Resources, Government of Yukon

ISSN 1718-8342 (online version)

Yukon Geological Survey publications can be obtained from:
Yukon Geological Survey
102-300 Main Street
Box 2703 (K-102)
Whitehorse, Yukon, Canada Y1A 2C6

email geology@yukon.ca

Yukon Geological Survey website https://yukon.ca/en/science-and-natural-resources/geology

In referring to this publication, please use the following citation:
Yukon Geological Survey, 2026. Yukon Exploration and Geology 2025. A. Stuart, L.H. Weston and S.K. Schultz (eds.), Yukon Geological Survey, Government of Yukon, 272 p.

Front cover photograph: Surficial geology mapping along Charcoal Ridge, Tombstone Territorial Park. The view is to the west, and the Dempster Highway is visible in the background. (Photo by Moya Painter, Yukon Geological Survey.)

Preface

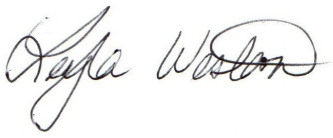
The Yukon Exploration and Geology (YEG) volume continues to evolve and with that, we introduce a fully digital publication for this year. The YEG remains a key annual publication by the Yukon Geological Survey (Energy, Mines and Resources, Government of Yukon) and highlights geoscience research and activities across the Yukon from the previous year. Although you will no longer see a printed volume, we continue to provide the same format that comprises an overview section followed by a series of technical papers. The overview includes summaries of the Yukon Geological Survey's (YGS) staff activities, as well as exploration and development overviews for both the hardrock and placer industries in the Yukon; the technical papers consist of a number of current research reports on various geoscience projects across the territory. The YEG volume is available in digital format only and can be downloaded from our website (along with all other Yukon Geological Survey publications) at https://data.geology.gov.yk.ca/.

As in previous volumes, YEG 2025 aims to provide the most up-to-date information on mining and mineral exploration activity in the Yukon, both in the hardrock and placer sectors. We also strive to deliver the most current geoscience research in the Yukon, for example, this year, thanks to the hard work of some of our YGS staff and their co-authors, we are able to present some preliminary observations on the December 6, 2025 M_W7.0 earthquake that took place in southwest Yukon—the largest onshore earthquake in Canada in the last 75 years.

As always, the success of this publication relies on the continued contributions from prospectors, exploration and government geologists, mining companies, and academic students, all of whom are willing to contribute to public geoscience for the benefit of the scientific community, the public, and the mineral industry of the Yukon. Their work is greatly appreciated.

More importantly, I would like to acknowledge the support from our 14 Yukon First Nation partners whose Lands and Traditional Territories we continue to work on. Without their engagement and support, the valuable geoscience data that is gathered by industry, government and academia would not happen. We look forward to strengthening and fostering honest and meaningful partnerships with all Yukon First Nations.

I hope you enjoy the volume. Any input or suggestions you may have to improve future YEG publications are welcome. Please contact us at geology@yukon.ca.



Leyla Weston

Congratulations to Carolyn Relf on her retirement!

Director, Yukon Geological Survey from 2008 to 2025

Carolyn graduated from Queen's University with a BSc in Geological Sciences in 1984. She moved on to Memorial University and completed an MSc in 1987 in geochemistry and mineral chemistry before finally completing her studies in geology with a PhD back at Queen's University in structural geology, metamorphic petrology, and Archean tectonics (1992). Her fieldwork, which took place in the arctic regions of Canada, had her well poised for a future career in the northern territories. And so began Carolyn's 30+ successful years as a woman in geology, at a time when women were estimated to make up less than 15% of this discipline.





Carolyn's first 16 years of her career in the public sector began in Yellowknife with the Northwest Territories (NWT) Geological Survey. She started as a project geologist mapping throughout NWT and Nunavut and not long after, moved into management to become the Chief Geologist. In that time, Carolyn also worked as an adjunct professor at the University of Alberta (2000–2007) leading an invaluable initiative that took qualified 4th year students every year to complete a field course that focused on bedrock mapping skills. This program not only gave the students exceptional skills for their future geological careers, but it also resulted in advancing the geological understanding of various parts of the territory.

In 2008, Carolyn moved with her husband and daughter to take on the role as Director of the Yukon Geological Survey (YGS) for the next 18 years. It was evident from the day that Carolyn began at YGS that she had a wealth of experience in a leadership role; however, it is her incredible character that brought so much success to the team. Carolyn is a passionate geoscientist and her leadership style is inclusive, collaborative, and full of authenticity and humour. She always took the time to engage with all her staff and recognize everyone's contributions to the organization, which included a talented and diverse team of geoscientists. Through her vision and support, the YGS not only advanced geological knowledge in the territory, but also became a place where young geoscientists grew into world-class professionals. She also saw the value in engaging beyond the survey and always put a strong emphasis on building and maintaining strong relationships with industry, federal government partners, academia and Yukon First Nation governments. Carolyn's tireless efforts and dedication to the organization was admirable. She was an incredible mentor and role model for many of us at the YGS, and her professionalism, integrity, and wonderful sense of humour will be greatly missed. From your YGS family, we wish you all the best in your future adventures, of which we are certain there will be many!





Yukon Geological Survey staff

Back (left to right): *Laurent Cogotti, Dustin Rainey, Panya Lipovsky, Chad Côté, Alex Brubacher, David Moynihan, Derek Cronmiller, Jan Dettmer, Moya Painter, Theron Finley.*
Middle (left to right): *Tamara Annau, Emilie Stewart-Jones, Spencer Skerget.*
Front (left to right): *Tyler Ambrose, Amanda O'Connor, Sarah Schultz, Tiera Naber, Leyla Weston.*
Missing: *Rosie Cobbett, Patrick Sack, Sarah Ellis, Sydney van Loon, Amy Stuart.*

Yukon Geological Survey

Yukon Geological Survey staff are located in two buildings in Whitehorse: the Elijah Smith Building at 300 Main Street, room 102, and the H.S. Bostock Core Library at Mile 918 on the Alaska Highway.

Operations

Elijah Smith Building

Rainey, Dustin – Director, (867) 332–4192 ..... dustin.rainey@yukon.ca

Annau, Tamara – Supervisor, Finance & Operations, (867) 667–8508 ..... tamara.annau@yukon.ca

H.S. Bostock Core Library

Dettmer, Jan – Geoscience Research Manager, (867) 332–4163 ..... jan.dettmer@yukon.ca

Bedrock Geology

H.S. Bostock Core Library

Ambrose, Tyler – Project Geologist, (867) 667–5175 ..... tyler.ambrose@yukon.ca

Cobbett, Rosie – Project Geologist, (867) 455–2802 ..... rosie.cobbett@yukon.ca

Moynihan, David – Project Geologist, (867) 455–2805 ..... david.moynihan@yukon.ca

Schultz, Sarah – Project Geologist, (867) 332–0846 ..... sarah.schultz@yukon.ca

Vacant – Head, Bedrock Geology

Vacant – Project Geologist

Surficial Geology

H.S. Bostock Core Library

Cronmiller, Derek – Head, Surficial Geology, (867) 332–4961 ..... derek.cronmiller@yukon.ca

Finley, Theron – Surficial Geologist, (867) 334–4531 ..... theron.finley@yukon.ca

Lipvosky, Panya – Surficial Geologist, (867) 667–8520 ..... panya.lipovsky@yukon.ca

Painter, Moya – Permafrost Geologist, (867) 667–8514 ..... moya.painter@yukon.ca

Stewart-Jones, Emilie – Transportation Geohazard Specialist (joint position with Transportation Planning Branch, HPW), (867) 332–2530 ..... emilie.stewart-jones@yukon.ca

van Loon, Sydney – Placer Geology Technician, (867) 332–3324 ..... sydney.vanloon@yukon.ca

Minerals Geology

H.S. Bostock Core Library

Sack, Patrick – Head, Minerals Geology, (867) 667–3203 ..... patrick.sack@yukon.ca

Brubacher, Alex – Economic Geologist, (867) 334–6314 ..... alex.brubacher@yukon.ca

Ellis, Sarah – Economic Geologist, (867) 332–9263 ..... sarah.ellis@yukon.ca

Naber, Tiera – Economic Geologist, (867) 456–3828 ..... tiera.naber@yukon.ca

Skerget, Spencer – Core Library Manager, (867) 393–6492 ..... spencer.skerget@yukon.ca

Vacant - Mineral Assessment Geologist

Technical Services & Outreach

Elijah Smith Building

Stuart, Amy – Manager, Technical Services, (867) 332–7865 ..... amy.stuart@yukon.ca

Cogotti, Laurent – Geological Spatial Database Administrator, (867) 471–0502 ..... laurent.cogotti@yukon.ca

Côté, Chad – Geological Spatial Database Administrator, (867) 393–7186 ..... chad.cote@yukon.ca

O'Connor, Amanda – Outreach Geologist, (867) 332–9376 ..... amanda.oconnor@yukon.ca

Weston, Leyla – Outreach Geologist, (867) 393–7187 ..... leyla.weston@yukon.ca

Vacant – Publications Technician

Yukon Exploration and Geology 2025

Table of Contents

Yukon Geological Survey overview, 2025

Dustin Rainey 1

Yukon placer mining development and exploration overview, 2025

Sydney van Loon 19

Yukon hardrock mining, development and exploration overview, 2025

Spencer W. Skerget and Tiera V. Naber 39

A preliminary HVSR investigation of the shallow structure of the Teslin fault, southern Yukon

Daniel O. Afolabi, Hersh Gilbert, Jeremy M. Gosselin and Jan Dettmer 75

Stratigraphic, geochronological, and geochemical constraints on the genesis of Late Cretaceous volcanic rocks in the Sixtymile district of west central Yukon, Canada (NTS 116C/2, 115N15)

Emilia Butty, Patrick J. Sack, Matthew Leybourne and James Crowley 91

Preliminary investigation of seismic site conditions in Whitehorse (Kwänlin), Yukon, from passive seismic methods

Jamie Friesen Byer, Jeremy M. Gosselin, Jan Dettmer and Hersh Gilbert 119

The December 6, 2025 M_w7.0 earthquake in Yukon, Canada: Tectonic significance and observations of ground failure

Theron Finley, Jeremy M. Gosselin, Katherine M. Biegel, Panya S. Lipovsky, Derek C. Cronmiller, Andrew J. Schaeffer and Jan Dettmer 131

Current tectonics of the Richardson Mountains, northwestern Canada, from preliminary double-difference earthquake relocations

Andrew J. Schaeffer, Jeremy M. Gosselin, Pascal Audet, John F. Cassidy and Collin Paul 149

Preliminary analysis of the sequence stratigraphy and geochemistry of the Portrait Lake Formation at Macmillan Pass, Yukon, Canada

Sarah K. Schultz, Octavian Catuneanu and John B. Gordon 167

Ordovician to Devonian stratigraphy of Nááts'įhch'oh National Park Reserve, Northwest Territories

Sarah K. Schultz and Merilie A. Reynolds 191

Mapping geohazards to support climate adaptation on Yukon's transportation network

Emilie Stewart-Jones and Moya Painter 207

Assessing Miles Ridge landslide activity using an integrated ground-RPAS-satellite approach

John Stix, Justin Roman, Margaret Kalacska, Oliver Lucanus, Panya S. Lipovsky and Pablo Arroyo-Mora 221

In-situ monazite geochronological constraints on the timing of vein formation and gold mineralization in the Klondike gold district, western Yukon

Brodie A. Stroh, Tyler K. Ambrose, Murray M. Allan and Matthjis A. Smit 239

Yukon Geological Survey list of publications and data releases for 2025 267

Yukon Geological Survey overview, 2025

*Dustin Rainey**
Yukon Geological Survey

Rainey, D., 2026. Yukon Geological Survey overview, 2025. *In*: Yukon Exploration and Geology, 2025, A. Stuart, L.H. Weston and S.K. Schultz (eds.), Yukon Geological Survey, Government of Yukon, p. 1–17.

Introduction

The Yukon Geological Survey (YGS) underwent considerable change in 2025, mostly in response to the retirement of two key individuals. Carolyn Relf retired as Director after 17 years of leading the YGS. Shortly after Relf's departure, Maurice Colpron retired from his role as Head of Bedrock Geology. These two individuals contributed greatly to expanding the geological understanding of the Yukon, which directly resulted in significant injection of funding into the territory in the form of research dollars and industry investment in mineral exploration. Those of us remaining at the YGS are thankful to have been able to learn from their approach to pursuing scientific excellence. Following his retirement, Colpron was granted the status of Emeritus Scientist, allowing him to continue advancing his research interests and to provide mentorship to YGS staff.

The past three years have seen considerable changeover in YGS staff. In addition to eight new people joining the YGS in 2024, Relf led a reorganization of the branch that added a Geoscience Research Manager and a Technical Services Manager, both of which report to the Director. In 2024, Amy Stuart brought her Government of Yukon (YG) information technology expertise to the YGS to be the Technical Services Manager. In February 2025, Jan Dettmer became the Geoscience Research Manager after leaving a full-time geophysics professorship at the University of Calgary. After 15 years in YG's Assessment and Abandoned Mines branch, Dustin Rainey became the new Director of the YGS at the end of March 2025. The new management team brings a wealth of knowledge and experience in geoscience research, information technology, finance and public service; together they look forward to leading and supporting the YGS team.

Broader trends that impacted the YGS in 2025 include the continued rise in the price of gold (surpassing C$6000 per ounce in October), a national interest and focus on critical minerals, ongoing landscape modification by landslides, advancement of land use planning projects, and the ever-increasing involvement of First Nations in territorial decision-making. A Yukon First Nation dedication to mining was best exemplified by Selkirk First Nation's purchase of the Minto Mine, which is a past-producer of copper, gold and silver. Despite considerable ongoing challenges, significant progress was made in managing the Eagle Gold Mine heap leach failure that occurred in June 2024, and governments and industry continue to await the outcome of the sales process being led by the Receiver. Within the context of these geopolitical factors, this report provides an overview of YGS's 2025 staff project highlights and activities across the territory.

* dustin.rainey@yukon.ca

Yukon Geological Survey personnel and branch changes

The YGS delivers on its public geoscience mandate through four units led by the Director and two managers, with support from the Finance and Operations Supervisor (Fig. 1). Under the coordination of the Geoscience Research Manager, the Bedrock Geology, Minerals Geology and Surficial Geology units (Bedrock, Minerals and Surficial units) are responsible for delivering the geoscience research program. The Technical Services unit provides the necessary technological and collaborative expertise that enables the public to use YGS's services and products.

As in 2024, there were significant changes in staff throughout 2025. The most significant changes were the retirements of both Carolyn Relf and Maurice Colpron within a three-month period. Their retirements marked the end of a generation of leading geoscience experts in their fields. In particular, Colpron's years of bedrock mapping and geology research with the YGS led to the significant advancement of our understanding of the evolution of the northern Cordillera and in particular, the tectonic evolution of the Yukon. Their collective efforts provided a base geoscientific understanding of the Yukon that continues to attract considerable investment dollars for research purposes and for natural resource exploration. The geological puzzle that is the landscape of the Yukon will always require bedrock and surficial mappers to make maps that communicate their findings to the public. As of December 2025, the YGS was actively recruiting a new head to lead the bedrock unit to continue advancing the understanding of Cordilleran tectonics in the Yukon.

Prior to her retirement, Relf had the foresight to reorganize the branch so that the Director would be supported by two managers. As the new Director, I appreciate her recognition that it would be challenging for a single individual to fill a role she expertly managed for 17 years. With that context, I would like to introduce myself and provide a brief overview of my background and what I bring to the YGS team. After starting in technical roles, I moved on to project management, then followed that with nearly

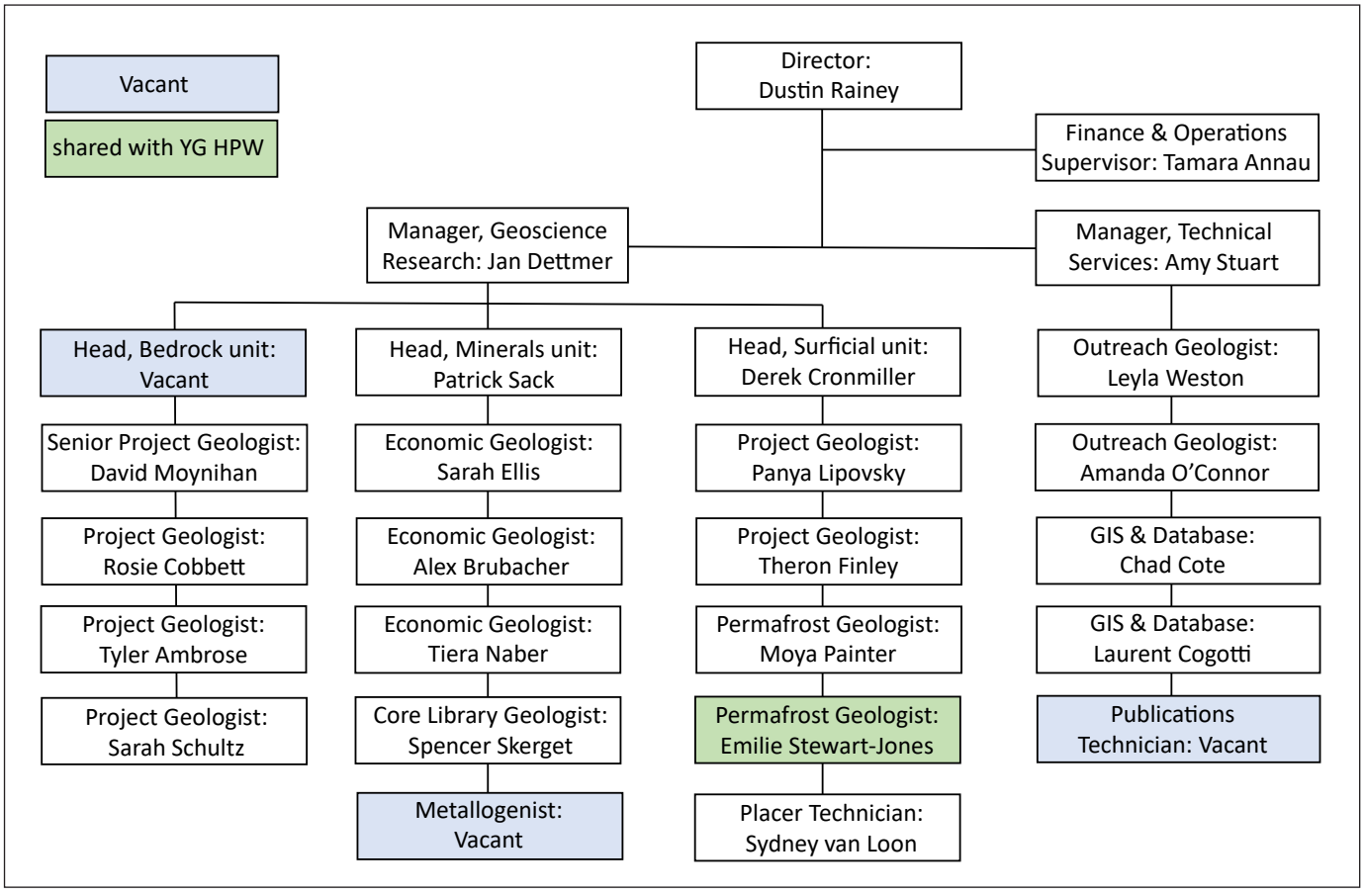


Figure 1. *Organizational chart for the Yukon Geological Survey. HPW – Department of Highways and Public Works.*

a decade of personnel management. This allows me to understand how management can support the needs of staff by reducing their administrative burden. I conducted my PhD research at the University of Alberta studying how relict Holocene carbonate spring deposits in the Rocky Mountains of Alberta and British Columbia could be used as terrestrial paleoclimate indicators. I spent five years as a Project Geologist in the mineral exploration industry seeking precious and base metals in Mexico, British Columbia and the Yukon. In the 15 years prior to joining the YGS, I was part of YG's Assessment and Abandoned Mines (AAM) branch, which is a project management group tasked with managing and remediating abandoned mines in the territory. In that role, I worked with multidisciplinary engineering and environmental teams to apply geoscientific principles to solve issues related to Metal Leaching and Acid Rock Drainage (ML/ARD). Historically, geological surveys focused on using geoscience knowledge to discover mineral and energy resources. My experience with abandoned mines leads me to believe that geological surveys are also well positioned to consider the potential environmental effects of geological mine waste, and how its impact across the entire mining life cycle could be reduced. During my time with AAM, I acquired considerable experience planning and scheduling complex projects, managing large budgets, coordinating diverse teams, and ensuring engagement with local communities and First Nations. As the Director of YGS, I am more than happy to manage these types of administrative tasks so that the staff can focus on their technical expertise to advance public geoscience.

My experience in mining and paleoclimates is complemented by Jan Dettmer's academic experience in geophysics and Amy Stuart's understanding of the technologies that underpin the functioning of YG. Dettmer completed his PhD at the University of Victoria where he developed methods in computational geophysics that have broad applicability to research areas of interest to the YGS such as seismology, geohazard assessment and geothermal potential. Dettmer's wide breadth of understanding of earth systems processes makes him ideally suited to provide an integrating role for research conducted by the Bedrock, Minerals and Surficial units. His technical background combined with his experience as a professor and researcher at the University of Calgary provides YGS geoscientists with strong mentorship and the expectation that they conduct rigorous scientific research.

Including Dettmer and myself, four new staff were hired by YGS in 2025. Theron Finley joined the Surficial Geology unit in August, immediately after completing his PhD at the University of Victoria, where he studied active tectonics of Cascadia and the Yukon. Finley's research on the potential for there to be large magnitude earthquakes on the Tintina fault created global media attention while he was driving through remote northwestern British Columbia on his way to start a new research career with YGS. The YGS is pleased to have him join the team and for him to continue his research. Laurent Cogotti came from YG's Department of Education in June to join the YGS as a Geological and Spatial Database Administrator in the Technical Services unit. Cogotti is with YGS until September 2026 while Brett Elliot is away working for the Department of Tourism and Culture on a temporary assignment. There was an additional change in the Technical Services unit in 2025 with the departure of Bailey Staffen, GIS Technician, who converted her temporary role at the Department of Education into a permanent one. The Technical Services unit is currently in the process of hiring a Publications Technician to support the development of YGS's many products. Finance and Operations Supervisor, Tamara Annau, who originally joined the YGS on a temporary assignment, transitioned into a permanent position. Annau fills a critical role in ensuring that contracts are in place to support field operations and post-field season laboratory analyses, and brings exceptional expertise in helicopter contracting. Economic Geologist Sarah Ellis initiated an education leave in autumn to begin an MSc at the University of Alberta studying the mineral potential of intrusions in western Yukon. Ellis is expected to return to her duties at the YGS in spring 2026. Kristy Kennedy, Project Geologist in the Surficial unit, continues in her secondment role with Kluane First Nation as Director of Lands, Resources and Heritage. An important role of geological surveys is the training of future geoscientists. In support of this mandate, YGS employed seven summer students as field assistants in 2025.

Despite the loss of historical experience and knowledge that comes with retirements and departures, new YGS staff are well-positioned to continue to provide high quality geoscience services to all Yukoners. As the new Director, I am proud to have joined the YGS and feel privileged to lead such a dedicated and high-performing team. The YGS staff constantly share new earth science discoveries and demonstrate what it means to be committed public servants (Fig. 2).



Figure 2. *Permafrost Geologists Moya Painter and Emilie Stewart-Jones assess the headscarp of an active rock glacier that is encroaching on the North Canol highway near Macmillan Pass at a rate of approximately 1 m per year.*

Yukon Geological Survey resources

The 2025-26 operating budget for YGS totaled $2 863 000 (Table 1). This represents a reduction of $131 060 from the previous year mainly due to an end of funding for highway geohazard assessments from Crown-Indigenous Relations and Northern Affairs Canada (CIRNAC). The operating budget provides the financial means for the YGS to deliver on its mandate of providing geoscience information to the public. The YGS data website (https://data.geology.gov.yk.ca/) has been a valuable resource for me throughout my geoscience career in the Yukon, and continues to set an example for how geological surveys can effectively distribute geoscience information as raw datasets, maps and technical reports. The YGS also maintains Facebook and Instagram accounts to share information about activities, public events, staffing opportunities and research discoveries. Some of those discoveries are shared at the end of this volume in a list of 2025 publications.

Yukon Geological Survey staff are distributed across two offices in Whitehorse. Sharing space with the Mining Recorder in the Elijah Smith Building are the Director, Finance and Operations Supervisor, and the Technical Services unit. The Geoscience Research Manager and staff, who comprise the three research units, are based at the H.S. Bostock Core Library on the Alaska Highway, commonly referred to as the Core Library. In addition to hosting office and laboratory space, the Core Library serves as a repository for rock and drill core material from Yukon mineral properties

Table 1. Yukon Geological Survey funding for fiscal year 2025-26. All funding is from the Government of Yukon.

Source	Funding for	Amount
YGS operational budget	Geoscience program	$1 330 000
Our Clean Future funds	Permafrost geohazards	$100 000
Yukon Mineral Exploration Program	Program grants	$1 433 000
Total		**$2 863 000**

and YGS projects. Spencer Skerget with the Minerals unit manages the facility, which also houses a public core logging space and lapidary laboratory. In addition to regular use by YGS staff, the facility was used 52 days by 27 different external clients in 2025. Clients from industry and academia collectively pulled 4700 m of drill core from the collection for viewing or sampling. The publicly available online database was updated with 110 drillholes with either additional original data (core logs, analyses) or updated high-resolution drill core photographs. In 2025, three drillholes totaling 978 m were donated to the drill core collection from the Mint mineral occurrence in southwest Yukon. Due to ever-expanding holdings, drill core donation criteria are becoming more rigid as the facility is now over 95% storage capacity.

Geoscience planning

The YGS is implementing the five-year plan completed in 2024. The primary planning process involved internal YGS workshops that were held separately by the Bedrock, Minerals and Surficial units. The workshops helped identify emerging interests and generated project ideas across all units.

Over the current five-year implementation cycle, incorporating the results of the workshops will be influenced by Jan Dettmer's vision for integrating research across the three units, and the individual research strengths of the YGS team, many of whom are new to the survey in the past three years. Dominant themes that continue to attract YGS resources include First Nations' considerations regarding geoscience activities within their Traditional Territories, land use planning, geohazard identification/monitoring, high gold prices, critical minerals, and the impacts of mining on Yukon's people and environment. With the Eagle Gold Mine heap leach failure still garnering a lot of public attention, YGS is considering how public geoscience can contribute to reducing environmental impacts from future mining projects. Many YGS staff are adept at mineralogy and understanding the fundamental principles that govern Metal Leaching and Acid Rock Drainage (ML/ARD). For an economic geologist, understanding sphalerite as an ore mineral of zinc readily extends to recognizing its potential to be harmful to aquatic life if improperly managed. Geoscientists do not design and operate mine waste facilities, but their ability to understand both the small scale mineralogy and big picture interactions with the landscape allow them to identify gaps in knowledge that may prove helpful in mitigating future mining issues.

The YGS continues to capitalize on successful established collaborations, such as the Minerals Technical Liaison Committee (TLC). The TLC was established shortly after devolution as a means for representatives from the placer industry, the hardrock exploration industry, and academia to share their thoughts on gaps in geoscience knowledge that could be filled by YGS research. Yukon Geological Survey economic geologist Sarah Ellis began an MSc degree in 2025 through the University of Alberta partly in response to a TLC request for YGS to assess the potential for intrusions in western Yukon to host mineralization. Another partnership is the sharing of a permafrost geologist, Emilie Stewart-Jones, between YGS and Government of Yukon's Department of Highways and Public Works (HPW) to better understand and manage the impacts of degrading permafrost on the Yukon's highway network. Summer 2025 also saw the implementation of an innovative partnership between the YGS, Parks Canada and Champagne and Aishihik First Nations (CAFN). Bedrock Geologist Rosie Cobbett led field explorations in Kluane National Park with CAFN citizens to better understand how the interactions of bedrock near the old Johobo mine and water quality in the Kathleen Lake watershed impact spawning of Kokanee salmon. One aspect of the YGS that is not as well known outside of the group is the level of intense research interaction between YGS geoscientists and university researchers. By having a wide-ranging knowledge network, YGS staff are able to keep well-informed of the latest developments in evolving technologies (e.g., the use of core scanning and artificial intelligence [AI] technologies for better understanding critical mineral deposits). Surficial and bedrock mapping remain essential for providing foundational geoscience data, while also enabling geoscientists to think more broadly about the impacts of geological time on the infrastructure of our modern lives. This strong culture of collaboration and engagement with the broader academic community is also reflected in YGS's involvement in national geoscience initiatives.

In conjunction with Yukon University, the YGS is preparing to host GAC-MAC 2027. This event, organized by the Geological Association of Canada (GAC®) and the Mineralogical Association of Canada (MAC), is the premiere annual geoscience conference in Canada. It was previously held in Whitehorse in 2016 and will once again provide a venue to showcase YGS research and the Yukon's rich geology.

For detailed descriptions of YGS work planning, readers are encouraged to review the Yukon Geological

Survey 2024 overview (Relf, 2025). The following sections provide updates on activities performed by the YGS in 2025. Readers with additional project ideas are encouraged to submit their input via geology@yukon.ca.

Geothermal energy, geophysical research and seismology

With no external funding for geothermal energy available for 2025, geothermal-related work was limited to the release of two publications documenting work completed to date. The first report, Open File 2025-7, summarizes the current state of knowledge for geothermal indicators in the Yukon (Sternbergh and Colpron, 2025). The report compiled geothermal datasets and summarized previously unpublished, contracted geothermal studies, as well as research conducted by the YGS between 2016 and 2024. More than 20 thermal springs are described, and water chemistry for these springs and selected boreholes are presented. The second report, Open File 2025-8, was a collaboration between the YGS, Innovate Geothermal Ltd. and HPW to assess geothermal potential in Whitehorse (Witter, 2025). The work involved performing an analysis of geoscience data in a 13 by 15 km area in the northern part of Whitehorse to better understand the potential for geothermal energy resources that, if present, could be used for heating purposes. The primary goal of the project was to analyze and interpret a variety of pre-existing and newly acquired geological and geophysical datasets to evaluate where geothermal reservoirs may be present within the study area. To construct a 3D geological model, researchers performed 2D map interpretation and geophysical inversion modelling of gravity and magnetic survey data. Discussions of warm springs may lure readers to explore the woods around Whitehorse, however be forewarned that the sub-twenty degree Celsius springs are not optimal for soaking.

Prior to his retirement, Maurice Colpron was the lead YGS researcher of geothermal-related projects. With Colpron's departure, Dettmer is an ideal researcher to fill the gap due to his geophysical research in studying geothermal potential in British Columbia and the Yukon. In his current Geoscience Research Manager role, Dettmer continues to work on quantifying seismic site amplification in Haines Junction and Whitehorse in collaboration with the Geologic Survey of Canada. The Haines Junction assessment was completed for 14 sites and published as a peer-reviewed study. Around Whitehorse, data analyses were completed for one site located in the Ibex Valley (glaciolacustrine soil) and one site located near the Takhini ball diamonds (fluvial soil), published in this volume (Byer et al., this volume). New data were recorded at the sites of the Mountain View Golf Course (glaciofluvial/glaciolacustrine) and Hidden Valley Elementary School (glaciolacustrine). A collaboration with the University of Calgary continues to support the study of geothermal potential near Teslin. Seismic data were analyzed with spectral methods to provide new constraints about the elastic properties of Quaternary sediments and bedrock that is affected by multiple strands of the Teslin fault in this region (Afolabi et al., this volume).

As extensive as geological time is, a M7.0 strike-slip earthquake in Kluane National Park on December 6, 2025 was a visceral reminder that geological time always includes the present. The epicentre, and hundreds of aftershocks, were located just east of Mount Logan in a very remote part of the Yukon. Despite temperatures of -40°C across the territory for the week following the earthquake, YGS staff chartered a helicopter and took advantage of a favourable weather window on December 12, 2025 to examine the impacts to the area. The earthquake triggered significant landslides of rock and ice, and the majority were initiated on the slopes of Mt. King George, a 3741 m tall peak (Fig. 3). Despite 2 m of fault slip occurring at 5 km depth, there was no clear evidence of the Earth surface rupturing. It is possible however, that a surface rupture was hidden by glacier ice. The earthquake occurred between the southerly Fairweather fault and the northerly Totshunda fault in an area where there are relatively few previously recorded earthquakes. This earthquake provides evidence to support the existence of a hypothesized connection between these faults where extensive glaciated terrain makes research difficult (Finley et al., this volume).

Minerals overview

Following a re-staffing of the Minerals unit in the past two years and Patrick Sack shifting into the head position, the team is getting well-acquainted with the geology of Yukon mineral deposits and occurrences. The Minerals staff also spend considerable time furthering connections amongst the broad network of industry and academic professionals involved in mineral exploration. Companies with advanced stage exploration projects such as Snowline Gold Corp. and Fireweed Metals Corp. (Fig. 4) are well-funded to continue their work. In contrast, it appears Eagle Gold Mine's 2024 heap leach failure has negatively impacted investors choosing to

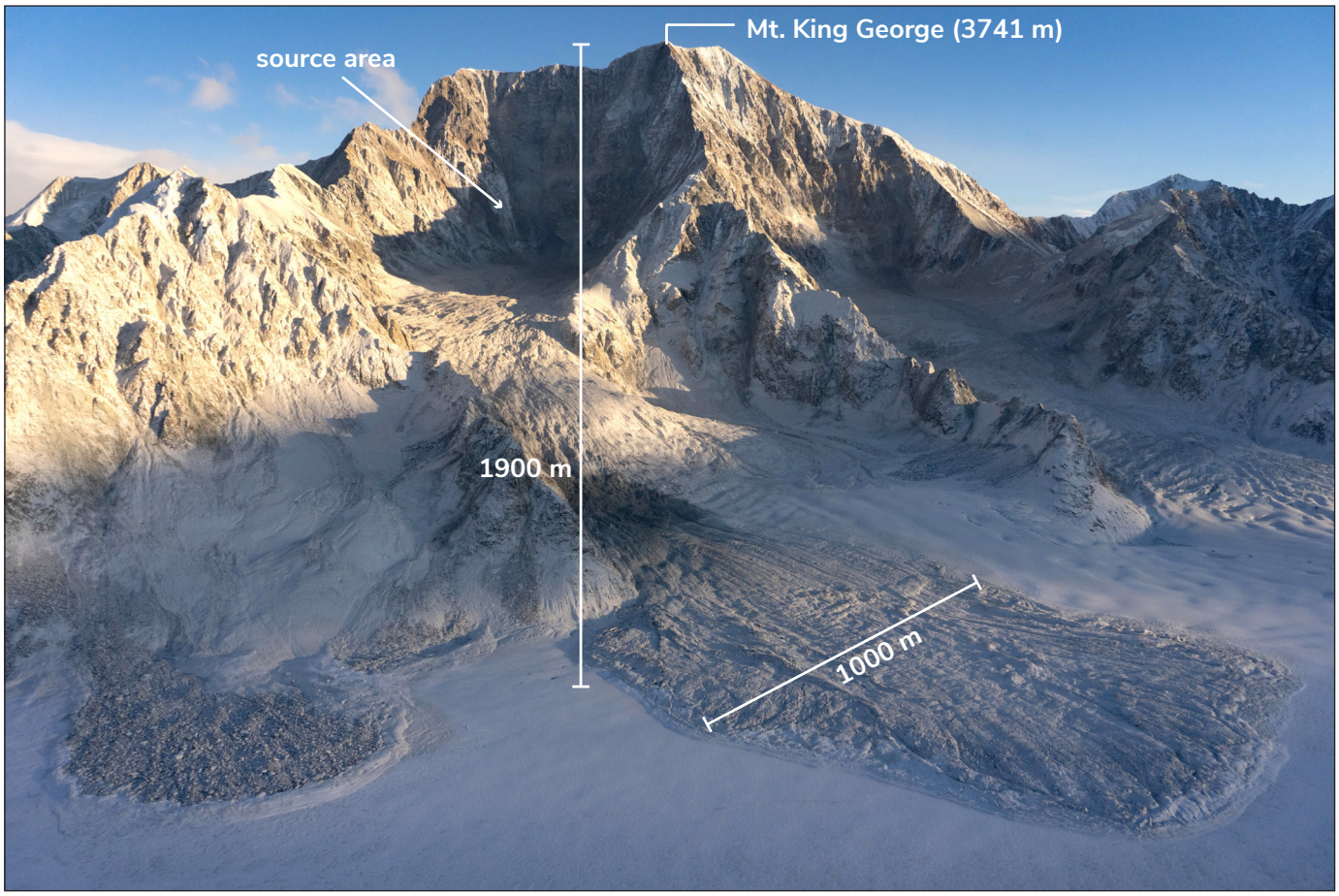


Figure 3. *Large landslides on the southwest side of Mount King George. The main debris lobe on the right is approximately 1000 m wide. The elevation difference between the peak and the glacier is approximately 1900 m.*

risk capital on early-stage projects in the Yukon. This is likely one reason why the demand for funding from the YGS Yukon Mineral Exploration Program (YMEP) remains strong. Following release of the Independent Review Board's (IRB) heap leach failure report with preventative recommendations (Smith and Konrad, 2025), and the initiation of a sales process to move the project out of receivership, it is hoped that confidence, and investment, in the Yukon's mining and exploration sector will continue to increase in 2026.

Maintaining access to large tracts of land for exploration is an ongoing concern of the mineral exploration industry. At the same time, First Nations and other Yukoners place paramount importance



Figure 4. *Core processing facility at Fireweed Metals Corp.'s Macpass project.*

on the responsible use of the land by industry. Land use planning has been identified as a key mechanism to bridge this gap, providing certainty to industry that they can explore their claims while ensuring that exploration activities do not hinder future land uses.

The YGS is contributing geoscience data to support the early stages of land use planning by leading the development of territory-wide mineral potential mapping. This work is particularly timely given the advancement of the Dawson Regional Land Use Plan, ongoing discussions regarding a potential national park in the Teetł'it Gwinjik (Peel River) watershed, and collaborative efforts between Ross River Dena Council, the Government of Yukon, and Parks Canada to explore options for a potential new protected area in the Tū Łı́dlini (Ross River) region.

In December 2024, YGS issued a request for proposals to engage a contractor to develop a series of commodity-specific mineral potential maps for the Yukon. The successful contractor, New Zealand-based Kennex Ltd., is producing maps based on mineral systems and deposit models relevant to the Yukon's various geological domains, such as the Selwyn basin and Intermontane terranes. A pan-Yukon approach has been adopted to ensure consistency across assessments, allowing each subsequent land use plan to begin with an established mineral potential mapping framework. Within the YGS Minerals unit, Patrick Sack and Alex Brubacher are leading the mineral potential mapping work.

Minerals activities

In addition to overseeing the Minerals unit, Sack is a respected leader within the branch, owing to his long tenure with YGS and extensive understanding of the interactions between tectonics and metallogeny. He was a co-author on Open File 2025-9 that reported U-Pb zircon ages for Paleogene magmatic rocks from the Ruby Range of southwestern Yukon (Israel, et al., 2025). Sack is also co-supervising two MSc thesis students: Keagan Parry (University of Alberta; co-supervisor Pillar Lecumberri-Sanchez) completed his thesis in 2025 on Banyan Gold Corp.'s AurMac property, while Maria Carter (Simon Fraser University; co-supervisor Dan Gibson) continues with her MSc thesis project at Trifecta Gold Ltd.'s Mount Hinton property that began in 2024. These two studies are part of a suite of four, staged thesis projects planned between 2023 and 2030 in the Dublin Gulch-Keno area. The Eagle Gold Mine heap leach failure may disrupt plans for a third MSc study of Victoria Gold Corp.'s Raven deposit and alternatives are being assessed.

In addition to database updates and processing of YMEP funding applications, staff from the Minerals unit spent as much time as possible setting foot on exploration properties. Sarah Ellis spent a lot of time on properties with intrusion-hosted gold deposits and in spring 2025, published her insights in Open File 2025-3 (Ellis, 2025). In the fall, she also began her MSc at the University of Alberta with a project focused on the geology and metallogeny of Oligocene–Miocene magmatic rocks in southwest Yukon and their association with porphyry system mineralization. As part of this project, Ellis completed her field season in June–July 2025 in collaboration with Project Geologist Rosie Cobbett, and will continue with another field season in 2026.

Before joining YGS, Alex Brubacher worked for Newmont Corporation at the Coffee Gold project, now owned by Fuerte Metals Corporation. In collaboration with project staff, Brubacher co-authored Open Files 2025-5 and 2025-6, which are a property-scale geology map and an accompanying report describing the geology and gold mineralization (Kitchen et al., 2025a,b). During the field season, Brubacher spent two weeks visiting various exploration sites, collecting samples for ongoing Minerals unit research, and tracking exploration activities to contribute to the annual hardrock overview (Skerget and Naber, this volume). In September he spent two weeks logging representative fences at the Revenue deposit, and collecting short wave infrared spectroscopy alteration data to complement the Geological Survey of Canada's (GSC) full tensor mag survey of the deposit completed in October 2024.

Skarn deposits at Mactung and Whitehorse Copper received a lot of attention in the Yukon in 2025, which aligns with Tiera Naber's project to develop a Yukon skarn atlas. In the summer, she conducted 13 property visits across central and eastern Yukon where she liaised with prospectors and exploration geologists, and collected samples from several skarn and porphyry systems associated with tungsten, tin and gold mineralization. In the spring, Naber visited three communities with Amanda O'Connor, from YGS's outreach geology team, to teach elementary students about geoscience. At the Yukon Geoscience Forum in November, Naber pressented the annual Yukon hardrock mining and exploration overview (Skerget and Naber, this volume).

The Minerals unit manages important spatial databases that contain minerals-related data, including MINFILE (mineral occurrence data), GARDEd (surficial geochemical data from assessment reports), and Drill Core (drill core data). Mineral occurrence data are key inputs into mineral potential mapping. In 2025, the inaugural physical rock properties database was released. The dataset contains magnetic susceptibility and/or specific gravity measurements for more than 5800 samples across the Yukon along with their associated locations, lithology and map unit. Following the release, data was collected from an additional 480 samples to be included in a future update. Also ongoing is a YGS-British Columbia Geological Survey (BCGS) project to scan and digitize data from historical assessment reports containing critical minerals data. This Cordillera-wide project is being funded by the GSC through their Critical Minerals and Geoscience Data (CMGD) program. The Yukon's share of the funding ($250 000 over three years) is being used to convert scanned geochemical data from assessment reports into a digital format and capture it in the GARDEd database.

Mineral industry liaison

The big drivers behind spending by the Yukon mineral industry in 2025 were the high price of gold and the demand for critical minerals. Despite there being no hardrock gold production in the Yukon in 2025 to take advantage of the gold price, half of the estimated $200 million in exploration expenditures by 51 explorers across 77 projects were directed at hardrock gold projects. Demand for the critical metals copper, zinc (lead is reported with zinc even though it is not considered a critical mineral) and tungsten accounted for nearly 43% of remaining exploration expenditures, and silver covered the remaining 7%. Silver is also the lone bright spot on the Yukon's mining horizon with Hecla Mining Company's Keno Hill silver project being the only producing hardrock mine in the territory with an estimated production revenue for 2025 of $158 million from ~3 Moz silver. Geologists from the Minerals unit visit dozens of hardrock exploration properties to track exploration progress over the field season and to better understand the health of the industry in any given year. Highlights of the 2025 hardrock exploration season are presented in this volume (Skerget and Naber, this volume).

Placer Geology Technician Sydney van Loon, with YGS's Surficial unit, is YG's main point of contact with the placer industry as evidenced by her 90 placer operation site visits over 60 field days in summer 2025. During van Loon's visits to operations in the Yukon's eleven placer mining areas, she recorded observations of the equipment, mining process and geology. Prior to kicking off the 2025 field season, she published the 2021–2023 Yukon placer mining industry report (van Loon, 2025) and began compiling data for the 2024–2026 edition. van Loon co-hosted a public family event at the Dawson City Museum during Gold Show with YGS outreach staff in May, including a panning station for kids using local gold donated by placer miner Adrian Hollis (Fig. 5). After the mining season ended, she organized and hosted the annual Yukon Placer Forum in November, which attracted around 100 attendees. She also delivered the 2025 Yukon placer industry overview at Yukon Geoscience Forum, supported by a poster, and prepared the Yukon placer mining 2025 development and exploration overview in this issue (van Loon, this volume).



Figure 5. *To support YGS outreach activities during Gold Show, placer miner Adrian Hollis donated gold that YGS geologists mixed with Dawson City road gravel for kids to pan.*

Unlike hardrock, the gold price has catapulted the placer industry into its highest production year since 1997. By November, reported placer gold production was at 104 367 crude ounces. In 2025, the Yukon generated C$400 million in placer gold revenue with an average gold price of C$4811 per ounce. Going into the 2025 season at Gold Show in Dawson City, placer operators and supporting industries continued with their appeal to government to develop solutions to the permitting backlog that resulted from numerous ten-year water licences coming up for renewal. After Gold Show in May, many projects that were seeking approvals for previously approved work were issued temporary licence extensions to enable them to operate in summer 2025. Though not a perfect solution, these actions by YG seemed to have contributed to a Yukon Placer Forum in November where participants could focus more on solving technical challenges of placer mining, rather than discussing permitting challenges; a C$400 million season eases the pain too. A prosperous industry also enables groups like the Klondike Placer Miners Association to contribute $500 000 to ensure ongoing support of food programs at Dawson City schools. A truly commendable act of community support.

Yukon Mineral Exploration Program highlights

The YMEP provides partial risk capital to locate, explore and develop mineral projects to an advanced exploration stage. The hardrock Grassroots Module allocates up to $25 000 per project and does not require matching or leveraged funds. Up to $50 000 per project is available through the Target Evaluation Module and $40 000 through the Placer Module, both of which require leveraged funds. For the 2025 exploration season, the program had $1.4 million available and received 67 applications (40 hardrock and 27 placer). Funding was approved for 39 projects (20 hardrock and 19 placer). It is anticipated that the YMEP contributions will leverage an additional $2.4 million in private sector spending.

To stimulate investment in critical minerals in the Yukon, the YMEP evaluation criteria were recently updated to include extra weighting for projects that primarily target critical minerals. In response to concerns regarding YG First Nation consultation obligations, reimbursements were not available for claim staking or for work conducted off claim. More detailed summaries of YMEP highlights are presented in the hardrock and placer exploration overview papers in this volume (Skerget and Naber; and van Loon, respectively).

Geohazards and surficial geology studies

Staff with the Surficial unit conduct research on Yukon's changing landscapes and they regularly receive reports and inquiries from members of the public who observe rapid changes associated with slope instabilities (Fig. 6). Derek Cronmiller, head of the Surficial unit, advanced his study of permafrost landslides in the Klondike, completing two weeks of fieldwork and is now finalizing results of the study as it nears completion. He tested new geochronological approaches using cosmogenic ^{81}Kr to date sediments up to a few million years old at a pilot study at Silver Creek with Brent Ward of Simon Fraser University. Cronmiller also collaborated with Yukon University to develop the Klondike module for their Virtual Geology project giving an overview of Beringian geology, placer mining and permafrost hazards. He supported paleontological researchers studying Quaternary mammal evolution by helping interpret and date fossil-bearing sediments exposed along riverbanks in the Old Crow Basin. He also accompanied other members of the YGS team for several field campaigns, helping newer staff familiarize themselves with field techniques and logistics.

In 2025, YGS's Surficial unit hired a new project geologist, Theron Finley, who started in August. Finley



Figure 6. *Aerial photo of the May 2025 Burma Road landslide located on the east bank of the Yukon River; view is to the north. The landslide is 950 m long, up to 250 m wide and approximately 20 ha. This landslide is one of several that have been featured on 'The Landslide Blog' through guest posts authored by the YGS (https://eos.org/thelandslideblog/yukon-river-1).*

participated in a range of surficial geology fieldwork, including placer visits, landslide monitoring, glacial-limit mapping and regional mapping in the Tombstone Range. He led a paleoseismic trench investigation on the Tintina fault to establish the timing and frequency of past earthquakes and worked toward publishing manuscripts on the Eastern Denali fault and the Rocky Mountain–Tintina fault system. Finley also launched a new collaboration with Dr. Tiegan Hobbs of the GSC on seismic hazard and risk modelling for the Tintina fault and began planning a multi-year surficial mapping, geochronology, and landslide research program in the Tintina Trench/Clear Creek region.

Panya Lipovsky's fieldwork this year largely focused on the Tombstone Territorial Park and the Ogilvie Mountains, where she spent two weeks improving surficial geology and geohazard mapping, better constraining glacial limits and chronology in the area as well as contributing to the Tombstone Territorial Park Weekend on the Rocks outreach event. She is currently finalizing a landscape hazard susceptibility map for the Haines Junction area, which integrates landslide, permafrost and hydrological hazards. She is also providing support for Whitehorse area groundwater investigations led by YG's Water Resources branch and Yukon University.

Lipovsky helped facilitate several academic research studies related to landslides in southwest Yukon. She and Cronmiller visited the unique Mount Martha Black frozen slope creep-debris avalanche in Kluane National Park in collaboration with Carleton University researchers, and Lipovsky presented some of their results at the GeoManitoba conference in Winnipeg. She also supported a team from the University of Montreal who tested an automated drone docking system at the Miles Ridge landslide near the White River bridge (Stix et al., this volume) and performed drone-based monitoring of Alaska Highway deformation near Beaver Creek. Additionally, Lipovsky supported Simon Fraser University researchers, Catalina Pino-Rivas and Sergio Sepulveda, who are investigating potential earthquake-induced landslides at the Sheep Mountain landslide and the Aishihik landslide near Canyon.

Emilie Stewart-Jones continued to develop an integrated geodatabase combining the highway geohazard inventory, inspections data, and existing highway permafrost feature mapping. She enabled offline data collection and automated syncing for the 2025 field season. She mapped 831 new geohazards (934 including late-2024 work) across Yukon highways using reports, satellite imagery, lidar mapping, field inspections and maintenance staff input. She completed inspections along major routes including most of the Alaska, South Klondike, Dempster, North Canol, and part of the North Klondike highways, while coordinating closely with highway foremen (Stewart-Jones and Painter, this volume). Together with colleagues, she completed feature mapping for several highway corridors, expanding the total mapped features to 3092. Stewart-Jones also completed a detailed assessment of rockfall hazards in Rabbit's Foot Canyon (Whitehorse) for HPW.

Moya Painter, YGS's permafrost geologist, completed permafrost feature mapping on the Alaska Highway and North Klondike Highway, and jointly mapped the Dempster and North Canol highway corridors with Emilie Stewart-Jones. She installed new permafrost monitoring equipment in the Macpass region and drilled multiple new boreholes at key locations including Two-Mile Hill (Whitehorse), Tombstone Territorial Park, and sites along the Dempster and North Canol highways. Painter collected data from 38 YGS ground-temperature monitoring stations and updated temperature and geotechnical records through October 2024. She also conducted a 10-year hazard-map review in Old Crow, acquiring new lidar to assess landscape change since 2016, and carried out field checks of permafrost features and geohazards in the North Canol and Macpass areas.

Bedrock mapping

The biggest change to the Bedrock unit was the July retirement of long-time Head of Bedrock and Cordilleran tectonics expert Maurice Colpron. The team has lost an exceptional leader, but they still have access to his expertise and mentorship as a YGS Emeritus Scientist. Emeritus status enables Colpron to continue working on geoscience projects that he is passionate about and allow him to continue to contribute to the YGS. An example of Colpron's continued participation in YGS activities was his involvement with the Bedrock and Minerals units organization and delivery of a one day short course at the Yukon Geoscience Forum on the geological and metallogenic framework of the Yukon. In addition to his co-authorship of two geothermal open files, Colpron was the lead author on Open File 2025-4 which included new geochronological and geochemical data for Permian rocks of the western Yukon-Tanana terrane (Colpron et al., 2025b), and on Open File 2025-10, the updated Yukon Bedrock Geology Map (Colpron, et al., 2025a). It is anticipated that a new head of the bedrock unit will be hired in early 2026.

Even without a unit head, the four bedrock mappers in the unit proceeded with their multi-year efforts to better resolve ongoing questions about the amalgamation of Yukon's terranes and implications for natural resource assessment. For instance, this summer, Senior Bedrock Geologist David Moynihan mapped areas of the southern Englishmans Range to revise the decades-old mapping. Moynihan selected areas near Dorsey Lake, focusing on documenting the stratigraphy of the Klinkit Group, establishing the distribution of Permian volcanic rocks (Butsih Formation) and identifying previously unrecognized major structural boundaries within this part of Yukon-Tanana terrane (Fig. 7). Geochemical and geochronological investigations in support of the mapping are underway, including conodont microfossil analysis at GSC laboratories. The area around the Seagull and Hake batholiths contains abundant tin and tungsten skarn mineralization, and Economic Geologist Tiera Naber joined the fieldwork to investigate occurrences in and around the JC tin prospect. Moynihan plans to continue with his mapping and metallogenic studies in summer 2026.

It was a big year for Rosie Cobbett who completed her PhD at Memorial University researching the magmatic and tectonic record of Cambrian–Ordovician rift history of the Laurentian margin of western North America. Read more about Cobbett's findings in YGS' first open file of 2025 (Open File 2025-1; Cobbett et al., 2025). Achieving this milestone allowed her the space and time to conduct some alternate geological activities such as collaborating with CAFN to investigate the geology around the historic Johobo mine in Kluane National Park to better understand the contributions of bedrock geology to metal contamination in surface waters near the mine site and their impacts on Kokanee Salmon spawning. Champagne and Aishihik First Nations citizens and YGS staff formed a joint field camp in Kluane National Park where they shared land practices and each learned about what is important to CAFN Land Guardians and YGS staff alike. With Ediacaran fauna attracting more attention in north-central Yukon, Cobbett is also the YGS lead for collaborating with YG Heritage branch and the First Nation of Na-Cho Nyäk Dun (FNNND) to improve collection and storage protocols for fossils found on FNNND Traditional Territory. She also expanded into mentorship, teaching and outreach by providing cross-unit support to assist Sarah Ellis in strengthening her bedrock mapping skills as part of her MSc fieldwork. Cobbett also participated in improving the bedrock geology map of Tombstone Territorial Park to enhance communication of the park geology to the public. She also taught the 2025 fall semester of structural geology at Yukon University.

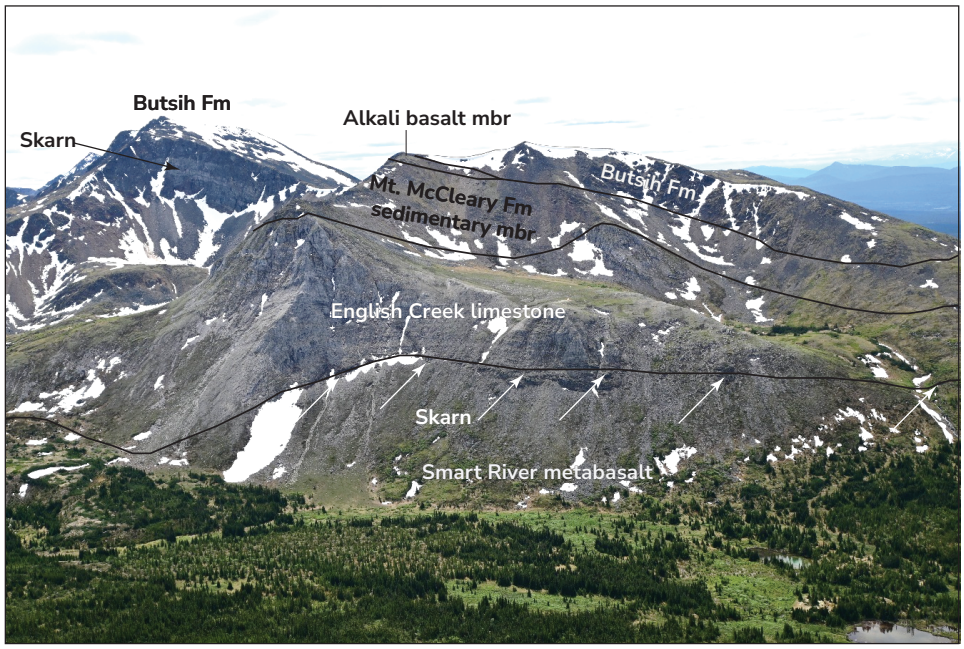


Figure 7. *View facing south along the Englishmans Range, indicating the stratigraphy in the type area of the Klinkit Group in the Yukon. Relief from valley bottom to peak is approximately 450 m.*

Sarah Schultz continued with a multi-year project studying the shale geochemistry of Late Devonian units in the Selwyn basin region. The project aims to document the evolution of deep-water depositional systems and create a sequence stratigraphic framework through an integrated sedimentological and geochemical dataset. It is exciting that a sequence stratigraphic approach, normally associated with oil and gas exploration, is being applied to metals exploration in the Yukon. Fieldwork in 2025 focused on core logging in the Howards Pass region (Schultz et al., this volume) and an initial reconnaissance trip to Nááts'įhch'oh National Park Reserve to further expand on the model that was developed in the Macmillan Pass region by

Schultz in 2024 (Schultz and Reynolds, this volume). Samples were collected at Howards Pass from the core for XRF and organic carbon isotopes through mudstone-dominated intervals of the Portrait Lake Formation. This dataset will be leveraged to facilitate regional correlations between the two lead-zinc mineralization districts to explain the distribution and extent of deposition, mineralization, and systems tract development.

Tyler Ambrose is in the process of wrapping up several projects as he prepares for a half-year sabbatical starting in spring 2026. Due to Ambrose's upcoming break, he had a much less intense field season compared to previous years and spent more time in the office working on the final report and maps for the Rackla River area, in the southern Wernecke Mountains. He has a paper in review with the GSA Bulletin that combines geochronology and mapping to constrain the Paleoproterozoic and Mesoproterozoic evolution of the Yukon. He is also working on another project involving Pb isotopes and Ag-Pb-Zn mineralization in the Ogilvie platform. Ambrose has already been thinking ahead and planning for his return when he will focus on a project in the Pelly Mountains to investigate the evolution of the Cassiar Platform. In summer 2025, he spent time engaging with Ross River Dena Council (RRDC) citizens sharing his research ideas and listening to concerns they may have. To further communicate his plans, Ambrose was joined by a young RRDC Land Guardian for a day of helicopter-supported rock sampling on ridges in his proposed field area.

Technical services

The primary means for YGS to share its products are through publications and online databases. The Technical Services unit, under the guidance of Amy Stuart since August 2024, consistently delivers high-quality digital and printed materials. Technical services are mainly delivered by Stuart and two Geological and Spatial Database Administrators, Chad Côté and Laurent Cogotti. Outreach Geologist Leyla Weston also plays a large role in editing annual publications. The unit is soon to be supported by a Publications Technician, who will begin in January 2026. Despite not having a fully staffed unit in 2025, the YGS published the 2024 Yukon Exploration and Geology (YEG), 2021-2023 Placer Industry Report, ten Open Files, and one Miscellaneous Report. Additionally, YGS authors were published in eleven peer-reviewed journals.

Considerable time was spent in 2025 performing GIS work, updating databases and performing critical system infrastructure upgrades. Coinciding with Maurice Colpron's retirement was the release of a new 2025 bedrock geology map with updated online data. New in 2025 was the release of a rock properties dataset as was discussed in the Minerals activities section of this paper. Also newly developed was an internal placer database to streamline data entry during Sydney van Loon's site visits to placer operations. This should allow for more standardized data entry and more efficient data consolidation for compiling the next placer industry report. Côté and Cogotti rebuilt YGS's web mapping applications and spatial data delivery tools in the newest technology and retired applications that had little use or irrelevant information. The primary YGS data website (https://data.geology.gov.yk.ca/) and the permafrost database are being rebuilt on this new infrastructure to make them more efficient and to have better search capabilities. To assist with more efficient budget tracking and to improve utility, a new project budget management system is being developed and will be ready for use in the new fiscal year. The Technical Services unit demonstrates that effective communication tools are just as important as fieldwork for disseminating information about rocks. Without this team, it would be difficult for the public to access and appreciate the great work being done by YGS geoscientists.

Outreach and First Nation engagement

The Technical Services unit includes two Outreach Geologists, Leyla Weston and Amanda O'Connor. Perhaps with geology in the Yukon being very prominent in our day to day lives and landscapes, it sometimes seems as though two Outreach Geologists are not enough to manage all of the engagement requests that the YGS receives from the public who want to know more about the geology around them. A large part of the outreach requests are for visits to Whitehorse area schools where our outreach team hosted four rock and mineral identification workshops, five Water Week workshops, two deep dives on mining with grade 7 students at Elijah Smith Elementary School, and three presentations on the geological framework of the Yukon, which is a newly developed module for secondary-level students.

Field-based activities for the Whitehorse public included eleven field trips to the Whitehorse copper belt, two excursions to Miles Canyon, two visits to the

Takhini retrogressive thaw flow west of Whitehorse, two rounds of the Riverdale compass course, and a stop at the clay cliffs. Other Whitehorse outreach activities include a YGS presence at the Yukon Heritage Fair, YGS's organization and the recruitment of volunteer judges for the Yukon-Stikine STEM Expo event, and activity booths at the Canada Games Centre for Mining Week and for Yukon Geoscience Forum Family Day (Fig. 8).

The YGS was also actively involved in outreach activities elsewhere in the Yukon. During Mining Week, while Weston engaged with the public in Whitehorse, O'Connor was in Teslin participating in a Land Camp with the school and meeting with Teslin Tlingit Council. She then continued east to Watson Lake for a school visit and a meeting with the Liard First Nation Lands and Resources Department. Other community outreach activities included a public hike in Kluane National Park with Parks Canada, Tombstone Territorial Park Weekend on the Rocks with Yukon Parks, and Tombstone Park interpreters pre-season glacial history and bedrock geology training. The outreach team also helped support with judging the Haines Junction Science Fair, as well as participating in the CAFN career fair. Additionally, the YGS outreach team collaborated with the Yukon Palaeontology Program in facilitating a field trip to the dinosaur trackway near Ross River with schools from Faro and Ross River. O'Connor also visited the community of Mayo to deliver hands-on geoscience activities at one of First Nation of Na-Cho Nyäk Dun's Land Camps.

In 2025, the YGS took time to reflect on their approach to First Nation engagement and to consider ways to improve this process. In February, the YGS hired IRP (Inspired Reconciliation Potential - https://www.irpotential.com/) to hold a reconciliation workshop aimed at teaching YGS staff about approaches for building trusting relationships with Yukon First Nations. The founders of IRP are Yukon First Nation women who excel at teaching individuals from government and public organizations how to consider First Nation ways of knowing, being and doing. The YGS staff have been willing to adjust their approach to geoscience work to align more with input received from First Nations upon whose Traditional Territories YGS staff wish to conduct research. With the YGS being involved in land use planning by leading mineral potential mapping, geologists are expanding their traditional roles from helping delineate natural resources, to also helping First Nations better understand the geological conditions of their lands. Going forward, the education and engagement of YGS's mineral potential mapping project will be a major focus for the YGS. The more that First Nations understand the geology around them, the more empowered they will be to participate in decision-making that affects their environment and their lives.

Knowing that First Nations have many demands on their time, the YGS and the GSC initiated a pilot project in 2023 to coordinate their engagement with First Nations governments. The intent is to reduce engagement fatigue by jointly communicating both of the surveys' proposed activities in each Yukon First Nation Traditional Territory. In addition to written letters to First Nations,

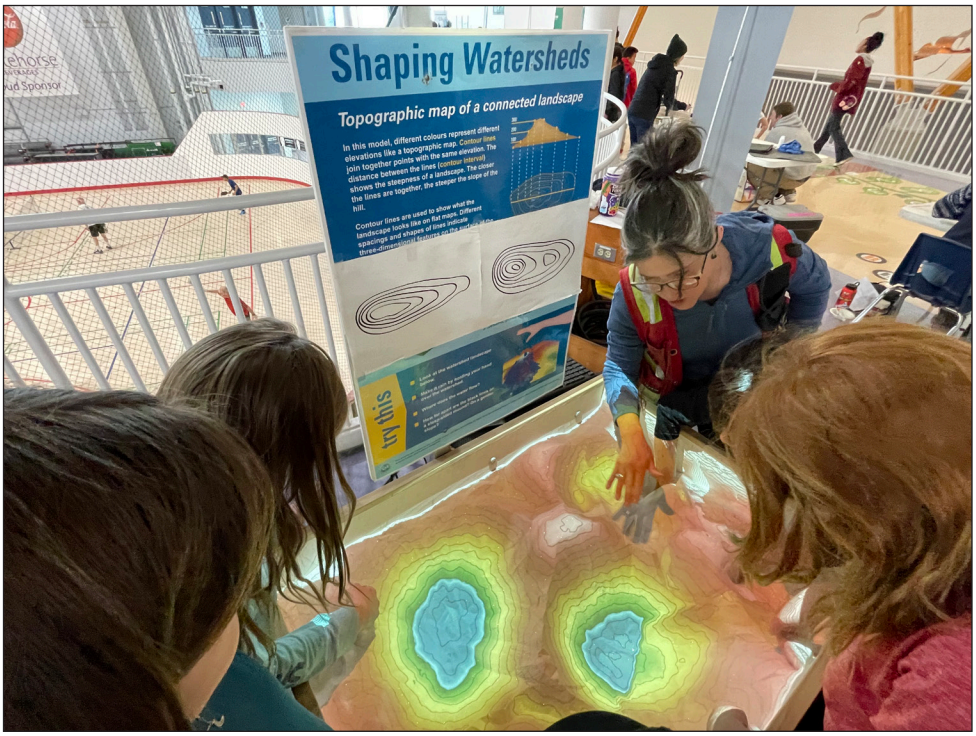


Figure 8. *Outreach Geologist Leyla Weston showing students YGS's Augmented Reality Sandbox at Yukon Chamber of Mines' Mining and Geology Week Discovery Day event in May.*

staff try to have in-person meetings before and after the field season, to share work outcomes and next steps. In conjunction with these community meetings, YGS always makes efforts to also schedule a school visit. The YGS has active projects across the Yukon and staff were able to have in-person community meetings with nearly half of the Yukon's First Nations over the past year. To further strengthen these relationships, a model of continuous communication and regular updates is being introduced to ensure First Nations are kept apprised of both immediate and long-term plans.

Summary

The YGS team carried out its 2025 program under the direction of a new branch management trio who came into their positions with no recent experience at the Yukon Geological Survey or any other geological survey. With the retirements of the long-time Director and Head of Bedrock, several decades of combined Yukon geoscience knowledge left the collective group in a three-month window. Under these conditions, it is understandable that a staff where over half of the people are new to their positions in the past three years may have been concerned about the future direction of the YGS. My hope is that this overview summary of some of our activities is proof that the YGS is as active and diverse in its geoscience knowledge and experience as it ever has been. I offer my thanks to Carolyn Relf, Maurice Colpron and the geologists who came before them and dedicated time and effort to the YGS, building the reputation that Jan, Amy and I inherited and intend to uphold.

The YGS will carry out its 2026 program under new political direction from the Yukon Party as a result of the November territorial election. The Eagle Gold Mine's future and its impact on the territory's sentiment toward mining should become clearer as the sales process evolves. Selkirk Copper Mines exploration at Minto will advance toward a 2027 production decision and the potential for a Yukon First Nation to be a significant shareholder of a producing mine on its own land. The near-term global political landscape suggests that an elevated gold price could continue and that demand will remain high for Yukon's abundance of copper, zinc, tungsten and silver. Yukon Geological Survey staff are open to growing our interests and how we direct our resources to answering Yukon's geoscience questions. The Yukon is a large territory and much of the surficial and bedrock geology has yet to be mapped, so there are boundless discoveries of scientific and economic interest that await. More critical minerals need to be found and responsibly developed. Geohazards need to be monitored and studied to reduce impacts on our lives and infrastructure. Melting permafrost is freeing sulphide minerals, and releasing metals and acid into northern Yukon waters. Land use planning is required for those areas of the Yukon where little knowledge exists of the mineral resource potential. First Nations want to know more about resources on their Traditional Territories to aid in their own decision-making. The YGS is here and ready to help overcome these challenges.

References

Afolabi, D., Gilbert, H., Gosselin, J. and Dettmer, J., 2026 *(this volume)*. A preliminary HVSR investigation of the shallow structure of the Teslin fault, southern Yukon. *In:* Yukon Exploration and Geology 2025, A. Stuart, L.H. Weston and S.K. Schultz (eds.), Yukon Geological Survey, Government of Yukon, p. 75–89.

Byer, J.F., Gosselin, J.M., Dettmer, J. and Gilbert, H., 2026 *(this volume)*. Preliminary investigation of seismic site conditions in Whitehorse (Kwänlin), Yukon, from passive seismic methods. *In:* Yukon Exploration and Geology 2025, A. Stuart, L.H. Weston and S.K. Schultz (eds.), Yukon Geological Survey, Government of Yukon, p. 119–130.

Cobbett, R.N., Beranek, L.P., Colpron, M., Piercey, S.J., Crowley, J.L., Strauss, J.V. and Taylor, J.F., 2025. Geochemistry and geochronology of Cambrian and Upper Ordovician mafic igneous rocks along the Dawson fault zone, Yukon. Yukon Geological Survey, Government of Yukon, Open File 2025-1, 42 p. plus appendices.

Colpron, M., Ambrose, T., Cobbett, R. and Moynihan, D. (compilers), 2025a. Yukon Bedrock Geology Map. Yukon Geological Survey, Government of Yukon, Open File 2025-10, 1:1 000 000 scale map and legend.

Colpron, M., McClelland, W.C., Piercey, S.J., Kroeger, E.D.L., Crowley, J.L. and Gehrels, G.E., 2025b. New geochronological and geochemical data for Permian rocks of the western Yukon-Tanana terrane, Klondike district, Yukon. Yukon Geological Survey, Government of Yukon, Open File 2025-4, 35 p. plus appendices.

Ellis, S.H.M., 2025. Preliminary observations from four reduced intrusion-related gold deposits, Selwyn basin, Yukon. Yukon Geological Survey, Government of Yukon, Open File 2025-3, 46 p. plus appendices.

Finley, T., Gosselin, J.M., Biegel, K.M., Lipovsky, P.S., Cronmiller, D.C., Schaeffer, A.J. and Dettmer, J., 2026 (*this volume*). The December 6, 2025 M_w 7.0 earthquake in Yukon, Canada: Tectonic significance and observations of ground failure. *In:* Yukon Exploration and Geology 2025, A. Stuart, L.H. Weston and S.K. Schultz (eds.), Yukon Geological Survey, Government of Yukon, p. 131–148.

Israel, S., Murphy, D., Sack, P.J. and Crowley, J.L., 2025. U-Pb zircon geochronological data for Paleocene to Eocene magmatic rocks in southwest Yukon. Yukon Geological Survey, Government of Yukon, Open File 2025-9, 36 p. plus digital appendices.

Kitchen, J.G., Brubacher, A.D., Essman, J., Valli, F., Johansson, P., Kocay, B., Crowley, J.L. and Larson, K.P., 2025a. Geology and bedrock mapping updates at the Coffee Project gold deposit: implications for deposit classification. Yukon Geological Survey, Government of Yukon, Open File 2025-6, 50 p. plus appendices.

Kitchen, J.G., Essman, J.E., Brubacher, A.D. and Johansson, P., 2025b. Bedrock geology map of the Coffee Project, Dawson Range, Yukon (parts of NTS 115J/13, 14 and 15). Yukon Geological Survey, Government of Yukon, Open File 2025-5, scale 1:50 000.

Relf, C., 2025. Yukon Geological Survey 2024 overview. *In:* Yukon Exploration and Geology Overview 2024, L.H. Weston, A. Stuart, S.K. Schultz, A.D. Brubacher and D.C. Cronmiller (eds.), Yukon Geological Survey, Government of Yukon, p. 1–20.

Schultz, S.K., Catuneanu, O. and Gordon, J.B., 2026 (*this volume*). Preliminary analysis of the sequence stratigraphy and geochemistry of the Portrait Lake Formation at Macmillan Pass, Yukon, Canada. *In:* Yukon Exploration and Geology 2025, A. Stuart, L.H. Weston and S.K. Schultz (eds.), Yukon Geological Survey, Government of Yukon, p. 167–190, plus digital appendix.

Schultz, S.K. and Reynolds, M.A., 2026 (*this volume*). Ordovician to Devonian stratigraphy of Nááts'įhch'oh National Park Reserve, Northwest Territories. *In:* Yukon Exploration and Geology 2025, A. Stuart, L.H. Weston and S.K. Schultz (eds.), Yukon Geological Survey, Government of Yukon, p. 191–205.

Skerget, S.W. and Naber, T.V., 2026 (*this volume*). Yukon hardrock mining, development and exploration overview, 2025. *In:* Yukon Exploration and Geology Overview 2025, A. Stuart, L.H. Weston and S.K. Schultz (eds.), Yukon Geological Survey, Government of Yukon, p. 39–74.

Smith, M. and Konrad, J.M., 2025. Victoria Gold Corp. Eagle Gold Mine June 2024 Heap Leach Failure. Independent Review Board (compilers). Submitted June 30, 2025, 141 p. plus appendices, https://www.pwc.com/ca/en/car/victoria-gold/assets/victoria-gold-117_020725.pdf.

Sternbergh, S. and Colpron, M., 2025. Summary of geothermal indicators in the Yukon. Yukon Geological Survey, Government of Yukon, Open File 2025-7, 92 p. plus appendices.

Stewart-Jones, E. and Painter, M., 2026 (*this volume*). Mapping geohazards to support climate adaptation on Yukon's transportation network. *In:* Yukon Exploration and Geology 2025, A. Stuart, L.H. Weston and S.K. Schultz (eds.), Yukon Geological Survey, Government of Yukon, p. 207–219.

Stix, J., Roman, J., Kalacska, M., Lucanus, O., Lipovsky, P. and Arroyo-Mora, P., 2026 (*this volume*). Assessing Miles Ridge landslide activity using an integrated ground-RPAS-satellite approach. *In:* Yukon Exploration and Geology Overview 2025, A. Stuart, L.H. Weston and S.K. Schultz (eds.), Yukon Geological Survey, Government of Yukon, p. 221–237.

van Loon, S., 2025. Yukon Placer Mining Industry 2021 to 2023. Yukon Geological Survey, Government of Yukon, 269 p.

van Loon, S., 2026 *(this volume)*. Yukon placer mining development and exploration overview, 2025. *In:* Yukon Exploration and Geology Overview 2025, A. Stuart, L.H. Weston and S.K. Schultz (eds.), Yukon Geological Survey, Government of Yukon, p. 19–38.

Witter, J.B., 2025. Analysis of geoscience data for geothermal exploration in the Whitehorse area, Yukon. Yukon Geological Survey, Government of Yukon, Open File 2025-8, 53 p. plus appendices.

Yukon placer mining development and exploration overview, 2025

*Sydney van Loon**
Yukon Geological Survey

van Loon, S., 2026. Yukon placer mining development and exploration overview, 2025. *In*: Yukon Exploration and Geology, 2025, A. Stuart, L.H. Weston and S.K. Schultz (eds.), Yukon Geological Survey, Government of Yukon, p. 19–38.

Introduction

Placer mining in the Yukon for the 2025 season reported the highest crude gold total in 28 years, exceeding the last record high reported in 1997 (116 383 crude ounces). From April 1 to November 1, 2025, reported placer gold production totalled 104 367 crude ounces, ranking 11th highest in the past 50 years. A total of 165 placer operations contributed to production, a slight increase from 156 in 2024, reflecting expanded activity and leasing by established operators rather than new entrants. The Dawson Mining District continued to host the majority of operations (68%), followed by the Whitehorse Mining District (18%) and the Mayo Mining District (14%). Elevated gold prices were the primary economic driver in 2025, which averaged C$4811 per ounce (US$3476/oz) over the reporting period, and reached a record high of C$6114 per ounce on October 20, 2025. Using a gold price averaged over the entire season, reported production represents an estimated C$401 million in placer gold revenue, highlighting the industry's continued economic importance to the Yukon.

Climate for mining

Winter began early in October 2024, bringing widespread snowfall across central and southwestern Yukon. From October 2024 to March 2025, temperatures were near to slightly below seasonal averages and precipitation ranged from 75 to 150% of normal (Government of Yukon, 2025a). Snowfall was above average in parts of central and northern Yukon, including Dawson and Old Crow, resulting in a substantial late-season snowpack.

Spring was slow to arrive in April, when daily maximums in Dawson averaged 8°C and the mean temperature was 1.5°C. Overnight freezing persisted throughout most of the month, delaying ground thaw and early start-up at some Dawson-area operations (Government of Yukon, 2025b). By May, daytime highs averaged 15°C and stable conditions allowed sluicing to begin by mid-month (Government of Yukon, 2025c).

Summer weather was favourable across most of the territory. Temperatures in July and August were warmer than normal throughout the Yukon, and Dawson, Mayo and Whitehorse all recorded above-average mean temperatures. September remained notably warm across most of the Yukon, reporting mean monthly temperatures ranging from 8°C at Burwash Landing to 10.4°C at Whitehorse, approximately 1 to 3°C above normal. Precipitation varied from 32% of normal at Whitehorse to over 130% at Burwash Landing and Dawson. In October, mean temperatures remained warmer than normal across most communities, ranging from 0.1°C at Burwash Landing to 3°C in Whitehorse, representing anomalies of 1.2 to 3.5°C above normal. Precipitation was generally below normal at Whitehorse (40% of normal) and Mayo (69% of normal), whereas Dawson recorded 194% of normal precipitation, marking a notably wetter month in central Yukon (G. Bramwell, pers. comm., 2025). Mild conditions persisted into the fall across much of the territory, which extended the mining season in most placer mining areas and supported the ability for some operations to sluice into early November.

* sydney.vanloon@yukon.ca

Gold production summary

The 2025 season marked a significant year for the Yukon placer industry resulting in a reported gold production from April 1 to November 1, 2025 of 104 367 crude ounces. This is the highest reported placer gold production since 1997, reflecting strong industry performance despite a year characterized by elevated operating costs and shifting regulatory and labour conditions. Favourable spring conditions and an extended fall sluicing window further contributed to elevated production across most placer mining areas. The total placer production revenue from April 1 to November 1, 2025, amounted to C$401 million with an average gold price of C$4811 per ounce (Fig. 1).

The Yukon is divided into eleven placer mining areas: 1. Bonanza-Hunker; 2. Dominion-Sulphur, Indian River; 3. South Klondike; 4. Fortymile, Sixty Mile, Moosehorn; 5. Clear Creek-McQuesten; 6. Mayo, Keno; 7. Big Creek, Nansen, Hayes-Canadian; 8. Livingstone; 9. Kluane, Ruby Range, Kimberley; 10. Nisutlin-Pelly, Whitehorse South; and 11. Watson, Hyland (Fig. 2). In 2025, the five leading placer mining areas were Dominion-Sulphur, Indian River (57 391 crude ounces), Fortymile, Sixty Mile, Moosehorn (14 003 crude ounces), Bonanza-Hunker (11 561 crude ounces), South Klondike (10 047 crude ounces), and Mayo-Keno (5114 crude ounces). Dominion-Sulphur, Indian River accounted for 55.0% of the total Yukon placer gold production, followed by Fortymile, Sixty Mile, Moosehorn at 13.4% and Bonanza-Hunker producing 11.1% (Fig. 3).

The number of active operations remained relatively consistent, increasing slightly from 156 in 2024 to 165 in 2025. Of these, 68% were in the Dawson Mining District, 18% in the Whitehorse Mining District, and 14% in the Mayo Mining District. The increase does not reflect new mining areas or an influx of new operators; instead, it is largely attributed to expansions by established operations and, in several cases, next-generation miners initiating activity on existing ground.

Development highlights

Bonanza-Hunker placer mining area

Placer gold production in the Bonanza-Hunker placer mining area totalled 11 561 crude ounces in 2025, a 31% decrease from 16 764 crude ounces in 2024. The main contributors in 2025 were Bonanza Creek

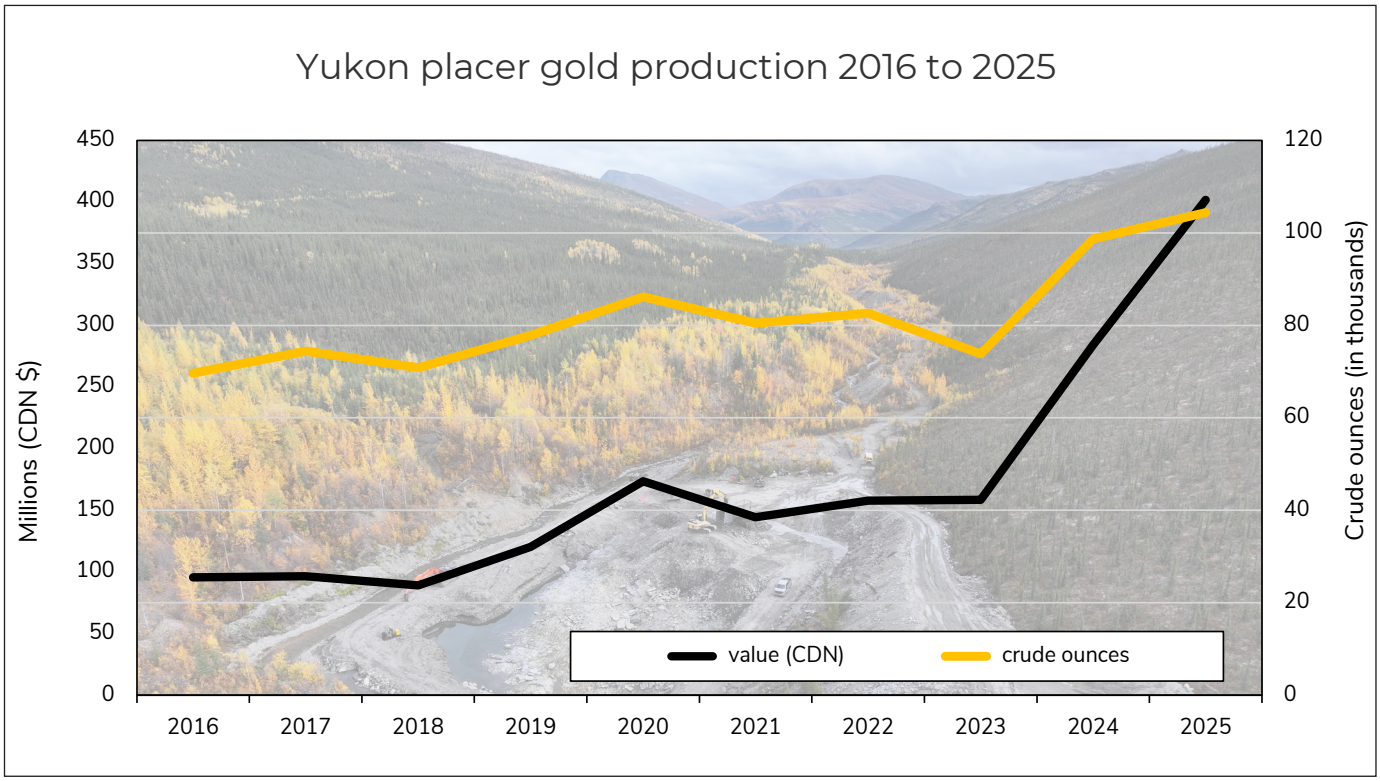


Figure 1. *Yukon placer gold production in Canadian dollars over the past ten years including most recent production from April 1 to November 1, 2025. The chart displays crude ounces produced and the total value.*

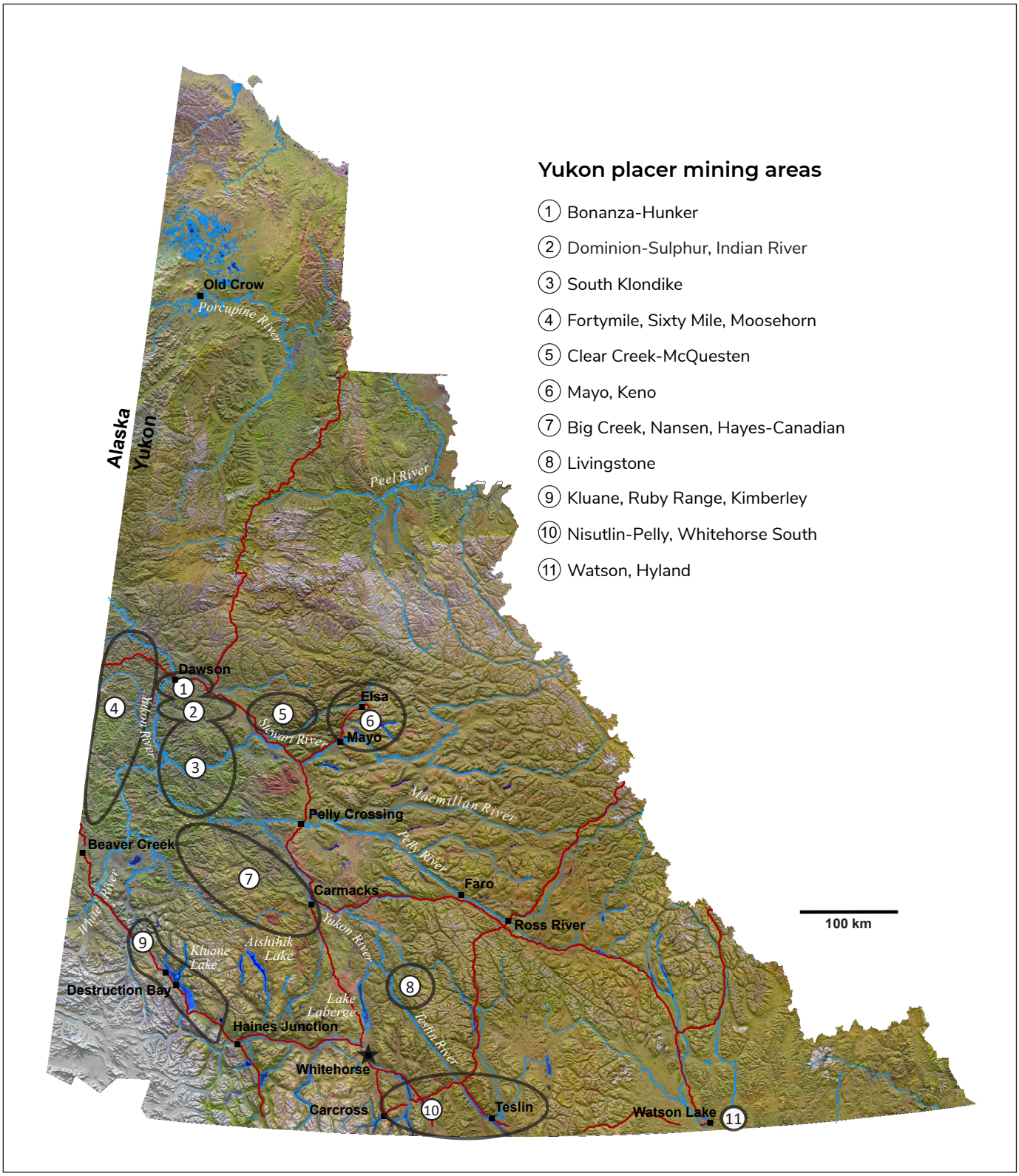


Figure 2. *Placer-mining areas of the Yukon.*

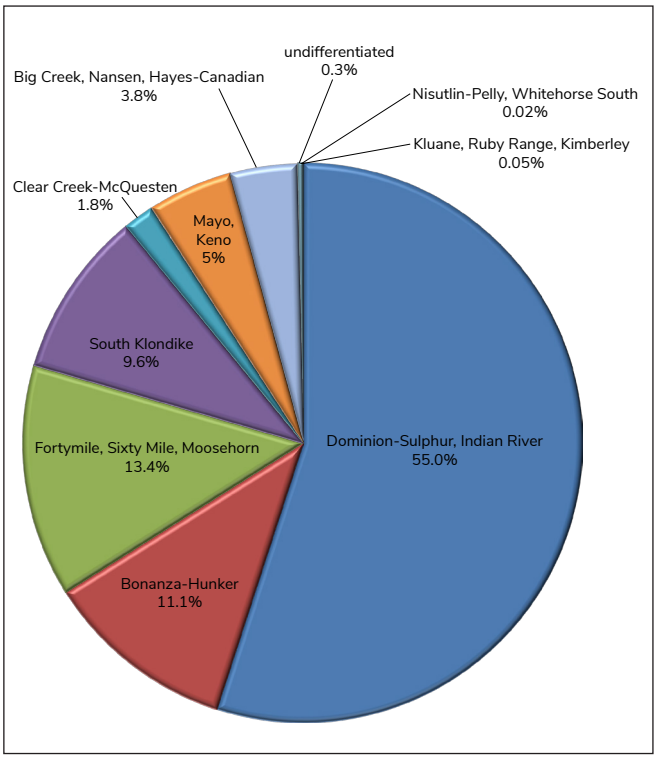


Figure 3. *Distribution of placer gold production by placer mining area, based on royalties reported from April 1 to November 1, 2025.*

(7358 crude ounces), Hunker Creek (2065 crude ounces), Hattie Gulch (648 crude ounces), Last Chance Creek (618 crude ounces), and Adams Creek (337 crude ounces; Fig. 4).

In spring 2025, Rodal Placers sold their property on Eldorado Creek, located upstream from the confluence with Glacier Gulch, to Le Fevre and Company Property Agents Ltd. The new operator ran a small, two to three-person crew and undertook an exploration-focused season supported by the Yukon Mineral Exploration Program (YMEP). The project targeted two primary areas: potential side pay on the left limit buried beneath a colluvial apron, and a large rockslide on the right limit that fans into the Eldorado Creek valley. Thirty-five sonic drill holes totaling 229 m (750 ft), along with three test pits, were completed to assess these two areas (Fig. 5). Pay gravel was confirmed beneath the slide, and evidence of old-timer workings was observed in the deposit, which led to focussing mining efforts along the toe of the fan to evaluate the thickness and lateral extent of the paleo-Eldorado Creek floodplain into the right limit.

FellHawk Enterprises Ltd. continued leasing ground on Bonanza Creek from R. Berglund and D. Trudeau for a fifth consecutive season, having initiated work on the property in 2021. All mining activity was focused on the left limit of Bonanza Creek, using a crew of up to six people. The company completed sonic drilling to evaluate the potential for remnant in-situ Bonanza Creek gravel that may have been missed by historical dredging due to its proximity to the valley wall, as well as side pay buried beneath hydraulic tailings. Drilling results confirmed the presence of in-situ pay extending beneath the Bonanza Creek road. As a result, the focus of the 2025 season was to relocate the road and progressively mine upstream along the left limit.

In February 2024, Northern Shoveler Resources Ltd. purchased three claims on Hunker Creek from M. Wierda. The claims are located between Hester and Independence creeks and were formerly part of a larger block of claims held by the late D. Gould. The ground was previously dredged, but the company is evaluating remnant in-situ gravel preserved on bedrock beneath tailings. In August, the operation moved to a new property in the Mayo Mining District.

H3 Mining Corporation continued mining on Hattie Gulch throughout the 2025 season, following their acquisition of the property in 2024. A 20-person crew focused on the concurrent development of cuts on both the left and right limits of Hattie Gulch, situated on top of Australia Hill. Mining targeted the lowermost 9 m (30 ft) of White Channel gravel directly overlying bedrock. Crews alternated between the two limits, stripping and sluicing simultaneously, as they waited for thaw to progress. The stratigraphy on the left limit consists of 20 m (66 ft) of lower White Channel gravel overlain by 21 m (70 ft) of upper White Channel gravel. This season, H3 Mining Corporation received YMEP funding to support a drilling campaign on both limits of Hattie Gulch. The program successfully delineated the lateral extent of pay as the company continues to mine into the slope on both sides of the gulch.

Jerusalem Mining began work on Too Much Gold Creek in 2025, after optioning the ground from the Too Much Gold ownership group (Fig. 6). The left-limit tributary of the Klondike River is situated immediately downstream from Allgold Creek. Extensive exploration has occurred in the drainage, including hand shafting and drilling; furthermore, operators have received YMEP funding to support various programs over the years. A seven-person crew was active throughout the 2025 season, completing a cut 366 m (1200 ft) long, averaging 36 m (120 ft) wide, and 3.7 m (12 ft) deep. In the valley

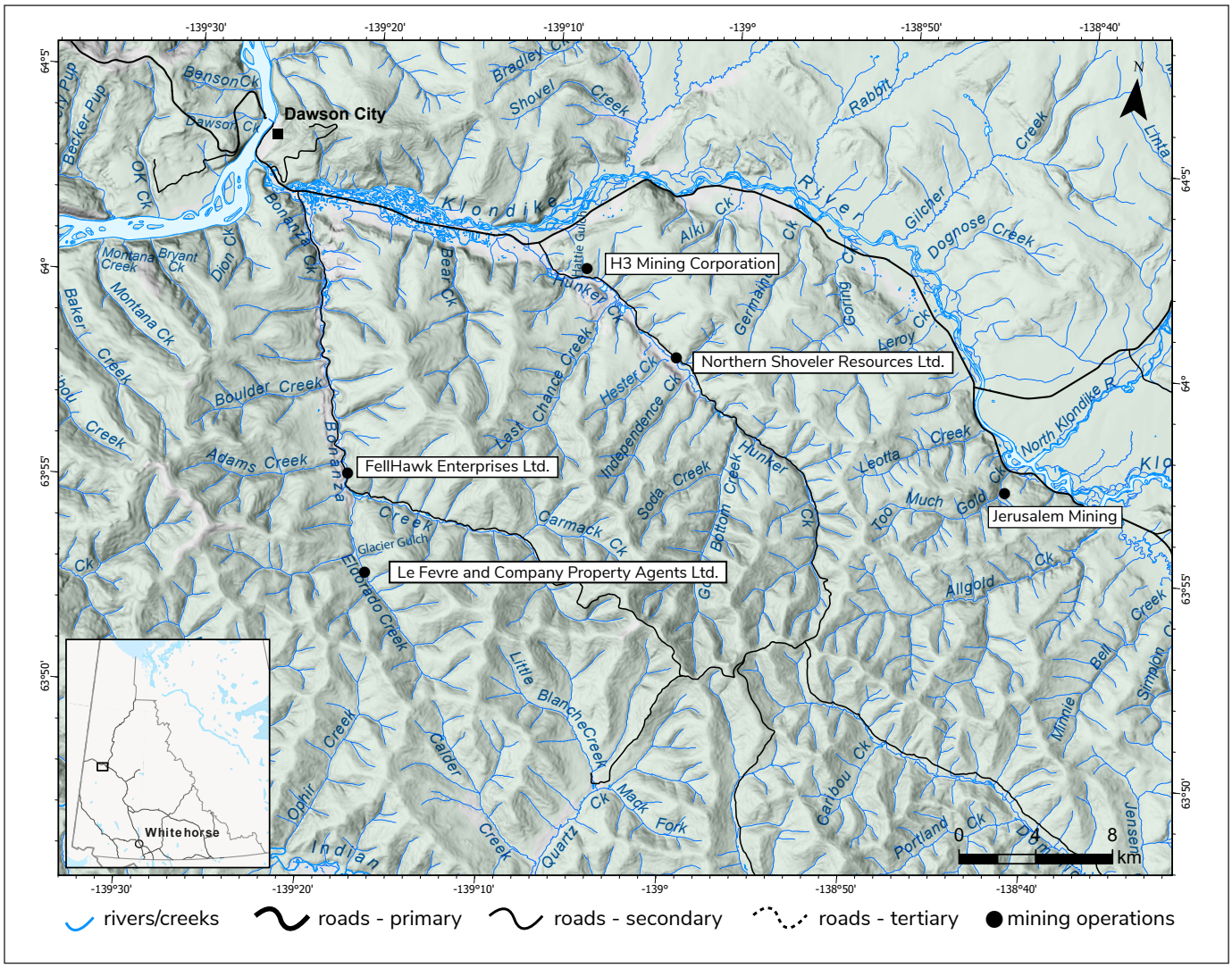


Figure 4. *Locations of highlighted placer operations in the Bonanza-Hunker placer mining area.*



Figure 5. *Le Fevre and Company Property Agents Ltd. completed 35 sonic drill holes on Eldorado Creek in June 2025 through the YMEP program. The drill rig is shown on the left limit of the creek (right side of image). The view is looking upstream.*

bottom, an observed section measured 3.4 m (11 ft) in total thickness to bedrock, and depth increased at the base of the slope where a colluvium apron thickened. The pay unit is a compact, poorly sorted, matrix-supported gravel containing subrounded clasts. A high-energy depositional setting was interpreted due the presence of weathered bedrock fragments in the lowermost 0.6 m (2 ft) of the gravel. The recovered gold is predominantly fine grained and has a fineness of 82%.

Dominion-Sulphur, Indian River placer mining area

The Dominion-Sulphur, Indian River placer mining area remained the top producer in 2025, reporting 57 391 crude ounces, a 24% increase from 46 217 crude ounces in 2024. The area continued as the leading contributor to Yukon placer gold production, accounting for 55.0% of the territory's total reported ounces. The top producing drainages in 2025 were Indian River (17 409 crude ounces), Dominion Creek (16 896 crude ounces), Sulphur Creek (7562 crude ounces), Eureka Creek (7416 crude ounces), and Montana Creek (3163 crude ounces; Fig. 7).

Armstrong Mining commenced their first season of mining in 2025, operating on a large claim block leased from Klondike Gold Corp. The 239 placer claim block is situated in the Indian River valley, encompassing the mouth of Montana Creek and extending downstream. The claims had not been extensively mined since 316 Mining was active in 2015. The operation employed a nine-person crew and had an ambitious first year completing seven cuts by July without conducting pre-season stripping (Fig. 8). They quickly caught up, using two Komatsu 475 bulldozers in tandem to strip muck and a sandy, pebble gravel. Cuts ranged from 6 to 9 m (20–30 ft) in total thickness, and sluicing targeted the lowermost 3 m (10 ft), which included auriferous gravel and several feet of bedrock. Material was processed at a rate of 115 m³ (150 yd³)/hr using a Macon T600 trommel.

The company 16406 Yukon Inc. holds a large claim block that covers an area on mid-Montana Creek and continues up Steele Creek, a right-limit tributary of Montana Creek. Significant exploration began in 2023, including an extensive sonic drill program. Results from the drilling guided mining in 2024 and 2025, and efforts focused on the left limit of the modern Montana Creek valley, along the rim of a low-level bench that extends the length of the drainage into the Indian River valley. A five-person crew mined an average of 1.2 m



Figure 6. *Jerusalem Mining's sluicing operation on Too Much Gold Creek in 2025. The view is looking upstream.*

(4 ft) of pay gravel overlying bedrock that is composed of a conglomerate unit rich in quartz pebbles (mapped as the Indian River Formation). Minimal stripping was required (maximum of 3 m [10 ft]), and the material was composed of black muck and fine pebble gravel.

DK Gold Inc. continued mining on Green Gulch, a left-limit tributary of upper Sulphur Creek, focusing on two target areas during the 2025 season. DK Gold Inc. worked in collaboration with Lucky Dog Mining, employing up to eight people. On the upper part of the drainage, the crew used a single water monitor to thaw several metres of frozen black muck and massive ice in an area that had been extensively mined by old-timers. At the mouth of Green Gulch, immediately upstream from its confluence with Sulphur Creek, DK Gold identified a new target on the left limit. Initial interest in the area was piqued by the presence of an exposed historical shaft at surface; this prompted a sonic drill program in the spring of 2025. They stripped a cut 84 by 98 m (275 × 320 ft) on the left limit of lower Green Gluch and completed sluicing 3/4 of the cut. Figure 9 displays some of the coarse gold recovered in the lowermost cut, including a 28 g (1 oz) nugget.

In 2025, L. Humrickhouse returned for a second season leasing ground from R. Stuart on Caribou and Dominion creeks. In 2024, mining was focused on Caribou Creek; the operation shifted into the Dominion Creek valley for the 2025 season. A five-person crew investigated in-situ gravel that was believed to occur beyond the historical dredge limit, which led to the discovery of a mid-level bench deposit. The deposit is composed of gravel up to 1.5 m (5 ft) in thickness at

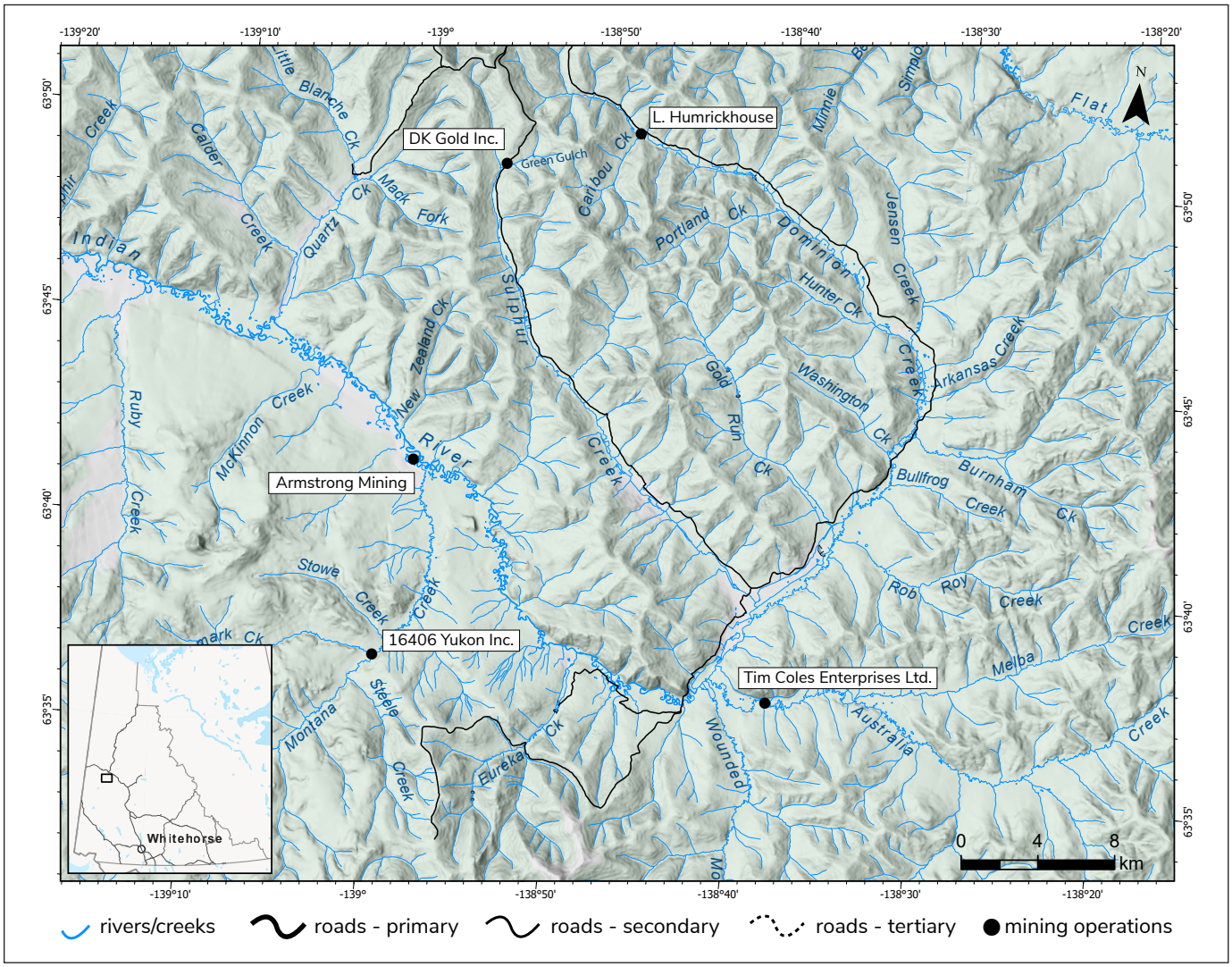


Figure 7. *Locations of highlighted placer operations in the Dominion-Sulphur, Indian River placer mining area.*

the rim. It is characterized by pervasive oxidation and contains a high concentration of weathered clasts. Minimal stripping was required along the outer edge of the bench, consisting of 3 m (10 ft) of overburden. The thickness of overburden increases toward the hillslope and is overlain by a colluvial apron. Fine gold was recovered from the bench deposit.

Tim Coles Enterprises Ltd. returned for his second season mining on Australia Creek, working claims leased from Metallic Minerals Corp. Equipment was moved into the drainage late in the 2024 season. An eight-person crew operated approximately 2.5 km upstream from the confluence with the Indian River, in the vicinity of ground previously worked by Little Flake Mining in 2023. In preparation for the 2025 season, 30 sonic drill holes were completed to inform the mine plans for both the 2025 and 2026 seasons. Mining efforts targeted a bedrock reef previously intercepted by Little Flake Mining at the upstream end of their cut. Coarse gold was associated with the reef, suggesting it may have functioned as a trap (Fig. 10). Gold recovered from the site has a fineness ranging from 86 to 88%.

Fortymile, Sixty Mile, Moosehorn placer mining area

Fortymile, Sixty Mile and Moosehorn placer mining area production increased in 2025, reporting 14 003 crude ounces, up from 12 794 crude ounces in 2024. For the first time in the past ten years, the Fortymile, Sixty Mile, Moosehorn placer mining area ranked as the second highest producer, contributing 13.4% of the Yukon's total placer production. Continued growth



Figure 8. *Mining cuts on the Indian River, outlined by white dashed lines, completed by Armstrong Mining as of July 2025.*

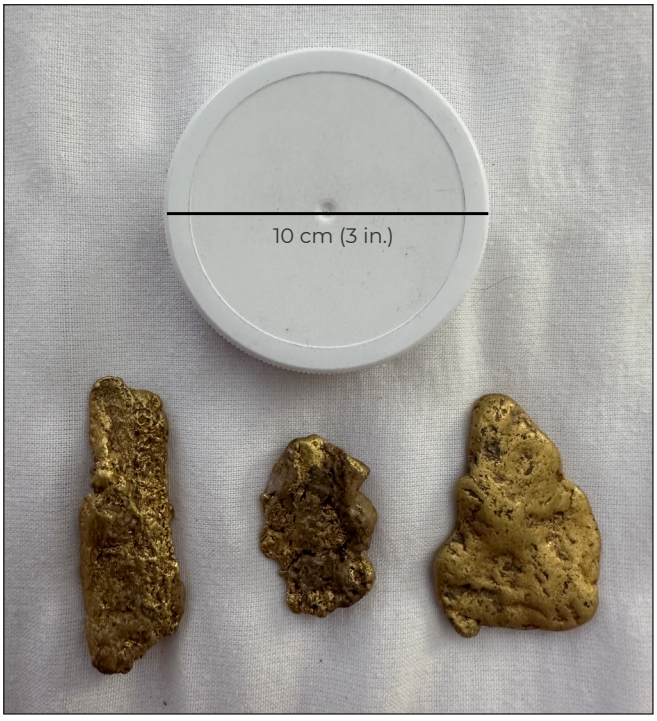


Figure 9. *Coarse gold recovered from Green Gulch by DK Gold Inc. The largest nugget weighs 28 g (1 oz).*

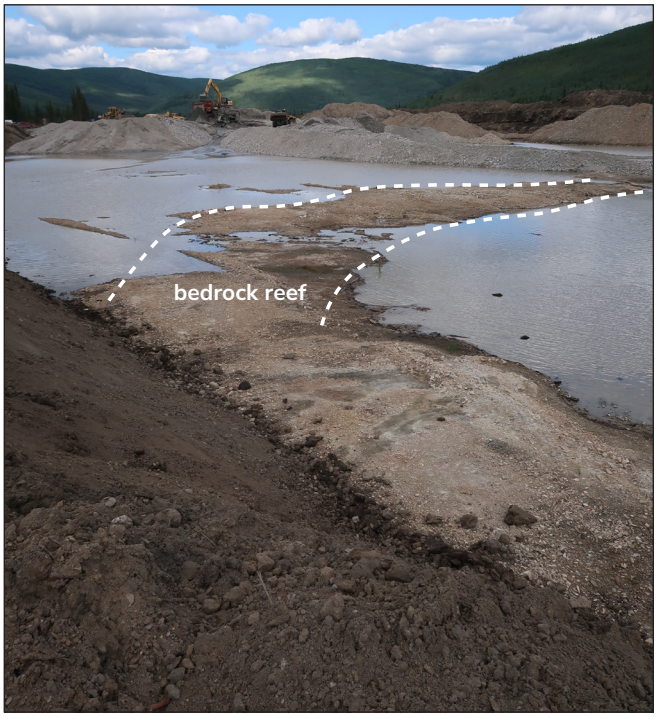


Figure 10. *Bedrock reef exposed in Tim Coles Enterprises Ltd. cut in 2025 on Australia Creek (delineated by white dashed lines).*

reflects expanded workings and strengthened output from core contributors within the placer mining area. The Sixty Mile River remained the dominant producer, reporting 10 176 crude ounces and accounting for most of the area's total production. Additional contributors included Browns Creek (1123 crude ounces), Ten Mile Creek (772 crude ounces), Kate Creek (tributary of Great Bear Creek; 505 crude ounces), and Glacier Creek (237 crude ounces; Fig. 11).

In 2025, H. Clopp leased Cheryl and Ralph creeks, both left-limit tributaries of Fifty Mile Creek, from claim owner R. Nordling. Equipment was mobilized in early July, and ground was opened on lower Cheryl Creek, approximately 0.8 km upstream from the confluence with the Fifty Mile River. Mining focused on a 4.6 m (15 ft)-thick section, targeting the lowermost 0.6 m (2 ft) of auriferous gravel and up to 0.6 m (2 ft) of bedrock composed of variably oxidized muscovite schist (Fig. 12). A boulder lag present at the bedrock contact marked a high-energy depositional environment and defines the pay layer. Prospecting efforts were aimed at delineating the extent of a paleochannel that appears to be continuous along the right limit. This channel was not reworked during incision on lower Cheryl Creek. However, evidence of significant downcutting is observed below a left-limit bench where the modern creek level is incised 9.1 m (30 ft) within the current valley bottom.

Favron Enterprises Ltd. and Northern Envy continued their operations in the West Yukon area, marking their second year of sluicing high volumes of pay. Following camp mobilization in September 2024, the operation ran at full capacity throughout the 2025 season, with a crew of up to 13 people. By July, four large cuts

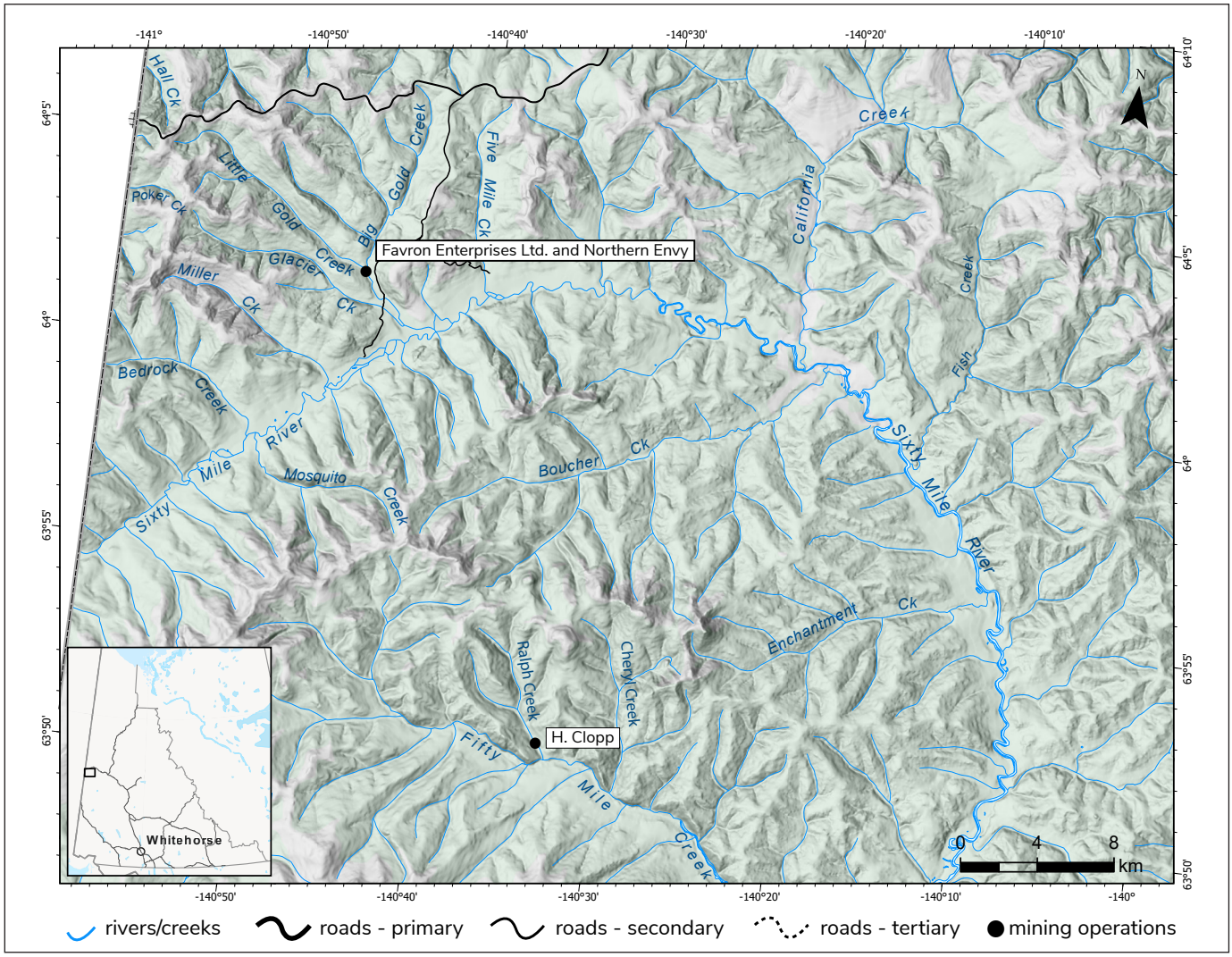


Figure 11. *Locations of highlighted placer operations in the Fortymile, Sixty Mile and Moosehorn placer mining area.*

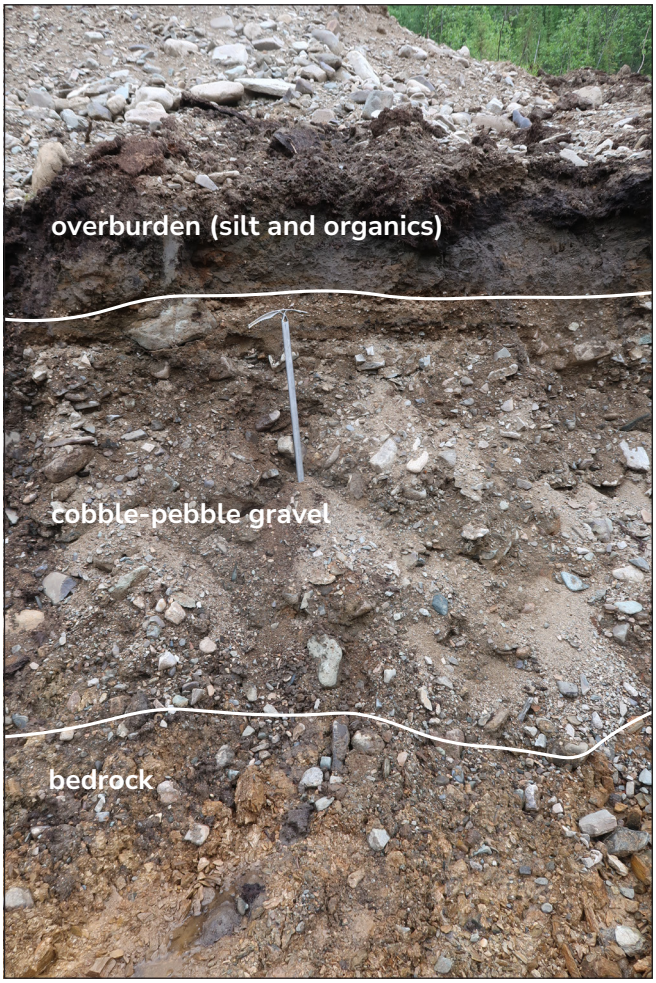


Figure 12. *Section exposed on lower Cheryl Creek in July 2025. An ice axe for scale measures 0.9 m (3 ft).*

had been completed, and a fifth cut was underway on the right limit of Glacier Creek. Cut 1, measuring approximately 32 500 m² (350 000 ft²), was situated between Glacier and Big Gold creeks, which flow parallel to one another before they meet the Sixty Mile River. Cut 2, which is the largest at 46 500 m² (500 000 ft²), was situated on the far left limit of Big Gold Creek near its confluence with the Sixty Mile River valley. Cut 3 was located in the centre of the valley, adjacent to historic dredge tailings on the right limit. Cut 4 measured 55 700 m² (600 000 ft²) and averaged 6 m (20 ft) in depth, and consisted of 3 m (10 ft) of mud overlying 3 m (10 ft) of gravel. Recovered gold has an average fineness of 84%, and 90% of the gold grain population is rice-sized or smaller. Extensive sonic drilling was completed across the property, and drill holes were spaced at 30 m (100 ft) intervals along fences set every 150 m (500 ft). This comprehensive drill program provided detailed resource calculations to support a multi-year mine plan. They sluiced a total of 191 139 m³ (250 000 yd³) of pay gravel in 2025.

South Klondike placer mining area

The South Klondike placer mining area reported 10 047 crude ounces in 2025, representing a 12% decrease from 11 417 crude ounces in 2024. Henderson Creek remained the dominant contributor, producing 5627 crude ounces, or more than half of the area's total output. Other top contributors were Black Hills Creek (1456 crude ounces), Scroggie Creek (1136 crude ounces), Barker Creek (680 crude ounces), and Brewer Creek (403 crude ounces; Fig. 13). The overall decrease reflects reduced output from several secondary drainages due to a shift in active operations, while core production from Henderson Creek remained stable.

The Maisy May drainage, which has had limited activity in recent years, was a hub of mining activity during the 2025 season. The most significant development was a change in ownership: Bedrock Mining Company Inc. sold the property to FellHawk Enterprises Ltd. in the fall of 2024. The 2025 season marked FellHawk Enterprises first year of sluicing on the creek, commencing in July after relocating from their former operation on North Henderson Creek. Operating with a four-person crew, FellHawk Enterprises targeted potential side pay that had not undergone mechanized mining during the 1970s. Historic air photos were used to identify those areas that remained untouched. Work focused on a single cut on the left limit, situated 1.7 km downstream from the mouth of Patton Creek. The cut measured 24 m (80 ft) wide and 207 m (680 ft) long (Fig. 14). Pay was considered to be the lowermost 0.9 to 1.2 m (3–4 ft) of a unit of pervasively oxidized, high-energy, poorly sorted gravel in contact with bedrock.

Two additional sluicing operations were active on lower Maisy May Creek in 2025, which were both on leased ground from 40419 Yukon Inc. Full Throttle Gold Syndicate Inc., who tested the property during the 2024 season, commenced a full year of mining in 2025. The company also received support from YMEP, which helped to fund a sonic drill program to evaluate the potential of bench deposits in the lower part of the drainage. Mining targeted both limits of the valley, and they processed material with a Gold Machine 250 trommel at a rate of 122 m³ (160 yd³)/hr. The pay gravel averages 1.2 m (4 ft) in thickness, and overlies a highly undulating bedrock surface with a well-defined boulder lag at the contact. The recovered gold is predominantly fine grained, and has an assay fineness of 78%. The largest nugget weighed 8 g.

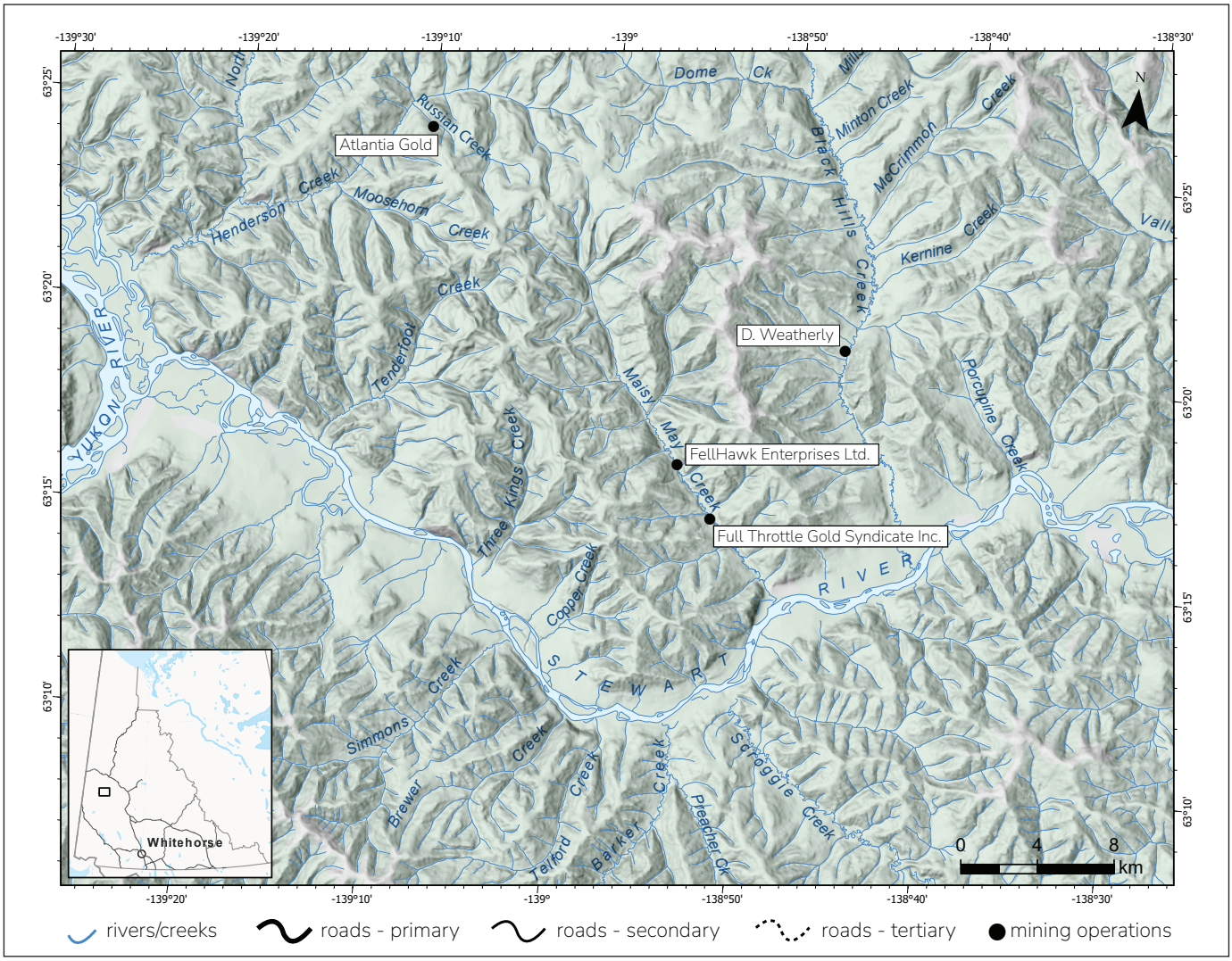


Figure 13. *Locations of highlighted placer operations in the South Klondike placer mining area.*

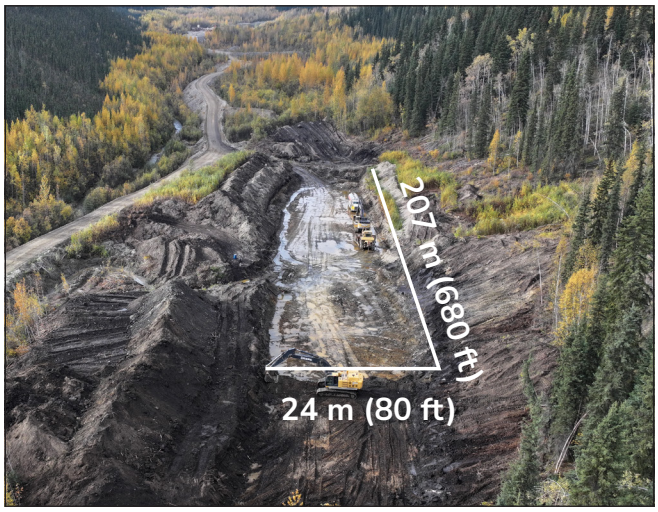


Figure 14. *Fellhawk Enterprises Ltd. left-limit cut, situated 1.7 km downstream from Patton Creek. The view is looking upstream.*

In 2025, D. Weatherly shifted his operation from Dome Creek and mid Black Hills Creek to a new site on lower Black Hills Creek, where he leased ground from T. Nixdorf. This location represents the lowermost active placer operation in the Black Hills drainage and had been inactive for a number of years prior to Weatherly's move. An eight-person crew was employed throughout the season. Mining focused on two settings: a right-limit bench and the modern valley bottom (Fig. 15). The bench cut measured 81 by 114 m (265 × 375 ft), while the valley-bottom cut measured 152 by 87 m (500 × 285 ft). In the valley bottom, operators stripped 1.8 m (6 ft) of pebble gravel and sand before reaching the pay unit, which consisted of a cobble-pebble gravel.

Atlantia Gold continued mining on Russian Creek, a left-limit tributary of upper Henderson Creek. The company has been steadily advancing upstream since



Figure 15.
D. Weatherly's two cuts on Black Hills Creek completed in 2025; a right-limit bench cut and a modern, valley-bottom cut. The view is looking upstream.

2016 and is now active approximately 2.5 km above the confluence with Henderson Creek. In 2025, the operators mined rim to rim where, at that location, the valley bottom is 40 m (130 ft) wide. The operation employed between three and five people throughout the season. Stripping included 3.0 to 3.7 m (10–12 ft) of black muck and organic material overlying 0.9 to 1.5 m (3–5 ft) of pay gravel, all of which was sluiced. Notably, as mining progressed upstream, the gold recovered became slightly coarser. An incised bedrock gutter was identified within the drainage, measuring 2.4 to 3.0 m (8–10 ft) wide and up to 1.2 m (4 ft) deep. This feature is highly sinuous and represents a meandering channel carved into bedrock and could be responsible for the increase in recovery of coarse gold.

Clear Creek-McQuesten placer mining area

Placer production in the Clear Creek-McQuesten placer mining area increased in 2025, reporting 1864 crude ounces, up from 1143 crude ounces in 2024. This represents a 63% increase from the previous year and reflects strengthened output from a limited number of active operators. Clear Creek remained the dominant contributor, producing 1733 crude ounces, while Barlow Creek reported 130 crude ounces. Although overall production volumes in this placer mining area remain modest, the 2025 increase highlights continued activity and scale of the active operations in the area (Fig. 16).

Scott and Son Mining resumed their operations from the same location as last year but progressing further downstream. Mining took place on the main stem of Clear Creek, 7.5 km downstream from the confluence of the upper forks of the creek. An eight-person crew targeted right-limit side pay that had been overlooked by earlier mining (Fig. 17). The pay averaged 1.2 m (4 ft) in thickness and has a maximum thickness of up to 1.8 m (6 ft). Gold distribution and concentration is controlled by faulting in the modern valley bottom. A series of cross-cutting faults were observed by the operator and was noted to have contributed to the high grades recovered on the downstream side. The pay gravel is a compact, high-energy, boulder-cobble gravel, and all gravel encountered was sluiced as pay.

Mayo, Keno placer mining area

Placer production in the Mayo, Keno area increased in 2025, reporting 5114 crude ounces, up from 4354 crude ounces in 2024. This reflects a 17% increase from the previous year and steady activity across several established drainages. The district contributed 5% of the Yukon's total placer gold production in 2025. Highet Creek was the leading contributor, producing 1701 crude ounces, followed by Granite Creek with 1570 crude ounces. Additional production was reported from Owl Creek (544 crude ounces), Minto Creek (534 crude ounces), and Ross Creek (317 crude ounces; Fig. 18).

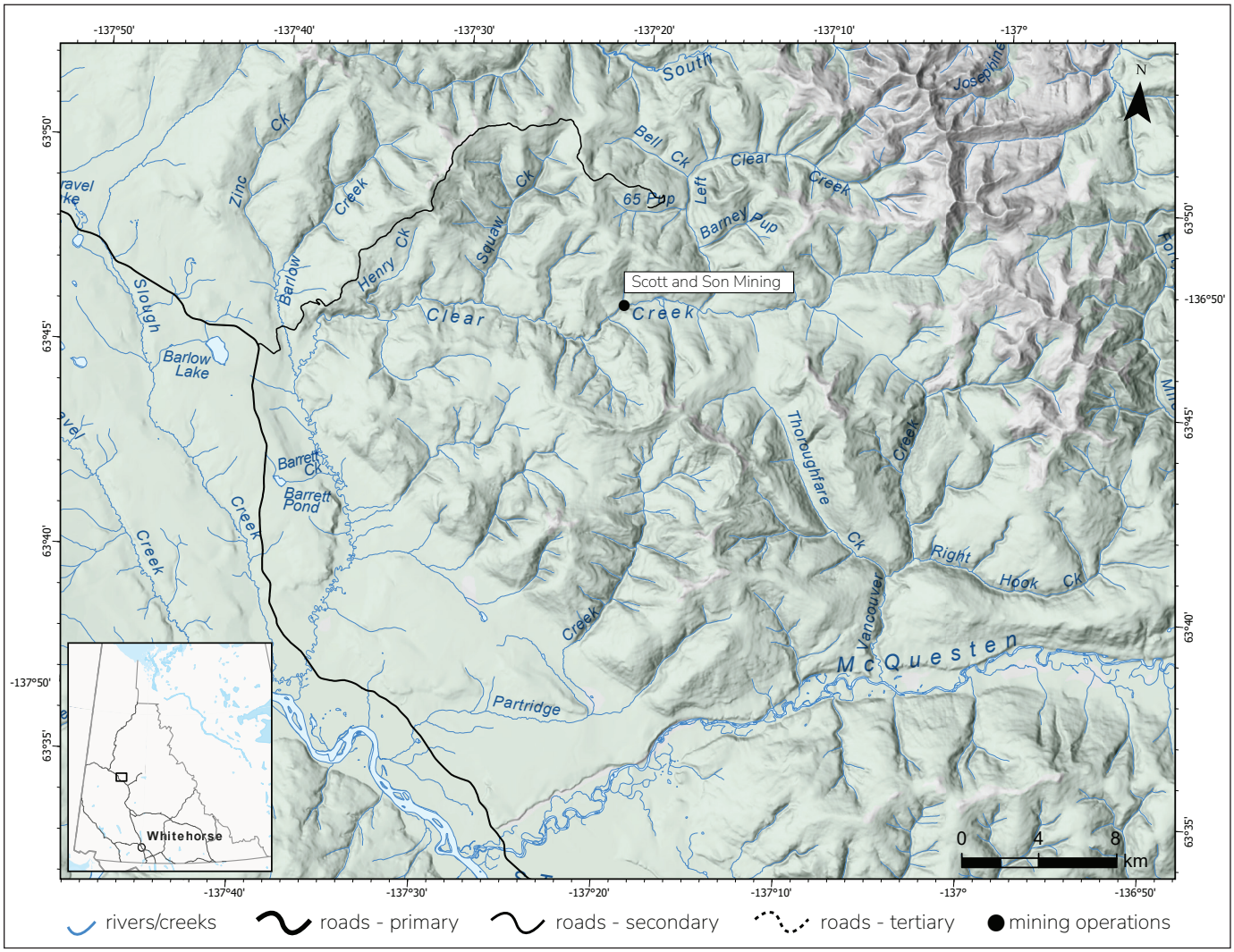


Figure 16. *Location of the highlighted placer operation in the Clear Creek-McQuesten placer mining area.*



Figure 17. *Scott and Son Mining's operation on Clear Creek, 7.5 km downstream from the confluence of the upper forks of Clear Creek. The view is looking upstream.*

Taylor Mining and Reclamation Ltd. initiated mining on their Upper Duncan Creek claims during the 2025 season, approximately 1.8 km upstream from the confluence with Duncan Creek proper (Fig. 18). The ground was staked in 2023, and a three-person crew undertook their first year of production following an extensive exploration program in the drainage that included geophysics on a bench deposit (resistivity and lidar surveys) and sonic drilling. Historical activity on the property dates back to the early 1980s, when Nugget Drilling & Company was active in the drainage; they were followed by C. Barchan who continued to mine in the area through to the mid-1990s. The current cut, measuring 15 by 41 m (50 × 135 ft), had been previously disturbed and is presumed to have been incompletely excavated by earlier cat-mining methods. The bedrock surface is highly undulating and extensively fractured, conditions that would have been difficult to mine effectively using cat-mining methods

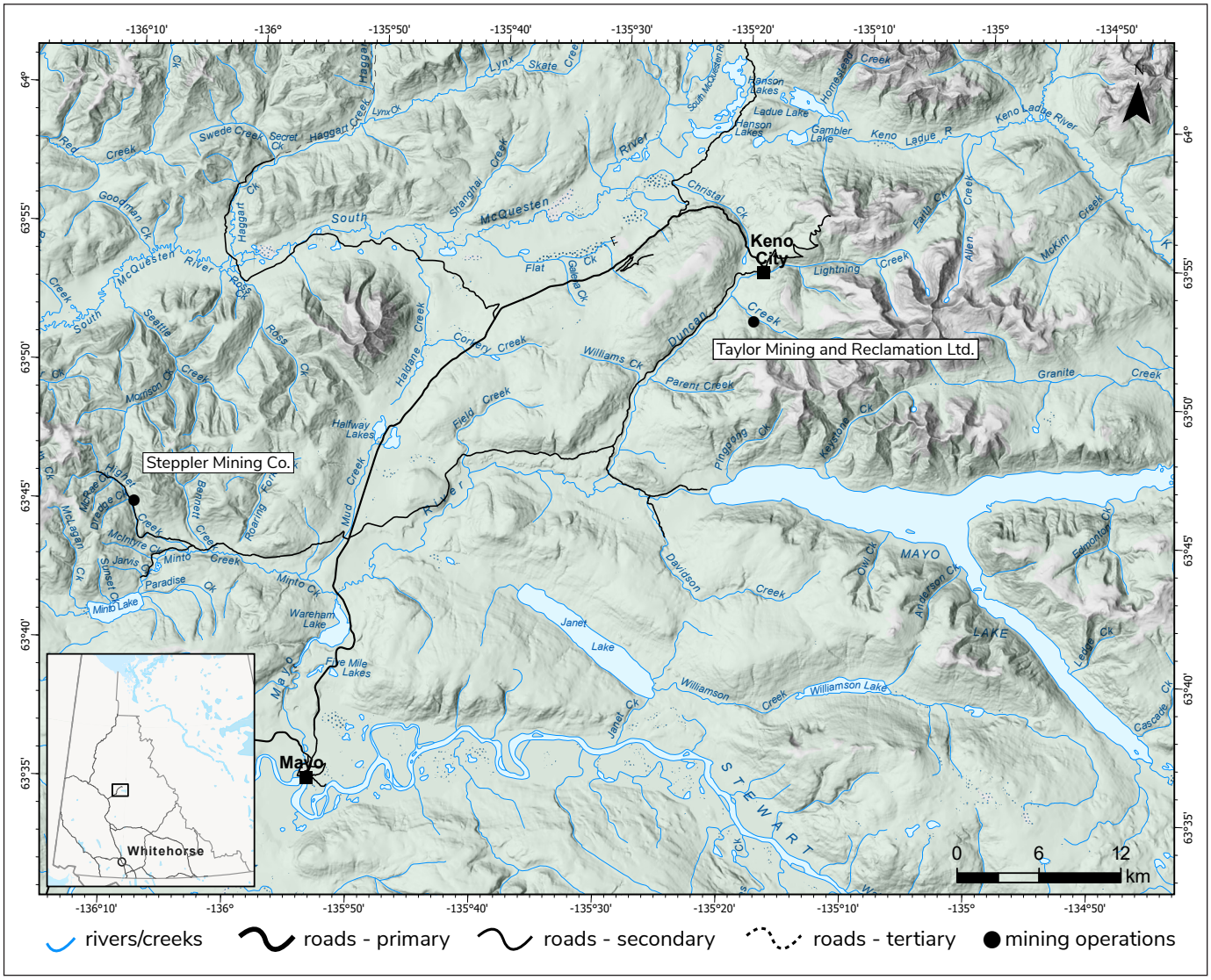


Figure 18. *Locations of highlighted placer operations in the Mayo, Keno placer mining area.*

(Fig. 19). The total thickness of the section in the cut was 6 m (20 ft), and all material was sluiced using a scalping deck plant capable of processing 57 m³ (75 yd³)/hr.

Steppler Mining Co. continued mining on Highet Creek at the mouth of Dredge Creek with a four-person crew, shifting from the left limit in 2024 to the right limit in 2025. The operation began on a lower right-limit bench, where 19 000 m³ (25 000 yd³) of material was sluiced. By mid season they relocated upstream to an area that had been previously dredged and later cat mined, and current efforts targeted side pay, as well as other areas untouched by previous mining. Earlier cat mining terminated on a graphitic schist layer thought to be bedrock; however, C. Steppler identified it as false bedrock and exposed a paleo Highet Creek channel preserved beneath. Coarse gold, including nuggets weighing up to 7 g (1/4 oz), were recovered from the right limit in 2024, whereas gold grains recovered on the left limit in 2025 were finer grained. The coarse component of the gold recovered in 2025 is shown in Figure 20. The graphitic schist unit was poorly exposed at the time of the site visit but it may represent a slide or an overhanging feature incised by the paleochannel.

Whitehorse Mining District

The Whitehorse Mining District is comprised of four placer mining areas: 1. Big Creek, Nansen, Hayes-Canadian; 2. Livingstone; 3. Kluane, Ruby Range, Kimberley; and 4. Nisutlin-Pelly, Whitehorse South. Reported production in the Whitehorse Mining District is predominantly derived from Big Creek, Nansen,



Figure 19. *Undulating and blocky bedrock surface exposed in Taylor Mining and Reclamation Ltd.'s cut on upper Duncan Creek in 2025.*



Figure 20. *Coarse gold recovered from Steppler Mining Co.'s operation on Highett Creek in 2025.*

Hayes-Canadian placer mining area, reporting 4% of the Yukon's total production as of November 1, 2025. The top three producing drainages in the Whitehorse Mining District are Nansen Creek (1508 crude ounces), Canadian Creek (tributary of the Yukon River; 1254 crude ounces) and Seymour Creek (779 crude ounces; Figs. 21 and 22), all of which are drainages in the Big Creek, Nansen, Hayes-Canadian placer mining area.

Following their 2024 season on upper Nansen Creek, Reno Contracting relocated their operation southeast to Victoria Creek, a tributary of the Nisling River. Mining was conducted under a water licence held by Mammoth Mining Inc., purchased earlier in the year. A six-person crew focused on a right-limit tributary of Victoria Creek, dedicating the early part of the season to testing and completing 765 m³ (1000 yd³) of bulk samples across several units. The 2025 exposure consisted of three units overlying a clay layer that acted as a false bedrock. Unit 1, from 0 to 1.8 m (0–6 ft), consists of Nansen till; unit 2, a periglacial gravel, extends from 1.8 to 4.0 m (6–13 ft); and unit 3, from 4.0 to 6.7 m (13–22 ft), comprises Klaza till. The periglacial gravel between the two till units was identified as the most economic material (Fig. 23). Drilling (using a privately owned rig) was used to inform the size and dimension of the cut for the 2025 season, targeting deep ground where total depth to bedrock was 26 m (85 ft). Material was processed using a shaker-deck plant at a rate of 45 to 75 m³ (60–100 yd³)/hr.

Ownership on Back Creek in the Nansen area shifted this season when L. Hearn sold the claim block to Jopebo Mining Inc., a company based in Namibia (southern Africa). This was the operator's second year on the ground, as they gradually increased capacity at the site, operating a daily single shift with a six-person crew. Sonic drilling of 21 holes in 2024 directed this year's mining efforts. The targeted pay unit is a pre-glacial gravel on the left limit, where 1.8 m (6 ft) of material was sluiced, including the uppermost part of bedrock. A trommel processed material at a rate

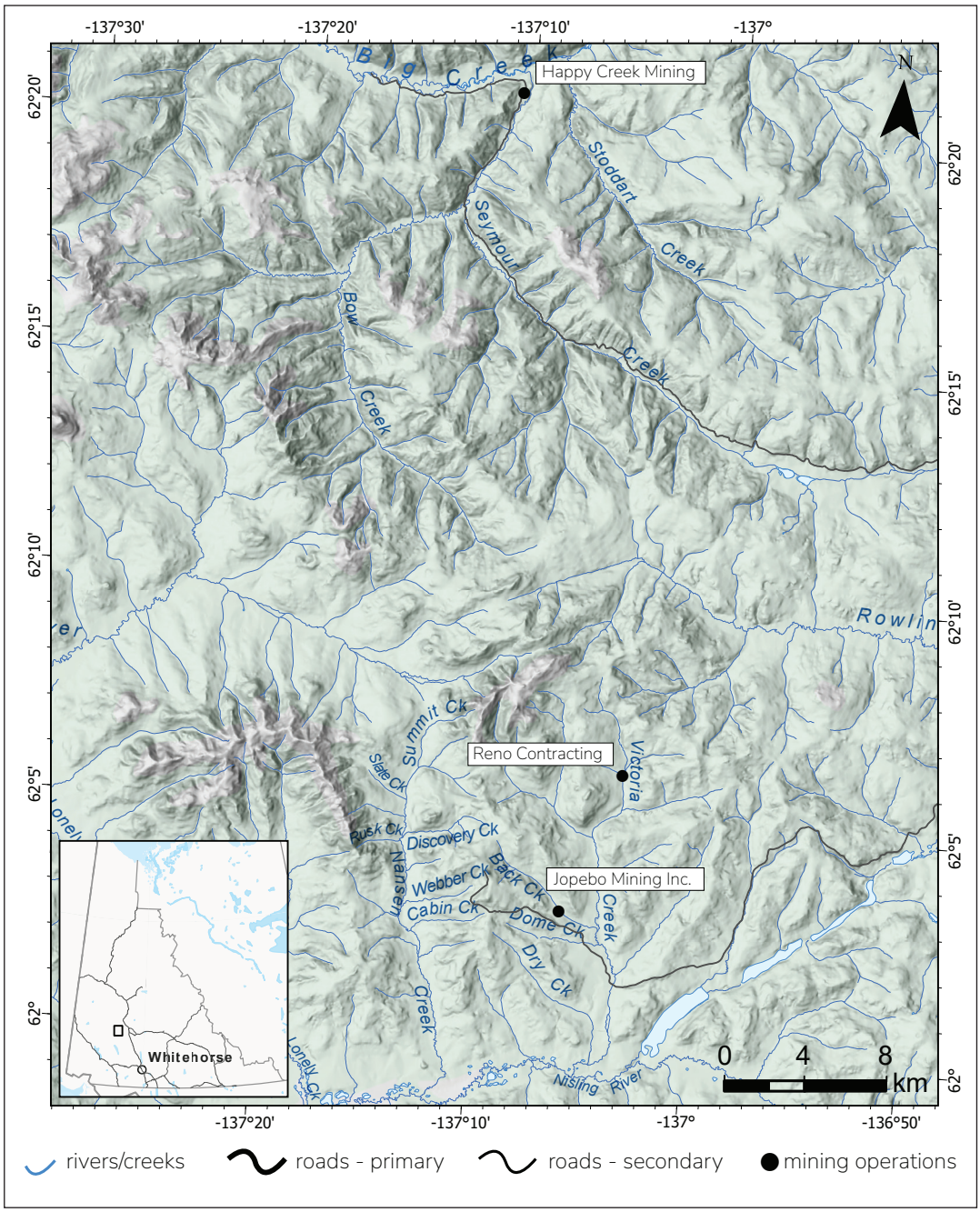


Figure 21. *Locations of highlighted placer operations in the Whitehorse Mining District.*

of 31 m³ (40 yd³)/hr. Much of the season was spent exploring the ground to assess and delineate the pay zone. Gold recovered has a fineness of 70%, and the largest nugget recovered weighed 6.8 g (<1/4 oz).

Happy Creek Mining opened up their property on lower Seymour Creek for the first time during the 2025 season, operating with a crew of up to five people. Mining was focused on the left limit of Seymour Creek, immediately upstream from its confluence with Big Creek. The company had long sought to test the potential of low-level bench deposits in the area, particularly those with possible influence from Big Creek. A total of five distinct bench levels are present along lower Seymour Creek, and the lowest bench is situated approximately 4.6 m (15 ft) above the modern creek level (Fig. 24). Stripping conditions were favourable, with only 0.6 m (2 ft) of moss and tephra overburden. All underlying gravel was sluiced as pay. The gravel is a clast-supported, cobble-dominated unit with a medium to coarse sand

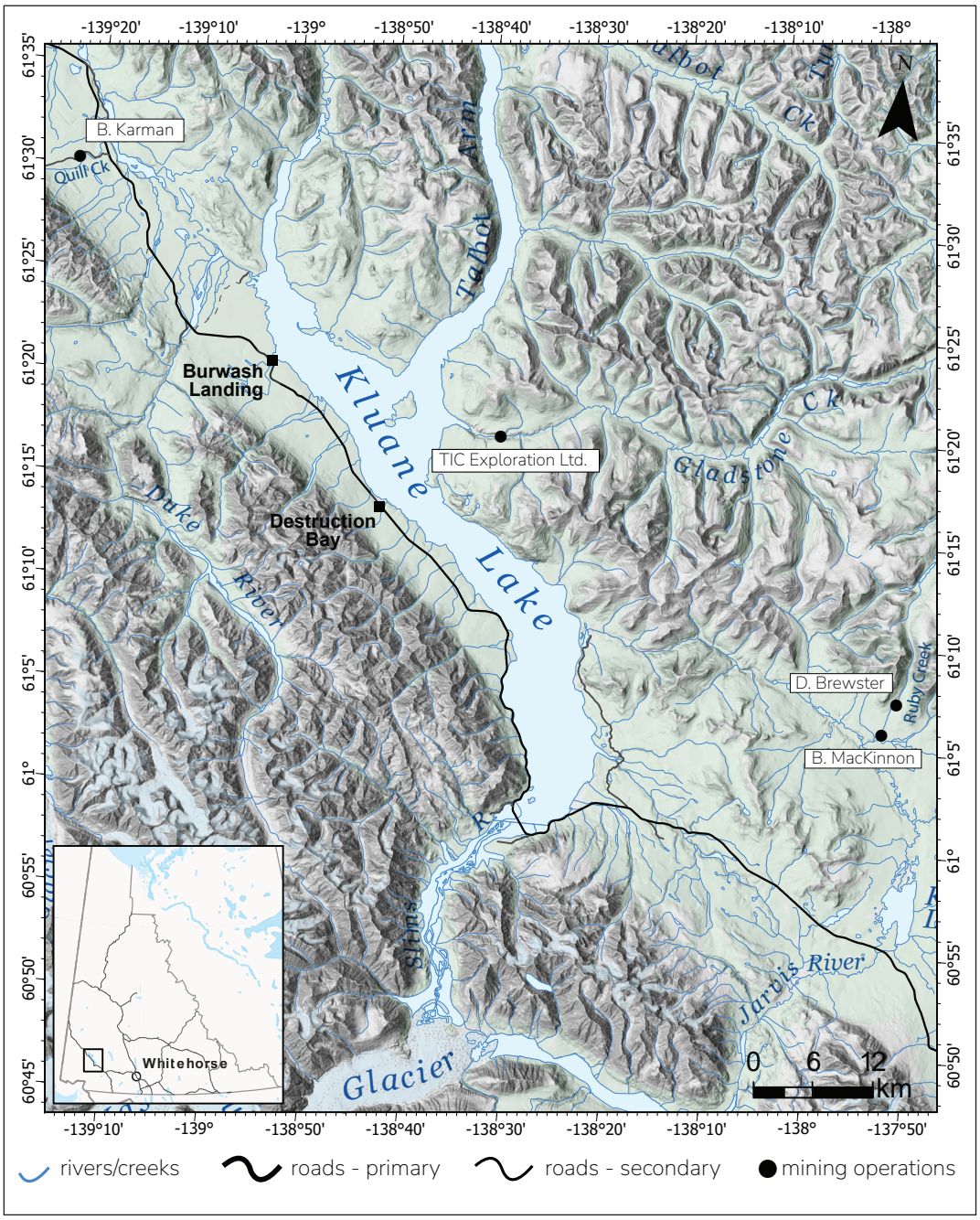


Figure 22. *Locations of highlighted placer operations in the Ruby Range area, within the Kluane, Ruby Range, Kimberley placer mining area.*

matrix. It is moderately sorted, and contains minor boulders throughout. The gold that was recovered is fine grained. Material was processed at a rate of 54 m³ (70 yd³)/hr using a shaker plant.

A change of ownership occurred in the Kluane region in October 2024, when B. Karman purchased nine claims on lower Quill Creek. The ground had been held by J. Nicols since 2001, and minimal activity was reported over the past several seasons. Karman mobilized equipment to the site and initiated mining in mid-summer 2025. Mining efforts were focused on the left limit, below the mouth of a canyon.

Two operations were active on Ruby Creek, a tributary to the Jarvis River. Both are one-person operations (B. MacKinnon and D. Brewster), and they have been present in the drainage since the 1980s; MacKinnon

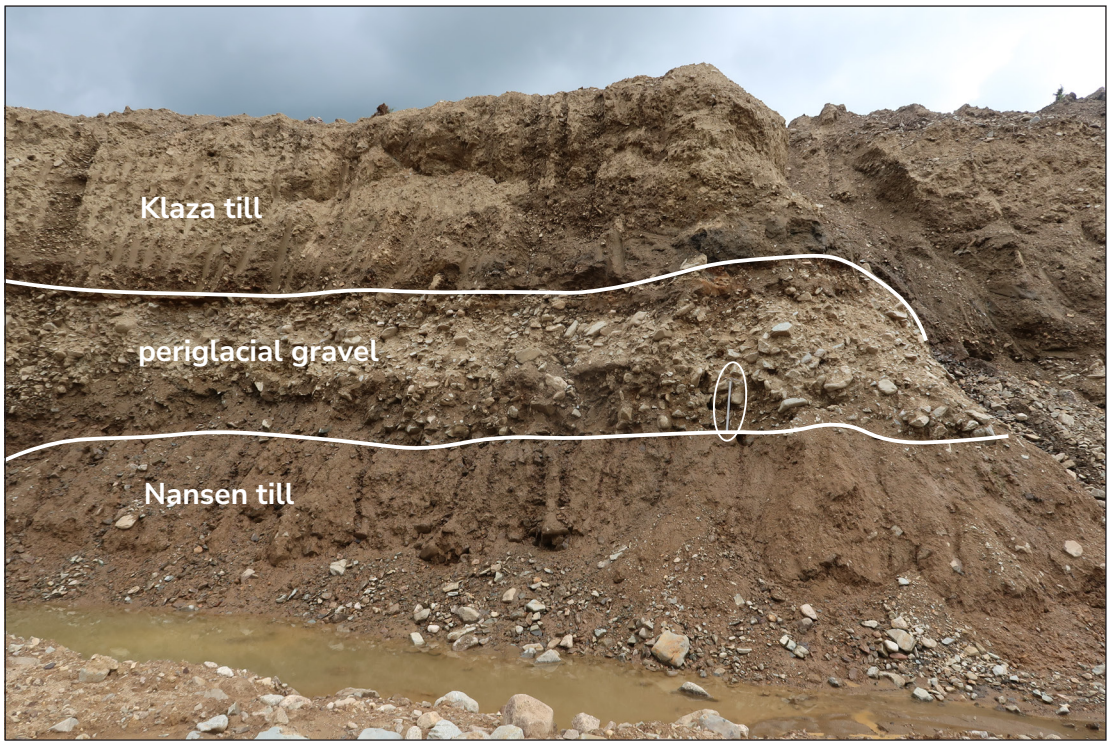


Figure 23. *Exposed section at Reno Contracting's cut on Victoria Creek in 2025. The total section depth was 6.7 m (22 ft) and consisted of three units, situated on a false bedrock of clay. An ice axe for scale (circled in white) measures 0.9 m (3 ft).*



Figure 24. *Five distinct bench levels on lower Seymour Creek at Happy Creek Mining's property. The dashed white lines indicate the different bench elevations.*

mined the lower reaches of the creek, while Brewster focused upstream. Mining targeted reworked modern Ruby Creek gravel overlying a compact till that acts as a false bedrock. At MacKinnon's 2025 cut, a low-level, right-limit bench is present, but appears to be defined by the till surface rather than by a re-incised Ruby Creek channel. The modern creek gravel contains a boulder lag both at surface and along the till contact. Pay gravel thickness ranges from 2.4 to 3.7 m (8–12 ft), all of which was sluiced as pay.

TIC Exploration continued mining on Gladstone Creek (tributary to Kluane Lake), advancing into a deep, right-limit cut located upstream from their camp, 5.9 km up the drainage from its confluence with Kluane Lake. They also mined a second site (upstream from the right-limit cut) 7.5 km from the confluence with Kluane Lake, where they sluiced modern Gladstone Creek gravel. This right-limit cut is one of their deepest targets to date since they began mining in 1992. Operating with a six-person crew, they mined a section 37 m (120 ft) deep, which is composed of till and glacial lake sediments overlying a gravel unit. They sluiced the lowermost 1.2 m (4 ft) of material where the gravel becomes coarser and a boulder layer marks the start of pay (Fig. 25). The operation used a unique mining style that relies exclusively on excavators, moving pay to the plant through three to four excavator relays to efficiently manage material at depth.

Summary

The resilience of the Yukon placer mining industry has been demonstrated for decades, and stable production was maintained through fluctuating gold prices, shifting market conditions, and evolving regulatory requirements. In 2025, the industry reported an estimated C$401 million in placer gold revenue, the highest on record, which was primarily driven by elevated gold prices. Operators have sustained activity during periods of significantly lower gold values, making this year's strong revenue particularly notable. Most production was derived from the Dominion-Sulphur, Indian River placer mining area, which accounted for 55% of the Yukon's total and hosts several of the largest operations in the territory. Production increases were also recorded in multiple placer mining areas, including Clear Creek-McQuesten (63% increase); Mayo, Keno (20% increase); Fortymile, Sixty Mile,



Figure 25. *TIC Exploration Ltd.'s operation on Gladstone Creek in 2025. They mined in two locations throughout the season. The view is looking downstream, toward Kluane Lake.*

Moosehorn (10% increase); and Big Creek, Nansen, Hayes-Canadian (7% increase). Another highlight of the 2025 season was the reported production from the Watson, Hyland placer mining area, marking the first documented output from this region since 1981. Despite regulatory delays and a shifting political landscape, the placer industry continues to move forward and remains one of the Yukon's most significant economic contributors. Increases in four placer mining areas, modest growth in the number of active sluicing operations, and renewed production from a long-dormant placer region all point to sustained strength and a positive outlook for the Yukon's placer mining industry.

Acknowledgments

A sincere thank you to the Yukon placer mining community, and particularly to miners and their crews, for their continued support, openness, as well as their willingness to share their time during site visits throughout the season (Fig. 26). The ability to document active operations and observe geology is made possible through the willingness of operators to share knowledge, provide site access, and walk through their cuts in the field. This collaboration is deeply valued and essential to the ongoing work of documenting and understanding the Yukon's placer industry.



Figure 26. *Gold recovered during a site visit, illustrating the support and openness of Yukon placer operators who continue to provide access, share knowledge, and allow us to walk through active cuts in the field.*

References

Government of Yukon, 2025a. Yukon Snow Survey Bulletin and Water Supply Forecast, March 1, 2025. Water Resources Branch, Department of Environment, Government of Yukon, https://yukon.ca/sites/default/files/2025-03/env-snow-bulletin-march-2025.pdf [accessed November, 2025].

Government of Yukon, 2025b. Yukon Snow Survey Bulletin and Water Supply Forecast, April 1, 2025. Water Resources Branch, Department of Environment, Government of Yukon, https://yukon.ca/sites/default/files/2025-04/env-snow-bulletin-april-2025.pdf [accessed November, 2025].

Government of Yukon, 2025c. Yukon Snow Survey Bulletin and Water Supply Forecast, May 1, 2025. Water Resources Branch, Department of Environment, Government of Yukon, https://yukon.ca/sites/default/files/2025-05/env-snow-bulletin-may-2025-en.pdf [accessed November, 2025].

Yukon hardrock mining, development and exploration overview, 2025

Spencer W. Skerget and Tiera V. Naber‡*
Yukon Geological Survey.

Skerget, S.W. and Naber, T.V., 2026. Yukon hardrock mining, development and exploration overview, 2025. *In*: Yukon Exploration and Geology 2025, A. Stuart, L.H. Weston and S.K. Schultz (eds.), Yukon Geological Survey, Government of Yukon, p. 39–74.

Introduction

Hardrock mineral exploration activity in the Yukon increased in 2025 coinciding with record high prices of gold and silver, as well as the progression of numerous exploration projects into the advanced stage. In 2025, eight updated mineral resources estimates (MRE) were released and many exploration companies announced late-season capital raises and expanded programs. At the time of writing, the Yukon Geological Survey (YGS) estimated exploration expenditures in the territory to be $180M[1] for the year, based on company press releases, System for Electronic Document Analysis and Retrieval (SEDAR) postings, and conversations with industry parties. This estimate of exploration expenditures is up 24% compared with $145M in 2024 (Fig. 1). Development expenditures for 2025 are estimated to be $99M, up by 148% compared with $40M in 2024. In summary, combined exploration and development expenditures are up 51% for a total of $280M compared with $185M in 2024.

Mineral production is estimated to be $158M, down 16% from $190M in 2024 (Fig. 2). This decrease is primarily due to the closure of the Eagle Gold Mine in 2024 after the site's heap leach facility failed. In August 2024, the Government of Yukon launched an Independent Review Board to investigate the causes and factors that led to the failure; the final report was released June 30, 2025 (Smith and Konrad, 2025). Hecla Mining Company's Keno Hill Mine is currently the only operating hardrock mine in the territory and continues to work towards full capacity.

There were 78 active exploration projects in the territory in 2025 (Fig. 3; Appendix A), which is comparable to 2022, 2023 and 2024 (Fig. 4). Twenty of these projects were supported by the Yukon Mineral Exploration Program (YMEP). In 2025, the majority (approximately 67%) of active exploration projects occurred within the Traditional Territories of the First Nation of Na-Cho Nyäk Dun (26%), Kaska Dena Nations (16%), Selkirk First Nation (13%), and the Tr'ondëk Hwëch'in (12%; Fig. 5). The estimated exploration expenditures within these Traditional Territories were $207M for the First Nation of Na-Cho Nyäk Dun, $53M for the Kaska Dena Nations (Ross River Dena Council and Liard First Nation), $28M for Selkirk First Nation, and $16M for Tr'ondëk Hwëch'in First Nation (Fig. 5)[2].

As of October 31, 2025, 2841 claims had been staked in 2025, representing a 46% decrease compared with 2024 (Fig. 6). In 2025, the Dawson Mining District retains the most claims staked (41%; 1167 claims), followed by the Whitehorse Mining District (31%; 887 claims), the Mayo Mining District (26%; 749 claims) and the Watson Lake Mining District (2%; 48 claims; Fig. 7). A total of 169 981 claims remain in good standing, up 4% from 164 000 in 2024. With respect to the

* spencer.skerget@yukon.ca
‡ tiera.naber@yukon.ca

[1] *All estimated expenditure projections are in Canadian dollars and reflect the current estimates as of November 27, 2025, and will not be finalized until the end of January 2026.*

[2] *Some projects and their associated expenditures are counted more than once where traditional territories overlap.*

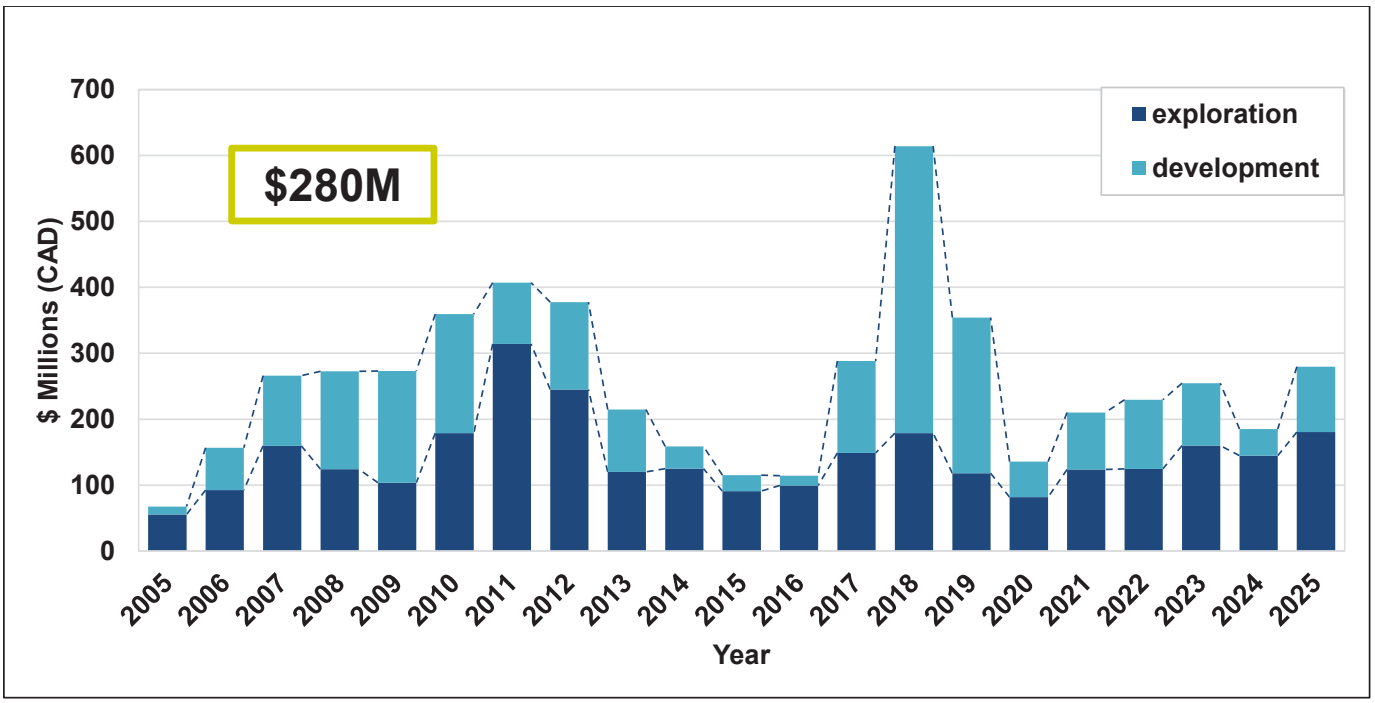


Figure 1. *Yukon Geological Survey's estimated exploration and development expenditures from 2005 to 2025.*

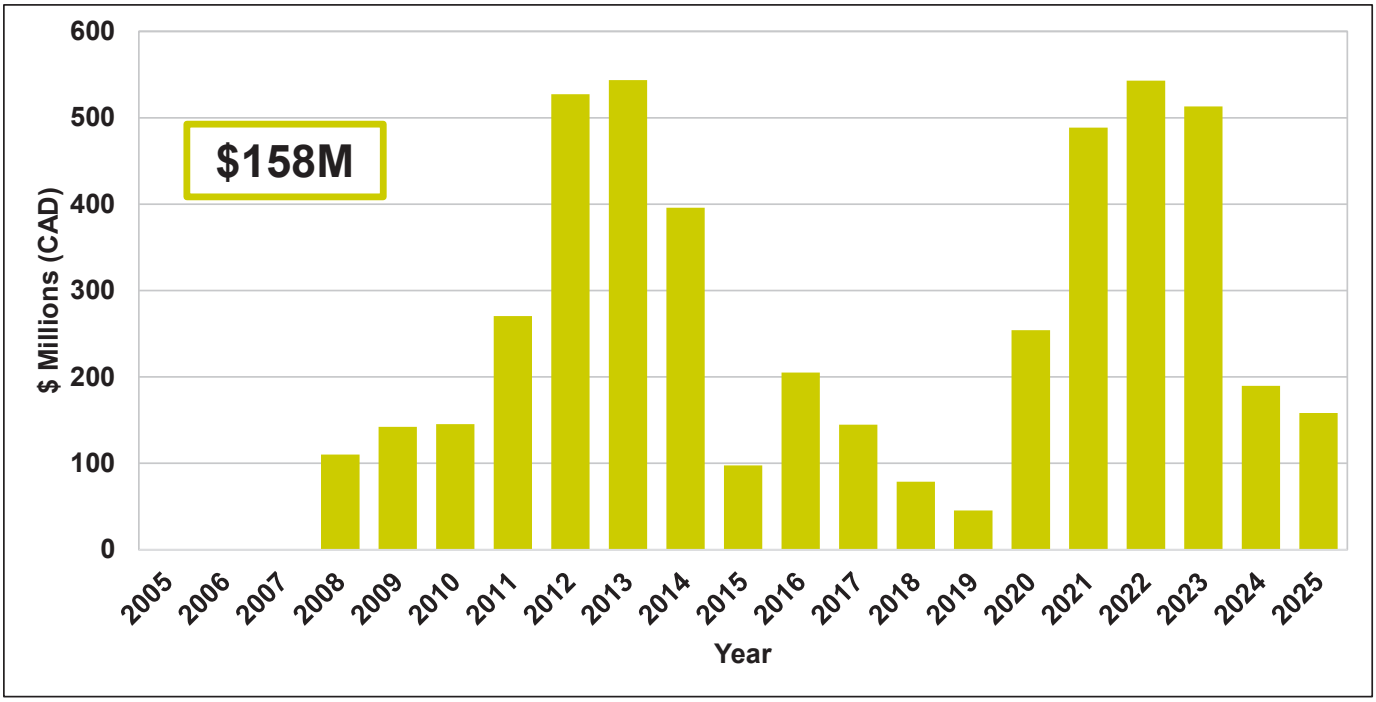


Figure 2. *Yukon Geological Survey's estimated mineral production values from 2005 to 2025.*

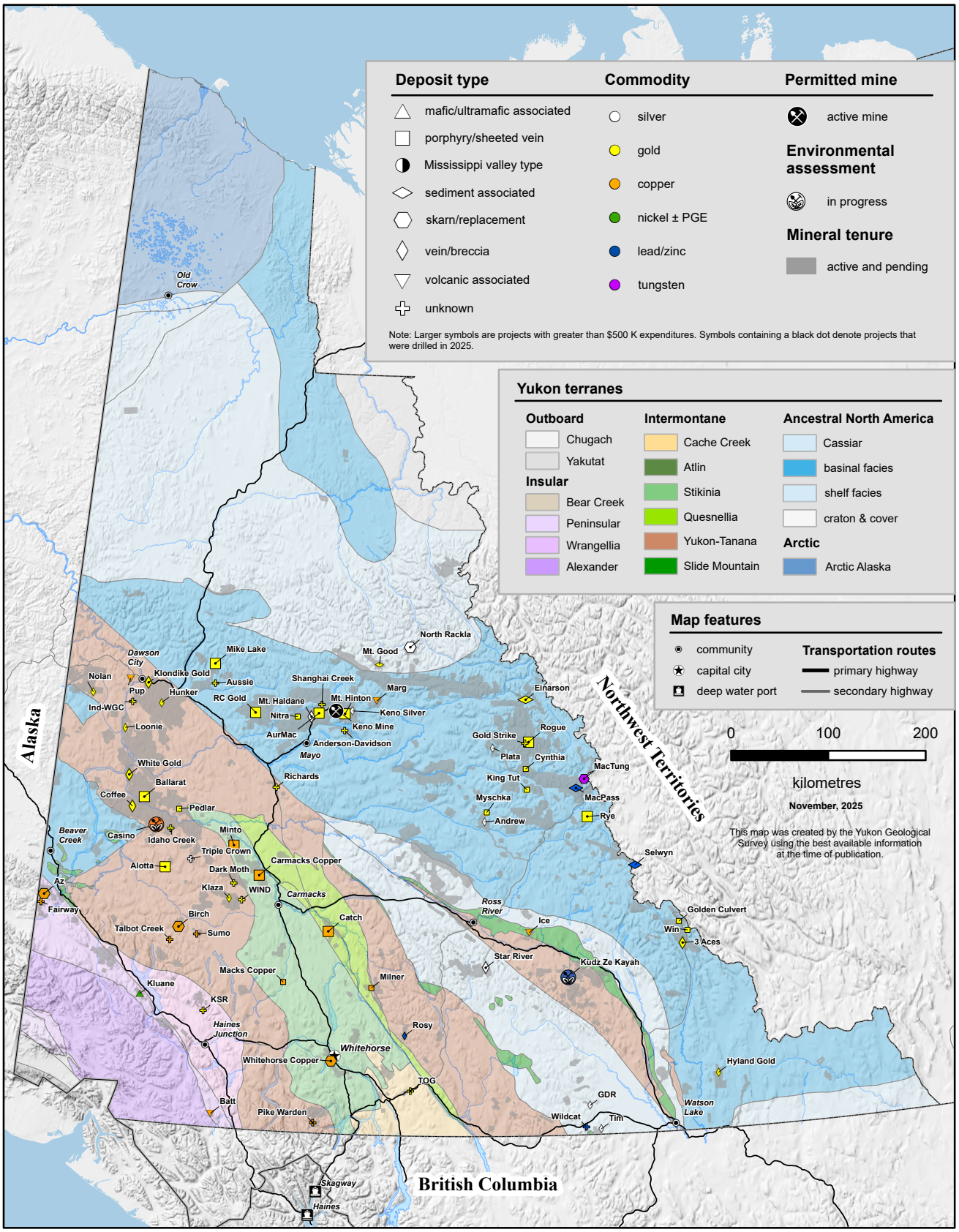


Figure 3. *Active hardrock projects in the Yukon as of November 30, 2025.*

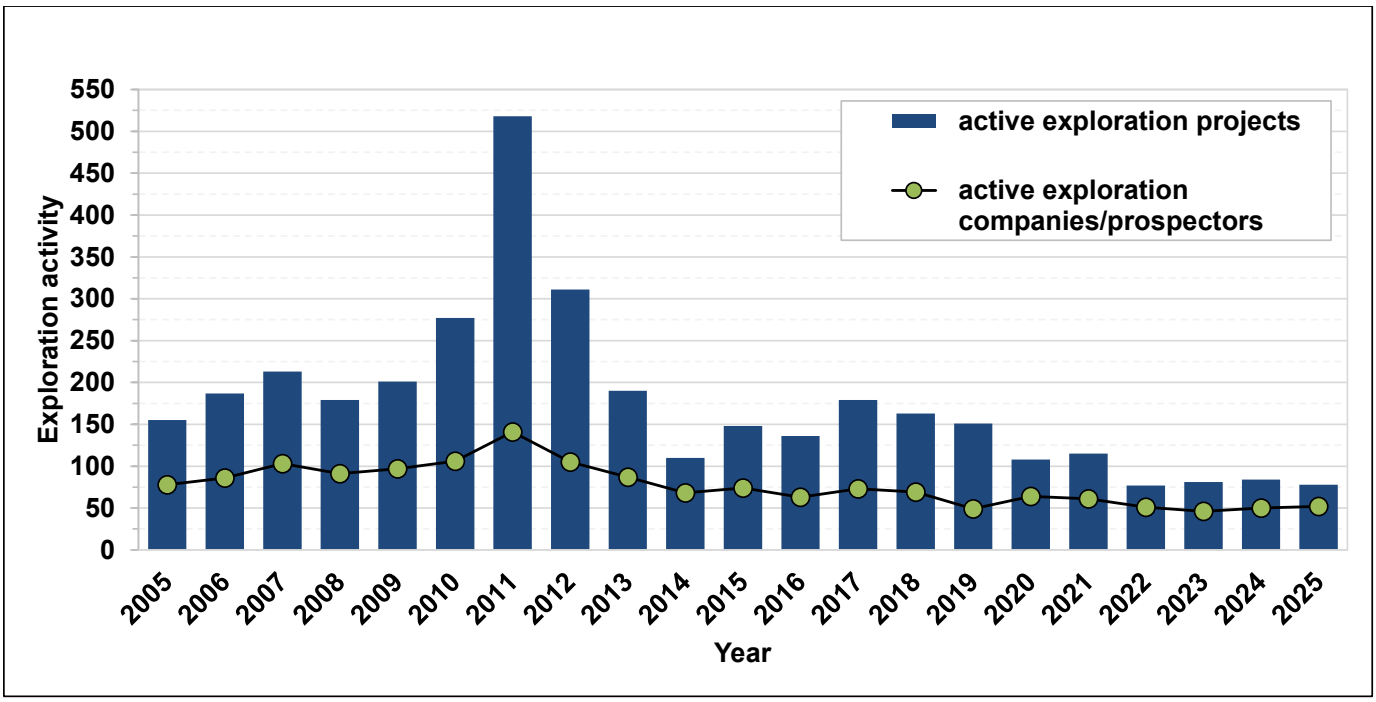


Figure 4. *Annual number of active exploration projects, as well as number of active companies and prospectors in the Yukon from 2005 to 2025.*

Traditional Territories in the Yukon, the majority of the claims staked in 2025 were within the First Nation of Na-Cho Nyäk Dun (32%; 1266 claims), the White River First Nation (15%; 617 claims), Tr'ondëk Hwëch'in First Nation (14%; 540 claims) and the Kluane First Nation (12%; 478 claims; Fig. 8)[3] .

In 2025, 50 projects, which were operated by 38 prospectors or companies, reported expenditures less than $500K per project, while 28 projects (managed by 22 companies) reported expenditures exceeding $500K per project. Of those 28 projects, 25 reported expenditures of over $1M. The primary commodity in terms of total exploration expenditure in the territory continues to be gold, representing 52% of spending ($93.8M), followed by copper (17.0%; $30.7M), lead-zinc (11.7%; $21.2M), tungsten (11.5%; $20.7M), silver (7.7%, $14.0M), and nickel + platinum group elements (PGE; <0.1%; $40K; Fig. 9). This distribution is similar to what was reported in 2024; however, there was a notable increase in relative exploration spending on copper and tungsten projects at the expense of lead-zinc projects. The percentage of exploration spending on gold projects was similar to 2024 despite record-high gold prices.

The total metreage of diamond, reverse circulation, and rotary air-blast drilling in 2025 is estimated to be at least 248 000 m in 834 holes across 26 projects. This represents a total metreage increase of 44% relative to 2024 (Fig. 10; Appendix B). Five projects in 2025 reported drilling metreage of greater than 25 000 m each.

Mining activity

Hecla Mining Company's Keno Hill mine was the only producing operation in the territory in 2025. The company reported production from the first three quarters of the year of 2.4 Moz of silver, 3032 tons lead, and 1810 tons zinc (Hecla Mining Company, 2025b). The operation averaged 307 tons per day during the first three quarters of 2025. The company is advancing operation programs including waste dump facilities, mine development programs, tailing capacity expansion, water treatment infrastructure upgrades, and related permitting execution to achieve their target rate of 440 tons per day (Hecla Mining Company, 2025a).

Surface and underground exploration at Keno Hill continued throughout 2025, which led to the identification of new mineralization 150 m down-

[3] *Some claims are counted more than once where traditional territories overlap.*

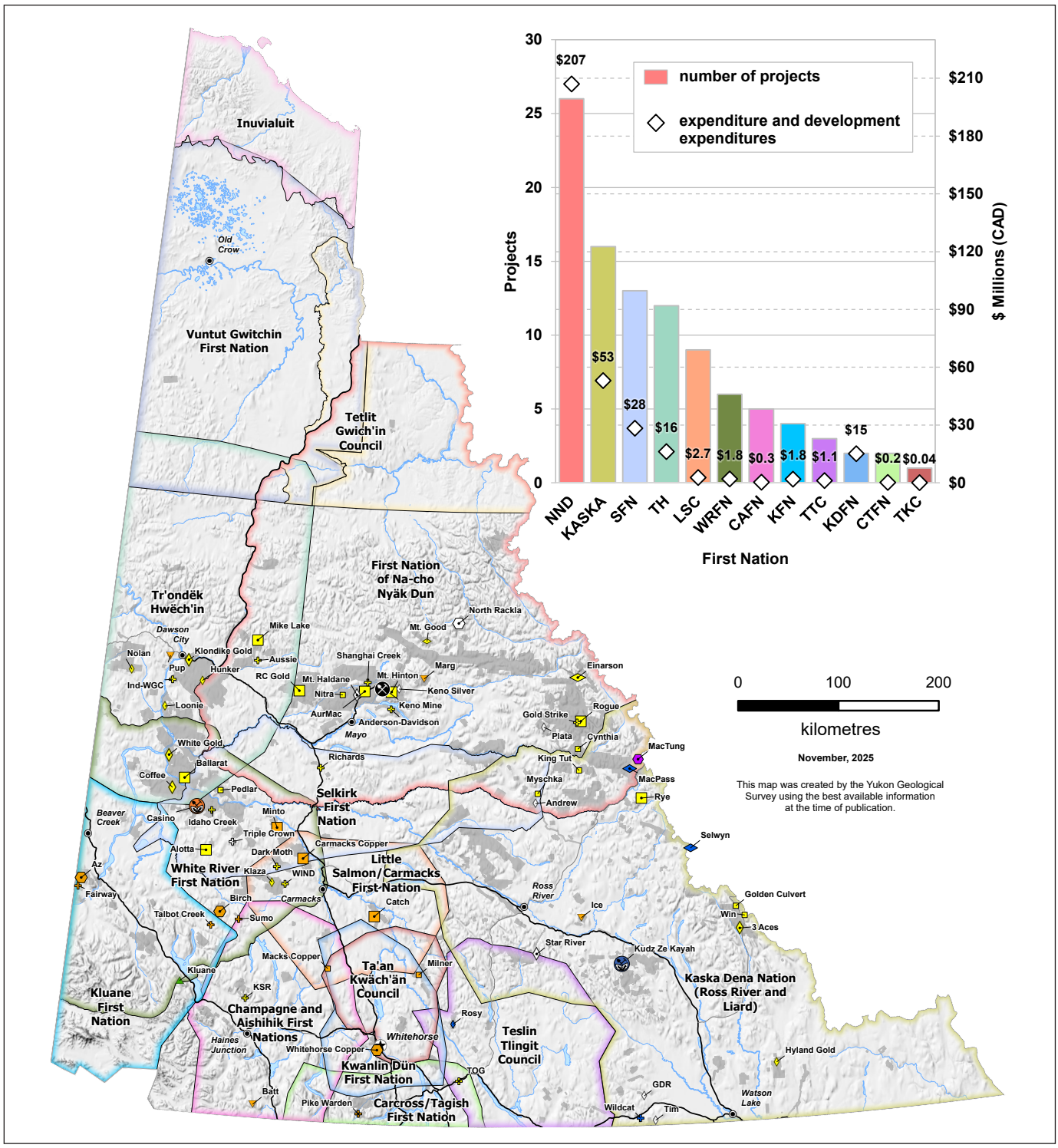


Figure 5. *Number of projects and exploration expenditures in 2025 across First Nations Traditional Territories in the Yukon. Note, several Yukon First Nations have overlapping traditional territorial boundaries, thus some projects and their associated expenditures may be counted in multiple instances. Exploration project symbology can be found in the legend of Figure 3. NND – First Nation of Na-Cho Nyäk Dun, KASKA – Kaska Dena Nations (includes Ross River Dena Council and Liard First Nation), SFN – Selkirk First Nation, TH – Tr'ondëk Hwëch'in, LSC – Little Salmon/Carmacks First Nation, WRFN – White River First Nation, CAFN – Champagne and Aishihik First Nations, KFN – Kluane First Nation, TTC – Teslin Tlingit Council, KDFN – Kwanlin Dün First Nation, CTFN – Carcross/Tagish First Nation, and TKC – Ta'an Kwäch'än Council.*

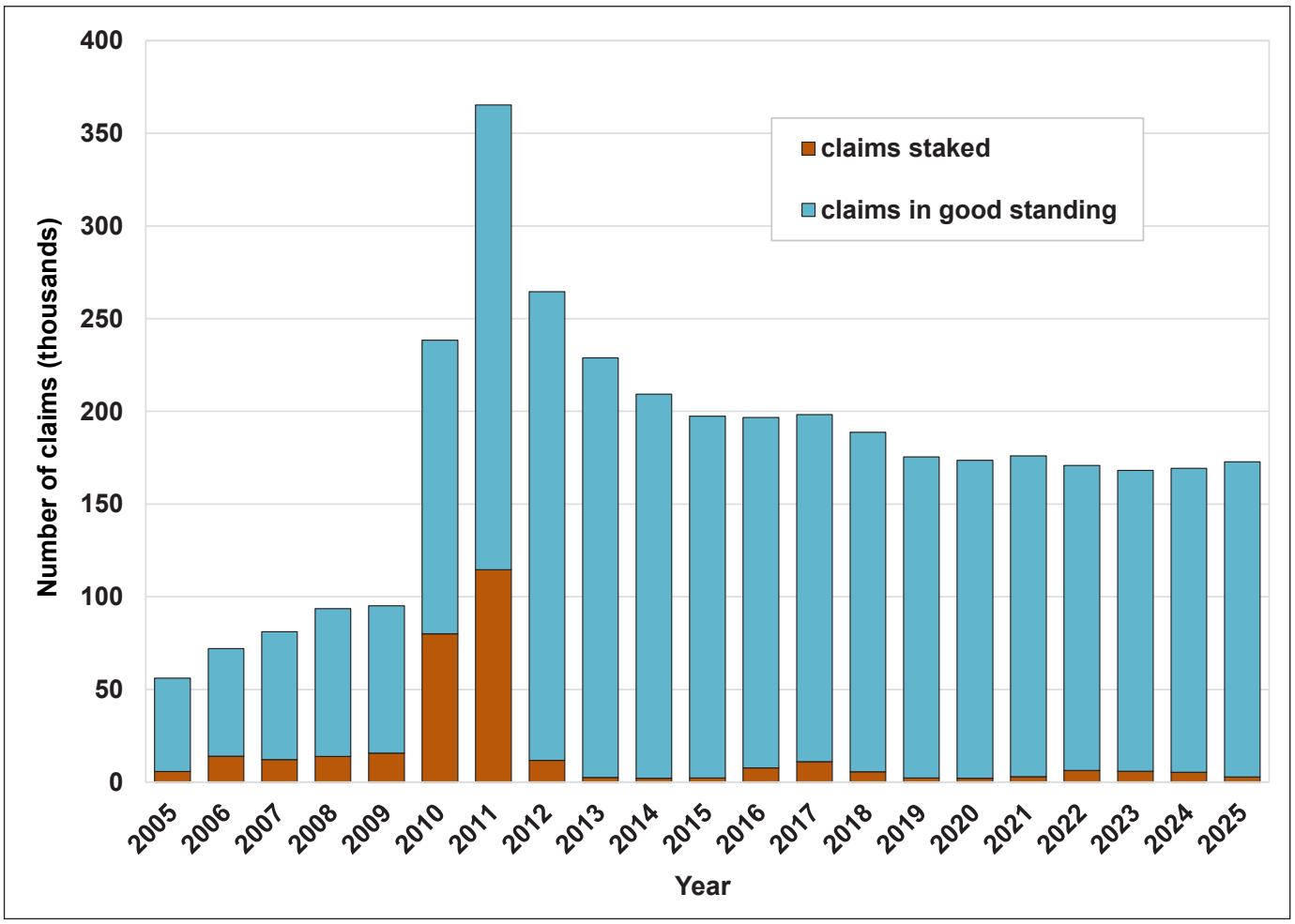


Figure 6. *Claim-staking activity in the Yukon from 2005 to 2025.*

plunge of existing reserves at the Bermingham deposit (Hecla Mining Company, 2025a). Highlights include 3.8 m of 1262 g/t Ag, 3.8% Zn, and 3.1% Pb at Bermingham Deep – Main Vein, and 0.6 m of 465 g/t Ag at Bermingham Deep – Footwall Vein.

At the formerly producing Victoria Gold Mine, the court appointed receiver, PricewaterhouseCoopers Incorporated, carried out remediation and environmental monitoring of the Eagle Gold Mine following the heap leach failure, and continued to meet the timelines issued by regulators. In August 2024, the Government of Yukon commissioned an independent technical review to investigate causes and contributing factors to the heap leach failure. In June 2025, the Independent Review Board (IRB) submitted their findings to the Government of Yukon, the Receiver, and the First Nation of Na-Cho Nyäk Dun. The report included 56 recommendations concerning changes to industry practices; changes to licensing, compliance, and enforcement; and updates to the Yukon Guidelines for Mine Waste Management Facilities (Smith and Konrad, 2025). Work is ongoing by the involved parties to understand and implement all recommendations outlined by the IRB (Government of Yukon, 2025a).

Key activities at the site in 2025 included construction of water storage ponds and groundwater monitoring infrastructure to permit interception, storage and treatment of site water. Stabilization work on the heap is ongoing and efforts are underway to recover gold from the facility. Revenue from asset sales, including gold, is aiding in funding remediation efforts. The Receiver is continuing to work with regulators to manage water and monitor site conditions (Government of Yukon, 2025b).

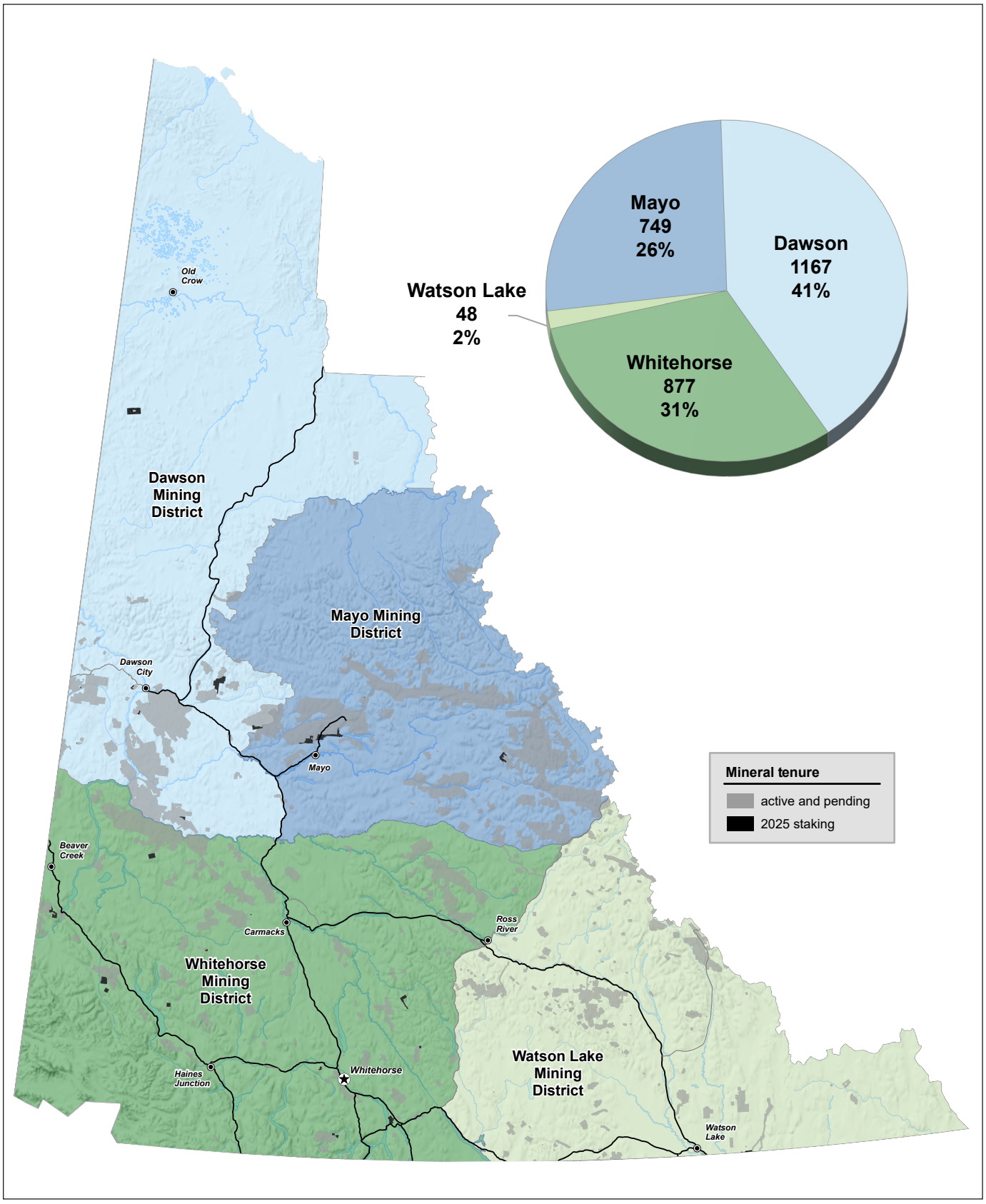


Figure 7. *Claim-staking activity during 2025 in the Yukon by mining district.*

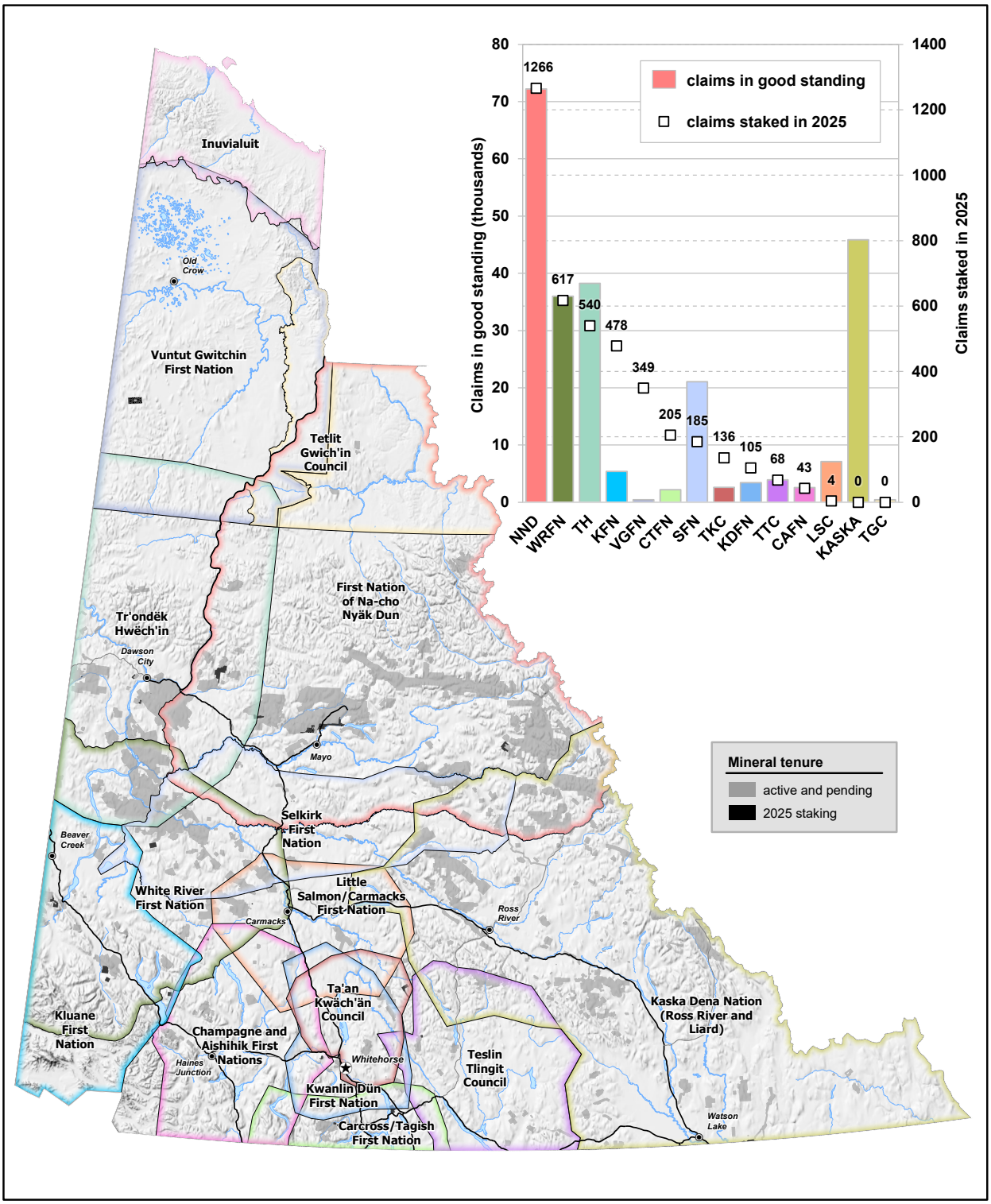


Figure 8. *Claim-staking activity in 2025 across Yukon First Nations' Traditional Territories. Note, several Yukon First Nations have overlapping traditional territorial boundaries, thus some projects and their associated mineral claim data may be counted in multiple instances. NND – First Nation of Na-Cho Nyäk Dun, WRFN – White River First Nation, TH – Tr'ondëk Hwëch'in, KFN – Kluane First Nation, VGFN – Vuntut Gwitchin First Nation, CTFN – Carcross/Tagish First Nation, SFN – Selkirk First Nation, TKC – Ta'an Kwäch'än Council, KDFN – Kwanlin Dün First Nation, TTC – Teslin Tlingit Council, CAFN – Champagne and Aishihik First Nations, LSC – Little Salmon/Carmacks First Nation, KASKA – Kaska Dena Nations (includes Ross River Dena Council and Liard First Nation), and TGC – Tetlit Gwich'in Council.*

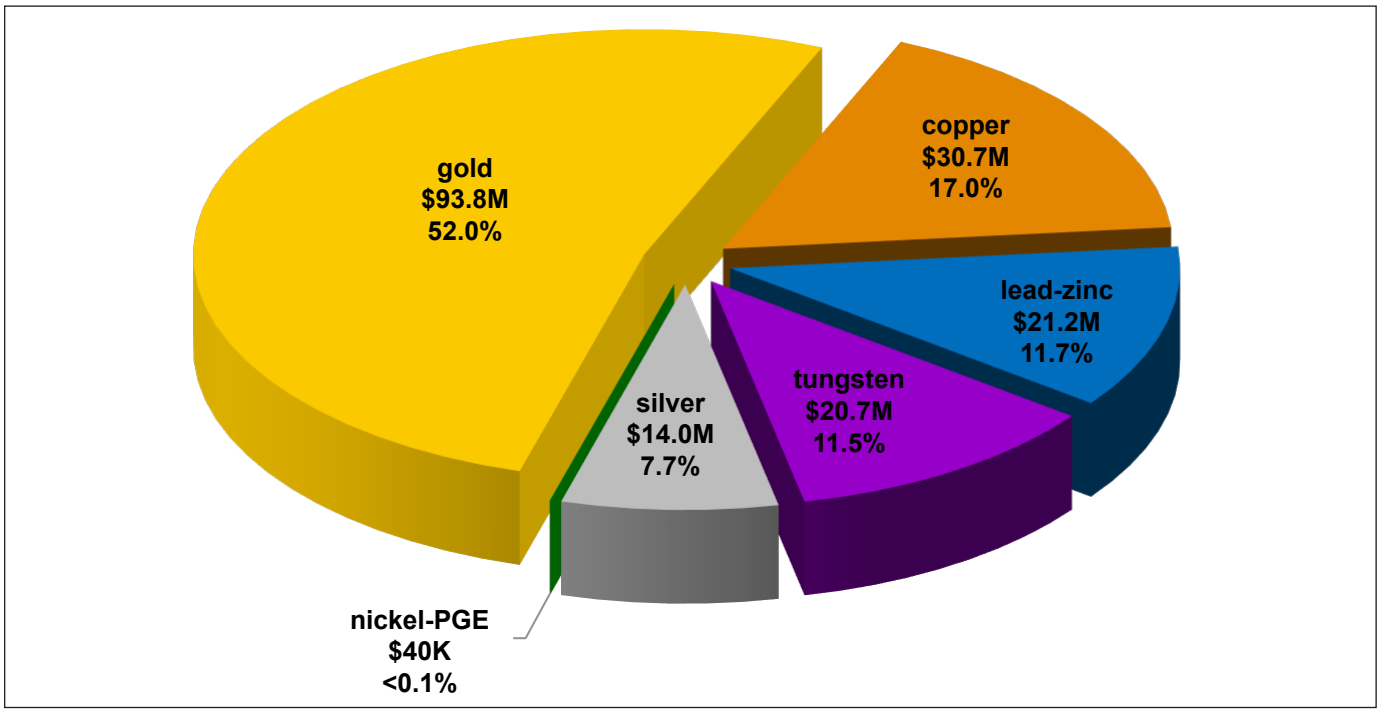


Figure 9. *Breakdown of 2025 exploration expenditures in the Yukon by commodity.*

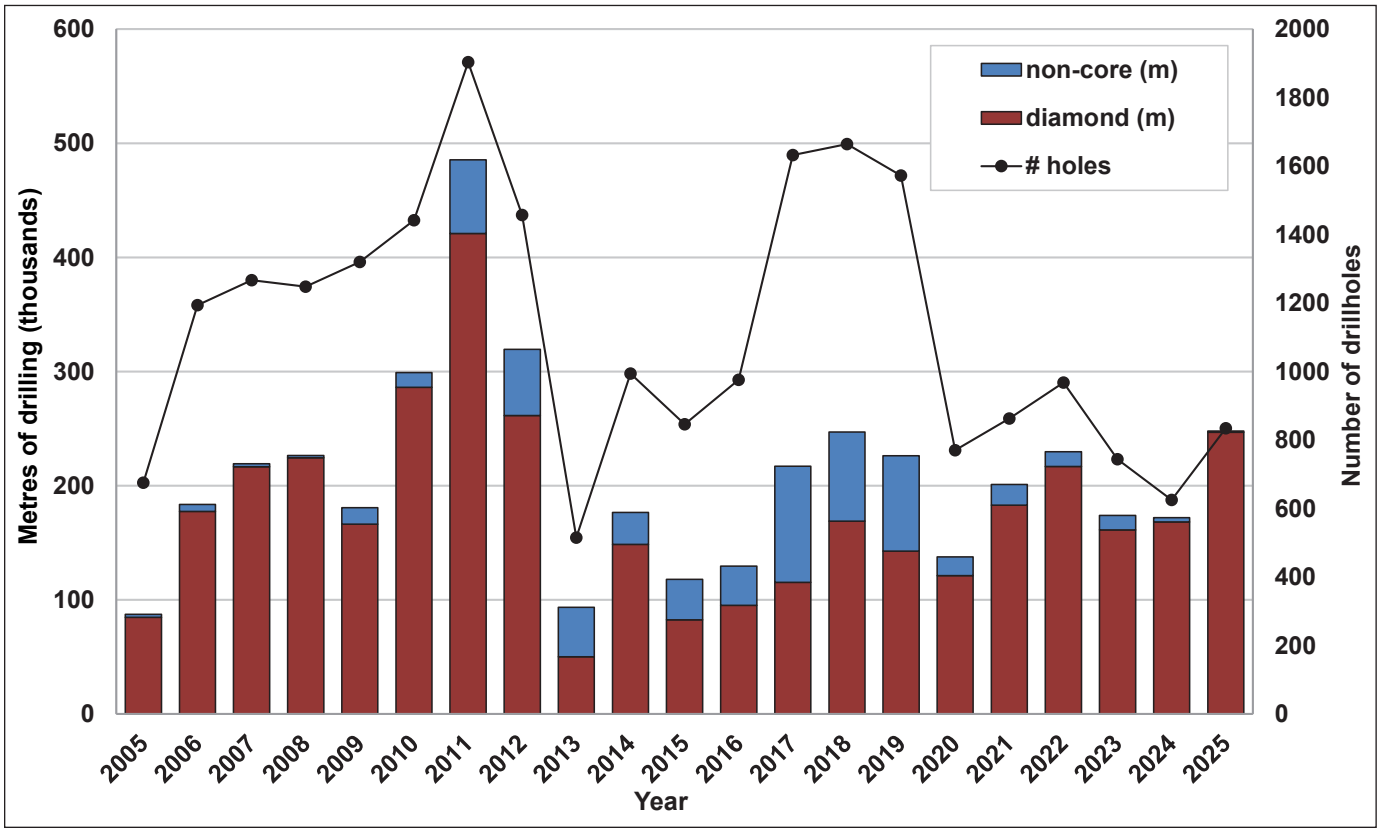


Figure 10. *Diamond drilling, and reverse circulation or rotary air-blast drilling in the Yukon from 2005 to 2025.*

Permitting and mine development

In June 2025, the Selkirk First Nation purchased the formerly producing Minto Mine and associated infrastructure and assets out of receivership (Venerable Ventures Ltd., 2025a). This represents the first time in Canadian history that an Indigenous government has assumed full legal ownership of a mine (Connors, 2025). As part of the arrangement, the Government of Yukon agreed to continue to fund ongoing care-and-maintenance and environmental monitoring of the site into 2026 using existing bonds on the property from the previous operator.

Following the sale, Selkirk First Nation entered an agreement with Venerable Ventures Ltd. to create a jointly held company, Selkirk Copper Mines Inc., to continue exploration, development and permitting activities at the mine site (Venerable Ventures Ltd., 2025a). In August 2025, a National Instrument (NI) 43-101 technical report was filed including an updated MRE for the project containing Indicated resources of 334 Mlbs Cu, 187 Koz Au, and 1.7 Moz Ag, and Inferred resources of 547 Mlbs Cu, 295 Koz Au, and 2.97 Moz Ag (Table 1; Bird and O'Farrell, 2025). The company commenced a 50 000 m diamond drill program in August aiming to evaluate high-priority targets, expand known mineralized zones, and collect updated geological data to support planned future trade-off studies (Venerable Ventures Ltd., 2025b). At the time of writing, the company had completed drilling of 98 holes across 26 000 m and a regional 1992 km^2 lidar survey for district-scale exploration (Selkirk Copper Mines Inc., 2025). The first holes of the program were drilled at the Minto North area, where results have successfully defined continued mineralization in that area (Fig. 11; Selkirk Copper Mines Inc., 2025). Assays from the first four holes of the drill campaign produced promising results. Drillhole 25SCM001, a 100 m southeastern step-out from previous drilling at the Minto North West zone, included a highlight of 8.7 m at 228.85 m of 5.21% Cu, 0.47 g/t Au, 26.68 g/t Ag, within a broader zone over 23.4 m containing 2.39% Cu, 0.32 g/t Au and 11.61 g/t Ag. The drillhole intersected strongly deformed migmatite hostrock with foliaform and disseminated bornite and chalcopyrite (Selkirk Copper Mines Inc., 2025).

BMC Minerals Ltd.'s Kudz Ze Kayah (KZK) project contains the ABM deposit (consisting of the ABM and Krakatoa zones). The ABM deposit is a replacement-style polymetallic volcanic-hosted massive sulphide (VHMS) deposit with a proposed open-pit and underground mine for zinc, silver, copper, gold and lead. The company received a positive decision document from the governments of Yukon and Canada in June 2022, approving the proposed mine to proceed to the regulatory phase (reaffirmed in March 2024 with specific terms and conditions; YESAB, 2024), and submitted Type A Water License and Quartz Mining License applications in September 2022.

In 2025, the company completed a Superconducting Quantum Interference Device Fixed-Loop Electro-

Table 1. Selkirk Copper Mines Inc.'s Indicated and Inferred Mineral Resource Estimate at the Minto property, effective April 7, 2025 (Bird and O'Farrell, 2025).

Type	Class	Tonnage (Kt)	Cu (%)	Au (g/t)	Ag (g/t)	Cu (Mlbs)	Au (Koz)	Ag (Koz)
Open pit	Indicated	6085	0.897	0.274	2.9	120.3	53.7	560.4
Open pit	Inferred	9496	0.702	0.162	2.4	146.9	49.3	738.4
Underground	Indicated	6504	1.489	0.636	5.6	213.5	132.9	1167.6
Underground	Inferred	14 162	1.281	0.539	4.9	399.9	245.4	2229.6
Total	Indicated	12 588	1.203	0.461	4.3	333.8	186.6	1728
Total	Inferred	23 658	1.048	0.387	3.9	546.8	294.7	2968.1

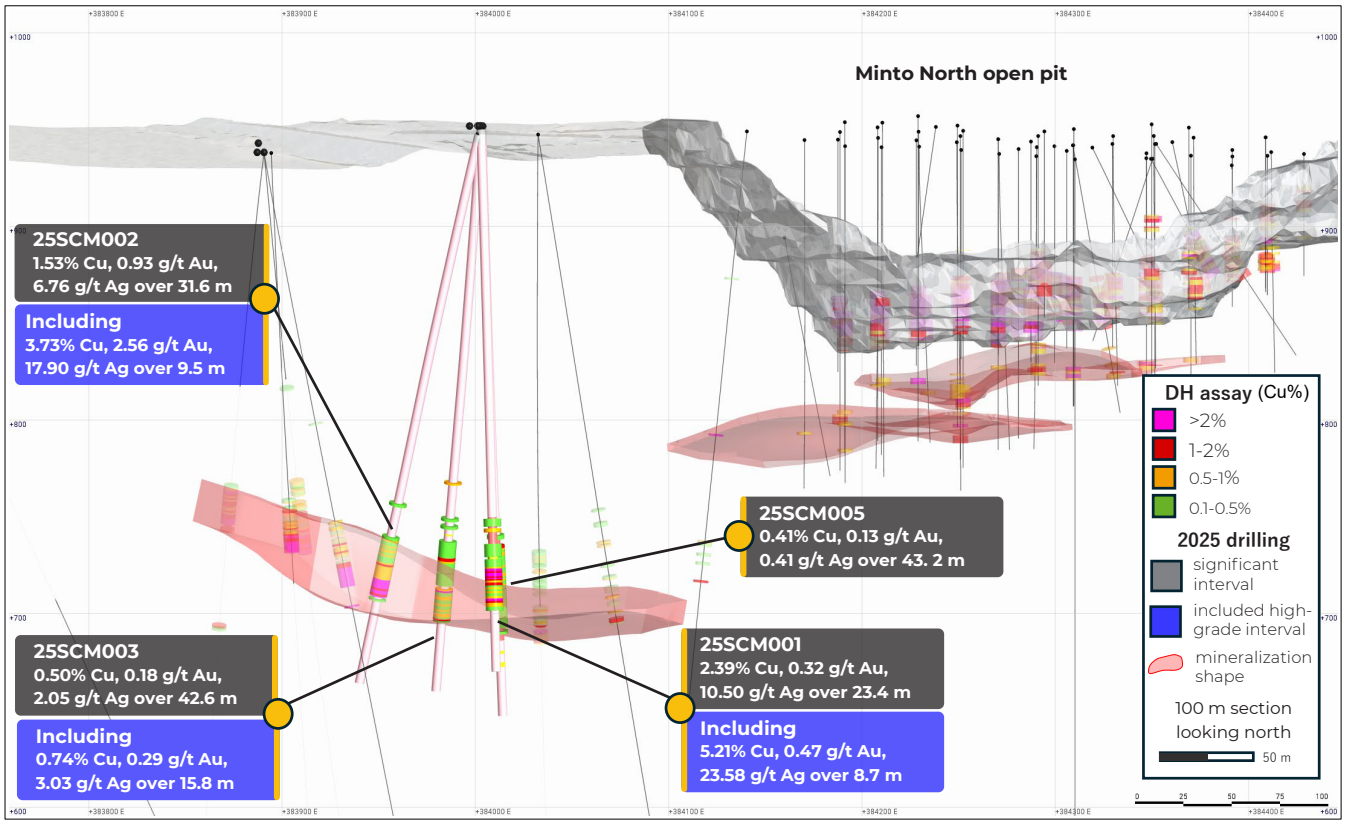


Figure 11. *Cross-section looking north-northeast, highlighting the Minto North West zone and showing select intersections from the Selkirk Copper Mines Inc.'s 2025 drill program (Selkirk Copper Mines Inc., 2025).*

magnetic (SQUID FLEM) survey covering Rhyolite Peak, Fuego and adjacent targets. A detailed structural study around the Fault Creek and East Fault areas was also conducted. Baseline environmental studies continued at KZK, positioning the project for future advancement.

Western Copper and Gold Corp.'s Casino project is one of Canada's largest undeveloped copper-gold porphyry deposits. The Casino project received strategic investments by Rio Tinto Corp. in 2024 ($5 M) maintaining Rio Tinto's ownership of approximately 9.7% of Western Copper and Gold's outstanding common shares (Western Copper and Gold Corp., 2024). In October 2025, the company submitted its Environmental and Socio-economic Effects Statement (ESE) representing an important step in the permitting process for the Casino project. In June 2025, Western Copper and Gold Corp. released and updated economic impacts assessment detailing the direct, indirect and induced effects of the proposed project (Western Copper and Gold Corp., 2025).

Following the acquisition of the Coffee Gold project from Newmont Corp., Vancouver-based exploration and development company, Fuerte Metals Corp., filed an NI 43-101 technical report and released an updated MRE consisting of a Measured and Indicated gold resource of 2.96 Moz at 1.15 g/t Au, and an Inferred gold resource of 0.8 Moz at 1.17 g/t Au (Table 2; Fuerte Metals Corp., 2025). Baseline economic and environmental studies on the project are ongoing. Fuerte Metals adds the Coffee Gold project to its portfolio of copper gold assets including those in Chile and Mexico (San Martin et al., 2025).

Exploration activities in 2025

Exploration activities and exploration-related expenditures were dominantly in the Mayo Mining District, which has been a consistent trend in the last few years. The Mayo Mining District comprises the Clear Creek, Keno and Mayo regions, as well as most of the Selwyn basin northwest of the North Canol Road (Fig. 3). The majority of exploration was focused on searching for reduced intrusion-related gold (RIRG), high-grade silver-lead-zinc veins, tungsten skarn and sediment-hosted massive sulphide.

Table 2. Fuerte Metals Corp.'s Measured, Indicated and Inferred Mineral Resource Estimate at the Coffee property, effective August 21, 2025 (San Martin et al., 2025).

Category	Tonnage (Kt)	Au (g/t)	Au (Koz)
Measured	1200	1.8	69
Indicated	78 846	1.14	2888
Inferred	21 200	1.17	800
Total	101 246		3757

Table 3. Snowline Gold Corp.'s Measured, Indicated, and Inferred Mineral Resource Estimate at the Valley Gold deposit, effective March 1, 2025 (SRK Consulting (Canada) Inc., 2025).

Category	Tonnage (Kt)	Au (g/t)	Au (Moz)
Measured	69.7	1.41	3.15
Indicated	134.3	1.11	4.79
Inferred	44.5	0.62	0.89
Total	248.5		8.83

Gold exploration projects

There were 39 active gold exploration projects in 2025. These projects accounted for 52.0% ($93.8M) of the total exploration expenditure.

Snowline Gold Corp. filed an updated MRE and an independent Preliminary Economic Assessment (PEA) for the Valley deposit at their Rogue project. The MRE incorporated recent exploration campaigns resulting in Measured and Indicated resources of 7.94 Moz at 1.21 g/t Au and Inferred resources of 0.89 Moz at 0.62 g/t Au (Table 3; SRK Consulting (Canada) Inc., 2025). The company continued exploration at the Rogue property with a 26 000-m drill program across 72 holes. Of this total, 20 000 m was allocated to advancing their understanding of the Valley deposit, and 6000 m was directed at regional targets (i.e., Cujo, Ramsey, Aurelius, Gracie, JP, Duke and Charlotte) on the property; some of these being drill-tested for the first time (Snowline Gold Corp., 2025a,c). Highlights at Valley include the intersection of a new zone of sheeted quartz veining along the previously untested eastern margin of the Valley intrusion, well beyond the extent of the current pit shell in drillhole V-25-143 (Figs. 12 and 13; Snowline Gold Corp., 2025b). Other work at Valley included geotechnical and surface characterization, surface and groundwater hydrology studies, and continued environmental baseline surveying, which has positioned the project for future potential permitting and development.

Exploration work also continued at Snowline's nearby orogenic Einarson project where 3500 m was drilled across eight holes. A major step-out drillhole at the Jupiter target returned a 5.5 m intercept at 2.6 g/t Au, 550 m beyond previous drilling (Snowline Gold Corp., 2025c).

Banyan Gold Corp. filed an NI 43-101 technical report supporting an updated pit-constrained MRE consisting of 2.274 Moz Au at 0.63 g/t in the Indicated category, and 5.453 Moz Au at 0.60 g/t in the Inferred category across the Powerline and Airstrip deposits at their AurMac Gold project (Table 4; Hantelmann et al., 2025). The company completed an exploration program at AurMac consisting of approximately 42 000 m across 193 drillholes focusing on advancing the understanding of mineralized domains in the Airstrip and Powerline deposits (Banyan Gold Corp., 2025a). The program also tested high-priority regional targets identified in previous geophysical and surface geochemical surveys. Highlights to date include 104.4 m at 0.82 g/t Au, including 33.2 m at 1.44 g/t Au in drillhole AX-25-679 at the southern extent of the Airstrip deposit (Banyan Gold Corp., 2025b). The company also completed a soil sampling program on their neighbouring Nitra project and filed an NI 43-101 report and updated MRE for their Hyland Gold project in southeast Yukon (Table 5; Armitage and Eggers, 2025).

Sitka Gold Corp. filed an NI 43-101 technical report and released an updated MRE for the near-surface Blackjack deposit at their RC Gold project, outlining an Indicated gold resource of 1.29 Moz at 1.01 g/t Au and an Inferred resource of 1.04 Moz at 0.94 g/t Au (Table 6; Simpson, 2025). Including the existing resource at Eiger, this brings the global resource for the RC Gold project to 2.8 Moz Au, more than double their total resource that was released in 2023.

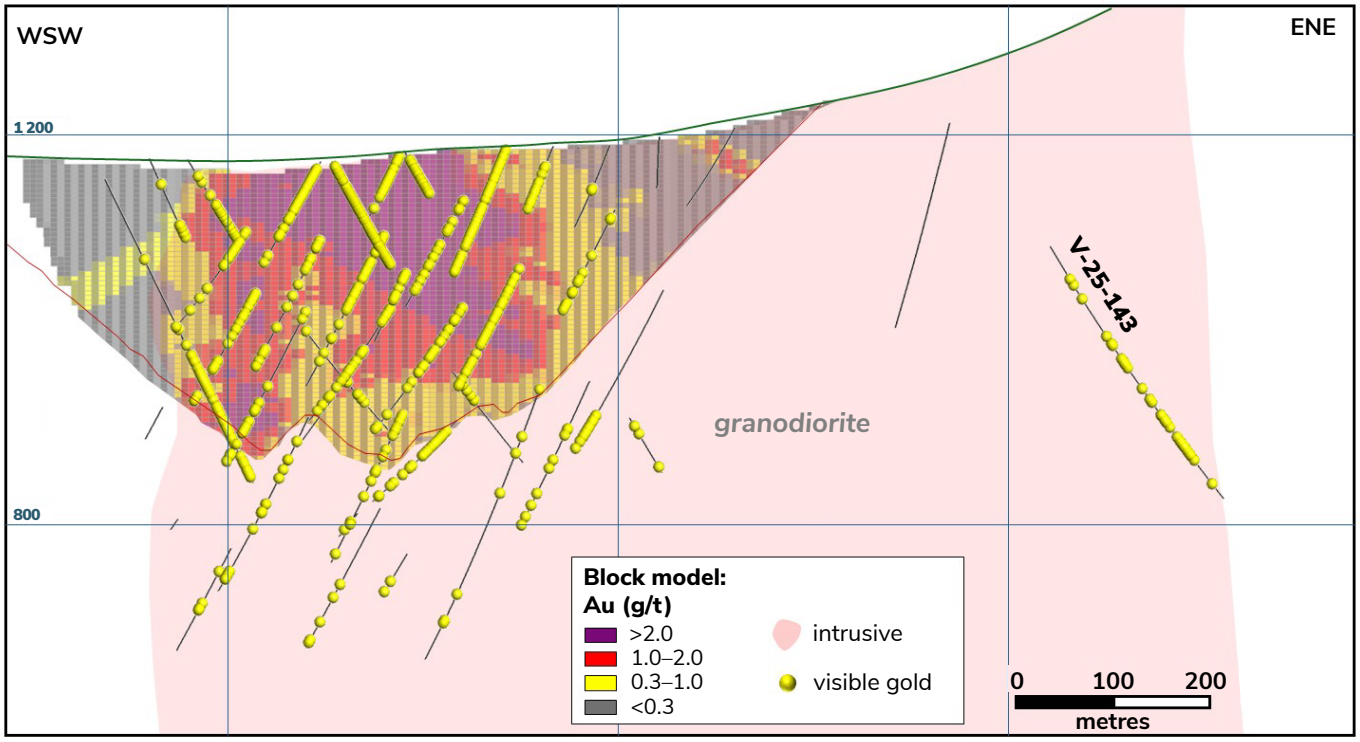


Figure 12. *Cross-section of Snowline Gold Corp.'s Valley deposit showing the location of step-out hole V-25-143 relative to the existing block model; WSW – west-southwest; ENE – east-northeast (Snowline Gold Corp., 2025b).*

Following the release, the company commenced exploration at the RC Gold project including approximately 32 000 m across 91 drillholes focusing on exploration at the Blackjack and Eiger deposits, as well as Rhosgobel, Pukelman, Saddle, Contact, Bear Paw and MayQu targets (Sitka Gold Corp., 2025). Of the 91 drillholes, 43 drillholes (12 722 m) were dedicated to Rhosgobel following the drilling success made there in 2024. Select drilling highlights at Rhosgobel returned 235.9 m at 1.11 g/t Au from surface and included 40.0 m at 2.01 g/t Au in drillhole DDRCRG-25-010; the elevated gold values are associated with quartz veining in feldspar megacrystic quartz monzonite (Sitka Gold Corp., 2025). The company also reported anomalous tungsten mineralization in the form of scheelite at the Rhosgobel target. This includes 75.50 m of 0.132% WO_3 in drillhole DDRCRG-24-002, which was reprocessed in 2025 for tungsten analysis.

Table 4. Banyan Gold Corp.'s Indicated and Inferred Mineral Resource Estimate at the AurMac property (Airstrip and Powerline zone), effective June 28, 2025 (Hantelmann et al., 2025).

Category	Tonnage (Kt)	Au (g/t)	Au (Moz)
Indicated (Airstrip)	27.7	0.69	0.611
Indicated (Powerline)	84.8	0.61	1.663
Inferred (Airstrip)	10.1	0.75	0.245
Inferred (Powerline)	270.4	0.6	5.208
Total	393		7.727

Table 5. Banyan Gold Corp.'s Indicated and Inferred Mineral Resource Estimate at the Hyland Gold property, effective September 1, 2025 (Armitage and Eggers, 2025).

Category	Tonnage (Kt)	Au (g/t)	Ag (g/t)	Au (Koz)	Ag (Koz)
Indicated	11272	0.93	7.27	337	2634
Inferred	3865	0.95	6.94	117	863
Total	15137			454	3497



Figure 13. *Photos of drill core from hole V-25-143. The interval shown is from 427.0 m to 443.5 m downhole and highlights light to intense sheeted quartz veins cutting the Valley intrusion. These sheeted quartz veins occur along the eastern edge of the Valley intrusion, which was previously assumed to be unmineralized (Snowline Gold Corp., 2025b).*

Seabridge Gold Inc. continued exploration at their 3 Aces project drilling 2442 m across 10 drillholes to advance their understanding of select targets. Additionally, the company conducted regional till sampling, a very low frequency (VLF)-magnetic survey, geologic mapping and prospecting.

Klondike Gold Corp. completed 5159 m across 31 diamond drillholes on their Klondike property. The drilling focused on testing major gold-bearing structures along the Eldorado Fault Corridor. Other activities included prospecting, geologic mapping and relogging to advance their understanding of key target areas (Klondike Gold Corp., 2025).

White Gold Corp. released an NI 43-101 technical report and updated MRE for its White Gold Project, which hosts four, near-surface gold deposits in close proximity that are interpreted to represent a structurally controlled orogenic gold system (White Gold Corp., 2025a). The updated resource includes an Indicated resource of 1.7 Moz at 1.53 g/t Au and an

Table 6. Sitka Gold Corp.'s Indicated and Inferred Mineral Resource Estimate at the Blackjack deposit, RC Gold property, effective January 21, 2025 (Simpson, 2025).

Category	Tonnage (Kt)	Au (g/t)	Au (Koz)
Indicated	39 962	1.01	1291
Inferred	34 603	0.94	1044
Total	74 565		2335

Inferred resource of 1.3 Moz at 1.22 g/t Au across the four deposits (Table 7; Arseneau, 2025). Exploration programs on the property continue to test the expansion potential of mineralized structures. White Gold Corp. drilled 2100 m at Golden Saddle and Arc deposit areas. Initial results from the program include 50.2 m of 6.9 g/t Au in the Golden Saddle Main zone in drillhole WHTG25D0218A. The interval is associated with quartz veining, brecciation and disseminated mineralization within altered felsic orthogneiss (White Gold Corp., 2025b). Exploration programs at White Gold's Nolan and Loonie properties were YMEP-supported and included 24 line-kilometres of induced polarization (IP) geophysics at Loonie and 32 line-kilometres of IP at Nolan.

Trifecta Gold Ltd. conducted exploration programs at their Mt. Hinton and Rye projects in 2025. A total of 753 m of diamond drilling was completed at Mt. Hinton, which was initiated as a follow-up on geophysical targets from previous projects. The drilling was also testing for evidence of a buried intrusion in the underexplored areas of the property (Trifecta Gold Corp., 2025c). At Rye, 1992 m of drilling was completed in six holes. The holes tested surface geochemical anomalies and associated sheeted veins identified in previous exploration programs within mid-Cretaceous intrusive rocks as well as surrounding hornfels (Trifecta Gold Corp., 2025b). Drillhole RY-25-01 intersected 224 m of hornfels (from surface) hosting sheeted quartz-pyrrhotite-chalcopyrite ± arsenopyrite ± scheelite veins with densities greater than 25 per metre (Fig. 14; Trifecta Gold Ltd., 2025a). In addition to the drill programs, 103 rock samples were collected at Mt. Hinton, and 66 at Rye. A highlighted quartz-vein rock sample at Rye returned 21.1 g/t Au and 8550 ppm bismuth (Trifecta Gold Ltd., 2025a).

Table 7. White Gold Corp.'s Indicated and Inferred Mineral Resource Estimate at the White Gold project, effective August 19, 2025 (Arseneau, 2025).

Type	Class	Tonnage (Kt)	Au (g/t)	Au (Koz)	Ag (Koz)
Open pit	Indicated	35 143	1.53	1730	2634
Open pit	Inferred	32 065	1.2	1242	863
Under-ground	Indicated	23	2.84	2	3497
Under-ground	Inferred	232	3.2	23	
Total		67 463		2997	

Prospector Metals Corp. conducted an exploration program at their ML project including 6649 m of diamond drilling in 39 holes testing seven different target areas (Prospector Metals Corp., 2025b). Mineralization at the Skarn Ridge target included 45.65 m of 2.11 g/t Au, 0.48% Cu, and 9.48 g/t Ag in hole ML25-010 in strongly calc-silicate altered calcareous siltstone containing disseminated and vein-controlled sulphides (Prospector Metals Corp., 2025a). A Highlighted result at the North Vein target includes 44 m of 13.79 g/t Au and 1.84% Cu in hole ML25-031 in the newly discovered Tess Zone north of the North Vein (Fig. 15; Prospector Metals Corp., 2025b). The North Vein and Tess targets are reported to have an association with jarosite alteration, and the discovery was followed up with geologic mapping and rock sampling.

Copper and nickel-platinum group elements exploration projects

There were 21 active copper exploration projects, and one active nickel-PGE project in 2025. These projects accounted for 17.0% ($30.7 M) of the total exploration expenditure.

Gladiator Metals Corp. continued exploration on their Whitehorse Copper project. Their initial planned program of 29 000 m of diamond drilling was extended to 50 000 m, targeting high-grade copper skarns throughout the Whitehorse Copper Belt (Gladiator Metals Corp., 2025b). Objectives included exploration and defining drill targets at Cowley Park, as well as exploration drilling at Chiefs Trend, Best Chance,



Figure 14. *Drill core from hole RY-25-01 at Trifecta Gold Ltd.'s Rye property; sheeted vein density is greater than 25 per metre and consists of quartz-pyrrhotite-chalcopyrite ± arsenopyrite ± scheelite (Trifecta Gold Ltd., 2025a).*

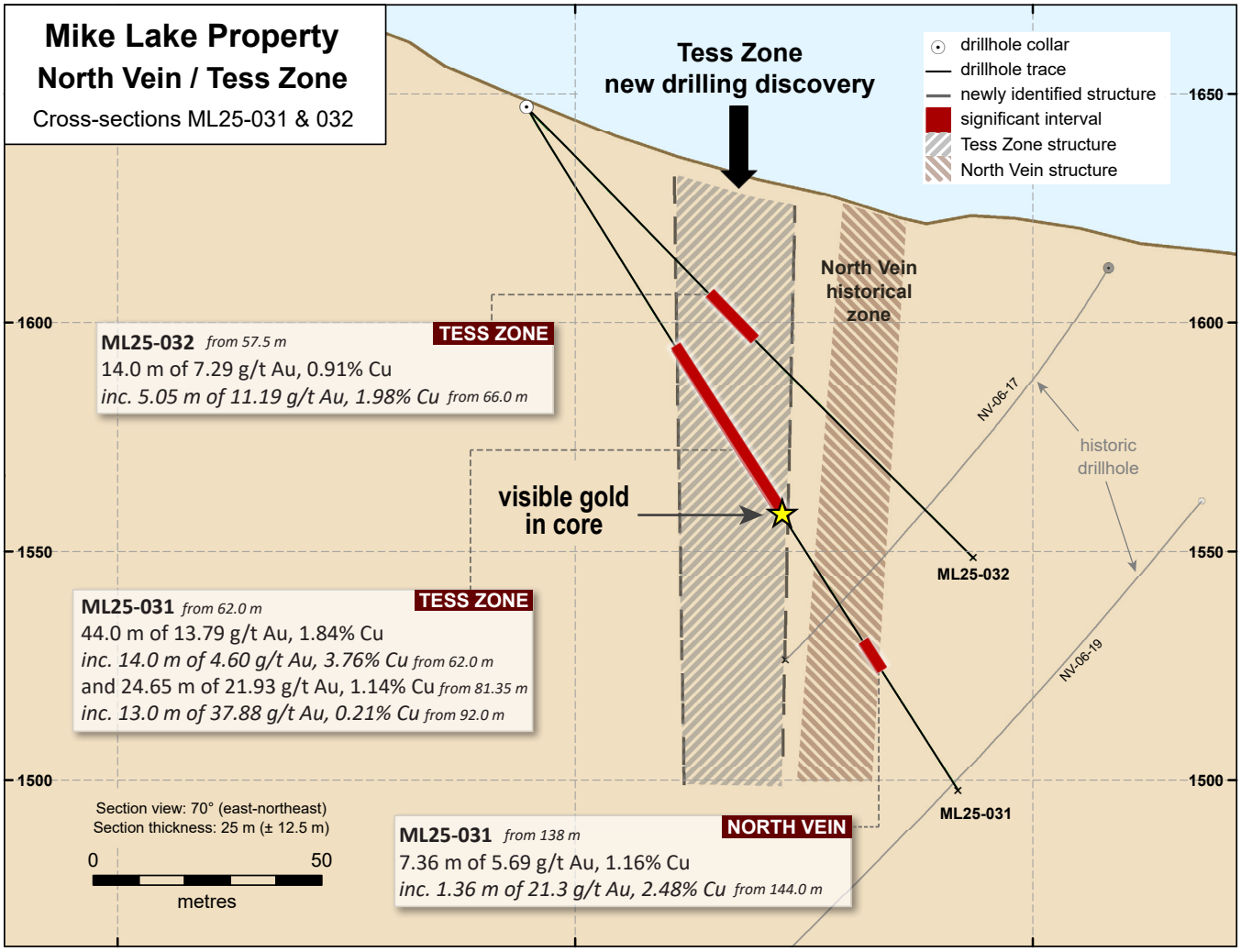


Figure 15. *Cross-section, looking east, showing the newly identified Tess zone in drillholes ML25-031 and ML25-032 at Prospector Metals Corp.'s ML project (Prospector Metals Corp., 2025a).*

Arctic Chief and Cub Trend. New geophysical targets were also identified. To date, highlighted intercepts at Cowley Park include 70.5 m at 1.13% Cu in skarn from hole CPG-094, as well as 55 m at 0.70% Cu in newly identified, granodiorite-hosted mineralization in CPG-092 (Fig. 16; Gladiator Metals Corp., 2025b). The company received a positive recommendation from the Yukon Environmental and Socio-Economic Assessment Board (YESAB) to proceed to a Class 3 License for their Whitehorse Copper project, a noteworthy milestone in the advancement of the project (Gladiator Metals Corp., 2025c).

Cascadia Minerals Ltd. conducted exploration programs across their diverse and expanding portfolio of copper and gold projects. In June, Cascadia Minerals Ltd. and Granite Creek Copper Ltd. announced a merger agreement whereby Cascadia Minerals acquired Granite Creek's flagship asset, the Carmacks project, located in the Minto copper district. Following completion of the agreement, Cascadia Minerals drilled 3848 m across 11 drillholes at the Carmacks Project focusing on step-out holes at the Carmacks Main Deposit (Fig. 17; Cascadia Minerals Ltd., 2025c). Initial results include 83.52 m of 0.89% Cu and 0.26 g/t Au in drillhole CD-25-033 at the 147 Zone (Cascadia Minerals Ltd., 2025d).

Cascadia Minerals continued exploration at their Catch project, including 741 m across three holes at the Amp Zone, where a surface sample returned 1065 g/t Au and 267 g/t Ag in 2024 (Cascadia Minerals Ltd., 2025a). The 2025 drill program at the Amp Zone did not identify the source of high-grade surface samples (Cascadia Minerals Ltd., 2025b). Geologic mapping and prospecting programs were conducted at their Milner

and Macks Copper projects (YMEP-supported), as well as at their Idaho Creek and Rosy projects.

Forge Resources Corp. carried out exploration at their Alotta project consisting of more than 2600 m of diamond drilling across nine holes. The program was designed to follow up on previous drilling at the Payoff and Severance targets, as well as the previously untested Commission and Alimony targets (Forge Resources Corp., 2025a). Drillhole ALT-25-012 intersected veined and altered granodiorite and porphyritic rocks including a 10 cm vein hosting coarse native gold at the Payoff Zone (Fig. 18; Forge Resources Corp., 2025b). Complete results are still pending, but the company has reported an intersection that includes 3.15 m of 45.01 g/t Au from hole ALT-25-012 at their Payoff Zone (Forge Resources Corp., 2025c).

Yukon Metals Corp. conducted work on their Birch, Talbot Creek, Fairway (YMEP-supported), Star River and Az properties in 2025. At Birch, a total of 1684 m was drilled over six holes that includes a highlight of 21.2 m of 0.30% Cu in skarn horizons hosted in schists adjacent to intrusive contacts (Yukon Metals Corp., 2025a). Additionally, a surface exploration program at Birch returned anomalous samples 2 km south of the 2025 drilling area. At Az, the company drilled 1489 m across five holes targeting the Chair Mountain and Southeast targets. Highlights from drilling include 14.4 m of 0.44% Cu associated with quartz-

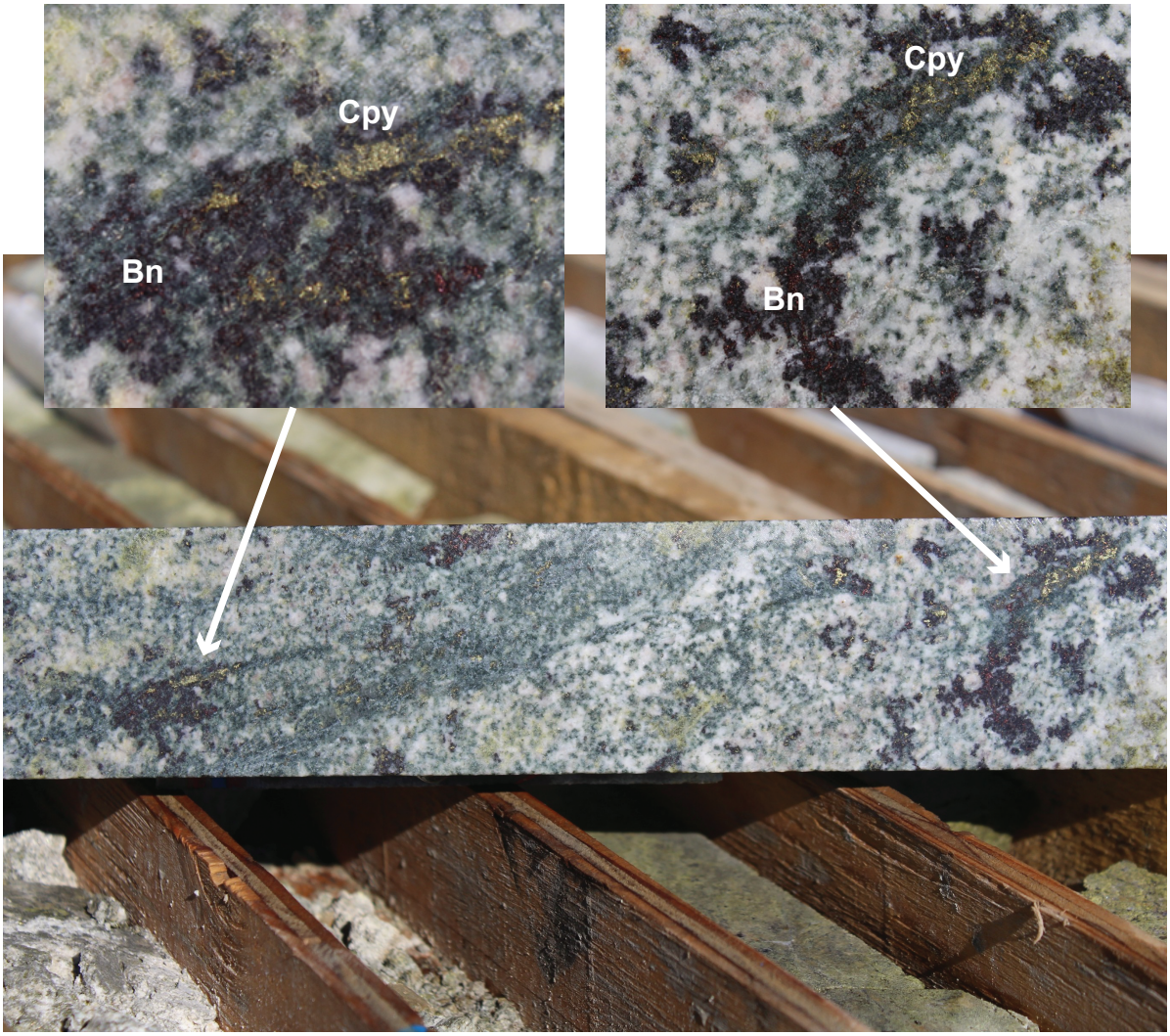


Figure 16. *Gladiator Metals Corp.'s newly identified granodiorite-hosted mineralization in drillhole CPG-092 at Cowley Park, Whitehorse Copper project. Mineralization consists of disseminated and blebby bornite (Bn) and chalcopyrite (Cpy) replacing chlorite-altered mafic minerals (Gladiator Metals Corp., 2025a).*

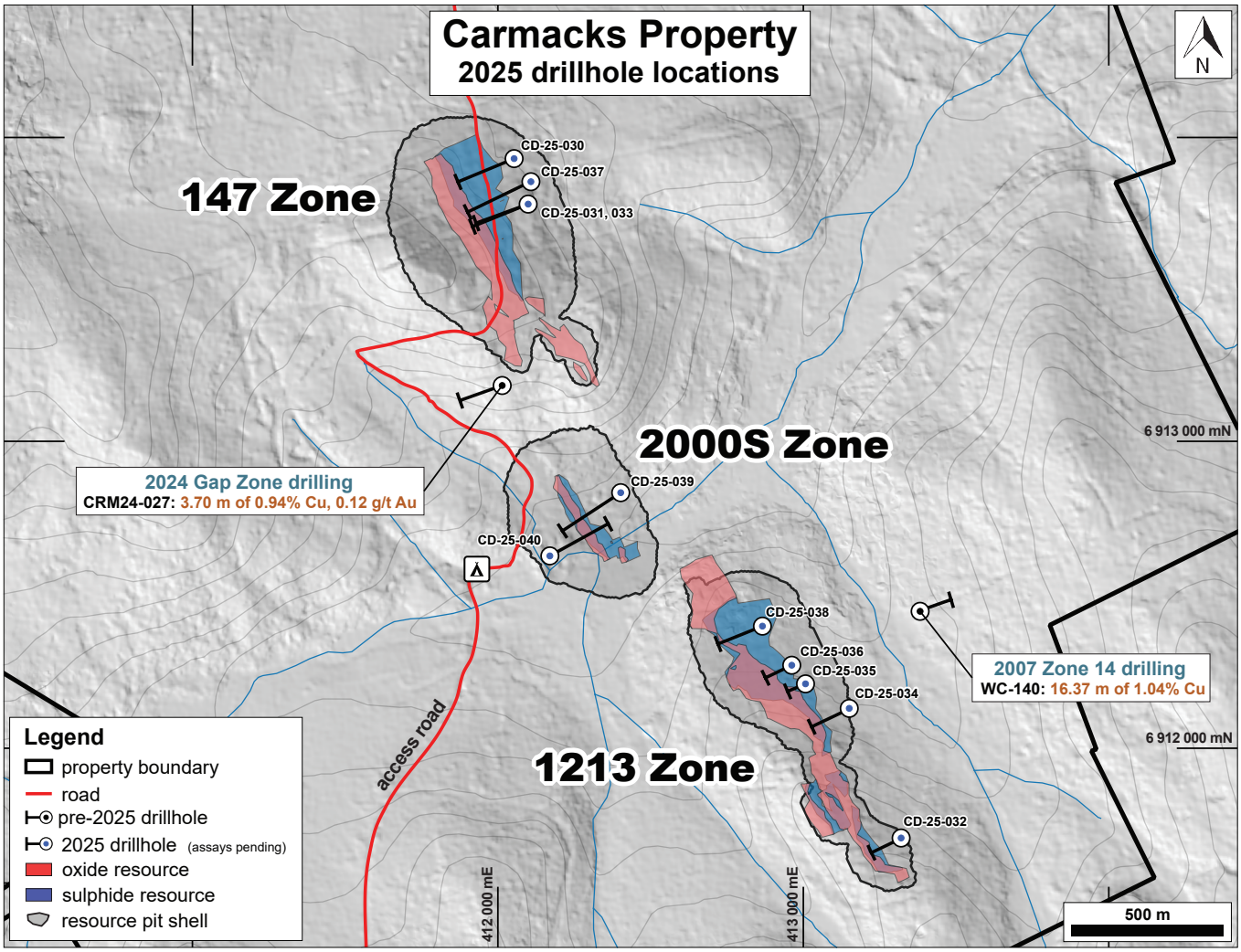


Figure 17. *Cascadia Minerals Ltd.'s 2025 drill plan for the Carmacks property. Drilling focused on step-out holes at the Carmacks Main deposit, with the goal of expanding sulphide resources (Cascadia Minerals Ltd., 2025c).*

carbonate veining in basalt, as well as volcaniclastic and siliciclastic rocks at the Chair Mountain target (Yukon Metals Corp., 2025b). The company interprets alteration, geochemistry and mineralogy to be indicative of a porphyry system. At Star River, 1591 m was drilled over eight holes targeting geophysical indicators in near-surface showings. Drill results were still pending at the time of writing, but the company reported intersections of vein swarms containing pyrite, arsenopyrite, quartz, ankerite and galena in quartzite and dolostone (Yukon Metals Corp., 2025c). Additionally, the company conducted prospecting and rock sampling, a gravity infill survey, and flew a high-resolution unmanned aerial vehicle (UAV) drone magnetic survey across the property. At Talbot and Fairway properties, Yukon Metals conducted mapping and surface sampling programs.

Silver, lead-zinc and tungsten exploration projects

A total of 15 silver and lead-zinc projects, as well as two tungsten exploration projects were active in 2025. Together, these projects accounted for 30.9% ($55.8 M) of the total exploration expenditure.

Fireweed Metals Ltd. conducted an exploration program at their Macmillan Pass lead-zinc project consisting of 8723 m across 24 drillholes. The drill program advanced high-priority regional targets with 3791 m across 12 drillholes, and extensions around known deposits with 4932 m across 12 drillholes at the Tom and Boundary zones. Additionally, the company continued regional exploration efforts across their tenure and carried out focused and regional gravity and seismic surveys, mercury gas surveys, ambient noise

tomography, surface prospecting and geochemical sampling, and baseline environmental studies (Fireweed Metals Corp., 2025a). Drillhole TS25-001D1 at Tom South showcased the expansion potential of the deposit beyond the current resource having a 30 m true width (54.82 m core width) intersection of 18.20% Zn, 13.93% Pb and 161.0 g/t Ag in a down-dip test 115 m beyond known mineralization. The highlighted interval was associated with laminated to massive sphalerite, galena and minor chalcopyrite (Fig. 19; Fireweed Metals Corp., 2025b).

The company completed a program at their Mactung property to support an upcoming updated feasibility study. The program included 11 117 m of drilling across 66 drillholes, and ongoing environmental baseline field work. Of the total metreage drilled, 1545 m aimed to advance hydrological and geotechnical studies (Fireweed Metals Corp., 2025a). Drilling confirmed the high-grade nature of the deposit having intersections that included 12 m of 6.21% WO_3 in drillhole MT25-048 (Fireweed Metals Corp., 2025c). Mactung is a tungsten skarn deposit associated with a mid-Cretaceous granitic intrusion in eastern Yukon. The deposit straddles the border between the Yukon and Northwest Territories and is the largest known high-grade tungsten resource in the world (Fireweed Metals Corp., 2023).

Cantex Mine Development Corp. conducted a diamond drill program consisting of 3620 m across 16 holes at their North Rackla project. The program focused on continuing to understand regional targets including the Copper Zone, as well as follow up on previous programs at the Main Zone.

Silver North Resources Ltd. carried out exploration programs at their Haldane and Veronica silver properties. The YMEP-supported program at Veronica consisted of prospecting, geologic mapping and

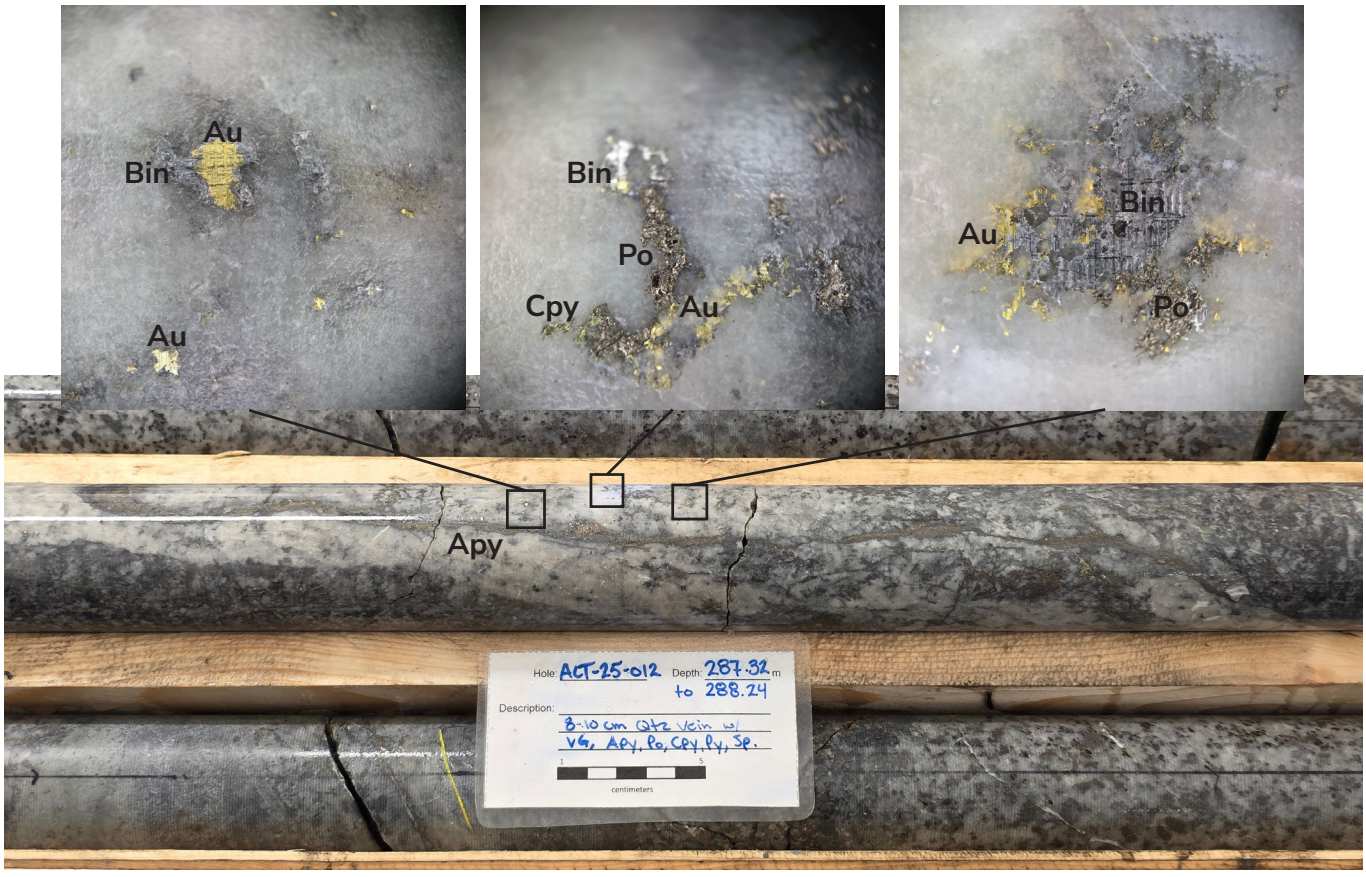


Figure 18. *Forge Resources Corp.'s Alotta project drill core showing a ~10 cm-wide quartz vein cutting granodiorite and containing coarse native gold (Au), bismuthinite (Bin), pyrrhotite (Po), chalcopyrite (Cpy) and arsenopyrite (Apy) in hole ALT-25-012. Pyrite, molybdenite and sphalerite also occur, but are not visible in this figure (Forge Resources Corp., 2025b).*

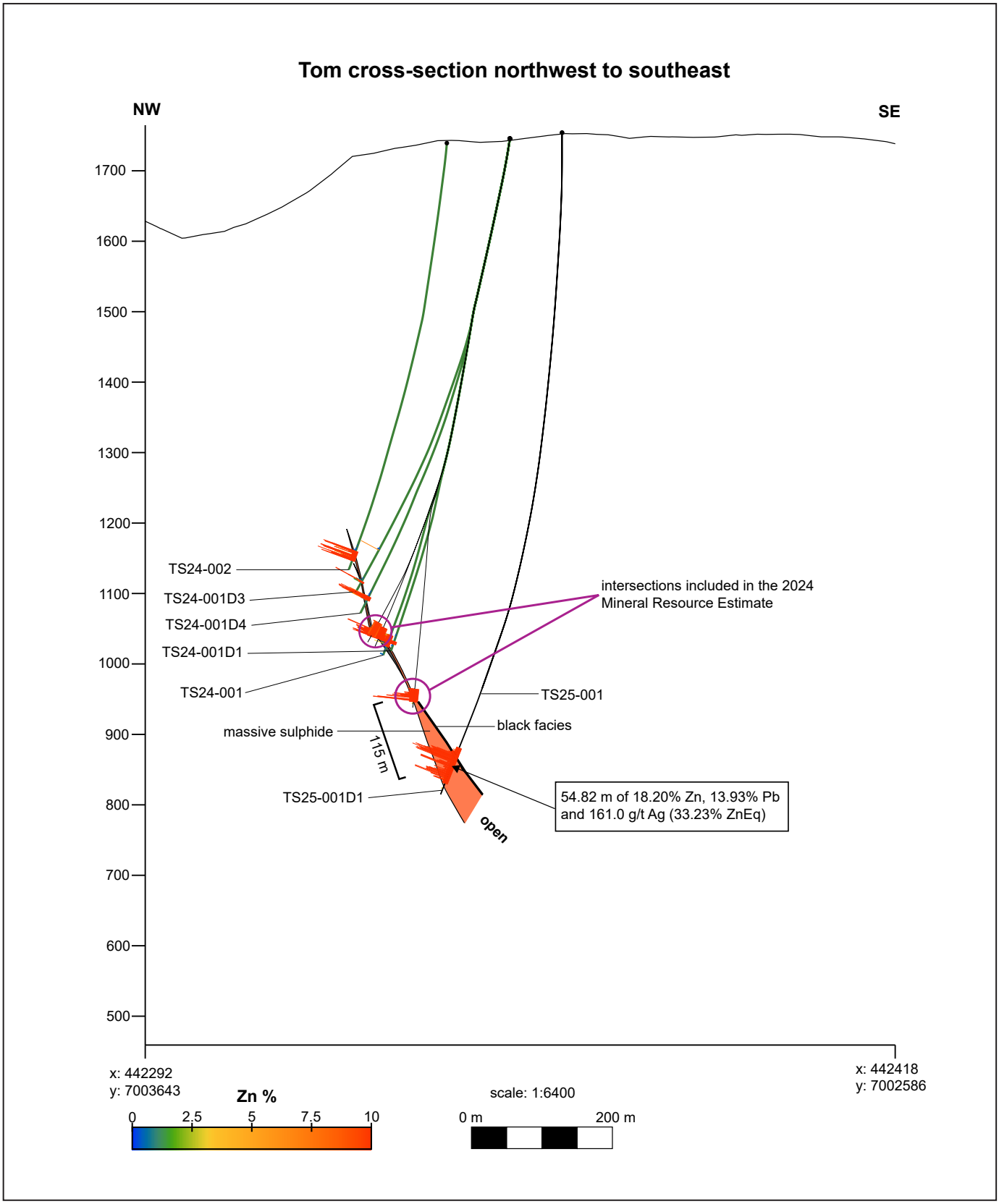


Figure 19. *Cross-section of 2025 drillholes at Fireweed Metals Corp.'s Tom South zone. Hole TS25-001D1 intersects mineralization 115 m beyond the drilling results that were included in the 2024 MRE; NW – northwest; SE – southeast (Fireweed Metals Corp., 2025b).*

surface geochemistry as a follow-up on an existing soil geochemical anomaly. The program identified float samples containing up to 2860 g/t Ag, as well as outcrop samples containing up to 33.7 g/t Ag (Silver North Resources Ltd., 2025a). At the Haldane silver property, the company drilled 1760 m across eight holes, which was designed to follow up on expansions of Keno-style, silver-lead-zinc mineralization at the Main Fault target. Results included a highlighted interval of 13.15 m of 818 g/t Ag and 1.39 g/t Au (Silver North Resources Ltd., 2025b).

Honey Badger Silver Inc. carried out exploration and data review programs at their Plata project. The YMEP-supported program focused on geologic mapping and sampling of new target areas to further assess the potential of the property (Honey Badger Silver Inc., 2025). The field program, in combination with the data review program, led to the identification of multiple new silver and gold zones (i.e., Canela, Inferno and Pimento).

Yukon Mineral Exploration Program

The Yukon Mineral Exploration Program (YMEP) is a Government of Yukon-funded program designed to support early-stage exploration by individual prospectors and companies. The funding supports placer and hardrock exploration projects by reimbursing a percentage of approved exploration expenditures. The program comprises three types of varying reimbursement rates and funding limits: hardrock projects are eligible for either the Grassroots or Target Evaluation modules, whereas placer projects can receive funding from a Target Evaluation module (Table 8). Applications for funding and submission of project proposals are due March 31st of each year. Detailed information on project modules, eligibility and levels of funding can be found in the YMEP guidebooks at https://yukon.ca/en/doing-business/funding-and-supports-business/apply-mineral-exploration-funding.

YMEP 2025

The total amount of YMEP funding available for the 2025–26 season was $1.4 M. The program was oversubscribed, and 71 applicants sought $2.5 M in funding. The breakdown of applications is shown in Table 8 and the geographic distribution of funded projects is shown in Figure 20. As of November 30, 2025, 39 applicants had funding agreements in place for the 2025–26 fiscal year: 20 (51%) hardrock and 19 (49%) placer; 7 projects withdrew their applications or were ineligible for funding. An estimated $3.8 M was spent on all YMEP-supported projects, $2.4 M from industry and $1.4 M from YMEP. Hardrock projects accounted for $1.7 M of all program spending: $1.0 M from industry and $700 K from YMEP. Placer projects accounted for $2.1 M: $1.4 M from industry and $700 K from YMEP.

In 2023, YGS modified the YMEP evaluation criteria for hardrock applications to encourage exploration for critical mineral targets. Up to 10% of the total application score was assigned to projects targeting critical minerals; 5% was assigned for projects that included critical minerals as a secondary target. In 2025, 19 hardrock projects included at least one critical mineral as a target. In 2024, the Focused Regional hardrock module was eliminated and the funding cap for the Grassroots module was increased to $25 000. These two changes resulted in 40% of hardrock projects being Grassroots in 2025, and 45% in 2024, levels not seen in the YMEP since the early 2000s.

Table 8. Yukon Mineral Exploration Program 2025-2026 application and funded project numbers.

Type	Reimbursement percentage	Module	Total applicants	Total approved	Active	Withdrawn/ ineligible
Hardrock	100	Grassroots	15	**10**	**8**	**3**
Hardrock	50	Target Evaluation	28	**13**	**12**	**2**
Placer	50	Target Evaluation	28	19	19	2
Total			**71**	**42**	**39**	**7**

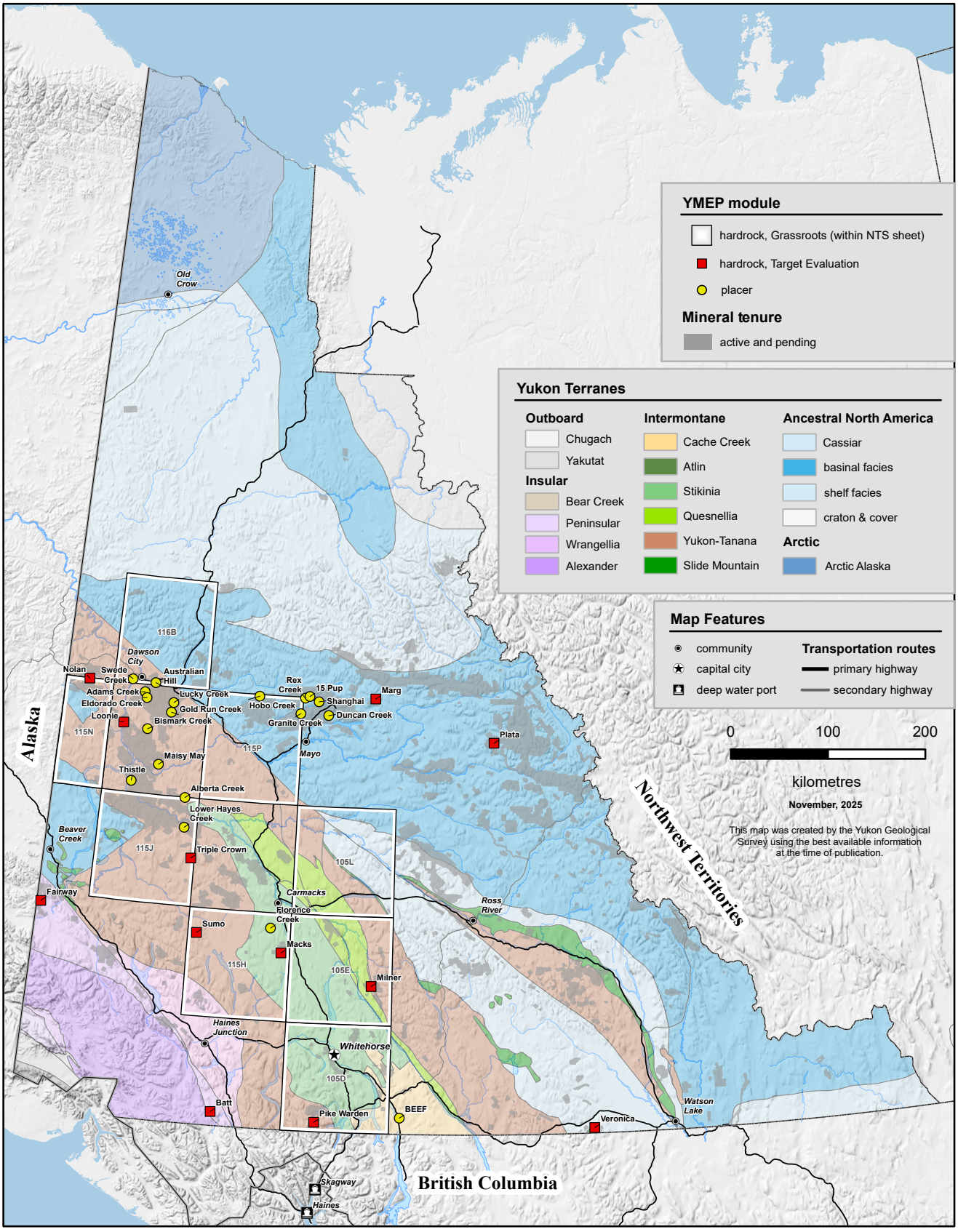


Figure 20. *Geographical distribution of YMEP-supported projects in the Yukon for the 2025-26 fiscal year.*

Impacts of YMEP

The intent of the YMEP program is to support early-stage projects and stimulate new mineral discoveries in the Yukon. Several indicators can be used to measure the success of the program, including local economic benefits, leveraged dollars, new discoveries, and option agreements. The economic benefits of the program not only include the potential for same-year discoveries and long-term investment, but also short-term local spending in the territory. In 2021, the YGS began collecting data from YMEP recipients to quantify the local economic impact of the program. Feedback received from 2024 YMEP recipients shows that 73% of total project expenditure stayed in the Yukon (Fig. 21).

YMEP 2025 project spotlights and discoveries

Projects that result in new discoveries or significant advancement of a target can lead to further investment in mineral exploration in the Yukon. Every year, several YMEP-funded projects stand out. Some projects raise additional funding on equity markets to conduct further work during the same field season; others enter into property option agreements. New discoveries can fuel property and district-scale exploration, and some progress to advanced stages of exploration. This section highlights one project from each of the three YMEP modules that returned exciting results in 2025, as well as a project that has seen ongoing YMEP investment and continues to yield promising results.

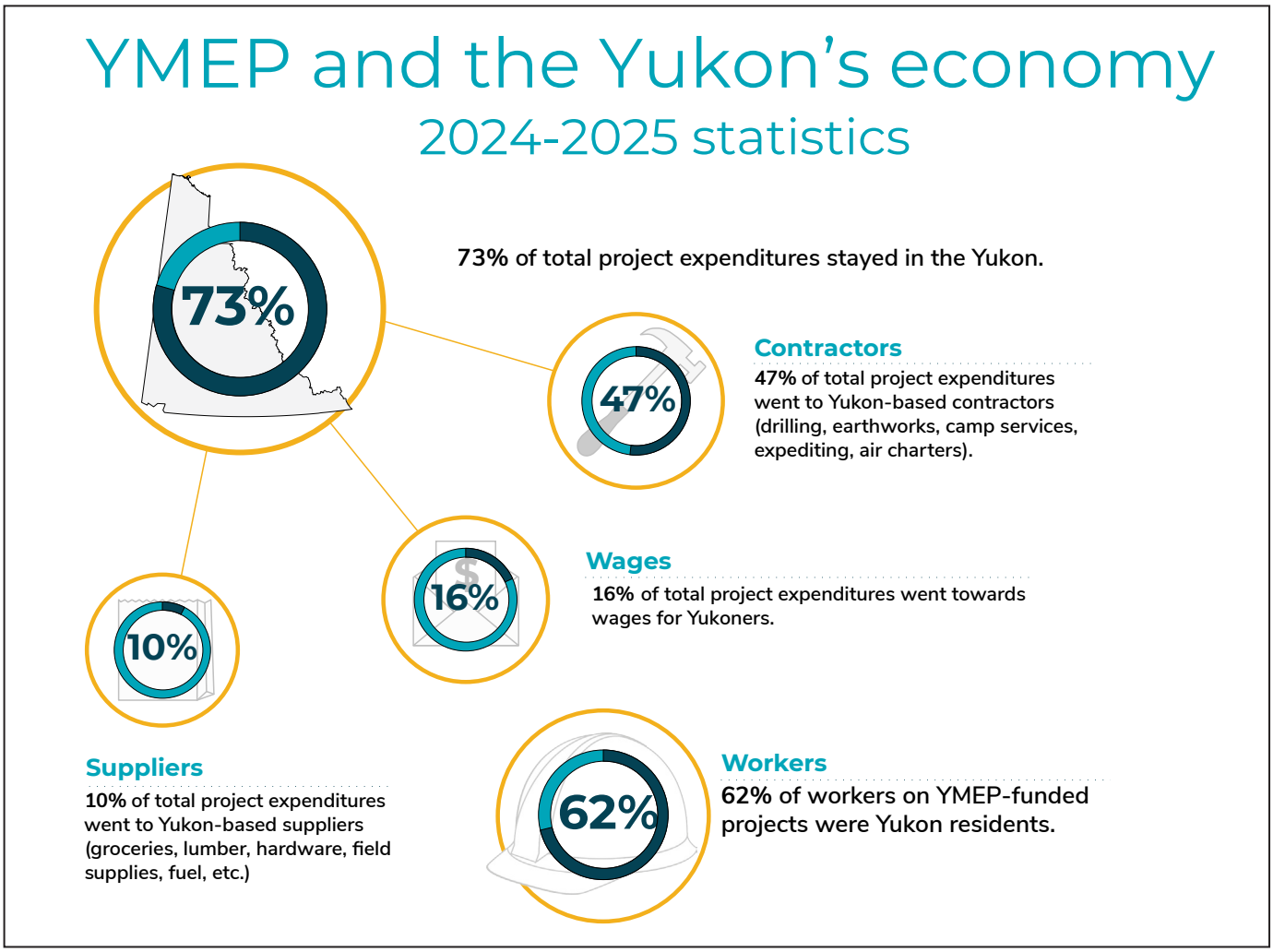


Figure 21. *Breakdown of expenditures from YMEP-funded projects in the Yukon for the 2024-25 fiscal year.*

Grassroots module:

Amauta Geo Solutions carried out a Grassroots module program (YMEP Project 25-001) consisting of soil sampling, geological mapping and prospecting to evaluate mineralization styles found at the King Lake property and the associated Suits MINFILE occurrence (Yukon MINFILE 105D 104; Yukon Geological Survey, 2020). The property previously produced a hand sample with 11.5% Cu and 2 g/t Au in 2007. The property is located approximately 25 km west-northwest of Whitehorse, centered over the King Lake pluton, a multiphase granodiorite to monzonite suite with a crystallization age of 216.35 ± 0.23 Ma by U-Pb geochronology (Sack et al., 2020). The YMEP-supported program identified soil and rock samples with anomalous values of gold, copper, molybdenum, and other supportive pathfinder elements. A highlighted rock sample returned assay values of 10.8% Cu and 1.2 g/t Au (Fig. 22). The strongest mineralization was observed in quartz carbonate veins containing malachite, chalcopyrite, bornite and pyrite.

Target Evaluation module:

Strategic Metals Ltd. completed a YMEP-supported exploration project at their Batt property in southwest Yukon (YMEP Project 25-048). The property is underlain by volcanic and volcaniclastic rocks intruded by diorite and granodiorite, and later porphyritic sills. Previous exploration on the property identified anomalous copper, cobalt and gold occurrences with characteristics of both porphyry and volcanogenic massive sulphide mineralization. The 2025 program included hand trenching, rock sampling and mapping of known occurrences to improve the understanding of the two distinct mineralization styles. Additionally, prospecting was carried out to identify new mineral occurrences. A 54 m hand trench (Fig. 23) was excavated across the known Main Ridge occurrence where a 5 m interval returned 0.52 g/t Au, 0.61% Cu and 935 ppm Co. A sample of quartz veining in silicified basalt returned 0.65% Cu located 100 m away from the identified mineralization. This new showing will be investigated further in future programs.

Placer module:

Le Fevre and Company Property Agents Ltd. conducted a YMEP-supported placer exploration program on Eldorado Creek in the Bonanza-Hunker region (YMEP Project 25-038). Eldorado Creek has a long, rich history of placer gold production dating back to the gold rush, and new discoveries of unworked horizons continue to be made through continued exploration. The program consisted of three test pits and 35 sonic drillholes totaling 230 m to investigate the potential on the left and right limits of the valley for side pay and paleo-Eldorado Creek deposits buried by landslide debris. The program successfully delineated favourable mineralization and will aid in optimizing future production.

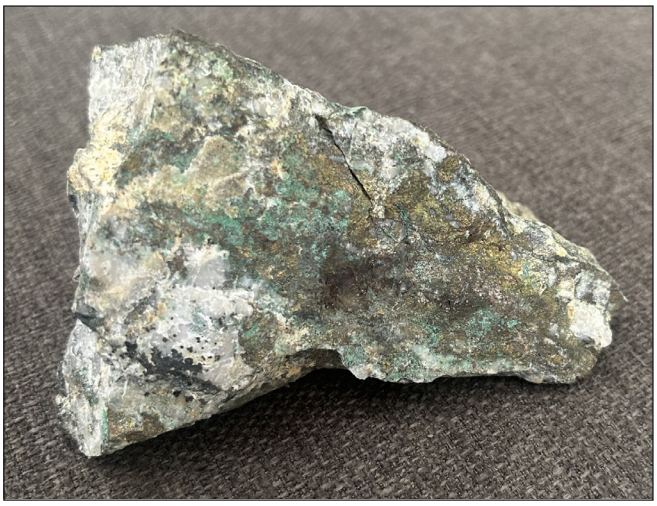


Figure 22. *Rock sample consisting of massive quartz-carbonate vein containing malachite, chalcopyrite, bornite and pyrite from Amauta Geo Solution's King Lake YMEP-supported project.*

Pike Warden project: ongoing success

Transition Metals Corp. received Target Evaluation funding for their Pike Warden property located in southern Yukon (YMEP Project 25-036). The property is situated within the Intermontane belt along the northern margin of the Bennett Lake volcanic complex. Polymetallic mineralization with elevated gold, silver, copper, lead and zinc has been found to have a structural spatial association. The 2025 program continued to build on previous YMEP-funded programs by focusing on mapping, surface sampling, and 8.9 km of IP geophysics. Rock samples from the program returned up to 1.9% Cu and 409 g/t Ag (Fig. 24; Transition Metals Corp., 2025a). The exploration program further defined targets in the Copper Junction area and identified four new showings for additional work. Following the YMEP-supported program, the company executed an inaugural drill program in the fall consisting of 504 m across two drillholes, which tested high-priority targets in the Copper Junction area. Analytical results are pending (Transition Metals Corp., 2025b).



Figure 23. *A hand trench completed at Strategic Metals Ltd.'s YMEP-supported Batt project.*

Summary

Record high gold and silver prices, high commodity prices, and numerous exploration projects progressing into the advanced stage, made 2025 a remarkable year for exploration in the Yukon. In 2025, exploration and development expenditures in the Yukon increased 51% from 2024. The 2025 exploration expenditures are projected to surpass the last high, which occurred in 2018. Numerous companies reported new discoveries and mid-season capital raises, leading to expanded exploration programs. Eight updated MREs were released in the Yukon this year.

This overview is not a comprehensive list of exploration activities in the Yukon but is meant to showcase significant developments in mining and exploration activity in the Yukon, including a mix of early and advanced exploration, infrastructure upgrades, regulatory review progressions, as well as new ownership models, particularly involving Indigenous governments. Additionally, many results were not available at the time of writing, and the reader is encouraged to continue to visit company websites for up-to-date program results in the Yukon.

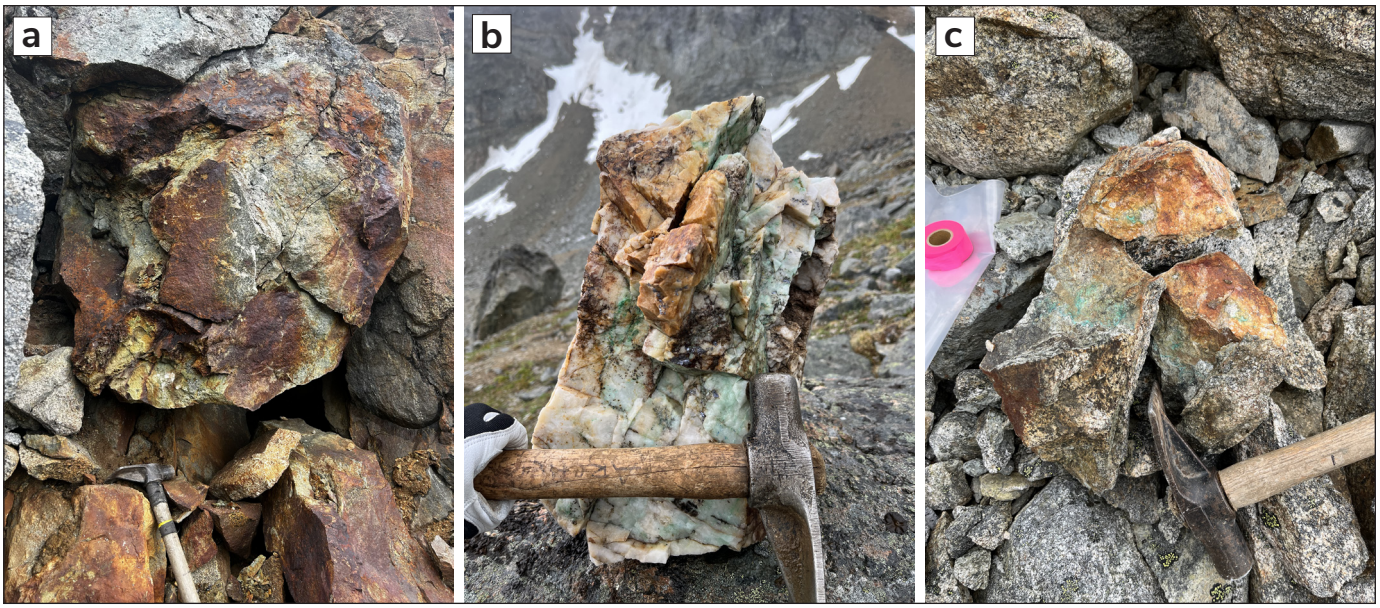


Figure 24. *Select photos of mineralized rock samples from Transition Metals Corp.'s Pike Warden project:* **(a)** *bedrock exposure rich in sulphides;* **(b)** *malachite-stained vein quartz from the Copper Junction target area; and* **(c)** *heavily malachite-stained granodiorite with minor molybdenite (Transition Metals Corp., 2025a).*

References

Armitage, A. and Eggers, B., 2025. Technical Report on the Mineral Resource Estimate for the Hyland Gold Project, Yukon Territory, Canada. NI 43-101 technical report prepared by SGS Canada Inc. for Banyan Gold Corp. Submitted October 24, 2025, 98 p., https://banyangold.com/site/assets/files/5429/hyland_gold_project_2025_43101_technical_report_including_mre_for_banyan_gold_25_10_24.pdf.

Arseneau, G., 2025. 2025 Technical report for the White Gold Project, Dawson Range, Yukon, Canada. NI 43-101 technical report prepared by Arseneau Consulting Services Inc. for White Gold Corp. Submitted August 19, 2025, 214 p., https://www.sedarplus.ca.

Banyan Gold Corp., 2025a. Banyan Gold commences fully funded 30 000+ metre diamond drill program at AurMac Project, Yukon. News release, March 27, 2025, https://banyangold.com/news-releases/2025/banyan-gold-commences-fully-funded-30-000-metre-diamond-drill-program-at-aurmac-project-yukon/ [accessed 30/10/2025].

Banyan Gold Corp., 2025b. Banyan intersects 1.44 g/t Au over 33.2 m, within 104.4 m at 0.82 g/t Au and extends mineralization between deposits, AurMac Project, Yukon, Canada. News release, September 4, 2025, https://banyangold.com/news-releases/2025/banyan-intersects-1.44-g-t-au-over-33.2m-within-104.4m-at-0.82-g-t-au-and-extends-mineralization-between-deposits-aurmac/ [accessed 30/10/2025].

Bird, S. and O'Farrell, T., 2025. NI 43-101 2025 Mineral Resource Estimate update for the Minto Property, Yukon, Canada. NI 43-101 technical report prepared by Moose Mountain Technical Services for Venerable Ventures Ltd. Submitted August 5, 2025, 167 p., https://www.sedarplus.ca [accessed 30/10/2025].

Cascadia Minerals Ltd., 2025a. Cascadia provides exploration update, announces AGM results and grant of options. News release, June 26, 2025, https://cascadiaminerals.com/cascadia-provides-exploration-update-announces-agm-results-and-grant-of-options/ [accessed 30/10/2025].

Cascadia Minerals Ltd., 2025b. Cascadia provides exploration update and appoints Vice President of Exploration. News release, September 9, 2025, https://cascadiaminerals.com/cascadia-provides-exploration-update-and-appoints-vice-president-of-exploration/ [accessed 30/10/2025].

Cascadia Minerals Ltd., 2025c. Cascadia completes drill program at its Carmacks Copper-Gold Project, Yukon. News release, October 16, 2025, https://cascadiaminerals.com/cascadia-completes-drill-program-at-its-carmacks-copper-gold-project-yukon/ [accessed 30/10/2025].

Cascadia Minerals Ltd., 2025d. Cascadia Minerals drills 83.52 m of 0.89% copper with 0.26 g/t gold at the Carmacks Copper-Gold Project. News release, November 4, 2025, https://cascadiaminerals.com/cascadia-drills-83-52-m-of-0-89-copper-with-0-26-g-t-gold-at-the-carmacks-copper-gold-project-yukon/ [accessed 05/11/2025].

Connors, S., 2025. Selkirk First Nation partners with venture firm to take over Minto mine. APTN News, July 16, 2025, https://www.aptnnews.ca/national-news/selkirk-first-nation-partners-with-venture-firm-to-take-over-minto-mine [accessed 01/12/2025].

Fireweed Metals Corp., 2023. Fireweed Metals announces mineral resources for the Mactung project: the largest high-grade tungsten deposit in the world. News release, June 13, 2023, https://fireweedmetals.com/fireweed-metals-announces-mineral-resources-for-the-mactung-project-the-largest-high-grade-tungsten-deposit-in-the-world/ [accessed 08/12/2025].

Fireweed Metals Corp., 2025a. Fireweed Metals commences 2025 field program. News release, June 4, 2025, https://fireweedmetals.com/fireweed-metals-commences-2025-field-program/ [accessed 30/10/2025].

Fireweed Metals Corp., 2025b. Fireweed intersects 30 m true width of 33.2% zinc equivalent in 115 m step-out at Tom South. News release, September 23, 2025, https://fireweedmetals.com/fireweed-intersects-30-m-true-width-of-33-2-zinc-equivalent-in-115-m-step-out-at-tom-south/ [accessed 30/10/2025].

Fireweed Metals Corp., 2025c. Mactung Project update. News release, November 24, 2025, https://fireweedmetals.com/mactung-project-update/ [accessed 26/11/2025].

Forge Resources Corp., 2025a. Forge Resources announces mobilization for 2025 drill program at Alotta Project, Yukon. News release, June 3, 2025, https://www.forgeresourcescorp.com/news/forge-resources-announces-mobilization-for-2025-drill-program-at-alotta-project-yukon [accessed 30/10/2025].

Forge Resources Corp., 2025b. Forge Resources intersects additional visible gold in first hole of phase II Alotta drill program, Yukon. News release, September 30, 2025, https://www.forgeresourcescorp.com/news/forge-resources-intersects-additional-visible-gold-in-first-hole-of-phase-ii-alotta-drill-program-yukon [accessed 30/10/2025].

Forge Resources Corp., 2025c. Forge Resources drills 45.01 g/t gold over a core length of 3.15 m starting 286.0 metres at Payoff Zone at Alotta Project, Yukon. News release, November 20, 2025, https://www.forgeresourcescorp.com/news/forge-resources-drills-45-01-g-t-gold-over-a-core-length-of-3-15-m-starting-at-286-0-metres-at-payoff-zone-at-alotta-project-yukon [accessed 01/12/2025].

Fuerte Metals Corp., 2025. Fuerte announces transformational acquisition of the Coffee Project from Newmont Corporation. News release, September 15, 2025, https://fuertemetals.com/news/fuerte-announces-transformational-acquisition-of-the-coffee-project-from-newmont-corporation/ [accessed 30/10/2025].

Gladiator Metals Corp., 2025a. Gladiator discovers new zone in first drilling below 200 m at Cowley. News release, August 11, 2025, https://www.gladiatormetals.com/news/gladiator-discovers-new-zone-in-first-drilling-below-200m-at-cowley [accessed 30/10/2025].

Gladiator Metals Corp., 2025b. Gladiator identifies new targets at Little Chief & Cowley Park. News release, October 16, 2025, https://www.gladiatormetals.com/news/gladiator-identifies-new-targets-at-little-chief-cowley-park [accessed 30/10/2025].

Gladiator Metals Corp., 2025c. Gladiator continues to deliver near-surface high-grade copper-gold intercepts at Cowley Park with 14 m @ 2.36% copper and 2.78 g/t gold. News release, October 29, 2025, https://www.gladiatormetals.com/news/gladiator-continues-to-deliver-near-surface-high-grade-copper-gold-intercepts-at-cowley-park-with-14m-2-36-copper-and-2-78-g-t-gold [accessed 30/10/2025].

Government of Yukon, 2025a. Statement from Minister Streicker on the Government of Yukon's response to the recommendations of the Eagle Gold Mine Independent Review Board. News release, September 25, 2025, https://yukon.ca/en/node/28135 [accessed 30/10/2025].

Government of Yukon, 2025b. Government of Yukon provides update on remediation of Victoria Gold's Eagle Gold Mine. News release, September 25, 2025, https://yukon.ca/en/node/28133 [accessed 30/10/2025].

Hantelmann, T., Jutras, M. and Malhortra, D., 2025. Technical report AurMac Property Mayo Mining District, Yukon Territory, Canada. NI 43-101 technical report prepared by JDS Energy and Mining Inc. for Banyan Gold Corp. Submitted August 20, 2025, 337 p., https://banyangold.com/site/assets/files/5390/banaur07e_ni_43-101_technical_report_2025_08_20.pdf.

Hecla Mining Company, 2025a. Hecla reports second quarter 2025 results. News release, August 6, 2025, https://ir.hecla.com/News--Media/news-releases/news-details/2025/Hecla-Reports-Second-Quarter-2025-Results/default.aspx [accessed 30/10/2025].

Hecla Mining Company, 2025b. Hecla reports third quarter 2025 results. News release, November 5, 2025, https://ir.hecla.com/News--Media/news-releases/news-details/2025/Hecla-Reports-Third-Quarter-2025-Results/default.aspx [accessed 06/11/2025].

Honey Badger Silver Inc., 2025. Honey Badger Silver identifies two new zones: Inferno and Pimento containing silver, gold, lead, and zinc at Plata, Yukon. News release, November 19, 2025, https://honeybadgersilver.com/honey-badger-identifies-two-new-zones-inferno-and-pimento-containing-silver-gold-lead [accessed 28/11/2025].

Klondike Gold Corp., 2025. Klondike Gold update on Phase 2 exploration program. News release, October 13, 2025, https://www.klondikegoldcorp.com/klondike-gold-update-on-phase-2-exploration-program/ [accessed 30/10/2025].

Prospector Metals Corp., 2025a. Prospector initial drill results include 45.65 m of 2.11 g/t Au, .48% Cu; new "Skarn Ridge-Bueno" mineralized corridor extends along trend 1.5 kilometres. News release, September 2, 2025, https://prospectormetalscorp.com/news/prospector-initial-drill-results-include-45.65m-of-2.11-g-t-au-48-cu-new-skarn-ridge-bueno-mineralized-corridor-extends-along/ [accessed 30/10/2025].

Prospector Metals Corp., 2025b. Prospector drills new discovery: hole ML25-31 intersects 13.79 g/t Au and 1.84% Cu over 44 m, includes higher-grade interval of 21.93 g/t Au over 24.65 m. News release, October 1, 2025, https://prospectormetalscorp.com/news/prospector-drills-new-discovery-hole-ml25-31-intersects-13.79-g-t-au-and-1.84-cu-over-44m-includes-higher-grade-interval-of/ [accessed 30/10/2025].

Sack, P.J., Colpron, M., Crowley, J.L., Ryan, J.J., Allan, M.M., Beranek, L.P. and Joyce, N.L., 2020. Atlas of Late Triassic to Jurassic plutons in the Intermontane terranes of Yukon. Yukon Geological Survey, Open File 2020-1, 365 p.

San Martin, A., Holloway, A. and Murahwi, C., 2025. NI 43-101 technical report for the 2025 Mineral Resource Estimate update on the Coffee Gold Project, Yukon, Canada. NI 43-101 technical report prepared by Micon International for Fuerte Metals Corp. Submitted October 6, 2025, 130 p., https://www.sedarplus.ca.

Selkirk Copper Mines Inc., 2025. Selkirk Copper announces initial drill results – successfully expands Minto North West Zone with a high-grade intercept of 5.21% Cu, 0.47 g/t Au, 26.68 g/t Ag over 8.7 m within a broader zone of 2.39% Cu, 0.32 g/t Au and 11.61 g/t Ag over 23.4 m in drill hole 25SCM001. News release, December 01, 2025, https://selkirkcopper.com/selkirk-copper-announces-initial-drill-results-successfully-expands-minto-north-west-zone-with-a-high-grade-intercept-of-5-21-cu-0-47-g-t-au-26-68-g-t-ag-over-8-7-m-within-a-broader-zone-o/ [accessed 01/12/2025].

Silver North Resources Ltd., 2025a. Initial exploration program at Silver North's Veronica property completed. News release, August 20, 2025, https://silvernorthres.com/initial-exploration-program-at-silver-norths-veronica-property-completed/ [accessed 30/10/2025].

Silver North Resources Ltd., 2025b. Silver North intersects 13.15 metres averaging 818 g/t silver and 1.39 g/t gold from 249.9 m depth at the Haldane Silver Property, Keno district, Yukon. News release, November 17, 2025, https://silvernorthres.com/silver-north-intersects-13-15-metres-averaging-818-g-t-silver-and-1-39-g-t-gold-from-249-9-m-depth-at-the-haldane-silver-property-keno-district-yukon/ [accessed 26/11/2025].

Simpson, R., 2025. Clear Creek property, RC Gold Project NI 43-101 technical report Dawson Mining District, Yukon Territory. NI 43-101 technical report prepared by GeoSim Services Inc. for Sitka Gold Corp. Submitted January 21, 2025, 98 p., https://www.sedarplus.ca.

Sitka Gold Corp., 2025. Sitka Drills 235.9 metres of 1.11 g/t gold from surface, including 40.0 metres of 2.01 g/t gold and 10.0 metres of 5.29 g/t gold, further confirming a near-surface higher-grade gold zone at its Rhosgobel Discovery, RC Gold Project, Yukon. News release, September 18, 2025, https://sitkagoldcorp.com/sitka-drills-235-9-metres-of-1-11-g-t-gold-from-surface-including-40-0-metres-of-2-01-g-t-gold-and-10-0-metres-of-5-29-g-t-gold-further-confirming-a-near-surface-higher-grade-gold-zone-at-its-rhosgo/ [accessed 30/10/2025].

Smith, M. and Konrad, J.M., 2025. Victoria Gold Corp. Eagle Gold Mine June 2024 Heap Leach Failure. Submitted June 30, 2025, Independent Review Board (compilers), 141 p. plus appendices, https://www.pwc.com/ca/en/car/victoria-gold/assets/victoria-gold-117_020725.pdf.

Snowline Gold Corp., 2025a. Snowline Gold commences fully funded 30 000 m exploration and project advancement program. News release, May 20, 2025, https://snowlinegold.com/2025/05/20/snowline-gold-commences-fully-funded-30000-m-exploration-and-project-advancement-program/ [accessed 30/10/2025].

Snowline Gold Corp., 2025b. Snowline Gold identifies new gold zone near its Valley deposit and provides regional exploration update. News release, August 7, 2025, https://snowlinegold.com/2025/08/07/snowline-gold-identifies-new-gold-zone-near-its-valley-deposit-and-provides-regional-exploration-update/ [accessed 30/10/2025].

Snowline Gold Corp., 2025c. Snowline Gold extends strike length by 550 m and Intersects 6.8 g/t gold over 9.0 m at its Jupiter target, Einarson project, Yukon. News release, September 24, 2025, https://snowlinegold.com/2025/09/24/snowline-gold-extends-strike-length-by-550-m-and-intersects-6-8-grams-per-tonne-gold-over-9-0-m-at-its-jupiter-target-einarson-project-yukon/ [accessed 30/10/2025].

SRK Consulting (Canada) Inc., 2025. Independent preliminary economic assessment for the Rogue project Yukon, Canada. Prepared for Snowline Gold Corp., Vancouver, BC. Submitted August 27, 2025, as a revision of the report dated July 30, 2025, 192 p., https://snowlinegold.com/wp-content/uploads/2025/09/Snowline_-_PEA_-_NI41-303_report-lr.pdf.

Transition Metals Corp., 2025a. Transition Metals defines multiple drill-ready copper porphyry and epithermal gold-silver targets at Pike Warden. News release, September 9, 2025, https://www.transitionmetalscorp.com/news/transition-metals-defines-multiple-drill-ready-copper-porphyry-and-epithermal-gold-silver-targets-at-pike-warden [accessed 24/11/2025].

Transition Metals Corp., 2025b. Drilling initiated at Transition Metals' polymetallic Pike Warden project, Yukon. News release, October 6, 2025, https://www.transitionmetalscorp.com/news/drilling-initiated-at-transition-metals-polymetallic-pike-warden-project-yukon [accessed 30/10/2025].

Trifecta Gold Ltd., 2025a. Trifecta Gold Ltd. is drilling sheeted quartz veins at Rye property, Yukon. News release, August 28, 2025, https://trifectagold.com/news/2025/trifecta-gold-ltd-is-drilling-sheeted-quartz-veins-at-rye-property-yukon/ [accessed 24/11/2025].

Trifecta Gold Ltd., 2025b. Trifecta Gold completes 2025 drilling program at the Rye Project, Yukon. News release, September 18, 2025, https://trifectagold.com/news/2025/trifecta-gold-completes-2025-drilling-program-at-the-rye-project-yukon/ [accessed 30/10/2025].

Trifecta Gold Ltd., 2025c. Trifecta Gold provides exploration updates for the Rye and Mount Hinton projects, Yukon. News release, September 30, 2025, https://trifectagold.com/news/2025/trifecta-gold-provides-exploration-updates-for-the-rye-and-mount-hinton-projects-yukon/ [accessed 30/10/2025].

Venerable Ventures Ltd., 2025a. Venerable Ventures enters into definitive agreement with Selkirk First Nation with respect to Selkirk Copper Mines Inc., announces $30 million brokered private placement offering. News release, August 26, 2025, https://www.newsfilecorp.com/release/263913/Venerable-Ventures-Enters-into-Definitive-Agreement-with-Selkirk-First-Nation-with-Respect-to-Selkirk-Copper-Mines-Inc.-Announces-30-Million-Brokered-Private-Placement-Offering [accessed 30/10/2025].

Venerable Ventures Ltd., 2025b. Venerable Ventures announces start of 50 000 m drill program at the Minto Copper-Gold-Silver Mine. News release, September 8, 2025, https://www.newsfilecorp.com/release/265576/Venerable-Ventures-Announces-Start-of-50000-m-Drill-Program-at-the-Minto-CopperGoldSilver-Mine [accessed 30/10/2025].

Western Copper and Gold Corp., 2024. Western Copper and Gold announces completion of C$5 million financing with Rio Tinto. News release, May 6, 2024, https://www.westerncopperandgold.com/news-and-resources/news-release/western-copper-and-gold-announces-completion-of-c5-million-financing-with-rio-tinto/ [accessed 30/10/2025].

Western Copper and Gold Corp., 2025. Western Copper and Gold announces submission of Environmental and Socio-Economic Effects statement for the Casino Project. News release, October 6, 2025, https://www.westerncopperandgold.com/news-and-resources/news-release/western-copper-and-gold-announces-submission-of-ese-statement/ [accessed 30/10/2025].

White Gold Corp., 2025a. White Gold Corp. files Technical Report demonstrating significant 44% increase in Indicated Resources to 1 732 300 oz gold (35.2 million tonnes grading 1.53 g/t) and 13.4% increase in Inferred Resources to 1 265 900 oz gold (32.2 million tonnes grading 1.22 g/t) at its flagship White Gold Project, Yukon, Canada. News release, October 6, 2025, https://whitegoldcorp.ca/news/2025/white-gold-corp-files-technical-report-demonstrating-significant-44-increase-in-indicated-resources-to-1732300-oz-gold-352-million-tonnes-grading-153-gt-and-134-increase-in-inferred-resources-to-1265900-oz-gold-322-million-ton [accessed 30/10/2025].

White Gold Corp., 2025b. White Gold Corp. increases high-grade gold mineralization at Golden Saddle intersecting 6.9 g/t gold over 50.2 metres in the Main Zone and expands the high-grade footwall breccia and hanging wall mineralization. News release, November 4, 2025, https://www.whitegoldcorp.ca/news/2025/white-gold-corp-increases-high-grade-gold-mineralization-at-golden-saddle-intersecting-69-gt-gold-over-502-metres-in-the-main-zone-and-expands-the-high-grade-footwall-breccia-and-hanging-wall-mineralization [accessed 05/11/2025].

YESAB, 2024. Yukon Environmental and Socio-economic Assessment Act Decision Document – executive committee screening. March 8, 2024, 61 p., https://yesabregistry.ca/projects/5942a72b-b77d-403d-83d6-bc2ffffc0c7b/activity.

Yukon Geological Survey, 2020. Yukon MINFILE - A database of mineral occurrences. Yukon Geological Survey, Government of Yukon, https://data.geology.gov.yk.ca/Occurrences/ [accessed 06/11/2025].

Yukon Metals Corp., 2025a. First drill hole confirms high-grade copper skarn mineralization at the Birch Project. News release, October 15, 2025, https://yukonmetals.com/news/news-2025/all-do-not-delete/first-drill-hole-confirms-high-grade-copper-skarn-mineraliza2025-10-15-040503 [accessed 30/10/2025].

Yukon Metals Corp., 2025b. Yukon Metals confirms large copper-bearing system at the AZ project. News release, September 18, 2025, https://yukonmetals.com/news/news-2025/all-do-not-delete/yukon-metals-confirms-large-copper-bearing-system-at-the-az-2025-09-18-040502 [accessed 30/10/2025].

Yukon Metals Corp., 2025c. Yukon Metals commences inaugural drill program at its Star River project. News release, August 25, 2025, https://yukonmetals.com/news/news-2025/star-river/yukon-metals-commences-inaugural-drill-program-at-its-star-river-project [accessed 30/10/2025].

Appendix A. Exploration projects active in 2025.

Owner/Optioner	Project	Prior commodity	Deposit type	Work type
Seabridge Gold Inc.	3 Aces	gold	vein/breccia	PR, GEO, GPA, GCS, DD, CR
Forge Resources Corp	Alotta	gold	porphyry/sheeted vein	DD
Mayo Lake Minerals Inc.	Anderson-Davidson	gold	unknown	GCS
Banyan Gold Corp.	AurMac	gold	porphyry/sheeted vein	DD, MRE
H. Coyne & Sons Ltd.	Aussie	gold	unknown	GCS
Yukon Metals Corp.	Az	copper	skarn/replacement	PR, GEO, GPA, GCS, GCR, DD
Stakeholder Gold Corp.	Ballarat Project	gold	porphyry/sheeted vein	PR, GEO, GCS, DD
Strategic Metals Ltd.	Batt	copper	volcanic-associated	PR, GEO, GCR, TR
Arsenault, Chris	Big Ray	copper	porphyry/sheeted vein	GCS, GCR, PR, GEO
Yukon Metals Corp.	Birch	copper	skarn/replacement	PR, GEO, GCS, GCR, DD
Cascadia Minerals Ltd.	Carmacks Copper	copper	porphyry/sheeted vein	DD
Western Copper and Gold Corp.	Casino	copper	porphyry/sheeted vein	GPG, GCS, CR, ES, ENV
Cascadia Minerals Ltd.	Catch	copper	porphyry/sheeted vein	PR, GCS, GCR, DD
Fuerte Metals Corporation	Coffee Project	gold	vein/breccia	MRE
Newmont Corporation	Coffee Project	gold	vein/breccia	ENV
Snowline Gold Corp.	Cynthia	gold	porphyry/sheeted vein	AP, RS
Harris, Bill	Dark Moth	gold	unknown	PR, GEO, GCS, GCR, TR
Snowline Gold Corp.	Einarson	gold	sediment-associated	PR, GEO, GPA, GCS, GCR, DD
Yukon Metals Corp.	Fairway	copper	unknown	GCS, GCR, PR, GEO
Burke, Ryan	Fyfe	copper	unknown	GCS, GCR, RS
Silver North Resouces	GDR	silver	vein/breccia	PR, GCS, GCR, TR
Gold Strike Resources Corp.	Gold Strike 2	gold	unknown	GCS, GCR, GCSS, PR
Lode Gold	Golden Culvert	gold	porphyry/sheeted vein	GEO, GCS, GCR
Hulstein, Roger	Goldorak	gold	unknown	PR, GEO, GCS, GCR, GCT

Abbreviations

AP – aerial photography
CR – road construction
CS – claim staking
DD – diamond drilling
ENV – environmental study
ES – economic study
GCR – geochemistry rocks
GCS – geochemistry soils
GCRS – geochemistry ridge and spur
GCST – geochemistry stream sediments
GEO – geology
GPA – aerial geophysics
GPG – ground geophysics
MRE – mineral resource estimate
MTL – metallurgy
PR – prospecting
RC – reverse circulation drilling
RS - remote sensing
TR – trenching
UW – underground work

Appendix A. (continued) Exploration projects active in 2025.

Owner/Optioner	Project	Prior commodity	Deposit type	Work type
White Gold Corp.	Hunker	gold	vein/breccia	GCS
Banyan Gold Corp.	Hyland Gold	gold	vein/breccia	ES
Bastion Minerals	Ice	copper	volcanic-associated	GCS
Cascadia Minerals Ltd.	Idaho Creek	gold	unknown	PR, GEO, GCR
White Gold Corp.	Ind-WGC	gold	unknown	GCS
Hecla Mining Company	Keno Mine	silver	vein/breccia	DD, UW
Metallic Minerals Corp.	Keno Silver	silver	vein/breccia	PR, GEO, GCS
Amauta Geo Solutions	King Lake (Suits)	copper	unknown	PR, GCS, GCR
Onyx Gold Corp.	King Tut	gold	porphyry/sheeted vein	GCR, PR, GEO, AP
Rockhaven Resources Ltd.	Klaza	gold	vein/breccia	GCR, TR
Klondike Gold Corporation	Klondike Gold	gold	vein/breccia	PR, GEO, DD
Stillwater Critical Minerals Corp.	Kluane Project	nickel-PGE	mafic/ultramafic-associated	PR, GEO, GCS, GCR
Fage, Isaac	KSR	gold	unknown	PR, GEO, GPA, GPG, GCS, GCR
BMC Minerals Ltd.	Kudz Ze Kayah	zinc-lead	volcanic-associated	GPA
White Gold Corp.	Loonie	gold	vein/breccia	GPG
Cascadia Minerals Ltd.	Macks Copper	copper	porphyry/sheeted vein	GCS, GCR, PR, GEO
Fireweed Metals Ltd.	MacMillan Pass	zinc-lead	sediment-associated	PR, GPG, GCS, GCR, DD, MRE
Fireweed Metals Ltd.	Mactung	tungsten	skarn/replacement	DD, MRE, ENV, MTL
Azarga Metals Corp.	Marg	copper	volcanic-associated	GCR, MRE
Prospector Metals Corp.	Mike Lake	gold	porphyry/sheeted vein	CS, PR, GEO, DD
Cascadia Minerals Ltd.	Milner	copper	porphyry/sheeted vein	GCR, PR, GEO
Selkirk Copper Mines Inc.	Minto Mine	copper	porphyry/sheeted vein	DD, RS
Trifecta Gold Ltd.	Mount Hinton	gold	porphyry/sheeted vein	PR, GCR, DD

Abbreviations

AP – aerial photography
CR – road construction
CS – claim staking
DD – diamond drilling
ENV – environmental study
ES – economic study
GCR – geochemistry rocks
GCS – geochemistry soils
GCRS – geochemistry ridge and spur
GCST – geochemistry stream sediments
GEO – geology
GPA – aerial geophysics
GPG – ground geophysics
MRE – mineral resource estimate
MTL – metallurgy
PR – prospecting
RC – reverse circulation drilling
RS - remote sensing
TR – trenching
UW – underground work

Appendix A. (continued) Exploration projects active in 2025.

Owner/Optioner	Project	Prior commodity	Deposit type	Work type
Cantex Mine Development Corp.	Mt. Good	gold	sediment-associated	PR, GEO
Silver North Resources	Mt. Haldane	silver	vein/breccia	DD, AP, RS
Renegade Exploration Limited	Myschka	gold	porphyry/sheeted vein	PR, GEO, GPA
Banyan Gold Corp.	Nitra	gold	porphyry/sheeted vein	GCS
White Gold Corp.	Nolan	gold	vein/breccia	GPG
Cantex Mine Development Corp.	North Rackla	silver	skarn/replacement	DD
Mann, Bill	ORC	tungsten	unknown	GCS, GCR, PR, GEO
White Gold Corp.	Pedlar	gold	porphyry/sheeted vein	GPG
Transition Metals Corp.	Pike Warden	copper	unknown	GEO, GPG, GCR, DD
Honey Badger Silver Inc.	Plata	silver	vein/breccia	PR, GEO, GCS, GCR
Sitka Gold Corp.	RC Gold	gold	porphyry/sheeted vein	GPG, GCS, DD
44984 Yukon Inc.	Richards	gold	unknown	GPG
Snowline Gold Corp.	Rogue	gold	porphyry/sheeted vein	PR, GEO, GPA, GCS, GCR, GCRS, DD, RC, ES, MRE, ENV, AP, RS, MTL
Cascadia Minerals Ltd.	Rosy	zinc-lead	vein/breccia	PR, GCR
Trifecta Gold Ltd.	Rye	gold	porphyry/sheeted vein	PR, GEO, GCR, DD
Selwyn Chihong Mining Ltd.	Selwyn Project	zinc-lead	sediment-associated	MTL
T2 Metals	Shanghai Creek	gold	unknown	PR, GCS, GCR
Yukon Metals Corp.	Star River	silver	vein/breccia	DD, GCR, PR, GPA, GPG
Burke, Ryan	Sumo	copper	unknown	GPG, GCS, GCR
Yukon Metals Corp.	Talbot Creek	copper	unknown	PR, GEO, GCS, GCR
Hulstein, Roger	Taut	copper	unknown	PR, GEO, GCS, GCR, TR
Coeur Mining Inc.	Tim	silver	vein/breccia	GEO
Higher Ground Exploration	TOG	gold	unknown	GCR, DD

Abbreviations

AP – aerial photography
CR – road construction
CS – claim staking
DD – diamond drilling
ENV – environmental study
ES – economic study
GCR – geochemistry rocks
GCS – geochemistry soils
GCRS – geochemistry ridge and spur
GCST – geochemistry stream sediments
GEO – geology
GPA – aerial geophysics
GPG – ground geophysics
MRE – mineral resource estimate
MTL – metallurgy
PR – prospecting
RC – reverse circulation drilling
RS - remote sensing
TR – trenching
UW – underground work

Appendix A. (continued) Exploration projects active in 2025.

Owner/Optioner	Project	Prior commodity	Deposit type	Work type
Strategic Metals Ltd.	Triple Crown	silver	unknown	PR, GEO, GCR, TR
Kreft, Bernie	Val-Jual	gold	unknown	GCS, GCR
White Gold Corp.	White Gold	gold	vein/breccia	GPG, GCS, DD
Gladiator Metals	Whitehorse Copper	copper	skarn/replacement	GPG, DD
Lee, Gary	Wildcat	zinc-lead	unknown	GCS
Lode Gold	Win	gold	porphyry/sheeted vein	GCS, GCR, GEO
Hood, William C.	WIND	gold	unknown	GEO, GPG
Renegade Exploration Limited	Yukon Base Metal Project (Andrew)	silver	vein/breccia	ENV

Abbreviations

AP – aerial photography
CR – road construction
CS – claim staking
DD – diamond drilling
ENV – environmental study
ES – economic study
GCR – geochemistry rocks
GCS – geochemistry soils
GCRS – geochemistry ridge and spur
GCST – geochemistry stream sediments
GEO – geology
GPA – aerial geophysics
GPG – ground geophysics
MRE – mineral resource estimate
MTL – metallurgy
PR – prospecting
RC – reverse circulation drilling
RS - remote sensing
TR – trenching
UW – underground work

Appendix B. Drilling summary 2025.

Owner/Optioner	Project name	DDH		RC/RAB	
		# of holes	metres	# of holes	metres
Banyan Gold Corp.	AurMac	193	42 000		
Cantex Development Corp.	North Rackla	16	3620		
Cascadia Metals Ltd.	Carmacks Copper	11	3848		
Cascadia Metals Ltd.	Catch	3	742		
Fireweed Metals Ltd.	Mactung	66	11 117		
Fireweed Metals Ltd.	MacMillan Pass	24	8723		
Forge Resources Corp.	Alotta	9	2686		
Gladiator Metals	Whitehorse Copper	52+*	50 000		
Hecla Mining Company	Keno Mine	11	6586		
Higher Ground Exploration	TOG	10	700		
Klondike Gold Corporation	Klondike Gold	31	5159		
Prospector Metals Corp.	Mike Lake	39	6649		
Seabridge Gold Inc.	3 Aces	10	2442		
Selkirk Copper Mines Inc.	Minto	98+*	26 000		
Silver North Resources	Mt. Haldane	8	1760		
Sitka Gold Corp.	RC Gold	91	31 841		
Snowline Gold Corp.	Rogue	72	26 775	48	1027
Snowline Gold Corp.	Einarson	8	3580		
Stakeholder Gold Corp.	Ballarat Project	**	2500		
Transition Metals Corp.	Pike Warden	2	504		
Trifecta Gold Ltd.	Rye	6	1992		
Trifecta Gold Ltd.	Mount Hinton	2	753		
White Gold Corp.	White Gold	5	2100		
Yukon Metals Corp.	Birch	6	1684		
Yukon Metals Corp.	Star River	8	1591		
Yukon Metals Corp.	Az	5	1489		

Abbreviations

DD – diamond drilling

RC/RAB - reverse circulation/rotary air blast

+ At time of writing, drilling program is still in progress and actual number of drillholes unconfirmed*

*** At time of writing, number of drillholes unconfirmed*

A preliminary HVSR investigation of the shallow structure of the Teslin fault, southern Yukon

Daniel O. Afolabi and Hersh Gilbert*
Department of Earth, Energy, and Environment, University of Calgary

Jeremy M. Gosselin
Natural Resources Canada, Geological Survey of Canada–Pacific

Jan Dettmer
Department of Earth, Energy, and Environment, University of Calgary
Yukon Geological Survey

Afolabi, D.O., Gilbert, H., Gosselin, J.M. and Dettmer, J., 2026. A preliminary HVSR investigation of the shallow structure of the Teslin fault, southern Yukon. *In*: Yukon Exploration and Geology 2025, A. Stuart, L.H. Weston and S.K. Schultz (eds.), Yukon Geological Survey, Government of Yukon, p. 75–89.

Abstract

This study investigates the shallow subsurface structure of the Teslin fault zone in southern Yukon using the horizontal-to-vertical spectral ratio (HVSR) method. By recording continuous ambient seismic noise on 5 Hz geophones deployed at over 100 sites across the Teslin and Eastern Teslin faults between July and August 2023, we seek to delineate variations in resonance frequency and amplitude related to geologic and structural features. Data were processed to isolate low-noise intervals, and HVSR curves were calculated to estimate changes in sediment structure, impedance contrasts and near-surface heterogeneities. Our observations reveal distinct spatial variations in HVSR signatures that correlate with mapped terranes and fault strands. Low-frequency, high-amplitude HVSR peaks correspond to a thicker sedimentary layer within fault-bounded basins, whereas high-frequency, low-amplitude responses reflect thin sediment cover over bedrock. Comparisons with Bouguer gravity anomalies indicate consistent spatial correlations between low resonance frequencies and more negative gravity anomalies. These findings demonstrate that the Teslin fault serves as a lithologic and structural boundary, as well as showcases the value of single-station passive-seismic methods for mapping variability in subsurface structure that is masked by sediment overburden. This study provides a foundation for future joint inversions of surface-wave dispersion, gravity, and magnetic data, which will help refine models of shallow seismic properties to better support geothermal assessments in southern Yukon.

Plain language summary

This study investigates regions around the Teslin fault in southern Yukon to better understand the structure of the shallow Earth. The Teslin region is known for its complex geology, where different rock units and past fault movements have created a complex geologic patchwork. This geologic structure influences how water and heat move through the uppermost part of the crust. To explore what lies below the surface, we continuously recorded the natural vibrations of the ground shaking at more than 100 locations during the summer of 2023. These small vibrations, caused by wind, rivers, storms and human activity, travel differently through soft sediments than through solid rock. By examining these vibrations at each site, we were able to estimate changes in the speeds that the ground vibrations travel and variations in the thickness of soils or sediments that overlie bedrock. Our results indicate clear changes in the subsurface that align with known faults and different rock types. The Teslin fault appears to mark a location of changing subsurface structures. Understanding the shallow structure of the Teslin fault and adjacent areas helps identify the pathways of heat and fluid in the shallow subsurface, which is important for geothermal assessment. This study also provides a framework for future, more detailed investigations of the Teslin fault in this region.

* daniel.afolabi@ucalgary.ca

Introduction

Southern Yukon is characterized by a network of crustal-scale faults that exert control on its geology and tectonics. The major fault systems include the Denali, Teslin and Tintina faults which extend to lengths of >2000 km and have accommodated hundreds of kilometres of right-lateral displacement (Fig. 1; Mortensen, 1992; Snyder et al., 2005). Collectively, these faults define major terrane boundaries within the northern Canadian Cordillera and have accommodated accretionary and later Cenozoic deformation (de Keijzer et al., 2000; Fisher et al., 2007; Yukon Geological Survey, 2011). Their long-lived tectonic activity has generated extensive fracture networks, fault gouge, and disrupted stratigraphy, producing the pronounced geologic complexity characteristic of the region (Mortensen, 1992).

Large strike-slip faults, such as the Denali and Teslin, are known to generate broad zones of deformation comprising fractured, altered rock volumes and damage zones (Stevens and Erdmer, 1996; Fisher et al.,

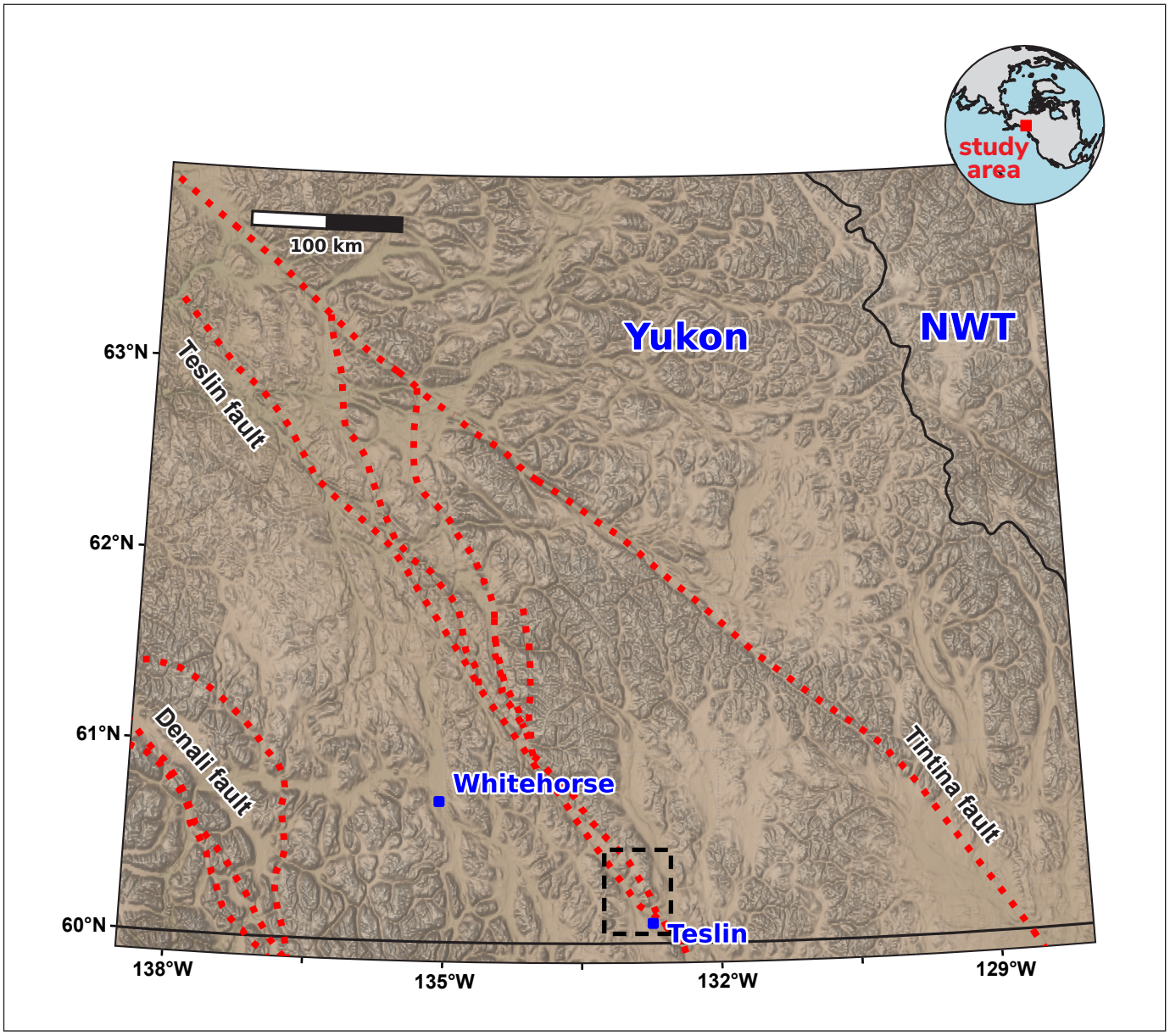


Figure 1. *Map of the Yukon and Northwest Territories (NWT), Canada, indicating the locations of the Denali, Teslin and Tintina faults (red dashed lines). The locations of Whitehorse and Teslin are indicated by blue squares. The inset map indicates the position of the study area in northwestern North America. The black dashed outlined box presents the approximate extent of the study area.*

2007; Witter, 2023). These damage zones can extend hundreds of metres to kilometres from the main fault core, depending on lithology and slip history (Caine et al., 1996; Faulkner et al., 2010). In southern Yukon, such zones are particularly well developed where faults juxtapose contrasting terranes; for example, the Denali fault separating the Kluane schist from Mesozoic sedimentary packages, or the Teslin fault bounding plutonic intrusions against Paleozoic–Mesozoic sediments. The resulting heterogeneity is manifested in variable sediment accumulation, disrupted stratigraphy and complex seismic velocity structures (Gilbert et al., 2006; McDermott et al., 2019; Estève et al., 2021).

The Teslin fault zone in southern Yukon is characterized by the juxtaposition of diverse lithological terranes and the presence of multiple fault strands and subsidiary structural features (Fig. 2; de Keijzer et al., 2000; Larson, 2002; Hayward, 2015). Locally, the fault bifurcates into multiple strands and subsidiary shear zones, incorporating slivers of Quesnellia and Atlin terranes within a structurally intricate duplex system (Larson, 2002; Witter, 2023). This bifurcation has produced localized pull-apart basins and strike-slip duplex structures along the fault zone, representing zones of transtensional deformation that promote intense brittle fracturing, interconnected fracture networks, and enhanced structural permeability (Caine et al., 1996; de Keijzer et al., 2000; Faulkner et al., 2010). Structural depressions such as the Fox Creek trough, interpreted as a fault-related, pull-apart basin infilled with low-density sediments, exemplify this process and may provide pathways for geothermal fluid circulation within the strike-slip duplex system (Witter, 2023). This connectivity has the potential to influence hydrothermal flow and the distribution of geothermal resources within the Teslin fault corridor (Witter, 2023).

Recent geophysical and geologic investigations reveal pronounced lithologic contrasts across the Teslin fault (de Keijzer et al., 2000; Snyder et al., 2005; Hildes, 2022; Witter, 2023). The northeastern domain is underlain by Neoproterozoic to Paleozoic metamorphic rocks of the Yukon-Tanana terrane, primarily quartzite and schist, whereas the southwestern domain consists of Mesozoic chert, shale, carbonate and volcanic rocks of the Cache Creek terrane (Fig. 2; Witter, 2023; Sternbergh and Colpron, 2025). Intrusive bodies, including the Early Cretaceous Deadman Creek pluton (Fig. 2), further diversify the subsurface geology and influence local heat flow.

The interplay between fault-controlled fracture systems, lithologic variability and moderate regional heat flow likely affects the geothermal potential of the Teslin area. Although the Teslin fault is considered tectonically inactive, it preserves a legacy of deformation characterized by fractured and altered rock volumes that may sustain residual structural permeability (Colpron et al., 2021; Witter, 2023). This permeability, combined with the favourable thermal conditions of the region, underscores the potential for geothermal development around the Teslin fault zone. However, the subsurface characterization of the region remains limited due to sparse near-surface geophysical data (de Keijzer et al., 2000; Larson, 2002; Monger and Price, 2002; Fraser et al., 2018; Witter, 2023).

Passive seismic methods, such as the horizontal-to-vertical spectral ratio (HVSR) technique, offer a practical and non-invasive means of imaging shallow geologic structures. The HVSR method uses ambient seismic noise to identify resonance frequencies generated by seismic impedance contrasts, allowing estimation of sediment thickness, bedrock depth and subsurface layering (Lane et al., 2008; Haefner et al., 2011; Stannard and Meyers, 2018). Building on the success of HVSR applications in mapping basin geometry and fault-related structures in other geologic settings (Haefner et al., 2011; Stannard and Meyers, 2018; Berumen-Borrego et al., 2024), this study applies the HVSR technique to data collected along transects crossing the Teslin fault zone as a preliminary step toward addressing existing data gaps.

Specifically, we employ HVSR surveys to delineate spatial variations in the thickness of sedimentary layers and impedance contrasts within the shallow structures surrounding the Teslin fault and its eastern strand. Based on these observations, we explore the continuity of fault-controlled structures and their relationship to the configuration of geologic units. Characterizing these features will contribute to constraining the near-surface architecture and permeability distribution, which is needed for future heat-flow modelling and geothermal assessment. Ultimately, this study seeks to enhance the geologic understanding of the Teslin fault zone and demonstrate the utility of HVSR as a cost-effective tool for early geothermal exploration in structurally complex and data-scarce regions.

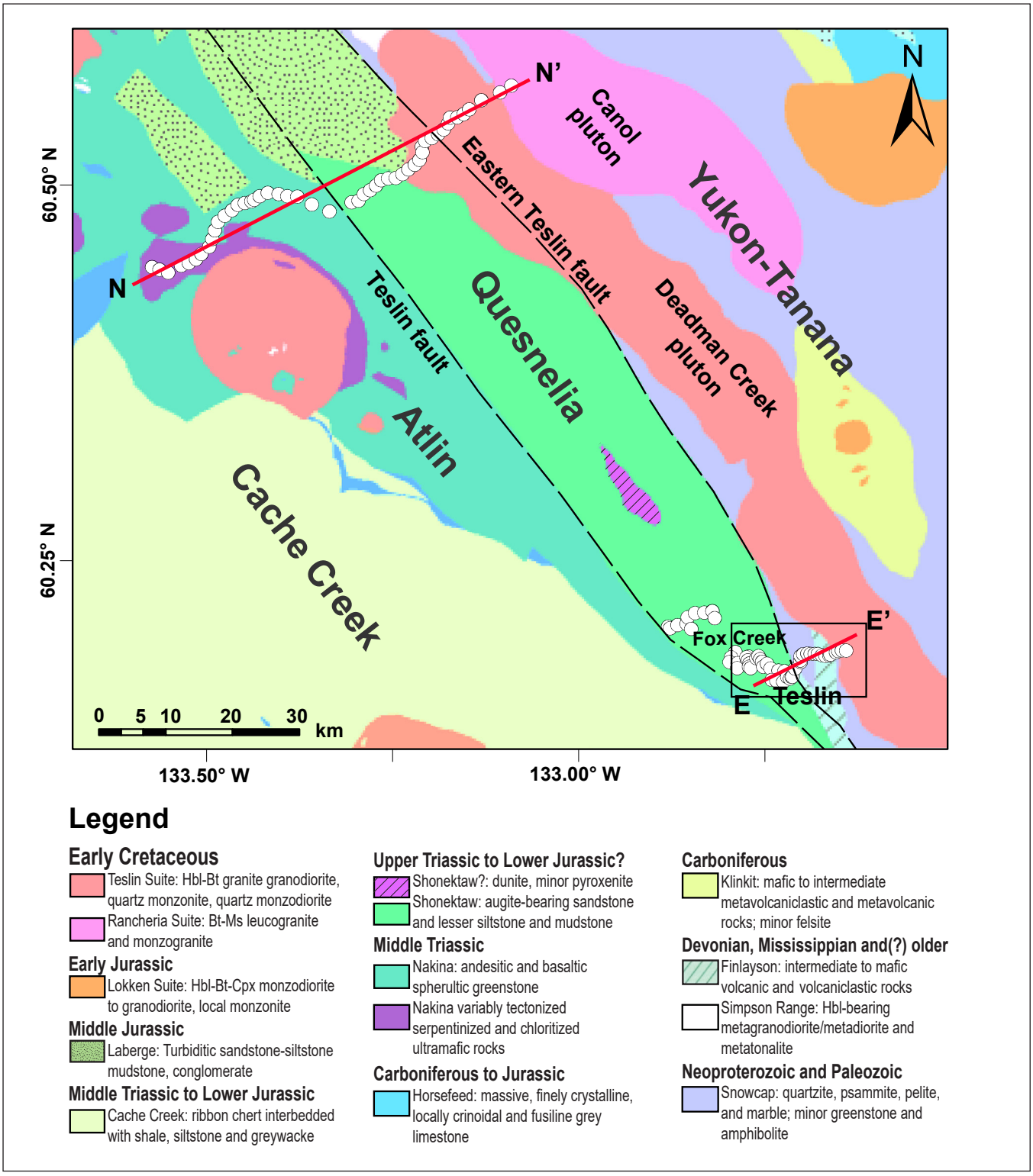


Figure 2. *Geological map (Yukon Geological Survey, 2023) of the Teslin fault near the town of Teslin including locations of the Yukon-Tanana, Quesnellia, Atlin and Cache Creek terranes. Faults are indicated by black dashed lines. Geophone locations are displayed as white circles. Locations of profiles N-N' and E-E' presented in Figures 5 and 6 are displayed as red lines. The box with the black outline represents the area with the available Bouguer anomaly map (presented in Figure 7). Bt – biotite; Cpx – clinopyroxene; Hbl – hornblende; and Ms – muscovite.*

Geologic and tectonic setting of the Teslin fault zone

Southern Yukon, located in the northern Canadian Cordillera, comprises a complex collage of terranes that accreted during the Mesozoic and Cenozoic, including the Yukon-Tanana (YTT), Stikinia, Wrangellia, Quesnellia, Atlin and Cache Creek terranes (Monger and Price, 2002; Colpron et al., 2007, 2022). These terranes are juxtaposed along sharp structural boundaries formed by thrusting, subduction and crustal deformation (Evenchick et al., 2005; Johnston and Canil, 2007). The Teslin fault, a northwest-trending, right-lateral, strike-slip system is a major feature separating key terranes (Colpron et al., 2021; Witter, 2023). The fault zone contains Paleozoic–Mesozoic metavolcanic rocks juxtaposed with Triassic–Jurassic chert and carbonates of the Cache Creek terrane (Yukon Geological Survey, 2011), and records multiple deformation phases, including early sinistral ductile shearing and mylonitization (Early Jurassic–mid-Cretaceous) followed by later dextral transpressional motion (Late Cretaceous–Tertiary; de Keijzer et al., 2000; Larson, 2002). Despite the current low level of activity along the Teslin fault, the structural inheritance and fracture network of the fault zone continue to influence the regional tectonic framework, resource distribution and crustal permeability.

The surficial geology near the Teslin fault consists of variable Quaternary deposits, including till, glaciofluvial sand and gravel, outwash terraces, and colluvial material (Witter, 2023). These sediments overlie faulted bedrock units composed mainly of quartzite, volcanic and meta-intrusive rocks (Denny, 1952; Witter, 2023). The distribution and thickness of sediments are highly irregular due to glacial advance, meltwater reworking and postglacial surface processes. Locally, surficial sediments are stratigraphically complex, which influences interpretations of shallow structure (Morison and Klasen, 1997; Witter, 2023). The observations of HVSR resonant frequencies presented here provide needed constraints for resolving sediment thickness.

Method

Data acquisition

For this study, the HVSR method was used because of its ease in data processing and sensitivity to seismic discontinuities in shallow structure (e.g., Nakamura, 1989, 2008; Cipta et al., 2018; Berumen–Borrego et al., 2024). Continuous seismic data was collected to examine the structure of the Teslin fault zone and surrounding area near the village of Teslin in southern Yukon (Fig. 2). Continuous seismic signals were recorded using the three-component Inova Hawk 5-Hz nodal geophones. Each seismic sensor records three orthogonal components of ground motion (vertical, north–south and east–west) at 250 Hz, allowing flexibility for both microtremor and higher-frequency ambient noise applications. The continuous recordings were made between July and August 2023 at a total of 104 locations in the study area.

Data processing

Using a combination of the open-source Obspy (Beyreuther et al., 2010; Krischer et al., 2015) and HVSRPY Python software (Vantassel et al., 2021, 2023), we processed the continuous three-component raw recordings and performed HVSR measurements. Initially, we processed an entire day of data and found time variable peaks whose amplitudes changed with noise level throughout the day. To improve the reliability of HVSR measurements, only segments of data from the quietest period of each day were retained for further analysis. To find these quiet time windows, we first filtered the continuous recordings between 0.5 and 25 Hz using a four-pole Butterworth bandpass filter. The standard deviation of these filtered waveforms was then calculated using a three-hour, long-moving time window. Following testing shorter and longer time windows, ranging between one hour to an entire day of data, we selected the three-hour window because it produced HVSR curves with clearer peaks, higher amplitudes and fewer spurious peaks. The three-hour long windows with the lowest standard deviation across all three components from each day of recording were used for stacking and further analysis. We found the quiet period varied from day to day and occurred mostly during the middle of the night local time. This time windowing approach reduced the influence of temporally varying signals and spurious noise.

The HVSRPY workflow provides a reproducible, and standardized framework that complies with the SESAME (2004) recommendations for ambient-noise spectral ratio estimation (Cox et al., 2020). Further details of the data processing and window selection/rejection can be found in the description of HVSRPY (Cox et al., 2020; Vantassel et al., 2023). The initial steps of HVSRPY processing remove linear trends from the quiet three-hour segments and cut the timeseries into 100-second windows. A cosine (Tukey) taper with

a 10% width was applied to the start and end of each window to suppress edge-related spectral leakage (Konno and Ohmachi, 1998). The HVSR calculations followed the method described by Nakamura (1989) as implemented within HVSRPY in which each time window was transformed into the frequency domain using a fast Fourier transform. To reduce spectral variability and highlight dominant resonance behaviour, the resulting curves were smoothed using the logarithmic Konno-Ohmachi filter with a bandwidth coefficient b=40 (Konno and Ohmachi, 1998). The stacked HVSR curves and peak resonant frequencies presented here for each station are calculated based on the average values of the HVSR curves from the quiet hours (i.e., lowest noise variance) determined for each day. The lowest-frequency peaks on each HVSR curve are automatically identified using an algorithm that selects the fundamental resonant frequency (f_0) with sufficiently high amplitude. These f_0 peaks are interpreted to represent the primary impedance contrast associated with the thickness and velocity of sediments overlying bedrock. Because f_0 is controlled by both the thickness of the sedimentary layer and their average shear wave velocity, there are tradeoffs interpreting HVSR in terms of either parameter (Fig. 3). For example, low frequency HVSR peaks can result from the layers overlying bedrock either being thick or comprised of material with low shear wave velocities. Conversely, thin layers or layers comprised of high velocity material can contribute to high-frequency HVSR peaks.

Interpreting HVSR curves are inherently non-unique. Different subsurface structures can yield identical Rayleigh-wave ellipticity or spectral ratio signatures (Hobiger et al., 2013). Consequently, and in line with recommendations from recent sensitivity analyses (SESAME, 2004), we limit our interpretation to comparing relative changes in HVSR between stations rather than attempting to derive absolute models. In this study, variations in f_0 are evaluated in terms of their spatial patterns and are compared with Bouguer gravity anomalies to produce geologic interpretations.

Results

All the stations that we operated around Teslin were fully analyzed. We present HVSR curves for a subset of 37 sites from the Teslin survey to demonstrate changes in signal along two transects crossing the Teslin fault zone. The selected sites are representative of the full dataset and capture the range of HVSR responses and key structural variations. The selected HVSR curves presented here clearly demonstrate changes in site response across the study area. We also present the resonant frequencies for another 27 sites to compare with structures along the southern transect. The HVSR curves display clear peaks related to their fundamental resonant frequencies that range between 0.28 and 28 Hz, reflecting the changing and heterogenous structures around the Teslin fault. Viewing examples of HVSR spectrograms calculated for the continuous data recorded at two of the stations used here (E03 and N30) displays time variable signals that correlate with meteorological conditions (air temperature and wind speed) in Teslin (Fig. 4). Temperature and wind speed display strong diurnal variations throughout the observation period. Daily maximum temperatures reach

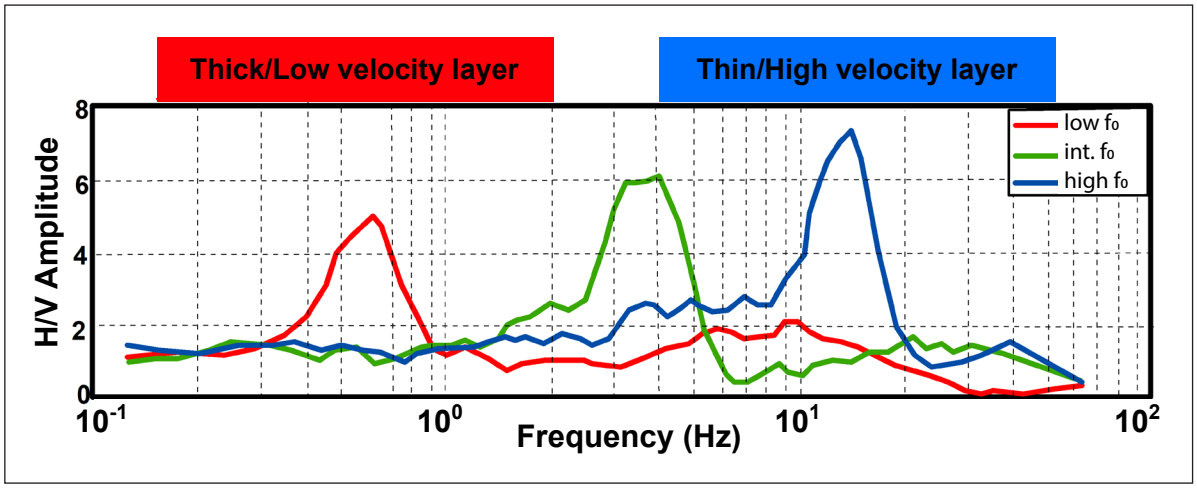


Figure 3. *Schematic illustration of HVSR measurements demonstrating the relationship between resonant frequencies (low – red, intermediate – green, high – blue), seismic wavespeeds and sediment thickness.*

approximately 25–28°C, while minimum temperatures drop to near ~5–10°C, consistent with daily cycles during the summer. Average daily wind speeds fluctuate around ~5–10 km/h with occasional short bursts exceeding 20 km/h. The HVSR spectrograms display distinct peaks that exhibit daily fluctuations in amplitude and peak frequencies. At station E03, two persistent peaks are observed at frequencies between 1.5–2.5 Hz and near 9 Hz (Fig. 4a). The high-frequency component exhibits a periodic pattern, with amplitude alternating between higher and lower values over the observation period. The HVSR amplitude for E03 is greatest in the 1.0–2.5 Hz range and displays consistent daily variation. A secondary pulse between 7 and 9 Hz also displays daily amplitude fluctuations, though with lower amplitude than the primary low-frequency peak. At station N30, a strong HVSR signal is observed between 2 and 3 Hz, with amplitudes ranging from approximately 3.5 to 5 (Fig. 4b). This signal also indicates daily variations in amplitude, like the pattern observed at E03. The recurring diurnal fluctuations in both stations indicate that the HVSR response varies over time, with clear frequency-dependent differences in amplitude stability and persistence. Despite these hourly variations in HVSR signals that appear to result from environmental effects on the ambient seismic noise wavefield, the spectrograms reveal that the peaks in resonant frequencies are consistent throughout the recording period. Further analysis presented below is based on average HVSR curves taken from the mean of the signal attained from the quiet recording period each day, which enables more reliable comparability between measurements from different sites.

Our analysis focuses on two profiles that transect the main traces of the Teslin fault and the Eastern Teslin fault. The HVSR results along profile N–N' are presented in Figure 5, and Figure 6 presents the corresponding results for the E–E' profile. These profiles provide coverage across zones of contrasting lithology and fault geometry, whereas facilitates analysis of site response across the fault. For each profile, the amplitudes of HVSR curves are plotted at the same scale, so relative amplitudes of the signals can be compared. The N–N' profile, with a length of nearly 38 km, spans the Teslin fault (TF) and samples the Nakina Formation (NK) at its

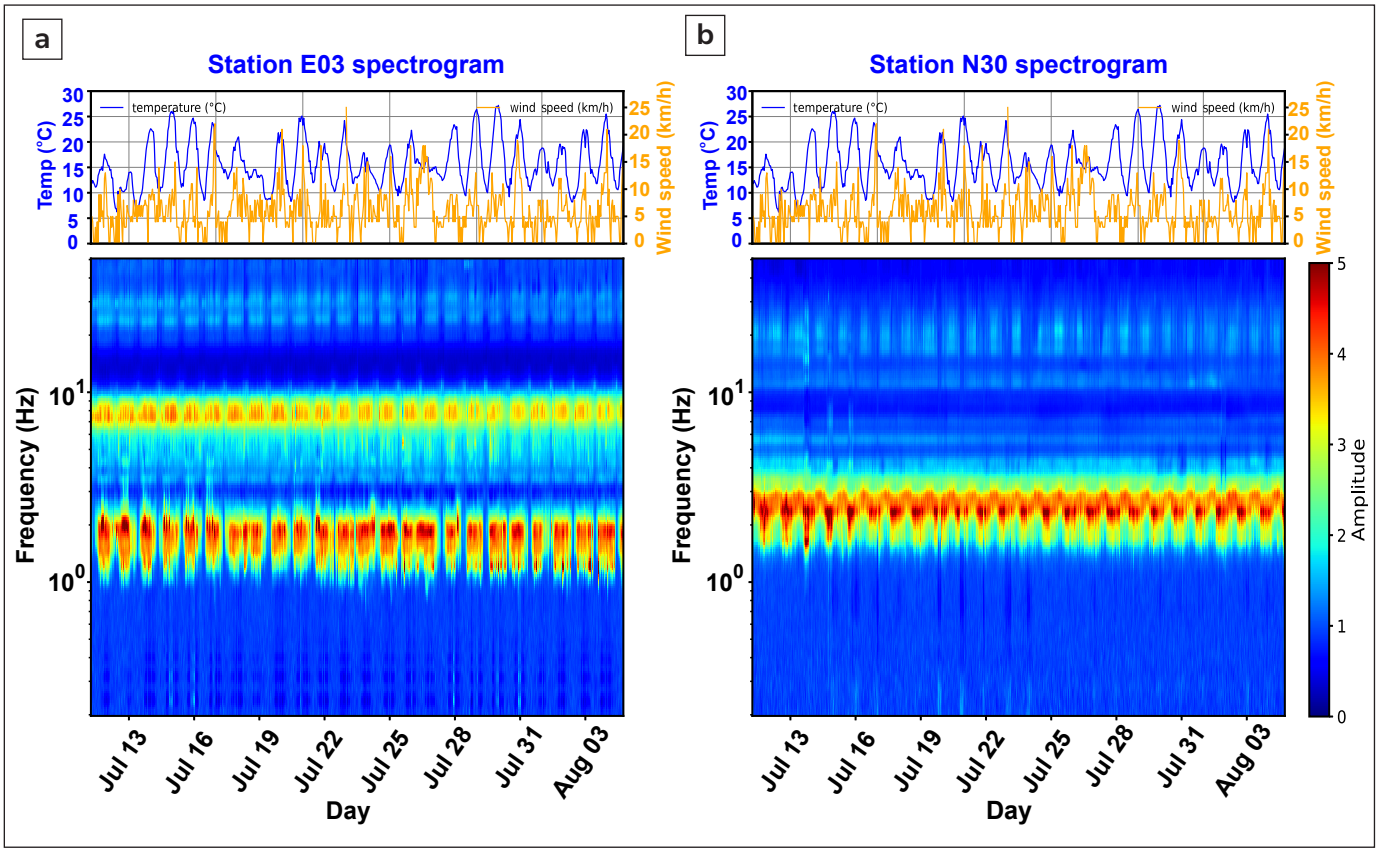


Figure 4. *Environmental conditions and HVSR variability at sites* ***(a)*** *N30 and* ***(b)*** *E03. Top panels illustrate temperature and wind speed. Bottom panels display a spectrogram depicting temporal variations of HVSR signals between July 11 and August 5, 2023. The weather data was downloaded from Environment and Climate Change, Canada for the Teslin area, Yukon.*

southwestern end. Its central segment extends across the Shonektaw formation (ST) and the Teslin suite (TS), and ends at the Canol pluton (CP) to the northeast. Profile E–E' extends for ~7 km and crosses the Eastern Teslin fault from the Shonektaw formation (ST) in the west, to multiple geologic blocks associated with the Finlayson (FN) and Snowcap (SC) assemblages, as well as the Teslin suite (TS) in the east.

Topography along profile N–N' rises from ~750 m in the southwest to ~1450 m in the northeast (Fig. 5a). Elevations remain subdued (750–900 m) across the low-relief Nakina Formation, then dip slightly near the Teslin fault. Farther east, the terrain steepens across the Shonektaw formation and Teslin suite, reaching >1100 m near the Eastern Teslin fault. The highest relief occurs in the northeast, where elevations sharply exceed 1300 m over the Canol pluton. The surface elevations exhibit moderate relief, with localized depressions and ridges located close to mapped fault zones, particularly near the Teslin fault and between geologic units (Fig. 5a). The HVSR profile illustrates the spatial variation in the stacked HVSR curves including the frequencies and amplitudes of their peaks (Fig. 5b). Southwest of the Teslin fault, stations between horizontal offsets of 0 and 7 km, are located within the tectonized portion of the Nakina Formation and display HVSR curves with double or multiple peaks, and peak resonant frequencies between 0.6 and 2 Hz. This part of the transect possesses moderate topographic relief. Between horizontal offsets of 7 and 18 km along this profile, the HVSR peaks shift to higher frequencies while maintaining multi-peaked spectra. Resonant frequencies increase from 0.6 Hz in the eastern part of the andesitic and basaltic Nakina Formation to ~2 Hz west of the Teslin fault where f_0 deceases to ~1 Hz at the fault. The lack of large variations in resonant frequency among stations within this region of the Nakina Formation suggests laterally consistent seismic response and that the area only exhibits modest structural variations.

Stations farther to the east between horizontal offsets of 18 and 23 km, spanning the Teslin and Eastern Teslin faults, are located within the Shonektaw formation and exhibit some of the highest amplitude HVSR curves observed in this study. The HVSR curves within this interval exhibit single, well-defined peaks with resonant frequencies ranging between 1 and 3 Hz. Compared with the lower-frequency, multi-peaked responses southwest of the Teslin fault, this section displays higher and more uniform resonant frequencies. Along sections of the profile east of offsets of 25 km, the resonant frequencies increase gradually to the northeast, accompanied by an increase in amplitude. Northeast of the Eastern Teslin fault, between 23 and 38 km, the HVSR curves display multiple frequency peaks. The spectra in this region are dominated by higher-frequency peaks between ~3.5 and 15 Hz with resonant frequencies that increase to the northeast, within the Deadman Creek pluton of the Teslin suite, and the Canol pluton (Fig. 5c). A change in f_0 occurs at the Eastern Teslin fault within the Teslin suite at a horizontal offset ~27 km.

The topography along profile E–E' is lower than that found along N-N' and ranges from ~690 to 760 m (Fig. 6a). Elevations remain near ~700 m across the Shonektaw formation, with a small depression at the Eastern Teslin fault followed by a modest rise to ~730 m over the Finlayson and Snowcap assemblages. The topography reaches its maximum elevation within the Deadman Creek pluton of the Teslin suite, along this profile. The stacked HVSR curves along the E–E' transect (Fig. 6b) display clear variations in amplitude, shape, and resonant frequency across the 7 km profile. In the southwestern segment of the line, between horizontal offsets of 0 and 2.2 km within the Shonektaw formation, the curves exhibit multiple broad peaks with f_0 values of ~1.5–2.2 Hz. The stations within this unit display high HVSR amplitudes with only subtle shifts in peak frequencies. Where the profile intersects the Finlayson assemblage, between horizontal offsets of ~2.2 and 2.5 km, the HVSR signals exhibit reduced amplitudes compared to the Shonektaw formation (Fig. 6c). The HVSR peaks in the Finlayson assemblage are narrower, and the curves indicate less variability in their frequency content. Between horizontal offsets of ~2.5 to 4 km across the Snowcap assemblage, the HVSR curves shift to a single peak with resonant frequencies between ~3.5 and 10 Hz. The HVSR signals within the Snowcap assemblage possess reduced amplitudes compared to those sampling other units (Fig. 6b). Returning to sampling the Finlayson assemblage between horizontal offsets of ~4 to 5.3 km, the HVSR peaks shift to lower frequencies and have a single peak from 1.3 to 2 Hz. In the easternmost segment of the profile, spanning horizontal offsets of approximately 5.3 to 7 km, where stations cross from the Snowcap assemblage into the Teslin suite (Fig. 6c), the HVSR curves vary in peak frequency and amplitude. Resonant frequencies increase from ~2 to ~3.5 Hz and HVSR curves possess multiple peaks.

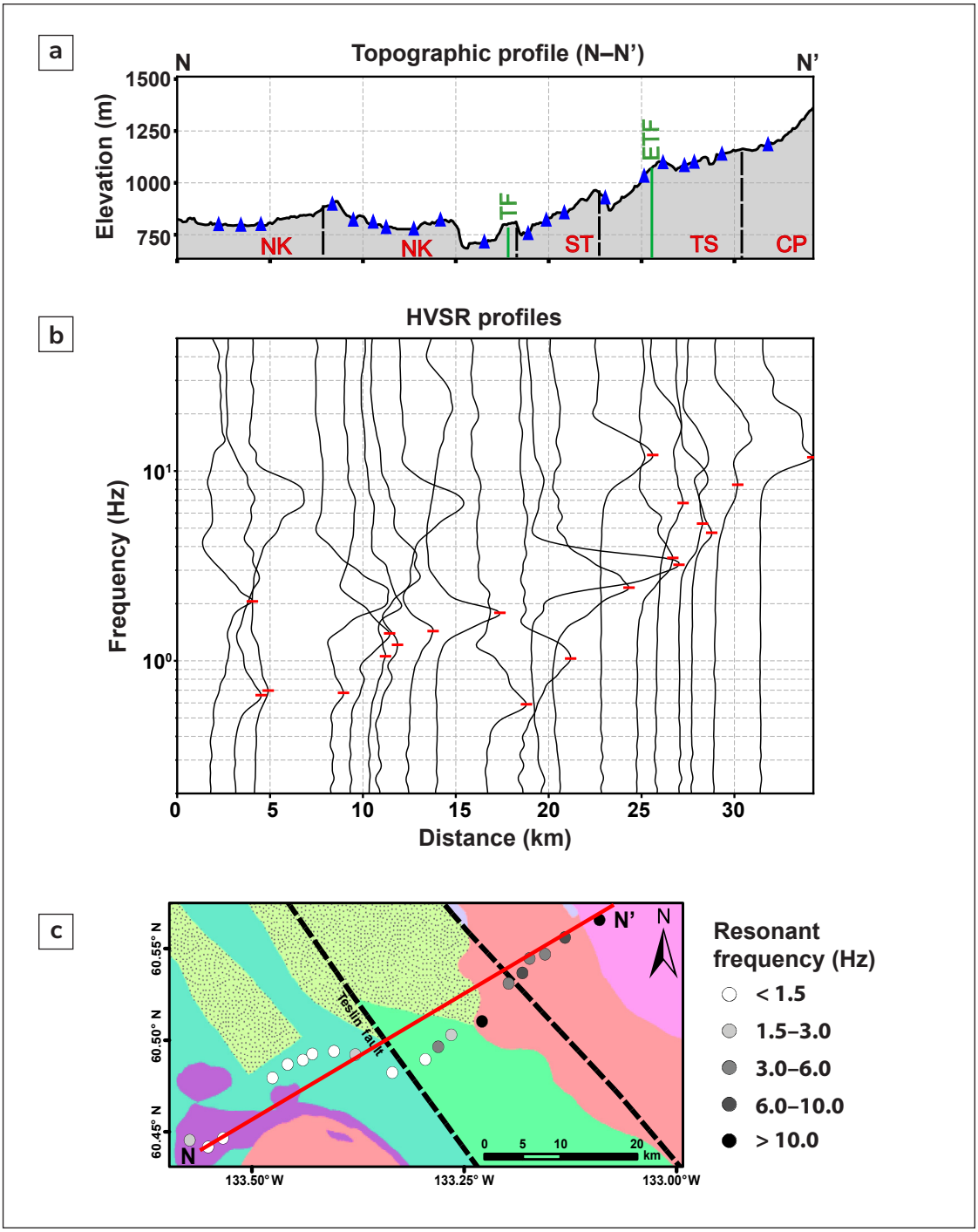


Figure 5. *Horizontal-to-vertical spectral ratio (HVSR) results along the N–N' transect.* ***(a)*** *Topographic profile along the transect. Geophone locations are indicated by blue triangles. Locations of fault surface traces are indicated by green lines. TF – Teslin fault; ETF – Eastern Teslin fault. Boundaries between mapped geologic units are depicted as dashed lines. Geologic units are labeled: western part of the Nakina Formation (NK) consists of variably tectonized serpentinized and chloritized ultramafic rocks, and to the east, consists of andesitic and basaltic spherulitic greenstone; ST – Shonektaw formation; TS – Teslin suite; CP – Canol pluton.* ***(b)*** *HVSR curves for geophones along transect N–N'. The red lines on the HVSR profile represent the measured resonant frequency of the site.* ***(c)*** *Geologic map illustrating the stations in the northern transect of the Teslin fault project on profile N–N'. Geophone locations are displayed as circles, coloured according to measured resonant frequency. Fault traces are indicated by dashed lines and are labeled. See legend of geologic units in Figure 2.*

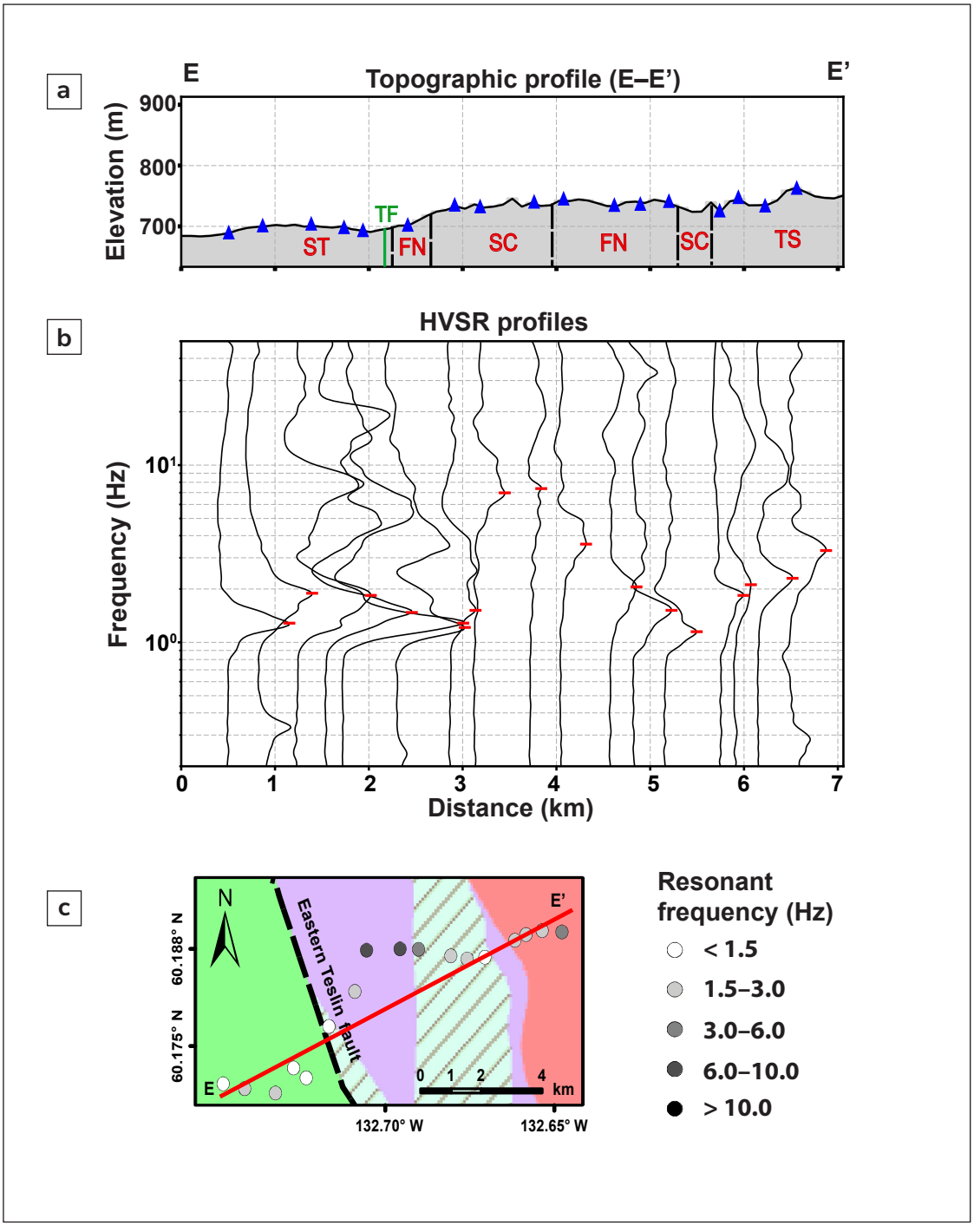


Figure 6. *Horizontal-to-vertical spectral ratio (HVSR) results along the E–E' transect. Details as in Figure 5. Geologic units are labeled: ST – Shonektaw formation; FN – Finlayson assemblage; SC – Snowcap assemblage; TS – Teslin suite. See legend of geologic units in Figure 2.*

Discussion

Implications for boundaries in bedrock geology

Horizontal-to-vertical spectral ratio (HVSR) observations across a broad region surrounding the Teslin fault and its surrounding area reveal several consistent patterns. We find that the locations of changes in HVSR curves and peak frequencies observed here display similarities between the locations of faults and geologic units around the Teslin fault in southern Yukon. The characteristics of the HVSR curves including the amplitude and widths of HVSR peaks, the frequencies of those peaks, and whether the curves possess single or multiple peaks, all appears to vary between geologic units. Lithologic transitions between geologic units are accompanied by changes in HVSR signature, which suggests that changes in bedrock units, and the contrasting seismic properties between the bedrock units and their overlying layers, contribute to the observed HVSR signatures.

The HVSR curves from sites sampling the Nakina Formation on the western segment of the N–N' transect (offsets <18 km; Fig. 5b), display broad peaks with increasing amplitudes from <1 Hz up to 7–8 Hz. The systematic increase in HVSR peak amplitudes from the tectonized ultramafic Nakina Formation in the west, to the andesitic and basaltic Nakina Formation in the east toward the centre of the transect indicates that variations in bedrock lithology accompany changes in contrasting seismic properties between the bedrock and overlying sediments. In this context, the greater HVSR peak amplitudes in the central part of the transect suggests that the difference in seismic properties between the underlying bedrock and surficial deposits is greater than that found for the units to the west.

Sites within the Shonektaw formation of the Quesnellia terrane possess the highest amplitude HVSR peaks along both the N–N' and E–E' profiles (Figs. 5b and 6b). The large seismic contrast between bedrock within the Shonektaw formation, comprised of sandstone, siltstone and mudstone, and the overlying sedimentary layers can be inferred from the strong HVSR peaks displayed in the central part of N–N' and the western end of E–E'. Isolating the factors responsible for the increased impedance contrast within the Shonektaw formation will require further analysis and modelling. The observations presented here indicate that the history of deformation that shaped the region bound by the Teslin and Eastern Teslin faults has imparted the geologic blocks with a distinct structural signature. Additionally, crustal-scale seismic observations from the SNORCLE lines have been interpreted to indicate that parts of Quesnellia have been thrust onto the Stikinia terrane (e.g., Evenchich et al., 2005). Such episodes of terrane overthrusting would produce intracrustal seismic discontinuities and impart signatures of deformation.

The HVSR curves for the stations sampling the Teslin suite, on the eastern sides of both the N–N' and E–E' profiles, exhibit broad peaks that extend from 2 Hz to as high as 10 Hz or greater (Figs. 5c and 6c). The structural configuration responsible for HVSR peaks at high frequencies could be a shallow layer that is either thin or characterized by low seismic velocities (Fig. 4). A thin layer of sediments fits expectations for the area of the Teslin suite at high elevations above 1 km sampled along N–N'. Further modelling will be necessary to constrain the source of broad peaks that extend to high frequencies within the area of the Teslin suite along E–E' at lower elevations.

HVSR and Bouguer gravity anomalies

In addition to the HVSR changes that align with changes in geology and fault locations, the spatial distribution of HVSR derived resonant frequencies follows a similar trend to the distribution of Bouguer gravity anomalies. Our sampling along the E–E' profile and other stations near Teslin are located within the area of a recent gravity survey (Figs. 2 and 7; Witter, 2023). Stations characterized by low-resonant frequencies (<1.5 Hz), are located within regions of more negative Bouguer anomalies (Fig. 7). Conversely, higher–frequency responses (6–28 Hz) are concentrated in regions characterized by less negative Bouguer gravity anomalies (Fig. 7). The pattern of resonant frequencies follows a trend in which higher frequencies coincide with the locations of gravity highs on either side of the Eastern Teslin fault (Fig. 7). Closer to the fault, we observe resonant frequencies decrease to lower values as Bouguer anomaly values decrease to more negative values. The similar patterns in Bouguer anomalies and resonant frequencies highlight the complimentary nature of these datasets in delineating basin geometry, sediment fill, and near-surface structural variability, particularly across complex zones such as the Teslin fault. Additionally, the observed coincidence of gravity anomalies with HVSR signatures suggests they are influenced by common structural sources such as the distribution of faults and changes in the thickness of shallow sedimentary cover.

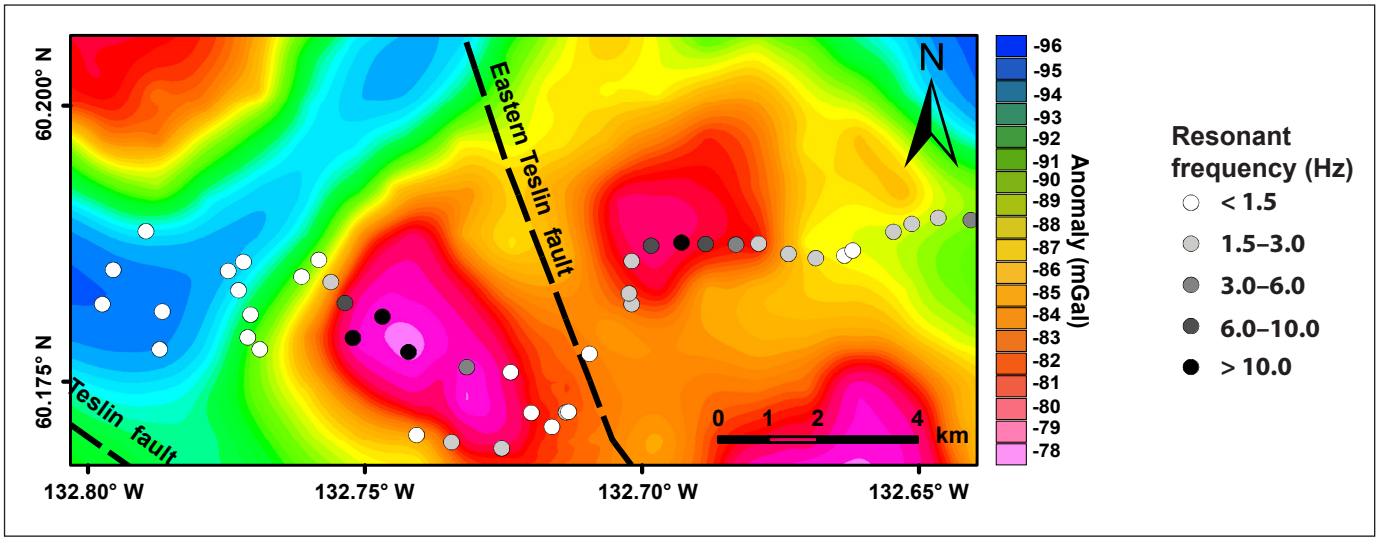


Figure 7. *Comparison between Bouguer gravity anomaly and HVSR measurements. Bouguer gravity anomaly map is modified from Witter (2023). Circles denote geophone locations, coloured according to measured resonant frequency. Fault traces are indicated by black dashed lines and are labeled.*

Conclusions

The HVSR investigation across the Teslin fault zone provides new insights into its shallow architecture. The results reveal distinct spatial variations in resonant frequency and amplitude that correlate with mapped geologic units, fault strands and topographic features. These observations delineate the Teslin and Eastern Teslin faults as structural boundaries separating zones of contrasting subsurface seismic properties. Identifying similar patterns in resonance frequencies and Bouguer anomalies points to the sensitivity of both sets of observations to the same subsurface structures. In summary, these preliminary results find that the Teslin fault and its surrounding features serve as lithologic and structural boundaries that influence the distribution of sediment thickness and contrasting seismic properties. Future work will focus on formal, joint inversion of multiple geophysical data types to create detailed models of the subsurface for future geothermal exploration.

Acknowledgments

We extend our gratitude to the Teslin Tlingit Council for allowing us to conduct field measurements on their land. We also acknowledge the financial support from the University of Calgary, Yukon Geological Survey, and from the Natural Sciences and Engineering Research Council of Canada through Alliance Grant ALLRP-580887-22 and Discovery Grants awarded to Hersh Gilbert and Jan Dettmer. A constructive critical review by Collin Paul helped improve this report.

References

Berumen-Borrego, F., Gilbert, H., Dettmer, J., Gosselin, J.M. and Shahsavari P., 2024. Shear-wave velocities from broadband HVSR measurements for geothermal resource assessment near Burwash Landing, Yukon. *In:* Yukon Exploration and Geology 2023, L.H. Weston and Purple Rock Inc. (eds.), Yukon Geological Survey, p. 1–15.

Beyreuther, M., Barsch, R., Krischer, L., Megies, T., Behr, Y. and Wassermann, J., 2010. ObsPy: A python toolbox for seismology. Seismological Research Letters, vol. 81, no. 3, p. 530–533, https://doi.org/10.1785/gssrl.81.3.530.

Caine, J.S., Evans, J.P. and Forster, C., 1996. Fault zone architecture and permeability structure. Geology. vol. 24, no. 11, p. 1025–1028, https://doi.org/10.1130/0091-7613(1996)024<1025:FZAAPS>2.3.CO;2.

Cipta, A., Cummins, P., Dettmer, J., Saygin, E., Irsyam, M., Rudyanto, A. and Murjaya, J., 2018. Seismic velocity structure of the Jakarta Basin, Indonesia, using trans-dimensional Bayesian inversion of horizontal-to-vertical spectral ratios. Geophysical Journal International, vol. 215, no. 1, p. 431–449, https://doi.org/10.1093/gji/ggy289.

Colpron, M., Nelson, J.L. and Murphy, D.C., 2007. Northern Cordilleran terranes and their interactions through time. GSA Today, vol. 17, no. 4–5, p. 4–10, https://doi.org/10.1130/GSAT01704-5A.1.

Colpron, M., Hayward, N. and Crowley, J.L., 2021. Potential heat production from the Seagull and Teslin plutonic suites, southern Yukon: Geochemistry, geochronology, rock physical properties, and 3D geophysical inversion of Bouguer gravity data. *In:* Yukon Exploration and Geology 2020, K.E. MacFarlane (ed.), Yukon Geological Survey, p.47–72.

Colpron, M., Sack, P.J., Crowley, J.L., Beranek, L.P. and Allan, M.M., 2022. Late Triassic to Jurassic magmatic and tectonic evolution of the Intermontane terranes in Yukon, Northern Canadian Cordillera: Transition from arc to syn-collisional magmatism and post-collisional lithospheric delamination. Tectonics, vol. 41, no. 2, p. 1–32, https://doi.org/10.1029/2021TC007060.

Cox, B.R., Cheng, T., Vantassel, J.P. and Manuel, L., 2020. A statistical representation and frequency-domain window-rejection algorithm for single-station HVSR measurements. Geophysical Journal International, vol. 221, no. 3, p. 2170–2183, https://doi.org.10.1093/gji/ggaa119.

de Keijzer, M., Mihalynuk, M.G. and Johnston, S.T., 2000. Structural investigation of an exposure of the Teslin fault, northwestern British Columbia. Geological Survey of Canada, Natural Resources Canada, Current Research 2000-A5, p. 1–10.

Denny, C.S., 1952. Late Quaternary geology and frost phenomena along the Alaska Highway, Teslin Lake to Whitehorse, Yukon Territory. U.S. Geological Survey Bulletin, 983–C, p. 73–118.

Environment and Climate Change Canada, n.d. Historical Data Climate. Government of Canada, https://climate.weather.gc.ca/historical_data/search_historic_data_stations_e.

Estève, C., Gosselin, J.M., Audet, P., Schaeffer, A.J., Schutt, D.L. and Aster, R.C., 2021. Surface-wave tomography of the northern Canadian Cordillera using earthquake Rayleigh wave group velocities. Journal of Geophysical Research: Solid Earth, vol. 126, no. 8, p. 1–22, https://doi.org/10.1029/2021JB021960.

Evenchick, C.A., Gabrielse, H. and Snyder, D.B., 2005. Crustal structure and lithology of the northern Canadian Cordillera: alternative interpretations of SNORCLE seismic reflection lines 2a and 2b. Canadian Journal of Earth Sciences, vol. 42, p. 1149–1161.

Faulkner, D.R., Jackson, C.A.L., Lunn, R.J., Schlische, R.W., Shipton, Z.K., Wibberley, C.A.J. and Withjack, M.O., 2010. A review of recent developments concerning the structure, mechanics and fluid flow properties of fault zones. Journal of Structural Geology, vol. 32, no. 11, p. 1557–1575, https://doi.org/10.1016/j.jsg.2010.06.009.

Fisher, M.A., Pellerin, L., Nokleberg, W.J., Ratchkovski, N.A. and Glen, J.M.G., 2007. Crustal structure of the Alaska Range orogen and Denali fault along the Richardson Highway. *In:* Tectonic growth of a collisional continental margin: Crustal evolution of southern Alaska, K.D. Ridgway, J.M. Trop, J.M.G. Glen and J.M. O'Neill (eds.), Geological Society of America Special Paper, https://doi.org/10.1130/2007.2431(03).

Fraser, T.A., Grasby, S.E., Witter, J.B., Colpron, M. and Relf, C., 2018. Geothermal studies in Yukon–Collaborative efforts to understand ground temperature in the Canadian North. Geothermal Resources Council Transactions, vol. 43, p. 891–903.

Gilbert, R., Desloges, J.R., Lamoureux, S.F., Serink, A. and Hodder, K.R., 2006. The geomorphic and paleoenvironmental record in the sediments of Atlin Lake, northern British Columbia. Geomorphology, vol. 79, no. 1-2, p. 130-142, https://doi.org/10.1016/j.geomorph.2005.09.021.

Haefner, R.J., Sheets, R.A. and Andrews, R.E., 2011. Evaluation of the horizontal-to-vertical spectral ratio (HVSR) seismic method to determine sediment thickness in the vicinity of the South Well Field, Franklin County, Ohio. Ohio Journal of Science, vol. 110, no. 4, p. 77–85.

Hayward, N., 2015. Geophysical investigation and reconstruction of lithospheric structure and its control on geology, structure, and mineralization in the Cordillera of northern Canada and eastern Alaska. Tectonics, vol. 34, no. 10, p. 2165–2189, https://doi.org/10.1002/2015TC003871.

Hildes, D., 2022. YGS-20221024 Logistic Report on Teslin area gravity survey. YGS-20221024 logistic report prepared by Aurora Geosciences Ltd., Yukon Geological Survey, Submitted October 22, 2022, 266 p.

Hobiger, M., Cornou, C., Wathelet, M., Di Giulio, G., Knapmeyer-Endrun, B., Renalier, F., Bard, P.-Y., Savvaidis, A., Hailemikael, S., Le, B.N., Ohrnberger, M. and Theodoulidis, N., 2013. Ground structure imaging by inversions of Rayleigh wave ellipticity: Sensitivity analysis and application to European strong-motion sites. Geophysical Journal International, vol. 192, no. 1, p. 207–229, https://doi.org/10.1093/gji/ggs005.

Johnston, S.T. and Canil, D., 2007. Crustal architecture of southwestern Yukon and implications for Cordilleran terrane accretion. Tectonics, vol. 26, no. 2, p. 1–18, https://doi.org/10.1029/2006TC001950.

Konno, K. and Ohmachi, T., 1998. Ground-motion characteristics estimated from spectral ratio between horizontal and vertical components of microtremor. Bulletin of the Seismological Society of America, vol. 88, p. 228–241, https://doi.org/10.1785/BSSA0880010228.

Krischer, L., Megies, T., Barsch, R., Beyreuther, M., Lecocq, T., Caudron, C. and Wassermann, J., 2015. ObsPy: A bridge for seismology into the scientific Python ecosystem. Computational Science and Discovery, vol. 8, no. 1, p. 1–17, https://doi.org/10.1088/1749-4699/8/1/014003.

Lane, J.W., Jr., White, E.A., Steele, G.V. and Cannia, J.C., 2008. Estimation of bedrock depth using the horizontal-to-vertical (H/V) ambient-noise seismic method. *In:* Symposium on the Application of Geophysics to Engineering and Environmental Problems, April 6–10, 2008, Philadelphia, Pennsylvania, Proceedings: Denver, Colorado, Environmental and Engineering Geophysical Society, 13 p.

Larson, K.P., 2002. Microstructural analysis of the Teslin fault, northern Canadian Cordillera. British Columbia Geological Survey, Geological Fieldwork 2001, Paper 2002-1, 3 p.

McDermott, R.G., Ault, A.K., Caine, J.S. and Thomson, S.N., 2019. Thermotectonic history of the Kluane Ranges and evolution of the eastern Denali fault zone in southwestern Yukon, Canada. Tectonics, vol. 38, no. 8, p. 2983–3010, https://doi.org/10.1029/2019TC005545.

Monger, J.W.H. and Price, R.A., 2002. The Canadian Cordillera: Geology and tectonic evolution. CSEG Recorder, vol. 27, no. 2, p. 17–36.

Morison, S.R. and Klassen, R.W., 1997. Surficial geology, Teslin, Yukon Territory, Geological Survey of Canada, Open File Map 1891A, scale 1:125 000.

Mortensen, J.K., 1992. Pre-mid-Mesozoic tectonic evolution of the Yukon-Tanana terrane, Yukon and Alaska. Tectonics, vol. 11, p. 836–853, https://doi.org/10.1029/91TC01169.

Nakamura, Y., 1989. A method for dynamic characteristics estimation of subsurface using microtremor on the ground surface. Railway Technical Research Institute, Quarterly Reports, vol. 30, no. 1, https://trid.trb.org/view/294184.

Nakamura, Y., 2008. On the H/V spectrum. The 14th World Conference on Earthquake Engineering, Beijing, China, October 12–17, 2008.

SESAME, 2004. Guidelines for the implementation of the H/V spectral ratio technique on ambient vibrations: Measurements, processing and interpretation. SESAME European Research Project WP12, p. 1–62.

Snyder, D.B., Roberts, B.J. and Gordey, S.P., 2005. Contrasting seismic characteristics of three major faults in northwestern Canada. Canadian Journal of Earth Sciences, vol. 42, no. 7, p. 1223–1237, https://doi.org/10.1139/e05-0276.

Stannard, D. and Meyers, J., 2018. Near surface passive seismic HVSR surveying for mineral exploration, regolith mapping and other applications. *In*: EAGE–HAGI 1st Asia Pacific Meeting on Near Surface Geoscience & Engineering, Yogyakarta, Indonesia, April 9–13, 2018, Program with Abstracts, vol. S401, p. 1–6, https://doi.org/10.3997/2214-4609.201800392.

Sternbergh, S. and Colpron, M., 2025. Summary of geothermal indicators in the Yukon. Yukon Geological Survey, Government of Yukon, Open File 2025-7, 92 p. plus appendices.

Stevens, R.A. and Erdmer, P., 1996. Structural divergence and transpression in the Teslin tectonic zone, southern Yukon Territory. Tectonics, vol. 15, no. 6, p. 1342–1363, https://doi.org/10.1029/96TC01134.

Vantassel, J.P., Cox, B.R. and Brannon, D.M., 2021. HVSRweb: An open-source, web-based application for horizontal-to-vertical spectral ratio processing. International Foundation Congress and Equipment Expo 2021, p. 1–10, https://doi.org/10.1061/9780784483428.005.

Vantassel, J.P., Stolte, A.C., Wotherspoon, L.M. and Cox, B.R., 2023. AutoHVSR: A machine-learning-supported algorithm for the fully-automated processing of horizontal-to-vertical spectral ratio measurements. ArXiv, 25 p., https://arxiv.org/abs/2304.05559.

Witter, J.B., 2023. Analysis of geoscience data for geothermal exploration along the Teslin fault near Teslin, Yukon. Yukon Geological Survey, Government of Yukon, Open File 2023-3, 48 p.

Yukon Geological Survey, 2011. A digital atlas of terranes for the northern Cordillera. Yukon Geological Survey, http://data.geology.gov.yk.ca/Compilation/2, [accessed 15/11/2025].

Yukon Geological Survey, 2023. Yukon Digital Bedrock Geology. Yukon Geological Survey, http://datatest.geology.gov.yk.ca/Compilation/3, [accessed 22/10/2025].

Stratigraphic, geochronological, and geochemical constraints on the genesis of Late Cretaceous volcanic rocks in the Sixtymile district of west central Yukon, Canada (NTS 116C/2, 115N/15)

Emilia Butty
Queen's Facility for Isotope Research, Department of Gological Sciences and Geological Engineering, Queen's University
Yukon Geological Survey

*Patrick J. Sack**
Yukon Geological Survey

Matthew Leybourne
Queen's Facility for Isotope Research, Department of Gological Sciences and Geological Engineering, Queen's University

James Crowley
Boise State University

Butty, E., Sack, P.J., Leybourne, M. and Crowley, J., 2026. Stratigraphic, geochronological, and geochemical constraints on the genesis of Late Cretaceous volcanic rocks in the Sixtymile district of west central Yukon, Canada (NTS 116C/2, 115N/15). *In*: Yukon Exploration and Geology 2025, A. Stuart, L.H. Weston and S.K. Schultz (eds.), Yukon Geological Survey, Government of Yukon, p. 91–117, plus digital appendices.

Abstract

In the Yukon, Late Cretaceous rocks are associated with significant porphyry systems that are of interest from mineral exploration, mineral potential and land use planning perspectives. The Sixtymile district of west-central Yukon contains rocks thought to be of this age, but their origin is largely unknown due to poor geochronological and geochemical constraints. In this contribution geologic mapping, U-Pb zircon geochronology, whole-rock geochemistry, and strontium (Sr), neodymium (Nd), and lead (Pb) whole-rock isotopes are used to characterize Late Cretaceous volcanic rocks in the Sixtymile district. Bedrock geology in the Sixtymile district is composed of a Yukon-Tanana terrane metamorphic basement overlain by undeformed and unmetamorphosed Cretaceous sedimentary and volcanic rocks. The Cretaceous rocks have a consistent stratigraphy consisting of a basal sedimentary unit, a middle andesitic unit, and an upper basaltic andesite unit. Four new U-Pb magmatic zircon ages that range between 69.779 ± 0.020 and 69.802 ± 0.020 Ma from the andesitic component of the volcanic stratigraphy demonstrate the volcanic event was short lived and lasted a maximum of 60 000 years. Late Cretaceous volcanic rocks are dominantly subalkaline and have continental arc geochemical signatures: 1) thorium/ytterbium (Th/Yb) versus niobium/ytterbium (Nb/Yb) values plot in the volcanic arc field; 2) extended trace element plots reveal negative Nb and titanium (Ti) anomalies and positive lead (Pb) anomalies; and 3) high field strength elements (HFSE) and light rare earth elements (LREE) are depleted compared to large ion lithophile elements (LILE). Additionally, isotope ratios reveal $^{87}Sr/^{86}Sr_i$ of 0.7050 to 0.7056, $^{143}Nd/^{144}Nd_i$ values of 0.5124 to 0.5126, εNd_i values of -1.9 to 1.1, and elevated Pb isotope ratios. We suggest that the Sixtymile district Late Cretaceous volcanic rocks are consistent with a relatively primitive continental magmatic arc setting.

* patrick.sack@yukon.ca

Plain language summary

This paper describes the geology of the Sixtymile district of western Yukon and presents data on the age of volcanic rocks from the area, and how the magmas that formed the volcanic rocks were generated. The geology of the Sixtymile district consists of a basement of metamorphic rocks overlain by sedimentary and volcanic rocks. The sedimentary and volcanic rocks were mostly preserved in a small basin (approximately 7 by 15 km) formed along the Sixtymile-Pika fault. The volcanic rocks in the Sixtymile district are 69.8 million years old and likely erupted in less than 60 000 years. The chemistry of the volcanic rocks suggests that they are the products of subduction-related magmatism.

Introduction

Late Cretaceous (ca. 84 to 68 Ma) volcanic rocks in the northern Cordillera are widely distributed southwest of the Tintina fault where they extend from northwestern British Columbia, through the Yukon and into Alaska (Fig. 1). Additionally, Late Cretaceous rocks are associated with significant porphyry systems (porphyry, epithermal and skarn deposits; Fig. 2) and are of interest from mineral exploration, mineral potential and land use planning perspectives. In the Yukon, these rocks include the Windy-Table, Open Creek, Tslansanlin and Carmacks group volcanic rocks which have mostly been investigated at regional mapping scales (1:50 000 to 1:250 000; e.g., Tempelman-Kluit, 1974, 1984, 2009; Grond et al., 1984; Mortensen, 1988, 1996; Ryan et al., 2013; Bordet et al., 2019). A few localized studies related to mineralization (Glasmacher and Friedrich, 1992; Smuk, 1999) or petrogenesis (Francis and Minarik, 2008) have also been completed.

It is generally recognized that a coarse conglomerate or breccia makes up the lowest Late Cretaceous stratigraphy followed by an andesitic volcanic and volcaniclastic package capped by basaltic flows and breccias (e.g., Payne et al., 1987; Johnston et al., 1996; Tempelman-Kluit, 2009). A shallowly dipping (<10˚) unconformity is locally recognized between the andesitic and basaltic components of the stratigraphy (e.g., Johnston et al., 1996; Francis and Minarik, 2008), but the entire volcanic package is thought to be genetically related and regionally flat lying. The current understanding of the magmatic setting and petrogenesis of these rocks is hampered by the lack of high quality, precise geochronological and geochemical control on the volcanic stratigraphy (e.g., Grond et al., 1984; Lowey et al., 1986). Partially based on these limited data, a continental arc magmatic setting has been ascribed to the more andesitic components of the stratigraphy (e.g., Morris et al., 2014), whereas a continental flood basalt, hot-spot related petrogenesis (Johnston et al., 1996) is primarily based on samples from the upper basaltic rocks.

One of the locales in the Yukon with Late Cretaceous magmatic rocks is the Sixtymile district along the Yukon-Alaska border (Mortensen, 1988, 1996; Rimando et al., 2022). In this area, Late Cretaceous volcanic rocks are primarily found within a pull-apart graben formed at a stepover along the orogen-normal, Cretaceous Sixtymile-Pika fault system (Fig. 2; Mortensen, 1996; Allan et al., 2017). The area has been regionally mapped (1:50 000 and 1:250 000; Mortensen, 1988; 1996), but the Late Cretaceous volcanic rocks have not been characterized in detail, and prior to this study, were undated. This paper describes the Late Cretaceous geology of the Sixtymile district in detail and reports four new chemical abrasion-isotope dilution-thermal ionization mass spectrometry (CA-TIMS) U-Pb ages for volcanic strata along with 27 whole-rock lithogeochemical analyses and six whole-rock Sr, Nd and Pb isotope analyses. We use this new data to constrain the stratigraphy for the Sixtymile district and interpret a continental magmatic arc origin for the volcanic rocks.

Regional geology

The bedrock geology of the Sixtymile district consists of metamorphic basement overlain by Cretaceous volcanic and sedimentary rocks (Mortensen, 1988, 1996) dissected by the 130 km-long Sixtymile-Pika fault system (Allan et al., 2017). The metamorphic basement is primarily of Yukon-Tanana terrane affinity; however, towards the southern margin of the district, the Fiftymile fault, a low-angle extensional fault, juxtaposes the Fiftymile batholith of autochthonous North American affinity against the parautochthonous Yukon-Tanana terrane rocks (Fig. 3, Mortensen, 1996; Dusel-Bacon and Mortensen, 2024).

Yukon-Tananaterranehasalowermostmetasedimentary assemblage of parautochthonous North American affinity (Snowcap assemblage) overlain by up to three volcanic arc or back-arc packages separated by unconformities (Finlayson, Klinkit and Klondike

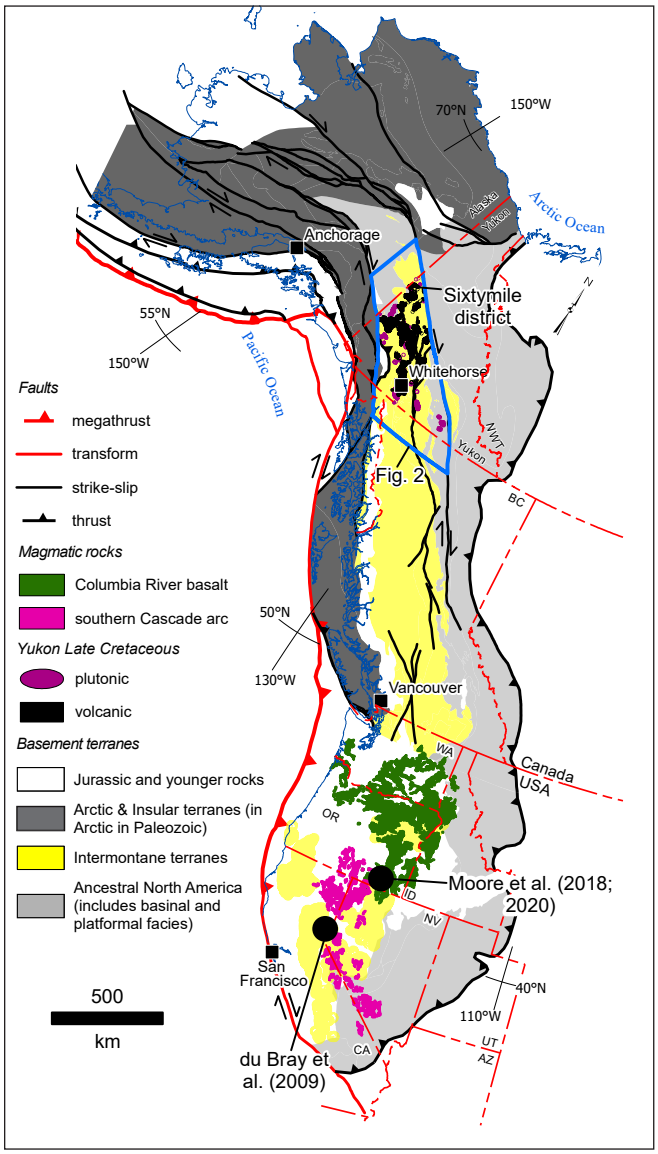


Figure 1. *Tectonic realms of the northern North American Cordillera (modified after Colpron et al., 2007). Continental USA geology from Garrity and Soller (2009). Black dots represent the location of the du Bray et al. (2009) and Moore et al. (2018 and 2020) studies. Figure 2 is delineated by blue outline.*

assemblages, respectively; Colpron et al., 2006; Dusel-Bacon et al., 2006). In the Sixtymile district, only the Finlayson and Klondike assemblages are recognized (Fig. 3). Locally, the Finlayson assemblage is a mix of quartzose and graphitic metasedimentary rocks and Mississippian micaceous schist of metavolcanic origin (Nasina assemblage of Mortensen, 1988) and coeval intermediate composition orthogneiss of the Simpson Range suite. The Klondike assemblage is a Permian meta-igneous package of felsic schist (Mortensen, 1988). There are also a few slivers of ultramafic rocks near the margins of a thrust-bound package of the Klondike assemblage (Fig. 3).

The majority of $^{40}Ar/^{39}Ar$ analyses of biotite and muscovite for the Sixtymile district are Early to Middle Jurassic and are associated with exhumation from mid-crustal levels during initial accretion of the Yukon-Tanana terrane with the western margin of North America (Johnston and Erdmer, 1995; Colpron et al., 2022; Colpron et al., 2025). Following exhumation to upper crustal levels, domains with mid-Cretaceous $^{40}Ar/^{39}Ar$ cooling ages formed in autochthonous rocks with Late Devonian intrusions such as the Fiftymile batholith (Dusel-Bacon et al., 2002; Dusel-Bacon and Mortensen, 2024). These mid-Cretaceous cooling domains are interpreted as windows through the upper parautochthonous Yukon-Tanana plate into the lower autochthonous North American plate (e.g., Staples et al., 2016). Coeval with mid-Cretaceous extension was the deposition of the Indian River Formation, a succession of pebble conglomerate, sandstone, siltstone and ash-fall tuff up to 500 m thick (Lowey, 1984). After deposition of the mid-Cretaceous Indian River Formation, Late Cretaceous volcanic and sedimentary rocks such as those in the Sixtymile district were deposited. Cretaceous and younger deformation in the Sixtymile region was brittle in nature and is dominated by the northeast-striking Sixtymile-Pike fault zone that extends from the Denali fault to the Tintina fault and accommodates up to 17 km of sinistral displacement (Allan et al., 2017). The Sixtymile-Pika fault also appears to have influenced the emplacement, and/or preservation of the Late Cretaceous magmatic rocks in the area (Allan et al., 2013).

Local geology

Thirty days of geological mapping (1: 25 000 scale) were conducted in 2023 and 2024 in the Sixtymile district (Figs. 3 to 5). Access to the Sixtymile district is from the Top of the World Highway. Mapping was conducted via foot-traverses, and access was by truck and all-terrain vehicles. The Sixtymile district was not glaciated in the Quaternary (Duk-Rodkin, 1996) and the landscape consists of rolling hills separated by over-steepened valleys with thick forest coverage and relatively deep weathering, all of which result in poor bedrock exposure. Because of the poor bedrock exposure, changes in felsenmeer composition are used to map the approximate location of contacts. Additionally, a few key man-made exposures in quarry pits and placer excavations also help determine relationships between units.

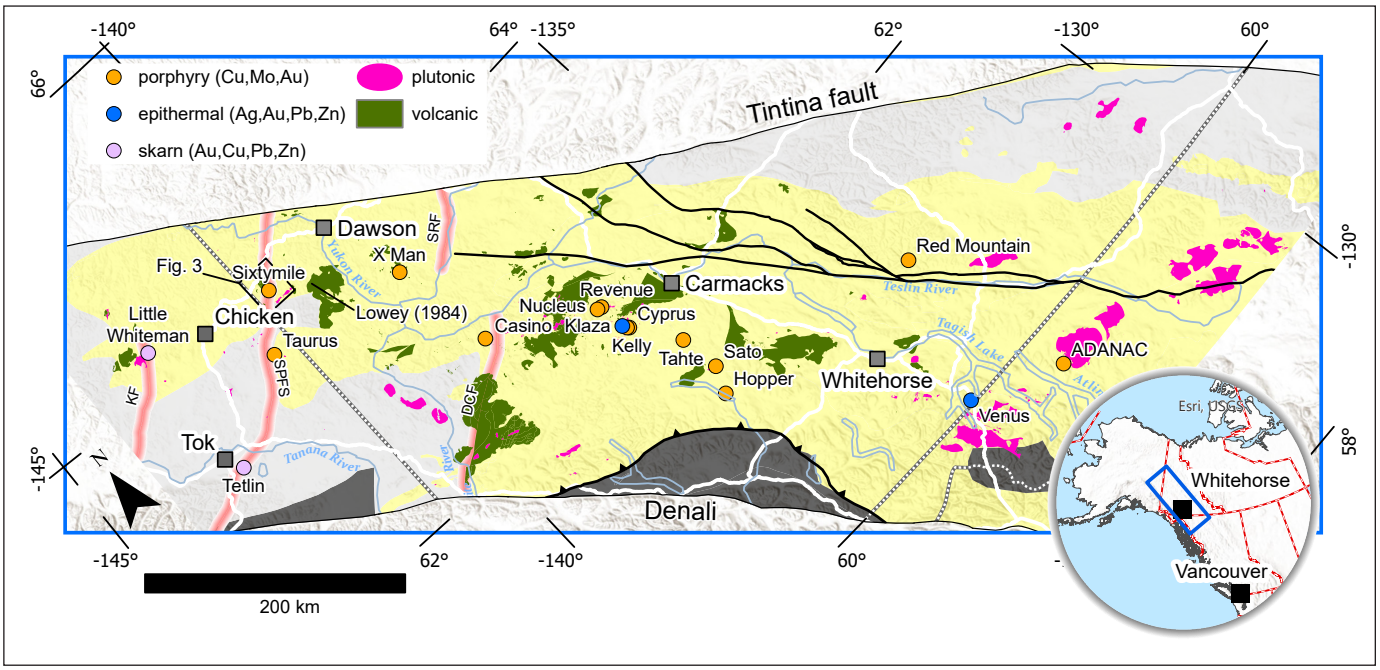


Figure 2. *Simplified bedrock geology map of eastern Alaska, southwest Yukon and northeast British Columbia, including Cretaceous-orogen normal faults (red lines: Ketchumstuk fault (KF); Sixtymile-Pika fault system (SPFS); Stewart River fault (SRF); and Dip Creek fault (DCF)), as well as Late Cretaceous magmatic rocks and mineral occurrences (modified from Allan et al., 2017). Basement terrane colours same as Figure 1.*

Metamorphic basement

The Sixtymile district basement geology is comprised of metamorphic rocks (Figs. 3 and 6). The oldest of these consist of the Late Devonian Grass Lakes suite, which is a coarse-grained, foliated granodiorite with rounded plagioclase crystals up to 3–5 cm in diameter. These intrusions are found on the southern boundary of the map area (Dusel-Bacon and Mortensen, 2024). Most of the district is underlain by Late Devonian to Early Mississippian quartzite and metavolcanic rocks of the Finlayson assemblage and their coeval metaplutonic equivalent, the Simpson Range suite. The quartzite is white to dark grey, thinly to thickly layered, and contains carbonaceous foliations. The metavolcanic rocks are pale green and include chlorite and quartz-rich layers (Fig. 6g). The metaplutonic rocks are equigranular, foliated, hornblende-bearing and of granodiorite composition. The youngest basement units are mostly found in a thrust-bound panel of Permian, silver-grey, muscovite-chlorite-quartz schists of the Klondike assemblage, and small lozenges of red-brown weathering ultramafic rocks of the Dawson-Clinton Creek assemblage (Mortensen, 1988).

Late Cretaceous conglomerate

The stratigraphically lowest rocks investigated in detail in this study are a sedimentary unit that overlies the metamorphic basement and consists of unmetamorphosed, poorly consolidated sedimentary rocks. These rocks weather easily and are poorly preserved, and most exposures occur in road and placer workings; a few natural exposures are found near the Top of the World highway and to the north in creek banks and confluences. Where observed in outcrop, this unit is dominated by matrix to clast-supported, pebble to cobble conglomerate with a sandy matrix (Fig. 6h). The sandstone matrix is white-beige in colour and grains are 0.1 to 0.3 mm in diameter. The clasts are rounded to subrounded, black, white and beige in colour, and 0.5 mm to >5 cm in diameter. The lithologies are metamorphic and quartz in composition. At the confluence of Little Gold and Big Gold creeks, an extensive excavation 3 m high exposes a section that includes a spheroidal-weathering, coarse-grained sandstone, a thin coal seam, a 15 cm-thick tuff unit, as well as the matrix-supported pebble conglomerate. The tuff is light grey, very fine-grained and has quartz eyes and biotite phenocrysts. Higher in the Late Cretaceous stratigraphy, there are minor occurrences of coarse-sandstone; the best exposures of which are along the Sixtymile road.

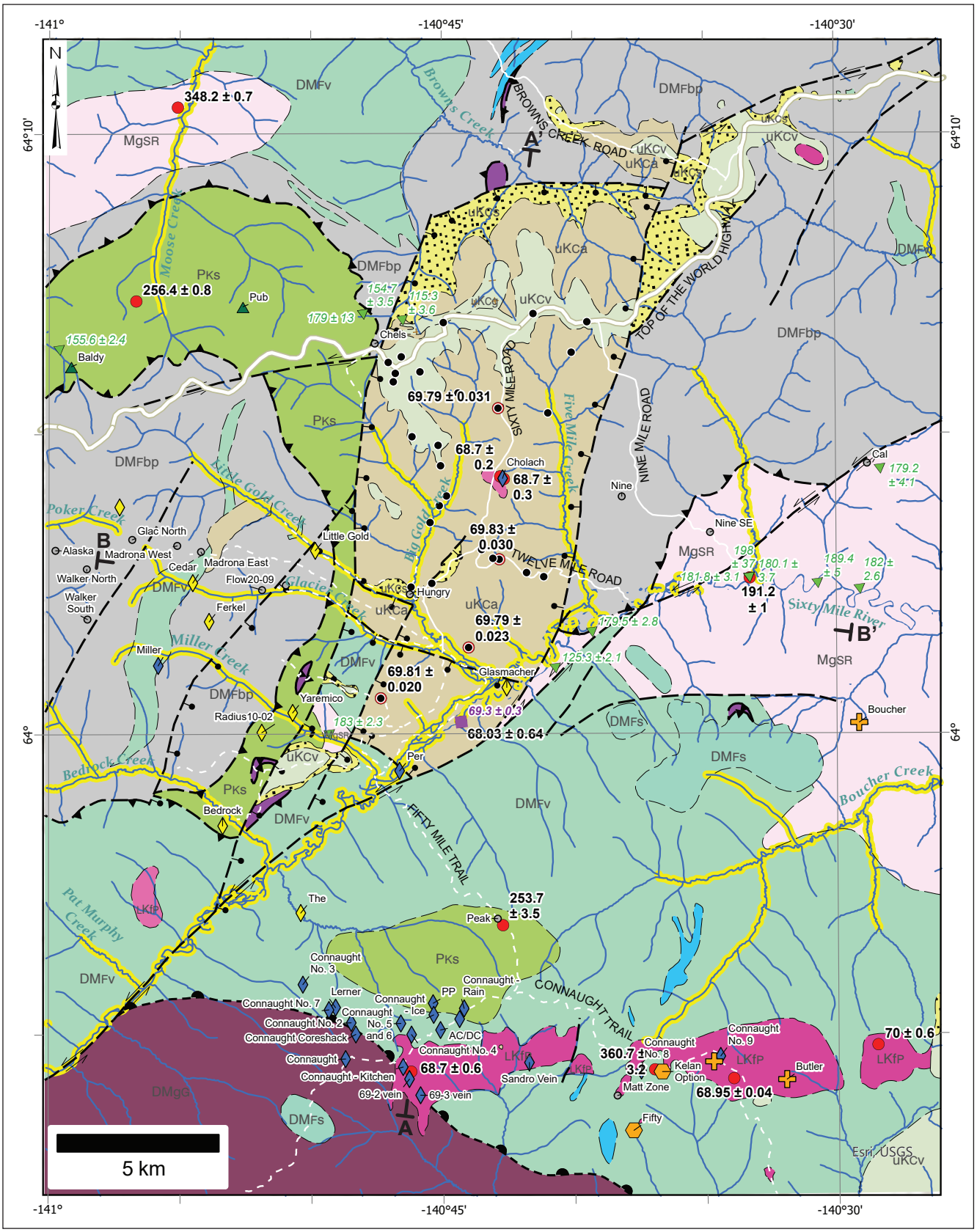


Figure 3. *Bedrock geology map of the Sixtymile district. See legend on following page (Sack et al., in prep).*

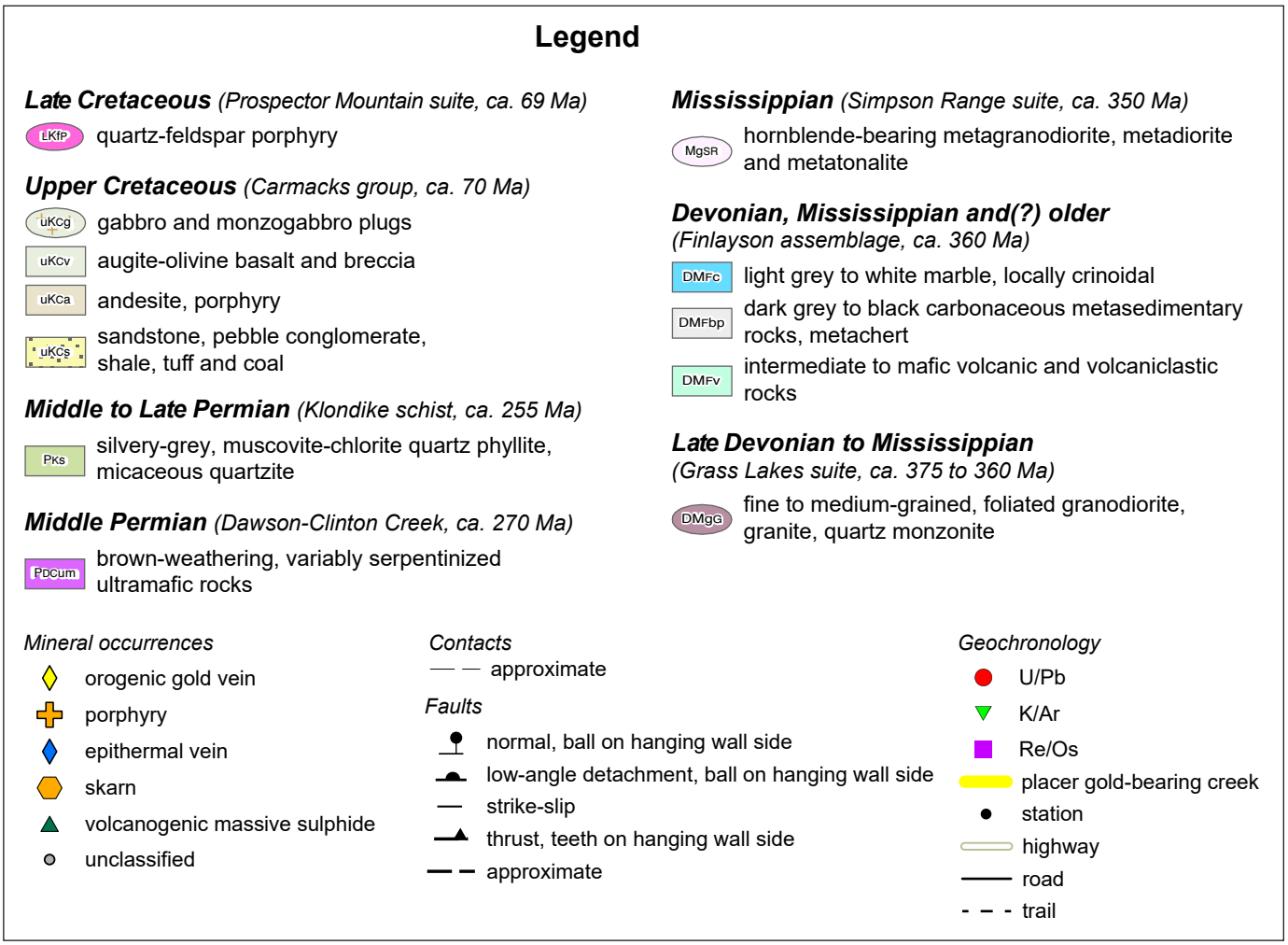


Figure 3 (legend). *Bedrock geology map of the Sixtymile district (Sack et al., in prep).*

Late Cretaceous volcanic rocks

Andesitic rocks

The most widespread unit reported in detail in this study is an unfoliated andesitic unit. This unit is typically found immediately above the basal conglomerate from approximately 670 to 980 m elevation and is approximately 300 m thick. It extends from near the Top of the World Highway, south to the Sixtymile River (Fig. 3), and constitutes most of the rocks exposed within the graben. The andesitic rocks are massive flows, crystal tuffs, and block and ash flows (Fig. 6a,e). They are light to dark grey and contain plagioclase ± hornblende, biotite, quartz and pyroxene phenocrysts. The phenocrysts in the andesite unit are primarily plagioclase (≤80%), and subordinate amounts of hornblende (≤15%) and biotite (≤5%) in a plagioclase-rich matrix (Fig. 7a-h). In rare samples, quartz phenocrysts are visible in thin section where they make up to 5% of the rock. The plagioclase phenocrysts vary in size from 0.5–2 mm near the top of the succession, to 2–3 mm near the bottom. Trace pyroxene phenocrysts are seen near the top of the unit, but not in the lower stratigraphy. Hornblende and biotite phenocrysts range from <1–2 mm in diameter. Progressing down section, the plagioclase and hornblende phenocrysts increase in size and abundance. Biotite is limited to the lower sections of the succession.

Basaltic andesitic rocks

The upper basaltic andesite unit is at least 200 m thick and found at higher elevations (≥980 m) in the northern part of the study area around the Top of the World Highway (Fig. 3). The basaltic andesite unit is unfoliated, dense, dark grey to black on fresh surfaces, and weathers dark brown (Fig. 6d). It is

generally massive, but surfaces can show differential weathering with a pseudo-fragmental texture suggestive of a monomictic breccia. Plagioclase phenocrysts are 0.5–1 mm and surrounded by an aphanitic groundmass; in some samples, small pyroxene crystals (<0.5 mm) are observed (Fig. 7e). The phenocrysts are dominantly plagioclase (80%) with subordinate amounts of pyroxene (7%), hornblende (5%), olivine (3%) and opaque minerals (probably magnetite; 5%). Hornblende, biotite and quartz are very fine-grained and only identifiable in thin section (Fig. 7a–f).

Late Cretaceous(?) intrusive rocks

Three types of intrusive rocks crosscut the Late Cretaceous volcanic rocks. Hornblende-biotite granodiorite and hornblende diorite intrude the andesitic unit in drill core in the Sixtymile valley near the Per occurrence, as well as basement units along the southern margin of the map near the Connaught occurrences (Fig. 3). These intrusions are associated with porphyry mineralization (Allan et al., 2017). Pyroxene porphyritic gabbro to monzogabbro bodies intrude the andesitic and basaltic andesite units at higher elevations. These intrusions weather brown-red and have up to 25% equant pyroxene, 7–10 mm in size, in an aphanitic groundmass (Fig. 6f). Dense, dark green to black aphanitic mafic dykes crosscut the andesitic unit (Fig. 6e). These dykes can have small pyroxene phenocrysts less than 0.2 mm in diameter and resemble the basaltic andesite unit implying they could be feeder dykes to that unit.

Methods

Analytical methods are briefly summarized here and are described in more detail in Appendices A and B. Geochronological data were collected at Boise State University using laser ablation-inductively coupled plasma mass spectrometry (LA-ICPMS) and chemical abrasion-isotope dilution-thermal ionization mass spectrometry (CA-TIMS) of U-Th-Pb in zircon. Whole-rock geochemical analyses were done by Analytical Laboratory Services (ALS) Geochemistry on samples prepared with a mild steel mill and analyzed with X-ray fluorescence spectroscopy (XRF) and ICPMS after fusion and four acid digestion. Whole-rock pulps were also analyzed at the University of Melbourne for Sr, Nd, Pb isotope compositions.

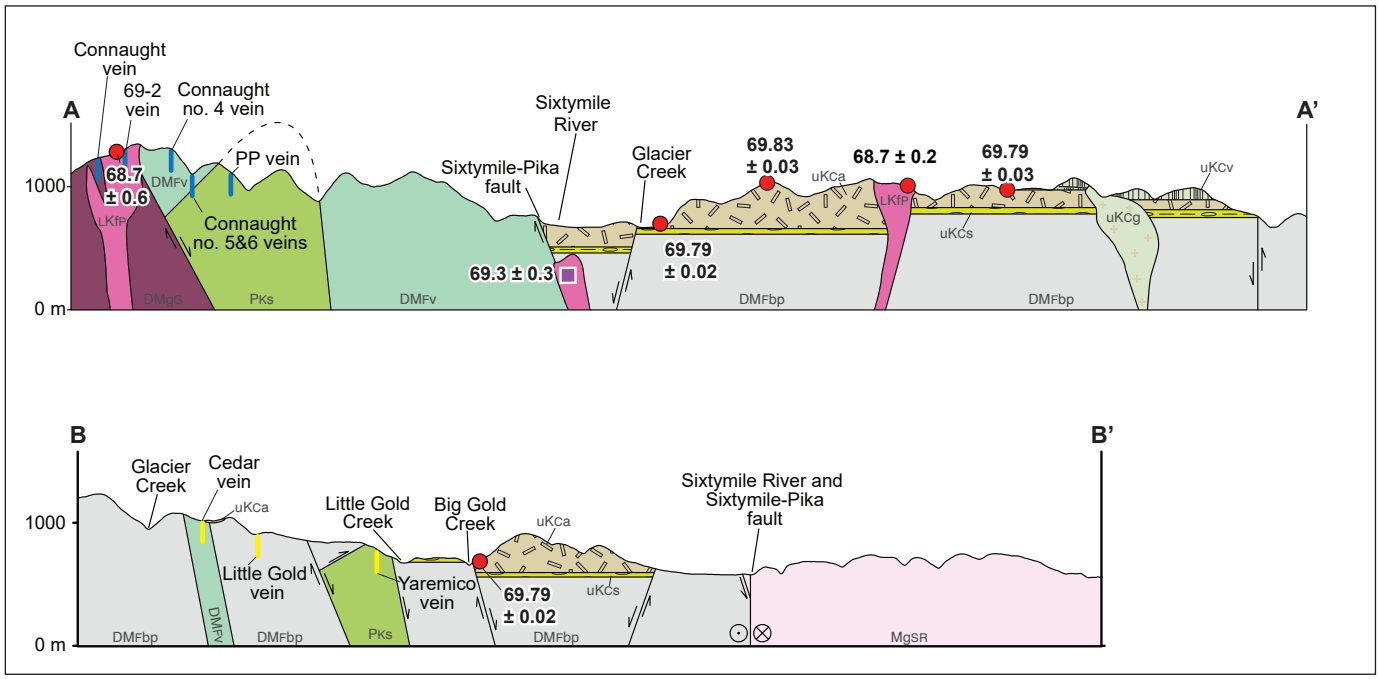


Figure 4. *Long-section (A–A') and cross-section (B–B') through the Sixtymile district. Section locations shown on Figure 3. Legend same as Figure 3. Three times vertical exaggeration.*

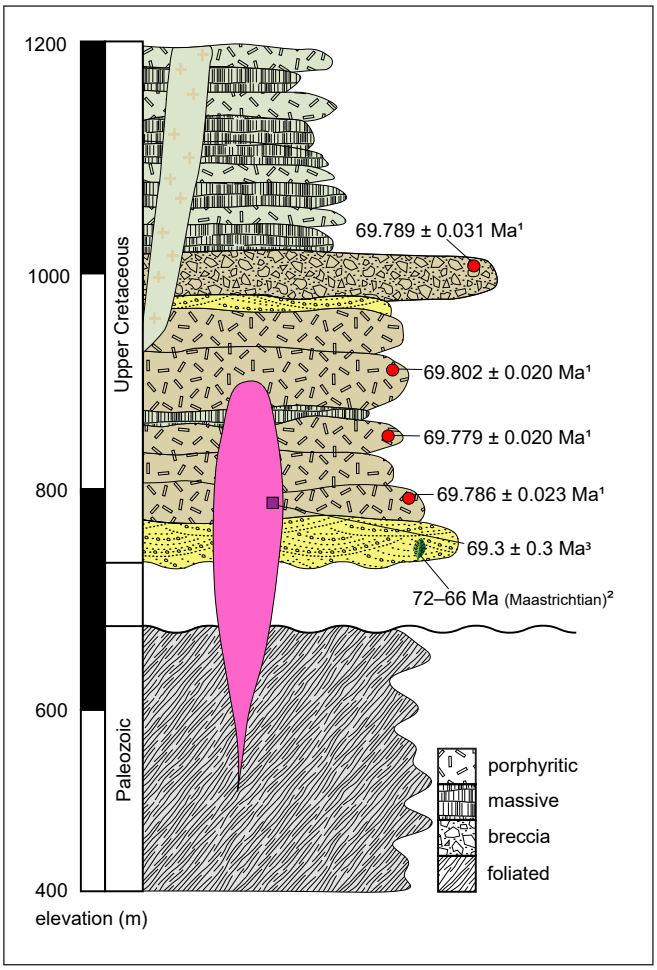


Figure 5. *Cretaceous stratigraphy of the Sixtymile district. Colours and age symbols same as Figure 3. Superscripts on age dates are as follows: 1 – this study; 2 – Lowey (1984); 3 – Allan et al. (2017).*

Results

Geochronology

New geochronological data tightly constrain the age of Late Cretaceous magmatism in the Sixtymile district. Four samples from throughout the Late Cretaceous volcanic stratigraphy were analyzed for U-Pb LA-ICPMS and CA-TIMS zircon geochronology. All dates and ages are 206Pb/238U unless otherwise stated. Data for cathodoluminescence (CL) imaging and LA-ICPMS analyses are in Appendix A. Chemical abrasion-thermal ionization mass spectrometry data are in Table 1.

Sample 23PS053-1 is a pink-orange weathering plagioclase porphyritic andesite collected from a hilltop on Twelve Mile Road (Fig. 3) near the middle of the andesitic unit (Fig. 5). This sample yielded three populations of zircon: Paleozoic to Mesozoic, mid-Cretaceous, and Late Cretaceous (Fig. 8; Appendix A). The Paleozoic to Mesozoic population is dark in CL and displays oscillatory zoning; grains are elongate (≥3:1 aspect ratio), and have LA-ICPMS dates between 368 and 207 Ma. The mid-Cretaceous grains are stubby (≤2:1 aspect ratio), rounded, display moderate brightness with sector zoning, and have LA-ICPMS dates between 119 and 95 Ma. The Late Cretaceous population of grains display dark to moderate lightness in CL, are elongate with sharp crystal faces, and have LA-ICPMS dates between 73.5 and 65.0 Ma. The Paleozoic to Mesozoic and mid-Cretaceous grains are interpreted to be inherited, whereas the Late Cretaceous grains are interpreted as volcanic in origin. The weighted mean age of 18 Late Cretaceous LA-ICPMS analyses is 69.4 ± 0.7 Ma; the oldest three Late Cretaceous grains are interpreted to be antecrysts, and the youngest two grains are believed to have undergone minor Pb-loss. Six zircon grains analyzed by CA-TIMS yielded concordant $^{206}Pb/^{238}U$ dates that range from 69.845 ± 0.050 to 69.771 ± 0.040 Ma (Table 1); all six grains have a weighted mean age of 69.802 ± 0.020 Ma (MSWD = 1.5, probability of fit = 0.19, n = 6/6). The weighted mean age of 69.802 ± 0.020 Ma is interpreted as the crystallization age of this sample.

Sample 23PS004-2 is a medium grey to brown andesitic block and ash pyroclastic rock (Fig. 6a and Fig. 9) located near the top of the andesite unit (Fig. 5) in a quarry pit on the main Sixtymile access road (Fig. 3). This sample yielded three populations of zircon: Paleozoic to Mesozoic, mid-Cretaceous and Late Cretaceous (Fig. 10; Appendix A). The Paleozoic to Mesozoic population yields elongate (≥3:1 aspect ratio), euhedral to subhedral zircons that exhibit various CL zoning (sector, concentric and rim/core relationships), and have LA-ICPMS dates between 356 and 205 Ma. The mid-Cretaceous population yields stubby to elongate subhedral grains displaying sector CL zoning, and have LA-ICPMS dates between 113 and 100 Ma. The Late Cretaceous population yields elongate (≥3:1 aspect ratio), euhedral zircons exhibiting weak to no CL zoning, and have LA-ICPMS dates between 72.6 and 68.2 Ma. The Paleozoic to Mesozoic and mid-Cretaceous grains are interpreted to be inherited, whereas the Late Cretaceous grains are interpreted as volcanic in origin. The weighted mean $^{206}Pb/^{238}U$ age of the four youngest LA-ICPMS analyses is

68.7 ± 1.2 Ma. Four zircon grains analyzed by CA-TIMS yielded concordant $^{206}Pb/^{238}U$ dates between 169.806 ± 1.246 and 69.781 ± 0.051 Ma (Table 1) and have a weighted mean age for the three youngest of 69.789 ± 0.031 Ma (MSWD = 0.2, probability of fit = 0.86, n = 3/4). The weighted mean age of 69.789 ± 0.031 Ma is interpreted as the crystallization age of this sample.

Sample 23PS064-1 is a green-brown andesitic crystal tuff (Figs. 6b and 11) located near the bottom of the andesite unit (Fig. 5), 2 km northwest of the mouth of Big Gold Creek (Fig. 3). This sample yielded four populations of zircon: Paleoproterozoic, Paleozoic to Mesozoic, mid-Cretaceous and Late Cretaceous (Fig. 11; Appendix A). A single stubby, rounded zircon was analyzed and displayed a moderate CL response, and has a Paleoproterozoic



Figure 6. *Field photographs of select outcrops and hand samples:* **(a)** *pyroclastic breccia;* **(b)** *crystal tuff;* **(c)** *massive plagioclase porphyritic andesite;* **(d)** *plagioclase porphyritic basaltic andesite;* **(e)** *mafic dike cross-cutting andesitic block and ash flow; quarry face is approximately 3 m high;* **(f)** *pyroxene porphyritic monzogabbro;* **(g)** *chlorite-muscovite-quartz schist; and* **(h)** *pebble conglomerate.*

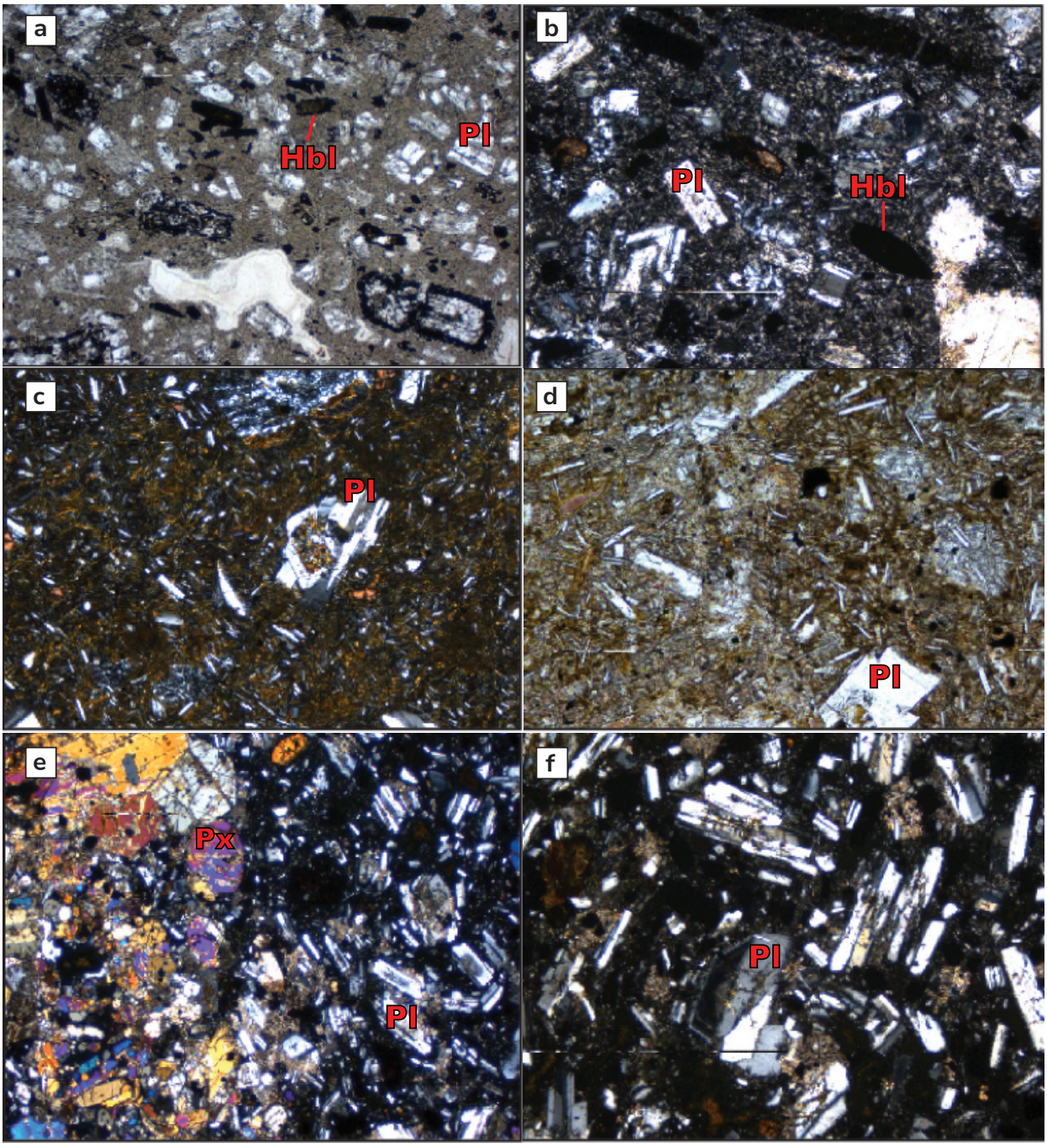


Figure 7. *Photomicrographs of select samples:* **(a)** *23PS017-1 (plagioclase, quartz, hornblende andesite porphyry) in plane polarized light (PPL) at 2.5x magnification and field of view (fov) is 10 mm across;* **(b)** *23PS017-1 in cross-polarized light (XPL) at 5x magnification and fov is 5 mm across;* **(c)** *23PS038-1 (plagioclase, hornblende, biotite andesite porphyry) in XPL at 5x magnification (fov 5 mm across);* **(d)** *23PS038-1 in XPL at 10x magnification and fov is 2.5 mm across;* **(e)** *23PS006-1 (plagioclase, pyroxene basaltic andesite) in XPL at 10x magnification (fov 2.5 mm across); and* **(f)** *23PS006-1 in XPL at 5x magnification (fov 5 mm across). Mineral abbreviations from Whitney and Evans (2010); Hbl – hornblende; Pl – plagioclase; Px – pyroxene.*

Table 1. CA-TIMS U-Pb zircon data table.

								Radiogenic Isotope Ratios										Isotopic Dates									
Sample	LA-ICPMS label	Th / U	$^{206}Pb^*$ x10^{-13} mol	mol % $^{206}Pb^*$	Pb^* (pg)	Pb_c (pg)	Pb^*/Pb_c	$^{206}Pb/^{204}Pb$	$^{208}Pb/^{206}Pb$	$^{207}Pb/^{206}Pb$	% err	$^{207}Pb/^{235}U$	% err	$^{206}Pb/^{238}U$	% err	corr. coef.	$^{207}Pb/^{206}Pb$	±	$^{207}Pb/^{235}U$	±	$^{206}Pb/^{238}U$	±	include in weighted mean?	*Weighted mean calculations (2 sigma errors)*		
(a)		(b)	(c)	(c)	(c)	(c)	(c)	(d)	(e)	(e)	(f)	(e)	(f)	(e)	(f)		(g)	(f)	(g)	(f)	(g)	(f)				
23PS053-1																										
z5	67	0.306	0.6068	99.77%	14	0.12	121	7701	0.098	0.047525	0.114	0.071351	0.170	0.010894	0.072	0.8724	74.6232	2.707	69.981	0.115	69.845	0.050	x	$^{206}Pb/^{238}U$ ± random (+tracer) [+decay constant]	MSWD =	1.48
z3	60	0.595	1.5704	99.91%	40	0.12	342	20069	0.191	0.047503	0.076	0.071301	0.138	0.010891	0.072	0.9369	73.5253	1.815	69.933	0.093	69.828	0.050	x	**69.802 ± 0.02 (0.03) [0.08]**	pof =	0.19
z1	55	0.615	1.6259	99.91%	42	0.13	326	19028	0.197	0.047472	0.087	0.071235	0.147	0.010888	0.071	0.9232	71.9517	2.074	69.871	0.099	69.810	0.049	x		n =	6
z2	74	0.749	1.1910	99.81%	32	0.19	169	9554	0.240	0.047468	0.089	0.071216	0.148	0.010886	0.071	0.9173	71.7443	2.11	69.853	0.1	69.797	0.050	x			
z4	62	0.696	1.7114	99.91%	45	0.13	353	20169	0.223	0.047468	0.070	0.071198	0.135	0.010883	0.072	0.9578	71.7765	1.672	69.836	0.091	69.779	0.050	x			
z6	69	0.400	0.2804	99.44%	7	0.13	52	3219	0.128	0.047472	0.167	0.071195	0.239	0.010882	0.057	1.2279	71.9446	3.96	69.833	0.161	69.771	0.040	x			
23PS004-2																										
z5	63	0.318	0.4564	99.54%	10.9	0.18	62	3918	0.101	0.052017	0.230	0.191344	0.789	0.026691	0.743	0.957	285.12	5.27	177.78	1.29	169.806	1.246		$^{206}Pb/^{238}U$ ± random (+tracer) [+decay constant]	MSWD =	0.2
z4	54	0.933	1.7496	99.90%	48.6	0.14	347	18693	0.299	0.047407	0.079	0.071128	0.140	0.010887	0.072	0.930	68.72	1.88	69.77	0.09	69.800	0.050	x	**69.789 ± 0.031** (0.037) [0.084]	pof =	0.86
z3	70	0.719	0.1747	99.01%	4.6	0.15	32	1814	0.230	0.047568	0.444	0.071354	0.493	0.010884	0.090	0.616	76.78	10.54	69.98	0.33	69.785	0.062	x		n =	3
z2	62	0.897	0.3578	99.55%	9.9	0.14	73	3976	0.288	0.047345	0.189	0.071015	0.240	0.010884	0.073	0.792	65.57	4.49	69.66	0.16	69.781	0.051	x			
23PS064-1																										
z6	99	0.321	0.6690	98.48%	15.9	0.85	19	1200	0.103	0.050850	0.265	0.135954	0.315	0.019400	0.077	0.721	233.02	6.11	129.43	0.38	123.860	0.095		$^{206}Pb/^{238}U$ ± random (+tracer) [+decay constant]	MSWD =	0.8
z2	88	1.448	2.1386	99.86%	66.8	0.25	264	12676	0.464	0.047387	0.094	0.071110	0.152	0.010888	0.071	0.908	67.70	2.23	69.75	0.10	69.812	0.049	x	**69.786 ± 0.023** (0.031) [0.082]	pof =	0.55
z5	102	0.549	0.2238	98.43%	5.6	0.30	19	1149	0.176	0.047558	0.426	0.071358	0.478	0.010887	0.083	0.691	76.29	10.11	69.99	0.32	69.803	0.058	x		n =	5
z1	85	1.124	1.9507	99.89%	56.7	0.19	306	15753	0.360	0.047447	0.079	0.071176	0.140	0.010885	0.072	0.930	70.70	1.89	69.81	0.09	69.789	0.050	x			
z3	91	0.836	0.3998	99.34%	10.9	0.22	49	2743	0.268	0.047522	0.213	0.071269	0.261	0.010882	0.076	0.729	74.47	5.06	69.90	0.18	69.769	0.053	x			
z4	82	0.955	1.4756	99.81%	41.2	0.23	180	9680	0.306	0.047472	0.085	0.071184	0.146	0.010880	0.071	0.928	71.96	2.02	69.82	0.10	69.760	0.050	x			
23PS074-1																										
z3	110	0.817	1.0300	99.85%	28	0.12	223	12358	0.262	0.047458	0.064	0.071203	0.138	0.010886	0.072	1.026	71.25	1.51	69.84	0.09	69.799	0.050	x	$^{206}Pb/^{238}U$ ± random (+tracer) [+decay constant]	MSWD =	0.7
z6	106	0.931	1.1037	99.86%	31	0.13	233	12596	0.298	0.047482	0.086	0.071232	0.147	0.010885	0.073	0.923	72.47	2.04	69.87	0.10	69.792	0.051	x	**69.779 ± 0.020 (0.03) [0.08]**	pof =	0.62
z4	107	0.757	1.1416	99.89%	30	0.10	297	16710	0.243	0.047473	0.081	0.071211	0.142	0.010884	0.071	0.934	72.01	1.92	69.85	0.10	69.785	0.050	x		n =	6
z1	111	0.752	1.2895	99.91%	34	0.09	370	20852	0.241	0.047453	0.077	0.071178	0.139	0.010884	0.072	0.935	71.03	1.82	69.82	0.09	69.782	0.050	x			
z7	121	0.645	0.7973	99.82%	21	0.12	176	10201	0.207	0.047505	0.092	0.071253	0.153	0.010883	0.071	0.929	73.60	2.19	69.89	0.10	69.779	0.049	x			
z2	112	0.765	2.1006	99.93%	56	0.13	434	24384	0.245	0.047465	0.070	0.071152	0.134	0.010877	0.072	0.953	71.61	1.66	69.79	0.09	69.739	0.050	x			

(a) z1, z2, etc. are labels for analyses composed of single zircon grains that were annealed and chemically abraded (Mattinson, 2005).

(b) Model Th/U ratio calculated from radiogenic $^{208}Pb/^{206}Pb$ ratio and $^{207}Pb/^{235}U$ date.

(c) Pb* and Pbc are radiogenic and common Pb, respectively. mol % $^{206}Pb^*$ is with respect to radiogenic and blank Pb.

(d) Measured ratio corrected for spike and fractionation only. Pb fractionation correction for analyses done with tracer solution BSU1B is 0.16 ± 0.03 (1 sigma) %/amu (atomic mass unit) for single-collector Daly analyses, based on recent analyses of EARTHTIME ^{202}Pb-^{205}Pb ET2535 tracer solution.

(e) Corrected for fractionation and spike. Common Pb in zircon analyses is assigned to procedural blank with composition of $^{206}Pb/^{204}Pb$ = 18.04 ± 0.61%; $^{207}Pb/^{20}4Pb$ = 15.54 ± 0.52%; $^{208}Pb/^{204}Pb$ = 37.69 ± 0.63% (1 sigma). $^{206}Pb/^{238}U$ and $^{207}Pb/^{206}Pb$ ratios corrected for initial disequilibrium in $^{230}Th/^{238}U$ using a $D_{(Th/U)}$ of 0.20 ± 0.05 (1 sigma).

(f) Errors are 2 sigma, propagated using algorithms of Schmitz and Schoene (2007) and Crowley et al. (2007).

(g) Calculations based on the decay constants of Jaffey et al. (1971). $^{206}Pb/^{238}U$ and $^{207}Pb/^{206}Pb$ dates corrected for initial disequilibrium in $^{230}Th/^{238}U$ using a $D_{(Th/U)}$ of 0.20 ± 0.05 (1 sigma).

core ($^{207}Pb/^{206}Pb$ date of 1837 ± 44 Ma). The Paleozoic to Mesozoic population yields stubby to elongate (1:1 to 3:1 aspect ratio) euhedral zircons with mainly sector and core zoning, and having LA-ICPMS dates between 382 and 153 Ma. The mid-Cretaceous population yields mostly stubby (≤2:1 aspect ratio), rounded zircons with varied CL zoning (weak to none, sector), and LA-ICPMS dates between 121 and 97 Ma. The Late Cretaceous population yields euhedral zircons with various CL zoning (weak to none, sector, oscillatory), and are mostly elongate (≥3:1 aspect ratio); LA-ICPMS dates range between 77.0 and 65.4 Ma. The Paleoproterozoic, Paleozoic to Mesozoic and mid-Cretaceous grains are interpreted to be inherited, whereas the Late Cretaceous grains are interpreted as volcanic in origin. The weighted mean $^{206}Pb/^{238}U$ age of the 24 youngest LA-ICPMS analyses is 69.1 ± 0.9 Ma. Six zircon grains analyzed by CA-TIMS yielded concordant $^{206}Pb/^{238}U$ dates between 123.860 ± 0.095 and 69.760 ± 0.050 Ma (Table 1), and have a weighted mean age for the four youngest of 69.786 ± 0.023 Ma (MSWD = 0.8, probability of fit = 0.55, n = 5/6). The weighted mean age of 69.786 ± 0.023 Ma is interpreted as the crystallization age of this sample.

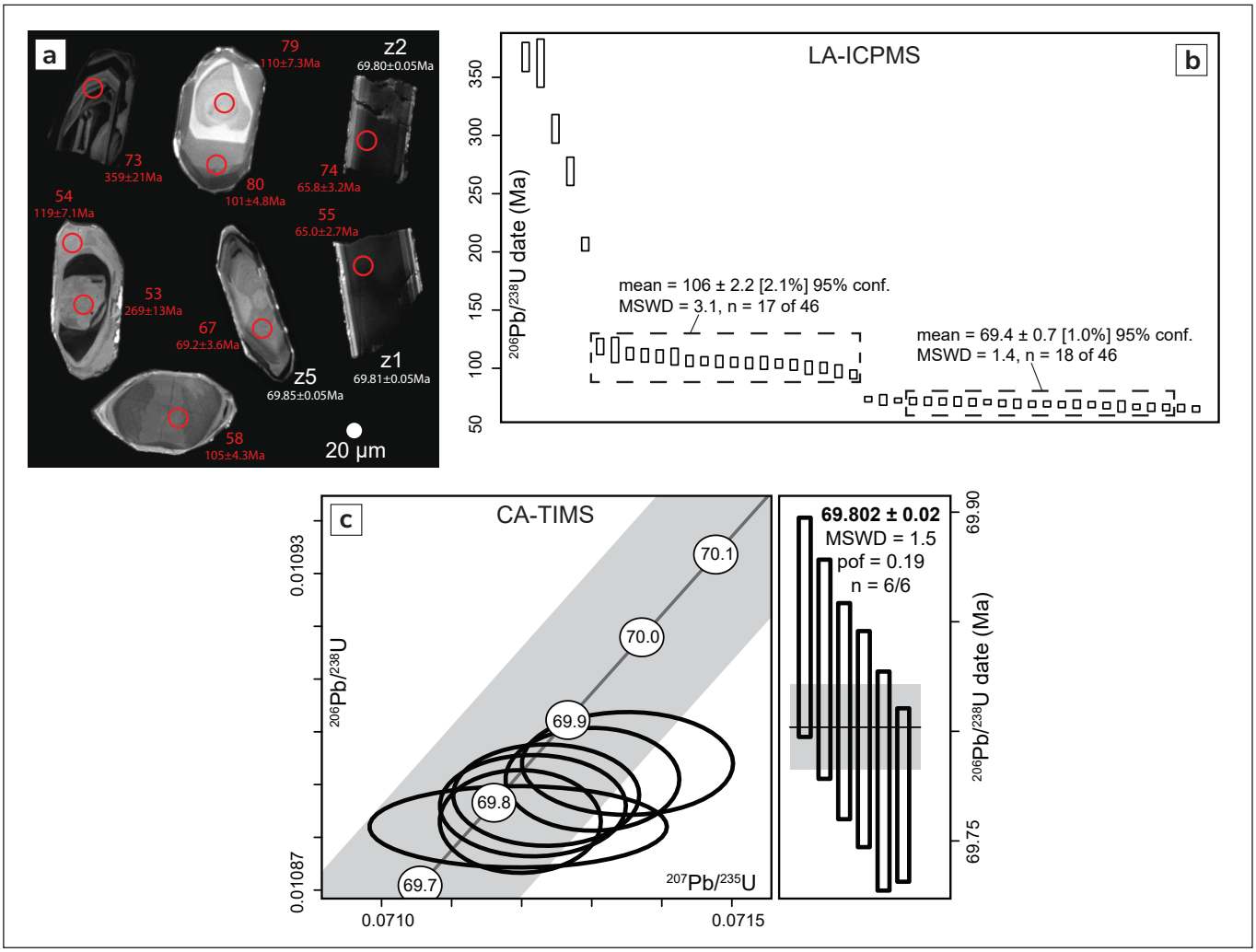


Figure 8. *Sample 23PS053-1 U-Pb geochronological results.* ***(a)*** *Cathodoluminescence images of representative igneous zircons. Red labels indicate LA-ICPMS analysis number and age with associated error; the red open circle indicates the location of the analysis spot; white analysis number and age with associated error refers to grain analyzed by CA-TIMS.* ***(b)*** *Ranked plot of LA-ICPMS $^{206}Pb/^{238}U$ dates.* ***(c)*** *Concordia diagram (left) and ranked $^{206}Pb/^{238}U$ dates (right) for zircons analyzed by CA-TIMS. Grey horizontal bar shows calculated weighted mean with error. Analyses included in weighted mean age calculations (light grey horizontal bar) are bold; analyses with thin lines are not used in calculations. The light grey band around Concordia (dark grey line) shows the decay constant uncertainties. Errors in all plots are at 2σ. MSWD – mean squared weighted deviation; pof - probability of fit; n – number of analyses included in age calculation.*

Sample 23PS074-1 is a purple-weathering, plagioclase porphyritic andesite collected on the ridge between Miller and Glacier creeks (Fig. 3), near the middle of the andesitic unit (Fig. 5). This sample yields mostly Late Cretaceous zircon with one Paleozoic grain and three mid-Cretaceous grains (Fig. 12; Appendix A). The Paleozoic grain is dark in CL with oscillatory zoning, elongate (≥3:1 aspect ratio), and has a LA-ICPMS date of 386 Ma. The three mid-Cretaceous grains are stubby (≤2:1 aspect ratio) and rounded with moderate brightness, sector zoning, and have LA-ICPMS dates between 108 and 99 Ma. The Late Cretaceous population of grains display dark to moderate brightness in CL, are elongate (≥3:1 aspect ratio) with sharp crystal faces, and have LA-ICPMS dates between 74.5 and 59.1 Ma. The Paleozoic to Mesozoic and mid-Cretaceous grains are interpreted to be inherited, whereas the Late Cretaceous grains are interpreted as volcanic in origin. The weighted mean age of 20 Late Cretaceous LA-ICPMS analyses is 68.9 ± 0.8 Ma; the oldest four Late Cretaceous grains are interpreted to be antecrysts, and the youngest eight grains are believed to have undergone minor Pb-loss. Six zircon grains analyzed by CA-TIMS yield concordant $^{206}Pb/^{238}U$ dates that range from 69.799 ± 0.050 to 69.739 ± 0.050 Ma (Table 1), all six grains have a weighted mean age of 69.779 ± 0.020 Ma (MSWD = 0.7, probability of fit = 0.62, n = 6/6). The weighted mean age of 69.779 ± 0.020 Ma is interpreted as the crystallization age of this sample.

Whole-rock geochemistry

Major and trace element compositions for the 27 samples are in Appendix B. Loss on ignition (LOI) for the samples are mostly between <1 to 10%. The Sixtymile district samples are mostly intermediate in composition with calc-alkaline to high potassium (K) calc-alkaline affinity (Fig. 13). The samples have between 66 and 49 wt% SiO_2, 18.1 and 14.2 wt% Al_2O_3, 3.8 to 0.4 wt% K_2O, ≤6.0 wt% Na_2O, and TiO_2 between 1.0 and 0.3 wt%. Field and petrographic observations in conjunction with the low to moderate

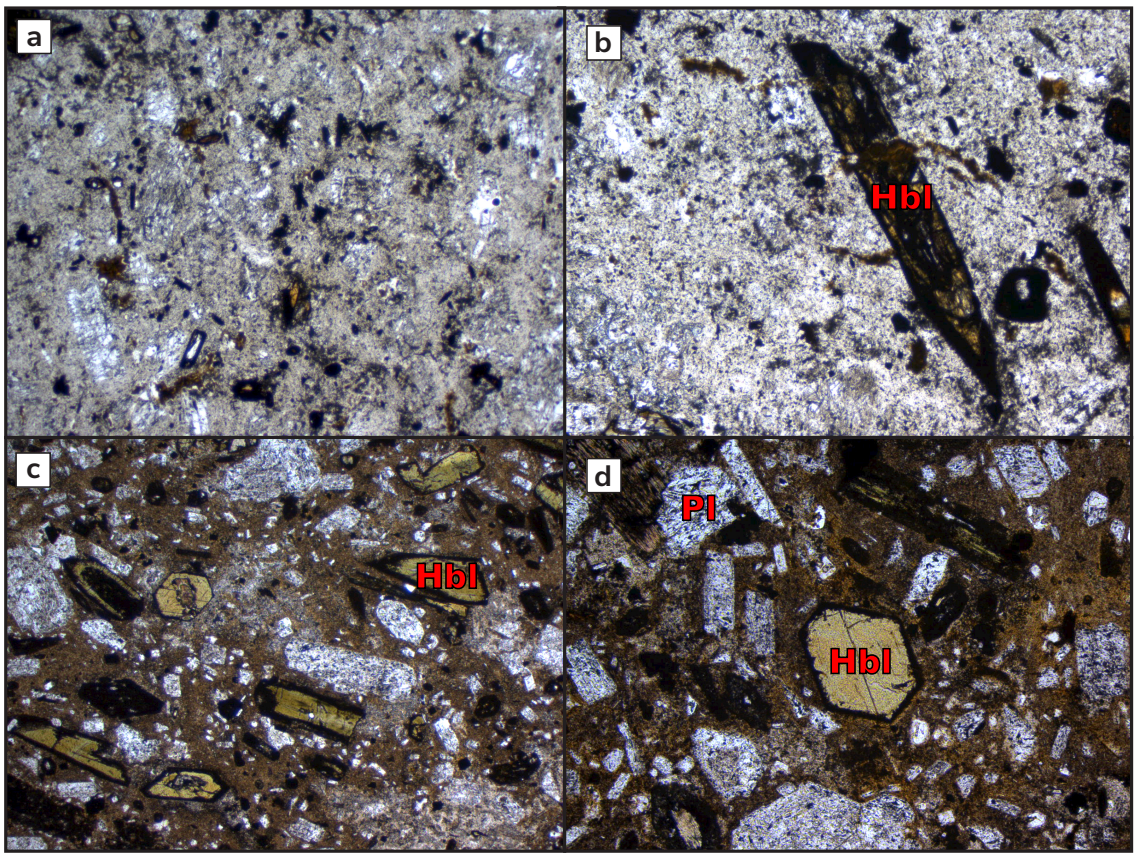


Figure 9. *Thin sections of the geochronology samples:* ***(a)*** *23PS004-2 in PPL at 2.5x magnification (field of view (fov) 10 mm across);* ***(b)*** *23PS004-2 in PPL at 5x magnification (fov 5 mm across);* ***(c)*** *23PS064-1 in PPL at 2.5x magnification (fov 10 mm across); and* ***(d)*** *23PS064-1 in PPL at 5x magnification (fov 5 mm across). Mineral abbreviations from Whitney and Evans (2010); Hbl – hornblende; Pl – plagioclase.*

LOI values, as well as scattered data on mobile element diagrams (e.g., Fig. 13), indicate that most samples have undergone at least minor alteration. Because of the alteration, rock classifications are derived from the Zr/Ti versus Nb/Y immobile element diagram, where the samples plot mainly in the andesite to basaltic andesite fields (Fig. 13).

The high field strength elements (HFSE) are relatively immobile with values that range from 92 to 150 ppm zirconium (Zr), 6.4 to 10.7 ppm niobium (Nb), 2.6 to 7.6 ppm thorium (Th), 12.1 to 22.4 ppm yttrium (Y), 0.3 to 0.7 ppm tantalum (Ta), and 2.3 to 3.6 ppm hafnium (Hf). The large ion lithophile elements (LILE) are more enriched in the samples and have concentrations of 808 to 1765 ppm barium (Ba), 552 to 996 ppm strontium (Sr), 36.6 to 87.1 ppm rubidium (Rb), 0.58 to 25.3 ppm cesium (Cs), and 0.02 to 0.09 ppm thallium (Tl). Trace element patterns for the samples show significant variation for the light rare earth elements (LREE) and are less variable for the heavy REE (HREE). Normalized against primitive

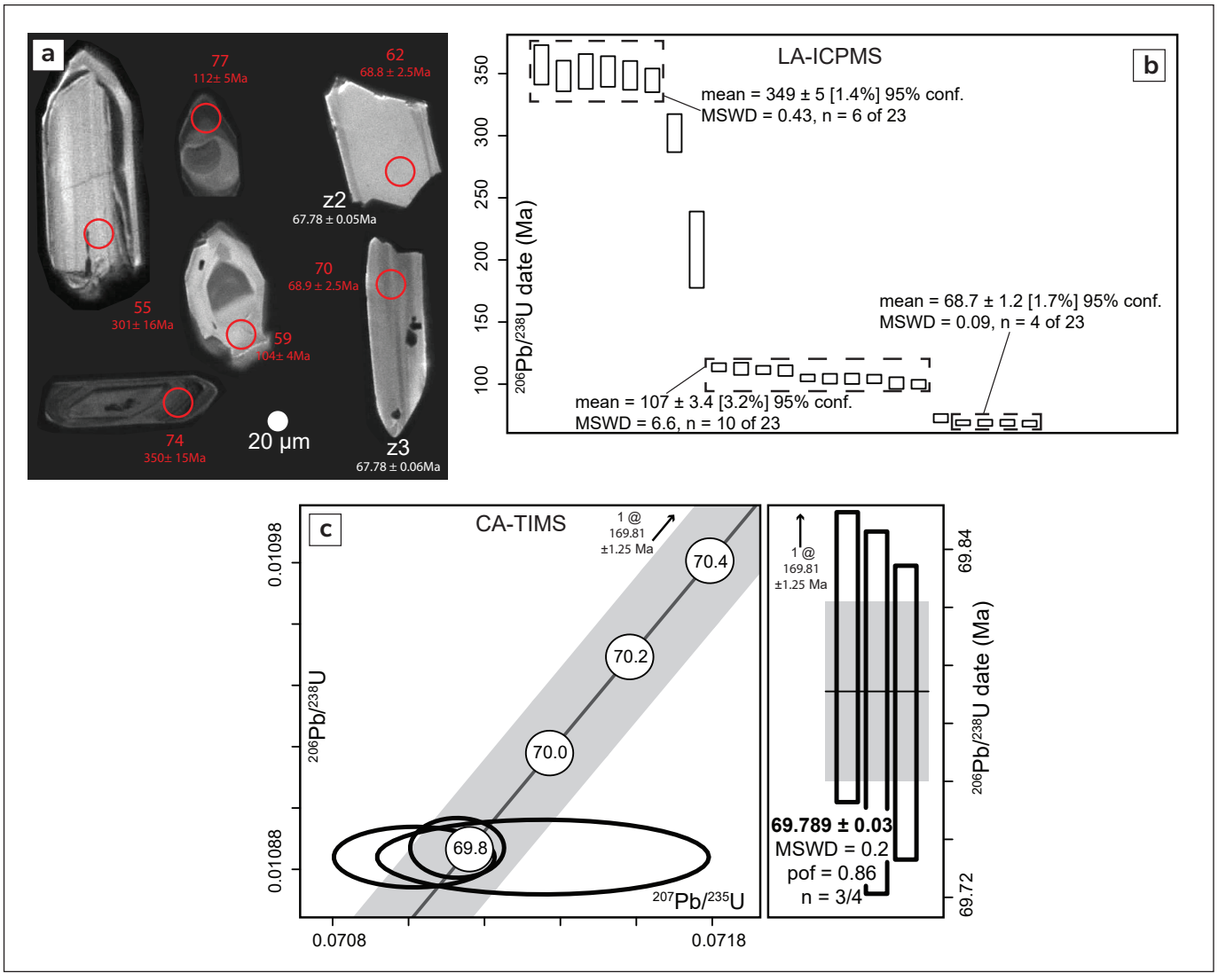


Figure 10. *Sample 23PS004-2 U-Pb geochronological results.* ***(a)*** *Cathodoluminescence images of representative igneous zircons. Red labels indicate LA-ICPMS analysis number and age with associated error; the red open circle indicates the location of the analysis spot; white analysis number and age with associated error refers to grain analyzed by CA-TIMS.* ***(b)*** *Ranked plot of LA-ICPMS $^{206}Pb/^{238}U$ dates.* ***(c)*** *Concordia diagram (left) and ranked $^{206}Pb/^{238}U$ dates (right) for zircons analyzed by CA-TIMS. Grey horizontal bar shows calculated weighted mean with error. Analyses included in weighted mean age calculations (light grey horizontal bar) are bold; analyses with thin lines are not used in calculations. The light grey band around Concordia (dark grey line) shows the decay constant uncertainties. Errors in all plots are at 2σ. MSWD – mean squared weighted deviation; pof – probability of fit; n – number of analyses included in age calculation.*

mantle values (Sun and McDonough, 1989), the LREE are enriched (La_N/Sm_N = 6.2) with moderately fractionated HREE (Gd_N/Yb_N = 2.02) and an overall negative slope (La_N/Yb_N = 9.6; Fig. 14). Barium content within all samples is high, averaging 1289 ppm with a range of 808–1765 ppm. Zirconium content for the samples has an average of 124.5 ppm, whereas Y, lanthanum (La), cerium (Ce), praseodymium (Pr), and Nd are in the tens of ppm. The trace elements do not show significant variation with increasing SiO_2. Plots of immobile REE ratios normalized to the primitive mantle display negative Ta, Nb, and Ti anomalies (e.g., Fig 14).

The Late Cretaceous volcanic rocks have $^{87}Rb/^{86}Sr$ ratios between 0.1529 and 0.3392, initial $^{87}Sr/^{86}Sr$ values ranging between 0.7050 and 0.70555, $^{143}Nd/^{144}Nd_i$ values ranging between 0.51244 and 0.5126, and εNd_i values of -1.9 to 1.1 (Table 2; Fig. 15). The values for the samples are 19.35 to 19.50 for $^{206}Pb/^{204}Pb$, 15.63 to 15.66 for $^{207}Pb/^{204}Pb$, 39.02 to 39.07 for $^{208}Pb/^{204}Pb$, 0.035 to 0.8080 for $^{207}Pb/^{206}Pb$, and 2.0095 to 2.0162 for $^{208}Pb/^{206}Pb$.

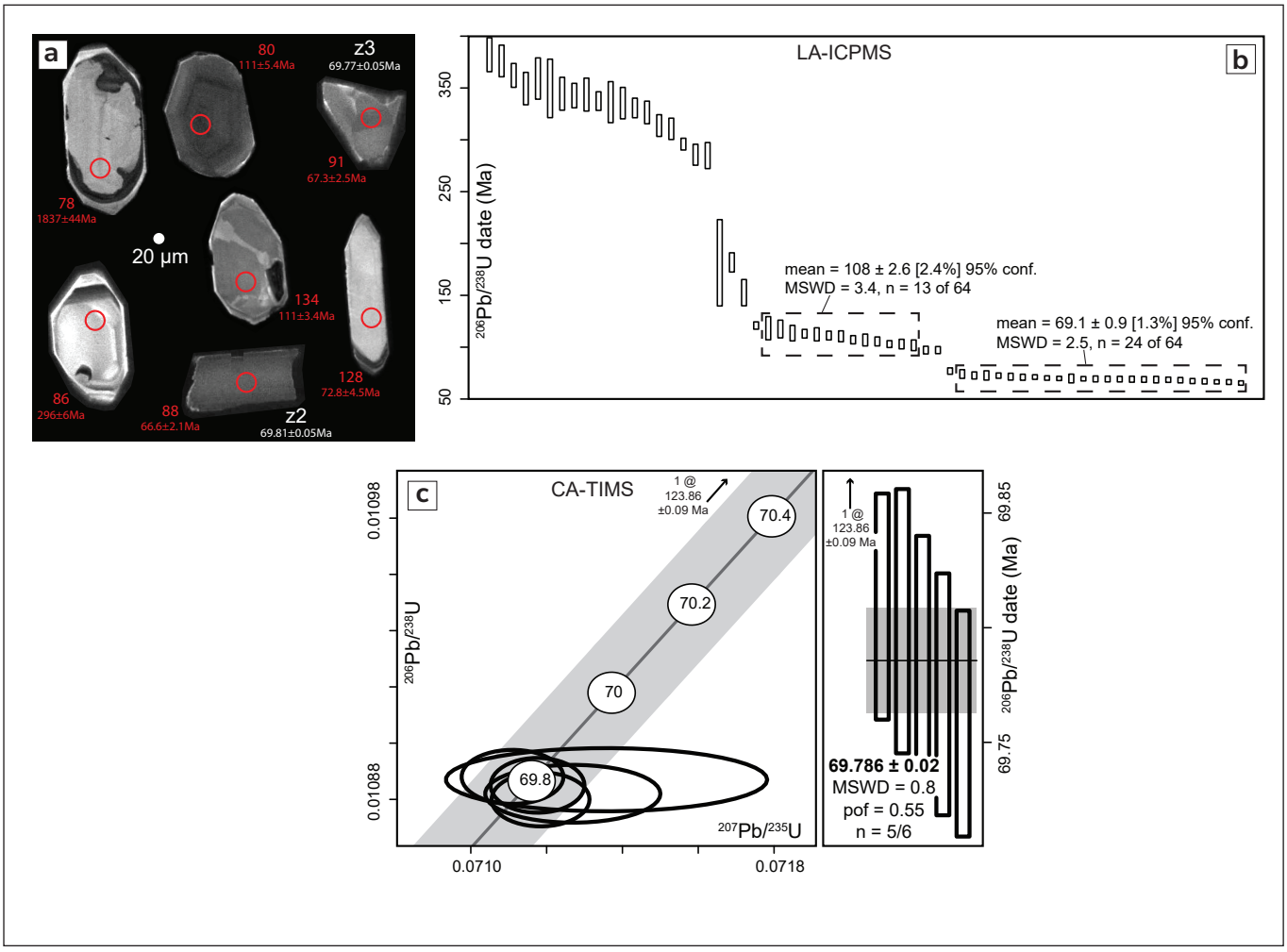


Figure 11. *Sample 23PS064-1 U-Pb geochronological results.* ***(a)*** *Cathodoluminescence images of representative igneous zircons. Red labels indicate LA-ICPMS analysis number and age with associated error; the red open circle indicates the location of the analysis spot; white analysis number and age with associated error refers to grain analyzed by CA-TIMS.* ***(b)*** *Ranked plot of LA-ICPMS $^{206}Pb/^{238}U$ dates.* ***(c)*** *Concordia diagram (left) and ranked $^{206}Pb/^{238}U$ dates (right) for zircons analyzed by CA-TIMS. Grey horizontal bar shows calculated weighted mean with error. Analyses included in weighted mean age calculations (light grey horizontal bar) are bold; analyses with thin lines are not used in calculations. The light grey band around Concordia (dark grey line) shows the decay constant uncertainties. Errors in all plots are at 2σ. MSWD – mean squared weighted deviation; pof – probability of fit; n – number of analyses included in age calculation.*

Table 2. Radiogenic isotope data for Late Cretaceous volcanic rocks in the Sixtymile district.

Sample	23PS040-1	23PS006-1	23PS028-1	23PS031-1	23PS043-1	23PS010-1
Lithology	basaltic andesite	basalt	basaltic andesite	basaltic andesite	basaltic andesite	basalt
Latitude	64.10336	64.11686	64.04378	64.08274	64.11453	64.11441
Longitude	-140.78421	-140.69200	-140.68574	-140.76922	-140.65775	-140.74912
Rb (ppm)	43.5	58.4	58.4	87.1	77.3	63.6
Sr (ppm)	822	714	552	742	834	562
$^{87}Sr/^{86}Sr$	0.7051	0.7058	0.7057	0.7056	0.7053	0.7059
2σ	0.000016	0.000006	0.000010	0.000019	0.000016	0.000021
$^{87}Rb/^{86}Sr$	0.1529	0.2364	0.3058	0.3392	0.2679	0.3271
$^{87}Sr/^{86}Sr_i$	0.70500	0.70555	0.70543	0.70527	0.70503	0.70555
Nd (ppm)	8.05	17.8	17.3	19.7	26	21.6
Sm (ppm)	4.46	4.58	3.2	4.16	5.74	5.06
$^{143}Nd/^{144}Nd$	0.5127	0.5125	0.5126	0.5126	0.5126	0.5127
2σ	0.0000053	0.0000059	0.0000067	0.0000069	0.0000059	0.0000049
$^{147}Sm/^{144}Nd$	0.3351	0.1556	0.1119	0.1277	0.1335	0.1417
$^{143}Nd/^{144}Nd_i$	0.5125	0.5124	0.5126	0.5126	0.5125	0.5126
εNd_i	-0.0358	-1.9210	0.9575	0.5096	-0.1040	1.1440
Pb (ppm)	12	6	12	10	10	6
$^{206}Pb/^{204}Pb_{corr}$	19.40	19.50	19.36	19.35	19.41	19.44
2σ	0.006	0.006	0.006	0.006	0.006	0.006
$^{207}Pb/^{204}Pb_{corr}$	15.63	15.66	15.64	15.64	15.64	15.63
2σ	0.005	0.005	0.005	0.005	0.005	0.005
$^{208}Pb/^{204}Pb_{corr}$	39.02	39.22	39.02	39.02	39.07	39.06
2σ	0.023	0.024	0.023	0.023	0.023	0.023
$^{207}Pb/^{206}Pb_{corr}$	0.81	0.80	0.81	0.81	0.81	0.80
$^{208}Pb/^{206}Pb_{corr}$	2.01	2.01	2.02	2.02	2.01	2.01

Discussion

Field relationships

The unfoliated sedimentary and volcanic rocks in the Sixtymile district form a relatively consistent stratigraphy with basal sedimentary rocks above a regional unconformity. In the main part of the graben, the sedimentary rocks appear to be conformably overlain by the andesitic unit. However, in the few instances where the basal sedimentary rocks are seen outside the graben, such as along the road to Miller Creek, as well as on the floors of old gravel pits along the Top of the World Highway, the andesitic unit is not present, and basaltic andesite directly overlies the sedimentary rocks. The age of the 'sub-Carmacks' sedimentary rocks has not been directly constrained in the Sixtymile district, and we note a lack of volcanic clasts in the conglomerate. On the lower Sixtymile River, sedimentary rocks that have a Masstrichtian fossil plant assemblage are interbedded with andesitic volcanic rocks (Lowey, 1984; 72–66 Ma, Late Cretaceous). At the time of

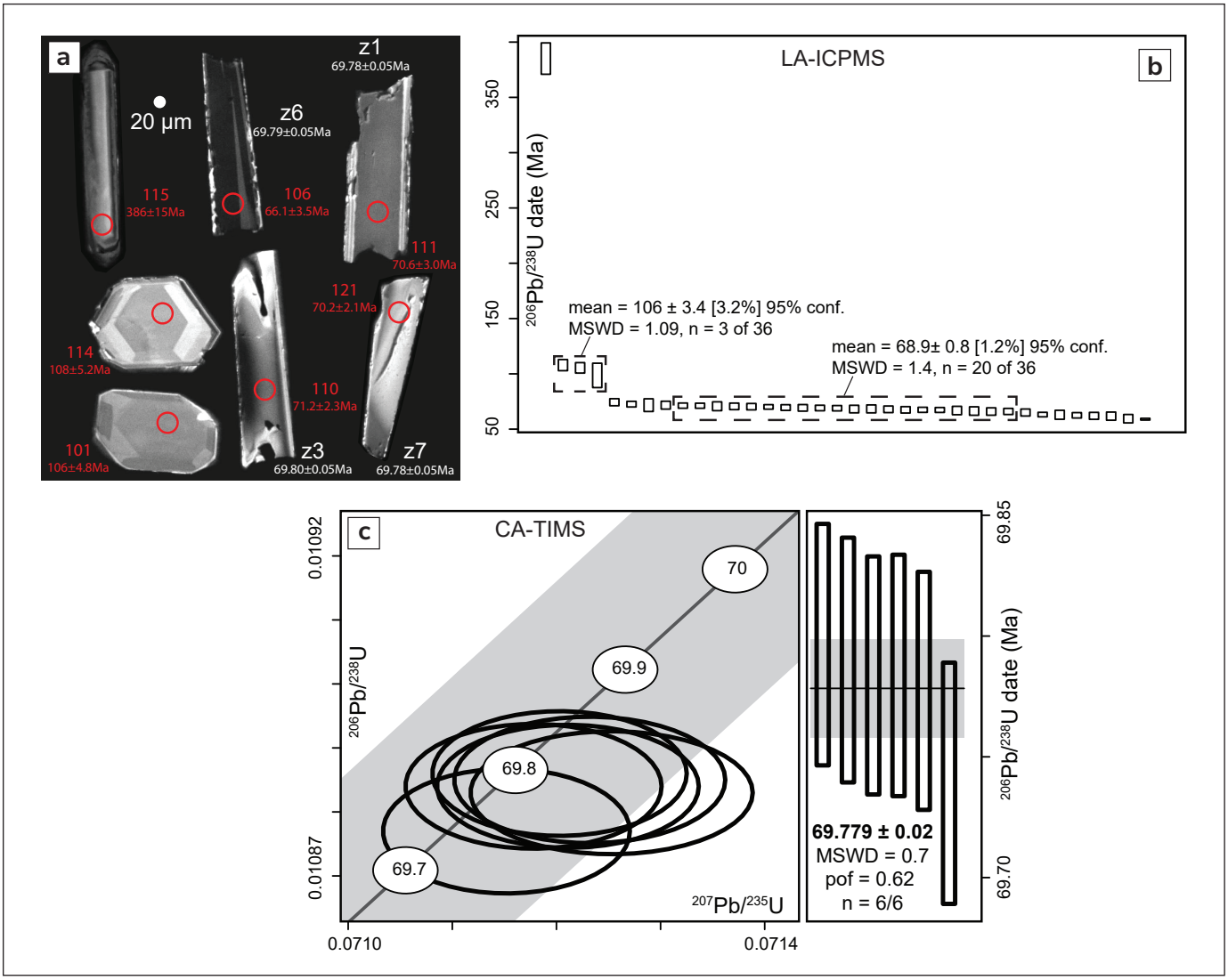


Figure 12. *Sample 23PS074-1 U-Pb geochronological results.* ***(a)*** *Cathodoluminescence images of representative igneous zircons. Red labels indicate LA-ICPMS analysis number and age with associated error; the red open circle indicates the location of the analysis spot; white analysis number and age with associated error refers to grain analyzed by CA-TIMS.* ***(b)*** *Ranked plot of LA-ICPMS* $^{206}Pb/^{238}U$ *dates.* ***(c)*** *Concordia diagram (left) and ranked* $^{206}Pb/^{238}U$ *dates (right) for zircons analyzed by CA-TIMS. Grey horizontal bar shows calculated weighted mean with error. Analyses included in weighted mean age calculations (light grey horizontal bar) are bold; analyses with thin lines are not used in calculations. The light grey band around Concordia (dark grey line) shows the decay constant uncertainties. Errors in all plots are at 2σ. MSWD – mean squared weighted deviation; pof – probability of fit; n – number of analyses included in age calculation.*

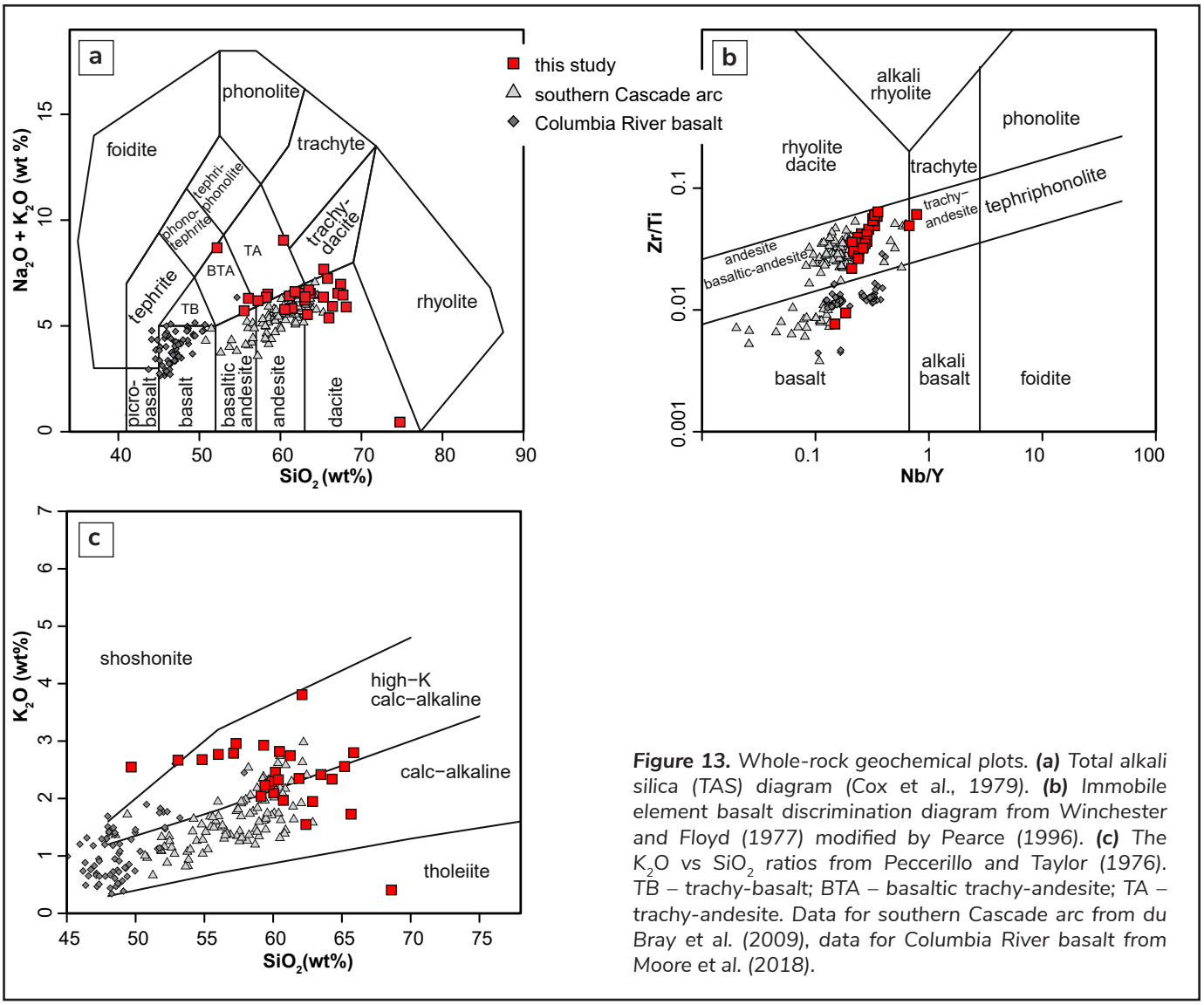


Figure 13. *Whole-rock geochemical plots.* ***(a)*** *Total alkali silica (TAS) diagram (Cox et al., 1979).* ***(b)*** *Immobile element basalt discrimination diagram from Winchester and Floyd (1977) modified by Pearce (1996).* ***(c)*** *The K_2O vs SiO_2 ratios from Peccerillo and Taylor (1976). TB – trachy-basalt; BTA – basaltic trachy-andesite; TA – trachy-andesite. Data for southern Cascade arc from du Bray et al. (2009), data for Columbia River basalt from Moore et al. (2018).*

writing, a sample of quartz-phyric tuff interbedded with the conglomerate unit was being analyzed for U-Pb zircon dating. If successful, this sample would constrain the depositional age for the sedimentary rocks.

Locally, the thickness of the sedimentary rocks is difficult to constrain precisely, but outside of the graben, such as on the road to Miller Creek, the bottom and top are discernible by colour changes in ditch material and suggest a true thickness of less than 20 m. The thickest part appears to be within the graben north of the Top of the World Highway, where there is at least 100 m of elevation change from the upper contact with the andesitic unit to where the unit truncates against a normal fault. The bottom of the sedimentary unit in contact with the metamorphic basement is not exposed in this area. Lowey (1984) estimated the thickness of the Late Cretaceous sedimentary rocks on the Lower Sixtymile River to be 200 m.

The volcanic rocks in the Sixtymile district are a mixture of relatively vent proximal facies, including block and ash flow, autoclastic breccia and massive, coherent flows with subordinate distal facies such as ash (tuff) deposits. The volcanic rocks appear to be part of the same magmatic cycle, as indicated by their similar immobile chemistry (see below) and a gradational mafic phenocryst assemblage. The basal andesite is hornblende-bearing throughout, but is biotite-bearing in its lower sections, and pyroxene-bearing in its upper sections as it transitions to a basaltic andesite; the basaltic

andesite has pyroxene ± olivine phenocrysts. The contact between the andesite and basaltic andesite on our map is inferred to be a transitional contact, not a sharp contact. We interpret these rocks to be from a single magmatic cycle having slightly more evolved compositions at the start that get increasingly juvenile as the cycle progresses.

Geochronology

Our four new U-Pb zircon CA-TIMS ages from throughout the andesitic component of the stratigraphy all overlap within error, indicating that these rocks erupted in less than 60 ka (total age range of 69.822 to 69.763 ka including internal errors). This tightly constrains the age of the volcanic event in the Sixtymile district to ca. 69.8 Ma. The age of the upper basaltic andesite unit is not directly constrained, except in that it is younger than the andesitic part of the stratigraphy. Plutonism in a slightly larger area around the Sixtymile district, and where constrained by high precision CA-TIMS U-Pb zircon ages, is less than one million years younger than volcanism (Fig. 15). This is consistent with observations of plutonic rocks crosscutting volcanic rocks within the study area, and emphasizes that the overall magmatic event was still short in duration (<1 m.y.).

All four samples analyzed for U-Pb zircon had inherited Paleozoic to Mesozoic grains (plus one sample with a Paleoproterozoic grain) and mid-Cretaceous grains. The Paleozoic grains are predominantly euhedral, elongate and match local units well, and include Devonian to Mississippian populations (Finlayson Assemblage), Permian grains (Klondike Assemblage), and a few Jurassic grains (Minto suite). The mid-Cretaceous grains differ in that they are generally stubby and rounded. Although a few scattered intrusions of this age occur to the south, there are not many local sources for mid-Cretaceous zircons. One possibility is that these mid-Cretaceous grains are sourced from the underlying sedimentary unit. This could imply the sediment source for those rocks was to the south where there are mapped mid-Cretaceous

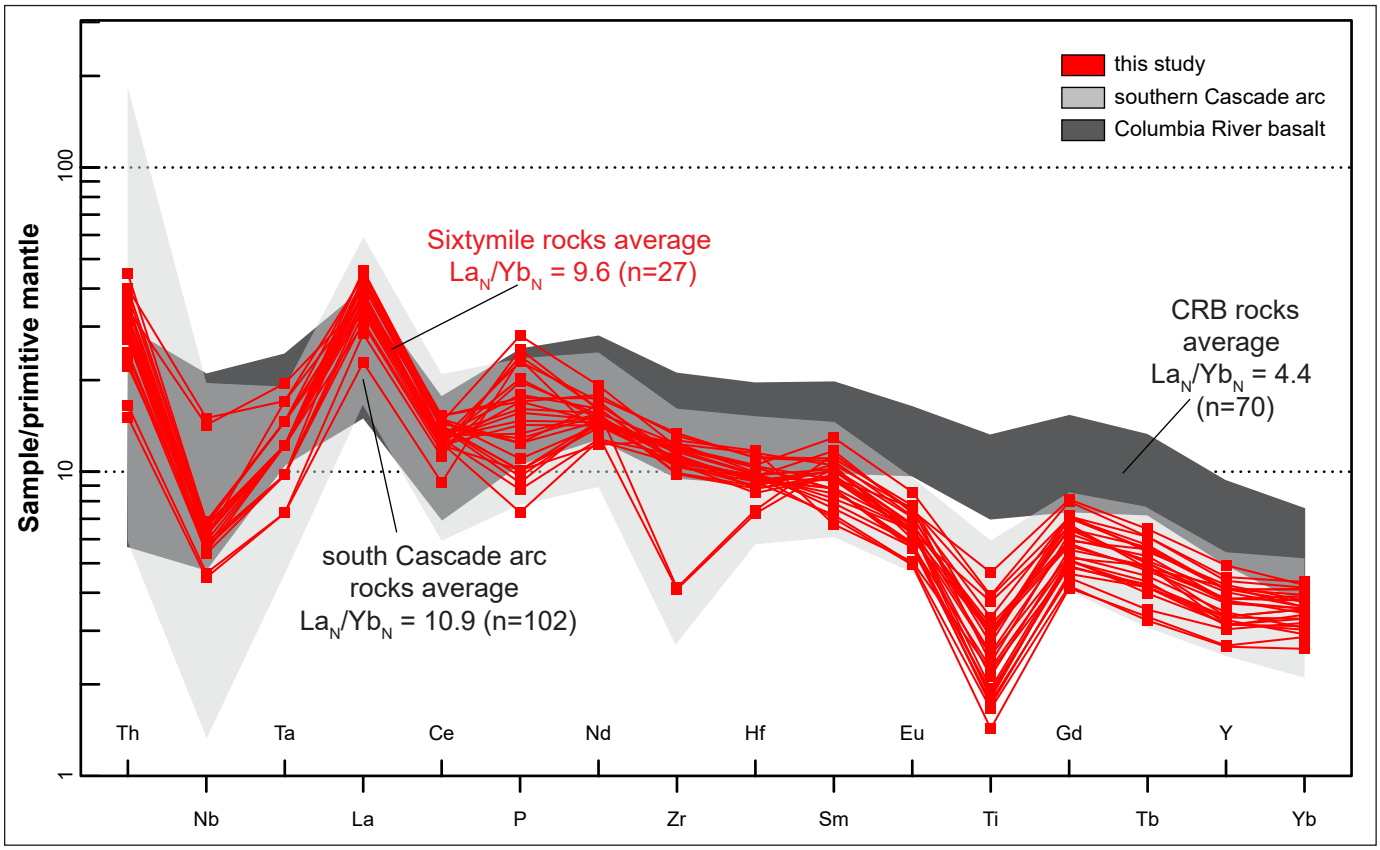


Figure 14. *Immobile rare earth element (REE) spider plot normalized to primitive mantle (Sun and McDonough, 1989). Symbols and data same as Figure 13.*

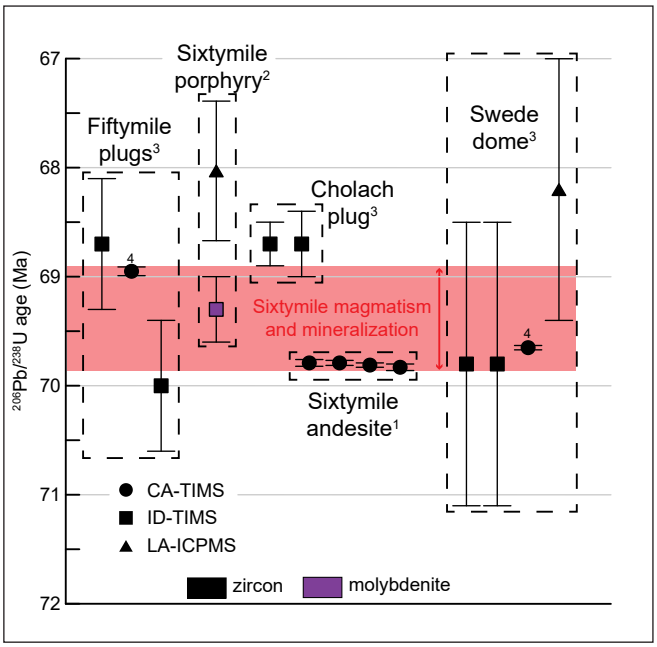


Figure 15. *Summary of Late Cretaceous geochronological data for the Sixtymile area. Superscripts: 1 – this study; 2 – Allen et al. (2017); 3 – Mortensen (Yukon Geological Survey, 2023); and 4 – Sack (Yukon Geological Survey, 2023).*

intrusions within the Fiftymile batholith. The latter interpretation would be consistent with Lowey (1984), who suggested a southern sedimentary source and noted rare kyanite in the sandy matrix of conglomerate units, potentially sourced from the autochthonous North American rocks in that region (e.g. Dusel-Bacon et al., 2002). However, we note that there are scattered mid-Cretaceous plutons to the north and east as well.

Geochemistry

Assessment of alteration

The iron oxides visible in thin section suggest the samples are weakly weathered. The minor carbonate and clay that replaces plagioclase and amphibole phenocrysts may be evidence of a CO_2-rich fluid interacting with the volcanic rocks (e.g., Wynne et al., 1998). Low to moderate loss on ignition values and the observations above suggest the rocks have undergone minor alteration (Appendix B), but when comparing the total-alkali-silica (TAS) diagram (Le Bas et al., 1986) or K_2O versus SiO_2 (Peccerillo and Taylor, 1976) with the Nb/Y versus Zr/Ti diagram (Pearce, 1996), the mobile element (e.g., SiO_2, Na_2O, K_2O) classifications are slightly more felsic and alkalic suggesting some element mobility. The andesitic and basaltic andesite classification used here is based on petrography and the Nb/Y versus Zr/Ti diagram of Pearce (1996). Because of the apparent element mobility, we mostly restrict our geochemical interpretations to those based on immobile elements.

Tectonic setting

The andesitic and basaltic andesite samples are very similar geochemically (Figs. 13 to 16). Based on the similar geochemistry and the phenocryst assemblage discussed above, we interpret these rocks to be part of the same magmatic event and thus genetically related. Despite possible mobility of some elements, major element geochemical compositions for all the rocks in this study straddle the calc-alkaline and high-K calc-alkaline fields of Peccerillo and Taylor (1976). Continental crust is geochemically modelled as intermediate in composition and contains elevated incompatible trace elements such as Th and Nb relative to Yb (Rudnick, 1995). The high values of both Th/Yb (>1) and Nb/Yb (3–10) are consistent with recycled material incorporated from the crust. This can be seen on various geochemical discrimination diagrams where our samples plot in the calc-alkaline compressional arc field (Fig. 16a), the volcanic arc field (Fig. 16b), the continental arc basalt (CAB) field (Fig. 16c), and to the bottom right of the volcanic arc discrimination line, in a field characteristic of continental arcs (Fig. 16d).

The Late Cretaceous volcanic rocks are depleted in HFSE and LREE relative to LILE, a pattern consistent with an arc setting (Basta et al., 2017). The immobility and low solubility of HFSE relative to LILE causes different melting behaviours during subduction (Zack et al., 2002). As a down-going slab dehydrates, it releases fluids with mobile LILE, but the immobile HFSE remain in the slab. This decoupling leads to their respective enrichment and depletion as evident in Figure 14. Trace element diagrams normalized to primitive mantle reveal distinct volcanic arc chemical signatures such as negative Nb, Ta and Ti anomalies (Fig. 14). The negative Ta-Nb trough anomaly is typical for volcanic arc settings and is consistent with crustal contamination (Xia, 2014). The trace element geochemistry suggests crustal contamination was involved in the formation of the Late Cretaceous volcanic rocks in the Sixtymile district.

Supporting evidence for a continental arc setting comes from Sr-Nd-Pb radiogenic isotopes. Magmas

that have interacted with crustal rocks are more abundant in Rb compared to primitive magmas (Rollinson et al., 2021) a pattern evident in our dataset. The Rb/Sr values for oceanic basalts are less than 0.1 and magmas derived entirely from continental crust can be up to 2.0 (Rollinson et al., 2021). The Sixtymile district samples $^{87}Rb/^{86}Sr$ (0.1529–0.3392) values are indicative of juvenile magma that interacted with continental crust. In the mantle source diagram ($^{87}Sr/^{86}Sr$ versus $^{143}Nd/^{144}Nd$) the samples plot just below bulk earth (BE) in the enriched mantle (EM1) field, suggesting an enriched mantle source (Rollinson et al., 2021). Additionally, positive εNd_i values are consistent with depleted mantle reservoirs and negative εNd_i values are consistent with an enriched mantle or crustal source (Allègre and Rousseau, 1984). Magmas that have interacted with crustal rocks have more evolved Pb isotope ratios as lead is sensitive to crustal processes and is highly concentrated in the crust. The elevated Pb isotopes in our data set are higher than the values typical for MORB or OIB, suggesting the magma has interacted with continentally derived rocks, such as rocks from the Yukon Tanana basement (Fig. 17).

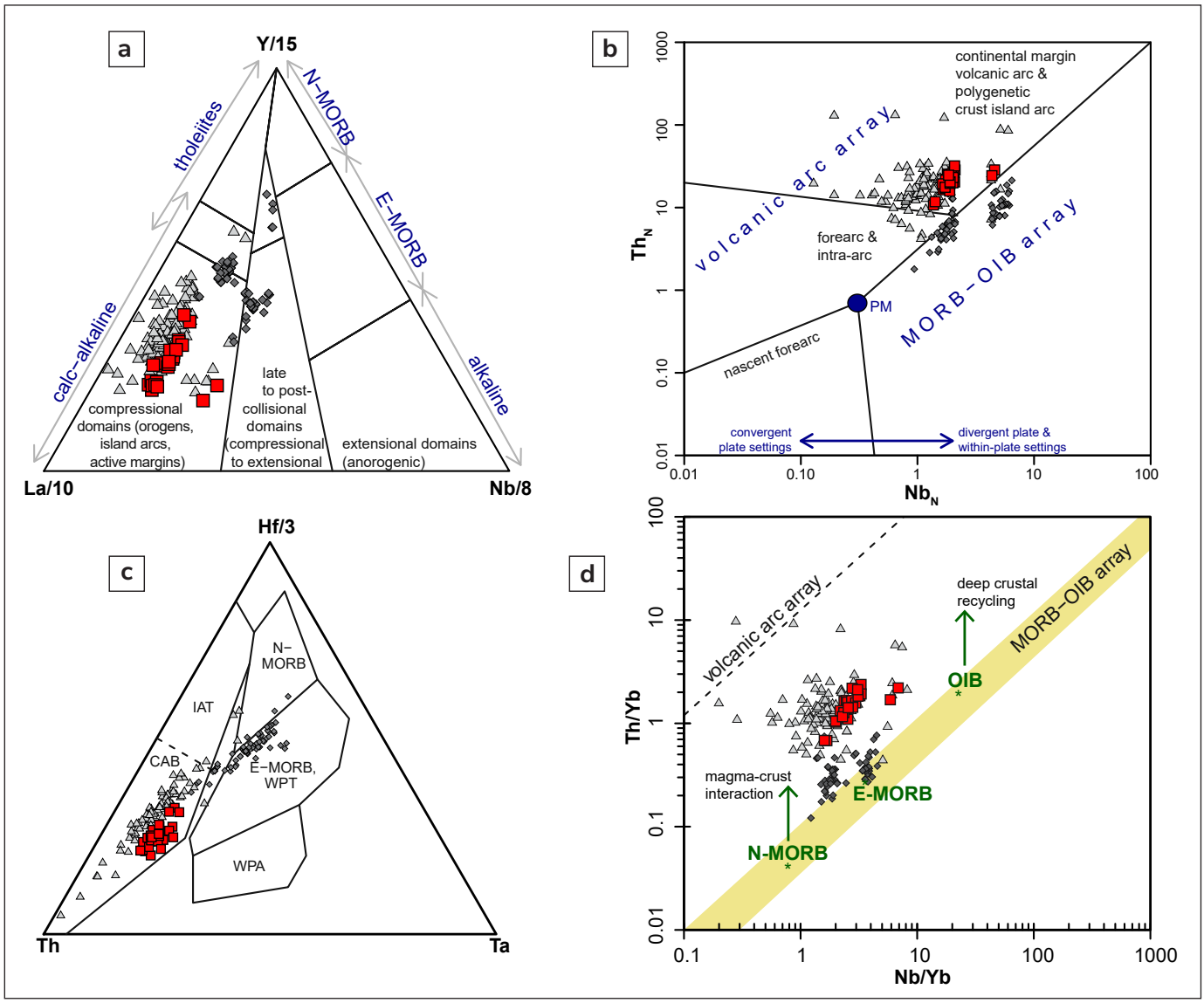


Figure 16. *Geochemical tectonic setting discrimination diagrams.* ***(a)*** *Crustal mixing or contamination (Cabanis and Lecolle, 1989).* ***(b)*** *Tectonic setting (Saccani, 2015).* ***(c)*** *Tectonic setting (Wood, 1980).* ***(d)*** *Basalt Th/Yb versus Nb/Yb diagram (Pearce, 2008). MORB – mid-ocean ridge basalt; N – normal; E – enriched; OIB – ocean island basalt; CAB – continental arc basalt; IAT – island arc tholeiite; WPT – within-plate tholeiite; and WPA – within-plate alkalic. Symbols and data same as Figure 13.*

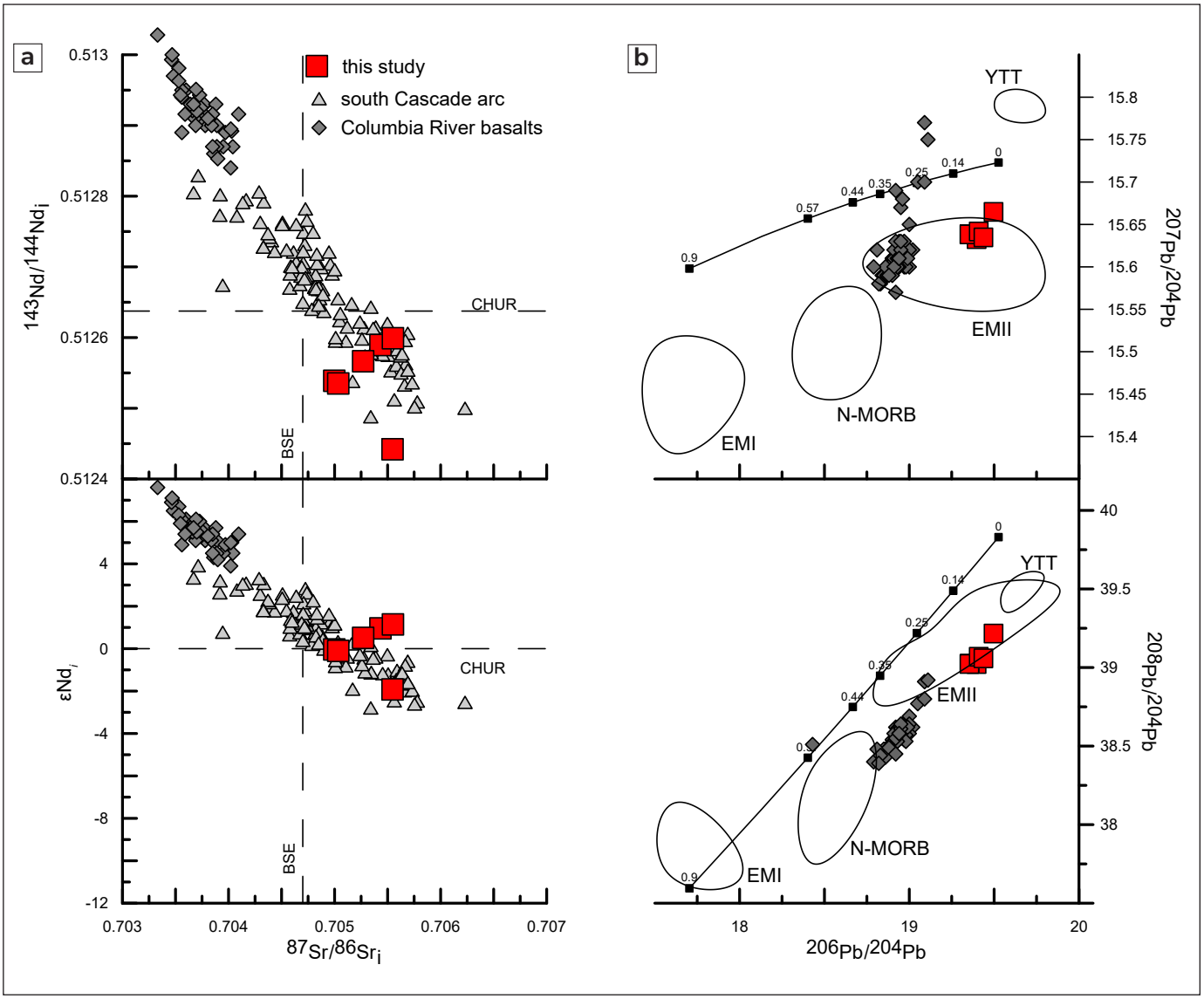


Figure 17. *Whole-rock isotope plots for Sixtymile volcanic rocks.* **(a)** *Initial Nd and εNd_i vs. initial Sr. Data for southern Cascade arc from du Bray et al. (2009), and data for Columbia River basalt from Moore et al. (2020). BSE – bulk silicate Earth; CHUR – chondritic uniform reservoir.* **(b)** *Plot of ^{207}Pb and ^{208}Pb vs ^{206}Pb. Data for enriched mantle I (EMI), enriched mantle II (EMII) and ocean island basalt (OIB) fields from Hart (1988); normal-mid ocean ridge basalt (N-MORB) from Ito et al. (1987); and Columbia River basalt from Moore et al. (2020). Yukon Tanana terrane (YTT) fields are based on samples of Sulphur Creek suite and Snowcap assemblage with data from Selby et al. (1999). Shale curve from Godwin and Sinclair (1982) and appears valid for parautochthonous terranes (Mortensen et al., 2006); ages in Ga.*

Summary

Late Cretaceous magmatic rocks across the northern Cordillera include small, high-level, calc-alkaline felsic to intermediate plutons (e.g., Friend, 2022) that are broadly coeval, and possibly comagmatic, with more widespread subaerial intermediate to mafic volcanic rocks of the Carmacks group (Grond et al., 1984; Woodsworth et al., 1991; Johnston et al., 1996). The volcanic rocks display calc-alkaline trace element signatures, but the high MgO contents of the mafic rocks have been interpreted as evidence of a mantle source (Johnston et al., 1996; Francis and Minarik, 2008). A few possible tectonic settings have been suggested based on these characteristics, including magmatism associated with oblique east-dipping subduction (Souther, 1991), a mantle plume source (Johnston et al., 1996), and subduction-related magmatism followed by slab rupture (Friend, 2022).

In the Sixtymile district, the lower part of the Late Cretaceous rocks appear to be exposed. The basal conglomerate unit in contact with the metamorphic basement is clearly observed, and the overlying rocks are dominantly andesitic, transitioning to basaltic andesite in the uppermost parts of the preserved volcanic stratigraphy. The new U-Pb zircon and CA-TIMS ages obtained from the andesitic component of the stratigraphy constrain the volcanic event in the Sixtymile district to approximately 69.8 Ma. Though the other areas with Late Cretaceous volcanic rocks are not as well constrained geochronologically, it is generally thought that the upper, basaltic component is ca. 72 to 69 Ma (Grond et al., 1984; Lowey et al., 1986). Elsewhere in the Yukon, Late Cretaceous, intermediate calc-alkaline volcanic rocks are considerably older, e.g., Tlansanlin (Morris et al., 2014) and Open Creek (Bordet et al., 2019) rocks in southern Yukon, which are ca. 79 to 76 Ma.

Geochemical data and phenocryst assemblages throughout the volcanic sequence indicate that the andesitic and basaltic andesite units were generated by a single, genetically related magmatic event. Major and trace element patterns (high Th/Yb and Nb/Yb values, negative Nb-Ta-Ti anomalies) and radiogenic Sr-Nd-Pb isotopes support a subduction setting with crustal contamination. These results differ from interpretations of Carmacks volcanic rocks having a mantle plume source (Johnston et al., 1996), characterized by shoshonitic magnesium-rich lavas and alkaline signatures. Instead, the Sixtymile district rocks lack these alkaline signatures and are more typical of young, primitive continental arc magmatism, supporting a subduction-related origin (e.g., Friend, 2022).

Conclusions

The geologic mapping, U-Pb zircon geochronology, whole-rock geochemistry, and Sr-Nd-Pb isotopic analyses presented in this study refine the understanding of Late Cretaceous volcanic rocks in the Sixtymile district. We suggest the Sixtymile volcanic sequence represents part of a Late Cretaceous continental magmatic arc system based on the following data:

1. Bedrock geology consists of a Yukon-Tanana terrane metamorphic basement overlain by relatively undeformed and unmetamorphosed Cretaceous sedimentary and volcanic rocks. The Cretaceous rocks have a consistent stratigraphy including a sedimentary basal unit, an andesitic middle unit, and a basaltic andesite upper unit.

2. Four new U-Pb zircon CA-TIMS ages from the andesitic component tightly constrain the volcanic event to ca. 69.8 Ma.

3. Whole-rock geochemical data indicate the volcanic rocks are dominantly sub-alkaline with continental arc geochemical signatures: (a) Th/Yb versus Nb/Yb ratios plot within the volcanic arc field; (b) extended trace element patterns reveal negative Nb-Ta anomalies and positive Pb anomalies; and (c) HFSE and LREE are depleted compared to LILE.

4. Isotopic values of $^{87}Rb/^{86}Sr$ (0.1529 - 0.3392), $^{143}Nd/^{144}Nd_i$ (0.51244 to 0.5126; εNd values of -1.9 to 1.1), and relatively enriched $^{206}Pb/^{204}Pb$ (19.35 to 19.50), $^{207}Pb/^{204}Pb$ (15.63 to 15.66), $^{208}Pb/^{204}Pb$ (39.02 to 39.07) suggest juvenile magma interaction with continental crust, consistent with a continental arc setting.

Acknowledgments

The authors would like to thank Mike MacDougall, Jayce Murtagh, John Flynn, Laurie Downes and other placer operators for access, advice on where to camp, and generally welcoming us to the Sixtymile area. Jim Ryan, Jan Dettmer and Jim Mortensen provided constructive criticism on earlier drafts of this manuscript.

References

Allan, M.A., Mortensen, J.K., Hart, C.J.R., Bailey, L.A., Sanchez, M.G., Ciolkiewicz, W., McKenzie, G.G. and Creaser, R.A., 2013. Magmatic and metallogenic framework of west-central Yukon and eastern Alaska. In: Tectonics, Metallogeny and discovery: The North American Cordillera and similar accretionary setttings, M. Colpron, T. Bissig, B.G. Rusk and J.F.H. Thompson (eds.), Society of Economic Geologists, p. 111–168.

Allan, M.M., Mortensen, J., Sanchez, M.G. and Hart, C.J.R., 2017. Structural and geochronological controls on Late Cretaceous porphyry and epithermal mineralization of the orogen-transverse Sixtymile-Pika fault system, Yukon and Alaska. Internal unpublished report, Mineral Deposits Research Unit, Vancouver, BC, 34 p.

Allègre, C.J. and Rousseau, D., 1984. The growth of the continent through geological time studied by Nd isotope analysis of shales. Earth and Planetary Science Letters, vol. 67, no. 1, p. 19–34.

Basta, F.F., Maurice, A.E., Bakhit, B.R., Azer, M.K. and El-Sobky, A.F., 2017. Intrusive rocks of the Wadi Hamad area, northeastern Desert, Egypt: Change of magma composition with maturity of Neoproterozoic continental island arc and the role of collisional plutonism in the differentiation of arc crust. Lithos, vol. 288, p. 248–263.

Bordet, E., Crowley, J.L. and Piercey, S.J., 2019. Geology of the eastern Lake Laberge area (105E), south-central Yukon. Yukon Geological Survey, Open File 2019-1, 120 p.

Cabanis, B. and Lecolle, M., 1989. Le diagramme La/10-Y/15-Nb/8; un outil pour la discrimination des series volcaniques et la mise en evidence des processus de melange et/ou de contamination crustale. The La/10-Y/15-Nb/8 diagram; a tool for distinguishing volcanic series and discovering crustal mixing and/or contamination. Comptes Rendus de l'Academie des Sciences, Serie 2: Mecanique, Physique, Chimie, Sciences de l'Univers, Sciences de la Terre, vol. 309, no. 20, p. 2023–2029.

Colpron, M., McClelland, W.C., Piercey, S.J., Kroeger, E.D.L., Crowley, J.L. and Gehrels, G.E., 2025. Revisiting the “Klondike Orogeny”: Permian to Jurassic development of the Yukon-Tanana terrane, northern Canadian Cordillera. Tectonics, vol. 44, no. 6, e2024TC008748, https://doi.org/10.1029/2024TC008748.

Colpron, M., Nelson, J.L. and Murphy, D.C., 2006. A tectonostratigraphic framework for the pericratonic terranes of the northern Canadian Cordillera In: Paleozoic evolution and metallogeny of pericratonic terranes at the ancient margin of North America, Canadian and Alaskan Cordillera, M. Colpron and J.L. Nelson (eds.), Geological Association of Canada, p. 1–23.

Colpron, M., Nelson, J.L. and Murphy, D.C., 2007. Northern Cordilleran terranes and their interactions through time. GSA Today, vol. 17, no. 4/5, p. 4–10.

Colpron, M., Sack, P.J., Crowley, J.L., Beranek, L.P. and Allan, M.M., 2022. Late Triassic to Jurassic magmatic and tectonic evolution of the Intermontane terranes in Yukon, northern Canadian Cordillera: Transition from arc to syn-collisional magmatism and post-collisional lithospheric delamination. Tectonics, vol. 41, no. 2, https://doi.org/10.1029/2021TC007060.

Cox, K.G., Bell, J.D. and Pankhurst, R.J., 1979. The interpretation of igneous rocks. Allen and Unwin, London, 450 p.

Crowley, J.L., Schoene, B. and Bowring, S.A., 2007. U-Pb dating of zircon in the Bishop Tuff at the millennial scale. Geology, vol. 35, p. 1123–1126.

du Bray, E.A., John, D.A., Putirka, K. and Cousens, B.L., 2009. Geochemical database for igneous rocks of the ancestral Cascades arc—southern segment, California and Nevada. United States Geological Survey, Data Series 439, 24 p.

Duk-Rodkin, A., 1996. Surficial geology, Dawson, Yukon Territory. Geological Survey of Canada, Open File 3288, scale 1:250 000.

Dusel-Bacon, C., Hopkins, M.J., Mortensen, J.K., Dashevsky, S.S., Bressler, J.R. and Day, W.C., 2006. Paleozoic tectonic and metallogenic evolution of the pericratonic rocks of east-central Alaska and adjacent Yukon. In: Paleozoic Evolution and Metallogeny of Pericratonic Terranes at the Ancient Pacific Margin of North America, Canadian and Alaskan Cordillera, M. Colpron and J.L. Nelson (eds.), Geological Association of Canada, p. 25–74.

Dusel-Bacon, C., Lanphere, M.A., Sharp, W.D., Layer, P.W. and Hansen, V.L., 2002. Mesozoic thermal history and timing of structural events for the Yukon–Tanana Upland, east-central Alaska: 40Ar/39Ar data from metamorphic and plutonic rocks. Canadian Journal of Earth Sciences, vol. 39, no. 6, p. 1013–1051.

Dusel-Bacon, C. and Mortensen, J., 2024. New U-Pb geochronology and geochemistry of Paleozoic metaigneous rocks from western Yukon and eastern Alaska, cross-border synthesis, and implications for tectonic models. US Geological Survey Professional Paper 1888, 100 p., https://doi.org/10.3133/pp1888.

Francis, D. and Minarik, W., 2008. Aluminum-dependent trace element partitioning in clinopyroxene. Contributions to Mineralogy and Petrology, vol. 156, p. 439–451.

Friend, M., 2022. Tectonomagmatic framework for Late Cretaceous postsubduction magmatism in west-central Yukon and southern Yukon. MSc thesis, University of British Columbia, Vancouver, British Columbia, 550 p.

Garrity, C.P. and Soller, D.R., 2009. Database of the geologic map of North America— Adapted from the map by J.C. Reed, Jr. and others (2005). US Geological Survey Data Series 424, https://pubs.usgs.gov/ds/424/.

Glasmacher, U. and Friedrich, G., 1992. Volcanic-hosted epithermal gold-sulphide mineralization and associated enrichment processes, Sixtymile River area, Yukon Territory, Canada. In: Yukon Geology, Volume 3, T.J. Bremner (ed.), Exploration and Geological Services Division, Yukon Region, Indian and Northern Affairs Canada, p. 271–291.

Godwin, C.I. and Sinclair, A.J., 1982. Average lead isotope growth curves for shale-hosted zinc-lead deposits, Canadian Cordillera. Economic Geology, vol. 77, no. 3, p. 675–690.

Grond, H.C., Churchill, S.J., Armstrong, R.L., Harakal, J.E. and Nixon, G.T., 1984. Late Cretaceous age of the Hutshi, Mount Nansen, and Carmacks groups, southwestern Yukon Territory and northwestern British Columbia. Canadian Journal of Earth Sciences, vol. 21, no. 5, p. 554–558.

Hart, S.R., 1988. Heterogeneous mantle domains: signatures, genesis and mixing chronologies. Earth and Planetary Science Letters, vol. 90, no. 3, p. 273–296.

Ito, E., White, W.M. and Göpel, C., 1987. The O, Sr, Nd and Pb isotope geochemistry of MORB. Chemical Geology, vol. 62, no. 3, p. 157–176.

Jaffey, A.H., Flynn, K.F., Glendenin, L.F., Bentley, W.C. and Essling, A.M., 1971. Precision measurements of half-lives and specific activities of 235U and 238U. Physical Review C, vol. 4, no. 5, p. 1889–1906.

Johnston, S.T. and Erdmer, P., 1995. Magmatic flow and emplacement foliations in the Early Jurassic Aishihik batholith, southwest Yukon: Implications for northern Stikinia. In: Jurassic Magmatism and Tectonics of the North American Cordillera, D.M. Miller and C. Busby (eds.), Geological Society of America Special Paper, https://doi.org/10.1130/SPE299-p65.

Johnston, S.T., Wynne, P.J., Francis, D., Hart, C.J.R., Enkin, R.J. and Engebretson, D.C., 1996. Yellowstone in Yukon: The Late Cretaceous Carmacks Group. Geology, vol. 24, no. 11, p. 997–1000.

Le Bas, M.J., Le Maitre, R.W., Streckeisen, A. and Zanettin, B., 1986. A Chemical Classification of Volcanic Rocks Based on the Total Alkali-Silica Diagram. Journal of Petrology, vol. 27, p. 745–750.

Lowey, G., 1984. The stratigraphy and sedimentology of siliciclastic rocks, west-central Yukon, and their tectonic implications. PhD thesis, University of Calgary, Calgary, Alberta, 620 p.

Lowey, G.W., Sinclair, W.D. and Hills, L.V., 1986. Additional K-Ar isotopic dates for the Carmacks Group (Upper Cretaceous), west-central Yukon. Canadian Journal of Earth Sciences, vol. 23, p. 1857–1859.

Mattinson, J.M., 2005. Zircon U/Pb chemical abrasion (CA-TIMS) method; combined annealing and multi-step partial dissolution analysis for improved precision and accuracy of zircon ages. Chemical Geology, vol. 220, no. 1-2, p. 47–66.

Moore, N.E., Grunder, A.L. and Bohrson, W.A., 2018. The three-stage petrochemical evolution of the Steens Basalt (southeast Oregon, USA) compared to large igneous provinces and layered mafic intrusions. Geosphere, vol. 14, no. 6, p. 2505–2532.

Moore, N.E., Grunder, A.L., Bohrson, W.A., Carlson, R.W. and Bindeman, I.N., 2020. Changing Mantle Sources and the Effects of Crustal Passage on the Steens Basalt, SE Oregon: Chemical and Isotopic Constraints. Geochemistry, Geophysics, Geosystems, vol. 21, issue 8, https://doi.org/10.1029/2020GC008910.

Morris, G.A., Mortensen, J.K. and Israel, S., 2014. U-Pb age, whole-rock geochemistry and radiogenic isotopic compositions of Late Cretaceous volcanic rocks in the central Aishihik Lake area, Yukon (NTS 115H) In: Yukon Exploration and Geology 2013, K.E. MacFarlane, M.G. Nordling and P.J. Sack (eds.), Yukon Geological Survey, p. 133–145.

Mortensen, J.K., 1988. Geology southwestern Dawson map area, Yukon. Geological Survey of Canada, Open File 1927, scale 1:250 000.

Mortensen, J.K., 1996. Geological compilation maps of the northern Stewart River area, Klondike and Sixtymile districts (115N/15, 16, 115O/13, 14 and Parts of 115O/15, 16). Indian & Northern Affairs Canada/Department of Indian & Northern Development: Exploration & Geological Services Division, Open File 1996-1(G), 43 p.

Mortensen, J.K., Dusel-Bacon, C., Hunt, J.A. and Gabites, J., 2006. Lead isotopic constraints on the metallogeny of middle and late Paleozoic syngenetic base-metal occurrences in the Yukon-Tanana and Slide Mountain/Seventymile terranes and adjacent portions of the North American miogeocline. In: Paleozoic Evolution and Metallogeny of Pericratonic Terranes at the Ancient Pacific Margin of North America, Canadian and Alaskan Cordillera, M. Colpron and J.L. Nelson (eds.), Geological Association of Canada, p. 261–279.

Payne, J., Gonzales, R.A., Akhurst, K. and Sisson, W.G., 1987. Geology of Colorado Creek (115-J/10), Selwyn River (115-J/9) and Prospector Mountain (115-I/15) map areas. Indian and Northern Affairs, Open File 1987-3, p. 150.

Pearce, J.A., 1996. A user's guide to basalt discrimination diagrams. In: Trace element geochemistry of volcanic rocks, D.A. Wyman (ed.), Geological Association of Canada - Mineral Deposits Division, p. 79–113.

Pearce, J.A., 2008. Geochemical fingerprinting of oceanic basalts with applications to ophiolite classification and the search for Archean oceanic crust. Lithos, vol. 100, p. 14–48.

Peccerillo, A. and Taylor, S.R., 1976. Geochemistry of eocene calc-alkaline volcanic rocks from the Kastamonu area, Northern Turkey. Contributions to Mineralogy and Petrology, vol. 58, no. 1, p. 63–81.

Rimando, J., Peace, A.L., Geng, M., Verbaas, J. and Slade, H., 2022. Structural setting of the Sixtymile gold district, Yukon, Canada: Insights into regional deformation and mineralization from field mapping and 3D magnetic inversion. Minerals, vol. 12, no. 3, 29 p.

Rollinson, H.R., Rollinson, H. and Pease, V., 2021. Using geochemical data: to understand geological processes. 2nd ed., Cambridge University Press.

Rudnick, R.L., 1995. Making continental crust. Nature, vol. 378, no. 6557, p. 571–578.

Ryan, J., Zagorevski, A., Williams, S.P., Roots, C.F., Ciolkiewicz, W. and Chapman, J.B., 2013. Geology, Stevenson Ridge (northeast part), Yukon. Geological Survey of Canada, Geoscience map 116 (2nd edition, preliminary), scale 1:100 000.

Saccani, E., 2015. A new method of discriminating different types of post-Archean ophiolitic basalts and their tectonic significance using Th-Nb and Ce-Dy-Yb systematics. Geoscience Frontiers, vol. 6, no. 4, p. 481–501.

Sack, P.J. and Butty, E., (in prep). Bedrock geology map of the Sixtymile district, west-central Yukon (Parts of NTS 116C/1, 2 and 115N/15, 16). Yukon Geological Survey, scale 1:50 000.

Schmitz, M.D. and Schoene, B., 2007. Derivation of isotope ratios, errors and error correlations for U-Pb geochronology using 205Pb-235U-(233U)-spiked isotope dilution thermal ionization mass spectrometric data. Geochemistry, Geophysics, Geosystems (G3), vol. 8, no. Q08006.

Selby, D., Creaser, R.A. and Nesbitt, B.E., 1999. Major and trace element compositions and Sr–Nd–Pb systematics of crystalline rocks from the Dawson Range, Yukon, Canada. Canadian Journal of Earth Sciences, vol. 36, p. 1463–1481.

Smuk, K.A., 1999. Metallogeny of epithermal gold and base metal veins of the southern Dawson Range, Yukon. MSc thesis, McGill University, 188 p.

Souther, J.G., 1991. Volcanic Regimes. In: Geology of the Cordilleran Orogen in Canada, H. Gabrielse and C.J. Yorath (eds.), Geological Society of America, vol G2.

Staples, R.D., Gibson, H.D., Colpron, M. and Ryan, J.J., 2016. An orogenic wedge model for diachronous deformation, metamorphism, and exhumation in the hinterland of the northern Canadian Cordillera. Lithosphere, vol. 8, no. 2, p. 165–184.

Sun, S.-S. and McDonough, W.F., 1989. Chemical and isotopic systematics of oceanic basalts: implications for mantle composition and processes. In: Magmatism in the Ocean Basins, A.D. Saunders and M.J. Norry (eds.), Geological Society, London, p. 313–345.

Tempelman-Kluit, D.J., 1974. Reconnaissance geology of Aishihik Lake, Snag and part of Stewart River map-areas, west-central Yukon. Geological Survey of Canada, Paper 73-41, 97 p., (3 sheets).

Tempelman-Kluit, D.J., 1984. Geology of Laberge (105E) and Carmacks (115I) map areas, Yukon. Geological Survey of Canada, Open File 1101, scale 1:250 000.

Tempelman-Kluit, D.J., 2009. Geology of Carmacks and Laberge map areas, central Yukon: Incomplete draft manuscript on stratigraphy, structure and its early interpretation (ca. 1986). Geological Survey of Canada, Open File 5982, 399 p.

Whitney, D.L. and Evans, B.W., 2010. Abbreviations for names of rock-forming minerals. American Mineralogist, vol. 95, p. 187–187.

Winchester, J.A. and Floyd, P.A., 1977. Geochemical discrimination of different magma series and their differentiation products using immobile elements. Chemical Geology, vol. 20, p. 325–343.

Wood, D.A., 1980. The application of a Th-Hf-Ta diagram to problems of tectonomagmatic classification and to establishing the nature of crustal contamination of basaltic lavas of the British Tertiary volcanic province. Earth and Planetary Science Letters, vol. 50, no. 1, p. 11–30.

Woodsworth, G.J., Anderson, R.G., Armstrong, R.L., Struik, L.C. (Proterozoic, Paleozoic) and Heyden, P.v.d. (Coast Plutonic Complex), 1991. Plutonic Regimes. In: Geology of the Cordilleran Orogen in Canada, H. Gabrielse and C.J. Yorath (eds.), Geological Society of America, vol. G2, https://doi.org/10.1130/DNAG-GNA-G2.491.

Wynne, P.J., Enkin, R.J., Baker, J., Johnston, S.T. and Hart, C.J.R., 1998. The big flush: paleomagnetic signature of a 70 Ma regional hydrothermal event in displaced rocks of the northern Canadian Cordillera. Canadian Journal of Earth Sciences, vol. 35, p. 657–671.

Xia, L.-Q., 2014. The geochemical criteria to distinguish continental basalts from arc related ones. Earth-Science Reviews, vol. 139, p. 195–212.

Yukon Geological Survey, 2023. Yukon geochronology – a database of Yukon isotopic age determinations. Yukon Geological Survey, https://data.geology.gov.yk.ca/Compilation/22, [accessed 20/11/2025]

Zack, T., Kronz, A., Foley, S.F. and Rivers, T., 2002. Trace element abundances in rutiles from eclogites and associated garnet mica schists. Chemical Geology, vol. 184, no. 1-2, p. 97–122.

Preliminary investigation of seismic site conditions in Whitehorse (Kwänlin), Yukon, from passive seismic methods

*Jamie Friesen Byer**
Department of Earth, Energy, and Environment, University of Calgary

Jeremy M. Gosselin
Natural Resources Canada, Geological Survey of Canada–Pacific

Jan Dettmer
Yukon Geological Survey

Hersh Gilbert
Department of Earth, Energy, and Environment, University of Calgary

Byer, J.F., Gosselin, J.M., Dettmer, J. and Gilbert, H., 2026. Preliminary investigation of seismic site conditions in Whitehorse (Kwänlin), Yukon, from passive seismic methods. *In*: Yukon Exploration and Geology 2025, A. Stuart, L.H. Weston and S.K. Schultz (eds.), Yukon Geological Survey, Government of Yukon, p. 119–130.

Abstract

Although southwestern Yukon is tectonically active, with large historical and instrumentally recorded earthquakes, the seismic hazard in this region remains understudied compared to other regions of Canada. Ground shaking is influenced by source, path, and local geological effects, and local site conditions control the amplification and resonance of seismic energy. In this study, we use passive seismic recordings to constrain the seismic properties of the sediment for two sites in the Whitehorse (Kwänlin) area. Frequency-wavenumber beamforming is applied to ambient seismic noise from each site to extract surface-wave dispersion curves that contain information on sediment rigidity and subsurface structure. These dispersion curves are then used in a probabilistic inversion to determine one-dimensional shear-wave velocity models and associated uncertainties. Our results indicate that both sites are associated with seismic site class D, stiff soil. The results of this study improve the understanding of local seismic hazards in Kwänlin, lay the foundation for ongoing local seismic hazard investigations, and contribute to geohazard mitigation for northern Canada.

Plain language summary

Southwestern Yukon experiences large earthquakes, but these events have not been studied as extensively as those in other parts of Canada. The strength of earthquake ground shaking is influenced by the type of earthquake and by the ground materials—rock or sediment—beneath the surface. In this study, we use recordings of background Earth vibrations to measure sediment properties at two sites in the Whitehorse (Kwänlin) area. This information is useful for anticipating the severity of ground shaking during future earthquakes. Our results indicate that both sites can be classified as leading to a moderate increase in shaking severity compared to sites underlain with hard rock. These site classifications are used in building and infrastructure design under Canada's building code. Our work provides a step toward an improved understanding of natural hazards in Kwänlin, and lays a foundation for ongoing studies of regional sediment properties and local earthquake shaking hazards. Ultimately, this contributes to geohazard mitigation for northern Canada.

* jamie.byer@ucalgary.ca

Introduction

Whitehorse, Yukon, has an elevated risk of geohazards due to nearby active tectonics and rapid geomorphic processes. Northern communities such as Whitehorse also experience greater impacts of climate change as northern climates warm at more than double the global rate (Government of Yukon, 2022). Furthermore, a changing climate modulates geomorphic processes and can locally exacerbate geohazards (e.g., Dutta et al., 2008). Yukon is experiencing permafrost thaw, as well as more severe precipitation and wildfires (Government of Yukon, 2022). These can contribute to erosion, subsidence, landslides and increased severity of earthquake-induced ground shaking (Sun et al., 2017). Since spring 2022, multiple large landslides have occurred along the steep bluff that separates the Whitehorse airport from the downtown city centre (Brideau et al., 2024). These landslides caused disruptions to infrastructure and community access (Proulx, 2022), and highlight the need to better understand geohazards across Whitehorse to improve mitigation and community resilience.

The tectonics in southwestern Yukon are driven by the Yakutat microplate colliding and subducting beneath the North American plate (Bruhn et al., 2012; Gosselin et al., 2024). These active tectonics lead to rapid mountain building, erosion and earthquake activity (Fig. 1). Yukon is one of the most seismically active regions in Canada and has historically experienced numerous earthquakes of magnitude 6 and greater (Hyndman et al., 2005; Fig. 1). Seismicity from the nearby active Denali and Tintina faults (Eberhart-Phillips et al., 2003; Blais-Stevens et al., 2020; Biegel et al., 2024; Finley, 2025; Finley et al., 2025), as well as from the active plate boundary a few hundred kilometres to the southwest (Plafker, 1970; Doser, 2006), present significant additional hazards to the region. Geologically, the Yukon is part of the northern Canadian Cordillera, which formed through the accretion of magmatic arcs, continental arcs and oceanic basins onto the western margin of North America (Nelson et al., 2007). These accreted terranes have distinct geologic histories and are bounded by several large-scale faults (Kellett et al., 2017), mentioned above.

Earthquake hazards depend on the type and location of an earthquake, the propagation path of seismic energy, and local geological conditions (e.g., Kolaj et al., 2020). The Whitehorse trough sedimentary basin formed through accretion and was infilled by erosion during the Jurassic Period (White et al., 2012; van Drecht et al., 2022). Subsequent intrusive and volcanic activity produced plutonic and volcanic rocks that are now present in the subsurface. Because Whitehorse is proximal to several fault systems capable of generating large earthquakes, three-dimensional sedimentary basin structures that trap and amplify seismic energy are expected to influence ground motions in the area (e.g., Bard and Bouchon, 1980). The structure and properties of the sedimentary basin, its intrusions, and the contrast with the underlying crystalline basement may therefore exacerbate seismic hazard. Consequently, any knowledge on the seismic properties of rocks and sediments in the Whitehorse trough will improve our understanding of earthquake hazards.

At a local scale, earthquake shaking intensity and duration can be amplified by unconsolidated materials overlying bedrock due to resonance and seismic wave amplification (Anderson et al., 1986; Anderson et al., 1996), commonly referred to as seismic site effects. This study focuses on site effects associated with unconsolidated sediments and shallow bedrock within the upper ~100 m of the subsurface. In the Whitehorse area, unconsolidated sediments are predominantly less than 100 m thick and bedrock outcrops are sparse (Witter, 2025). These sediments were deposited during the McConnell Glaciation and include fine-grained silt and clay deposited in Glacial Lake Laberge (Lipovsky, 2023). The presence of these unconsolidated sediments of low rigidity overlying bedrock, combined with regional seismicity, has the potential to significantly increase the local seismic hazard.

The shear-wave velocity (V_S) is often used as a proxy for the rigidity of the soil/sediment at a site when evaluating conditions for earthquake engineering purposes. Specifically, the time-average V_S of the upper 30 m beneath a site (V_{S30}) is a useful parameter for the quantification of earthquake hazards. Furthermore, the National Seismic Hazard Model of Canada (Kolaj et al., 2020) assigns six specific site classes according to V_{S30} values measured or inferred at a site (Table 1). This allows for a more accurate application of the the National Building Code of Canada and highlights the importance of mapping near-surface geophysical properties throughout the Whitehorse area.

In this work, we used passive seismic recordings collected from two locations in Whitehorse to infer the one-dimensional (1D) near-surface Earth structure. Specifically, we apply frequency-wavenumber (f-k) beamforming to the ambient seismic noise recordings to extract surface-wave dispersion curves. The dispersion curves are then inverted using probabilistic

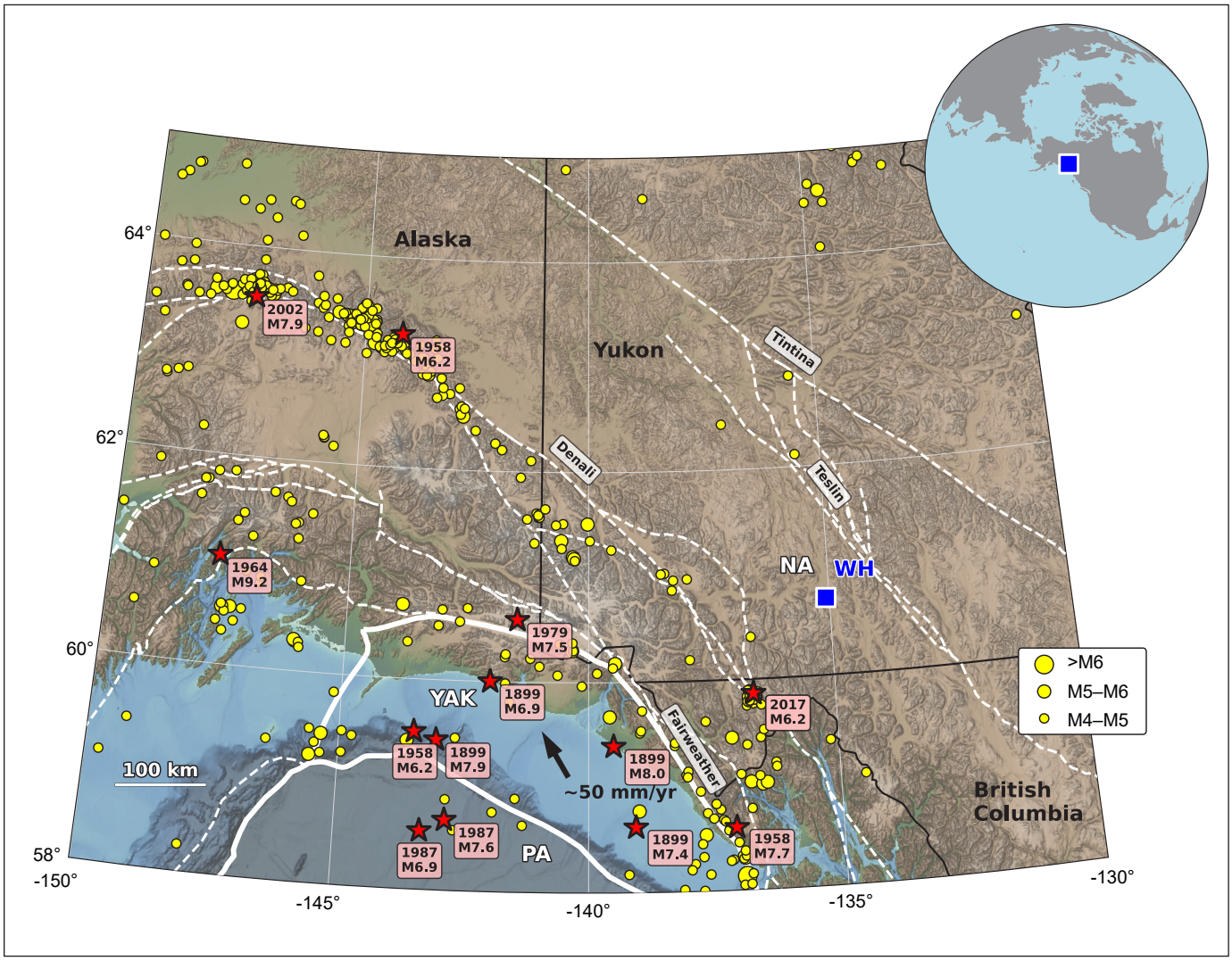


Figure 1. *Contributions to seismic hazards in southwestern Yukon. Instrumentally recorded earthquake epicentres (2000–2024) with magnitude ≥4 are represented by yellow circles, and significant earthquakes are represented by red stars. Major regional faults are indicated by dashed white lines, and the boundaries of the Pacific (PA), North American (NA), and Yakutat (YAK) tectonic plates are indicated by solid white lines. Provincial and territorial boundaries are marked with solid black lines. The location of Whitehorse (WH) is marked by the blue square.*

methods to estimate V_S profiles. Finally, the probability distributions of the V_{S30} values are determined from the inversion results and used to classify earthquake site hazards. The results of this work help improve the understanding of local seismic hazards in Whitehorse and lay the foundation for future microzonation analyses to understand the local variability in seismic hazards throughout the city and surrounding area. Ultimately, this will contribute to greater resilience of both the community and its infrastructure to geohazards.

Data and methods

Passive seismic array recordings

The passive seismic data used in this study were recorded on July 6, 2023 at two sites in the Whitehorse area (Fig. 2). Site A is in an agricultural field located along the Alaska Highway, approximately 20 km west of downtown Whitehorse, and site B is on a baseball field within the city limits. At each site, 14 Nanometrics Trillium Compact 120s broadband seismometers with Taurus seismographs were deployed in a cross-shaped configuration with a maximum station separation of approximately 100 m. The spacing between

instruments within the array increases outward, ranging from 5 to 45 m. This allows multiple and wider array apertures to collect data from a wider frequency band (Wathelet et al., 2008; Gosselin et al., 2018). These array apertures were chosen to target dispersion measurements over a specific frequency band that is sensitive to near-surface V_S over the depth extent that is relevant to seismic site amplification assessment (i.e., targeting the uppermost tens of metres).

The two site locations were selected based on several factors, including sufficient area to conduct passive seismic surveys, accessibility and relatively flat topography. In order to couple the seismometer to the ground, surface vegetation was removed beneath some instrument locations prior to installation. In addition, soft surficial materials beneath some instruments required that a ceramic tile be laid beneath seismometers to accurately level them. At site B, located on a baseball field, sufficient direct ground coupling could be achieved without tiles for all instruments. Synchronous ambient noise was collected on all instruments for approximately one hour with a sampling frequency of 100 Hz.

Table 1. The V_{S30} site classification used in Canada's national seismic hazard model (Kolaj et al., 2020).

Site class	Description	V_{S30} (m/s)
A	hardrock	1500
B	rock	760–1500
C	very dense soil and soft rock	360–760
D	stiff soil	180–360
E	soil with soft clay	<180
F	site-specific analysis required	—

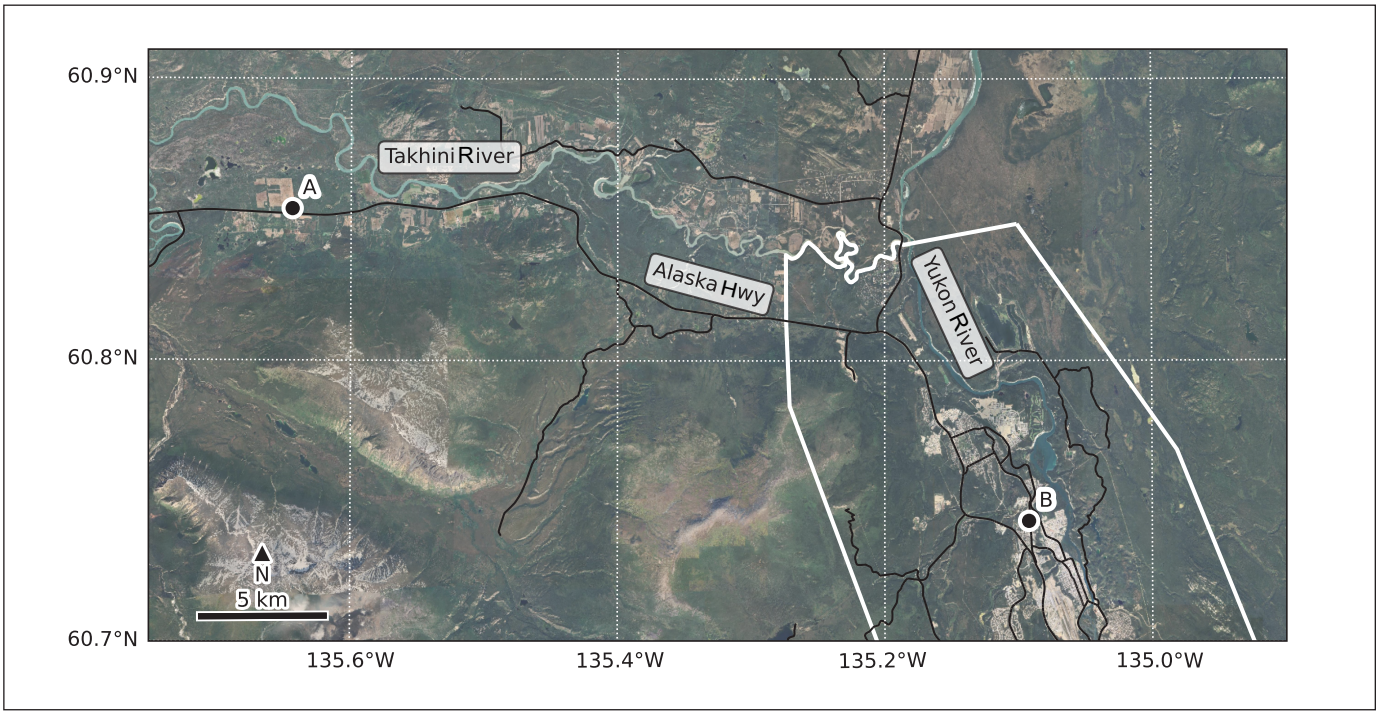


Figure 2. *The study area includes two focus site locations (labeled A and B). Whitehorse city limits (white lines), major roads (black lines) and rivers are also indicated.*

Frequency-wavenumber beamforming

The synchronous ambient seismic noise recordings were processed using Geopsy software (Wathelet et al., 2020) to perform frequency-wavenumber (f-k) beamforming and obtain fundamental-mode Rayleigh wave phase velocities as a function of frequency (i.e., dispersion). This beamforming approach estimates the propagation direction and speed of the dominant seismic signal propagating across the seismic array. The ambient seismic noise recordings are split into frequency-dependent time windows. For each time window, the beam power is calculated for a range of speeds and directions at the given frequency. The velocity with the maximum beam power is recorded for each time window, and this procedure is repeated for all time windows and all frequencies. The result is a distribution of phase velocities for each frequency.

The f-k beamforming analysis was performed for approximately 100 logarithmically-spaced frequencies between 1 and 15 Hz, assuming a phase velocity search grid between 200 and 2000 m/s. The approximately 1 hour of ambient seismic noise was divided into time windows with a frequency-dependent duration of 10 periods, with an overlap of 50%. Figure 3 illustrates the f-k beamforming results for all time windows and all frequencies, as well as the manually selected dispersion measurements retained for further analysis. Specifically, the dispersion data are taken as the median phase velocity of the time windows at each frequency. Measurement errors are taken to be the standard deviation at each frequency.

For site A, the dispersion curve is taken between 2.25 and 14.6 Hz, and for site B it is between 2.02 and 3.67 Hz and between 6.66 and 12.75 Hz. These frequency ranges were manually selected based on visual inspection of the f-k beamforming results and are frequencies where f-k results suggest sufficient constraint on phase velocity. These frequency limitations are likely due to a combination of site complexity, as well as the resolution and aliasing limits of the passive seismic array, which are dependent on the geometry and configuration of the array (Wathelet et al., 2008). For site A, at frequencies between about 5 and 8 Hz, and for site B at frequencies above approximately 10 Hz, phase velocities are near the lower processing bound of 200 m/s. Future work will investigate whether slower phase velocities, at higher frequencies, can be measured at these sites without the processing-imposed cutoff of our initial f-k beamforming analysis. For site B, at frequencies

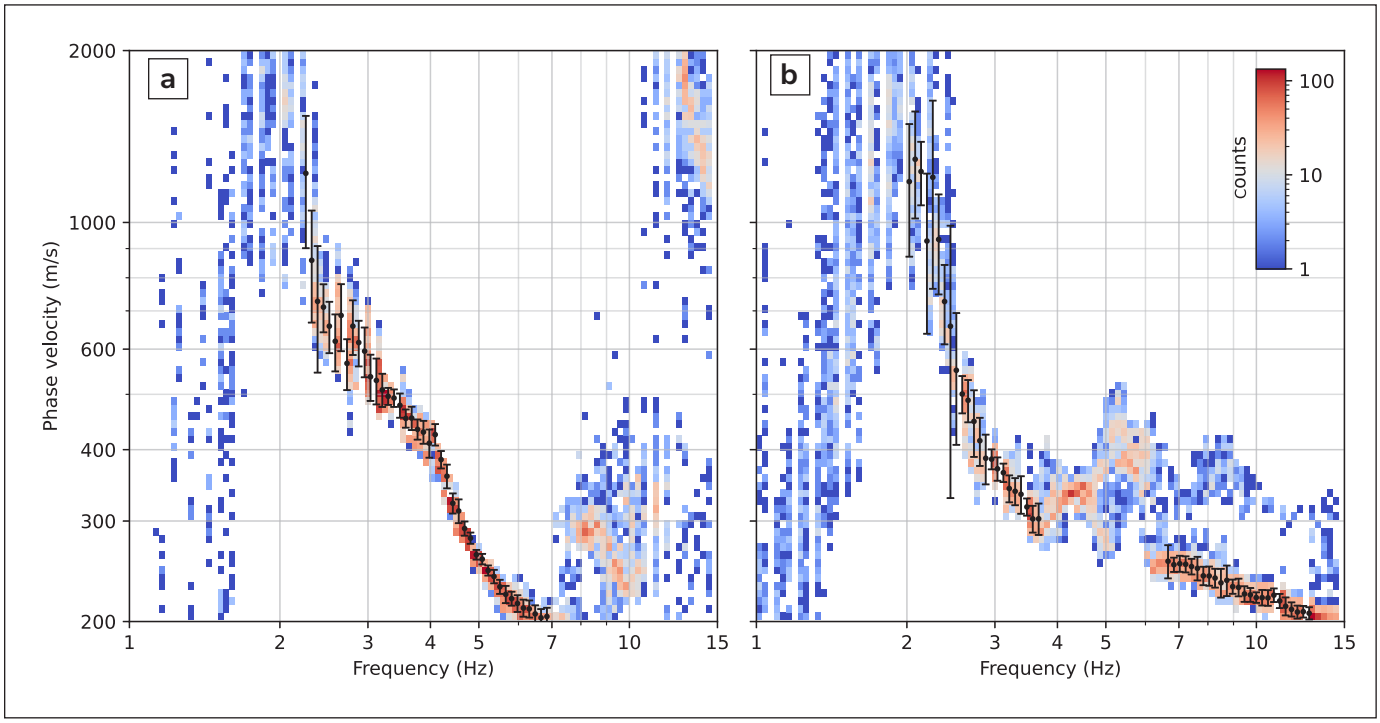


Figure 3. *Phase velocity dispersion from frequency-wavenumber (f-k) beamforming for* ***(a)*** *site A and* ***(b)*** *site B. Frequencies are chosen to be equidistant in log-space. Median phase velocities (black circles) and the standard deviations in phase velocity (error bars) are displayed, and represent the dispersion measurements used in subsequent analysis. The number of counts per bin are also illustrated by the colourbar.*

greater than 6.6 Hz, multiple phase velocity modes appear in the f-k results. At these frequencies, we qualitatively identify and remove the higher velocities associated with the second mode, which could bias our measurements (including the measurement errors). For site B, we exclude measurements between approximately 4 and 6 Hz due to the likely non-physical characteristics of the dispersion curve, which is expected to be smooth and nearly monotonic for phase velocities across frequencies. Further analysis is required to determine the cause of this processing result, though we speculate it may be partially due to the ambient seismic noise field during our 1-hour experiment. The final dispersion measurement selections for both sites suggest differences in near-surface site conditions.

Probabilistic inversion

Rayleigh wave dispersion is strongly dependent on V_S, and has a lesser sensitivity to density (ρ) and compressional-wave velocity (V_ρ; Xia et al., 1999). Consequently, dispersion curves can be used to infer V_S, and thereby the structure of the subsurface (Gosselin et al., 2022). For this problem, we parameterize the 1D Earth as a stack of layers over an infinite half-space, with unknown thicknesses and V_S. We determine V_ρ from V_S using a fixed V_ρ / V_S ratio of 1.75, and ρ using an empirical relation to V_ρ (Gardner et al., 1974). Since there are finite data, and these data have uncertainties, the inverse problem is non-unique, and many models can fit the data appropriately. In addition, the inverse problem is nonlinear as the sensitivity of the data to V_S depends on the model itself. To estimate 1D profiles of V_S from the computed dispersion curves and their uncertainties, we employ a probabilistic (Bayesian) Markov chain Monte Carlo (McMC) method (Molnar et al., 2010; Gosselin et al., 2022).

A posterior probability density (PPD) of the model parameters is estimated from a large ensemble of McMC samples dependent on the prior distribution, and on the data via a likelihood function. In this work, we assume that the prior distribution of the model parameters is uniform over a wide range of physically plausible values. The model parameters we infer are layer thicknesses and V_S. For both sites, we performed probabilistic inversions assuming several possible numbers of layers in the model. These inversions yielded similar results, leading us to qualitatively select a model consisting of three layers (two layers over a half-space) as the model with the minimum complexity required to explain our data. The prior bounds for the model parameters were chosen to be wide, yet physically plausible, to allow flexibility in the range of possible models that could be inferred to explain the data (Table 2). We used disba (Luu, 2024), a python implementation of Computer Programs in Seismology (Herrmann, 2013), to perform forward calculations that predict dispersion data for McMC model samples to evaluate model likelihood (i.e., data misfit). In this work, we assume a multi-variate Gaussian likelihood, with data errors at each frequency assumed to be independent and fixed to our measurement errors based on f-k processing (discussed above).

Results

Figure 4 displays the results of our passive seismic analysis for the data collected at site A. For illustration purposes, the figure bounds indicate the most pertinent region of the model and do not reflect the entire allowable prior model space. The configuration of the passive seismic array is delineated in Figure 4a, which highlights the extent (aperture) and configuration of the instruments deployed at the agricultural field site. We note that the minimum and maximum instrument separation distances are approximately 5 and 100 m, respectively. Figure 4b indicates the fit between the measured and predicted phase velocity dispersion data. Generally, the data predictions fall within the error bars for the field observations. The errors are larger for low frequencies, and this is reflected in the larger range in data predictions for low frequencies. We note a change in the trend of the dispersion curve at approximately 4 Hz, which is captured by the data predictions and is likely caused by a significant seismic impedance contrast beneath the site.

Table 2. Model parameter prior bounds.

Parameter	Site A		Site B	
	min	max	min	max
depth 1 (m)	5	50	5	50
depth 2 (m)	5	200	5	200
V_S1 (m/s)	100	750	100	750
V_S2 (m/s)	200	1250	200	1000
V_S3 (m/s)	500	3000	750	3000

We performed probabilistic inversions assuming several possible numbers of layers in the 1D V_S model. We note that results from these various inversions yield similar results. Qualitatively, we identify that a model consisting of three layers (two layers over a half-space) is the simplest model that can explain the data. The result of our probabilistic inversion at site A is displayed in Figure 4c and 4d. Specifically, we illustrate the marginal posterior density of V_S as a function of depth, as well as the marginal probabilities for layer interface depths. The inversion results provide evidence for a layer with V_S between 200 and 225 m/s, to a depth of around 20 m (between 15 and 22 m). The second layer has much larger uncertainty in both velocity and interface depth. Our results indicate a large contrast in V_S between the first and second layers and a gradual, monotonically increasing V_S below the first layer. The second interface depth ranges between 27 and 95 m, and inferred V_S values range between 325 and 850 m/s. Beyond approximately 100 m depth, V_S continues to increase, but with a significant increase in V_S uncertainty. This provides some evidence of higher velocities at depth below site A, but that V_S values at these depths are likely beyond the resolution limits of our measurements.

Figure 5 displays the results of our passive seismic analysis for the data collected at site B. As with site A, the figure bounds indicate the most pertinent region of the model and do not reflect the entire allowable prior model space. The configuration of the passive seismic array is delineated in Figure 5a, which highlights the extent (aperture) and configuration of the instruments deployed at the baseball field site. Similarly to site A, we note that the minimum and maximum instrument separation distances are approximately 5 and 100 m, respectively. Figure 5b indicates the fit between the measured and predicted phase velocity dispersion data. Generally, for high frequencies, the data predictions fall within the error bars for the field observations. However, the low frequency data predictions do not fall within the observed data error bars and indicate a systematic bias with under-prediction of phase velocities. The errors are larger for frequencies less than around 2.5 Hz., and this is reflected in the larger range in data predictions for low frequencies. The under-prediction of phase velocities at low frequencies suggests that the measured data require higher velocities than our model assumptions permit. Future work will further investigate the cause of this bias and the V_S values required to fit the data, and the plausibility of such high V_S values.

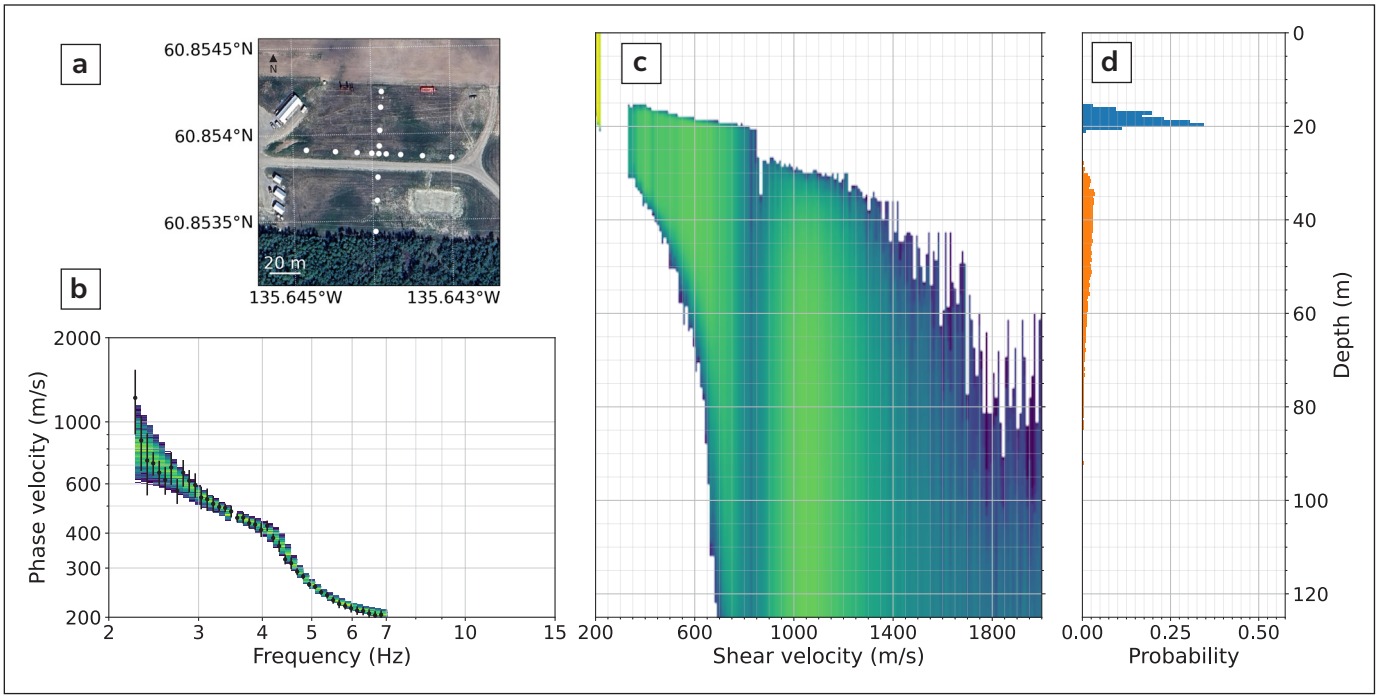


Figure 4. *Passive seismic analyses at site A.* ***(a)*** *Configuration of passive seismic array at site A.* ***(b)*** *Observed data (black markers with error bars) and predicted data (histogram); blue indicates low probability and yellow indicates high probability.* ***(c)*** *Marginal posterior probability density of shear-wave velocity (V_S) as a function of depth.* ***(d)*** *Marginal posterior probabilities for interface depths.*

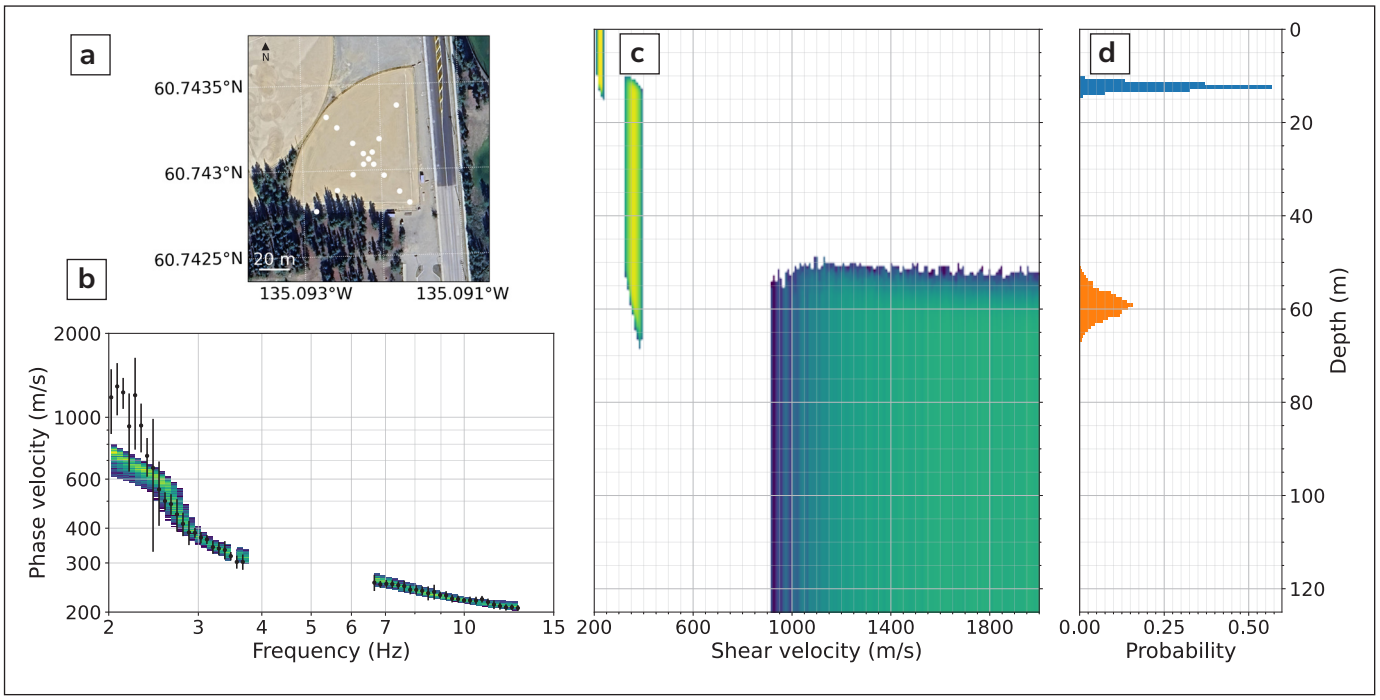


Figure 5. *Passive seismic analyses at site B.* ***(a)*** *Configuration of passive seismic array at site B.* ***(b)*** *Observed data (black markers with error bars) and predicted data (histogram); blue indicates low probability and yellow indicates high probability.* ***(c)*** *Marginal posterior probability density of shear-wave velocity (V_S) as a function of depth.* ***(d)*** *Marginal posterior probabilities for interface depths.*

The result of our probabilistic inversion at site B is displayed in Figure 5c and 5d. As discussed above, we assume a model consisting of two layers over a half-space. Specifically, we illustrate the marginal posterior density of V_S as a function of depth, as well as the marginal probabilities for layer interface depths. The inversion results provide evidence for a layer with V_S between 200 and 250 m/s, to a depth between 10 and 15 m. The second layer has V_S between 320 and 400 m/s, and interface depth between 52 and 57 m. Beneath the second layer is an effectively unconstrained half-space, with the data supporting V_S above the upper prior bound of 3000 m/s.

Discussion and conclusions

This section considers seismic engineering parameters that are summarized in Fig 6. The time-average V_S of the uppermost 30 m beneath a site (V_{S30}) is an important seismic engineering parameter that is used to accurately apply the National Building Code of Canada. Typically, methods that infer or measure V_{S30} report a single value. In this work, the V_{S30} values are computed for the ensemble of McMC models to obtain a posterior distribution of the V_{S30} values (Fig. 6a). This distribution quantifies the uncertainty of the V_{S30} results. Based on the values of V_{S30}, the site classification for both sites is D, stiff soil. For site A, the most probable value of V_{S30} is ~275 m/s, and the values range between 249 and 280 m/s. For site B, the most probable value of V_{S30} is ~285 m/s, and the values range between 275 and 295 m/s. These results suggest a moderate amplification potential in Whitehorse, compared to a reference site typically assumed to have V_{S30} = 760 m/s (Kolaj et al., 2020). Recently, a similar site classification was performed for 14 sites in the Haines Junction (Dakwäkäda) area (Gosselin et al., 2025). Estimates of the amplification potential in the Haines Junction area are generally less than for Whitehorse. However, the two Whitehorse sites we consider in this study are located in relatively soft sediments for the region. An analysis of more sites is required to understand how widespread our inference of low near-surface V_S estimates is throughout the Whitehorse area.

For complex stratigraphy sites, in situations where there is an impedance contrast in the upper 30 m beneath a site, V_{S30} may underestimate the site hazard (Castellaro et al., 2008; Lee and Trifunac, 2010). Since we infer that both sites have an impedance contrast within the top 30 m, computing the time-average of the uppermost

10 m beneath a site (V_{S10}) may be more indicative of near-surface sediment rigidity (Fig. 6b). However, V_{S10} has no regulatory significance for the seismic hazard model. For site A, the most probable value of V_{S10} is ~210 m/s. Values range between 195 and 218 m/s. For site B, the most probable value of V_{S10} is ~222 m/s, and values range between 208 and 232 m/s. Site B has velocities about 10 m/s faster than site A for both V_{S10} and V_{S30}. However, both sites have similar values that are nearly within their respective uncertainties. For both sites, the V_{S30}values are about 65 m/s faster than the V_{S10} values (Fig. 6), which illustrates how the V_{S30} values could under-predict seismic amplification hazard. The natural state of sediment rigidity at site B may be disrupted by the construction of the baseball diamond. The V_S of sediments beneath roads and other infrastructure can increase due to the changes in substrate sediment during contsruction (Gosselin et al., 2018). Yet, this effect is typically limited to the shallowest part of the subsurface and may not be resolved from our data due to the frequency band limitations in our measurement.

Limitations of this work include the assumption that Rayleigh-waves dominate the seismic ambient noise field on vertical-component recordings. The Earth is modelled as laterally homogeneous isotropic layers over the spatial extent of the array, which may not be accurate in an area with variable geology. Further, this assumption may not hold where sediment properties have a gradational change with depth, as results for site A suggest may be a possibility for depths greater than 20 m. The bandwidth for both sites is limited by the aperture and spacing of the array, which will influence the ability to resolve V_S in both the shallowest and deepest parts of the model. The results are also limited by the chosen f-k beamforming processing parameters, which allow only phase velocities between 200 and 2000 m/s. Furthermore, the probabilistic inversion depends on the assumption of the data error distribution. For this preliminary work, we assume independent, symmetric errors. The errors in the dispersion curves are likely covariant (Dettmer et al., 2012) at all frequencies and are asymmetric in the linear velocity space. Consequently, model uncertainty may be underestimated here.

Future work will include revisiting the f-k beamforming processing with wider velocity bounds to better constrain high frequencies, as well as investigating the

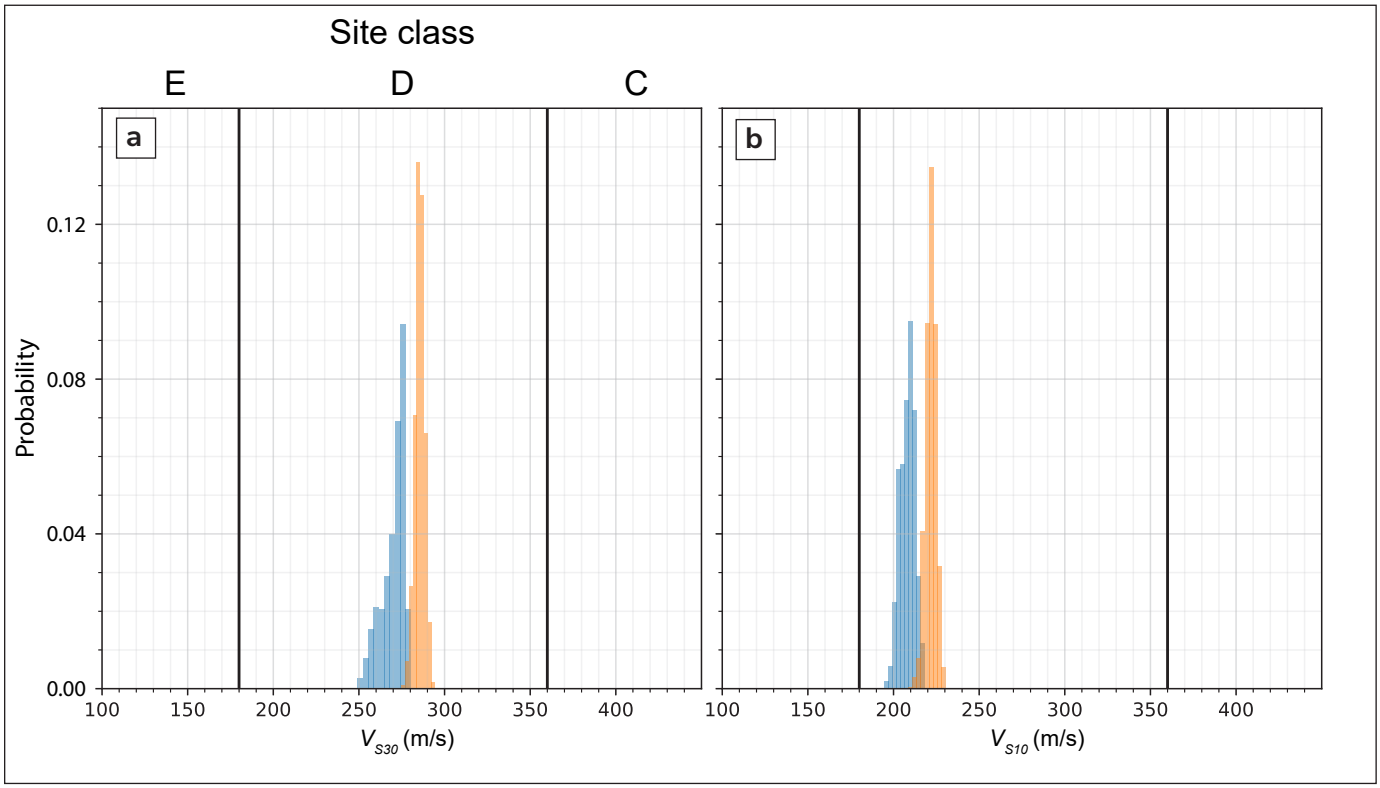


Figure 6. *Time-averaged velocity for* ***(a)*** *top 30 m (V_{S30}) and for* ***(b)*** *top 10 m (V_{S10}) for site A (blue) and site B (orange). Site classes are provided for V_{S30} where they are formally defined.*

under-prediction of phase velocities at low frequencies for site B. The under-prediction of low-frequency data implies that the data could require higher V_S values than allowed by the prior bounds, and so seismic resonances could be stronger than indicated by this initial model. We will also revisit the data error model, considering asymmetric and covariant data errors. Similar analysis will be performed for more sites throughout the Whitehorse area, incorporating additional data types (e.g., horizontal-to-vertical spectral ratios). Finally, we will extend the earthquake hazard analyses to consider site resonance, ground motion predictions and uncertainty quantification for all sites.

Although Whitehorse has no record of earthquakes in the immediate vicinity, it faces shaking hazards due to large earthquakes from the Aleutian subduction zone and moderate-sized earthquakes from closer, active faults. The larger and more distant earthquakes cause shaking at lower frequencies, while the moderate earthquakes cause shaking at higher frequencies. Characterizing shallow subsurface sediment conditions is important for understanding seismic wave amplification and resonance at local scales, and how the frequency content of various seismic sources may impact site-specific earthquake shaking. Furthermore, earthquake shaking can have implications for secondary hazards such as soil liquefaction or landslides. This work is important to understand the potential for landslide activation by shaking, particularly for the Whitehorse community. This preliminary research helps us better understand earthquake hazard for an understudied region, providing more information for the national hazard model, which has impacts for the community of Whitehorse, and other seismically active regions in Canada's North.

References

Anderson, J.G., Bodin, P., Brune, J.N., Prince, J., Singh, S.K., Quass, R. and Onate, M., 1986. Strong ground motion from the Michoacan, Mexico, earthquake. Science, vol. 233, no. 4768, p. 1043–1049.

Anderson, J.G., Lee, Y., Zeng, Y. and Day,S., 1996. Control of strong motion by the upper 30 meters. Bulletin of the Seismological Society of America, vol. 86, no. 6, p. 1749–1759, https://doi.org/10.1785/BSSA0860061749.

Bard, P.Y. and Bouchon, M., 1980. The two-dimensional resonance of sediment-filled valleys. Bulletin of the Seismological Society of America, vol. 75, no. 2, p. 519–541, https://doi.org/10.1785/BSSA0750020519.

Biegel, K.M., Gosselin, J.M., Dettmer, J., Colpron, M., Enkelmann, E. and Caine, J., 2024. Earthquake relocations delineate a discrete fault network and deformation corridor throughout southeast Alaska and southwest Yukon. Tectonics, vol. 43, no. 5, https://doi.org/10.1029/2023TC008140.

Blais-Stevens, A., Clague, J.J., Brahney, J., Lipovsky, P., Haeussler, P.J. and Menounos, B., 2020. Evidence for large Holocene earthquakes along the Denali fault in southwest Yukon, Canada. Environmental and Engineering Geoscience, vol. 26, no. 2, p. 149–166, https://doi.org/10.2113/EEG-2263.

Brideau, M.-A., Arenson, L.U., Porter, M., Mickey, A., Eshpeter, T. and Allen, T., 2024. The Whitehorse escarpment– preliminary landslide risk assessment. In: 77th Canadian Geotechnical Conference and the 16th Joint CGS/IAH-CNC Groundwater Conference, Montréal, QC, Canada.

Bruhn, R.L., Sauber, J., Cotton, M.M., Pavlis, T.L., Burgess, E., Ruppert, N. and Forster, R.R., 2012. Plate margin deformation and active tectonics along the northern edge of the Yakutat Terrane in the Saint Elias Orogen, Alaska, and Yukon, Canada. Geosphere, vol. 8, no. 6, p. 1384–1407, https://doi.org/10.1130/GES00807.1.

Castellaro, S., Mulargia, F. and Rossi, P.L., 2008. Vs30: Proxy for seismic amplification? Seismological research letters, vol. 79, no. 4, p. 540–543, https://doi.org/10.1785/gssrl.79.4.540.

Dettmer, J., Molnar, S., Steininger, G., Dosso, S.E. and Cassidy, J.F., 2012. Trans-dimensional inversion of microtremor array dispersion data with hierarchical autoregressive error models. Geophysical Journal International, vol. 188, no. 2, p. 719–734, https://doi.org/10.1111/j.1365-246X.2011.05302.x.

Doser, D. I., 2006. Relocations of earthquakes (1899–1917) in south-central Alaska. Pure and Applied Geophysics, vol. 163, no. 8, p. 1461–1476, https://doi.org/10.1007/s00024-006-0085-3.

Dutta, U., Yang, Z., Xu, G. and Haziribaba, K., 2008. Effect of seasonally frozen soil and permafrost on seismic site response. In: 14th World Conference on Earthquake Engineering, Beijing, China.

Eberhart-Phillips, D., Haeussler, P.J., Freymueller, J.T., Frankel, A.D., Rubin, C.M., Craw, P., Ratchkovski, N.A., Anderson, G., Carver, G.A., Crone, A.J., Dawson, T.E., Fletcher, H., Hansen, R., Harp, E.L., Harris, R.A., Hill, D.P., Hreinsdóttir, S., Jibson, R.W., Jones, L.M., Kayen, R., Keefer, D.K., Larsen, C.F., Moran, S.C., Personius, S.F., Plafker, G., Sherrod, B., Sieh, K., Sitar, N. and Wallace, W.K., 2003. The 2002 Denali fault earthquake, Alaska: A large magnitude, slip-partitioned event. Science, vol. 300, no. 5622, p. 1113–1118, https://doi.org/10.1126/science.1082703.

Finley, T., 2025. Neotectonics of major faults in the Canadian Cordillera. PhD thesis, University of Victoria, British Columbia, Canada, 151 p.

Finley, T., Nissen, E., Cassidy, J.F., Salomon, G., Leonard, L.J. and Froese, D., 2025. Large surface-rupturing earthquakes and a> 12 kyr, open interseismic interval on the Tintina fault, Yukon. Geophysical Research Letters, vol. 52, no. 14, https://doi.org/10.1029/2025GL116050.

Gardner, G., Gardner, L. and Gregory, A., 1974. Formation velocity and density—the diagnostic basics for stratigraphic traps. Geophysics, vol. 39, no. 6, p. 770–780, https://doi.org/10.1190/1.1440465.

Gosselin, J.M., Biegel, K.M., Dettmer, J., Gilbert, H., Colpron, M. and Enkelmann, E., 2024. Crustal stress near the Yakutat microplate collision from probabilistic earthquake focal mechanisms. Canadian Journal of Earth Sciences, vol. 62, no.4, p. 807–820, https://doi.org/10.1139/cjes-2024-0095.

Gosselin, J. M., Cassidy, J. F., Dosso, S. E. and Brillon, C., 2018. Probabilistic seismic-hazard site assessment in Kitimat, British Columbia, from Bayesian inversion of surface-wave dispersion. Canadian Geotechnical Journal, vol. 55, no. 7, p. 928–940, https://doi.org/10.1139/cgj-2017-0265.

Gosselin, J.M., Dettmer, J., Lipovsky, P. and Cronmiller, D., 2025. Seismic site amplification assessment in the Dakwäkäda (Haines Junction) area of Yukon, Canada, from probabilistic inference of passive seismic measurements. Canadian Geotechnical Journal, https://doi.org/10.1139/cgj-2025-0357.

Gosselin, J.M., Dosso, S.E., Askan, A., Wathelet, M., Savvaidis, A. and Cassidy, J.F., 2022. A review of inverse methods in seismic site characterization. Journal of Seismology, vol. 26, no. 4, p. 781–821.

Government of Yukon, 2022. Assessing climate change: Risk and resilience in the Yukon. Main Report, Government of Yukon, Whitehorse, 126 p, https://yukon.ca/sites/default/files/env/env-assessing-climate-change-risk-resilience-yukon-main-report.pdf.

Herrmann, R.B., 2013. Computer programs in seismology: An evolving tool for instruction and research. Seismological Research Letters, vol. 84, no. 6, p. 1081–1088, https://doi.org/10.1785/0220110096.

Hyndman, R., Cassidy, J., Adams, J, Rogers, G. and Mazzotti, S., 2005. Earthquakes and seismic hazard in the Yukon-Beaufort-Mackenzie. CSEG Recorder, vol. 30, no. 5, p. 32–67, https://www.seismescanada.rncan.gc.ca/hazard-alea/north-nord/Recorder_article.pdf.

Kellett, D., Ryan, J., Colpron, M., Zagorevski, A., Joyce, N., Zwingmann, H. and Kislitsyn, R., 2017. Report of activities, 2017, for Yukon tectonic evolution–late Mesozoic to Tertiary: GEM2 Cordillera project. Geological Survey of Canada Open File, vol. 8306, p. 14, https://publications.gc.ca/collections/collection_2018/rncan-nrcan/m183-2/M183-2-8306-eng.pdf.

Kolaj, M., Adams, J. and Halchuk, S., 2020. The 6th generation seismic hazard model of Canada. *In:* 17th World Conference on Earthquake Engineering, Sendai, Japan.

Lee, V.W. and Trifunac, M.D., 2010. Should average shear-wave velocity in the top 30 m of soil be used to describe seismic amplification? Soil Dynamics and Earthquake Engineering, vol. 30, no. 11, p. 1250–1258, https://doi.org/10.1016/j.soildyn.2010.05.007.

Lipovsky, P.S., 2023. Surficial geology and geohazards of the greater Whitehorse area. Yukon Geological Survey, Open File 2023-1, 67 p. plus appendices.

Luu, K., 2024. disba. https://pypi.org/project/disba/, [accessed 05/12/2025].

Molnar, S., Dosso, S.E. and Cassidy, J.F., 2010. Bayesian inversion of microtremor array dispersion data in southwestern British Columbia. Geophysical Journal International, vol. 183, no. 2, p. 923–940, https://doi.org/10.1111/j.1365-246X.2010.04761.x.

Nelson, J., Colpron, M. and Goodfellow, W., 2007. Tectonics and metallogeny of the British Columbia, Yukon and Alaskan Cordillera, 1.8 Ga to the present. In: Mineral Deposits of Canada: A Synthesis of Major Deposit Types, District Metallogeny, the Evolution of Geological Provinces, and Exploration Methods, Geological Association of Canada, Mineral Deposit Division, Special Publication 5, p. 755-791, https://cmscontent.nrs.gov.bc.ca/geoscience/publicationcatalogue/External/EXT060.pdf.

Plafker, G., 1970. Tectonics of the March 27, 1964, Alaska earthquake. US Government Printing Office, Washington, D.C., 74 p., https://doi.org/10.3133/pp543I.

Proulx, M., 2022. Road likely closed for days while city assesses risk after landslide, Whitehorse mayor says. CBC News, https://www.cbc.ca/news/canada/north/whitehorse-landslide-may-1-1.6437720, [accessed 05/12/2025].

Sun, H., Niu, F., Zhang, K. and Ge, X., 2017. Seismic behaviors of soil slope in permafrost regions using a large-scale shaking table. Landslides, vol. 14, no. 1, p. 1513–1520, https://doi.org/10.1007/s10346-017-0823-x.

van Drecht, L.H., Beranek, L.P., Colpron, M. and Wiest, A.C., 2022. Development of the Whitehorse trough as a strike-slip basin during early to middle Jurassic arc-continent collision in the Canadian Cordillera. Geosphere, vol. 18, no. 5, p. 1538–1562, https://doi.org/10.1130/GES02510.1.

Wathelet, M., Chatelain, J.-L., Cornou, C., Giulio, G.D., Guillier, B., Ohrnberger, M. and Savvaidis, A., 2020. Geopsy: A user-friendly open-source tool set for ambient vibration processing. Seismological Research Letters, vol. 91, no. 3, p. 1878–1889, https://doi.org/10.1785/0220190360.

Wathelet, M., Jongmans, D., Ohrnberger, M. and Bonnefoy-Claudet, S., 2008. Array performances for ambient vibrations on a shallow structure and consequences over VS inversion. Journal of Seismology, vol. 12, no. 1, p. 1–19.

White, D., Colpron, M., Buffett, G. and Lane, L., 2012. Seismic and geological constraints on the structure and hydrocarbon potential of the northern Whitehorse trough, Yukon, Canada. Bulletin of Canadian Petroleum Geology, vol. 60, no. 4, p. 239–255, doi:10.2113/gscpgbull.60.4.2.

Witter, J.B., 2025. Analysis of geoscience data for geothermal exploration in the Whitehorse area, Yukon. Yukon Geological Survey, Government of Yukon, Open File 2025-8, 53 p. plus appendices.

Xia, J., Miller, R.D. and Park, C.B., 1999. Estimation of near-surface shear-wave velocity by inversion of Rayleigh waves. Geophysics, vol. 64, no. 3, p. 691–700, https://doi.org/10.1190/1.1444578.

The December 6, 2025 M_w7.0 earthquake in Yukon, Canada: Tectonic significance and observations of ground failure

*Theron Finley**
Yukon Geological Survey

Jeremy M. Gosselin
Natural Resources Canada, Geological Survey of Canada–Pacific

Katherine M. Biegel
Earth and Planetary Sciences, University of California Davis

Panya S. Lipovsky and Derek C. Cronmiller
Yukon Geological Survey

Andrew J. Schaeffer
Natural Resources Canada, Geological Survey of Canada–Pacific

Jan Dettmer
Yukon Geological Survey

Finley, T., Gosselin, J.M., Biegel, K.M., Lipovsky, P.S., Cronmiller, D.C., Schaeffer, A.J. and Dettmer, J., 2026. The December 6, 2025 M_w7.0 earthquake in Yukon, Canada: Tectonic significance and observations of ground failure. *In*: Yukon Exploration and Geology 2025, A. Stuart, L.H. Weston and S.K. Schultz (eds.), Yukon Geological Survey, Government of Yukon, p. 131–148.

Abstract

The December 6, 2025 moment magnitude (M_w) 7.0 earthquake in southwestern Yukon was the largest onshore earthquake in Canada in over 75 years. It caused no casualties or damage to the built environment but offers insight into the complex active tectonics of the St. Elias orogen and hazards posed by major faults in the Yukon. It also caused widespread landslides and avalanche activity, providing an opportunity to study relationships between ground shaking and mass wasting. Here, we use double-difference relocation to refine the location of the mainshock and 3280 ensuing aftershocks. Based on satellite imagery and a reconnaissance flight to the epicentral area, we compile a preliminary inventory of over 200 landslides and other surface effects caused by the event. During the December 12, 2025 flight, no evidence of a surface rupture was observed. The areal extent of landslide occurrences was also considerably smaller than expected based on empirical data from past earthquakes, possibly due to the cold temperatures and presence of permafrost. The earthquake relocations and landslide distribution indicate that the main rupture and strongest shaking occurred beneath the Mt. King George massif. We infer that the rupture occurred on the southernmost section of the hypothesized Totschunda-Fairweather Connector fault. Slip initiated with strike-slip motion, rupturing northwestward, and may have activated a conjugate reverse fault toward the northwest segment of the rupture.

* theron.finley@yukon.ca

Plain language summary

On December 6, 2025 a major earthquake occurred in southwestern Yukon, near Mt. Logan (Canada's tallest peak) in the St. Elias Mountains. The earthquake had a magnitude of 7.0 and was the largest to have occurred beneath the Canadian landmass since 1946 (there have been larger earthquakes more recently, but these have been beneath the ocean). Thankfully, there were no deaths or injuries caused by the earthquake, and no damage to roads or buildings. Due to its shallow depth and location beneath mountainous terrain, the earthquake caused many landslides and avalanches. By studying this earthquake, we can learn more about ongoing tectonic activity in the St. Elias mountain range, which is complex and one of the most rapidly deforming regions on earth. We can also gain knowledge about the relationships between earthquakes and landslides. This information will help to better understand the risks that earthquakes and landslides pose to Yukon communities. In this paper we provide more accurate earthquake locations than were initially available following the earthquake. These give us a better idea of the location and orientation of the fault that broke in this earthquake. We also provide photos and observations of landslides from a helicopter flight we took to the site of the earthquake. Our more accurate earthquake locations, as well as the distribution of landslides, suggests that the earthquake mostly occurred beneath Mt. King George. It has long been theorized that a fault referred to as the Connector fault exists in this region, but it has been difficult to prove given the remoteness of the area and the heavily glaciated terrain. Our results provide strong evidence for the existence of the Connector fault.

Introduction

On December 6, 2025, a moment magnitude (M_w) 7.0 earthquake occurred in the remote icefields of southwest Yukon, beneath Mt. King George and the Hubbard Glacier in the St. Elias Mountains (Fig. 1). The earthquake occurred within Kluane National Park and the Traditional Territory of the Kluane First Nation. Though the area in the vicinity of the event is uninhabited, shaking was reported in many nearby Yukon communities, including throughout Whitehorse (Natural Resources Canada, 2025). This event was among the largest instrumentally recorded earthquakes in Canadian history, and the largest onshore/crustal event since 1946 (Cassidy et al., 2010). The rupture was shallow (<10 km) and consequently triggered extensive landslides and avalanches in the mountainous epicentral area, providing an excellent opportunity to study relationships between shaking and mass wasting. Moreover, the event is tectonically significant as it provides evidence of the hypothesized Fairweather-Totschunda Connector fault (CF) that serves as a structural link and mechanism for strain transfer within the St. Elias orogen, and which has been hypothesized for decades (e.g., Richter and Matson, 1971).

We provide an overview of the seismicity and ground failure associated with this event. We use double-difference relocation (Waldhauser and Ellsworth, 2000) to improve the relative precision of hypocentral locations of the mainshock and aftershocks. Analysis of the relocated events, combined with available moment tensor (MT) solutions, offer insights into the geometry and kinematics of the structures that hosted the recent earthquake sequence. Furthermore, we compile a preliminary landslide inventory based on satellite imagery and a reconnaissance flight to the area. Our results have implications for the understanding of neotectonics and natural hazards in the Yukon.

Background

Tectonic setting

The current tectonic setting of southwestern Yukon is primarily governed by the ongoing oblique collision of the Yakutat microplate (a thick and buoyant oceanic plateau), and its shallow subduction beneath North America (Fig. 1; Eberhart-Phillips et al., 2006; Christeson et al., 2010; Pavlis et al., 2019). Within this broader plate-boundary framework, deformation is especially concentrated in the St. Elias Mountains, where oblique convergence at the northeastern corner of the plate margin has driven rapid uplift and exhumation over the last 36 Ma (Finzel et al., 2011), producing one of the most rapidly deforming orogenic systems on Earth (Enkelmann et al., 2008). The active deformation is the cause for numerous major earthquakes observed in the region over the past 100+ years (Fig. 1). The Yakutat microplate remains mechanically coupled to the Pacific plate, which translates northward along the Queen Charlotte–Fairweather transform fault system

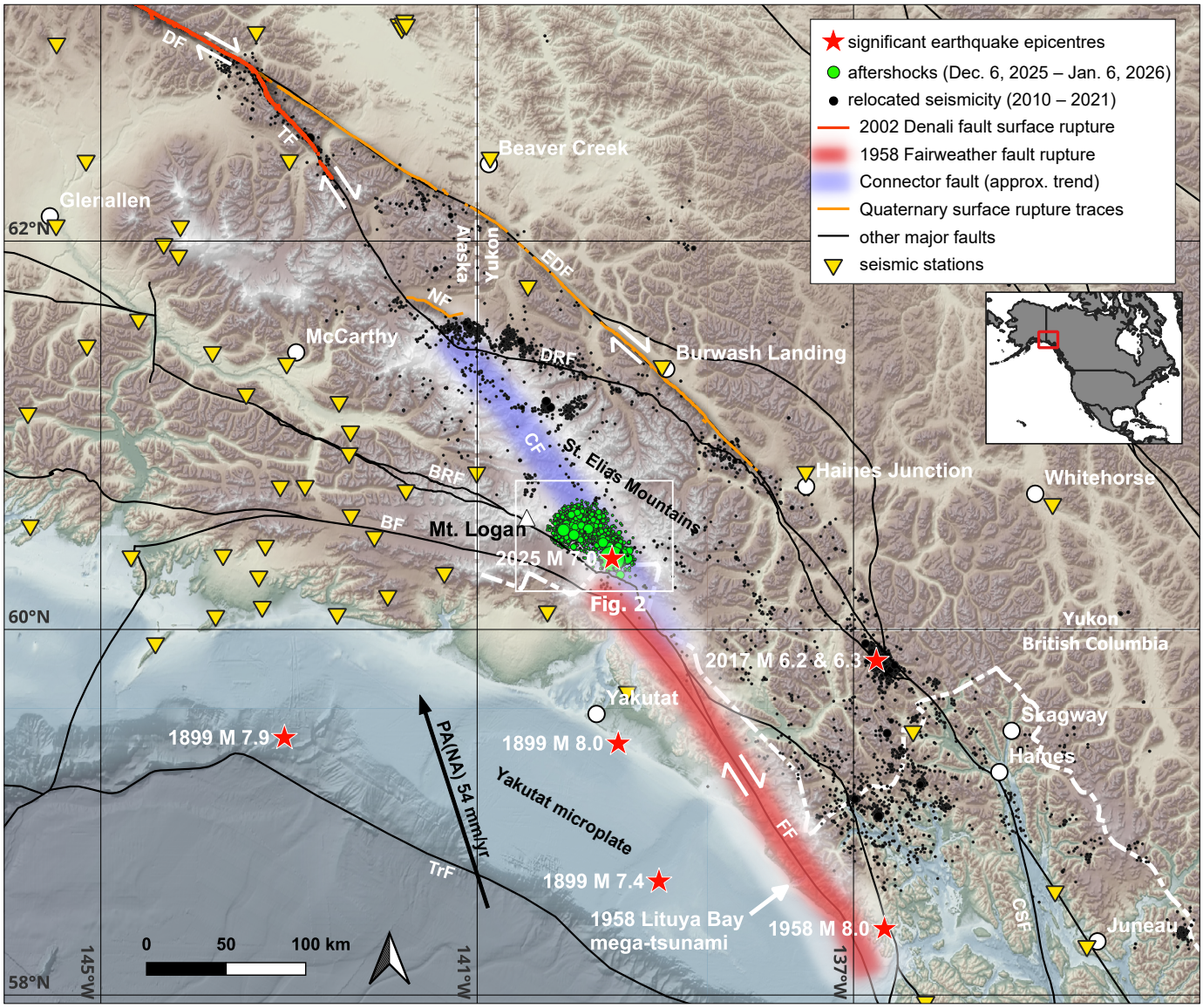


Figure 1. *Overview map of the regional tectonic setting of southwest Yukon and southeast Alaska including the December 6, 2025 mainshock and aftershock locations from the Natural Resources Canada (NRCan) earthquake catalogue. The approximate trace of the Connector fault (CF) is shown with the transparent blue polygon. Relocated background seismicity is from Biegel et al. (2024a). The 2002 M7.9 Denali fault (DF) rupture trace is from Haeussler (2009). The approximate 1958 M8 Fairweather fault (FF) rupture trace is from Doser (2010). The Eastern Denali fault (EDF) surface rupture traces are from Finley (2025). The Natazhat fault (NF) surface rupture trace is from Haeussler et al. (2024) based on Marechal et al. (2018). The locations of the 1899 earthquake sequence are from Doser (2006). Other major faults (black lines) are from the Yukon Geological Survey (2021): TF – Totschunda fault; DRF – Duke River fault; BRF – Border Ranges fault; BF – Bagley fault; TrF – Transition fault; CSF – Chatham Strait fault. Pacific Plate motion relative to North America (PA[NA]) is from the MORVEL model (DeMets et al., 2010).*

at the western margin of North America at a rate of >50 mm/yr. Further north, and to the west, the Pacific plate is subducting at the Alaska–Aleutian subduction zone. As a result, the tectonic regime of southwestern Yukon occupies a critical transition between transform motion, subduction, and continental collision, where the buoyant Yakutat crust exerts a strong control on upper-plate deformation (Plafker, 1987). Here, regional plate motion is partitioned between crustal shortening and a network of right-lateral strike-slip fault systems that accommodate lateral extrusion and strain transfer into the continental interior (Bruhn et al., 2012). It is within this remote, glaciated region of southwestern Yukon that the December 6, 2025 M_w7.0 earthquake occurred.

Earthquake-induced landslides in mountainous terrain

Earthquake-induced landslides are common in mountainous regions affected by shallow earthquakes, and represent a significant secondary hazard (Massey et al., 2018). When such events occur in populous regions, they have caused tens of thousands of deaths and significant economic losses beyond the direct effects of shaking (Keefer, 1984; Marano et al., 2010). Furthermore, in remote areas with limited transportation infrastructure, landslides can significantly impede emergency response to earthquakes if key roads are impacted (Bird and Bommer, 2004). Mapping landslide susceptibility can provide guidance on where the regions of highest hazard and risk are located (e.g., Behnia and Blais-Stevens, 2018). Additionally, earthquake-induced landslide prediction models can provide situational awareness to aid emergency response as well as generate estimates of landslide extent for hypothetical future earthquake scenarios (e.g., Nowicki Jessee et al., 2018). Such models are generally based upon empirical landslide inventories from past earthquakes. However, it is important to compile representative inventories for regions with specific climatic and geological conditions.

Many regions of the Yukon are susceptible to landslides (e.g., Brideau et al., 2026), particularly as slopes are becoming increasingly destabilized due to permafrost thaw (e.g., Clarke et al., 2024; Lipovsky and Huscroft, 2007). Moreover, many of Yukon's most active faults occur in mountainous terrain that could be susceptible to earthquake-induced landslides. For example, the Eastern Denali fault (EDF) occurs along the steep front range of the St. Elias Mountains (Fig. 1), posing a potential earthquake-induced landslide hazard to communities and infrastructure along the Alaska Highway corridor (Blais-Stevens et al., 2020; Finley, 2025). Potential earthquake-induced landslides related to prehistoric ruptures have been identified along the EDF (Everard, 1994; Whelan, 2022). More generally, landslides are known to threaten some of Yukon's communities (Brideau et al., 2007; Bodtker et al., 2023; Lipovsky, 2023) and though these are not necessarily linked to seismicity, it is important to understand how shaking might exacerbate the existing hazard. The December 6 event offers an opportunity to study seismically induced landslides in the Yukon.

Observations and interpretations

Seismic observations

The M_w7.0 mainshock occurred on December 6, 2025 at 20:41 UTC (13:41 Yukon Standard Time) at 60.37° N and 139.54° W, with a hypocentre location ~10 km east-northeast of Mt. Vancouver in the St. Elias Mountains (Fig. 1, Fig. 2). In this work, we consider 354 analyst-reviewed events drawn from the Natural Resources Canada (NRCan) National Earthquake Database (NEDB; Canadian Hazards Information Service, 1985), augmented by an additional 4193 automatic (i.e., not analyst reviewed) NRCan solutions within our study area between the occurrence of the mainshock on December 6, 2025 and the aftershocks of January 6, 2026 (Fig. 1).

To study the aftershock distribution, we use the double-difference (DD) relocation method (Waldhauser and Ellsworth, 2000), which improves relative precision for earthquake hypocentres. An advantage of the DD approach is that errors introduced by complex or unmodeled velocity structures along the propagation path from the earthquake source region to the recording station are reduced when proximal events are jointly relocated. The increased precision of relative hypocentre location can significantly improve event depths in otherwise sparsely instrumented settings (e.g., Biegel et al., 2024b) and can enable the identification and geometric characterization of discrete fault planes (e.g., Rubin et al., 1999; Biegel et al., 2024a). In the relocation, we use traditional arrival times for P and S-wave phases obtained from the NRCan solutions. These are supplemented with differential travel times based on waveform cross-correlations between event pairs. These data are jointly inverted using the SeisComP Real-Time Double-Difference (scrtdd) implementation of the DD algorithm (Scarabello et al., 2025; Helmholtz Centre Potsdam

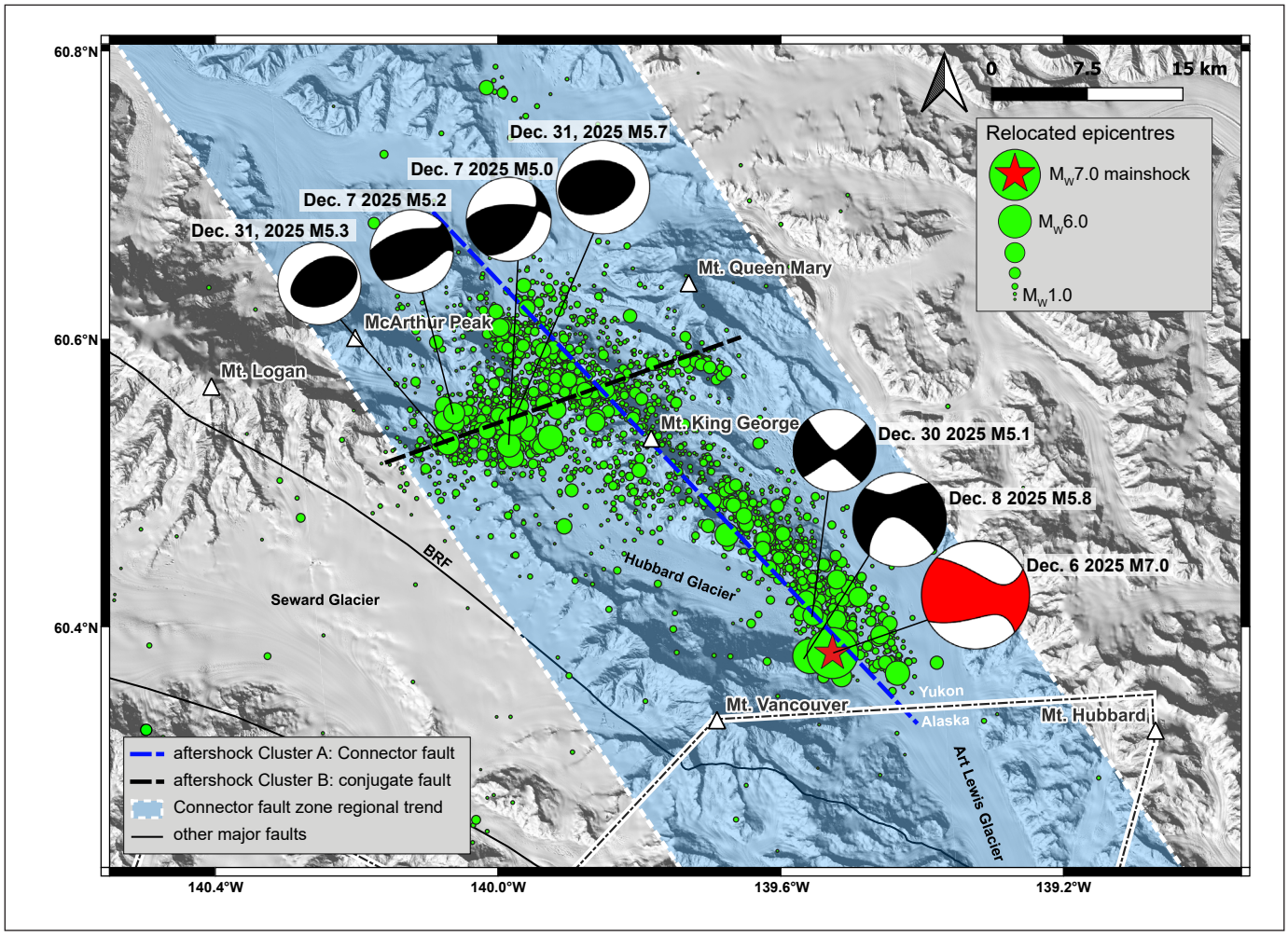


Figure 2. *Close-up view of the relocated aftershock sequence and inferred fault traces. The moment tensor (MT) solutions are shown for >M5 aftershocks where available (US Geological Survey, 2025a). See Figure 4 for 3D views of aftershocks. BRF – Border Ranges fault. Base map hillshade is from ArcticDEM version 4.1 (Porter et al., 2023).*

GFZ German Research Centre for Geosciences and gempa GmbH, 2008). For travel time predictions, we use the 1D seismic velocity model IASP91 (Kennett and Engdahl, 1991). Relocation algorithm parameters are mostly the same as in Schaeffer et al. (this volume). The only differences are an increased maximum number of neighbouring events per chain of 120, and reduced P and S-waveform cross correlation window lengths of ± 0.5s and ± 0.75s, respectively.

After relocation and application of quality control, 3280 aftershock locations are successfully updated (Fig. 2). The aftershocks mostly occurred to the northwest of the mainshock hypocentre and extended in this direction for ~50 km. Based on this observation, the mainshock rupture propagated toward the northwest and likely arrested in an area ~5 km east of McArthur Peak. To the northwest of Mt. King George, the distribution of epicentres is spread out laterally from this linear feature. An additional linear feature is apparent from the distribution of relocated aftershocks, particularly for events at the northwest end of the aftershock sequence. Overall, relocated event depths are predominantly shallower than 10 km, and the peak in the distribution of event depths occurs at ~4 km, supporting the shallow nature of the mainshock. The depth distribution is consistent with previous estimates of the crustal seismogenic layer thickness of <15 km in this area (Biegel et al., 2024b).

We carried out cluster analysis (e.g., Biegel et al. 2024a) of the relocated hypocentres. Clusters are first identified using the 'density-based spatial clustering of applications with noise' algorithm (DBSCAN; Ester et

al., 1996), in which the maximum distance to consider neighbours was set at 1.8 km, and the minimum number of neighbours to identify a cluster was set at 30. The DBSCAN algorithm identifies four potential clusters. Upon inspection, three of these clusters align along a single northwest–southeast structure and are reclassified as a single cluster. Because the remaining two clusters overlap, one fault planes is fit to each cluster using a least squares regression. Based on seismogenic layer thickness and distribution of relocated event depths, the maximum depth for the fault planes was chosen as 15 km. Subsequently, events are reclustered by proximity to one of these planes, and 10% of outlier events are excluded from the clustering based on the distance from the planes. Finally, we recalculate the least squares fits based on these re-sorted clusters which we name Cluster A and Cluster B (Fig. 3).

Using this clustering analysis, we identified two event clusters: Cluster A includes 1480 aftershocks, and Cluster B, 1155 aftershocks (Fig. 3). The remaining 270 aftershocks were unassigned. Cluster A has a dominant northwest–southeast-striking zone aligned with the inferred trace of the CF, and hosted the mainshock near its southern termination. The plane for Cluster A has a length of 60 km, a width of 15 km, and strike of 136°; the dip is 78° to the southwest. We interpret that this plane represents part of the CF. We note that a significant part of the fault plane solution for Cluster A is located beneath the Mt. King George massif. The fault for Cluster B is smaller in size and oriented at a conjugate strike of 250° with a dip of 86° to the north-northeast. The projected surface trace of the fault plane solution for both clusters is shown in Figure 2. We hypothesize that the mainshock may have included a complex rupture on multiple faults highlighted by the two clusters, but that the rupture initiated on the CF, and then triggered a rupture on a conjugate fault. The misfit from plane fitting for Cluster A is excellent, having an R2 value for the least squares planar fit of 0.95. However, misfit for Cluster B is lower (R2 = 0.39), and it is possible that multiple faults contribute to the poor least squares fit of Cluster B.

We further consider the spatial distribution of the largest aftershocks in the context of available MT solutions (Fig. 2). The MT solutions for the largest aftershocks along this feature exhibit dextral strike-slip mechanisms (Fig. 2). In contrast, the subsidiary conjugate lineament in the northwestern part of the aftershock cloud trends west-southwest to east-northeast and is associated with the largest aftershocks

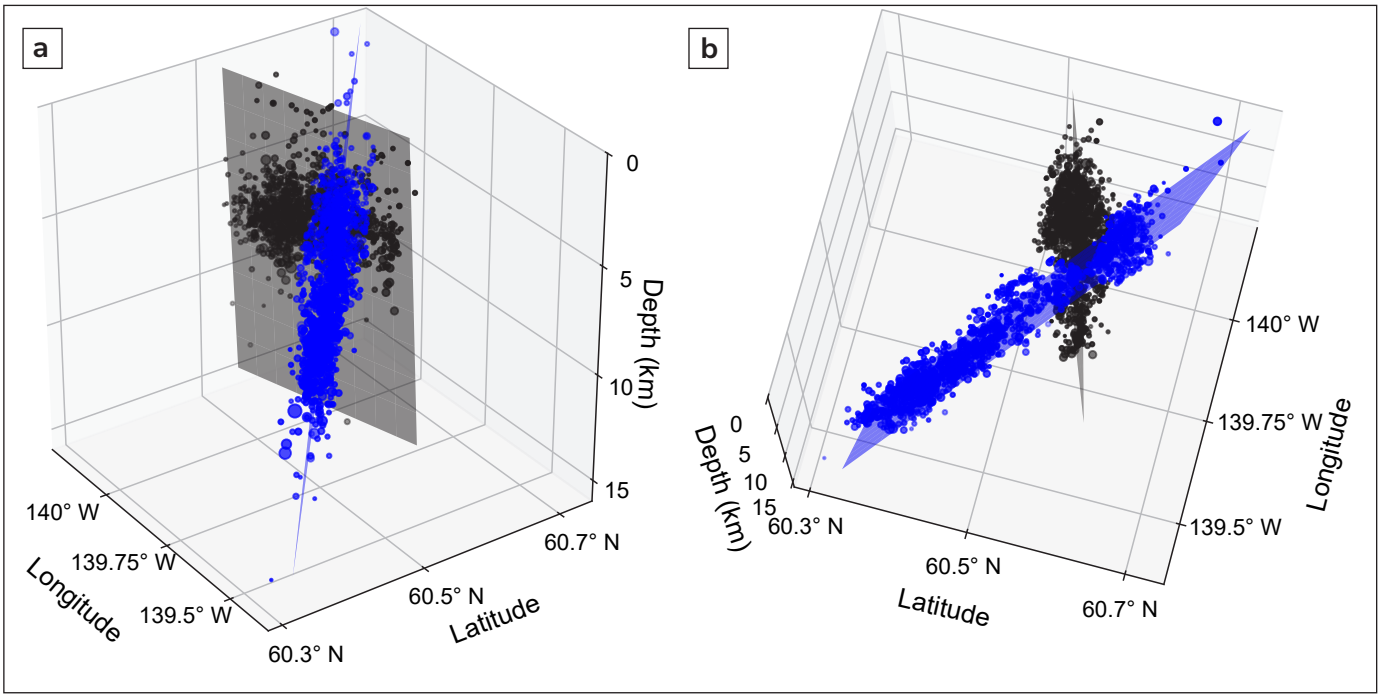


Figure 3. *Relocated aftershocks and inferred fault planes based on cluster analysis. Cluster A (blue) and Cluster B (black) are shown. Panel* ***(a)*** *view is oblique toward the northwest along strike of Cluster A fault plane. Panel* ***(b)*** *view is from overhead.*

exhibiting predominantly reverse mechanisms. Despite this variability in faulting style, available faulting mechanisms across the sequence share broadly similar P-axis orientations, consistent with a common regional stress field imposed by oblique convergence of the Yakutat microplate with North America (Gosselin et al., 2024). This pattern suggests rupture propagation and subsequent stress redistribution within a transpressional fault network, where strike-slip motion along the primary structure (CF) is locally accommodated or transferred onto conjugate, more contractional structures. The coexistence of strike-slip and reverse mechanisms, coupled with the segmented aftershock geometry, supports a model in which the December 6 earthquake activated multiple fault strands with differing orientations and kinematics within a shared regional stress regime. This hypothesis is further supported by the complexity of the MT solution of the mainshock, which exhibits oblique kinematics and suggests strain partitioning during a mechanically complex rupture process rather than slip on a single, planar fault. Furthermore, mainshock and some aftershock MT solutions show significant non-double-couple components, providing evidence that slip did not occur on a single, planar fault.

There does not appear to be a spatiotemporal pattern to the aftershock sequence between December 6 and December 31, 2025. However, a M_w5.7 aftershock on December 31 marked a resurgence in aftershock activity that is inconsistent with typical Omori-Utsu decay (Utsu et al., 1995). This event and the associated resurgence were located along the inferred conjugate fault planes with a reverse mechanism.

It is likely that the aftershock catalogue includes not only earthquakes but also landslides and cryospheric sources of seismic energy. To separate the various source types in the catalogue will require careful waveform examination that is currently ongoing. The superposition of multiple coincident seismic events complicates the analysis of seismic waveforms and can lead to a temporary increase in the magnitude of completeness of the earthquake catalogue. During our study period between December 6, 2025, and January 6, 2026, we note that there are two events of >M_w5 for which an MT solution is not reported. These events both occurred shortly after the mainshock on January 6, during a period of intense seismic activity that likely inhibited reliable MT estimation. The superposition of multiple seismic events may also preclude the conclusive assignment of source types in future analysis.

Surface effects and mass movement observations

Within minutes of the event on December 6, the US Geological Survey released an automated landslide probability map (Nowicki Jessee et al., 2018; Allstadt et al., 2022) that illustrated the elevated potential for landslides across a >2000 km^2 area with the highest probabilities on the slopes of Mt. Logan and Mt. Vancouver (US Geological Survey, 2025b). On December 9, Sentinel-1 radar change detection revealed numerous large slope failures (Eiden et al., 2025), though it was not immediately clear whether these were dominantly rock, ice or snow. With clearer weather, Landsat 8 and 9 images on December 10, 11 and 12 further confirmed the occurrence of numerous landslides. On December 12, the Yukon Geological Survey flew to the epicentral area to document the landslides and other surface effects before they could be obscured by further snowfall and glacial deformation. Our observations form the basis of a landslide inventory for this event.

Field observations on December 12, 2025 confirmed the occurrence of extensive landslides, snow and ice avalanches, and widespread damage to glaciers. Using satellite imagery (Landsat), our field observations, and nearly 2000 oblique aerial photographs taken from the helicopter, we map over 200 individual landslide initiation points and a subset of the largest runouts (Fig. 4). We distinguished landslides from snow and ice avalanches based on the texture and colour of the debris deposits, as well as the presence of a clear source-area scar in bedrock. Landslide activity was mainly concentrated on the Mt. King George massif (Fig. 4), where rock-ice avalanches and rockfall were the most common failure types. Bare rock was exposed on the majority of slopes of Mt. King George in contrast to surrounding peaks, which had largely retained their snow cover (Fig. 5).

The largest observed landslide was a rock and ice avalanche produced by a partial collapse of the southwest ridge of Mt. King George (Fig. 5a). The basal failure surface occurred along a southwest-dipping planar discontinuity oriented subparallel with the pre-existing slope angle (~35–40°) of the south flank of the ridge. The Mt. King George massif is underlain by Cambrian to Ordovician volcanic and sedimentary rocks which exhibit a northwest-striking foliation and dip between 30 and 60° to the northeast (Dodds and Campbell, 1992). The southwest flank of the massif is intruded by Jurassic to Cretaceous granite of the St. Elias plutonic suite. Notably the failure surface of

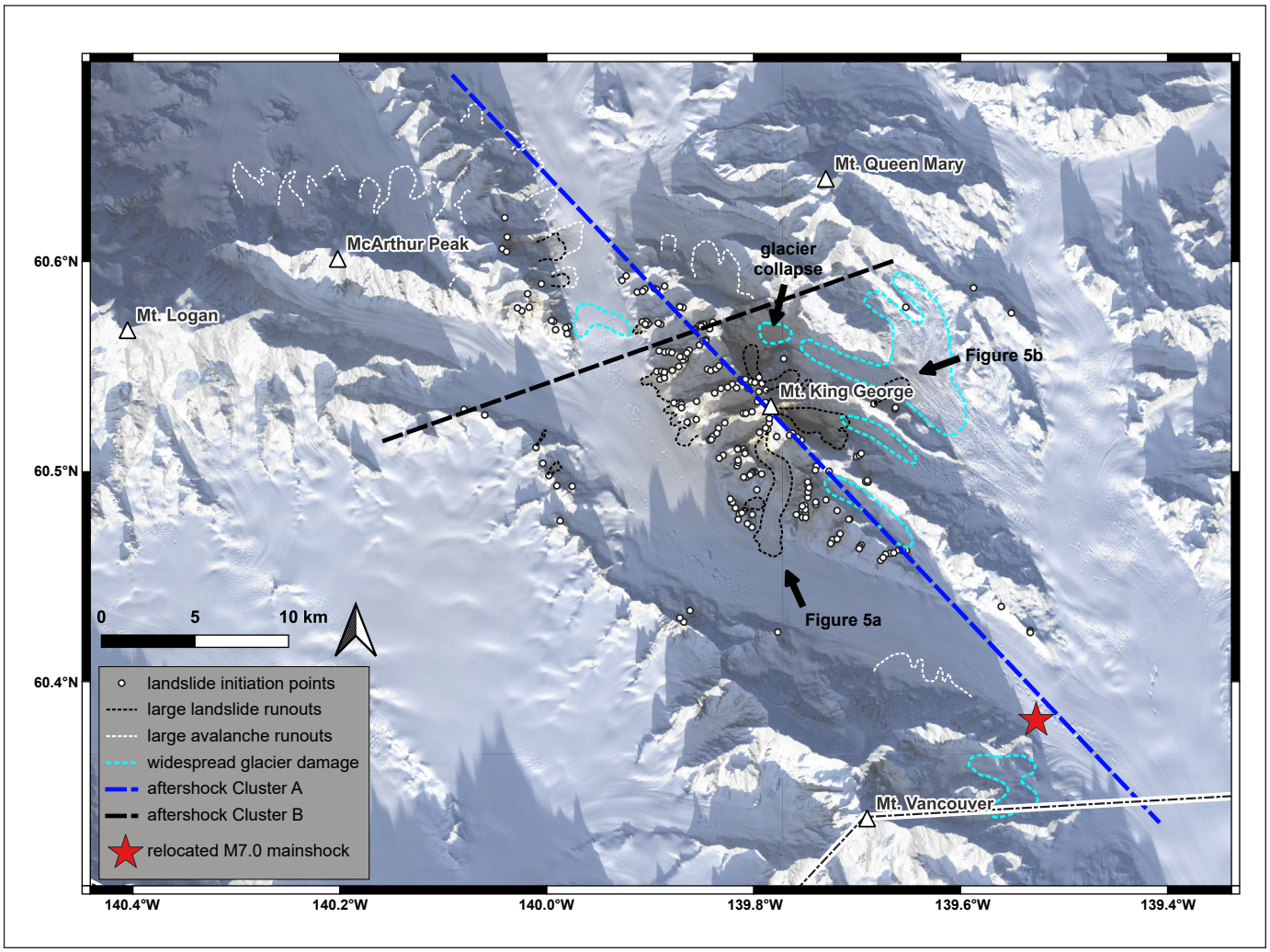


Figure 4. *Landslides and avalanches observed in the epicentral area during the December 12 reconnaissance flight. Landslides are concentrated around Mt. King George, whereas avalanches and areas of damaged glacial ice are more widespread. Base imagery is from a Landsat 8 pass on December 11, 2025.*

this slide is at a high angle to the local geological strike and dip, which was also apparent from the helicopter. The crown of the slide originated at approximately 3000 m above sea level and descended roughly 1300 m along a tributary glacier before coming to rest on the Hubbard Glacier, approximately 7.4 km from the source area (Fig. 5a). This corresponds to an overall travel angle of approximately 10°. Such high mobility is typical of rock avalanches on glaciers (Evans and Clague, 1988), where movement is enhanced by the low-friction surface of the glacier, entrainment of snow and ice, and by water inputs generated through frictional melting (Sosio et al., 2012). Several other rock and ice avalanches with similar mobility characteristics, but smaller overall dimensions, occurred in other tributary valleys on the southwest side of Mt. King George (Fig. 4).

On the northeast side of Mt. King George, several large rock falls and rock avalanches initiated on steep slopes (50–70°), falling at least 1700 m to the glacier below (Fig. 5b). Persistent rockfall and additional rock avalanches continued from existing slide scars for several days after the main earthquake, likely due to a combination of aftershocks and progressive failure of slopes that were damaged by the earthquake or destabilized by earlier failures. At least one entirely new rock avalanche occurred between December 11 and 12 as it only appeared on December 12 Landsat imagery and was apparent during our site visit (Fig. 5b). At the time of the overview flight, large dust clouds lingered in the air, obscuring our view of debris deposits on the glacier below (Fig. 5b). The large, active slide scar on the east face of the Mt. King George summit appeared to have water flowing down its centre,

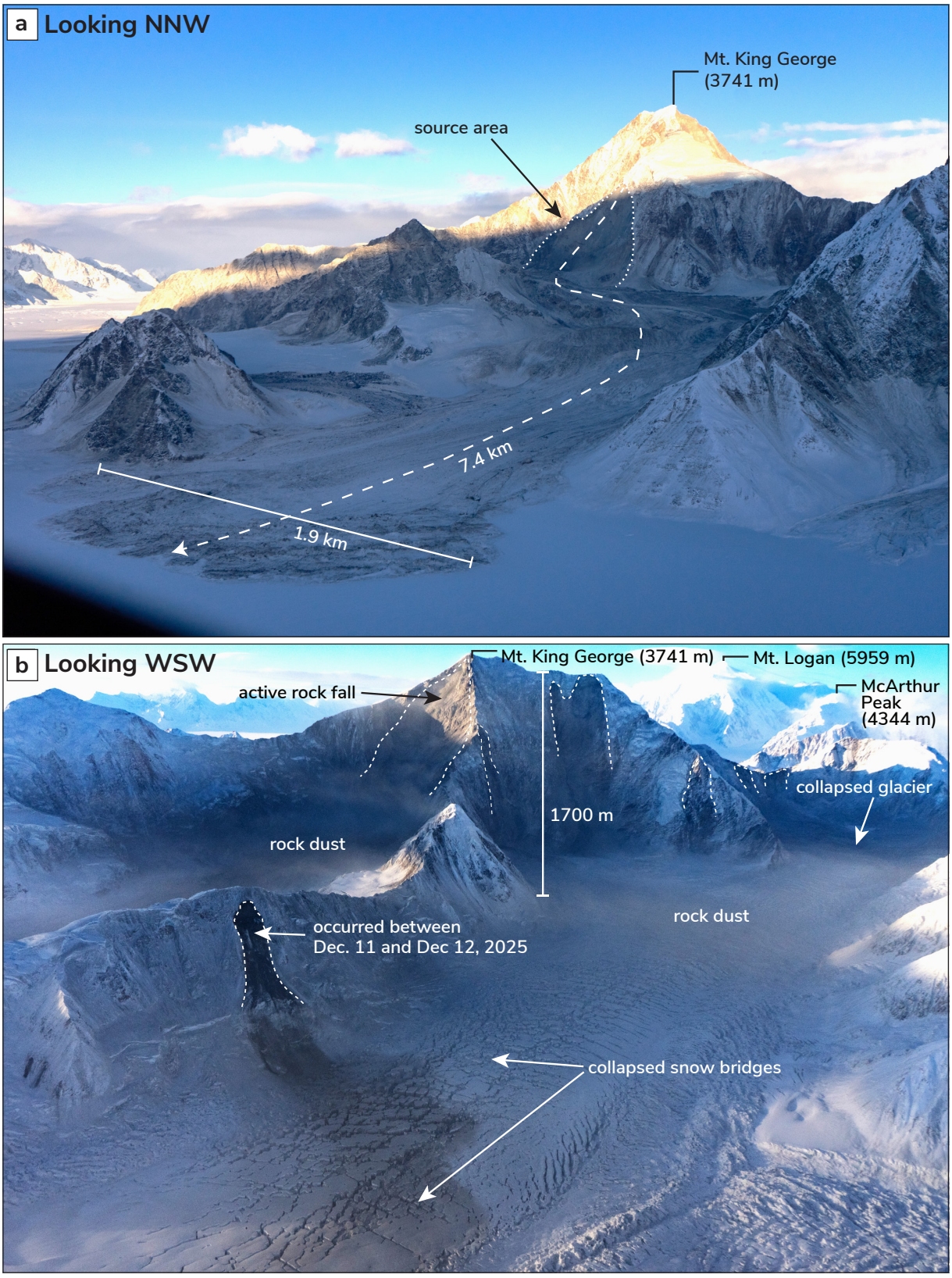


Figure 5. *Photos from December 12 reconnaissance flight over epicentral area:* ***(a)*** *largest landslide on west side of Mt. King George looking north-northwest (NNW); and* ***(b)*** *east side of Mt. King George looking west-southwest (WSW). White dashed lines indicate landslide source areas. See Figure 4 for photo locations.*

suggesting either discontinuous permafrost within the massif, or significant heating associated with slope failure. Beyond the Mt. King George massif, landslides were relatively limited. Two large landslides occurred on the east side of McArthur Peak, and several small point-source slides occurred on the arête between Mt. Vancouver and Mt. Logan (Fig. 4).

Snow avalanches were triggered in a much more extensive region than landslides (Fig. 4). Some of the largest snow avalanches occurred on the north and east aspects of Mt. King George and McArthur Peak (a sub-peak of Mt. Logan) and produced plumes that in some cases extended 2–3 km across the glacier at the base of the slopes from which they fell, covering hundreds of hectares each (Fig. 4). Based on their runout length and plume area, some of these avalanches are likely size 5, the largest and most destructive on the Canadian snow avalanche classification scale (Stethem et al., 2003). The apparent preference for aspect and the concentration of large avalanches at the northwest tip of the rupture could be related to directivity effects of strike-slip fault motion (e.g., Velasco et al., 2004), or simply local snowpack conditions at the time of the earthquake.

Damage to glaciers was also extensive; seracs (blocks and columns of ice between crevasses) were broken up and toppled by shaking, and in several locations, snow bridges over crevasses had collapsed (Fig. 5b). Particularly large areas of ice damage occurred on the east sides of Mt. King George and Mt. Vancouver (Fig. 4). There were also widespread failures of cornices and ice accumulations on ridgelines. Additionally, fresh cracking was observed at numerous ice-rock contacts at the margins of glaciers, possibly reflecting settling or dislodging of ice during shaking.

Despite the shallow rupture indicated by mainshock and aftershock relocations, we observed no clear evidence of fault surface rupture. However, it is possible that a surface rupture was hidden by thick glacial ice; adjacent glaciers in the St. Elias Mountains have been estimated to have thicknesses of >900 m based on airborne ice penetrating radar (Christine Dow, pers. comm.). Moreover, because the rupture appears to be directly beneath Mt. King George, a clear surface rupture could be obscured by the rugged topography and subsequent widespread slope failures. The apparent structural immaturity of the fault zone may also play a role in reducing its surface expression (e.g., Sethanant et al., 2023). Notably, a partial collapse of a low-angle glacier surface occurred between Mt. King George and Mt. Queen Mary (Fig. 4), an area adjacent to many of the most intense aftershocks at the intersection of the two linear clusters. It is conceivable that this collapse is related to a fault surface rupture beneath the glacier. However, this area of the glacier is covered by debris from a rock avalanche off the northeast face of Mt. King George, which could have also contributed to its collapse.

Discussion

Implications for the Connector fault, regional tectonics, and seismic hazard

The occurrence of the December 6 earthquake offers insight into the geometry and kinematics of the long-hypothesized CF that links the Fairweather and Totschunda fault systems and enables transfer of strike-slip motion. The concept attempts to reconcile plate-boundary kinematics across southeast Alaska and southwestern Yukon (Grantz, 1966; Richter and Matson, 1971; Lahr and Plafker, 1980). These early models provide a tectonically coherent explanation for how relative motion between the Pacific, North America, and Yakutat plates could be partitioned. This early work evolved into later plate-boundary reconstructions that emphasized distributed deformation (e.g., Marechal et al., 2015). However, subsequent regional syntheses continued to invoke a Fairweather–Totschunda linkage to explain long-term strain transfer and seismic moment balance in the region (e.g., Fletcher and Freymueller, 2003). Subsequent earthquake relocations by Doser (2014) delineated a possible trace of the CF. With improvements to the seismic network (Meighan et al., 2013; Busby and Aderhold, 2020), Biegel et al. (2024a) were able to relocate a larger catalogue of earthquakes (Fig. 1) and proposed a fault trace slightly west of that proposed by Doser (2014).

Geodetic observations provide independent support for the existence of the CF (e.g., Elliot et al., 2010; Elliott and Freymueller, 2020). In these tectonic block models, the proposed CF coincides with a zone of elevated shear strain and serves as a kinematic boundary between blocks rotating at different rates. Although the fault cannot be resolved as a single sharp velocity gradient from these data, its location is broadly consistent with subtle geomorphic lineaments that suggest long-term structural control. Similar geomorphic expressions characterize other intracontinental strike-slip transfer zones in Alaska and western North America, where cumulative slip is modest or partitioned across multiple strands, limiting the development of a clear surface

trace (e.g., Bemis et al., 2015; Koehler et al., 2012). Identification of a geomorphic expression along the CF is further complicated by its location in a remote, heavily glaciated region, where repeated glacial erosion and sediment redistribution can obscure or entirely remove surface fault scarps and offset landforms (Haeussler et al., 2008; Haeussler et al., 2017). The 2023 US National Seismic Hazard Model includes a discrete fault source representing the CF with a 13 mm/yr slip rate (Haeussler et al., 2024). Their fault trace is largely based on that of Doser (2014) and follows the trends of major valley glaciers as well as seismicity; however, they acknowledge there is uncertainty on its absolute location.

The December 6 M_w7.0 earthquake provides the clearest observational evidence to date for the existence, geometry, and kinematics of the long-postulated CF. Relocated aftershocks define a dominant northwest–southeast-trending structure consistent with the inferred regional trend of the CF (Fig. 2), with the mainshock initiating near its southern end and rupture propagating northward. Available MT solutions (US Geological Survey, 2025a) along the CF indicate predominantly strike-slip motion near the mainshock, transitioning to thrust-dominated mechanisms further northward, along conjugate structures. The activation of a subsidiary, east–west-oriented aftershock lineament suggests strain partitioning within this intracontinental transfer zone and highlights the likelihood of stress redistribution to adjacent faults. This concept is being evaluated through ongoing Coulomb stress modelling.

Importantly, this earthquake occurred on a structure lacking a previously mapped surface trace and within a local area of comparatively sparse historical seismicity, underscoring both the cryptic nature of the CF and its capacity to host large earthquakes. While Biegel et al. (2024a) documented a northern segment of the CF south of the Totschunda fault terminus based on relocated background seismicity (Fig. 1), the December 6 event demonstrates that this structure is through-going. Most previous studies (e.g., Doser, 2014; Haeussler et al., 2024) have inferred that the trace of the CF in this area occurs beneath, and is obscured by, the major valley glaciers (Hubbard and others). However, our earthquake relocations suggest that this segment of the fault is situated beneath the Mt. King George massif, and the landslide distribution further corroborates this location. The lack of a pre-existing surface expression could reflect the fact that erosion rates in this mountainous region are high, and preservation potential is limited. Moreover, it has been suggested that the CF is an incipient fault that is taking up strain that was previously accommodated by the Eastern Denali fault (Richter and Matson, 1971; Choi et al., 2021). The lack of clear topographic expression could therefore also reflect the structural immaturity of this developing fault zone.

Although the region in the immediate vicinity of the earthquake is uninhabited, this event presents several seismic hazard considerations. The southern tip of the rupture is 20–30 km from the approximate northern termination of the 1958 Fairweather fault ~M8.0 rupture (Doser, 2010). There is likely a large degree of spatial uncertainty on the northern part of the 1958 rupture. Doser (2010) places it on the main strand of the Fairweather fault (as depicted in Fig. 1), though it could conceivably have branched onto an eastern splay of the Fairweather fault mapped beneath the Art Lewis glacier (US Geological Survey, 2026), which is more directly aligned with the 2025 rupture (Fig. 2). Nevertheless, there appears to be a gap between the 1958 and 2025 ruptures that could have a lingering slip deficit, and Coulomb stress changes following the recent earthquake could promote future failure. Earthquake scaling relations indicate a 30 km fault length could cause an ~M6.8 earthquake, assuming a crustal seismogenic thickness of 15 km (Wells and Coppersmith, 1994). This section of fault passes near the heads of several glaciated fjords (Disenchantment Bay and Nunatak Fjord) where there is the potential for landslide generated tsunamis not unlike the 1958 Lituya Bay megatsunami (Fig. 1; Miller, 1960), or the recent Tracy Arm landslide southeast of Juneau (Read et al., 2025). To the north, there is an ~225 km section of fault between the 2025 rupture and the southern termination of the 2002 Denali earthquake on the Totschunda fault (Fig. 1). Geomorphic mapping by Marechal et al. (2018) provided evidence of rupture within the Quaternary on this section. If the entire section were to rupture at once, it could cause an ~M7.7 earthquake (Wells and Coppersmith, 1994); however, given the apparent structural immaturity, it is unclear whether it would do so in a single event, or in smaller sections.

Due to the remote location of the earthquake, no damage was reported (Natural Resources Canada, 2025). Ground shaking from the mainshock and several aftershocks was reported in the communities of Haines Junction, Burwash Landing and Whitehorse. However, the earthquake serves as a reminder of the seismic hazard in southwest Yukon, and the need to assess local variability of earthquake shaking intensity and duration due to site-specific geologic conditions (e.g., Gosselin et al., 2025; Byer et al., this volume).

This earthquake also offers an opportunity for ongoing research that compares ground-motion predictions to felt reports (specifically in the Yukon), which can improve estimates of shaking during more-damaging events that may occur in the future.

Relationships between mass movement and fault rupture

Based on our aftershock relocations, the Mt. King George massif directly overlies the fault rupture, and the landslide distribution is therefore reflective of the region where shaking was the strongest. Empirical relationships between earthquake magnitude and landslide distribution (Keefer, 1984; Rodriguez et al., 1999; Keefer, 2002) suggest that for a M7 earthquake, landslide activity is expected over an area between 1000 and 10 000 km^2. Our field observations indicate that the landslide distribution for this event was on the low end: the core area of landslides occurred over approximately 200 km^2 on the Mt. King George massif, and the most distal landslides occurred within an area of 500 km^2. The empirical data from past earthquakes further indicates that for M7 earthquakes, the expected maximum distance between the epicentre and rock falls and rock avalanches is between 100 and 200 km. Our field observations again place this event well below that, with a maximum distance of 35 km between the epicentre east of Mt. Vancouver, and the rock falls observed on the east side of McArthur peak. Measuring from the fault rupture plane defined by the aftershocks, maximum distances of 75 to 150 km are expected; however, in the case of this earthquake, maximum distances were around 11 km between the rupture plane and small landslides observed on the arête between Mt. Vancouver and Mt. Logan (Fig. 4). When compared to maps of shaking intensity, rock falls and rock avalanches typically require shaking of at least 4 on the Modified Mercalli Index (MMI), and the majority occur in zones of MMI 5 or greater. On the initial isoseismal maps generated by the US Geological Survey (2025b), MMI values of 5 occurred over an area >15 000 km^2, whereas the majority of landslides in this event occurred within the much smaller zone of MMI 7 or greater. It is worth noting however, that the sparse instrumentation in the epicentral region provides poor constraint on shaking intensity. The anomalously small area with seismically induced landslides may be due to the shallow depth of the rupture. Keefer (1984) observed that earthquakes with greater focal depths allow for sufficient shaking to trigger landslides over broader areas. We also speculate that local geological and climatic conditions (i.e., extreme cold and permafrost) may play a role in limiting the extent of landslides in this particular case study.

The US Geological Survey ground failure product estimates earthquake-induced landslide probability in near real-time based on estimated peak ground velocity (PGV) for the earthquake. It also considers global datasets of slope, lithology, land cover, climate, and soil wetness (Nowicki Jessee et al., 2018; Allstadt et al., 2022). Such a model could be applied proactively to earthquake hazard and risk scenarios for Yukon faults and the surrounding affected communities. Additionally, it could serve as a critical part of emergency response in future earthquakes. Nowicki Jessee et al. (2018) call for the collection of new comprehensive landslide inventories to improve the accuracy of these models, as well as inform region-specific models that take into consideration local variations in climate and geology. It is a goal of the Yukon Geological Survey to finalize the landslide inventory for this event to improve our understanding of potential hazard cascades faced by Yukon communities.

Conclusion

The December 6, 2025 M_w7.0 earthquake in southwestern Yukon was the largest continental earthquake in Canada in several decades and provides a rare opportunity to examine active tectonic processes in a remote, glaciated region. This earthquake sequence provides the most conclusive evidence to date for the existence and activity of the long-hypothesized Connector fault (CF), demonstrating that it is a through-going structure capable of hosting large-magnitude earthquakes despite the absence of a clear surface trace. Seismological observations indicate that this event involved a mechanically complex rupture, reflected by a large non-double-couple moment tensor solution. Analysis of relocated aftershocks (including relocation, cluster analysis, and fault-plane regression fitting), combined with available moment tensor solutions for the largest aftershocks suggests rupture occurred on at least two distinct fault segments. The mainshock initiated at the southern end of a southeast-striking segment of the CF and was dominated by dextral strike-slip motion, while the main event and subsequent aftershocks also activated an east-striking conjugate fault with reverse motion. The rupture complexity may reflect the structural immaturity of this incipient fault zone.

The shallow depth of rupture and its occurrence within a heavily glaciated, high-relief landscape led to widespread surface effects, including landslides and snow avalanches; preliminary observations indicate that these effects were concentrated near the Mt. King George massif. Notably, the areal extent of landslides

was considerably smaller than predicted based on empirical relations from past earthquakes, possibly due to the midwinter timing and widespread permafrost. Despite the shallow hypocentral depth, no surface rupture was observed, though it may be obscured by glacial ice or rugged topography. The damage to glacial ice, continuing rock fall, and lingering seismic hazard on adjacent fault segments will potentially pose an ongoing hazard for mountaineers and skiers who frequent the area. More broadly, the December 6, 2025 earthquake underscores the need for increased earthquake hazard awareness and preparedness in northern Canada, where large events may occur on unmapped or cryptic structures. Future research should focus on the integrated assessments of seismic hazard that explicitly consider interactions among earthquakes, landslides, geological site conditions, and climate-driven processes such as permafrost thaw, which may further exacerbate slope instability and compound risk in a rapidly changing Arctic and sub-Arctic environment.

Acknowledgments

This research occurred on the Traditional Territory of the Kluane First Nation. We thank Kate Allstadt, Elizabeth Eiden, Erin Jensen and other staff from the US Geological Survey for providing rapid satellite-based landslide mapping in support of our reconnaissance flight to the area. Horizon Helicopters provided a safe flight in extreme, cold conditions. We are very grateful to Leyla Weston and Amy Stuart for facilitating this last-minute addition to the Yukon Exploration and Geology volume.

References

Allstadt, K.E., Thompson, E.M., Jibson, R.W., Wald, D.J., Hearne, M., Hunter, E.J., Fee, J., Schovanec, H., Slosky, D. and Haynie, K.L., 2022. The US Geological Survey ground failure product: Near-real-time estimates of earthquake-triggered landslides and liquefaction. Earthquake Spectra, vol. 38, no. 1, p. 5–36, https://doi.org/10.1177/87552930211032685.

Behnia, P. and Blais-Stevens, A., 2018. Landslide susceptibility modelling using the quantitative random forest method along the northern portion of the Yukon Alaska Highway Corridor, Canada. Natural Hazards, vol. 90, p. 1407–1426, https://doi.org/10.1007/s11069-017-3104-z.

Bemis, S.P., Weldon, R.J. and Carver, G.A., 2015. Slip partitioning along a continuously curved fault: Quaternary geologic controls on Denali fault system slip partitioning, growth of the Alaska Range, and the tectonics of south-central Alaska. Lithosphere, vol. 7, no. 3, p. 235–246, https://doi.org/10.1130/L352.1.

Biegel, K.M., Dettmer, J., Igonin, N. and Eaton, D.W., 2024a. Double-pair double-difference relocation improves depth precision and highlights detailed 3D fault geometry for induced seismicity in Alberta, Canada. Seismological Research Letters, vol. 96, no. 3, p. 100–112, https://doi.org/10.1785/0220240194.

Biegel, K.M., Gosselin, J.M., Dettmer, J., Colpron, M., Enkelmann, E. and Caine, J.S., 2024b. Earthquake relocations delineate a discrete fault network and deformation corridor throughout southeast Alaska and southwest Yukon. Tectonics, vol. 43, no. 5, https://doi.org/10.1029/2023TC008140.

Bird, J.F. and Bommer, J.J., 2004. Earthquake losses due to ground failure. Engineering Geology, vol. 75, no. 2, p. 147–179, https://doi.org/10.1016/j.enggeo.2004.05.006.

Blais-Stevens, A., Clague, J.J., Brahney, J., Lipovsky, P., Haeussler, P.J. and Menounos, B., 2020. Evidence for large Holocene earthquakes along the Denali fault in southwest Yukon, Canada. Environmental and Engineering Geoscience, vo. 26, no. 2, p. 149–166, https://doi.org/10.2113/EEG-2263.

Bodtker, J., Cronmiller, D.C., Bond, J.D. and Shugar, D., 2023. The Sunnydale landslide, current understanding and research, Dawson (NTS 116B/3). *In:* Yukon Exploration and Geology 2022, K.E. MacFarlane (ed.), Yukon Geological Survey, p. 19–33.

Brideau, M.-A., Stead, D., Stevens, V., Roots, C., Lipovsky, P. and VonGaza, P., 2007. The Dawson City landslide (Dawson map area, NTS 116B/3), central Yukon. *In:* Yukon Exploration and Geology 2006, D.S. Emond, L.L. Lewis, and L.H. Weston (eds.), Yukon Geological Survey, p. 123–137.

Brideau, M.-A., Brayshaw, D., Hancock, C.-A., Lipovsky, P., Cronmiller, D., Lewkowicz, A., Blais-Stevens, A., Guthrie, R., Geertsema, M., Goetz, J., McGregor, C., Tannant, D., Friele, P., Clarke, J., Steelquist, A., Wong-Teichroeb, H., Ring, C. and Wells, G., 2026. Preliminary Canadian landslide database (13.0). Zenodo, https://doi.org/10.5281/zenodo.18216956.

Bruhn, R.L., Sauber, J., Cotton, M.M., Pavlis, T.L., Burgess, E., Ruppert, N. and Forster, R.R., 2012. Plate margin deformation and active tectonics along the northern edge of the Yakutat terrane in the Saint Elias orogen, Alaska, and Yukon, Canada. Geosphere, vol. 8, no. 6, p. 1384–1407, https://doi.org/10.1130/GES00807.1.

Busby, R.W. and Aderhold, K., 2020. The Alaska transportable array: As built. Seismological Research Letters, vol. 91, no. 6, p. 3017–3027, https://doi.org/10.1785/0220200154.

Byer, J.F., Gosselin, J.M., Dettmer, J. and Gilbert, H., 2026 (*this volume*). Preliminary investigation of seismic site conditions in Whitehorse (Kwänlin), Yukon, from passive seismic methods. *In:* Yukon Exploration and Geology 2025, A. Stuart, L.H. Weston and S.K. Schultz (eds.), Yukon Geological Survey, Government of Yukon, p. 119–130.

Canadian Hazards Information Service, 1985. Canadian National Earthquake Database. Natural Resources Canada, https://doi.org/10.17616/R3TD24, [accessed 08/01/2026].

Cassidy, J.F., Rogers, G.C., Lamontagne, M., Halchuk, S. and Adams, J., 2010. Canada's earthquakes: 'The good, the bad, and the ugly.' Geoscience Canada, vol. 37, no. 1, p.1–16.

Choi, M., Eaton, D.W. and Enkelmann, E., 2021. Is the Eastern Denali fault still active? Geology, vol. 49, no. 6, p. 662–666, https://doi.org/10.1130/G48461.1.

Christeson, G.L., Gulick, S.P., van Avendonk, H.J., Worthington, L.L., Reece, R.S. and Pavlis, T.L., 2010. The Yakutat terrane: Dramatic change in crustal thickness across the Transition fault, Alaska. Geology, vol. 38, no. 10, p. 895–898, https://doi.org/10.1130/G31170.1.

Clarke, H.C., Cronmiller, D.C., Ward, B.C. and Groeneveld, K.A, 2024. Permafrost-related landslides following a 2017 wildfire, Dempster Highway, Yukon (parts of NTS 116G/9 and 116H/12). *In:* Yukon Exploration and Geology Technical Papers 2023, L.H. Weston and Purple Rock Inc. (eds.), Yukon Geological Survey, p. 17–36.

DeMets, C., Gordon, R.G. and Argus, D.F., 2010. Geologically current plate motions. Geophysical Journal International, vol. 181, no. 1, p. 1–80, https://doi.org/10.1111/j.1365-246X.2009.04491.x.

Dodds, C.J. and Campbell, R.B., 1992. Geology, Mount St. Elias Map Area (115B &C[E1/2]), Yukon Territory. Geological Survey of Canada, Open File 2189, https://doi.org/10.4095/133475.

Doser, D.I., 2006. Relocations of earthquakes (1899–1917) in south-central Alaska. Pure and Applied Geophysics, vol. 163, no. 8, p. 1461–1476, https://doi.org/10.1007/s00024-006-0085-3.

Doser, D.I., 2010. A reevaluation of the 1958 Fairweather, Alaska, earthquake sequence. Bulletin of the Seismological Society of America, vol. 100, no. 4, p. 1792–1799, https://doi.org/10.1785/0120090343.

Doser, D.I., 2014. Seismicity of southwestern Yukon, Canada, and its relation to slip transfer between the Fairweather and Denali fault systems. Tectonophysics, vol. 611, p. 121–129, https://doi.org/10.1016/j.tecto.2013.11.018.

Eberhart-Phillips, D., Christensen, D.H., Brocher, T.M., Hansen, R., Ruppert, N.A., Haeussler, P.J. and Abers, G.A., 2006. Imaging the transition from Aleutian subduction to Yakutat collision in central Alaska, with local earthquakes and active source data. Journal of Geophysical Research: Solid Earth, vol. 111, no. B11, https://doi.org/10.1029/2005JB004240.

Eiden, E., 2025. Co-polarized synthetic aperture radar (SAR) change map between 11/28/2025 and 12/09/2025, Hubbard Glacier earthquake: US Geological Survey provisional data release, https://doi.org/10.5066/P14H7MVU.

Elliott, J.L., Larsen, C.F., Freymueller, J.T. and Motyka, R.J., 2010. Tectonic block motion and glacial isostatic adjustment in southeast Alaska and adjacent Canada constrained by GPS measurements. Journal of Geophysical Research: Solid Earth, vol. 115, no. B9, https://doi.org/10.1029/2009JB007139.

Elliott, J. and Freymueller, J.T., 2020. A block model of present-day kinematics of Alaska and western Canada. Journal of Geophysical Research: Solid Earth, vol. 125, no. 7, https://doi.org/10.1029/2019JB018378.

Enkelmann, E., Garver, J.I. and Pavlis, T.L., 2008. Rapid exhumation of ice-covered rocks of the Chugach-St. Elias orogen, southeast Alaska. Geology, vol. 36, no. 12, p. 915–918.

Ester, M., Kriegel, H.-P., Sander, J. and Xu, X., 1996. A density-based algorithm for discovering clusters in large spatial databases with noise. *In:* Proceedings of the 2nd International Conference on Knowledge Discovery and Data Mining (KDD-96), E. Simoudis, J. Han and U. Fayyad (eds.), p. 226–231.

Evans, S.G. and Clague, J.J., 1988. Catastrophic rock avalanches in glacial environments. *In:* Proceedings of the Fifth International Symposium on Landslides, Lausanne, Switzerland, vol. 2, p. 1153–1158.

Everard, K.A., 1994. Regional characterization of large landslides in southwest Yukon, with emphasis on the role of neotectonics. PhD thesis, University of British Columbia, Vancouver, British Columbia, Canada, 165 p.

Finley, T., 2025. Neotectonics of major faults in the Canadian Cordillera. PhD thesis, University of Victoria, British Columbia, Canada, 151 p.

Finzel, E.S., Trop, J.M., Ridgway, K.D. and Enkelmann, E., 2011. Upper plate proxies for flat-slab subduction processes in southern Alaska. Earth and Planetary Science Letters, vol. 303, no. 3–4, p. 348–360, doi:10.1016/j.epsl.2011.01.014.

Fletcher, H.J. and Freymueller, J.T., 2003. New constraints on the motion of the Fairweather fault, Alaska, from GPS observations. Geophysical Research Letters, vol. 30, no. 3, https://doi.org/10.1029/2002GL016476.

Gosselin, J.M., Biegel, K.M., Dettmer, J., Gilbert, H., Colpron, M. and Enkelmann, E., 2024. Crustal stress near the Yakutat microplate collision from probabilistic earthquake focal mechanisms. Canadian Journal of Earth Sciences, vol. 62, no. 4, p. 807–820, https://doi.org/10.1139/cjes-2024-0095.

Gosselin, J.M., Dettmer, J., Lipovsky, P. and Cronmiller, D., 2025. Seismic site amplification assessment in the Dakwäkäda (Haines Junction) area of Yukon, Canada, from probabilistic inference of passive seismic measurements. Canadian Geotechnical Journal, https://doi.org/10.1139/cgj-2025-0357.

Grantz, A., 1966. Strike-slip faults in Alaska, US Geological Survey Open File Report 66-53, 82 p.

Haeussler, P.J., Freymueller, J.T., Wesson, R.L. and Ekström, G., 2008. An overview of the neotectonics of interior Alaska: Far-field deformation from the Yakutat microplate collision. Active Tectonics and Seismic Potential of Alaska: American Geophysical Union Geophysical Monograph, p. 83–108.

Haeussler, P.J., 2009. Surface rupture map of the 2002 M7.9 Denali Fault earthquake, Alaska; digital data: US Geological Survey Data Series 422, http://pubs.usgs.gov/ds/422/.

Haeussler, P.J., Matmon, A., Schwartz, D.P. and Seitz, G.G., 2017. Neotectonics of interior Alaska and the late Quaternary slip rate along the Denali fault system. Geosphere, vol. 13, no. 5, p. 1445–1463, https://doi.org/10.1130/GES01447.1.

Haeussler, P.J., Bender, A.M., Powers, P.M., Koehler, R.D. and Brothers, D.S., 2024. Updating the crustal fault model for the 2023 national seismic hazard model for Alaska. *In:* Tectonics and Seismicity of Alaska and Western Canada: Earthscope and Beyond, N.A. Ruppert, M.A. Jadamec, and J.T. Freymueller (eds.), John Wiley & Sons Inc.

Helmholtz Centre Potsdam GFZ German Research Centre for Geosciences and gempa GmbH, 2008. The SeisComP seismological software package, GFZ Data Services, https://doi.org/10.5880/GFZ.2.4.2020.003.

Keefer, D., 1984. Landslides caused by earthquakes. Geological Society of America Bulletin, vol. 95, p. 406–421.

Keefer, D.K., 2002. Investigating landslides caused by earthquakes—A historical review. Surveys in Geophysics, vol. 23, no. 6, p. 473–510, https://doi.org/10.1023/A:1021274710840.

Kennett B.L.N. and Engdahl E.R., 1991. Traveltimes for global earthquake location and phase identification. Geophysical Journal International, vol. 105, no. 2, p. 429–465, https://doi.org/10.1111/j.1365-246X.1991.tb06724.x.

Koehler, R.D., Farrell, R.-E., Burns, P.A.C. and Combellick, R.A., 2012. Quaternary faults and folds in Alaska: A digital database. Miscellaneous Publication 141, Alaska Division of Geological & Geophysical Surveys, 33 p.

Lahr, J.C. and Plafker, G., 1980. Holocene Pacific–North American plate interaction in southern Alaska: Implications for the Yakataga seismic gap. Geology, vol. 8, no. 10, p. 483–486, https://doi.org/10.1130/0091-7613(1980)8%3C483:HPAPII%3E2.0.CO;2.

Lipovsky, P. and Huscroft, C., 2007. A reconnaissance inventory of permafrost-related landslides in the Pelly River watershed, central Yukon. *In:* Yukon Exploration and Geology 2006, D.S. Emond, L.L. Lewis and L.H. Weston (eds.), Yukon Geological Survey, p. 181–195.

Lipovsky, P.S., 2023. Surficial geology and geohazards of the greater Whitehorse area. Yukon Geological Survey, Open File 2023-1, 67 p. plus appendices.

Marano, K.D., Wald, D.J. and Allen, T.I., 2010. Global earthquake casualties due to secondary effects: A quantitative analysis for improving rapid loss analyses. Natural Hazards, vol. 52, no. 2, p. 319–328, https://doi.org/10.1007/s11069-009-9372-5.

Marechal, A., Mazzotti, S., Elliott, J.L., Freymueller, J.T. and Schmidt, M., 2015. Indentor-corner tectonics in the Yakutat-St. Elias collision constrained by GPS. Journal of Geophysical Research: Solid Earth, vol. 120, no. 5, p. 3897–3908, https://doi.org/10.1002/2014JB011842.

Marechal, A., Ritz, J.-F., Ferry, M., Mazzotti, S., Blard, P.-H., Braucher, R. and Saint-Carlier, D., 2018. Active tectonics around the Yakutat indentor: New geomorphological constraints on the eastern Denali, Totschunda and Duke River faults. Earth and Planetary Science Letters, vol. 482, p. 71–80, https://doi.org/10.1016/j.epsl.2017.10.051.

Massey, C., Townsend, D., Rathje, E., Allstadt, K.E., Lukovic, B., Kaneko, Y., Bradley, B., Wartman, J., Jibson, R.W., Petley, D.N., Horspool, N., Hamling, I., Carey, J., Cox, S., Davidson, J., Dellow, S., Godt, J.W., Holden, C., Jones, K., Kaiser, A., Little, M., Lyndsell, B., McColl, S., Morgenstern, R., Rengers, F.K., Rhoades, D., Rosser, B., Strong, D., Singeisen, C. and Villeneuve, M., 2018. Landslides triggered by the 14 November 2016 M_w7.8 Kaikōura earthquake, New Zealand. Bulletin of the Seismological Society of America, vol. 108, no. 3B, p. 1630–1648, https://doi.org/10.1785/0120170305.

Meighan, L.N., Cassidy, J.F., Mazzotti, S. and Pavlis, G.L., 2013. Microseismicity and tectonics of southwest Yukon Territory, Canada, using a local dense seismic array. Bulletin of the Seismological Society of America, vol. 103, no. 6, p. 3341–3346, https://doi.org/10.1785/0120130068.

Miller, D.J., 1960. The Alaska earthquake of July 10, 1958: Giant wave in Lituya Bay. Bulletin of the Seismological Society of America, vol. 50, no. 2, p. 253–266, https://doi.org/10.1785/BSSA0500020253.

Natural Resources Canada, 2025. Community internet intensity map. Earthquakes Canada, https://www.earthquakescanada.nrcan.gc.ca/recent/2025/20251206.2041/dyfi-en.php, [accessed 08/01/2026].

Nowicki Jessee, M.A., Hamburger, M.W., Allstadt, K., Wald, D.J., Robeson, S.M., Tanyas, H., Hearne, M. and Thompson, E.M., 2018. A global empirical model for near-real-time assessment of seismically induced landslides. Journal of Geophysical Research: Earth Surface, vol. 123, no. 8, p. 1835–1859, https://doi.org/10.1029/2017JF004494.

Pavlis, G.L., Bauer, M.A., Elliott, J.L., Koons, P., Pavlis, T.L., Ruppert, N., Ward, K.M. and Worthington, L.L., 2019. A unified three-dimensional model of the lithospheric structure at the subduction corner in southeast Alaska: Summary results from STEEP. Geosphere, vol. 15, no. 2, p. 382–406, https://doi.org/10.1130/GES01488.1.

Plafker, G., 1987. Regional geology and petroleum potential of the northern Gulf of Alaska continental margin. *In:* Geology and resource potential of the continental margin of western north America and adjacent ocean basins—Beaufort Sea to Baja California, p. 229–268.

Porter, C., Howat, I., Noh, M-J., Husby, E., Khuvius, S., Danish, E., Tomko, K., Gardiner, J., Negrete, A., Yadav, B., Klassen, J., Kelleher, C., Cloutier, M., Bakker, J., Enos, J., Arnold, G., Bauer, G. and Morin, P., 2023. ArcticDEM—Mosaics, Version 4.1, Harvard Dataverse, V1, https://doi.org/10.7910/DVN/3VDC4W [accessed 10/31/2025].

Read, C., Lyons, J., Stephani, E.A. and Staley, D.M., 2025. Oblique aerial photography and videography of the August 10, 2025 Tracy Arm landslide and tsunami, southeast Alaska, US Geological Survey, data release, https://www.usgs.gov/data/oblique-aerial-photography-and-videography-august-10-2025-tracy-arm-landslide-and-tsunami.

Richter, D.H. and Matson, N.A., Jr., 1971. Quaternary faulting in the eastern Alaska Range. Geological Society of America Bulletin, vol. 82, no. 6, p. 1529–1540.

Rodrıguez, C.E., Bommer, J.J. and Chandler, R.J., 1999. Earthquake-induced landslides: 1980–1997. Soil Dynamics and Earthquake Engineering, vol. 18, no. 5, p. 325–346, https://doi.org/10.1016/S0267-7261(99)00012-3.

Rubin, A.M., Gillard, D. and Got, J.-L., 1999. Streaks of microearthquakes along creeping faults. Nature, vol. 400, no. 6745, p. 635–641, https://doi.org/10.1038/23196.

Scarabello, L., Abdollahzadeh, M., Becker, J. and Pickle, R., 2025. Swiss-seismological-service/scrtdd: v1.8.9. Zenodo, https://doi.org/10.5281/zenodo.16797309.

Schaeffer, A.J., Gosselin, J.M., Audet, P., Cassidy, J.F. and Paul, C., 2026 (*this volume*). Current tectonics of the Richardson Mountains, northwestern Canada, from preliminary double-difference earthquake relocations. *In:* Yukon Exploration and Geology 2025, A. Stuart, L.H. Weston and S.K. Schultz (eds.), Yukon Geological Survey, Government of Yukon, p. 149–165.

Sethanant, I., Nissen, E., Pousse-Beltran, L., Bergman, E. and Pierce, I., 2023. The 2020 M_w6.5 Monte Cristo Range, Nevada, earthquake: Anatomy of a crossing-fault rupture through a region of highly distributed deformation. Bulletin of the Seismological Society of America, vol. 113, no. 3, p. 948–975, https://doi.org/10.1785/0120220166.

Sosio, R., Crosta, G.B., Chen, J.H. and Hungr, O., 2012. Modelling rock avalanche propagation onto glaciers. Quaternary Science Reviews, vol. 47, p. 23–40, https://doi.org/10.1016/j.quascirev.2012.05.010.

Stethem, C., Jamieson, B., Schaerer, P., Liverman, D., Germain, D. and Walker, S., 2003. Snow avalanche hazard in Canada—A review. Natural Hazards, vol. 28, p. 487–515, https://doi.org/10.1023/A:1022998512227.

US Geological Survey, 2025a. Advanced National Seismic System Comprehensive Earthquake Catalog, https://earthquake.usgs.gov/earthquakes, [accessed 08/01/2026].

US Geological Survey, 2025b. M 7.0 – 2025 Hubbard Glacier Earthquake Event Page, https://earthquake.usgs.gov/earthquakes/eventpage/us6000rsy1/executive [accessed 08/01/2026].

US Geological Survey, 2026. Quaternary fault and fold database for the United States. US Geological Survey, https://doi.org/10.5066/F7S75FJM [accessed 08/01/2026].

Utsu, T., Ogata, Y. and Matsu'ura, R.S., 1995. The Centenary of the Omori Formula for a Decay Law of Aftershock Activity. Journal of Physics of the Earth, vol. 43, no. 1, p. 1–33, https://doi.org/10.4294/jpe1952.43.1.

Velasco, A.A., Ammon, C.J., Farrell, J. and Pankow, K., 2004. Rupture directivity of the 3 November 2002 Denali fault earthquake determined from surface waves. Bulletin of the Seismological Society of America, vol. 94, no. 6B, p. S293–S299, https://doi.org/10.1785/0120040624.

Waldhauser, F. and Ellsworth, W.L., 2000. A double-difference earthquake location algorithm: Method and application to the northern Hayward fault, California. Bulletin of the Seismological Society of America, vol. 90, no. 6, p. 1353–1368, https://doi.org/10.1785/0120000006.

Waldhauser, F., 2001. hypoDD: A computer program to compute double-difference earthquake locations. Open-File Report 2001-113, US Geological Survey, https://doi.org/10.3133/ofr01113.

Wells, D.L. and Coppersmith, K.J., 1994. New empirical relationships among magnitude, rupture length, rupture width, rupture area, and surface displacement. Bulletin of the Seismological Society of America, vol. 84, no. 4, p. 974–1002, https://www.resolutionmineeis.us/sites/default/files/references/wells-coppersmith-1994.pdf.

Whelan, N., 2022. Geochronology of landslides in the Kluane Lake region, southwest Yukon. MSc thesis, Simon Fraser University. British Columbia, Canada, 165 p. plus appendices.

Yukon Geological Survey, 2021. Major Faults. Government of Yukon, https://open.yukon.ca/data/major-faults.

Current tectonics of the Richardson Mountains, northwestern Canada, from preliminary double-difference earthquake relocations

Andrew J. Schaeffer and Jeremy M. Gosselin*
Natural Resources Canada, Geological Survey of Canada - Pacific

Pascal Audet
University of Ottawa

John F. Cassidy
Natural Resources Canada, Geological Survey of Canada - Pacific

Collin Paul
Natural Resources Canada, Canadian Hazards Information Service

Schaeffer, A.J., Gosselin, J.M., Audet, P., Cassidy, J.F. and Paul, C., 2026. Current tectonics of the Richardson Mountains, northwestern Canada, from preliminary double-difference earthquake relocations. *In*: Yukon Exploration and Geology 2025, A. Stuart, L.H. Weston and S.K. Schultz (eds.), Yukon Geological Survey, Government of Yukon, p. 149–165.

Abstract

The Richardson Mountains (RM) of northwestern Canada form a tectonically active boundary between the northern Canadian Cordillera and stable North American craton. Although host to abundant seismicity, the RM modern geometry and kinematics remain poorly resolved. To better delineate active structures, we apply double-difference (DD) earthquake relocation to all seismicity in the Canadian National Earthquake Database (NEDB) between 2015 and 2021 (775 events). We jointly invert catalogue P and S-wave picks and waveform cross-correlation measurements with the *scrtdd* implementation of *HypoDD*.

The resulting 594-event catalogue reveals two zones. Along the eastern front of the central RM, DD relocations collapse into a sharply defined west-dipping plane extending from the surface to 35 km. Its approximate 75° dip and surface intersection with the Knorr fault suggest that contemporary deformation is reactivating a Paleozoic normal fault. In contrast, seismicity remains broadly distributed across the White Mountains and Barn uplifts, reflecting deformation partitioned among several interacting inherited structures within a complex deformation zone. A reduction in seismicity between these regions (in both original and relocated catalogues) may indicate structural segmentation or a locked segment with implications for seismic hazard.

These results demonstrate the effectiveness of DD relocation for resolving active tectonic structures in remote northern regions and provide a refined framework for future investigations. Continued incorporation of new data from the Western Arctic Regional Network of Seismographs (WARNS) will support improved assessments of crustal deformation and seismic hazard in Canada's North.

* andrew.schaeffer@nrcan-rncan.gc.ca

Plain language summary

The Richardson Mountains in northwestern Canada are situated at the junction between two very different parts of the continent: an active mountain belt to the west and a much older, stable region to the east. This area experiences many small earthquakes and has also produced large ones in the past, but the exact locations and behaviours of the faults that cause these earthquakes are not well understood. To improve this picture, we re-examined recent earthquakes recorded between 2015 and 2021 using methods that more precisely determine where each earthquake occurred. Out of hundreds of events, we were able to sharpen the locations of nearly 600 earthquakes. These improved locations reveal two main zones of activity. In the central Richardson Mountains, many earthquakes line up on a single, steeply sloping surface that reaches down to 35 km. This surface lines up with an ancient fault that originally formed hundreds of millions of years ago, suggesting that old structures in the region are being reactivated today. Farther north, earthquakes are more spread out. This pattern suggests that the deformation is spread over several older fault systems rather than along one main fault. Overall, this study provides a clearer picture of how the Richardson Mountains continue to deform and sets the stage for better understanding earthquake hazards in northern Canada.

Introduction

The Richardson Mountains (RM) represent a significant structural domain within the northern Canadian Cordillera (NCC), forming a narrow, north-trending range that marks the eastern limit of Cordilleran deformation in northern Yukon and the Northwest Territories (Hyndman et al., 2005b; Pinet, 2021), where they are juxtaposed to the stable North American craton. The formation and subsequent tectonic evolution of the RM are intrinsically linked to the development of the Beaufort Sea and the Canada Basin, reflecting a long history that began with continental rifting and culminated in complex Cenozoic strain transfer stemming from interactions along the Pacific margin (Mazzotti and Hyndman, 2002; Estève et al., 2022). Today, the RM region is tectonically active and hosts abundant earthquake activity. This seismicity not only presents valuable information that can enable a new understanding of the geological history and potential of the region, but also clearly identifies natural hazards to Canada's northern communities and development. In this work, we re-examine the modern earthquake catalogue across the RM region with the aim of precisely identifying reactivated structures. This is achieved using the double-difference (DD) relocation technique.

Tectonic Setting

The geological roots of the RM originate in the Richardson Trough (RT), a key paleogeographic feature that formed on the ancestral northwestern margin of Laurentia (Cecile et al., 1997; Eyster et al., 2017; Strauss et al., 2020). The RT is widely recognized as a rift basin on the southern margin of an ancestral Iapetus Ocean (Lane, 2007; Cecile et al., 2022), and specifically as a failed arm (aulacogen) of a triple rift system that developed during the early Paleozoic (Jeletsky, 1962; Cecile et al., 1997).

This trough separated the Yukon block (a basement high with relatively stable cratonic area to the west) from the Mackenzie/Peel Platform to the east (Morrow, 1999 ; Strauss et al., 2020). The RT experienced two major rift cycles that spanned the late Early Cambrian to early Middle Devonian (Cecile et al., 2022). For relevant geological maps and diagrams, see Figure 1 of Strauss et al. (2020) and Figures 1 and 2 of Cecile et al. (2022). The first cycle involved rifting from late-Early to middle-Late Cambrian, followed by post-rift subsidence lasting until the late Early Ordovician; the second cycle involved rifting from late Early Ordovician to Early Silurian, followed by post-rift subsidence lasting until the early Middle Devonian (Cecile et al., 2022). The trough accumulated a thick succession of deep-water sedimentary rocks, up to 3 km thick in the centre of the basin compared to 1 km on adjoining platforms (Cecile et al., 2022), known as the Road River Group, which ranges in age from the Late Cambrian to the early Middle Devonian (Strauss et al., 2020). This deep-water depositional setting, characterized by fine-grained carbonate and siliciclastic strata, has been compared in size and geometry to segments of the modern East African rift system, such as the Kenya Rift (Cecile et al., 1997; Cecile et al., 2022).

The modern Richardson Mountains correspond to the Richardson anticlinorium, a broad, gently north-plunging structure that resulted from the structural inversion of the RT (Pinet, 2021; Cecile et al., 2022). This inversion primarily occurred during the Late

Cretaceous to early Tertiary Laramide orogeny (Norris, 1985; Lane, 1996; Pinet, 2021), driven by east-directed compression associated with Cordilleran tectonics (Lane, 1996, 1998).

In Figure 1, we illustrate the modern configuration of the Yukon and westernmost Northwest Territories, including seismicity (yellow circles), major faults (dotted lines), defined faults (light grey lines) and the dominant terrane assemblages of Nelson et al. (2013). The RM are cut by the Richardson fault system (RFS), a major system of north-trending, curviplanar, near-vertical faults (Norris, 1985; Pinet, 2021). This array extends for nearly 600 km, originating in the Mackenzie Mountains and projecting north toward the Beaufort Sea (Gabrielse, 1991; Norris, 1997). The RFS accommodated early Paleozoic dextral strike-slip movement (Norris, 1985), but the subsequent Tertiary inversion involved primarily dip-slip reactivation and shortening (Norris, 1985; Lane, 1996).

The RM and their fault systems are critical elements in the regional tectonic framework that includes the Beaufort Sea and the origin of the Amerasia Basin (Canada Basin). Mesozoic rifting in Arctic North America led to the formation of the Canada Basin during the Jurassic–Cretaceous (Shephard et al., 2013; Faehnrich et al., 2025). Tectonic models for this opening involve counterclockwise rotation or translation of the Arctic Alaska terrane (Lane, 1997; Faehnrich et al., 2025).

Northward, the RFS is inferred to connect with fault systems defining the continental margin, potentially linking to the Husky Lakes fault system (HLFS; previously Eskimo Lakes fault zone) via the Bug Creek and Donna River faults (Lane, 1998; Pinet, 2021). The HLFS originated as a listric normal fault during the Late Jurassic–Early Cretaceous rifting (Stephenson et al., 1994; Lane, 1998). Later, tertiary contractional deformation inverted these extensional structures, contributing to the formation of the Beaufort foldbelt (Lane and Dietrich, 1995). Seismic data show that the Tertiary deformation front on the eastern side of the Richardson anticlinorium consists of a series of thrust faults, folds, and back thrusts, concentrated where Paleozoic platform carbonates transition into basinal shale (Rohr et al., 2011).

The Late Cretaceous–Tertiary deformation that inverted the RT was closely related to the subsequent formation of the Beaufort Sea fold and thrust belt (BSFTB), which extends offshore into the Beaufort-Mackenzie Basin (Lane, 2002 ; Estève et al., 2022), as indicated offshore in Figure 1. This fold belt resulted from east-west shortening caused by the collision of Arctic Alaska against the rigid North American craton (Estève et al., 2022). The RM, located at the edge of the craton, acted as a buttress that focused the escape and northward deformation of supra-crustal rocks into the Beaufort Sea (Lane, 1998; Estève et al., 2022).

The Porcupine fault system (PFS), located west of the RM, is a major northeast-striking fault zone that forms the southeastern boundary of the Arctic Alaska terrane (Colpron et al., 2019; Faehnrich et al., 2025). The PFS has recorded polyphase brittle–ductile deformation, including evidence of older sinistral displacement and younger dextral brittle movement (von Gosen et al., 2019). New geochronological data constrain Mesozoic deformation within the PFS to about 121 Ma (U-Pb dating of calcite veins), supporting translational or hybrid models for the opening of the Canada Basin that involved significant strike-slip motion of the Arctic Alaska terrane (McClelland et al., 2021; Faehnrich et al., 2025). The complex, contrasting kinematics observed in the RFS and PFS underscore the distributed nature of strain partitioning necessary to accommodate the convergence and rotations of crustal blocks within the northwestern Cordillera.

Seismicity

The RM region is one of the most seismically active zones along the eastern Cordillera mountain front in northwest Canada (Cassidy et al., 2005; Hyndman et al., 2005a; Hyndman et al., 2005b). This activity is proposed to be the result of far-field strain transfer originating from the oblique collision of the Yakutat terrane in the Gulf of Alaska, pushing the northern Cordilleran block northeastward (Mazzotti and Hyndman, 2002; Hyndman et al., 2005; Leonard et al., 2007). This rigid displacement of the upper crust, estimated at approximately 5 ± 4 mm/year relative to the stable North American craton, is accommodated in the RM primarily by strike-slip motion (Mazzotti and Hyndman, 2002; Leonard et al., 2007; Mazzotti et al., 2008; Rohr et al., 2011). An alternative driving mechanism for enigmatic Cenozoic deformation along the eastern margin of the NCC is rooted far from the active Pacific margin. Enkelmann et al. (2019) hypothesize that Early Oligocene deformation (~40–30 Ma) recorded through renewed exhumation in the RM is potentially related to stresses originating from the eastern boundary of the North American plate, located approximately 4000 km away. Specifically, this model links episodes of deformation and exhumation in the NCC to changes in the absolute plate motion of

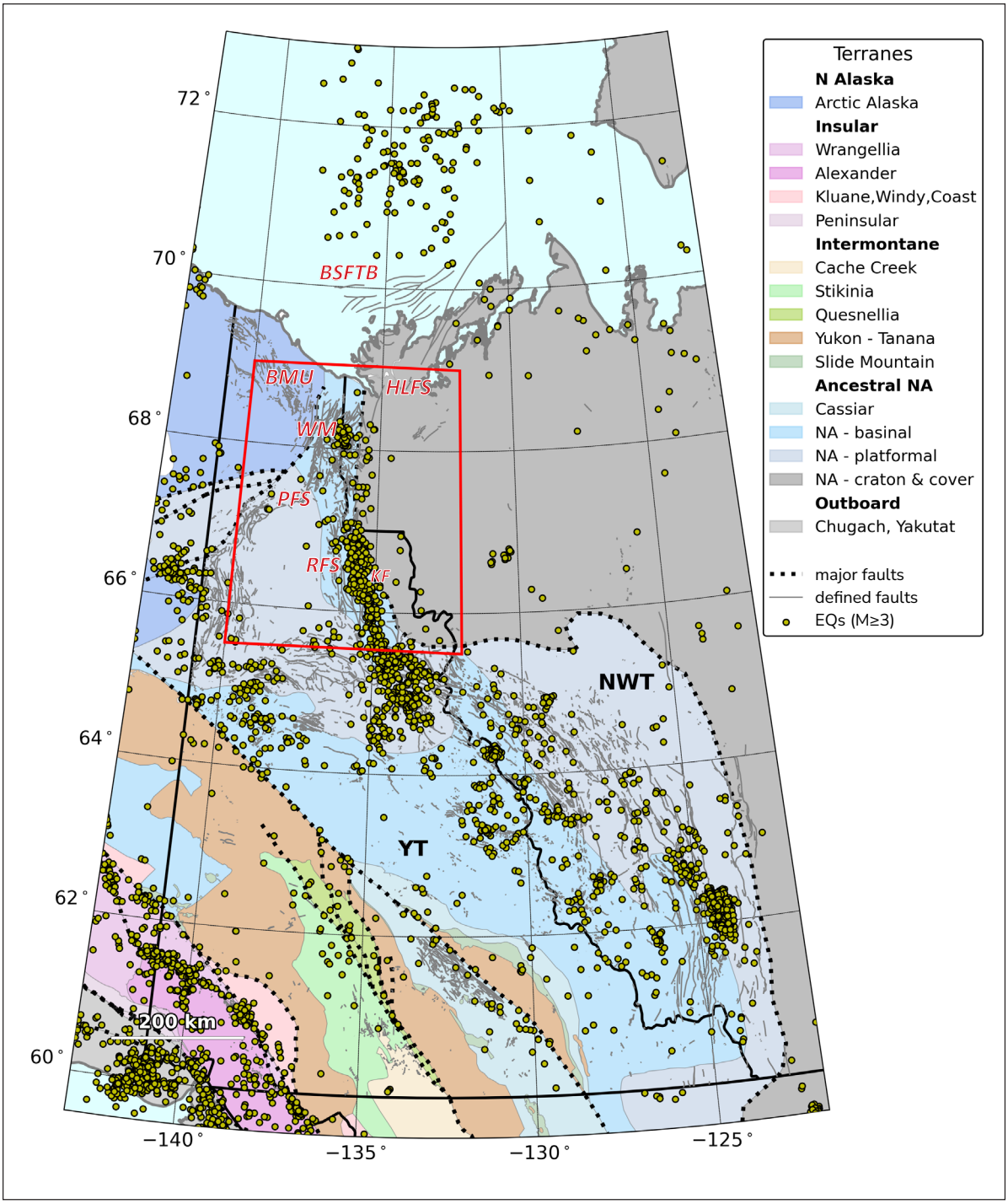


Figure 1. *Map of the Yukon and the westernmost region of the Northwest Territories. Terranes are taken from Nelson et al. (2013), and major faults are dashed lines and light grey lines denoting 'defined' faults extracted from the databases of the Yukon and Northwest Territories geological surveys (Yukon Geological Survey, 2016; Northwest Territories Geological Survey, 2018). Yellow circles denote the locations of earthquakes with M≥3.0. The red square denotes the Richardson Mountains study region illustrated in subsequent Figures 2 and 3. Labels denote regions discussed in the main text: BMU: Barn Mountains uplift; BSFTB: Beaufort Sea fold and hrust belt; HLFS: Husky Lakes fault system; KF: Knorr fault; PFS: Porcupine fault system; RFS: Richardson fault system; WM: White Mountain uplift.*

North America, particularly during periods when the plate's velocity increased and its motion was oriented at a high angle to the pre-existing structural grain of the Cordillera. This suggests that the opening of the North Atlantic Ocean provided the necessary far-field tectonic forcing (Enkelmann et al., 2019; Stephan and Enkelmann, 2025).

The RM remain seismically active today (Cassidy and Bent, 1993; Pinet, 2021), and seismicity is concentrated along the RFS, a system of steep north-south trending faults that extend northward toward the Beaufort Sea (Cassidy and Bent, 1993; Mazzotti and Hyndman, 2002; Hyndman et al., 2005; Pinet, 2021). The largest recorded earthquakes in this region occurred in close succession in 1940: M_S = 6.2 on May 29, and M_S = 6.5 on June 5 (Cassidy and Bent, 1993; Hyndman et al., 2005a; Hyndman et al., 2005b). These major events were complex ruptures, with focal depths ranging from 14.5 to 11 km for the May event, and 10 to 7 km for the June event, generally located in the mid to upper crust (Cassidy and Bent, 1993; Hyndman et al., 2005a; Hyndman et al., 2005b). In general, earthquakes in the RM are characterized by right-lateral strike-slip motion along the north-south trending planes (Cassidy and Bent, 1993; Cassidy et al., 2005). Structural analysis of the RFS shows that this dextral movement often affects previously tilted and deformed sedimentary successions, highlighting a history of polyphase deformation (Pinet, 2021). The orientation of the pressure axes for these earthquakes is northeast-southwest, consistent with the contemporary regional stress field that influences the entire northern Cordillera (Cassidy and Bent, 1993; Hyndman et al., 2005; Gosselin et al., 2024).

Focal mechanism studies, including analysis of 1940 events and subsequent moderate earthquakes (M_b = 4.8 in 1972 and M_b = 5.0 in 1976), consistently show a dominant right-lateral strike-slip faulting motion along the Richardson Mountains fault system (Cassidy and Bent, 1993; Cassidy et al., 2005; Hyndman et al., 2005b; Leonard et al., 2007; Pinet, 2021). For the 1940 events, the preferred interpretation is the right-lateral motion along north-south trending planes, consistent with mapped surface faults in the region (Cassidy and Bent, 1993). The pressure axes (maximum horizontal stress) determined from these focal mechanisms are oriented northeast-southwest (~N40°E), indicating that the contemporary regional stress field is reactivating the pre-existing, favourably oriented faults of the RFS (Cassidy and Bent, 1993; Mazzotti and Hyndman, 2002; Hyndman et al., 2005a; Hyndman, et al., 2005b). This compressional orientation is similar to that found in the northern Mackenzie Mountains, suggesting that both regions are driven by the same far-field stress, although the Mackenzie Mountains predominantly exhibit thrust faulting (Cassidy and Bent, 1993, 2025; Hyndman et al., 2005b).

A key feature of the seismicity is the lack of aftershocks for the 1940 Richardson Mountains earthquakes, which is consistent with the estimated low stress drops of 22 to 28 bars for these events, similar to other major earthquakes in the eastern Canadian Cordillera (Cassidy and Bent, 1993, 2025). The largest earthquakes in the region occur frequently in pairs or swarms, suggesting that stress triggering plays an important role (Cassidy and Bent, 1993, 2025; Cassidy et al., 2005). The RM represent a high seismic hazard zone, with an estimated return period for a potentially damaging earthquake (M≥5) of about 2–3 years (Cassidy et al., 2005; Hyndman et al., 2005). Based on the maximum geological and seismic extent of the main strike-slip fault system (estimated at 200 km), the maximum possible magnitude is estimated to be M_x = 7.5 (ranging from 7.2–7.8; Mazzotti and Hyndman, 2002; Hyndman et al., 2005a; Hyndman et al., 2005b). Despite the importance of the Richardson Mountains as a kinematic pivot point, the locus of current displacement and magnitude along the RFS is poorly constrained (Pinet, 2021).

Data and methods

Earthquake catalogues

The source of events used in this study is Canada's National Earthquake Database (NEDB; Canadian Hazards Information Service, 1985), originally created and curated by the Geological Survey of Canada (GSC), and now by the Canadian Hazards Information Service (CHIS) within Natural Resources Canada (NRCan). This database is the long-term primary national database for seismicity within and near Canada, and is used as the source of earthquake information for the Canadian National Seismic Hazard Model (CNSHM; Kolaj et al., 2023). Events within this catalogue have been located and reviewed by analysts since its inception, and historical earthquake epicentres were added through the archival study of reports of ground shaking and damage dating back hundreds of years. The 'modern' catalogue originated in 1985 when seismic data increased in availability.

In Figures 1 and 2 we plot events from the NEDB that have occurred since 1985, located within the study

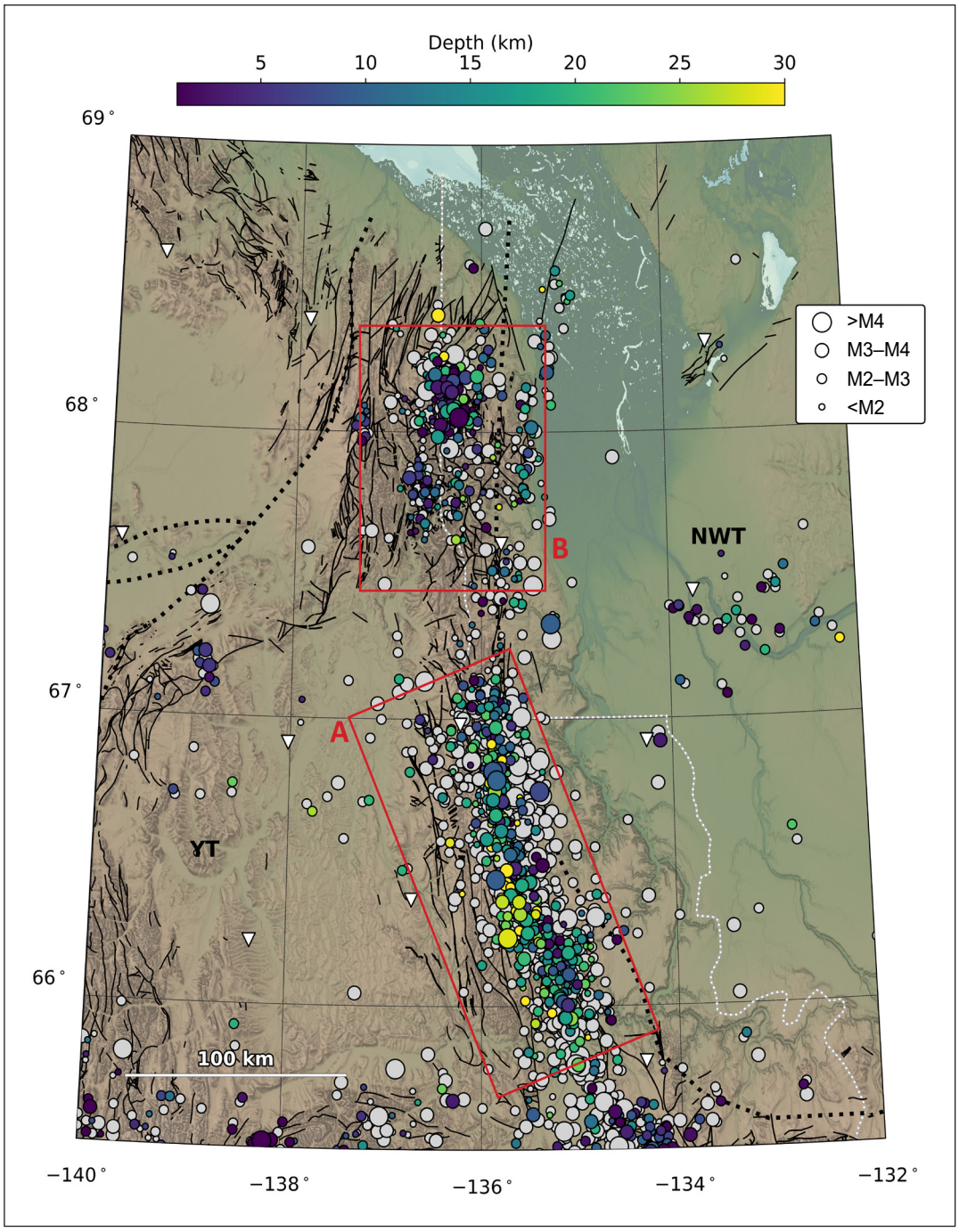


Figure 2. *Map of earthquakes extracted from the Canadian Hazards Information Service (CHIS) National Earthquake Database (NEDB; Canadian Hazards Information Service, 1985) for the region of interest. Earthquake magnitudes are indicated by the size of the circle, and the colour of the circle denotes the earthquake depth. The events coloured by depth are those events that occurred within the period for the relocation, from January 1, 2015 to December 31, 2021. The light grey circles denote the rest of the events in the NEDB, outside this time period. Inverted white triangles denote the location of operating seismic stations during this time period. Regions A and B are indicated by red boxes, as discussed in text.*

region. In Figure 1 only events M≥3.0 are illustrated to highlight seismically active areas in the broader regional context. In Figure 2, which focuses on our study region of the RM, we include all events in the NEDB sized according to event magnitude. Events for the time period between 2015 and 2021 are coloured according to depth and are used as input to the analysis in this work. Events indicated in grey are all remaining NEDB events outside this time period to illustrate the spatial distribution of events in the entire catalogue. Within the confines of the RM study region in Figure 2, there are a total of 1595 events in the NEDB, including 775 within the selected 2015 to 2021 period.

The distribution of these events is clearly concentrated in two regions associated with the RFS: the southern main strand between 66.5°N and 67.25°N (region A, Figs. 2 and 3), and a northern cluster centred around 68°N (region B, Figs. 2 and 3). The depths of seismicity within this region are poorly constrained between the surface and ~40 km depth. Some diffuse additional seismicity is observed off-axis of the RFS, potentially accommodating stress release on more localized structures to the west or reflecting uncertainties in event locations. Limited diffuse seismicity is also observed to the east, within the Mackenzie Delta region.

For this analysis, we extracted events in the period extending from January 1, 2015 to December 31, 2021 from the NEDB. This range is selected because it corresponds to the highest density of seismic station coverage in the area, due to the deployment of the USArray Transportable Array (TA; IRIS Transportable Array, 2003; Busby and Aderhold, 2020), in Alaska, Yukon, and the westernmost region of the Northwest Territories. The improved station coverage during this period enabled a significant reduction in the detection threshold and magnitude of completeness of the earthquake catalogue, resulting in significantly more recorded events (Ruppert and West, 2020). Although most of the TA stations were removed during 2021, a select number of these were retained by the GSC (PQ; Geological Survey of Canada, 2013) and CHIS (CN; Natural Resources Canada, 1975). Some of these adopted stations have contributed to the ongoing work of the Western Arctic Regional Network of Seismographs (WARNS; Schaeffer et al., 2025).

Double-difference relocation

We used the double-difference (DD) relocation method in order to better constrain the seismicity patterns throughout the RM region. The DD relocation method is a widely used seismological technique designed to improve relative earthquake hypocentres, and includes many successful applications. In many cases, the absolute location of events is also improved (Biegel et al., 2024b). Improved relative locations can illuminate active fault systems, allowing improved interpretation and understanding of geological processes. This methodology, typically implemented in software such as *HypoDD* (Waldhauser, 2001) or its advanced variants, leverages the additional information available when considering multiple events jointly, rather than independently located individual earthquakes.

The DD method is fundamentally a relative location technique that treats the estimation of the locations of all events within a cluster of earthquakes as a single inverse problem. Rather than considering the observed data as absolute travel times, the data are considered differential travel times (Waldhauser and Ellsworth, 2000; Waldhauser, 2001). Specifically, the data are the differences in travel times for events (within the same cluster) recorded by the same stations. The goal of the DD approach is to minimize the residuals for these differential travel times (i.e., the differences between observed and predicted differential travel times). Hence, the objective function for this problem is defined as a difference of differences, which is where the term double-difference originates. The DD method ultimately minimizes spatial distance errors between neighbouring events, allowing more precise identification of geological structures, such as active fault planes, with high fidelity (Waldhauser and Ellsworth, 2000; Waldhauser, 2001).

A fundamental inherent advantage to the DD approach is that if two earthquakes occur in near proximity, the paths that the seismic waves travel along to a recording seismic station will be similar, particularly outside of the earthquake source region. By treating the data as the difference in arrival times for this event pair, any errors introduced by complex or unmodeled velocity structures along the propagation path to the station are minimized. This process, known as common mode error suppression, focuses location sensitivity primarily on the region near the source (Jordan and Sverdrup, 1981; Got et al., 1994; Waldhauser and Ellsworth, 2000). This avoids the need for explicit station correction terms typical in older relocation methods (Douglas 1967; Waldhauser and Ellsworth 2000).

By reducing velocity-model and station-correction errors, DD relocations typically improve location precision by orders of magnitude compared to

traditional catalogue locations (Waldhauser and Ellsworth, 2000; Waldhauser and Schaff, 2008). This transformation collapses diffuse seismicity clusters into sharply defined structures (Got et al., 1994; Schaff et al., 2002; Wolfe, 2002). For example, studies on the Northern Hayward fault showed that DD relocations collapsed diffuse locations into sharp images, revealing previously hidden structures such as horizontal lines of hypocentres (Waldhauser and Ellsworth, 2000). This increased resolution allows seismicity to be restricted to specific geological units, providing excellent depth constraints, particularly valuable in induced seismicity studies (Rubin et al., 1999; Biegel et al., 2024b). Similar methods applied in southern Yukon have illuminated a network of discrete faults, as well as previously unknown faults, that accommodate deformation due to oblique collision of the Yakutat microplate with North America (Biegel et al., 2022; Biegel et al., 2024a).

In this work, we apply the DD algorithm by integrating two types of data into the inverse problem. First, traditional arrival times for the P and S-wave phases are obtained from the original NEDB. These catalogue data constrain the larger relative locations between distant earthquake clusters (multiplets) and uncorrelated events (Douglas, 1967; Waldhauser and Schaff, 2008). Second, for events with similar seismic waveforms ('doublets' or 'multiplets'), waveform cross correlations are used to measure the differential arrival times with sub-millisecond precision. These waveform cross-correlation data can yield measurements with precision orders of magnitude higher than manual phase selection (Poupinet et al., 1984; Schaff et al., 2004). Combining DD relocation catalogue data with waveform cross-correlation data is widely considered the most effective way to produce high-resolution event locations, and determine inter-event distances within multiplets to the highest accuracy (Poupinet et al., 1984; Waldhauser and Ellsworth, 2000).

We applied the DD approach to the selection of 775 earthquakes extracted from the NEDB, as outlined in the previous section. In this analysis, we used both the catalogue phase data and the calculated waveform cross-correlation data, inverting these simultaneously using the *scrtdd* (Scarabello et al., 2025) implementation of *HypoDD* integrated into the SeisComP software environment (Helmholtz Centre Potsdam GFZ German Research Centre for Geosciences and gempa GmbH, 2008). All combinations of waveform pairs for these events are cross correlated, and the resulting differential travel times are inverted with the catalogue phase arrival times to produce the final DD relocated catalogue. In this relocation analysis, we use a 1D reference model calculated from a regional average of the velocity model derived by Estève et al. (2022). For the DD relocation, we performed a number of iterations to explore the results based on selectable parameters in the software, and used the parameterizations below:

- a minimum of 4 defining phases common between stations;
- a minimum of 4 neighbouring events for each event in a chain;
- a maximum of 80 neighbouring events for each event in a chain;
- a maximum search ellipsoid of 10 km;
- P-wave minimum cross-correlation coefficient of 0.5;
- P-wave cross-correlation window of ± 0.75 s around the phase arrival;
- S-wave minimum cross-correlation coefficient of 0.5;
- S-wave cross-correlation window of ± 1.0 s around the phase arrival;
- waveforms band-pass filtered between 1–20 Hz;
- minimum signal to noise ration (SNR) of 2 for phases;
- noise window -3 s to -0.35 s prior to the phase arrival; and
- signal window -0.35 s to 1.0 s around the phase arrival.

Many of the selected parameters optimum values are dictated by the relative geometry of the stations and the events in the region (i.e., the distances between pairs of events and stations).

Results and discussion

Figure 3 illustrates our relocated earthquake catalogue for the RM region. It is apparent from examining the catalogue in map view that the quality control steps inherent to the DD workflow has removed some isolated seismicity (i.e., not in spatial clusters) that occurred throughout the region. It is important to note that this does not suggest that these events are not

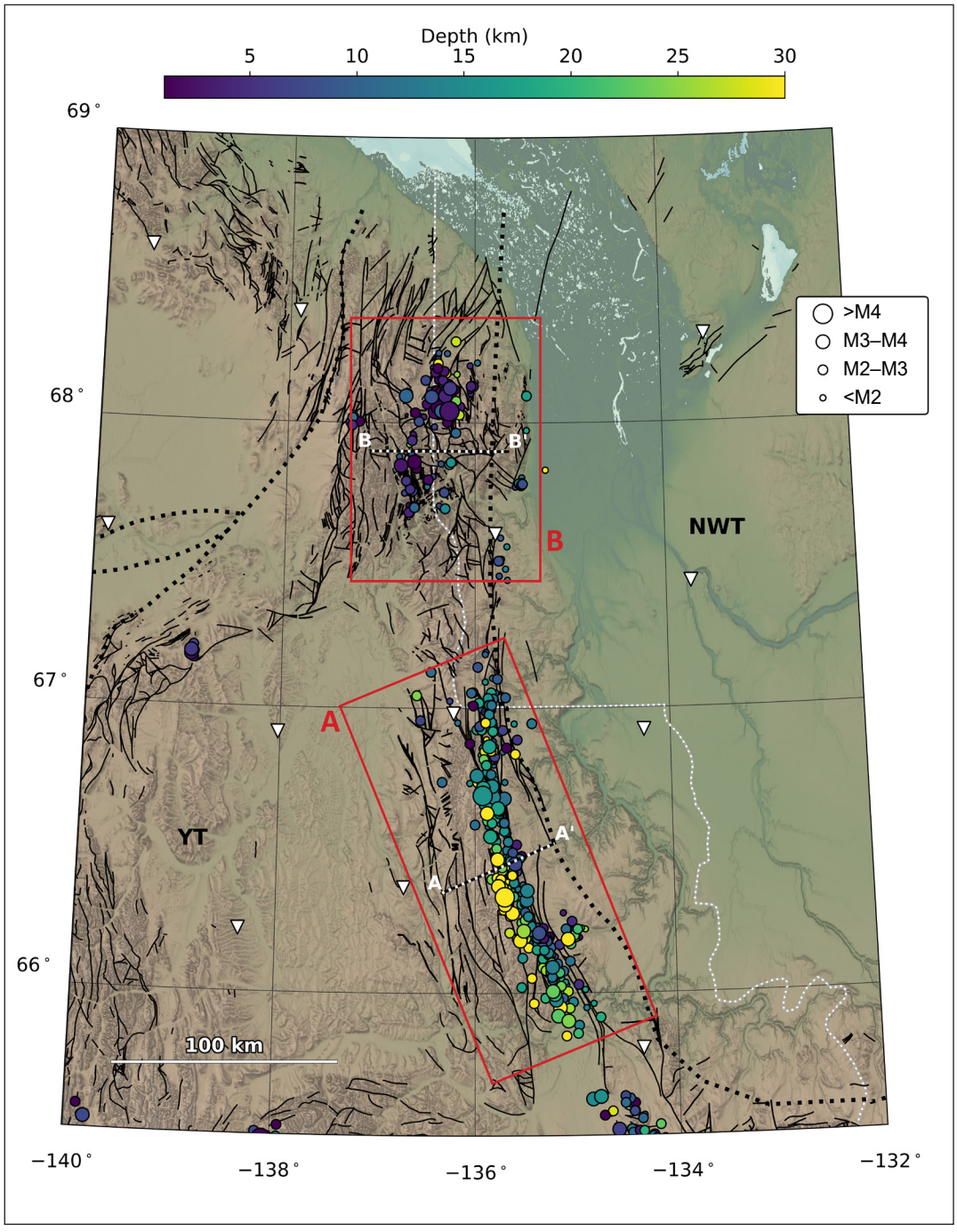


Figure 3. *Map view of the relocated catalogue of 594 earthquakes across the Richardson Mountains study region. Earthquake depths are denoted by the colour of the circle, and magnitudes by the size of the circle. Major faults are plotted as dotted lines and 'defined' faults as solid lines, from the Yukon Geological Survey (Yukon Geological Survey, 2016) and Northwest Territories Geological Survey (Northwest Territories Geological Survey, 2018) online repositories. Regions A and B are indicated by red boxes, as discussed in text. Two cross-sectional profiles, A–A' and B–B', are indicated by dashed lines, and illustrated in Figure 5.*

real, or that there is no seismicity where the events have been removed. Rather, this simply indicates that there is not sufficient seismicity to be robustly inverted within the DD framework. Therefore, the isolated events are excluded from our subsequent analysis. The final relocated catalogue includes 594 events.

The relocated earthquake catalogue highlights three main areas where seismicity meets the DD criteria for clustering, and as a result the spatial patterns of these events are much more clearly illuminated. The first area is the seismicity at the southernmost extent of the map, at the corner where the RM rotate and meet the Mackenzie Mountains. Second, moving northward, the most significant cluster of seismicity is associated with the main strand of the RFS, and locates predominantly along the easternmost front range of the RM, between approximately 65.75°N and 67.25°N. We refer to this region as A and denote the cross-section through it with profile A–A'. Finally, there is a more distributed zone of seismicity farther to the north, which we refer to as B, and illustrate with the cross-section profile B–B'. Region B seismicity occurs immediately to the north of the Richardson anticlinorium, within the White Mountains uplift of the Babbage basin (see Figure 2, Cecile et al., 2022). We observe a paucity of seismicity along the RM in the area between the main regions of seismicity A and B. We note that this lack of seismicity is also apparent in the original NEDB and is likely not due to the DD clustering and quality control processes. This may indicate that either regions A and B are distinct and disconnected, or that this intervening zone is presently locked.

Figure 4 illustrates the depth distributions of events in the NEDB catalogue and the relocated DD catalogue. The peaks in depth values for the NEDB are a result of fixing the depths manually by seismic analysts for most events when there were insufficient stations to constrain a free depth during the original location process. Different values of the fixed depth have been used over decades of the catalogue, resulting in the artificial peaks observed at 1, 5, 10, 15 and 20 km depths. In the relocated DD catalogue, it is clear that the depth distribution of events has been reallocated across the range; however, 2/3 to 3/4 of events are located to

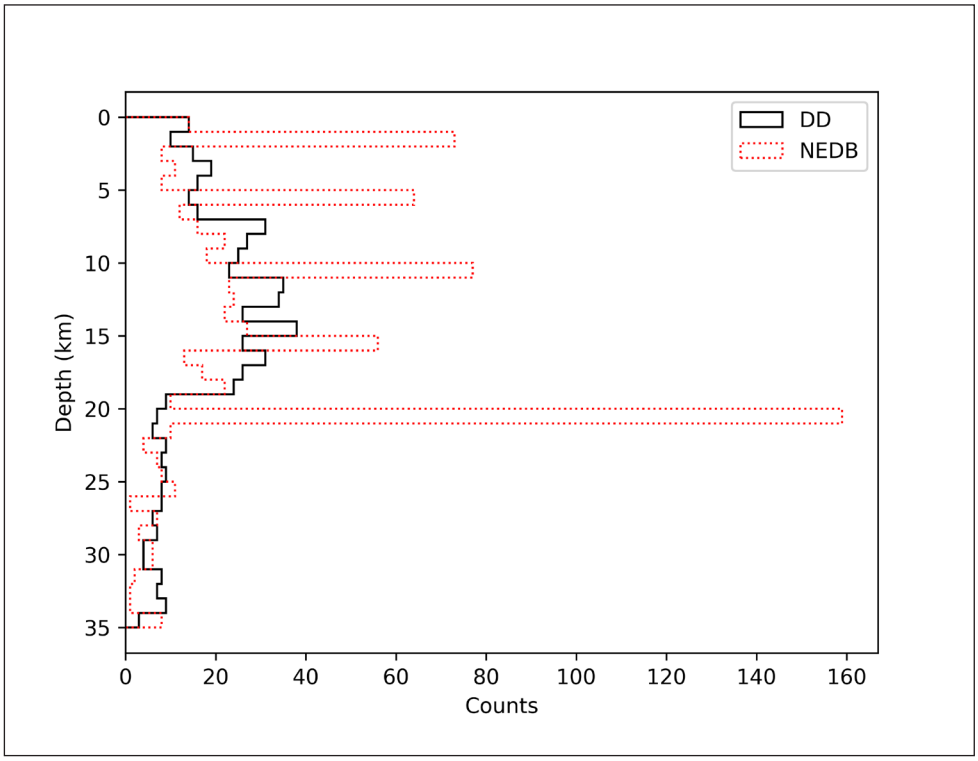


Figure 4. *Histograms of earthquake depths computed for the NEDB events (in red) within the Richardson Mountains study region and the relocated double-difference (DD) catalogue (in black). We note that the peaks in the depths of the NEDB depth distribution are due to common fixed event depths when free depths could not be constrained. These artifacts are removed by the DD relocation process.*

depths shallower than 20 km. Figure 5 illustrates the depths of seismicity along the profiles A–A' and B–B'. The profile locations are shown in Figure 3. All events within 20 km of the profile are projected onto it. The figure further highlights the catalogue artifacts due to manual selection of event depths in the NEDB, as well as the general diffusivity of seismicity.

Region A

Upon examination of region A in Figures 2 and 3, it is clear that the relocation procedure has significantly reduced the diffusivity of the pattern of seismicity, and events are concentrated along the easternmost edge of the RFS. Most of these events locate inboard of the inferred eastern limit of Cordilleran deformation (the dashed black line east of region A seismicity in Figure 3). Furthermore, the main branch of seismicity appears to align along a sub-linear feature dipping westward. The dip of this cluster of seismicity is clearly seen in cross-sectional view (Figure 5), and events at the eastern leading edge are shallower and deepen westward.

Figure 5a,c illustrates the vertical extent of seismicity for profile A–A'. The top panel (Fig. 5a) illustrates the NEDB catalogue along this profile: the grey circles are the complete NEDB, whereas those in red represent the window from 2015 to 2021 during the TA deployment and improved seismic station density. It is challenging to identify any consistent spatial pattern in the precise east–west concentration of seismicity, nor any specific pattern in depth, when considering the entire

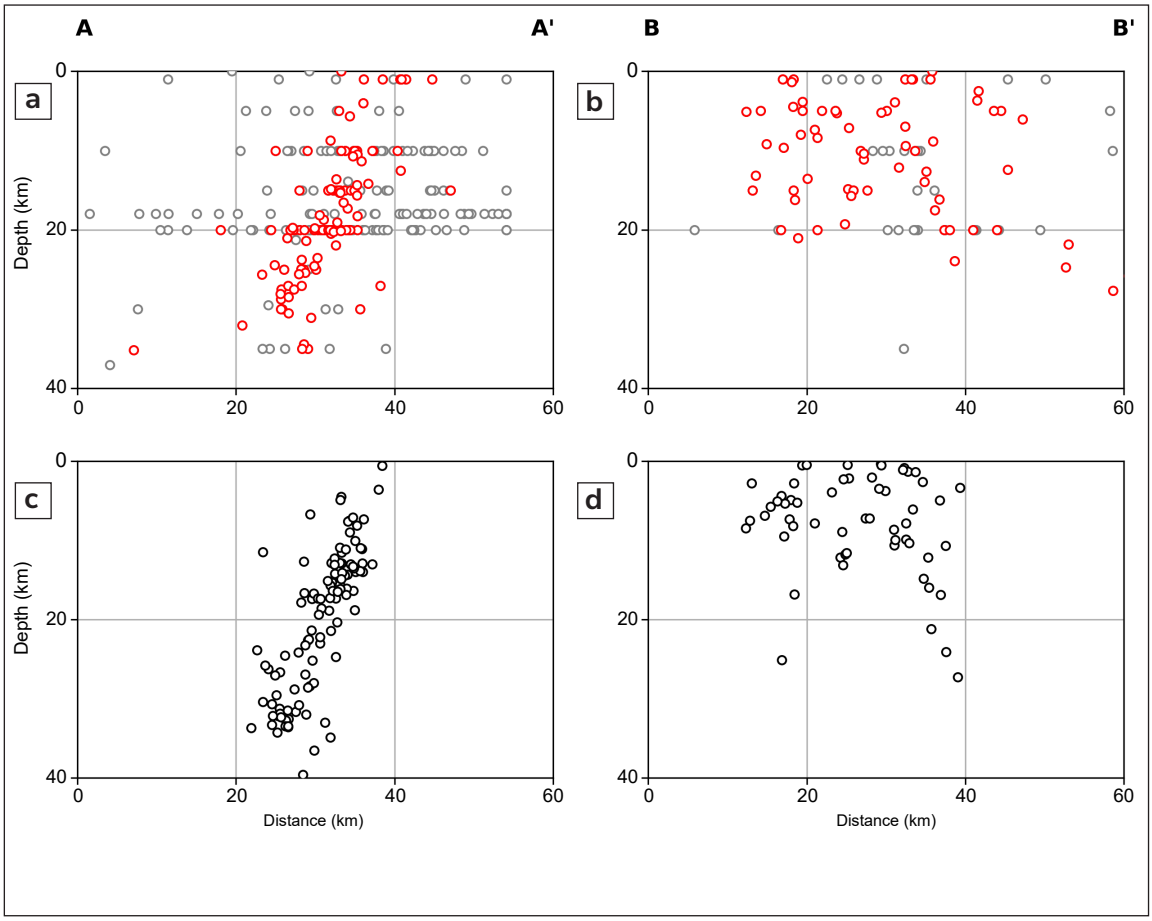


Figure 5. *Cross-sections of earthquake catalogues. Seismicity in the NEDB is displayed in plots* **(a)** *and* **(b)**. *Events considered for relocation are illustrated in red, other NEDB events (mostly outside of the 2015 to 2021 period) are illustrated in grey. Seismicity in the relocated catalogue is illustrated in plots* **(c)** *and* **(d)**. *Locations of cross sections (A–A' and B–B') are illustrated in Figure 3.*

NEDB. However, the relocated DD catalogue along A–A' (Fig. 5c), defines a clear, consistent westward-dipping structure, from near the surface to a depth of ~35 km, which is the inferred base of the crust (Audet et al., 2020). Based on the width of the seismicity across this depth range, we estimate the dip of this seismogenic zone to be ~75°. Both the depth and the dip of this seismogenic zone are consistent across the 150 km north–south extent. Notably, this seismicity is significantly deeper than observed in other parts of the Yukon (Drooff and Freymueller, 2023; Biegel et al., 2024a), highlighting the unique deformation in the RM area.

Extrapolating this dipping feature to the surface along most of its north–south length, it appears to intersect very closely with the surface trace of the easternmost segments of the Knorr fault, a normal fault that accommodated past rifting (e.g., Cecile et al., 1985; Cecile et al., 2022). The direction and dip of the seismogenic zoom we observe is compatible with modern seismicity reactivating an existing normal structure at depth.

Region B

Farther to the north, the seismicity of region B is not narrowly concentrated along the eastern front ranges of the RM, as is the case with seismicity in region A. Instead, here, we observe diffuse seismicity across the mountain range, despite the DD relocations. We note that the topographic expression is much wider in this region, as it incorporates a wider zone of deformation encompassing the White Mountains uplift, Barn uplift, and stretching to the British Mountains farther west. Along the southern boundary of this region, the PFS enters from the southwest, whereas the RFS enters from the south at the southeast corner. Finally, the HLFS departs to the northeast from the northernmost extent of the front ranges. This zone therefore records a complex interplay of pre-existing structures that supported significant amounts of deformation over hundreds of millions of years . In this context, the more distributed seismicity occurring across this region, suggests there is no single preferred active fault strand on which the seismicity has coalesced, in contrast to region A. Rather, seismicity clearly remains distributed across much of the width of the mountain range and active deformation zone.

The distribution of seismicity indicated in cross-section B–B' is illustrated in Figure 5b,d. Here, the differences between the starting NEDB catalogue and the relocated catalogue appear laterally less significant compared to region A. The apparent loss of seismicity east of the 40 km point along the profile is predominantly due to the clustering and quality control processes. The relatively sparse seismicity along the Bug Creek fault, the presumed active easternmost fault of the Aklavik Front Ranges, is retained as a consequence of selecting only those events suitable for inversion of differential travel times. However, we note that the relocation procedure indicates that much of the seismicity in region B is hosted on shallow (<10 km deep) structures, or that the seismogenic thickness of the crust in this area is more limited (Biegel et al., 2024a). This is consistent with previous observations of Estève et al. (2022), who propose the seismogenic thickness of the crust shallows northward through the RM, potentially due to increasing crustal temperatures.

Concluding remarks

This work re-examines a subset of the modern earthquake catalogue in northwestern Canada, along the RM, through application of the DD earthquake relocation process. Our relocated catalogue leads to several key findings, listed below.

- There is a reliability of inferred earthquake depths with the removal of catalogue artifacts due to manually fixed depths in the 0–20 km range.

- Much of the seismicity along the main branch of the RM is in close proximity to the surface expression of the Knorr fault and maintains a consistent ~75° westward dip along the entire ~150 km length of the easternmost edge of the RFS. This is compatible with reactivation of the normal fault surface of the Knorr fault.

- Seismicity farther north along the RM, within the complex White Mountains and Barn uplifts, is more diffuse without a dominant active structure.

These preliminary findings motivate the need for ongoing and additional study of active tectonics in the area. Specifically, the utilization of additional data recorded on seismic stations deployed recently through the WARNS initiative will enable further enhancement of earthquake catalogues. An outstanding tectonic question is the connection and relation of the Bug Creek fault to the HLFS. Additionally, the seismic quiescence along a ~75 km segment of the RM that we note from

both the NEDB and our relocated catalogue may imply a seismic gap or a change in seismogenic capacity of the crustal column. This has implications for maximum possible seismogenic fault size, and therefore seismic hazards. These questions will be addressed in future work. Our initial re-examination of the modern earthquake catalogue in the RM will contribute to improved understanding of the geological history and resource potential of the region, as well as support decision-making that mitigates natural hazards for Canada's northern communities.

Competing interests

The authors of this manuscript declare no competing interests.

Acknowledgments

We respectfully acknowledge and thank Yukon First Nations and Alaska Natives for providing access to their lands to install most of the seismic instruments used in this study. We are grateful to reviews from C. Estève (University of Vienna). Seismic data used in this study was obtained from the Earthscope Data Management Centre and the Canadian Hazards Information Service National Data Repository.

References

Audet, P., Schutt, D.L., Schaeffer, A.J., Estève, C., Aster, R.C. and Cubley, J.F., 2020. Moho variations across the northern Canadian Cordillera. Seismological Society of America, vol. 91, no. 6, p. 3076–3085.

Biegel, K., Gosselin, J.M. and Dettmer, J., 2022. Preliminary double-difference relocation earthquake catalogue for southwestern Yukon centred along the Denali fault zone. *In:* Yukon Exploration and Geology 2022, K.E. MacFarlane (ed.), Yukon Geological Survey, Government of Yukon, p. 1–18, plus digital appendices.

Biegel, K., Gosselin, J.M., Dettmer, J., Colpron, M., Enkelmann, E. and Caine, J.S., 2024a. Earthquake relocations delineate a discrete fault network and deformation corridor throughout southeast Alaska and southwest Yukon. Tectonics, vol. 43, no. 5, https://doi.org/10.1029/2023TC008140.

Biegel, K.M., Dettmer, J., Igonin, N. and Eaton, D.W., 2024b. Double-pair double-difference relocation improves depth precision and highlights detailed 3D fault geometry for induced seismicity in Alberta, Canada. Seismological Research Letters, vol. 96, no. 3, p. 100–112, https://doi.org/10.1785/0220240194.

Busby, R.W. and Aderhold, K., 2020. The Alaska transportable Array: As built. Seismological Research Letters, vol. 91, no. 6, p. 3017–3027, https://doi.org/10.1785/0220200154.

Canadian Hazards Information Service, 1985. Canadian National Earthquake Database. Natural Resources Canada, https://doi.org/10.17616/R3TD24 [accessed 15/11/2025].

Cassidy, J.F. and Bent, A.L., 1993. Source parameters of the 29 May and 5 June, 1940 Richardson Mountains, Yukon Territory, earthquakes. Bulletin of the Seismological Society of America, vol. 83, no. 3, p. 636–659, https://doi.org/10.1785/BSSA0830030636.

Cassidy, J.F. and Bent, A.L., 2025. The Mackenzie Mountains, Northwest Territories, earthquake sequence of 1953 to 1957. Canadian Journal of Earth Sciences, vol. 62, no. 4, p. 923–937, https://doi.org/10.1139/cjes-2024-0132.

Cassidy, J.F., Rogers, G.C. and Ristau, J., 2005. Seismicity in the vicinity of the Snorcle corridors of the northern Canadian Cordillera. Canadian Journal of Earth Sciences, vol. 42, no. 6, p. 1137–1148.

Cecile, M., Hutcheon, I.E. and Gardner, D., 1985. Geology of the northern Richardson anticlinorum. Geological Survey of Canada, Open File 875.

Cecile, M.P., Morrow, D.W. and Williams, G.K., 1997. Early Paleozoic (Cambrian to Early Devonian) tectonic framework, Canadian Cordillera. Bulletin of Canadian Petroleum Geology, vol. 45, no. 1, p. 54–74.

Cecile, M.P., Norford, B.S., Nowlan, G.S. and Uyeno, T.T., 2022. Lower Paleozoic stratigraphy and geology, Richardson Mountains, Yukon (with stratigraphic and paleontological appendices). Geological Survey of Canada, Bulletin 614, https://doi.org/10.4095/329454.

Colpron, M., Strauss, J.V. and McClelland, W.C., 2019. Detrital zircon U-Pb geochronological and Hf isotopic constraints on the geological evolution of North Yukon. *In:* Circum-Arctic Structural Events: Tectonic Evolution of the Arctic Margins and Trans-Arctic Links with Adjacent Orogens, K. Piepjohn, J.V. Strauss, L. Reinhardt and W.C. McClelland (eds.), Geological Society of America Special Paper, Geological Society of America, vol. 541, p. 397–437, https://doi.org/10.1130/2018.2541(19).

Douglas, A., 1967. Joint epicentre determination. Nature, vol. 215, p. 47–48.

Drooff, C. and Freymueller, J.T., 2023. New insights into the active tectonics of the northern Canadian Cordillera from an enhanced earthquake catalog. Journal of Geophysical Research: Solid Earth, vol. 128, no. 12, https://doi.org/10.1029/2023JB026793.

Enkelmann, E., Finzel, E. and Arkle, J., 2019. Deformation at the eastern margin of the northern Canadian Cordillera: Potentially related to the opening of the North Atlantic. Terra Nova, vol. 31, no. 3, p. 151–158, https://doi.org/10.1111/ter.12374.

Estève, C., Liu, Y., Koulakov, I., Schaeffer, A.J. and Audet, P., 2022. Seismic evidence for a weakened thick crust at the Beaufort Sea continental margin. Geophysical Research Letters, vol. 49, https://doi.org/10.1029/2022GL100158.

Eyster, A.E., Fu, R.R., Strauss, J.V., Weiss, B.P., Roots, C.F., Halverson, G.P., Evans, D.A.D. and Macdonald, F.A., 2017. Paleomagnetic evidence for a large rotation of the Yukon block relative to Laurentia: Implications for a low-latitude Sturtian glaciation and the breakup of Rodinia. Geological Society of America Bulletin, vol. 129, no. 1/2, p. 38–58.

Faehnrich, K., McClelland, W.C., Webb, L.E., Rasbury, E.T., Colpron, M. and Strauss, J.V., 2025. Cretaceous strike–slip displacement along the Porcupine fault system and potential links to the opening of the Canada Basin. Canadian Journal of Earth Sciences, vol 62, no. 10, https://doi.org/10.1139/cjes-2025-0013.

Gabrielse, H., 1991. Structural Styles. *In:* Geology of the Cordilleran Orogen in Canada, H. Gabrielse and C.J. Yorath (eds.), Geology of Canada, Geological Survey of Canada, p. 571–675.

Geological Survey of Canada, 2013. Public Safety Geoscience Program Canadian Research Network. International Federation of Digital Seismograph Networks. https://doi.org/10.7914/SN/PQ [accessed 30/11/2025].

Gosselin, J.M., Biegel, K.M., Dettmer, J., Gilbert, H., Colpron, M. and Enkelmann, E., 2024. Crustal stress near the Yakutat microplate collision from probabilistic earthquake focal mechanisms. Canadian Journal of Earth Sciences, vol. 62, no. 4, p. 807–820, https://doi.org/10.1139/cjes-2024-0095.

Got, J.-L., Fréchet, J. and Klein, F.W., 1994. Deep fault plane geometry inferred from multiplet relative relocation beneath the south flank of Kilauea. Journal of Geophysical Research, vol. 99, no. B8, p. 15375–15386.

Helmholtz Centre Potsdam GFZ German Research Centre for Geosciences and gempa GmbH, 2008. The SeisComP seismological software package, GFZ Data Services, https://doi.org/10.5880/GFZ.2.4.2020.003.

Hyndman, R.D., Cassidy, J.F., Adams, J., Rogers, G.C. and Mazzotti, S., 2005a. Earthquakes and seismic hazard in the Yukon-Beaufort Mackenzie. Canadian Society of Exploration Geophysicists, Recorder, vol. 30, no. 5, p. 32–43.

Hyndman, R.D., Flück, P., Mazzotti, S., Lewis, T.J., Ristau, J. and Leonard, L., 2005. Current tectonics of the northern Canadian Cordillera. Canadian Journal of Earth Sciences, vol. 42, no. 6, p. 1117–1136, https://doi.org/10.1139/e05-023.

IRIS Transportable Array, 2003. USArray Transportable Array. International Federation of Digital Seismograph Networks, https://doi.org/10.7914/SN/TA [accessed 30/11/2025].

Jeletsky, J.A., 1962. Pre-Cretaceous Richardson Mountains trough—Its place in the tectonic framework of Arctic Canada and its bearing on some geosynclinals concepts. Transactions of the Royal Society of Canada, vol. 56, no. 3, p. 55–84.

Jordan, T.H. and Sverdrup, K.A., 1981. Teleseismic location techniques and their application to earthquake clusters in the South-Central Pacific. Bulletin of the Seismological Society of America, vol. 71, no. 4, p. 1105–1130.

Kolaj, M., Halhcuk, S.C. and Adams, J., 2023. Sixth-generation seismic hazard model of Canada: Grid values of mean hazard to be used with the 2020 National Building Code of Canada (ver. 1.0). Geological Survey of Canada, Natural Resources Canada, Open File 8950, https://doi.org/10.4095/331497.

Lane, L.S., 1996. Geometry and tectonics of early Tertiary triangle zones, northeastern Eagle Plains, Yukon Territory. Bulletin of Canadian Petroleum Geology, vol. 44, p. 337–348.

Lane, L.S., 1997. Cretaceous and Tertiary. *In:* The Geology, Mineral and Hydrocarbon Potential of Northern Yukon Territory and Northwestern District of Mackenzie, D.K. Norris (ed.), Geological Survey of Canada, Natural Resources Canada, Bulletin 422, p. 301–318.

Lane, L.S., 1998. Late Cretaceous–Tertiary tectonic evolution of northern Yukon and adjacent Arctic Alaska. American Association of Petroleum Geologists Bulletin, vol. 82, no. 7, p. 1353–1371.

Lane, L.S., 2002. Tectonic evolution of the Canadian Beaufort Sea – Mackenzie Delta region: a brief review. Canadian Society of Exploration Geophysicists, Recorder, vol. 27, no. 2, p. 49–56.

Lane, L.S., 2007. Devonian–Carboniferous paleogeography and orogensis, northern Yukon and adjacent Arctic Alaska. Canadian Journal of Earth Sciences, vol. 44, no. 5, p. 679–694.

Lane, L.S. and Dietrich, J.R., 1995. Bedrock geology and offshore structural trends. *In:* Geological Atlas of the Beaufort-Mackenzie Area, J. Dixon (ed.), Geological Survey of Canada.

Leonard, L.J., Hyndman, R.D., Mazzotti, S., Nykolaishen, L., Schmidt, M. and Hippchen, S., 2007. Current deformation in the northern Canadian Cordillera inferred from GPS measurements. Journal of Geophysical Research, vol. 112, no. 11, p. 1–15, https://doi.org/10.1029/2007JB005061.

Mazzotti, S. and Hyndman, R.D., 2002. Yakutat collision and strain transfer across the northern Canadian Cordillera. Geology, vol. 30, no. 6, p. 495–498, https://doi.org/10.1130/0091-7613(2002)030<0495:YCASTA>2.0.CO;2.

Mazzotti, S., Leonard, L.J., Hyndman, R.D. and Cassidy, J.F., 2008. Tectonics, dynamics, and seismic hazard in the Canada–Alaska Cordillera. *In:* Active Tectonics and Seismic Potential of Alaska, J.T. Freymueller, P.J. Haeussler, R.L. Wesson and G. Ekström (eds.), vol 179, p. 297–319. AGU Geophysical Monograph Series, American Geophysical Union, https://doi.org/10.1029/179GM17.

McClelland, W.C., Strauss, J.V., Colpron, M., Gilotti, J.A., Faehnrich, K., Malone, S.J., Gehrels, G.E., Macdonald, F.A. and Oldow, J.S., 2021. Taters versus sliders: Evidence for a long-lived history of strike-slip displacement along the Canadian Arctic transform system (CATS). GSA Today, vol. 31, no. 7, p. 4–11, https://doi.org/10.1130/GSATG500A.1.

Morrow, D.W., 1999. Lower Paleozoic stratigraphy of northern Yukon Territory and northwestern District of Mackenzie. Geological Survey of Canada, Bulletin 538, 202 p., https://doi. org/10.4095/210998.

Natural Resources Canada, 1975. Canadian National Seismograph Network. Natural Resources Canada, https://doi.org/10.7914/SN/CN [accessed 30/11/2025].

Nelson, J.L., Colpron, M. and Israel, S., 2013. The Cordillera of British Columbia, Yukon, and Alaska: Tectonics and metallogeny. *In:* Tectonics, Metallogeny, and Discovery: The North American Cordillera and Similar Accretionary Settings, M. Colpron, T. Bissig, B.G. Rusk and J.F.H. Thompson (eds.), Society of Economic Geologists, https://doi.org/10.5382/SP.17.03.

Norris, D.K., 1985. Eastern Cordilleran foldbelt of Northern Canada: Its structural geometry and hydrocarbon potential. The American Association of Petroleum Geologists Bulletin, vol. 69, no. 5, p. 788–808.

Norris, D.K., 1997. Geological setting. *In:* The Geology, Mineral and Hydrocarbon Potential of Northern Yukon Territory and Northwestern District of Mackenzie, D.K. Norris (ed.), Geological Survey of Canada, Bulletin 422, p. 21–64, https://doi.org/10.4095/208886.

Northwest Territories Geological Survey, 2018. Geological compilation of Canada, NWT portion: Faults. Government of the Northwest Territories, https://ntgs-open-data-ntgs.hub.arcgis.com/datasets/NTGS::nwt-geology-gscmapd1860a/about?layer=0 [accessed 15/05/2025]. .

Pinet, N., 2021. Structural geology of the eastern Richardson Mountains, Yukon and Northwest Territories: Some field observations and a note of caution for palinspastic reconstructions. *In:* Yukon Exploration and Geology 2020, K.E. MacFarlane (ed.), Yukon Geological Survey, p. 1–18.

Poupinet, G., Ellsworth, W.L. and Fréchet, J., 1984. Monitoring velocity variations in the crust using earthquake doublets: An application to the Calaveras fault, California. Journal of Geophysical Research: Solid Earth, vol. 89, no. B7, p. 5719–5731.

Rohr, K.M.M., Lane, L.S. and MacLean, B.C., 2011. Subsurface compressional structures and facies transitions imaged by seismic reflection data, eastern margin of Richardson trough, Peel Plateau, Yukon. Bulletin of Canadian Petroleum Geology, vol. 59, no. 2, p. 131–146.

Rubin, A.M., Gillard, D. and Got, J.-L., 1999. Streaks of microearthquakes along creeping faults. Nature, vol. 400, no. 6745, p. 635–641.

Ruppert, N.A. and West, M.E., 2020. The impact of the USArray on earthquake monitoring in Alaska. Seismological Research Letters, vol. 91, no. 2A, p. 601–610, https://doi.org/10.1785/0220190227.

Scarabello, L., Abdollahzadeh, M., Becker, J. and Pickle, R., 2025. Swiss-seismological-service/scrtdd: v1.8.9. Zenodo, https://doi.org/10.5281/zenodo.16797309.

Schaeffer, A.J., Gosselin, J.M., Audet, P., Cairns, S., Colpron, M. and Elliott, B., 2025. The Western Arctic Regional Network of Seismographs (WARNS): History, challenges, and improvements in continuous broadband seismic data recordings in northwestern Canada. *In:* Yukon Exploration and Geology Technical Papers, 2024, L.H. Weston, A. Stuart, S.K. Schultz, A.D. Brubacher and D.C. Cronmiller (eds.), Yukon Geological Survey, Government of Yukon, p. 51–73.

Schaff, D.P., Bokelmann, G.H., Beroza, G.C., Waldhauser, F. and Ellsworth, W.L., 2002. High-resolution image of Calaveras Fault seismicity. Journal of Geophysical Research, vol. 107, no. B9, 16 p.

Schaff, D.P., Bokelmann, G.H., Ellsworth, W.L., Zanzerkia, E., Waldhauser, F. and Beroza, G.C., 2004. Optimizing correlation techniques for improved earthquake location. Bulletin of the Seismological Society of America, vol. 94, no. 2, p. 705–721.

Shephard, G.E., Müller, R.D. and Seton, M., 2013. The tectonic evolution of the Arctic since Pangea breakup: Integrating constraints from surface geology and geophysics with mantle structure. Earth-Science Reviews, vol. 124, p. 148–183, https://doi.org/10.1016/j.earscirev.2013.05.012.

Stephan, T. and Enkelmann, E., 2025. All aligned on the western front of North America? Analyzing the stress field in the northern Cordillera. Tectonics, vol. 44, no. 9, https://doi.org/10.1029/2025TC009014.

Stephenson, R.A., Dietrich, J.R. and Lane, L.S., 1994. Crustal structure and tectonics of the southeastern Beaufort Sea continental margin. Tectonics, vol. 13, p. 389–400.

Strauss, J.V., Allen, T.J., Malinowski, J., Feng, X., Fraser, T., Melchin, M.J., Taylor, J.F., Day, J., Gill, B.C. and Sperling, E.A., 2020. The Road River Group of northern Yukon, Canada: Early Paleozoic deep-water sedimentation within the Great American Carbonate Bank. Canadian Journal of Earth Sciences, vol. 57, no. 10, p. 1193–1219.

von Gosen, W., Piepjohn, K., McClelland, W.C. and Colpron, M., 2019. Evidence for the sinistral Porcupine shear zone in North Yukon (Canadian Arctic) and geotectonic implications. *In:* Circum-Arctic Structural Events: Tectonic Evolution of the Arctic Margins and Trans-Arctic Links with Adjacent Orogens, K. Piepjohn, J.V. Strauss, L. Reinhardt and W.C. McClelland (eds.), Geological Society of America Special Paper, Geological Society of America, vol. 541, p. 473–491, https://doi.org/10.1130/2019.2541(21).

Waldhauser, F., 2001. HypoDD: A computer program to compute double-difference earthquake locations. Open-File Report 01-113. US Geological Survey, https://doi.org/10.3133/ofr01113.

Waldhauser, F. and Ellsworth, W.L., 2000. A double-difference earthquake location algorithm: Method and application to the northern Hayward fault, California. Bulletin of the Seismological Society of America, vol. 90, no. 6, p. 1353–1368, https://doi.org/10.1785/0120000006.

Waldhauser, F. and Schaff, D.P., 2008. Large-scale relocation of two decades of northern California seismicity using cross-correlation and double-difference methods. Journal of Geophysical Research, vol. 113, no. B8, https://doi.org/10.1029/2007JB005479.

Wolfe, C.J., 2002. On the mathematics of using difference operators to relocate earthquakes. Bulletin of the Seismological Society of America, vol. 92, no. 8, p. 2879–2892.

Yukon Geological Survey, 2016. A Geological Compilation Map of the Yukon Territory Intended for Use by the Exploration Community, Prospectors and Geologists: Faults. GeoYukon, Government of Yukon, https://yukon.maps.arcgis.com/home/item.html?id=2695ad28cb2c421a95112313397b844d [accessed 15/05/2025].

Preliminary analysis of the sequence stratigraphy and geochemistry of the Portrait Lake Formation at Macmillan Pass, Yukon, Canada

*Sarah K. Schultz**
Yukon Geological Survey

Octavian Catuneanu
University of Alberta

John B. Gordon
Spectrum Geosciences

Schultz, S.K., Catuneanu, O. and Gordon, J.B., 2026. Preliminary analysis of the sequence stratigraphy and geochemistry of the Portrait Lake Formation at Macmillan Pass, Yukon, Canada. *In*: Yukon Exploration and Geology 2025, A. Stuart, L.H. Weston and S.K. Schultz (eds.), Yukon Geological Survey, Government of Yukon, p. 167–190, plus digital appendix.

Abstract

The Upper Devonian Earn Group is a clastic-dominated, deep-water succession that is intersected in outcrop and subsurface drill core throughout the Yukon. In east-central Yukon, the group is subdivided lithostratigraphically into the Portrait Lake and Prevost formations. The Portrait Lake Formation hosts significant lead-zinc ± silver (Pb-Zn ± Ag) mineralization in mudstone-dominated strata at three significant deposits in the Macmillan Pass region. The Portrait Lake Formation is well defined lithostratigraphically; however, a sequence stratigraphic approach to mapping the unit would allow for a better understanding of the evolution of the basin in relation to sedimentation and mineralization phases. By mapping the strata using this approach, it is possible to predict the distribution and extent of ore bodies in relation to the 3D variability of systems tracts and will allow for the prediction of where other ore bodies may exist in the Macmillan Pass district or in other areas of the Selwyn basin. This study presents the initial results of the core logging, x-ray fluorescence (XRF), and organic carbon isotope ($\delta^{13}C$) analyses that were conducted on four cores that were drilled at the Boundary, Jason and Tom properties.

Three major depositional processes have been identified, which include hemipelagic sedimentation, mass transport deposits (grainflow, mudflow, slump) and turbidites (high and low-density). Where coarser grained material that forms the grainflows, slumps and turbidite deposits are present, it is easier to identify stratigraphic horizons that separate depositional processes. This is due to distinct lithological and sedimentological contrasts between the strata above and below the contact. The mudstone-dominated units require additional geochemistry to identify subtle stratigraphic horizons and changes in depositional trends to facilitate regional correlations.

During the Late Devonian, the structural context of deposition shifted from that of a passive margin to an extensional setting. As extension occurs, coarse material is transported to the deep basin and accumulates in topographic lows of graben complexes. This causes the lateral and rapid juxtaposition of coarse-grained material with finer-grained material, complicating stratigraphic correlations in the region.

* sarah.schultz@yukon.ca

Plain language summary

This publication includes the initial geochemical dataset and descriptions for rocks that are between 388 and 359 million years old. The rocks that were studied for this dataset were deposited in deep water (water depths generally exceeding 1 km or more) where sediment (e.g., mud) settles to the ocean floor. Coarser grained material (sand and pebbles) is not typically expected to be found in deep-water deposits. When it is, it was generally brought to deeper water depths from underwater landslides (debris flows) or gravity-driven currents. This understanding is important when we try to interpret the paleogeography of a region and where economic deposits might be located. In the study area, critical minerals are found in the muddier sediment and generally contain lead-zinc ± silver (Pb-Zn ± Ag)-bearing minerals, such as sphalerite and galena that were formed as the mudstone was deposited, or shortly thereafter. These minerals are critical to Canada's drive for a green economy as they are used in the energy sector to build batteries and maintain wind turbines. This study aims to demonstrate where minerals occur in relation to the mudstone and sandstone intervals that were deposited hundreds of millions of years ago. It is challenging to see features in mudstone due to the fine-grained nature of these types of rocks. The geochemical study will inform us of subtle changes in the composition of the rocks, which will in turn allow us to map throughout the study area even in the finer grained units of rocks.

Introduction

The Yukon Geological Survey completed an initial study of Upper Devonian core that was drilled in the Macmillan Pass lead-zinc district. This study comprises a proposed four-year mapping project across east-central Yukon to create a high-resolution account of the sedimentology, stratigraphy and geochemistry of the Earn Group across the Selwyn basin region. The results of the project will be a sequence stratigraphic framework for the Earn Group using the 4-systems tract nomenclature (sensu Catuneanu et al., 2011). Herein, we present the initial results of our first year of data collection along with the objectives and goals for subsequent mapping years.

Location

The Earn Group was logged at Fireweed Metals' exploration property at Macmillan Pass during the summer of 2024. Macmillan Pass is located in east-central Yukon along the border with the Northwest Territories (Fig. 1). The site is accessible by driving the North Canol Road in the summer months when the barge at Ross River is operational.

The Macmillan Pass region hosts lead-zinc ± silver (Pb-Zn ± Ag) mineralization within mudstone-dominated intervals of the Late Devonian. The main deposits at Tom, Jason and Boundary are historical deposits that have received renewed interest when the property was acquired by Fireweed Metals. The company has been drilling seasonally and using the camp in the area since 2017.

Previous work – basin analysis and tectonism

From the Cambrian to Middle Devonian, rocks in the region were deposited in Selwyn basin, which was a deep-water depocenter along the northwestern margin of Laurentia (Figs. 2, 3; Gabrielse, 1967; Gordey and Anderson, 1993). Selwyn basin occurs basinward of the Mackenzie platform that is preserved to the northeast in outcrop belts of the Mackenzie Mountains. At Macmillan Pass, the Ordovician to Middle Devonian strata of the Road River Group comprise deposits that record basinal deep-water deposition. The Middle Devonian is marked by a volcanic suite known as the Macmillan Pass volcanics that separates the underlying Road River Group from the overlying Earn Group. The Earn Group is subdivided into the Portrait Lake Formation (Niddery Lake, Macmillan Pass and Fuller Lake members) and the Prevost Formation (Fig. 2).

The Devonian deposits logged in outcrop and core have been described lithostratigraphically in the literature for the Selwyn basin region (Carne, 1976; Gordey and Anderson, 1993; Cecile, 2000; Abbott, 2013). Fault-bound basins create the compartmentalization of sedimentary facies which results in rapid changes in the distribution of deep-water depositional environments over a relatively short distance. As a result, the naming conventions used to describe Devonian strata vary over relatively short distances within the Selwyn basin. For the present study, the nomenclature outlined in Abbott (2013) is adopted for the Macmillan Pass region (Figs. 1 and 2).

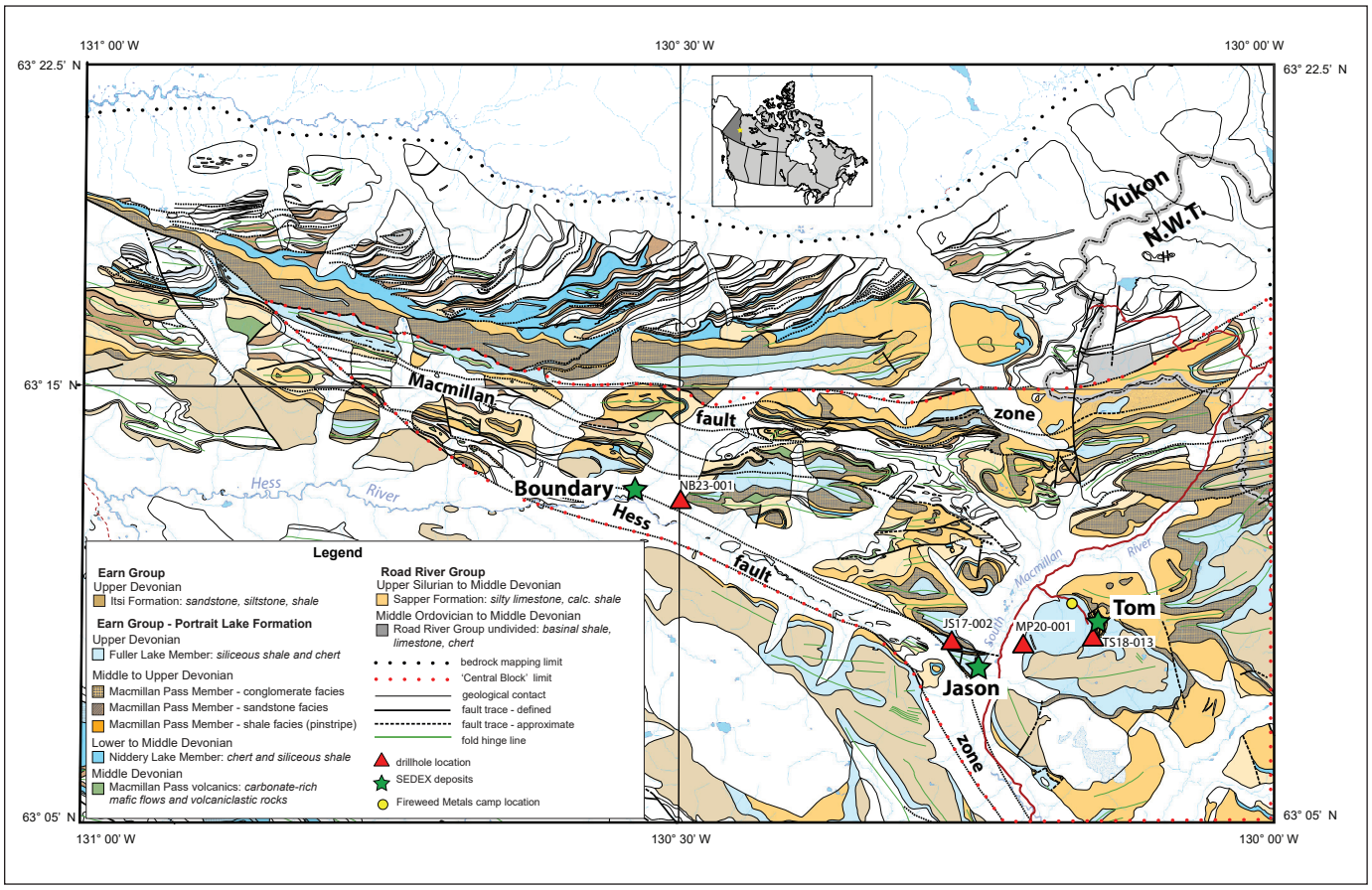


Figure 1. *Geological map of the Macmillan Pass region (after Abbott, 2013; modified from Fraser et al., 2021). Locations of the lead-zinc deposits and cores that were logged and sampled for this study are presented herein.*

During the deposition of the Late Devonian Portrait Lake Formation, the basin transitioned to an active convergent margin and the Macmillan Pass region experienced extensional events that were marked by the reactivation of normal faults in the region (Abbott and Turner, 1991; Nelson et al., 2006; Fraser et al., 2021). The syn-depositional fault reactivation creates horst and graben features in the region which localizes the deposition of coarse clastic material into the basin (Abbott and Turner, 1991; Fraser et al., 2021). The sub-seafloor replacement of barite by sphalerite and galena is inferred to have occurred syn and post-depositionally which resulted in the deposits at Tom, Jason and Boundary (Magnall et al., 2020; 2021; Grema et al., 2024). The strata at Macmillan Pass were later incorporated into the Mesozoic fold and thrust belt, complicating the correlation of stratigraphic units. It is inferred that major tectonic features mapped in the region (Fig. 1; Abbott, 2013) reflect pre-existing Devonian rift structures and divide the area into three distinct tectonic domains which include the North, Central and South blocks (Fig. 1; Abbott, 1983; Abbott and Turner, 1991).

Sequence stratigraphy

Sequence stratigraphy is a methodology of correlating stratal units based on the stacking patterns that develop in the sedimentary succession (Catuneanu et al., 2011). Changes in stratal stacking patterns are controlled by changes in accommodation and sedimentation in relation to fluctuations in relative sea level. Sequence stratigraphically significant surfaces mark changes in the observed stratal stacking patterns and can be traced regionally along depositional strike and down depositional dip. High-resolution sequence stratigraphic correlations require detailed facies analyses and a characterization of surfaces that mark changes in stratal stacking patterns to reconstruct the 3D variability of the sedimentary systems (Zecchin and Catuneanu, 2013; Catuneanu, 2019a,b). This is done to ensure that the deposits have been correctly assigned to their respective systems tracts and depositional systems to map the paleoshoreline and basin evolution (Ainsworth et al., 2017; Zecchin and Catuneanu, 2017).

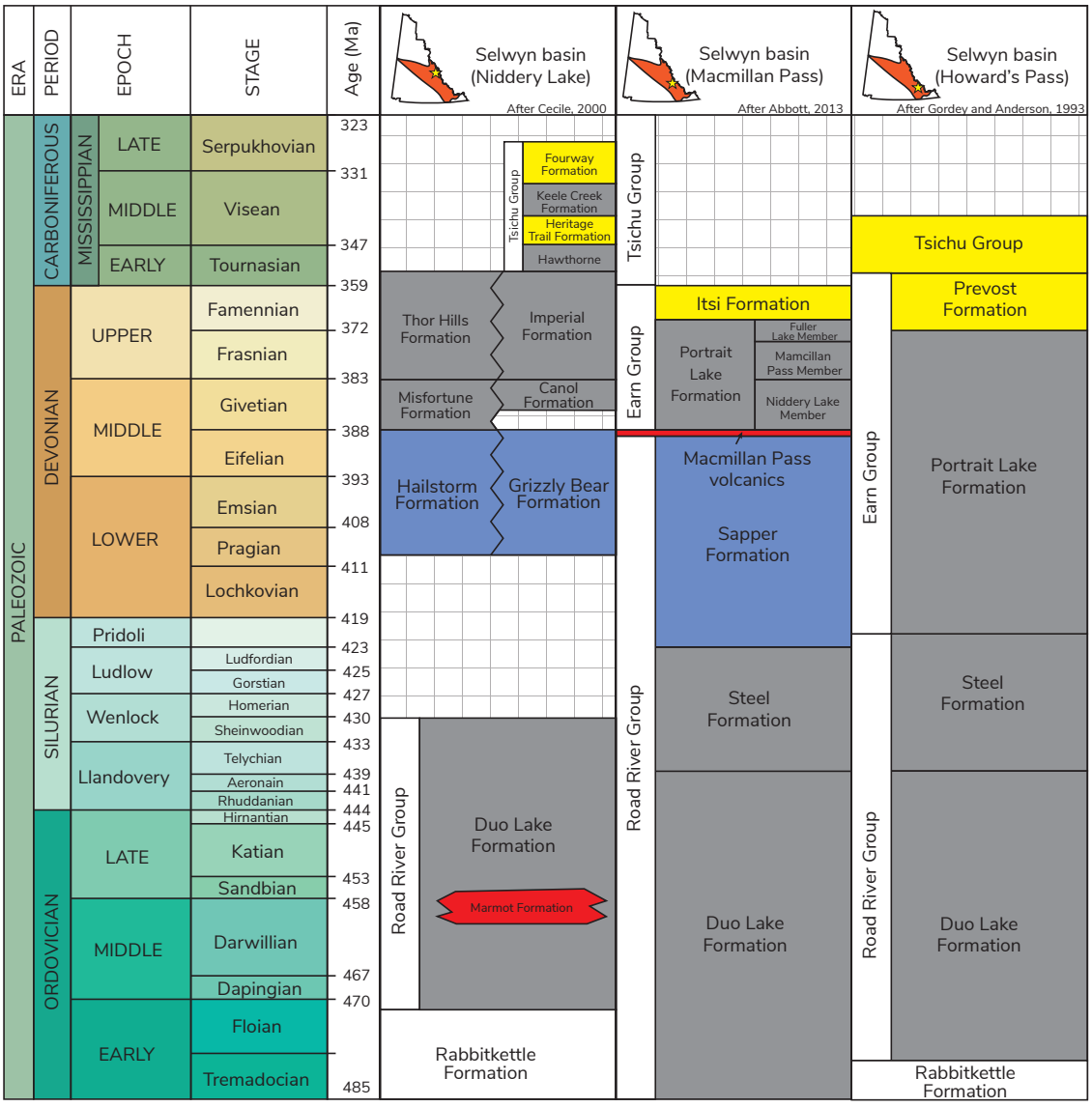


Figure 2. *Table of formations for the Macmillan Pass region (modified from Gordey and Anderson, 1993; Abbott, 2013). The colours on the table represent the following lithologies: yellow – sandstone; grey – shale; blue – limestone; red – volcanic rocks.*

This study follows the 4-systems tract nomenclature (Fig. 4; c.f. Catuneanu et al., 2011), which separates systems tracts into the highstand systems tract (HST; normal regression that follows a transgression); the falling-stage systems tract (FSST; forced regression); the lowstand systems tract (LST; normal regression that follows a forced regression); and the transgressive systems tract (TST). The sequence boundary selected for this study is the maximum flooding surface (MFS), which separates the underlying TST deposits from the overlying HST deposits (Fig. 4). This boundary was selected for the following reasons: it is readily identifiable through geochemical and sedimentological trends; it reflects trends of basin accommodation and subsidence (Galloway, 1989); and it can be used reliably to define cyclicity in the study area.

Sequence stratigraphy in deep-water settings

Deep-water settings are complex depositional systems to model due to the interplay between multiple allogenic and autogenic processes active during deposition; the co-existence of multiple sediment sources into a basin; and the mode of sediment transport into the basin (turbidity flows vs. mass-transport deposits; Catuneanu, 2022). As a result, depositional systems

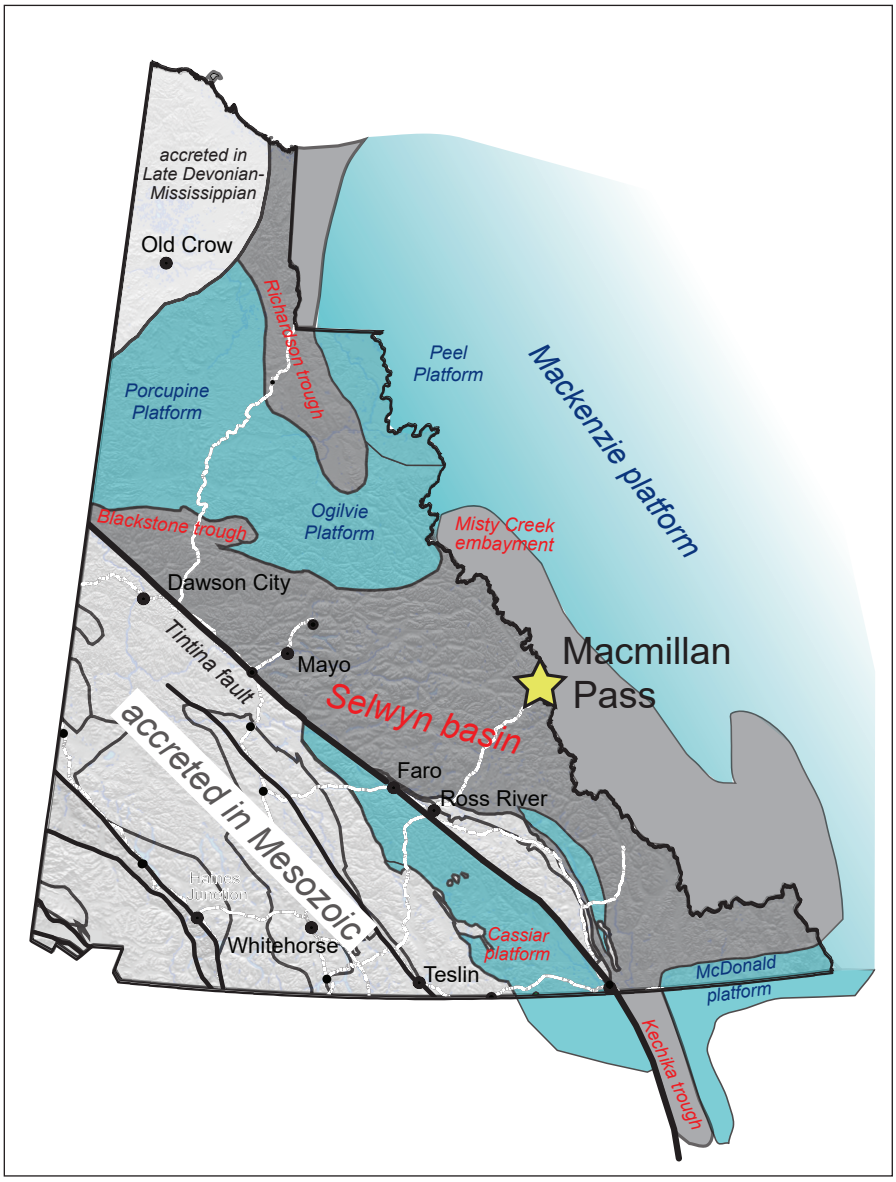


Figure 3. *Distribution of platforms and basins (after Nelson et al., 2006).*

may exhibit a high degree of variability along strike and down dip over a relatively short distance. In the absence of a sediment source, mud may accumulate in significant thicknesses through hemipelagic sedimentation, juxtaposing thick mudstone-dominated successions adjacent to sand-rich turbidites and mass transport deposits (Fig. 5).

Frameworks for the deep basin were developed initially for units that accumulated along a passive margin and were leveraged through the integration of 2D seismic datasets (Vail, 1987). In these models, turbidites can prograde significant distances into the deep basin and have well-developed lobe geometries with levee complexes (Fig. 4). Much of the literature for the deep basin has focused on creating stratigraphic frameworks and facies models for mapping passive margin depositional systems (e.g., Vail et al., 1977; Vail, 1987; Galloway, 1989; Posamentier and Allan, 1999).

Sequence stratigraphy in extensional settings

Sedimentary basins that form in active tectonic settings typically have tectonism outpacing the influence of sea level changes on stratigraphic cyclicity (Catuneanu, 2022). The resulting stratigraphic architectures are typically asymmetrical sequences with distinct variability in the distribution of sedimentary successions. Basin margins typically display higher rates of subsidence, particularly in fault-bound basins, due to the increase in the level of tectonic activity (Catuneanu, 2022). Clinoforms that develop in these settings are typically confined to graben features, and therefore significant lobe features do not develop well into the basin. Instead, the frequent tectonism promotes the collapse of unstable slopes and leads to the development of ramps that redirect sedimentation patterns (Catuneanu, 2022).

Extensional basins generally are subject to rapid changes in sedimentation rates and variations in accommodation. This variability may lead to the suppression of certain systems tracts forming, complicating the creation of a stratigraphic framework. In extensional basins with horst and graben features, the reactivation of fault-bounded features can lead to episodic sedimentation (Catuneanu, 2022), which can impose higher-frequency sequences of deposition (e.g., mass transport deposits and turbidites) into topographic lows in the basin (Fig. 5). Following the rapid creation of accommodation, periods of tectonic quiescence allow for sedimentation to infill topographic lows through hemipelagic sedimentation or through the deposition of mud-dominated turbidites (Fig. 5).

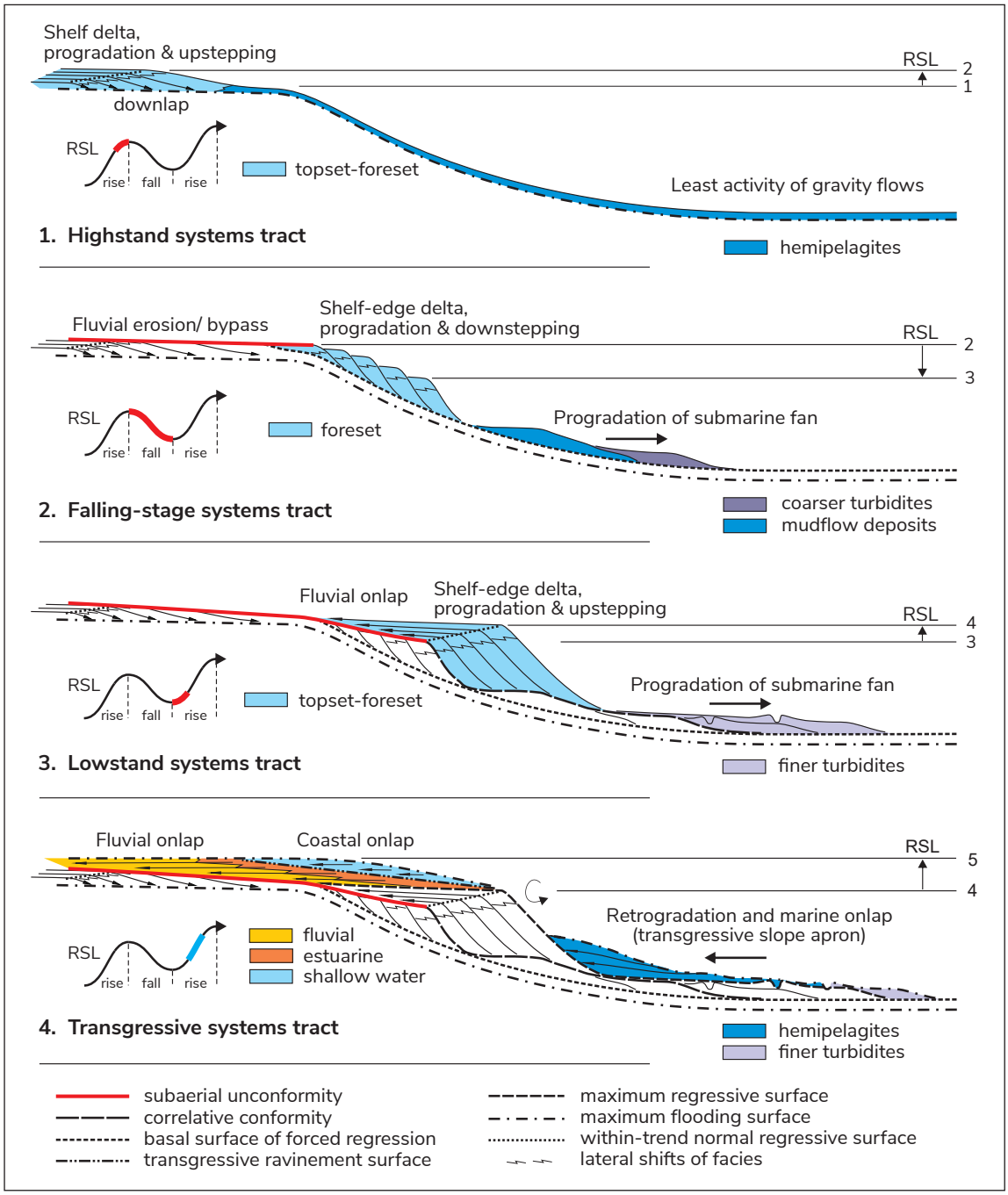


Figure 4. *Trends of sedimentation patterns that occur in siliciclastic passive margin settings (from Catuneanu, 2022). Departures in the expected trends are the result of allogenic and autogenic controls that are active during deposition and affect the accommodation and sedimentation conditions of the basin. RSL – relative sea level.*

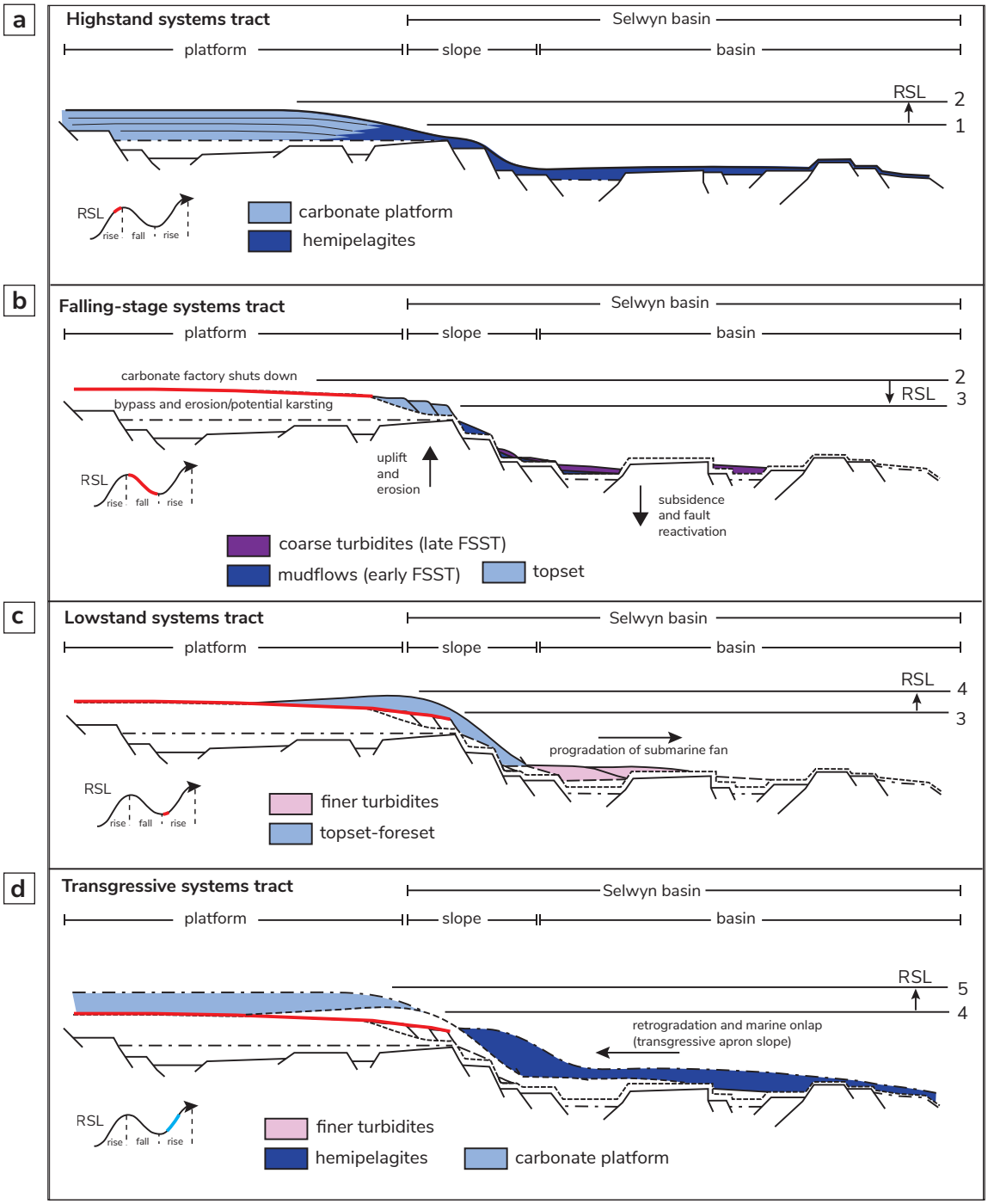


Figure 5. *Fault-bound basin sequence stratigraphic model (RSL – relative sea level). Refer to Figure 4 for the legend of the sequence stratigraphic surfaces.* ***(a)*** *Highstand systems tract (HST). During the deposition of the HST, carbonate platforms build out in a basinward direction in relation to sedimentation outpacing the rise RSL. In the deep basin, hemipelagic sedimentation is the predominant depositional process that occurs. Turbidites may accumulate; however, most continentally derived material is being deposited along the continental shelf.* ***(b)*** *Falling-stage systems tract (FSST). During the FSST, an extensional event occurs that creates a fall in RSL, causing horst and graben features to form or become reactivated in the deep basin. In the continental realm, the carbonate factory shuts down with the fall in sea level; bypass and erosion occur along the shelf. Coarse-grained material is deposited along the shelf to slope transition as shorelines and deltas downstep away from the previous landward position. During early stages of FSST, the slope becomes destabilized, which may result in mudflows being deposited in the deep basin. During the late stages of FSST, the coarse-grained turbidites form spill and fill patterns of sedimentation. The material is deposited in successive topographic lows until accommodation is filled and the material spills over to the next horst and graben feature.* ***(c)*** *Lowstand systems tract (LST). Following the drop in RSL, there is a rise which generates the deposition of the LST. This documents the farthest extent of deposition into the basin during this sequence of deposition. During this time, the continental slope builds in a basinward direction creating a wedge of material. In the deep basin, finer-grained turbidites infill the graben features, which results in localized deposition of sediment and atypical fan architecture.* ***(d)*** *Transgressive systems tract (TST). During the rise in RSL, hemipelagic sedimentation and the deposition of finer-grained turbidites occurs. In early TST, a healing-phase wedge may form in which hemipelagic sedimentation infills any remaining topographic lows in the region. With continued sea level rise, the slope may become destabilized, which results in slumps and mudflows of the slope into the deep basin. As sea level rises, deposition of the carbonate platform may resume. Note: figure is not to scale.*

Systems tracts in extensional settings

During the deposition of the HST, paleoshorelines and shallow-water systems prograde, along with the aggradation of continental topsets. At this time, sedimentation outpaces the rise in relative sea level, generating normal regressive stacking patterns. Slopes prograde in carbonate settings (i.e., 'carbonate shedding'), but less so in siliciclastic settings, where sediment supply to deep water diminishes as a result of topset aggradation. In the deep basin, hemipelagic sedimentation is a predominant depositional process, resulting in thick mudstone-dominated units. Turbidites may accumulate as mudstone-dominated heterolithic units, as most of the coarse-grained continentally derived material is being retained within the continental realm. The HST deposits in the deep basin overlie the maximum flooding surface (MFS) and are typically overlain by the basal surface of forced regression (BSFR) that develops at the base of the FSST deposits.

The deposition of the FSST occurs during the drop in relative sea level. In extensional settings, relative sea-level changes are commonly driven by tectonism. In carbonate realms, the carbonate factory shuts down with progressive subaerial exposure which results in sediment bypass and erosion along the shelf, potentially associated with karst features. In siliciclastic settings, coarse-grained material commonly bypasses the shelf as shorelines and deltas prograde and downstep toward the shelf edge. During early stages of FSST, mudflows and slumps are typically dominant in the deep basin, whereas late stages of FSST are conducive to coarser gravity flows such as turbidity currents and grainflows. The coarse-grained material is deposited in successive topographic lows down the slope until accommodation is filled and the material spills over to the next graben feature. Turbidite units that are deposited during the FSST may not have well-developed fan architectures and may be restricted to local depocenters such as half grabens. The FSST deposits overlie the BSFR and are overlain by a correlative conformity (CC), if an LST develops, or by a maximum regressive surface (MRS). The BSFR is identifiable as an erosional surface at the base of mudflow deposits or slumps, marking a stark change in the sedimentation patterns (Catuneanu, 2022). The CC in deep water is typically marked by a sharp decrease in grain size from the coarser FSST sediments below to the finer LST sediments above, due to the retention of coarser sediments on the shelf within the LST topset. In contrast, the MRS is more cryptic, within a gradational trend of decrease in the sediment grain size from LST into the TST (Catuneanu, 2022).

The subsequent rise in relative sea level leads to the deposition of the LST if the rates of sedimentation exceed the rates of relative sea-level rise at the shoreline. This documents the farthest extent of deposition into the basin during this sequence of deposition and likely reflects tectonic quiescence. During this time, the continental slope progrades, creating a 'lowstand wedge' of sediment clinoforms along the slope. In the deep basin, finer-grained turbidites infill the graben features, which results in localized deposition of sediment and atypical fan architecture. It is noted though that a significant development of the LST may be impeded by the rapid increase in accommodation that may accompany the reactivation of faults in extensional settings, making the development and/or identification of this systems tract challenging. The LST deposits overlie the CC, which are subsequently overlain by the MRS.

When the rise in relative sea level outpaces the rates of sedimentation at the shoreline, the deposition of the TST is initiated. During the rise in relative sea level, hemipelagic sedimentation and the deposition of finer grained turbidites occurs. During TST, a healing-phase wedge may form in which hemipelagic sedimentation infills any remaining topographic lows in the region. With continued sea level rise, the slope may become destabilized, which results in slumps and mudflows into the deep basin. A MFS overlies the TST and is often preserved as a cryptic gradational contact within a potentially condensed section.

Geochemistry

X-ray fluorescence (XRF) has proven to be a valuable tool when mapping sequences stratigraphically in mudstone-dominated successions (Sano et al., 2013; LaGrange et al., 2020; 2025; Harris et al., 2021). Commonly, these successions display subtle variabilities in their composition, lithology and sedimentology that is observable on a microscopic scale, or less commonly, a macroscopic scale. To accurately assess the subtle variabilities of mudstone in deep basins, geochemical analyses are becoming a common tool used to delineate changes in mudstone-dominated successions through whole rock geochemistry, x-ray fluorescence, x-ray diffraction (XRD), or total organic carbon (TOC). The geochemical dataset that is collected from mudstone-dominated intervals can be used to calculate proxies for terrestrial input, carbonate content in relation to distance from the continental shelf, grain size, marine anoxia, and basin restriction (LaGrange et al., 2020, 2025; Fraser et al., 2021).

Methods

Core logging

At Macmillan Pass, four cores were logged in July and August 2024 (Fig., 1; Table 1). Cores were selected based on vintage (younger than 2017 drilling programs), availability, length, as well as intersections including intervals of interest. One core was selected from each deposit in order to demonstrate the abrupt along-strike variations in sedimentation patterns that occur in the region. Core was logged onsite at the Tom property where the material is stored.

X-ray fluorescence (XRF) study

Results for the XRF study on the core from Macmillan Pass were completed in December 2024. In this study, 625 samples were collected from four cored intervals at a 2 m spacing and sent to Spectrum Geosciences Ltd. for analysis. The raw dataset for these cores is provided in Appendix A.

Samples were prepped for analysis by lightly washing the area before analysis to remove dust, mud or debris that could potentially influence the measurements. The sample points were collected using a portable XRF Bruker Tracer 5g model that is placed directly on the core surface. At the start of each analysis day, the XRF device analyzed a check standard to ensure all instrumentation was operating correctly. The data was quality checked and calibrated upon the completion of analysis of each core.

Samples were placed directly on the XRF analyzer window and were run using a 40 kV high-energy beam for 20 seconds to detect heavier elements, and with a 15 kV low-energy beam for 20 seconds to detect light elements. Samples in this study were run under air instead of vacuum purge or helium. This was done to increase accuracy for lighter elements such as silica (Si) and aluminum (Al). The drawback of running the sample under air is a lower detection value for sodium (Na; ~5% error margin).

Facies that contained conglomerate, breccia or significant mineralization were avoided in the sampling process. The clasts of the conglomerate contain reworked clasts in a mudstone to sandstone matrix. Given that each conglomerate facies is variable across the property, it was decided that the conglomerate would be excluded. Additionally, the mineralization was not sampled to avoid flooding the XRF results with an enrichment in iron (Fe), lead (Pb) and zinc (Zn) values.

Proxies

The geochemical data used in this study builds upon the work that was previously started at the Yukon Geological Survey by Fraser et al. (2021). In that study, values for terrigenous input, carbonate content and enrichment factors were calculated from whole-rock geochemistry from three cores at the Tom deposit. In this study, we also include a spectral gamma ray log. Additional proxies for basin restriction, anoxia, flooding surface markers and grain size will be calculated in subsequent studies once a larger dataset can be

Table 1. Summary of the core data analyzed in 2024.

Location	Hole #	Deposit	Location (Lat, Long)	Interval	Stratigraphic units	
					Formation	Members
Macmillan Pass	NB23-001	Boundary	63.214955°, -130.545624°	12–460 m	Portrait Lake	Fuller Lake, Macmillan Pass, Niddery Lake
					Sapper	Macmillan Pass volcanics
Macmillan Pass	TS18-103	Tom	63.160225°, -130.143376°	39–368 m	Portrait Lake	Fuller Lake, Macmillan Pass
Macmillan Pass	MP20-001	Jason South	63.151897°, -130.216625°	18–632 m	Portrait Lake	Fuller Lake, Macmillan Pass, Niddery Lake
Macmillan Pass	JS17-002	Jason	63.146910°, -130.252275°	9–197 m	Portrait Lake	Macmillan Pass

collected from the property to more accurately assess their utility as a correlation marker. The proxy trends are summarized in Table 2.

Terrigenous input (TIP)

The values for terrigenous input are calculated by the sum of weight percent oxides of Al_2O_3, TiO_2, Fe_2O_3, and K_2O (Ratcliffe et al., 2012). The calculated value is then plotted with the TiO_2 values to determine if the titanium is shelf-derived (e.g., rutile). If the values are determined to be terrestrially derived, an increase in the TIP (%) would relate to a change in the point source of deposition, which could reflect closer proximity of basinal deposition to the continental shelf. A decrease in this value could indicate that the distance away from shelf-derived material is increasing, which is expected during transgressive phases.

Carbonate content CaO (wt%) and MgO (wt%)

The carbonate content proxy is used to indicate the proximity to a carbonate sediment source. The farther distance from the continental shelf (i.e., carbonate source), the lower the values in CaO and MgO will be. These values increase when the units were deposited closer to the shelf.

Enrichment factor of molybdenum and vanadium

The enrichment values in elements like molybdenum and vanadium have typically been used to estimate redox conditions of bottom waters and have been used as a proxy for total organic carbon (TOC; Tribovillard et al., 2006). The enrichment factor for elements is calculated by normalizing the aluminum in the sample to the aluminum value calculated for the average shale (values provided in Tribovillard et al., 2006). This may be used as a proxy to estimate basin restriction at the time of deposition.

Spectral gamma ray log

A spectral gamma ray log is calculated from the XRF values to reflect fluctuations in lithology and to be used in stratigraphic correlations. Sedimentary rocks, and in particular shale, have distinct radioactive signatures that allows for the differentiation of lithological units. The gamma ray (GR) value is calculated as follows: $GR = 8(U_{ppm})+4(Th_{ppm})+16(K_2O_{\%})$. Low values of gamma ray indicate a sandier or siltier deposit. High values of gamma ray generally indicate a muddier or shalier deposit.

Organic carbon isotopes ($\delta^{13}C$)

Organic carbon isotopes are used in this study as potential marker horizons that can be correlated on a basin-wide or a global scale. The ratio of $^{13}C/^{12}C$ in oceans has fluctuated throughout time and significant markers that record negative and positive excursions of the isotope values are well documented in the rock record (Saltzman and Thomas, 2012). This study aims to use this marker on a local scale to add a broad chronostratigraphic component to the stratigraphic sections.

Select samples from the MP20-001 and NB23-001 cores were sent for organic carbon isotopes at the Saskatchewan Isotope Laboratory at the University of Saskatchewan. Samples were initially run at a 10 m interval spacing to determine if this type of analysis would be useful in creating local stratigraphic correlations. The first run was successful, and the remaining samples collected from MP20-001 and NB23-001 have been sent to infill the stratigraphic spacing to a 2 m interval.

Table 2. Proxy indicators for the x-ray fluorescence (XRF) study.

Proxy indicator	Trends in transgression	Trends in regression
CaO and MgO (wt%)	Decrease in values. Reflects a further distance away from the shelf and slope.	Increase in values. Reflects proximity to the continental shelf and slope.
Terrigenous input (TIP) $TIP = Al_2O_3 + TiO_2 + K_2O + Na_2O$	Lower values indicate less input from terrigenous sources. Titanium is heavier and less likely to travel far distances into the basin.	Higher values indicate more input from terrigenous sources.
Molybdenum enrichment (ppm) and vanadium enrichment (ppm)	Can become enriched in euxinic, anoxic or suboxic environments. Values possibly higher.	Values possibly lower in regressive packages that may reflect deposition in suboxic to oxic settings.

Results

Facies and depositional processes

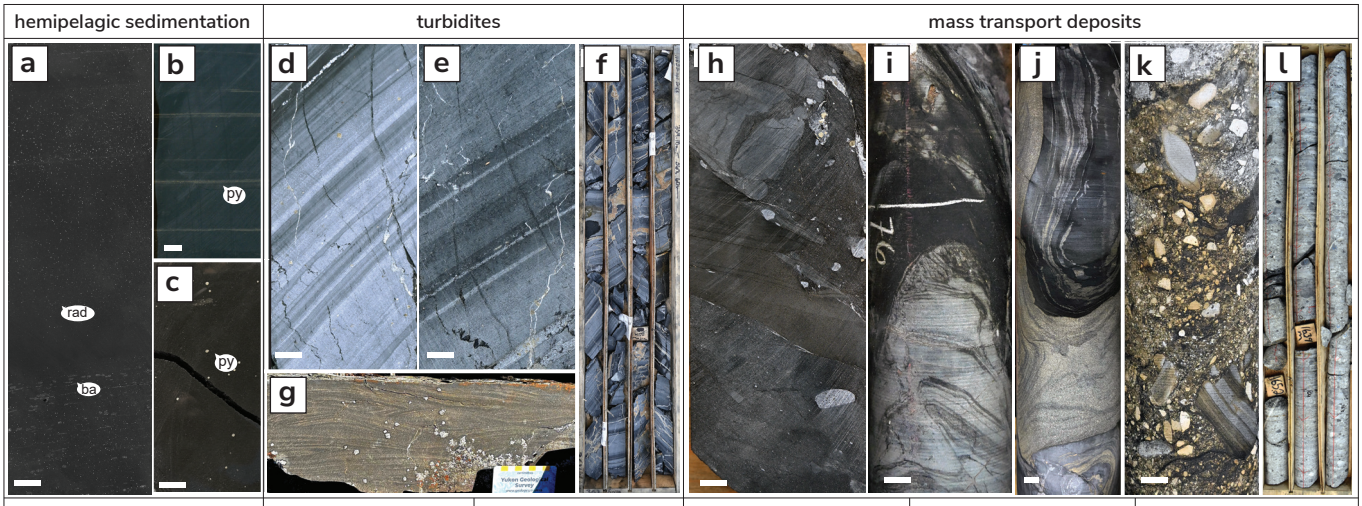
Facies have been documented and described from the cores that were logged in summer 2024. These descriptions are preliminary and will evolve when additional data is collected at the property. At present, 14 facies have been described and have been assigned to their corresponding depositional environments. The depositional environments have been grouped into the predominant depositional process that was active during deposition, which includes hemipelagic sedimentation, as well as turbidites and mass transport deposits. The facies are summarized in Figure 6 and Table 3.

XRF sequence stratigraphic surface classification

The geochemistry from the XRF study can be used to identify systems tracts and stratigraphic horizons. Additional data collected for this study in subsequent field seasons will follow and expand upon this identification criteria.

Maximum flooding surface (MFS)

The maximum flooding surface separates the underlying TST deposits from the overlying regressive deposits. The MFS is marked by the maximum decrease in the TIP values, a gradual increase in TOC above the surface, and the maximum decrease in carbonate



basinal plain	high-density turbidite	low-density turbidite	mudflow	slump	grainflow
Characteristics: Mudstone-dominated succession that contains chert-rich intervals. Radiolarians are common. Deposition by suspension settling occurs in all 4 systems tracts.	Characteristics: Sand-dominated heterolithic deposit. Usually displays an overall coarsening upwards sequence. Normally graded beds are common.	Characteristics: Mud-dominated heterolithic deposit. Usually displays an overall coarsening upwards sequence. Normally graded beds are common.	Characteristics: Matrix-supported conglomerate succession that contains chert clasts. The matrix ranges from mudstone to sandstone-dominated.	Characteristics: Matrix-supported conglomerate succession that contains chert clasts. The matrix ranges from mudstone to sandstone-dominated.	Characteristics: Sandstone-dominated succession that contains matrix and clast-supported conglomerate. Clasts are variable in lithology.
Systems tracts: FSST, LST, TST, HST	Systems tracts: FSST (late), LST	Systems tracts: LST, TST, HST	Systems tracts: FSST (early), TST (late)	Systems tracts: FSST, LST, TST	Systems tracts: FSST (late), LST
Photos: a, b, c	Photos: d, g	Photos: e, f	Photos: h	Photos: i, j	Photos: k, l

Figure 6. *Facies associations from core in the region.* ***(a–c)*** *Hemipelagic sedimentation containing radiolarians (rad), barite nodules (ba), and pyrite (py), which are common in this interval ([a] – MP20-001 at 409.6 m; [b] – MP20-001 at 135.8 m; [c] – MP20-001 at 322.5 m; scale bar is 1 cm in each photo).* ***(d–g)*** *Turbidite deposits that are heterolithic. Finer grained expressions of turbidites are found in (d)–(f) and show variable proportions of sandstone to mudstone. Current ripple lamination in photo (g) is from outcrop of the Prevost Formation where sandier expressions of turbidite deposition are preserved ([d] – NB23-001 at 366.45 m; [e] – NB23-001 at 349.7 m; [f] – NB23-001 box 88). In (d) and (e) the scale bar is 1 cm and in (f) the length of the core box is 1 m.* ***(h)*** *Mudflow from the Fuller Lake member that has re-entrained larger clasts and sandier debris (MP20-001 at 394.7 m; scale bar is 1 cm).* ***(i–j)*** *Slump deposits from the Macmillan Pass member. Soft-sediment deformation is common in these deposits indicating that the remobilization of sediment occurred before the unit was fully lithified ([i] – TS18-013 at 76 m; [j] – TS18-013 at 250.6 m; scale bar is 1 cm).* ***(k–l)*** *Conglomerate that formed from grainflows. Clasts are composed of ripped-up turbidite material and chert-rich pebbles. ([k] – JS17-002 at 87.3 m; [l] – TS18-013 box 50 from 162 to 165.4 m). In (k) the scale bar is 1 cm and in (l) the length of the core box is 1 m.*

Table 3. Initial summary descriptions of the facies associations and corresponding facies from core. BI – bioturbation index; vfgL – very fine grained lower; fgL – fine grained lower; mgL – medium grained lower; mgU – medium grained upper; vcgU – very coarse grained upper.

Depositional process	Facies	Sedimentology	Accessories / diagenesis	Trace fossils / fossils	Depositional environment
hemipelagic sedimentation	1 – carbonaceous mudstone/shale	• planar parallel lamination to apparently massive bedding	• disseminated pyrite	not observed	basinal plain
	2 – cherty mudstone/ shale with interlaminated siltstone	• weakly developed normally graded beds ranging from siltstone to mudstone • planar parallel lamination to apparently massive bedding • chert-rich intervals punctuated by interlaminated siltstone	• disseminated pyrite • clay content may be high • brecciation common in areas adjacent to faults	• radiolarians (can be locally replaced by pyrite)	basinal plain
	3 – carbonaceous to cherty mudstone/ shale	• planar parallel lamination to apparently massive bedding	• disseminated pyrite (may concentrate on bedding planes)	• radiolarians (can be locally replaced by pyrite)	basinal plain
turbidites	4 – pinstripe laminated mudstone/ siltstone/ sandstone with starved current ripple lamination	• normally graded beds from laminated/bedded vfgL – fgL sandstone to mudstone • starved current ripple lamination (less than 1 cm in crest height – lenticular bedding?)	• ankerite, siderite, quartz veins and sphalerite mineralization	not observed	low-density turbidite
	5 – mudstone-dominated heterolithic with normally graded beds	• normally graded beds from sandstone (vfgU – fgL) to mudstone • current ripple-laminated beds range in thickness from 2 to 5 cm • planar parallel lamination and apparently massive bedding in the mudstone and sandstone beds	• ankerite, siderite, and sphalerite mineralization • brecciation common in areas adjacent to faults	• *Planolites* (uncommon) • BI = 0; locally may be as high as 1	low-density turbidite
	6 – heterolithic mudstone/sandstone with granules	• heterolithic beds of sandstone (fgL – granule) interbedded with silty mudstone beds • sandstone beds range in thickness from 10–25 cm and form bedsets that are >1 m • mudstone interbeds are <20 cm thick	• ankerite, siderite, and sphalerite mineralization	not observed	high-density turbidite
	7 – sandstone-dominated heterolithic with current ripple lamination	• normally graded beds from sandstone (mgL – fgL) to siltstone • current ripple lamination, low-angle planar parallel lamination and planar parallel lamination • soft-sediment deformation	• carbonaceous debris • mudstone interbeds may be mineralized	not observed	high-density turbidite
	8 – apparently massive sandstone	• apparently massive bedding in coarser sandstone beds (granule – mgU)	• rip-up clasts of mudstone	not observed	channel complex
	9 – conglomerate with weakly developed imbrication	• granule to clast-sized conglomerate • fining upwards • clasts may show subtle imbrication	• not observed	not observed	channel complex
mass transport complex	10 – poorly sorted, clast-supported conglomerate	• poorly sorted conglomerate (clasts are granule to clast-sized) • matrix ranges from siltstone to sandstone (fgL – vcgU) • appears structureless to massive • clasts are subangular with low to moderate sphericity • clasts are primarily chert	• matrix and clasts may be mineralized (pyrite, ankerite)	not observed	grainflow
	11 – poorly sorted, matrix-supported conglomerate	• poorly sorted conglomerate (clasts are granule to clast-sized) • matrix ranges from mudstone to sandstone (vfgL – vcgU) • clasts may be rip-up clasts of the turbidite facies (clasts retain original sedimentary fabric)	• matrix and clasts may be mineralized (pyrite, ankerite)	not observed	grainflow
	12 – poorly sorted, matrix-supported conglomerate	• mudstone to siltstone matrix • larger granules and clasts are distributed randomly throughout • clasts tend to be angular and chert-rich	• disseminated pyrite	not observed	mudflow
	13 – syn-sedimentary deformed heterolithic mudstone	• soft-sediment deformation, syn-sedimentary faulting, convolute bedding • commonly are slumped deposits of the turbidite facies association	• disseminated pyrite, sandstone injectites	not observed	slump
	14 – syn-sedimentary deformed mudstone	• pyritized beds are deformed and may be inclined or overturned • mudstone matrix (may be chert-rich)	• pyrite nodules, sandstone injectites	not observed	slump

content. Above this horizon, the values in TIP, carbonate content and TOC increase. Additionally, the surface may be delineated by low values of the spectral gamma ray log (e.g., Fig. 7 at 260 m). Higher-frequency examples of the MFS follow similar geochemical trends.

Maximum regressive surface (MRS)

The maximum regressive surface separates the underlying regressive units from the overlying TST deposits. At this surface, there is an abrupt decrease in the TIP values, a decrease in the TOC above the surface, and an abrupt decrease in the carbonate content (e.g., Fig. 7 at 315 m). Below this surface, the values for TIP and carbonate content are generally high. The surface generally occurs within the fining-upward trends.

XRF geochemistry of systems tracts

Transgressive systems tract

The TST is marked by an overall decreasing trend in the TIP values, carbonate content and TOC values. In this study, the TST generally had TIP values that averaged around 10%, and carbonate content that averaged 2% MgO and 5% CaO. The TST trend generally indicates an overall decline in the terrigenous elements being delivered to the system.

Regressive systems tracts

This summary does not distinguish between which type of regression the mudstone units accumulated in, and it is noted that the mudstone accumulates in the HST, FSST and LST. The regressive systems tracts (HST, LST or FSST) are marked by an overall increasing trend in the TIP values, carbonate content and TOC values. Low values or declining trends for the enrichment of molybdenum (Mo) and vanadium (V) are observed in the deposits that accumulated in regression, which could indicate variable levels of redox that persisted throughout the deposition of the units.

X-ray fluorescence and organic carbon isotopes trends from core

Core NB23-001

The NB23-001 core contained syn and post-depositional mineralization throughout the mudstone-dominated successions and within the lobes of turbidites for the Niddery Lake and Macmillan Pass members (Figs. 6 and 7). Values for Pb, Zn and barium (Ba) are considerably higher in this core than the others that were analyzed for this study. In zones where these elements peak, the enrichment values for Mo and V also peak, which could indicate euxinic or reducing conditions occurring syn-depositionally. The calculated spectral gamma ray values were significantly higher in this core when compared to core that contained a lesser degree of mineralization. High values for the spectral gamma are coincident with zones where Mo and V enrichment spiked. It is possible that mineralization is skewing values for this calculation through the enrichment of uranium (U).

Between 375 to 425 m there is a transgressive systems tract preserved. Associated with this TST are high values for Zn and the enrichment factors of Mo and V. The TIP shows an overall decreasing trend, while the carbonate content is low. This zone of hemipelagic sedimentation is associated with syn and post-depositional mineralization. Although care was taken to avoid heavily mineralized zones, it is possible that the enrichment of the Zn, Pb and Ba is flooding the results of the XRF.

Overlying the mineralized zone of the Niddery Lake member (from 240 to 375 m) is a mudstone-dominated package of sediment that was deposited during a low-frequency regression. Higher-frequency sequences of transgression and regression are denoted by the fluctuating values for carbonate content, TIP and TOC. A low-density turbidite is observed from 320 to 375 m, and hemipelagic sedimentation or very distal extents of turbidite deposition are observed from 240 to 320 m.

From 6 to 240 m, grainflows and slumps are observed in core. Samples were taken from the mudstone-dominated intervals of the grainflows to incorporate some geochemical data into these sections. The grainflows, turbidites and slumps are characterized by high TIP values, but low values for TOC and carbonate content. Molybdenum and V are enriched in mineralized zones, which correspond to high values for Pb, Ba and Zn. This regressive package of sediment overlies a BSFR, which is distinguishable through sedimentological features that places coarse-grained, matrix-supported conglomerate erosively over top of mudstone-dominated units.

The $\delta^{13}C$ values range from -32 to -24‰, and two positive excursions of the isotopes occur at 450 and 310 m. The excursion at 310 m is coincident with the increase in terrigenous input. By tightening the interval spacing of samples that were sent for analysis, it is

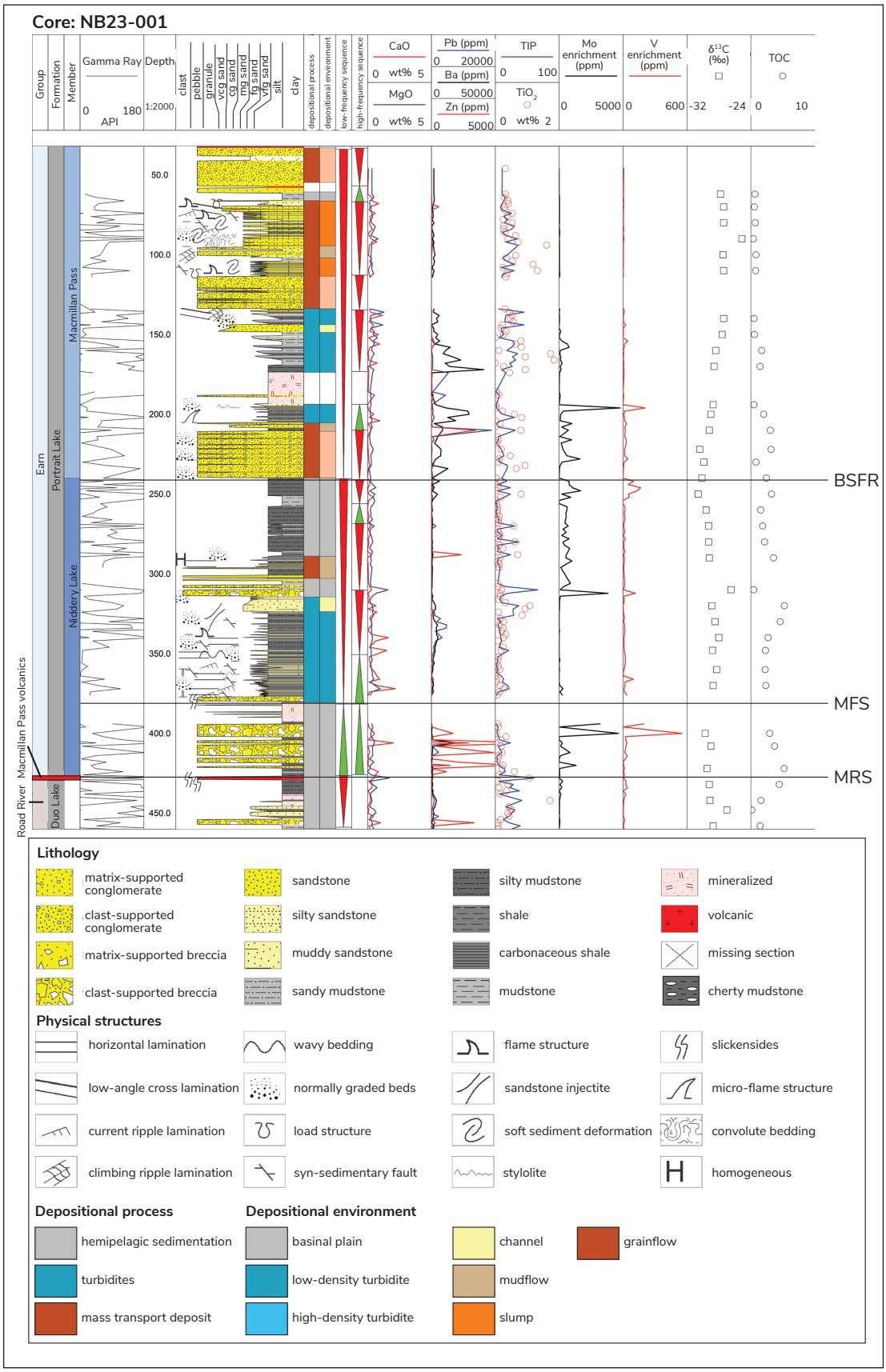


Figure 7. *Core log for NB23-001 and select geochemical proxies. For low and high-frequency sequences, red colour represents regression and green represents transgression.*

possible that the results may establish variations in the isotope fluctuations, which can be better tied to relative sea level trends.

Total organic carbon (TOC) fluctuates in relation to the mineralization and enrichment of Mo and V. The correlation between TOC and the enrichment factors appears to be a crude match. The incorporation of the additional carbon isotopes and TOC values with this core will increase the certainty of how TOC and the enrichment factors can be used to infer euxinic events.

Core JS17-002

The core from JS17-002 predominantly intersects a mass transport complex (Fig. 8). Samples were not taken in conglomerate intervals and large sections of the core have data gaps as a result. The slump features document higher values of terrigenous input (e.g., Fig 8 from 90 to 130 m), indicating that the material that forms the slumps had a higher degree of continentally derived material.

Core MP20-001

The MP20-001 core preserves a thick mudstone-dominated package of strata that accumulated by hemipelagic sedimentation or by the distal extent of turbidite progradation (Fig. 9). Hemipelagic sediments that accumulated during transgression tend to have lower values for CaO (wt%) and MgO (wt%), reflecting their increased distance away from the continental shelf. Additionally, lower values of TiO_2 and Zr (ppm) can be used as a proxy for the distance a deposit is from the shelf. Both elements are more dense and less likely to travel significant distances from the shelf or slope. Regressive packages of hemipelagic sedimentation tend to have higher values for CaO, MgO, TiO_2 and Zr. The increase in these oxides and elements reflect that the deposits are in closer proximity to the shelf and slope leading to an increase in terrestrial input.

The lower package of mudstone from 480 to 632 m is interpreted to have been deposited as a low-density turbidite that accumulated during an overall low-frequency regression (Fig. 9). The section contains a higher TIP value, higher carbonate content and higher TOC values. The Mo and V enrichment values generally show a decreasing trend. This section of regressive mudstone is marked by a decrease in carbonate content and TIP and this is inferred to be a MRS that is documented at 505 m. A slight negative excursion of the $\delta^{13}C$ isotope occurs over this horizon.

Hemipelagic sedimentation occurs above this marker between 410 to 505 m (Fig. 9). This package of

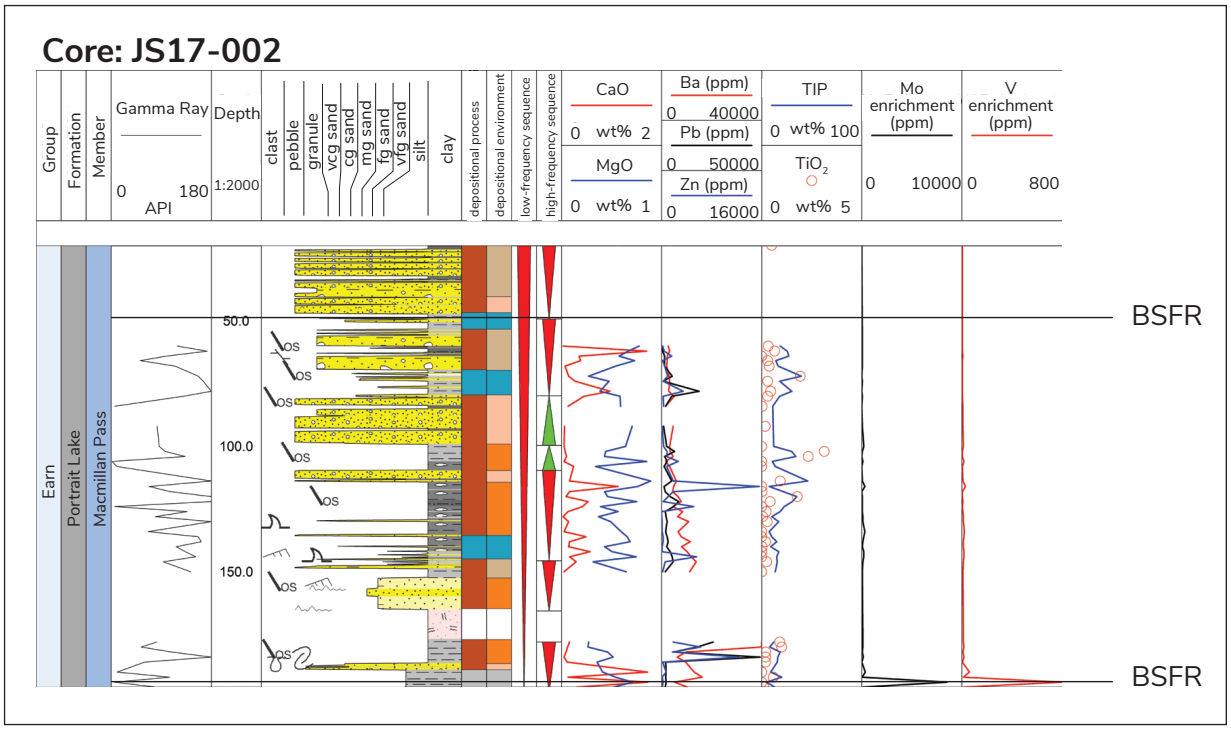


Figure 8. *Core log for JS17-002 and select geochemical proxies. Refer to Figure 7 for the legend. For low and high-frequency sequences, red colour represents regression and green represents transgression.*

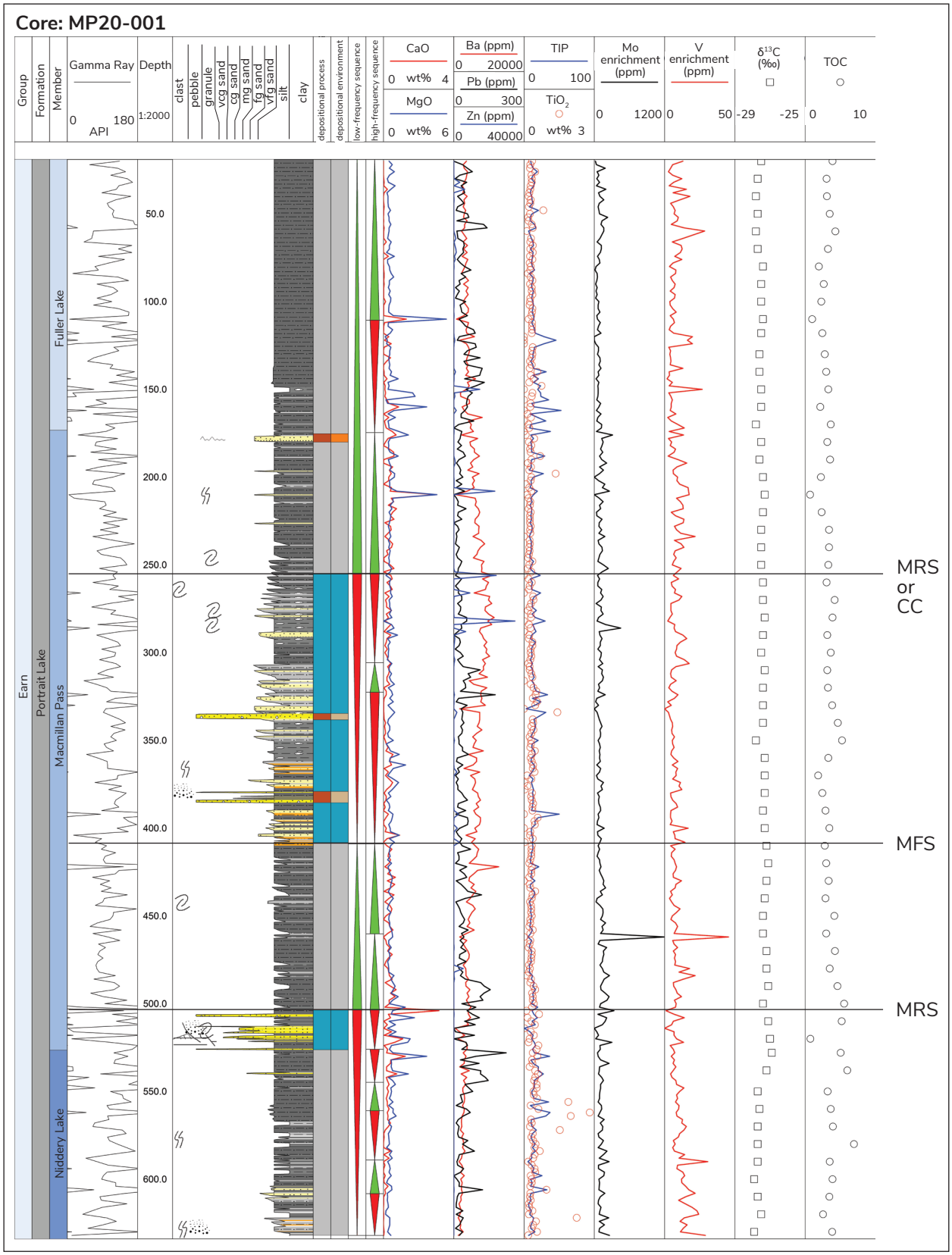


Figure 9. *Core log for MP20-001 and select geochemical proxies. Refer to Figure 7 for the legend. For low and high-frequency sequences, red colour represents regression and green represents transgression.*

sediment is characterized by low carbonate content, low TIP values and an overall decline in the TOC values. The unit is marked by a MFS, which includes the subtle increase in carbonate content, TIP and TOC values directly over the horizon. Within this package of mudstone, there are two lower-frequency transgressive systems tracts identified. The lower-frequency MFS is preserved at 460 m where there is a prominent spike in the enrichment of Mo and V.

A low-density turbidite is preserved from 260 to 410 m (Fig. 9). Within this unit there are two thin grainflow deposits that punctuate the turbidite deposition. This unit was deposited during an overall regression and is characterized by higher TIP values, variable carbonate content and high TOC values. The enrichment of V and Mo is low throughout this package of sediment. There are higher-frequency cycles of transgression and regression preserved in this section, which is reflected by the variable TIP and TOC signatures. This unit is overlain by a MRS or CC which is preserved as a significant change in the Pb, Zn and Ba trends over the contact and is coincident with a decrease in the TIP and TOC.

From the top of the core to 260 m a mudstone-dominated unit that accumulated through hemipelagic sedimentation is preserved. This unit is interpreted to have been deposited during a low-frequency transgressive event that contains higher-frequency regressive and transgressive packages. This succession displays overall lower TOC values, low TIP values and low carbonate content.

The $\delta^{13}C$ values range from -28 to -26‰ and display a lesser degree of positive or negative excursions of the carbon isotope. As the data points are separated at this time by a 10 m gap, it is possible that the current efforts to infill between points will demonstrate more variability of the isotopes over major stratigraphic horizons.

Core TS18-013

The Macmillan Pass member preserves low-density turbidites, slumps and grainflow features. The low-density turbidite facies occur between 330 to 375 m and 80 to 125 m (Fig. 10). The terrigenous input values for the turbidites are generally high, however the corresponding CaO and MgO values are low. These lower values could be due to diagenesis and alteration of carbonate material.

Slump features in this core tend to be rotational blocks of low-density turbidites that preserve internal deformation. The tops of slumps are invariably marked by abrupt changes in the terrigenous input proxy at 280 m, 225 m and 75 m. Values for terrigenous input abruptly drop at 65 m. This coincides with the transition from the deposition of the low-density turbidites of the Macmillan Pass member to the deposition of hemipelagic sedimentation of the overlying Fuller Lake member.

Discussion

Depositional processes

Facies described from core have been assigned to their corresponding depositional processes (Fig. 6; Table 3). The highest abundance of coarser grained sediment being transported to deep-water settings generally occurs during the falling-stage and lowstand systems tracts when a coarse sediment source would be available near the shelf edge (Fig. 5). Sedimentologically, identifying systems tracts in the coarser-grained units tends to be more straightforward when tying depositional trends to fluctuations in relative sea level. Where sediment deposition becomes finer-grained, these trends are more challenging to identify without the use of thin sections, downhole geophysical datasets, or XRF.

Depositional process 1: hemipelagic sedimentation

Hemipelagic sedimentation occurs within all four systems tracts. The input varies between terrigenous and biogenic, and sediment consists of clay and less commonly, silt-sized grains. In these deposits, sequence stratigraphic surfaces are gradational and cannot be identified using sedimentology alone. Commonly, these deposits contain radiolarians that may have been pyritized following their deposition.

The maximum flooding surface (MFS) and maximum regressive surface (MRS) separate out transgressive from regressive deposits. Within regressive packages, subtle increases in the CaO, MgO and terrigenous input values indicate a more proximal position to the shelf, which would likely occur during HST, LST or FSST. The MRS generally occurs within the fining upward trends in sedimentation and this is marked by the decrease in TIP and carbonate content (Figs. 7–10).

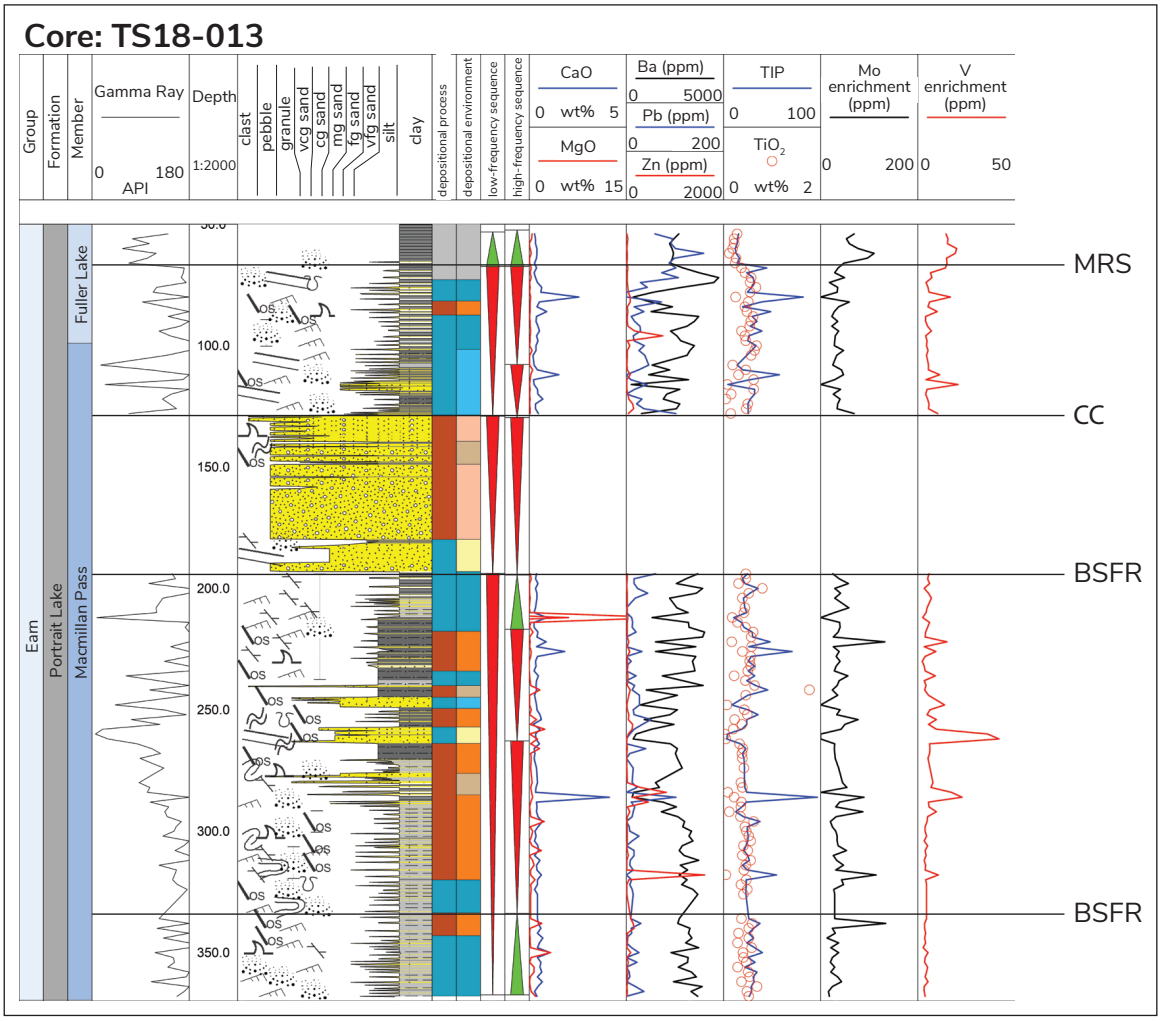


Figure 10. *Core log for TS18-013 and select geochemical proxies. Refer to Figure 7 for the legend. For low and high-frequency sequences, red colour represents regression and green represents transgression.*

Depositional process 2: turbidites

Turbidites form from gravity-driven turbidity currents in which sediment is supported from fluid turbulence and deposition is occurring through suspension settling (Dott Jr., 1963). Turbidites may form along the continental shelf, slope or deep basin.

The turbidites in this study have been classified as either belonging to high-density turbidites (sand-rich) or low-density turbidites (mud-rich). Although this classification is a broad grouping, it helps delineate the systems tracts that the turbidites may have accumulated in. High-density turbidites likely accumulated in the late FSST or LST due to an increase of coarse material accumulating near the shelf-edge margin and being redeposited in the deep basin. The low-density turbidites likely accumulated during late LST, early TST, or HST. In late LST and early TST, coarse material is no longer being delivered to the continental shelf, causing turbidites to become finer grained. In HST, much of the coarse material available in the basin is reworked in the continental realm and is less likely to be delivered to the deep basin.

Depositional process 3: mass-transport deposits

It is noted that the deposition of mass transport deposits occurs under the same gravity-driven processes as turbidite complexes; however, it is considered a lesser component to movement of sediment transport. Mass transport deposits in the study area can be categorized as either being deposited as a debris flow (grainflows and mudflows) or slumps.

Mudflows and grainflows are classified based on the material that was available along the shelf-slope break

when deposition and movement occurred. Grainflow deposits are characterized by poorly sorted, clast and matrix-supported conglomerate. In the study area, the clasts may be composed of re-entrained turbidite material, chert and quartz. Grainflow deposits are generally deposited in the FSST and LST, given that the matrix material is more sandstone-rich. Progressive lowering of sea level will result in sandstone and siltstone-rich intervals being deposited closer to the shelf-slope break.

Mudflows are documented in the area as matrix-supported conglomerate that are predominantly hosted in a mudstone matrix. Mudflows are most commonly deposited in the early stages of the FSST or in later stages of the TST.

Slumps consist of a coherent mass of sediment that undergoes rotational movements, which results in internal deformation of beds. The slumps in the Macmillan Pass region contain soft-sediment deformation, syn-sedimentary faulting, and convoluted bedding. These deposits are generally the remobilization of turbidite lobes into graben features, resulting in overturned or inclined bedding of thick packages of sediment (usually around 25 to 100 m in thickness). The movement of this slump material would have likely occurred as a result of, or during tectonic activity.

Depositional history

Niddery Lake member

The initial deposition that occurred in the Macmillan Pass region likely accumulated during a low-frequency sequence of regression (HST). The deposits are predominantly characterized by hemipelagic sedimentation and distal turbidite lobe deposition (Fig. 11a). The XRF geochemistry from the NB23-001 and MP-20-001 cores indicate that the Niddery Lake member preserves high-frequency sequences of transgression and regression (Figs. 7 and 8).

The Niddery Lake member is mudstone-dominated at the Boundary deposit (Fig. 7). Moving along depositional strike in the basin toward the Tom deposit (Fig. 10), the turbidite facies become more sandstone-rich. It is likely that either the lower depositional units at the Tom deposit are laterally equivalent to the mudstone-rich facies near the Boundary deposit; or the initiation of turbidite deposition near the Tom deposit was erosive in nature and removed the underlying mudstone units. The turbidites may have accumulated during a lowstand; however, minimal evidence for a fall in relative sea level at that time is preserved within the region. This could indicate that the FSST facies associations may be preserved in a more proximal position, and the lowstand fan has prograded a significant distance away from that region.

Macmillan Pass member

A significant tectonic event occurred that facilitated the rapid creation of accommodation space adjacent to fault margins, which resulted in the deposition of the falling-stage systems tract (Fig. 11b). This is documented by the thick conglomerate packages that are preserved (Figs. 7 and 9), as well as slump features of previously deposited turbidite material (Fig. 10). Following the syn-depositional tectonic reactivation, horst and graben features would have become pronounced topographic highs and lows in the region, redirecting sedimentation patterns (Fig. 11b).

Relative sea level would have fallen prior to, or during this time. The available source of material along the shelf-slope margin was coarse-grained, as indicated by the sandstone matrix that forms the conglomerate units in the Macmillan Pass area (Fig. 10). This indicates that the shorelines in proximal areas of the basin were downstepping in a seaward direction and depositing coarse-grained material in very distal regions of the continental shelf. This material would have then been transported to the deep basin following the extensional event.

In regions where the accommodation space is less pronounced and farther from fault margins, finer material tends to accumulate. This leads to the rapid juxtaposition and lateral transition of the coarser material that accumulates near fault margins into the finer grained deposits (Figs. 10 and 11b). In zones where horst features are prominent, coarse material will only begin to accumulate when the accommodation that is created in the grabens becomes filled. This leads to coarser material spilling out onto the horsts as coarse-grained lags and thin conglomerate packages (e.g., Fig. 9 at 340 m).

The Macmillan Pass member was deposited during a low-frequency fall in relative sea level. Limited evidence exists at this point in the study that indicates the preservation of a lowstand systems tract. This could be due to the rate of tectonism outpacing the fluctuations in relative seal level, thus suppressing the expression of the development of a lowstand fan. Alternatively, it may be that more data must be integrated to be able

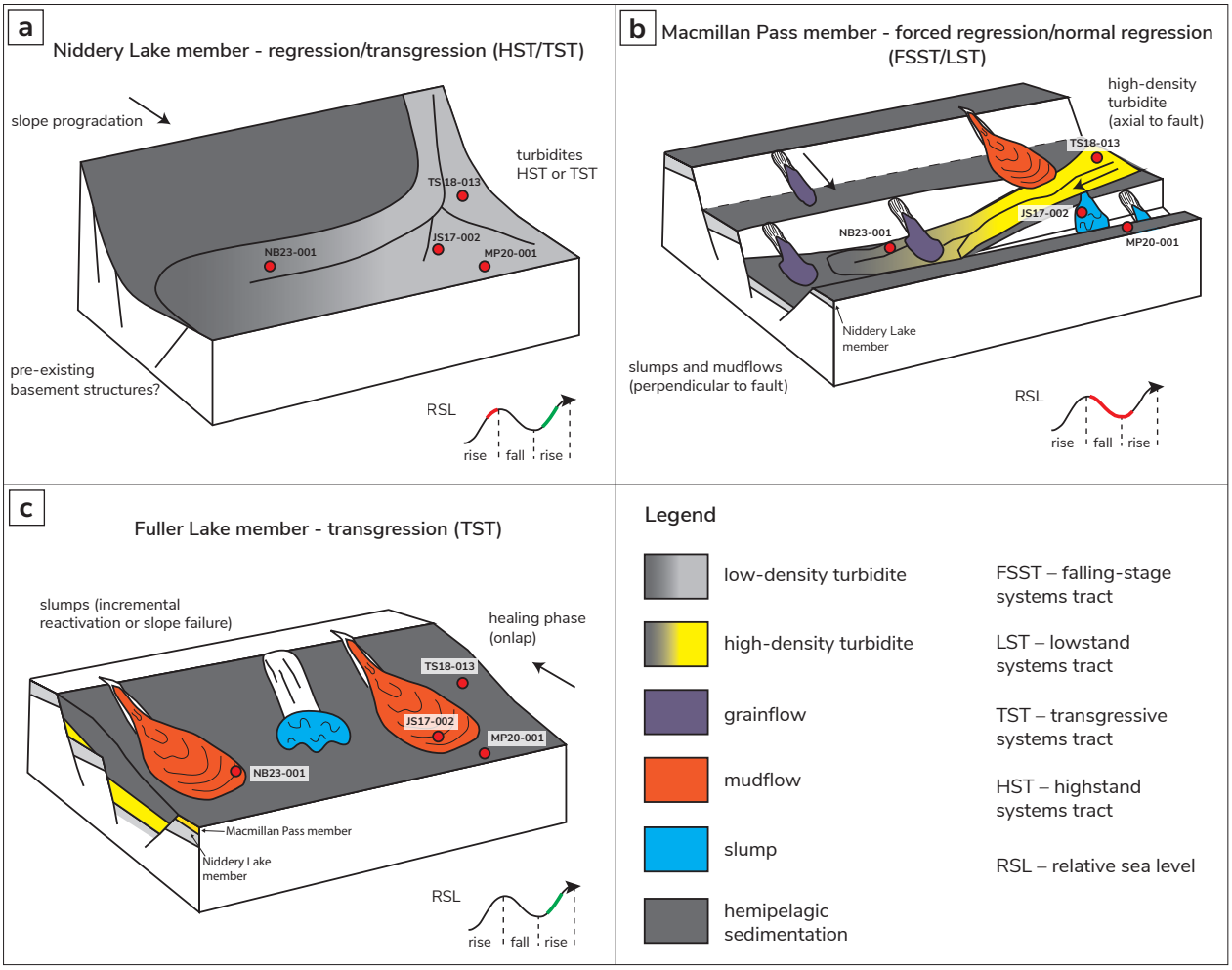


Figure 11. *Block diagram illustrating the orientation of sedimentation sources during the deposition of the Portrait Lake Formation.* ***(a)*** *Niddery Lake member that records deposition during transgression and highstand normal regression.* ***(b)*** *Macmillan Pass member that records deposition during forced regression. This is documented by the increase in coarse sand into the basin. Deposition of turbidites during this time is axial to the fault planes. The mass transport complexes are perpendicular to the fault plane orientation.* ***(c)*** *Fuller Lake member that records deposition during an overall transgressive phase in the basin history. This is documented by thick mudstone intervals that infill topographic lows in the region.*

to map the distribution of sediments that would have accumulated at that time.

Higher-frequency sequences of deposition are preserved within the overall falling-stage systems tract deposit of the Macmillan Pass member. Grainflows are commonly interstratified with low-density turbidite packages (Fig. 9), indicating local variation in the fluctuations of relative sea level. This is attributed to ongoing tectonism throughout the deposition of this member. Slumps and mudflows that are observed in this member may have been deposited during higher-frequency cycles of transgression or during progressive drops in relative sea level during the FSST.

Fuller Lake member

The Fuller Lake member is a mudstone-dominated interval that tends to contain more radiolarian-rich intervals indicating deposition during hemipelagic sedimentation. At the base of this unit, mudstone-dominated turbidites are present and they gradually grade into thick mudstone units with minor siltstone lamina. The Fuller Lake member likely reflects a healing phase of deposition during an overall transgressive period in the basin's history (Fig. 11c). Mudstone units infill the remaining topographic lows and form a thick package of sediment across the region. Slumps that have been termed 'diamictites' in previous studies

are prevalent in this unit, indicating that the slope is periodically destabilized. The presence of the slumps could mean that minor tectonic events are occurring syn-depositionally or that there are higher-frequencies of deposition superimposed on the lower resolution sequence. The geochemistry of the Fuller Lake member in the MP20-001 core indicates that there are short-lived periods of regression as is evidenced by the increase in carbonate content, terrigenous input and TOC values.

Next steps

Macmillan Pass

The along-strike variability in sediment supply, coupled with the localized occurrence of depositional elements, poses a challenge when correlating in deep-water settings. Turbidites in one location of the basin can abruptly be replaced laterally along-strike by hemipelagic mudstone. This is further complicated by syn-depositional fault reactivation that redirects and localizes sedimentation into graben features in the region. Careful sedimentologic analysis of the turbidites along with the clarification of the relative timing of deposition will refine the depositional model for the Earn Group in the Selwyn basin region.

Additional core logging and geochemical data must be collected in order to infill existing data gaps to create a consistent model. Completing the geochemical analyses throughout the mudstone intervals to identify the maximum regressive surface and the maximum flooding surface will be an integral part in the creation of this model. It is proposed that wireline log data be collected at key stratigraphic drillholes to facilitate meaningful mapping of the rock properties; this will also help determine the geophysical characteristics of the mudstone-dominated successions, and of the ore bodies.

Howards Pass

During the summer of 2025, work was initiated at Howards Pass where we began by infilling the stratigraphic gaps between the two major lead-zinc deposits in the region: Howards Pass and Macmillan Pass. Howards Pass is located approximately 100 km southeast of Macmillan Pass. The site is accessible by driving the Nahanni Range Road and the Howards Pass Access Road during the summer months. Travel along the Howards Pass Access Road is controlled by Selwyn Chihong Mining Ltd. and Parks Canada. Howards Pass records deposition in more distal settings, farther away from the transition of slope to basin.

At Howards Pass, three cores were logged and sampled in July and August 2025. Cores were selected based on vintage (2005–2010 drilling programs), length, and the intersection with the lower and upper boundaries of the Portrait Lake Formation. Hole DON-142 was drilled from the upper members of the Portrait Lake Formation into the mineralized rocks of the underlying Road River Group. Additional core is available outside of what was logged for the current study. The cores from holes XYC-208 and XYC-241 form a composite section from the Steel Formation into the upper informal members of the Portrait Lake Formation. These two holes are less than 800 m away from each other, were of newer vintage, and had overlapping strata preserved in them, which is why they were selected for creating the composite section. Core from drillhole XYC-241 was previously sampled in 2023 by John Xu from the University of British Columbia. To preserve the remaining material in the core, John has provided the samples he collected to Yukon Geological Survey (YGS) to be used in the XRF study.

Additional cores that intersect the Portrait Lake Formation are available for logging and sampling. Cores will infill the current stratigraphic gaps between the Don and XY properties. Outcrops that were logged by Gordey and Anderson (1993) and preserve mudstone-dominated sections will be given preference for sampling in the geochemistry study.

Nááts'įhch'oh National Park Reserve and Nahanni National Park

A sequence stratigraphic model is more robust when we understand the evolution of the paleoshoreline in relation to changes in deep-water packages of sediment. Platform and slope deposits that are age-equivalent to the deep-water Devonian strata are going to be sampled to compare geochemical markers, organic carbon isotopes, and the position of stratigraphically significant horizons to our current research. The next steps for this project include fly camping at outcrops that occur in Nááts'įhch'oh National Park Reserve and in Nahanni National Park. In these regions, proximal expressions of the Late Devonian strata are preserved in the Funeral, Grizzly and Sapper formations. This will assist with understanding the history of the basin as the various sedimentary systems evolved throughout the Ordovician to Late Devonian. A reconnaissance trip to these areas was conducted in August of 2025 (Schultz and Reynolds, this volume), and three key outcrops

were identified that will be sampled in the summer of 2026 for analysis. Additionally, mapping of outcrops that occur between Macmillan Pass and Howards Pass must be incorporated to bridge the stratigraphic gap between these two significant lead-zinc districts.

Acknowledgments

Thank you to Fireweed Metals for hosting the field crew in camp at Macmillan Pass and for providing access to the geochemical dataset collected by GeologicAI. Thank you to Rackla Metals and Selwyn Chihong for hosting the field crew in camp at Howards Pass. John Xu provided core material from hole XYC-241 to the YGS to use in future research. Thank you to Kieran McClenahan, Merilie Reynolds, Tiera Naber, Brock Palmer, Cameron Washi, Marissa Pimentel, Sophia Tafel and Piper Jostrand for your excellent assistance in the field and in the core shack. Thank you to Tiffany Playter for providing a critical review.

Parks Canada provided a Research Permit NAANPR-2025-46426 to Sarah Schultz and Merilie Reynolds (Northwest Territories Geological Survey) to conduct work in the parks. The multi-year permit was approved until 2027. In addition to this, a research permit was granted from the Northwest Territories Scientific Research License (No. 17563) to Merilie Reynolds to facilitate the start of the research in the Northwest Territories.

References

Abbott, J.G., 1983. Structure and stratigraphy of the Macmillan Fold Belt: Evidence for Devonian faulting. Exploration and Geological Services Division, Yukon Region, Indian and Northern Affairs Canada, Open File 1983-1, 16 p., 3 maps at 1:50 000 scale.

Abbott, J.G., 2013. Bedrock geology of the Macmillan Pass area, Yukon and adjacent Northwest Territories (NTS 105O/1, 2 and parts of 105O/7, 8, and 105P/4, 5; 1:50 000 scale). Yukon Geological Survey, Geoscience Map 2013-1.

Abbott, J.G. and Turner, R.J. 1991. Character and paleotectonic setting of Devonian stratiform sediment-hosted Zn, Pb, Ba deposits, Macmillan Fold Belt, Yukon. *In:* Mineral deposits of the northern Canadian Cordillera, Yukon-northeastern British Columbia, Geological Survey of Canada, Open File 2169, p. 99–136.

Ainsworth, R.B., Vakarelov, B.K., MacEachern, J.A., Rarity, F., Lane, T.I. and Nanson, R.A., 2017. Anatomy of a shoreline regression: Implications for the high-resolution stratigraphic architecture of deltas. Journal of Sedimentary Research, vol. 87, p. 425–459, doi:10.2110/jsr.2017.26.

Carne, R.C., 1976. Stratabound barite and lead-zinc barite deposits in eastern Selwyn Basin, Yukon Territory. Department of Indian and Northern Affairs, Open File Report EGS 1976-16, 41 p.

Catuneanu, O., Galloway, W.E., Kendall, C.G.S., Miall, A.D., Posamentier, H.W., Strasser, A. and Tucker, M.E., 2011. Sequence stratigraphy: Methodology and nomenclature. Newsletters on Stratigraphy, vol. 44, p. 173–245.

Catuneanu, O., 2019a. Model-independent sequence stratigraphy. Earth-Science Reviews, vol. 188, p. 312–318.

Catuneanu, O., 2019b. Scale in sequence stratigraphy. Marine and Petroleum Geology, vol. 106, 128–159.

Catuneanu, O., 2022. Principles of sequence stratigraphy (2nd edition). Elsevier Science, 494 p.

Cecile, M.P., 2000. Geology of the northeastern Niddery Lake map area, east-central Yukon and adjacent Northwest Territories. Geological Survey of Canada, Bulletin 553, 120 p.

Dott, R.H. Jr., 1963. Dynamics of subaqueous gravity depositional processes. AAPG Bulletin, vol. 47, no. 1, p. 104–128.

Fraser, T.A., Milton, J. and Gouwy, S.A., 2021. New geochemistry from old drill holes at the Tom property, Macmillan Pass, Yukon. *In:* Yukon Exploration and Geology 2020, K.E. MacFarlane (ed.), Yukon Geological Survey, p. 19–46.

Gabrielse, H., 1967. Tectonic evolution of the northern Canadian Cordillera. Canadian Journal of Earth Sciences, vol. 4, p. 271–298.

Galloway, W.E., 1989. Genetic stratigraphic sequences in basin analysis I: Architecture and genesis of flooding-surface bounded depositional units. AAPG Bulletin, vol. 73, no. 2, p. 125–142.

Gordey, S.P. and Anderson, R.G., 1993. Evolution of the northern Cordilleran miogeocline, Nahanni map area (105I), Yukon and Northwest Territories. Geological Survey of Canada, Memoir 428, 214 p.

Grema, H.M., Magnall, J.M., Gleeson, S.A., Milton, J.A., Wudarska, A., Schleicher, A.M. and Schulz, H-M., 2024. Mineralogy and paragenesis of the Boundary zone Zn-Pb±Ag deposit, Yukon, Canada. Economic Geology, vol. 119, no. 8, p. 1833–1859.

Harris, B.S., LaGrange, M.T., Biddle, S.K., Playter, T.L., Fiess, K.M. and Gingras, M.K., 2021. Chemostratigraphy as a tool for sequence stratigraphy in the Devonian Hare Indian Formation in the Mackenzie Mountains and Central Mackenzie Valley, Northwest Territories, Canada. Canadian Journal of Earth Sciences, vol. 59, no. 1, p. 1–17, https://cdnsciencepub.com/doi/10.1139/cjes-2020-0198.

LaGrange, M.T., Konhauser, K.O., Catuneanu, O., Harris, B.S., Playter, T.P. and Gingras, M.K., 2020. Sequence stratigraphy in organic-rich marine mudstone successions using chemostratigraphic datasets. Earth-Science Reviews, vol. 203, 103137, 16 p.

LaGrange, M.T., Harris, B.S., Biddle, S.K., Dhiman, S., Catuneanu, O., Konhauser, K.O., Terlaky, V. and Gingras, M.K., 2025. Integrating chemostratigraphy and sedimentology for sequence stratigraphy in an enigmatic Middle to Late Devonian mudstone. Sedimentologika, vol. 3, no. 1, p. 1–28. doi:10.57035/journals/sdk.2025.e31.1695.

Magnall, J.M., Gleeson, S.A. and Paradis, S., 2020. A new subseafloor replacement model for the Macmillan Pass clastic-dominant Zn-Pb ± Ba deposits (Yukon, Canada). Express Letter, Economic Geology, Bulletin of the Society of Economic Geologists, vol. 115, no. 5, p. 953–959.

Magnall, J.M., Gleeson, S.A., Poulton, S.W., Gordon, G.W. and Paradis, S., 2021. The importance of siliceous radiolarian-bearing mudstones in the formation of sediment-hosted Zn-Pb±Ag in the Selwyn basin, Yukon, Canada. Economic Geology, vol. 110, p. 2130–2146.

Nelson, J.L., Colpron, M., Piercey, S.J., Dusel-Bacon, C., Murphy, D.C. and Roots, C.F., 2006. Paleozoic tectonic and metallogenetic evolution of pericratonic terranes in Yukon, northern British Columbia and eastern Alaska. *In:* Paleozoic Evolution and Metallogeny of Pericratonic Terranes at the Ancient Pacific Margin of North America, Canadian and Alaskan Cordillera, M. Colpron and J.L. Nelson (eds.), Geological Association of Canada, Special Paper 45, p. 323–360.

Posamentier, H.W. and Allen, G.P., 1999. Siliciclastic sequence stratigraphy: Concepts and applications. SEPM Concepts in Sedimentology and Paleontology, vol. 7, 210 p., https://doi.org/10.2110/csp.99.07.

Ratcliffe, K.T., Woods, J. and Rice, C., 2012. Determining well-bore pathways during multilateral drilling campaigns in shale resource plays: An example using chemostratigraphy from the Horn River Formation, British Columbia, Canada. *In:* Proceedings from Eastern Australia Basin Symposium IV, Brisbane, Australia, p. 143–148, https://www.chemostrat.com/wp-content/uploads/2013/07/EABS4_Ratcliffe-et-al.pdf.

Saltzman, M.R. and Thomas, E. 2012. Carbon isotope stratigraphy. *In:* The Geologic Time Scale, F. Gradstein, J. Ogg, M.D. Schmitz and G. Ogg (eds.), Elsevier, p. 207–232. https://doi.org/10.1016/B978-0-444-59425-9.00011-1.

Sano, J.L., Ratcliffe, K.T. and Spain, D.R., 2013. Chemostratigraphy of the Haynesville Shale. *In:* Geology of the Hanyesville Gas Shale in East Texas and West Louisiana, U.S.A., U. Hammes and J. Gales (eds.), AAPG Memoir 105, p. 137–154.

Tribovillard, N., Algeo, T.J., Lyons, T. and Riboulleau, A., 2006. Trace metals as paleoredox and paleoproductivity proxies: An update. Chemical Geology, vol. 232, p. 12–32.

Vail, P.R., Mitchum, R.M.Jr. and Thompson, S.III., 1977. Seismic stratigraphy and global changes of sea level, Part 4: Global cycles of relative changes of sea level. *In:* Seismic Stratigraphy – Applications to Hydrocarbon Exploration, C.E. Payton (ed.), AAPG Memoir 26, p. 49–212.

Vail 1987. Seismic stratigraphy interpretation procedure. *In:* Atlas of Seismic Stratigraphy, A.W. Bally (ed.), AAPG Studies in Geology, no. 27, vol. 1, p. 1–10.

Zecchin, M. and Catuneanu, O., 2013. High-resolution sequence stratigraphy of clastic shelves I: Units and bounding surfaces. Marine and Petroleum Geology, vol. 39, p. 1–25.

Zecchin, M. and Catuneanu, O., 2017. High-resolution sequence stratigraphy of clastic shelves VI: Mixed siliciclastic-carbonate systems. Marine and Petroleum Geology, vol. 88, p. 712–723.

Ordovician to Devonian stratigraphy of Nááts'įhch'oh National Park Reserve, Northwest Territories

*Sarah K. Schultz**
Yukon Geological Survey

Merilie A. Reynolds
Northwest Territories Geological Survey

Schultz, S.K. and Reynolds, M.A., 2026. Ordovician to Devonian stratigraphy of Nááts'įhch'oh National Park Reserve, Northwest Territories. *In*: Yukon Exploration and Geology 2025, A. Stuart, L.H. Weston and S.K. Schultz (eds.), Yukon Geological Survey, Government of Yukon, p. 191–205.

Abstract

The Ordovician to Devonian sedimentary deposits of Selwyn basin have been studied in some detail in localities where mineralization of certain critical minerals (e.g., zinc, nickel, vanadium, etc.) is known to occur within these deep-water, mudstone-dominated strata. The coeval shallow-water sedimentary deposits of the Mackenzie platform have not received as much attention, nor have they been correlated basinwards to understand how the evolution of paleoshoreline successions affected deposition throughout the basin. This study applies a sequence stratigraphic framework to map shallow-water sedimentary deposits, integrating geochemical and chronostratigraphic data to correlate units and link shifts in sedimentation patterns to changes in relative sea level. Importantly, understanding how occurrences of critical metals such as the MacMillan Pass and Howard's Pass zinc-lead deposits fit within a sequence stratigraphic framework will help inform future exploration strategies within these districts.

Plain language summary

In August 2025, the Yukon Geological Survey (YGS) and the Northwest Territories Geological Survey (NTGS) began geological work in the Nááts'įhch'oh National Park Reserve investigating rocks that are approximately 486 to 359 million years old. Research on these rocks will contribute to understanding the natural history of Nááts'įhch'oh National Park Reserve, including the evolution of an ancient ocean shoreline and how mountain-building events and changing climate affected ancient ocean life. Furthermore, this information will provide an important puzzle piece for understanding why certain mineral deposits, like the MacMillan Pass and Howard's Pass zinc-lead deposits, formed where they did. This summer, three trips were made by helicopter to areas known to contain the rock intervals of interest in order to identify the most efficient way to carry out more detailed work in summer 2026.

* sarah.schultz@yukon.ca

Introduction

Nááts'įhch'oh National Park Reserve contains well-exposed sections of strata that accumulated in the Mackenzie platform (shallow-water carbonate deposition) and Selwyn basin (deep-water siliciclastic deposition) during the Paleozoic (Figs. 1 and 2). Current studies at the Howard's Pass and MacMillan Pass districts are being conducted on subsurface drill core that intersects the Ordovician to Devonian strata to understand the evolution of deep-water environments throughout this time (Xu et al., 2024; Schultz et al., this volume). To establish a regionally consistent stratigraphic framework and understand the evolution of the basin, deposition that occurs in the deep basin must be tied to its coeval shallow marine deposits. Such correlations will explain patterns in sedimentation as they relate to changes in relative sea level and tectonic events.

The goal for the first year of this project was to conduct several reconnaissance day trips to Nááts'įhch'oh National Park Reserve and Nahanni National Park to identify appropriate locations for multiday camps in 2026 and 2027. The permit for Nahanni National Park was put on hold until 2026 and as a result, only three of the four areas were visited during the 2025 field season. The areas were selected based on information available for outcrops logged by the Geological Survey of Canada in the 1960s and 1970s. At the selected locations, the outcrops intersect the Ordovician to Late Devonian shallow-water platform and slope sedimentary deposits. The outcrop in this region is patchy and discontinuous, and can have significant structural deformation, so the reconnaissance trips were necessary to determine which outcrops at each area would be suitable for sampling and logging in future years. The study was initially anchored on the Macmillan Pass and Howard's Pass areas where extensive drill cores are available to document the stratigraphy of the deep-water sedimentary deposits. Detailed stratigraphy will be established through whole-rock geochemistry, multi-element analysis by portable x-ray fluorescence (pXRF), and organic carbon isotopic analyses. The framework developed from continuous drill core will be expanded regionally to exposed sections in outcrops to develop a regional framework. The outcrop in the region records deposition in shallower water settings and along the transition to the continental slope. By incorporating observations from outcrop, it is possible to build sections that document the down-depositional dip variability of a basin and to map paleoshorelines regionally.

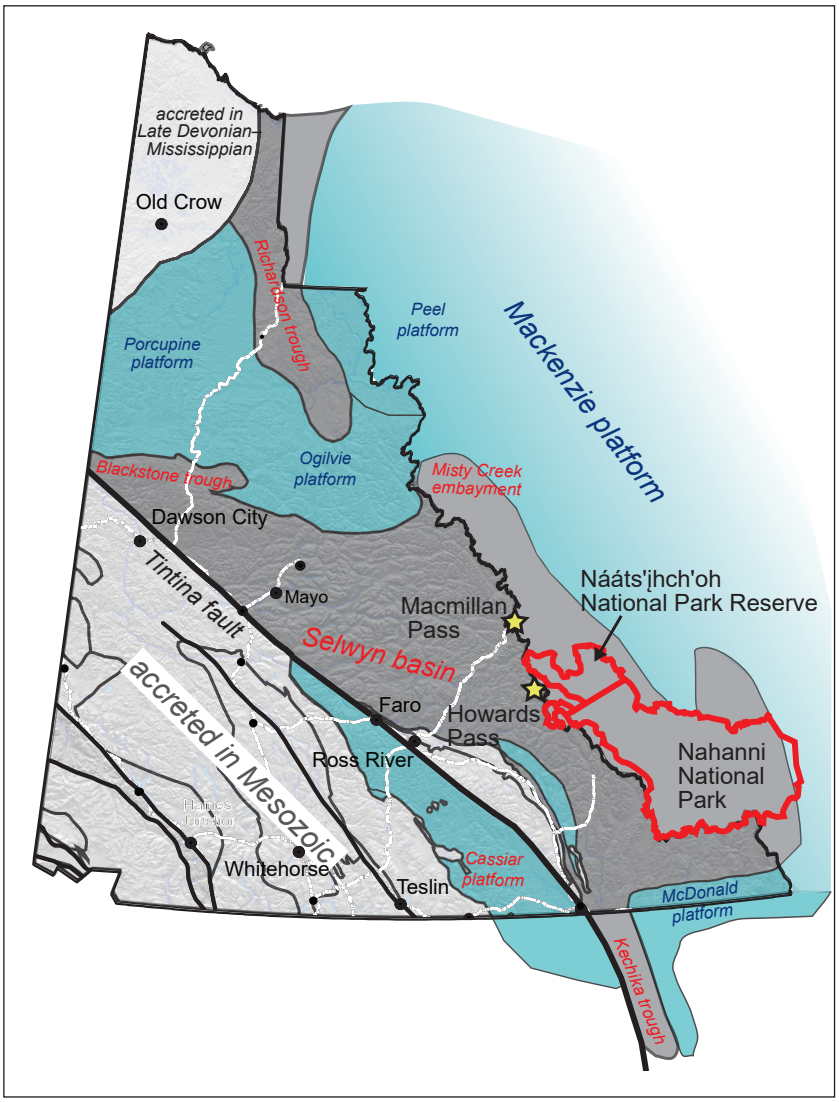


Figure 1. *Map illustrating the location of Selwyn basin and Mackenzie platform (after Fraser et al., 2021). The location of the park boundaries for Nááts'įhch'oh National Park Reserve and Nahanni National Park are denoted by red outlines.*

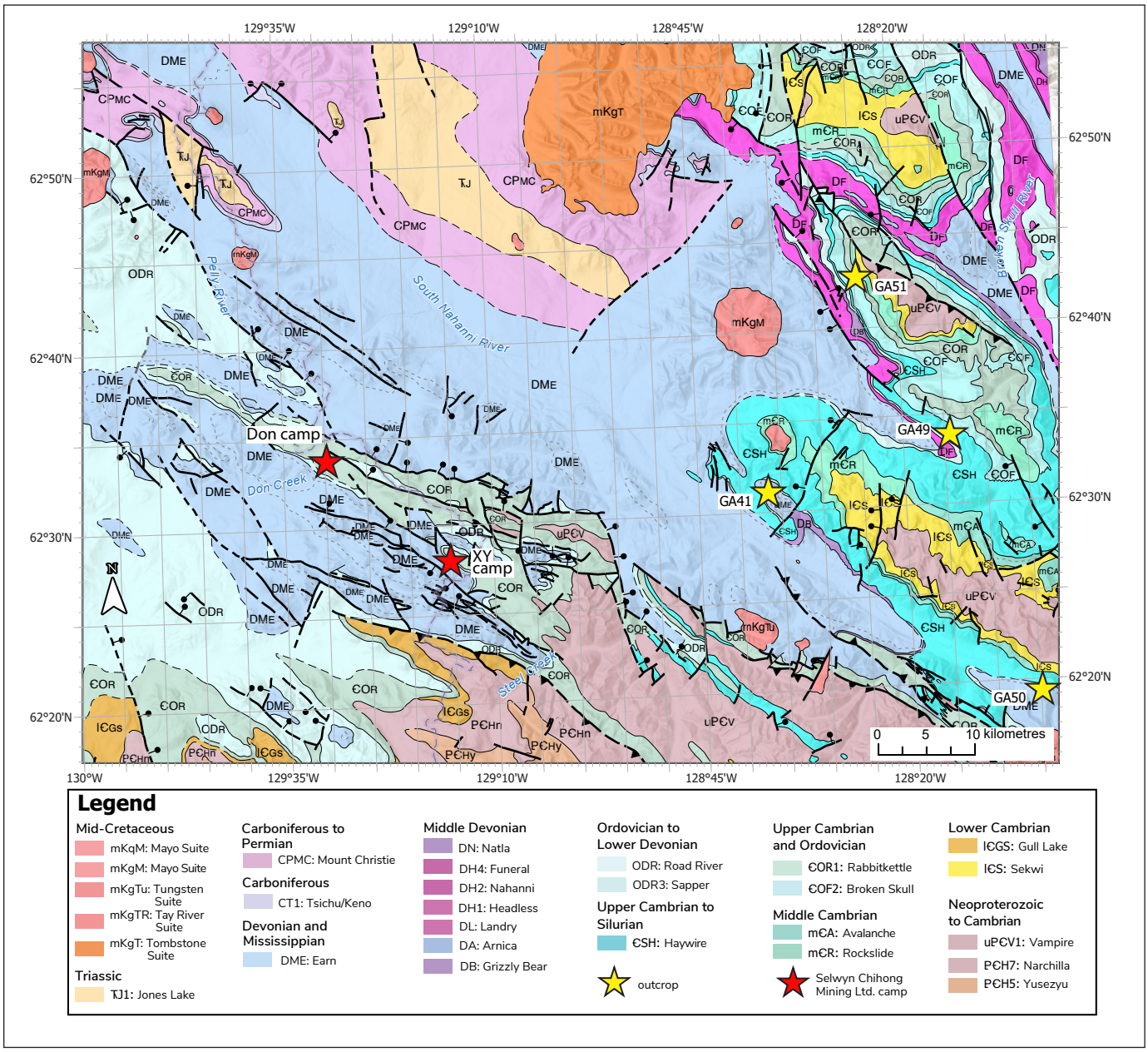


Figure 2. *Bedrock geology map (NTS 105/l) covering the study area and including the distribution of Ordovician and Devonian strata. The four main outcrops that were examined in this study are also shown (GA41, GA49, GA50, GA51).*

Study area and methods

The study area occurs within the Little Nahanni River map sheet (NTS 105/l; Fig. 2) and includes outcrops that were described in a Geological Survey of Canada report by Gordey and Anderson (1993). Areas with outcrops of sedimentary strata of the right age were selected based on that report and the areas of interest are located in Náátsʼįhch'oh National Park Reserve and Nahanni National Park. The location names used in this study (e.g., GA41) refer to the section numbers used by Gordey and Anderson (1993). The purpose of the 2025 field season was to do some initial reconnaissance to determine which outcrops would best support constructing a representative geochemical key for the shallow-water platform deposits. By doing this initial work, we can reduce the number of fly camps that would have to be set up in subsequent years, minimizing our environmental impact on the park.

Field sites were accessed by a helicopter that was based out of Selwyn Chihong Mining Ltd.'s mining

leases at the XY camp (occupied by Rackla Metals; Fig. 2). When selecting flight paths, we chose routes and landing areas that avoided wildlife corridors whenever possible. Additionally, we avoided flying during lambing season and stayed clear of known salt licks when possible.

Basin analysis and tectonism

The bedrock underlying the Little Nahanni River map area (NTS 105/l) form a westward-thickening package of sediment that accumulated from the mid-Proterozoic to the Middle Jurassic (Gordey and Anderson, 1993). During this time, the basin periodically experienced extensional or rifting events that resulted in changes in accommodation due to subsidence and fluctuations in regional sedimentation patterns. The rocks that were initially deposited during this time were later re-incorporated into the Mesozoic fold and thrust belt during mountain-building events, re-exposing the strata along ridges. The sedimentary deposits that accumulated during the Ordovician to Late Devonian experienced differing styles of tectonism, leading to variability in the distribution and extent of sedimentary facies within the Mackenzie platform and Selwyn basin.

Sequence stratigraphy

Sequence stratigraphy is a methodology of correlation in which changes in stratal stacking patterns of sedimentary depositional environments are tied to fluctuations in relative sea level (Catuneanu et al., 2011). In shallow marine carbonate successions, reef-building and marine organisms tend to be sensitive to changes in salinity, sedimentation, substrate consistency, and sunlight, allowing for fluctuations in relative sea level to be readily identified through abrupt changes in facies. These changes facilitate the identification of sequence stratigraphically significant horizons. In deep-water successions, variations in relative sea level are more difficult to identify due to many units being mudstone-dominated successions with limited macroscopic features (e.g., body fossils, trace fossils, sedimentary structures, etc.) to use for identifying changes in the sedimentary depositional systems. In these scenarios, whole-rock geochemistry, pXRF and organic/inorganic carbon isotopes are collected to document subtle geochemical variations that occur in relation to the position of relative sea level. These geochemical variations also occur in shallow marine successions and can be used to correlate basinward. In this study, organic and inorganic carbon isotopes, whole-rock geochemistry and pXRF will be conducted on the deposits collected from the parks. The initial framework for the deep-water deposits that is currently being developed from continuous drill core in the Macmillan Pass and Howard's Pass mineral districts (Schultz et al., this volume) will be expanded regionally to exposed sections in outcrops.

Previous work

The nomenclature of stratigraphic units in this study is lithostratigraphically divided into shallow water versus basinal sedimentary deposits (Fig. 3). The shallow-water stratigraphy of the platform (including the slope facies) occurs in the Mackenzie platform and follows the nomenclature proposed by Gabrielse et al. (1973) and Gordey and Anderson (1993). The stratigraphic nomenclature for the deep basin stratigraphy follows the units proposed by Cecile (1982, 2000) and Gordey and Anderson (1993). Age relationships between formations have been dated using conodont biostratigraphy, and previous work on the biostratigraphy is summarized in Gordey and Anderson (1993).

The deep-water Ordovician strata in the region have been extensively studied in drill core in the Howard's Pass mineral district (Morganti, 1979; Jonasson and Goodfellow, 1986; Gadd et al., 2016a; Slack et al., 2017; Kamal and Hickey, 2020; Xu et al., 2024). In this area, the basinal strata host lead-zinc deposits within mudstone-dominated successions of the Duo Lake Formation. The Devonian strata in this region contain only minor zinc-lead mineralization (Gadd et al., 2016b) and have received limited attention in the literature to date, particularly from a sedimentological viewpoint. In the study by Xu et al. (2024), pXRF data have been collected from numerous drill core that intersects the Duo Lake Formation. This study is creating a geochemical key for the Ordovician to Silurian deep-water sedimentary deposits that can be used in stratigraphic correlations elsewhere in the basin.

Gordey and Anderson (1993) conducted a study in the Little Nahanni River map sheet (NTS 105/l) and detailed the initial geological results from logging outcrop along exposed ridges in the region. A more detailed account and analysis of the sedimentology has not been conducted to date on many of these formations. This is an important area that links deep-water and shallow-water depositional trends; therefore, mapping the sedimentary facies and how they change throughout the area will be important for understanding the evolution of paleoshorelines.

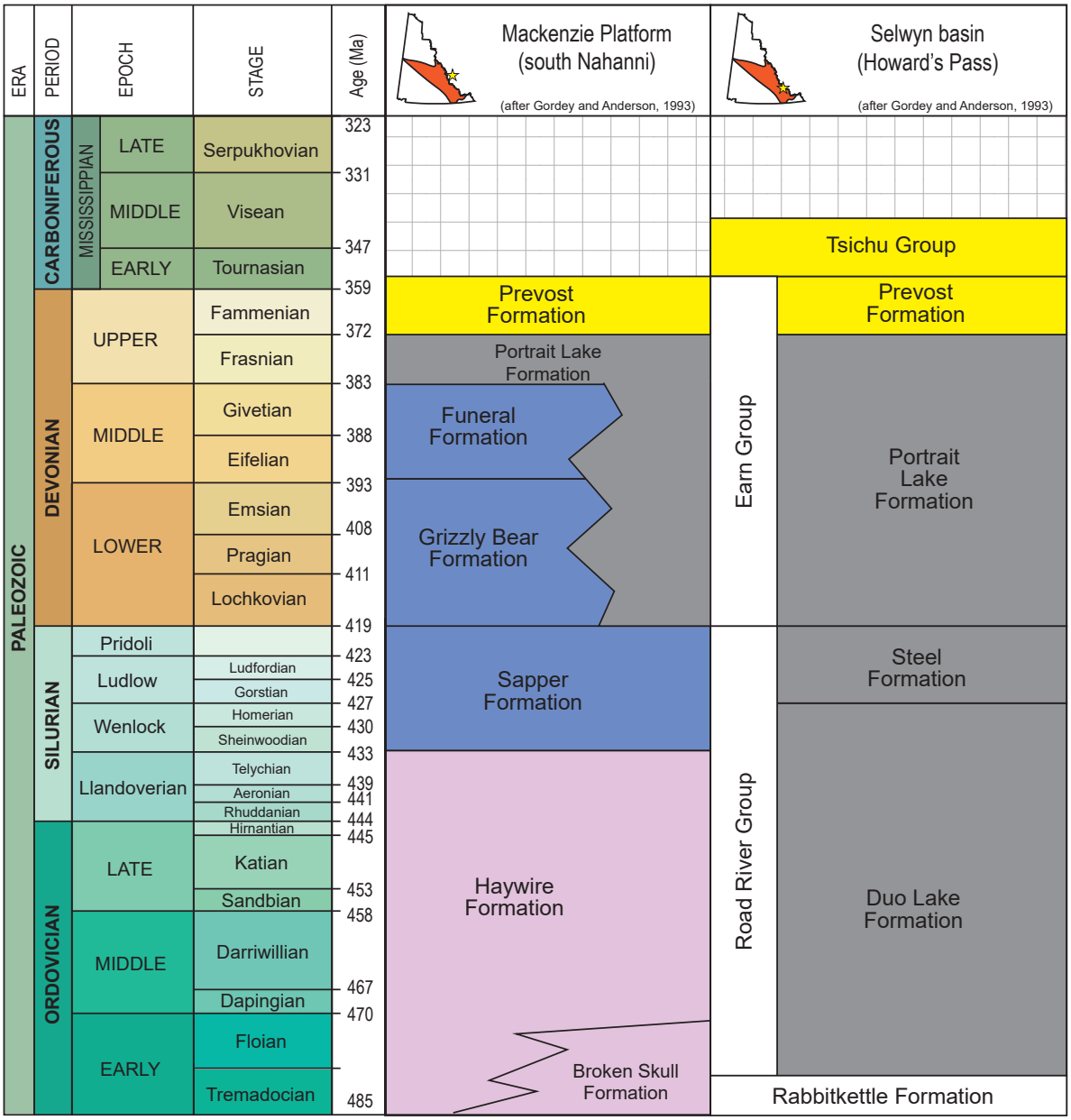


Figure 3. *Table of formations for the strata at Howard's Pass and the Mackenzie Mountains (after Gordey and Anderson, 1993).*

Platform stratigraphy

In the Mackenzie platform between the South Nahanni and Broken Skull rivers, the Paleozoic strata is composed of variable dolostone and limestone units that contain subordinate amounts of shale and sand (Figs. 2, 3). This reflects deposition along a carbonate platform and/or ramp, and the gradual transition to deeper, continental slope strata.

Haywire Formation

The Ordovician to Early Silurian Haywire Formation was first described and proposed as a formation by Gordey and Anderson (1993). This unit is comprised of dolostone that weathers white to light grey in colour and contains a variable amount of chert. The facies associated with the Haywire Formation are variable between outcrop localities. At the type-section of GA40, the unit is 639 m thick and is defined as a lithologically distinct unit from the underlying

Avalanche Formation based on the incorporation of sandstone into the Haywire Formation deposits. The upper contact at the type-section is faulted, and the section at GA41 is proposed as the type-contact for the transition from the Haywire Formation into the Sapper Formation. Gabrielse et al. (1973) suggested that the base of the Haywire Formation represents a significant regional unconformity across the basin. Some outcrops contain fossil material, which include crinoids, corals, brachiopods and disarticulated shelly debris (Gordey and Anderson, 1993).

It is suggested that the Haywire Formation records deposition in a shallow subtidal to intertidal environment (Gordey and Anderson, 1993). It is the outer shelf equivalent to the reefal units of the Rabbitkettle, Broken Skull and Sunblood formations (see Gabrielse et al., 1973; Gordey and Anderson, 1993).

Sapper Formation

The Sapper Formation is Silurian in age and was first described and proposed as a formation by Gordey and Anderson (1993). It is mapped as two distinctive informal members across the study area. The lowermost member is commonly referred to as the limestone member and is composed of light-grey weathering, thinly bedded limestone. The uppermost member is the silty member, which is comprised of limestone to dolostone that weathers to a distinctive tan-orange colour. At type-section GA51, the unit is 362 m thick. There, the basal 107 m is well preserved, and the remainder of the unit overlying this exposure is preserved as patchy outcrop.

It is proposed that the Sapper Formation was deposited along a shallow carbonate shelf below fairweather wave base (Gordey and Anderson, 1993). Fossils in this unit include graptolites, conodonts and other disarticulated shelly debris.

Grizzly Bear Formation

The Early Devonian Grizzly Bear Formation was first described by Gabrielse et al. (1973) as a distinct bioclastic limestone unit that can be used as a marker unit throughout the Little Nahanni River map sheet (NTS 105/I). In this area, the formation reaches a maximum thickness of approximately 200 m (Gabrielse et al., 1973; Gordey and Anderson, 1993). The formation unconformably overlies the Sapper Formation and is unconformably overlain by the Funeral Formation. The Grizzly Bear Formation is biostratigraphically constrained quite precisely by the presence of twin axial canal crinoid ossicles that are present at the base of the section (Gordey and Anderson, 1993). The Grizzly Bear Formation reflects deposition in a shallow marine setting near fairweather wave base to an offshore setting in a shoal depocentre along a carbonate platform. The correlative deep-basin strata is the Portrait Lake Formation.

Funeral Formation

The Middle Devonian Funeral Formation was first described by Douglas and Norris (1961) and was later redefined by Gabrielse et al. (1973). The formation is an orange-weathering, shaly to thinly bedded limestone succession. Like the Grizzly Bear Formation, the Funeral Formation is a lateral equivalent of the Portrait Lake Formation. No definitive depositional environment was proposed by Gordey and Anderson (1993) for the unit in the Nahanni map sheet; however, based on its stratigraphic position and sedimentology, it is likely that the unit was deposited between the offshore zone of the continental shelf to the continental slope.

Basin stratigraphy

Deep-water stratigraphy in the region records deposition as hemipelagic sedimentation, turbidites, and mass transport deposits (Schultz et al., this volume). At Howard's Pass, the deep-water sedimentary deposits are mudstone-dominated, making the delineation of stratigraphic units challenging without the addition of geochemical, biostratigraphic or organic carbon isotope studies.

Duo Lake Formation

The Ordovician to Silurian Duo Lake Formation was defined by Cecile (1982) and comprises of siliceous shale that preserves graptolites, chert and limestone nodules. The Duo Lake Formation contains significant Pb-Zn mineralization at Howard's Pass and has been studied extensively at that location for its potential to host base metal deposits (e.g., Morganti, 1979; Jonasson and Goodfellow, 1986; Xu et al., 2024). The Duo Lake Formation was deposited in a deep-water setting through hemipelagic sedimentation, contourites, or as the distal depositional extent of a turbidite lobe.

At Howard's Pass, the Duo Lake Formation also contains intervals with phosphorite beds or laminated fine-grained apatite (Gadd et al., 2016a; Slack et al., 2017). This, along with bulk rock geochemical data from Howard's Pass, led Slack et al. (2017) to reinterpret the Duo Lake Formation to have formed first

in a marginal basin that may have become increasingly restricted over time and later in an upper slope or outer shelf setting.

Steel Formation

The Late Silurian Steel Formation was defined by Gordey and Anderson (1993) at the GA14 type-section. At this section, the unit is approximately 143 m thick and comprised of siliceous mudstone beds that contain a varying degree of bioturbation. Bioturbation is observed as wispy laminae in outcrop. In core, trace fossils such as Zoophycos, Phycosiphon and Helminthopsis have been observed. The Steel Formation was deposited in an offshore to slope environment below fairweather wave base (Gordey and Anderson, 1993). The age of the unit is constrained based on the biostratigraphy of the underlying Duo Lake Formation and the overlying Portrait Lake Formation.

Portrait Lake Formation

The Devonian Portrait Lake Formation was defined by Gordey and Anderson (1993) at an outcrop in the Macmillan Pass region of the Niddery Lake map sheet (NTS 105/O). The unit is comprised of siliceous mudstone, chert, sandstone and conglomerate intervals. The conglomerate is prevalent in the Macmillan Pass region and is less predominant in the Howard's Pass region. The Portrait Lake Formation records deposition in a deep-water setting, and deposition occurred through hemipelagic sedimentation, turbidites and mass transport deposits (Gordey and Anderson, 1993; Schultz et al., this volume).

Prevost Formation

The Late Devonian Prevost Formation was defined by Gordey and Anderson (1993) at the type-section GA15. The section reaches thicknesses of up to 555 m; however, throughout much of the map area, the unit is not preserved. The Prevost Formation is separated lithologically into informal members that include a basal sandstone, a middle member that is siltstone and shale-dominated, and an upper member of sandstone and conglomerate. The Prevost Formation was deposited in a sand-rich turbidite succession through gravity-driven processes.

Results

The initial results of this study include rudimentary observations on the stratigraphic section. Each location below marks the start of the stratigraphic sections and is named based on the mapping by Gordey and Anderson (1993).

Section GA41 – 62.53167°N, 128.60833°W

This is the reference section for the basal contact of the Prevost Formation with the underlying Portrait Lake Formation and the contact between the Sapper and Haywire formations. In this interval, 330 m of Late Devonian rocks were logged along a ridge that was previously mapped by Gordey and Anderson (1993; Figs. 4 and 5). At this outcrop, the Haywire Formation was not included in the original logged section despite being exposed below the Sapper Formation. Additionally, below the ridge within the valley, a well-exposed outcrop of the Haywire Formation is preserved. A composite section is proposed to be created at this location in order to intersect a more continuous section of strata and include the basal units of the Haywire Formation.

The top of the Haywire Formation is well-exposed at this site (Fig. 6). At GA41, the Haywire Formation is a wavy-bedded, white-grey dolostone with thin carbonaceous laminae lining bedding plane surfaces; local discontinuous pyritic laminae and nodules were also observed. There is an increasing amount of chert toward the top of the unit. The chert is irregularly shaped and may preserve or replace fossil material or trace fossils (Fig. 7).

The Sapper Formation has patchy exposure at this section. The basal contact was inferred based on a colour change in the scree from the white to grey of the Haywire Formation to the darker grey of the limestone beds of the Sapper Formation (Fig. 7). The uppermost section of the Sapper Formation records a colour change to tan-orange strata that is poorly exposed in the scree. The upper contact with the Portrait Lake is preserved in scree and was inferred based on the change in colour from tan-orange to grey (Fig. 6).

The Portrait Lake Formation is preserved along the length of the ridge (Fig. 6). The exposure is patchy just above the contact with the Sapper Formation, but farther up the section there are more continuous intervals of outcrop inferred to be in place. Normally graded beds and chert-rich mudstone are observed in this unit.

The contact between the Portrait Lake Formation and the Prevost Formation is distinct at this section (Fig. 6). A few metres past this contact, the outcrop becomes unsafe to walk on. It was noted that the ridge to the north contained a similar section of strata that would be worth investigating during the proposed fly camp for this site to determine whether a composite section could be constructed through the upper units.

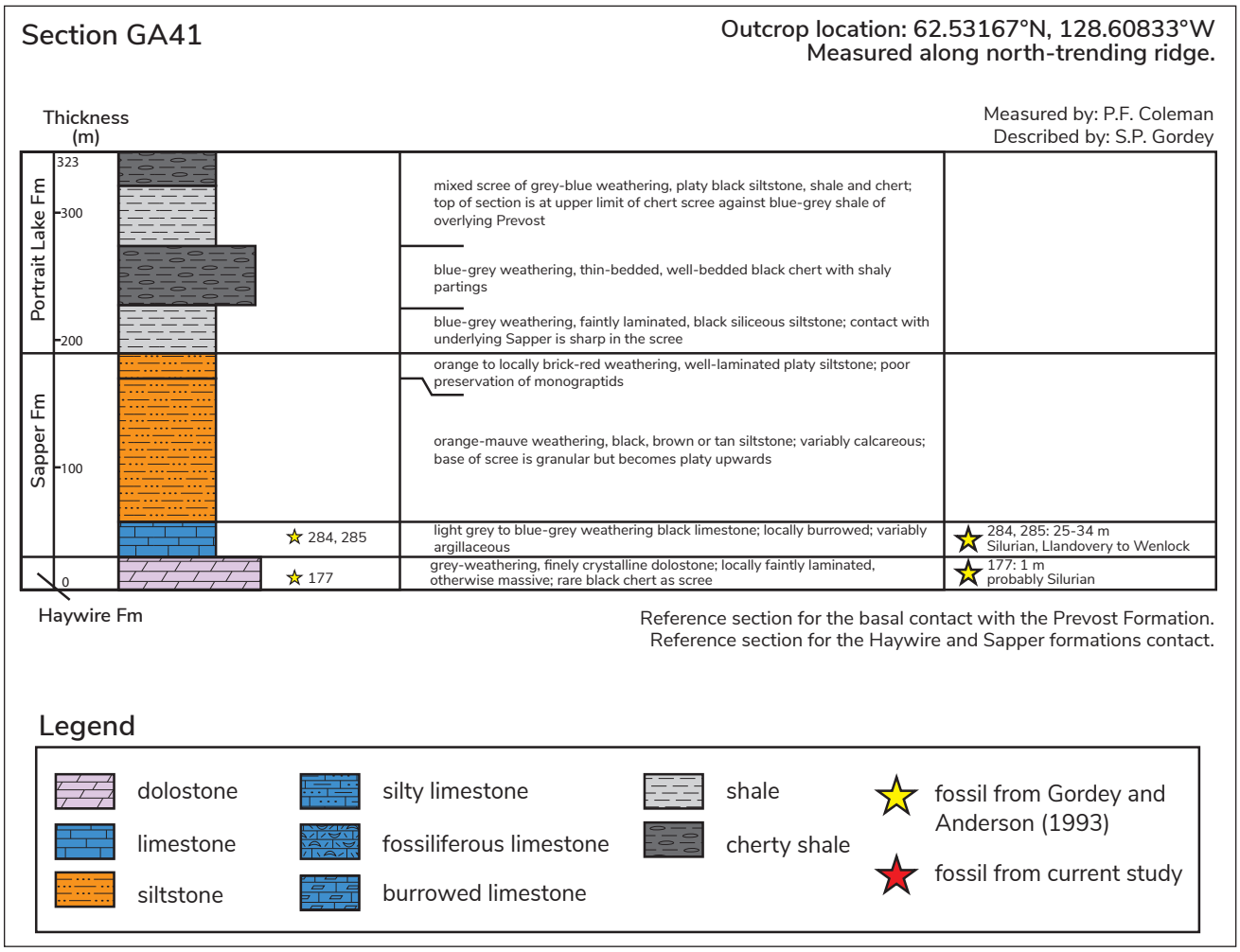


Figure 4. *Outcrop log from Gordey and Anderson (1993) for sections GA41. Fm – Formation.*

Section GA49 – 62.55°N, 128.29167°W

The GA49 section was visited due to multiple ridges in the area that preserve the Haywire, Portrait Lake and Funeral formations. The proposed future fly camp is situated lower down in the valley in an area that would be central to accessing the multiple surrounding ridges (Fig. 8a). Along these ridges, the exposure is patchy (e.g., Fig. 8b) and a composite section for the area would need to be constructed in order to detail a continuous section of strata.

During the reconnaissance day, the area that was covered at the GA49 section was more extensive than at locations GA41 and GA51. The visit allowed us to confirm that sufficient outcrop was present to warrant more work; however, more detailed preliminary observations about the formations were not documented due to time constraints. The locations of the most well-exposed outcrops were marked on the map to be revisited in 2026. These locations include sections logged by Gordey and Anderson (1993) as well as sections that preserve the Grizzly Bear and Haywire formations that may not have been visited during the initial study.

Section GA50 – 62.31833°N, 128.00333°W

This outcrop section was not visited in the 2025 field season as it is located outside of the area that was included in the permit issued by Parks Canada (Fig. 2). The Nahanni National Park area will be included in the 2026 or 2027 permit application to allow for further extensions of stratigraphic correlations in the region.

The strata at GA50 are preserved along a northwest-trending ridge. The basal contact between the Grizzly Bear and Portrait Lake formations is preserved in this area (Fig. 9; Gordey and Anderson, 1993). A fossil sample was taken by Gordey and Anderson (1993) in

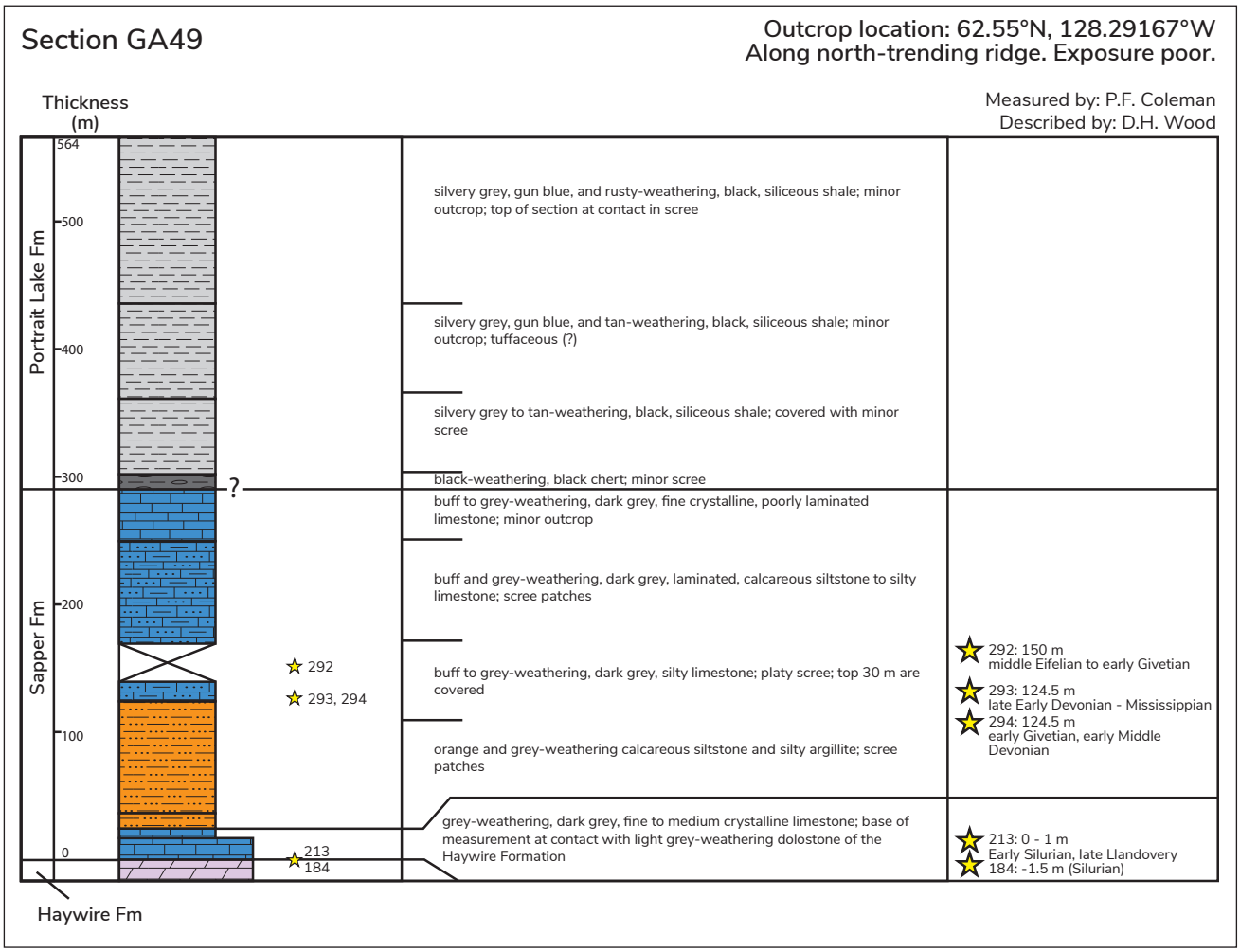


Figure 5. *Outcrop log from Gordey and Anderson (1993) for section GA49; Fm – Formation. See Figure 4 for legend.*

the Sapper Formation, but no additional fossil material was collected to refine the age relationships of the upper formations. It was noted by Gordey and Anderson (1993) that this section had a patchy distribution of outcrop, and detailed sampling through this section may be challenging.

Section GA51 – 62.7042°N, 128.43476°W

The GA51 section is the type-section for the Sapper Formation. The overlying Grizzly and Funeral formations are exposed along the top of a ridge. The Haywire and Broken Skull formations are preserved underlying the Sapper Formation.

At this field site, the Haywire Formation was not included in the log by Gordey and Anderson (1993; Fig. 9). From the reconnaissance trip, it was apparent that a significant amount of well-exposed outcrop preserves a continuous section of the Ordovician to Silurian Haywire Formation, including the contact with the overlying Sapper Formation. Based on previous mapping at this site, we estimate the thickness of the beds to be approximately 250 m.

Although this is the type-section for the Sapper Formation, it is noted that the top of the unit is poorly exposed due to cover by vegetation and scree. Along a ridge about 1–2 km to the southeast (Fig. 10a), there may be additional sections that could be logged to build a composite section for the Sapper Formation. The beds that are exposed weather light grey, and have a similar appearance to the lower limestone beds of the Sapper Formation that were observed at GA41.

The fossil material that was observed in the Grizzly Bear Formation and documented by Gordey and Anderson (1993) included stromatoporoids and disarticulated crinoid ossicles. The crinoids with twin axial canals suggest an age of approximately Emsian

to Eifelian (408–388 Ma). This section was visited at the end of the reconnaissance trip, and less time was available to look through the scree and outcrop material. It was noted however that a significant amount of the section remains in place along the ridge leading up to the summit of a mountain to the southwest (Fig. 10b). Transects along the southeastern and northeastern ridge will be completed to create a composite stratigraphic section that includes all strata from the Ordovician to Late Devonian.

Proposed research for 2026 and 2027

Fly camps will be established in 2026 at GA41, GA49 and GA51 for six to eight-day stays. At each study location, the most extensive and continuous outcrop will be logged and sampled at a 1 or 2 m interval. Samples weighing approximately 200 g will be collected at each interval and will be used for the geochemical study. Whole-rock and carbon isotope analyses tend to be destructive analytical methods, so only a small portion of the sample will be used for this

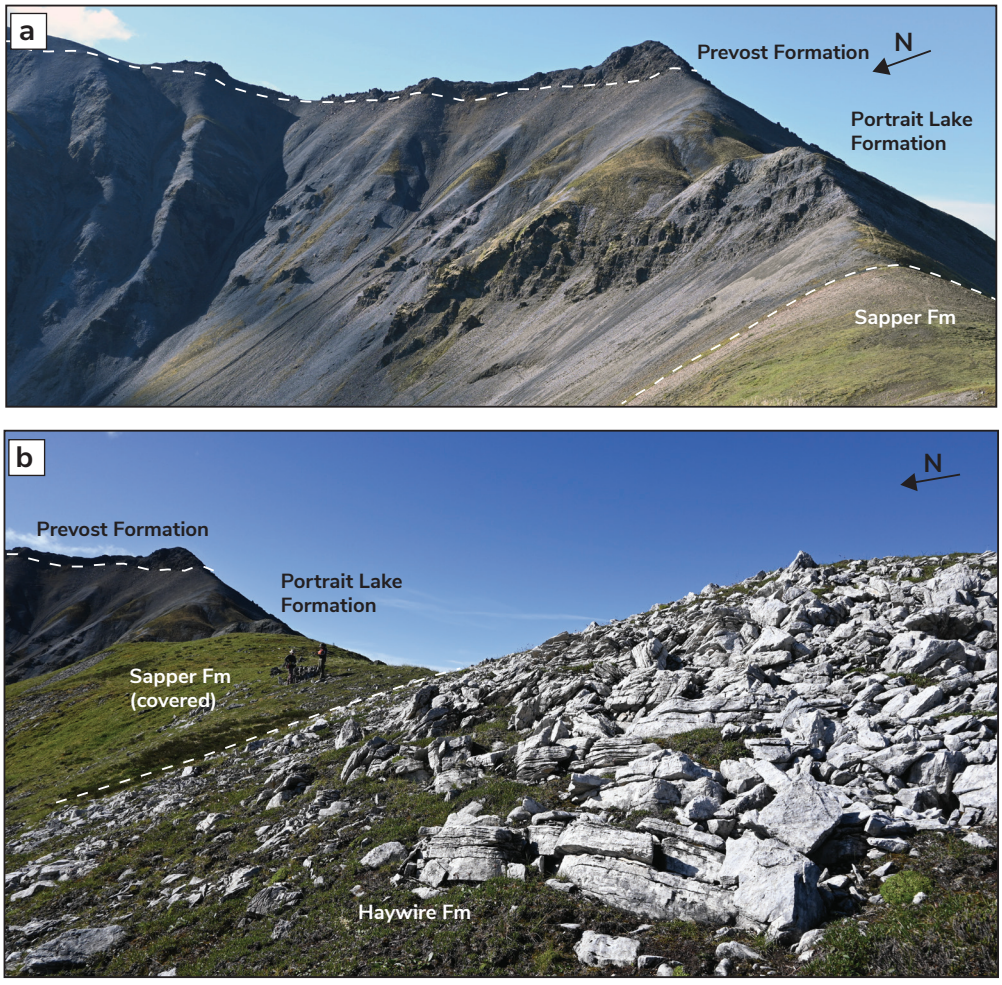


Figure 6. *Outcrop photos showing the location of formation contacts at section GA41.* ***(a)*** *The location of the contact between the Sapper and Portrait Lake formations is located at the transition from the tan-orange weathering scree into the overlying grey-weathering scree. The Portrait Lake Formation has chert-rich intervals that are well exposed along the ridge. The upper contact with the Prevost Formation is sharp in outcrop; however, the strata of the Prevost Formation form steep outcrop sections which will make them difficult to sample.* ***(b)*** *The Haywire Formation weathers white to light grey at this section. The upper contact with the Sapper Formation is not distinct as the lower beds of the Sapper Formation are covered at this section.*

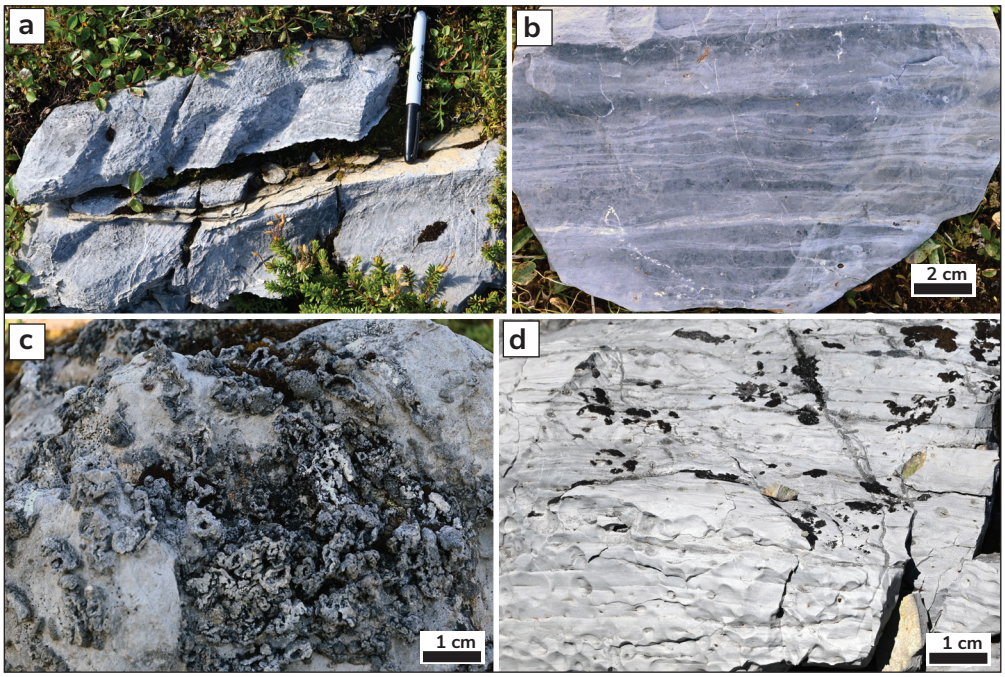


Figure 7. *Outcrop photos at GA41 section.* ***(a)*** *A bed of the Sapper Formation in place, near the base of the unit.* ***(b)*** *Limestone sample of the Sapper Formation near the base of the unit.* ***(c)*** *Nodular chert near the top of the Haywire Formation.* ***(d)*** *Wavy beds in the Haywire Formation containing preserved thin carbonaceous laminae.*

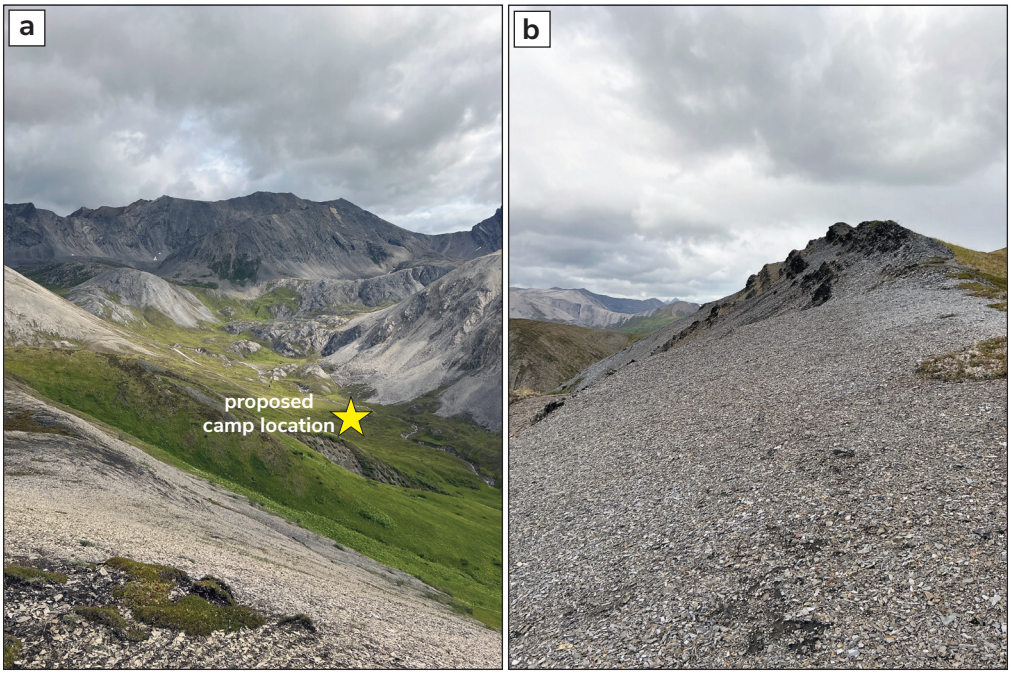


Figure 8. *Local area to GA49 section.* ***(a)*** *The proposed fly camp location is noted by the yellow star. The strata surrounding this camp is the Haywire Formation. View is to the northeast.* ***(b)*** *Portrait Lake Formation outcrop.*

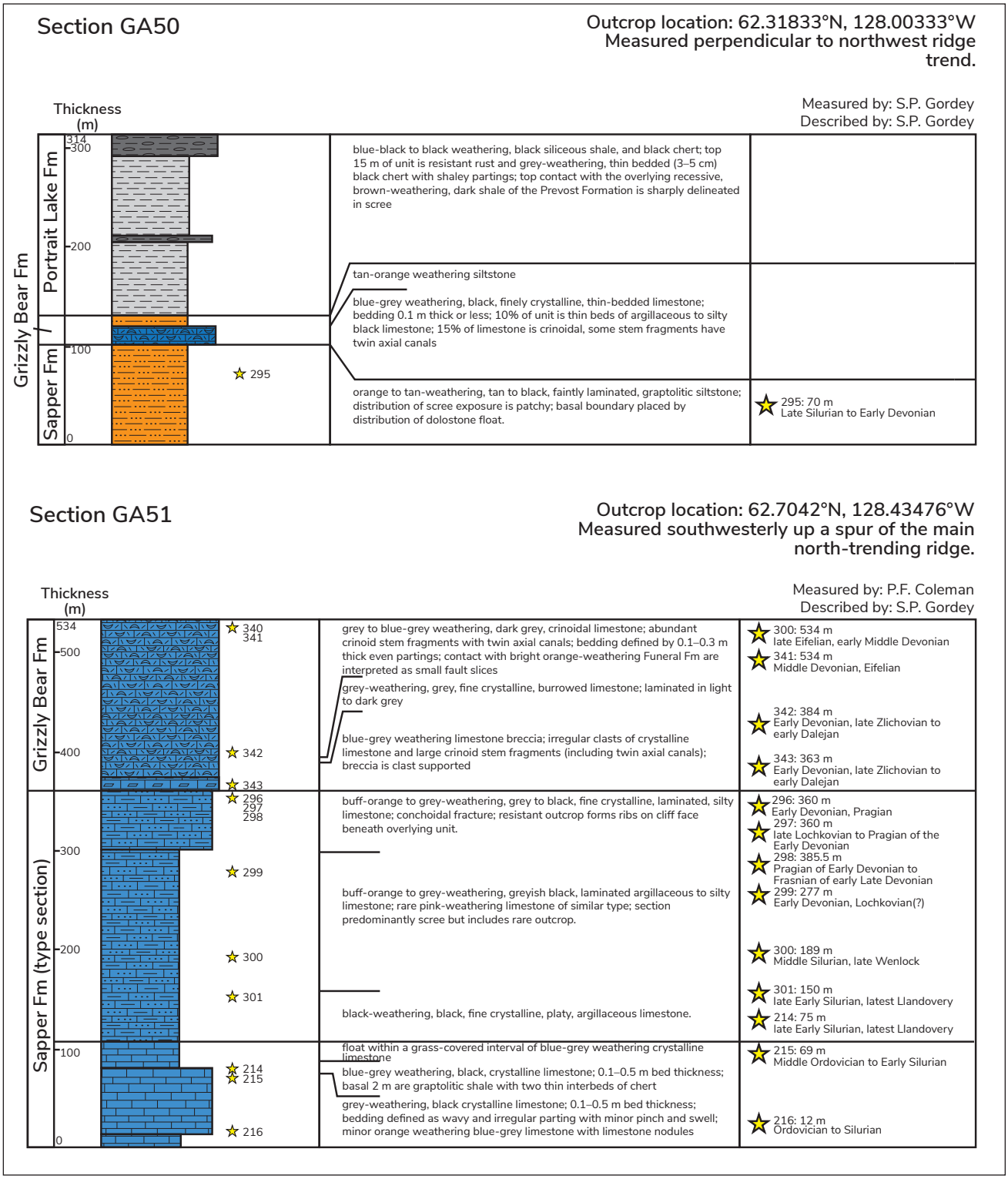


Figure 9. *Outcrop logs from Gordey and Anderson (1993) for sections GA50 and GA51; Fm – Formation. See Figure 4 for legend.*

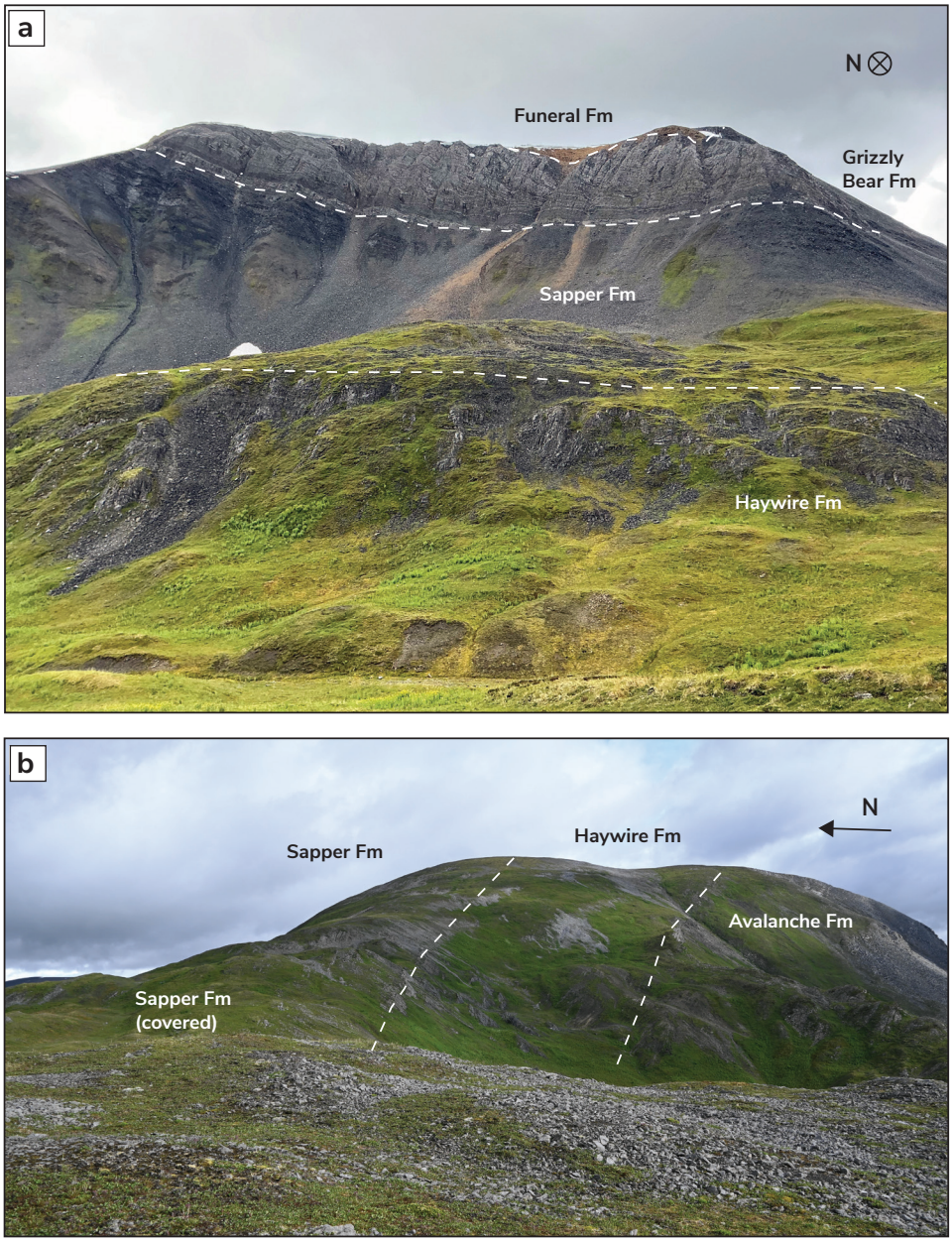


Figure 10. *Field photos of GA51 section.* ***(a)*** *Contacts between the Haywire, Sapper, Grizzly Bear and Funeral formations. The Grizzly Bear Formation forms cliffs at this section, with large boulders found in the scree at the base of the slope. It is possible that by walking along the ridge to the west that the unit will be able to be investigated further. The Funeral Formation is preserved as a thin orange unit that overlies the Grizzly Bear Formation. Outcrop locations to the southwest and northeast preserve thicker successions of this unit for building a composite stratigraphic section.* ***(b)*** *Contacts between the Avalanche, Haywire and Sapper formations. At this section, the basal 100 m of the Sapper Formation are exposed in outcrop. The rest of the unit is generally covered with a patchy distribution of outcrop. To the northeast and southwest of this location (within a few kilometres) there are other exposures of the unit that may be used to build a composite section.*

purpose. The remainder of the samples will be retained at the H.S. Bostock Core Library in an archive to be used in future studies.

Section GA40 is the representative type-section for the Haywire Formation and it may be included on the revised permit application that will be submitted to Parks Canada. If time permits, section GA50 will be visited for a reconnaissance trip. If there is not a significant amount of section exposed, it is possible that this site will be visited by one or two helicopter-supported day trips to compile less detailed stratigraphic columns that document the changes in sedimentology and the position of stratigraphic contacts.

In 2027, the YGS and NTGS may revisit the region to complete work that may not be accomplished in 2026. It is anticipated that this part of the research will take less than three weeks to complete. The results from this work will be published in subsequent Yukon Exploration Geology reports, in an MSc project, and in journal publications.

Acknowledgments

Thanks to Rackla Metals Inc. for providing helicopter support for the scout trips and to Rackla Metals and Selwyn Chihong Ltd. for hosting us in their camps. Thank you to Sophia Tafel for excellent assistance in the field. This study is funded by the YGS, NTGS, and a grant from Natural Resources Canada as part of the Critical Minerals Geoscience and Data Initiative (CMGD), delivered by the Geological Survey of Canada and awarded to NTGS. Multi-year research permits were granted by the Northwest Territories Scientific Research License (No. 17563) and by Parks Canada (NAANPR-2025-46425). Samples collected in this study will be stored in a repository at the H.S. Bostock Core Library and can be accessed by contacting the Yukon Geological Survey. This publication relates to the NTGS contribution #0168.

References

Catuneanu, O., Galloway, W.E., Kendall, C.G.S., Miall, A.D., Posamentier, H.W., Strasser, A. and Tucker, M.E., 2011. Sequence stratigraphy: Methodology and nomenclature. Newsletters on Stratigraphy, vol. 44, p. 173–245.

Cecile, M.P., 1982. The lower Paleozoic Misty Creek embayment, Selwyn basin, Yukon and Northwest Territories. Geological Survey of Canada, Bulletin 335, 78 p.

Cecile, M.P., 2000. Geology of the northeastern Niddery Lake map area, east-central Yukon and adjacent Northwest Territories. Geological Survey of Canada, Bulletin 553, 120 p.

Douglas, R.J.W. and Norris, D.K., 1961. Camsell Bend and Root River map-areas, Northwest Territories. Geological Survey of Canada, Paper 61-13, 36 p.

Fraser, T.A., Milton, J. and Gouwy, S.A., 2021. New geochemistry from old drill holes at the Tom property, Macmillan Pass, Yukon. *In:* Yukon Exploration and Geology 2020, K.E. MacFarlane (ed.), Yukon Geological Survey, p. 19–46.

Gabrielse, H., Blusson, S.L. and Roddick, J.A., 1973. Geology of Flat River, Glacier Lake and Wrigley Lake map-areas, District of Mackenzie and Yukon Territory, Part 1: general geology, structural geology, and economic geology. Geological Survey of Canada, Memoir 366, 153 p.

Gadd, M.G., Layton-Matthews, D. and Peter, J.M., 2016a. Non-hydrothermal origin of apatite in SEDEX mineralization and host rocks of the Howard's Pass district, Yukon, Canada. American Mineralogist, vol. 101, p. 1061–1071, doi:10.2138/am-2016-5550.

Gadd, M.G., Layton-Matthews, D., Peter, J.M. and Paradis, S.J., 2016b. The world-class Howard's Pass SEDEX Zn-Pb district, Selwyn Basin, Yukon. Part I: trace element compositions of pyrite record input of hydrothermal, diagenetic, and metamorphic fluids to mineralization. Mineralium Deposita, vol. 51, p. 319–342, doi:10.1007/s00126-015-0611-2.

Gordey, S.P. and Anderson, R.G., 1993. Evolution of the northern Cordilleran miogeocline, Nahanni map area (105I), Yukon and Northwest Territories. Geological Survey of Canada, Memoir 428, 214 p.

Jonasson, I.R. and Goodfellow, W.D., 1986. Sedimentary and diagenetic textures, and deformation structures within the Sulphide zone of the Howards Pass (XY) Zn-Pb deposit, Yukon and Northwest Territories. In: Mineral deposits of northern Cordillera, J.A. Morin (ed.), Canadian Institute of Mining and Metallurgy, Special Volume 37, p. 51–70.

Kamal, D. and Hickey, K.A., 2021. The geometry and kinematic history of Cordilleran deformation at the Howard's Pass shale-hosted massive sulphide deposit, Yukon: 1st year progress report. *In:* Yukon Exploration and Geology 2020, K.E. MacFarlane (ed.), Yukon Geological Survey, p. 137–156.

Morganti, J.M., 1979. The geology and ore deposits of the Howard's Pass area, Yukon and Northwest Territories: The origin of basinal sedimentary stratiform sulphide deposits. Unpublished PhD thesis, University of British Columbia, Vancouver, BC, 327 p.

Schultz, S.K., Catuneanu, O. and Gordon, J.K., 2026 (*this volume*). Preliminary analysis of the sequence stratigraphy and geochemistry of the Portrait Lake Formation at Macmillan Pass, Yukon, Canada. *In:* Yukon Exploration and Geology 2025, A. Stuart, L.H. Weston and S.K. Schultz (eds.), Yukon Geological Survey, Government of Yukon, p. 167–190.

Slack, J.F., Falck, H., Kelley, K.D. and Xue, G.G., 2017. Geochemistry of host rocks in the Howards Pass district, Yukon-Northwest Territories, Canada: implications for sedimentary environments of Zn-Pb and phosphate mineralization. Mineralium Deposita, vol. 52, p. 565–593, doi:10.1007/s00126-016-0680-x.

Xu, J., Hickey, K., Reynolds, M.A. and Kamal, D., 2024, Constructing the chemostratigraphy sequence around Zn-Pb mineralization using pXRF analysis on drill core, Howards Pass district. 2024 Yellowknife Geoscience Forum Abstract Volume, p. 41, https://cdn.fourwaves.com/static/media/filecontent/1d9de3e7-f172-428a-8cc4-159650c6db50/1ae5940c-0950-4544-8d2e-b562933d33b9.pdf.

Mapping geohazards to support climate adaptation on Yukon's transportation network

Emilie Stewart-Jones and Moya Painter*
Yukon Geological Survey

Stewart-Jones, E. and Painter, M., 2026. Mapping geohazards to support climate adaptation on Yukon's transportation network. *In*: Yukon Exploration and Geology 2025, A. Stuart, L.H. Weston and S.K. Schultz (eds.), Yukon Geological Survey, Government of Yukon, p. 207–219.

Abstract

The Government of Yukon's Department of Highways and Public Works and the Yukon Geological Survey are jointly developing a geohazard inventory and hazardous landform database to assess climate-driven hazards to Yukon's transportation network. Climate-change effects, such as accelerating permafrost thaw and an increase in extreme precipitation events, are contributing to a rise in geohazards that threaten the reliability and safety of major road corridors. The inventory integrates field observations, remote sensing, historical reports, and maintenance history to identify ten types of geohazards and eight hazardous landforms associated with permafrost thaw and slope deformation. As of November 2025, 934 geohazard points and over 3000 hazardous landforms have been mapped on the road network. Preliminary results highlight subsidence, icing and river encroachment as the most widespread geohazards. Case studies from the North Canol Road, South Klondike Highway and Dempster Highway illustrate how permafrost degradation, slope instability and extreme weather interact to impact transportation infrastructure. The hazard inventory and associated risk-assessment tools will support proactive adaptation, monitoring, and mitigation planning across the Yukon's road network.

Plain language summary

Much of Yukon's road network is exposed to hazards from permafrost, steep mountain slopes or rivers, making these areas vulnerable to problems such as ground settling from permafrost thaw, landslides, rockfalls and flooding. As climate changes, these hazards are becoming more common and more damaging, creating challenges for keeping roads safe and open. To help manage associated risk, the Yukon Geological Survey and the Government of Yukon's Department of Highways and Public Works are creating a territory-wide geohazard inventory and hazardous landform map. Using field inspections, imagery and road maintenance history, the project identifies where hazards are occurring, how they are changing over time, and which locations pose the greatest risk to roads. This information will help the Government of Yukon plan maintenance, prioritize risk mitigation projects, and reduce long-term costs. Furthermore, this will improve safety and reliability for people who travel these roads, and to the communities that are served by them.

* emilie.stewart-jones@yukon.ca

Introduction

The Yukon Geological Survey (YGS) and Highways and Public Works (HPW) are collaborating to create a geohazard inventory and hazardous landform database for Yukon roadways. Climate change in the Yukon is accelerating permafrost thaw and increasing extreme weather events such as extreme precipitation (Vincent et al., 2015), thereby raising the risk of geohazards such as slope failures, river flooding, erosion, and permafrost subsidence (Huscroft et al., 2004; Lantuit et al., 2008; Perrin and Jolkowski, 2022; Grenier et al., 2024). This trend poses increasing maintenance and safety challenges for transportation corridors as extensive segments of the territorial road network are built across permafrost terrain, along steep mountainous areas, or adjacent to rivers. Disruptions to the transportation network can delay other crucial systems such as food distribution (Perrin and Jolkowski, 2022) and fuel transport. Given the importance of road networks in the Yukon for community and resource access, there is a need to track geohazards to support proactive adaptation, maintenance planning, and risk reduction.

The Yukon's road network spans thousands of kilometres, stretching from the northern extent of British Columbia to the Arctic Circle. The climate is characterized as subarctic continental, marked by dry conditions, short cool summers, and long, cold winters having some of the greatest temperature extremes in Canada (Smith et al., 2004). Mean annual air temperatures range from about -2°C in the southern valleys to below -10°C along the Arctic coast. Annual precipitation varies widely with topography, from 250–300 mm in low-lying valleys to over 600 mm in higher mountain ranges, as orographic barriers influence the movement of maritime and Arctic air masses (Smith et al., 2004).

Permafrost is widespread across the Yukon, transitioning from continuous permafrost in the north, to discontinuous and sporadic zones in the south (Fig. 1; Smith et al., 2004). The thickness and temperature of permafrost vary considerably with latitude, elevation and surficial materials. Ground ice content varies considerably based on permafrost distribution, surficial geology, glacial history and paleo-vegetation (O'Neill et al., 2019). Ground ice content is often high in glaciolacustrine and organic-rich sediment, whereas materials like fluvial and glaciofluvial gravel are commonly ice poor. Permafrost degradation and thaw-related geohazards are increasingly evident across central and southern Yukon, particularly in response to climate warming and surface disturbance.

Recent analysis of maintenance-cost records for the territorial highway network in the Yukon revealed a clear linkage between climate-driven changes in permafrost environments and escalating infrastructure costs. Schetselaar and Burn (2024) show that annual climate-related maintenance expenditures (e.g., snow removal, icing control, landslide/washout repair) increased from approximately C$6.6 million in 1994–1999 to C$10.2 million in 2017–2022 (in constant 2021 dollars), with an average annual growth of roughly C$169 000. They further demonstrate that highway sections situated in extensive discontinuous and continuous permafrost zones incur per-kilometre maintenance costs more than 50% higher than those in areas of sporadic or isolated permafrost patches (Schetselaar and Burn, 2024).

Our geohazard inventory focuses on all major transportation corridors within the Yukon, and mapping has been completed for almost all high and medium-high priority roads (Fig. 1). Given the growing risks associated with climate-driven geohazards, a comprehensive inventory is crucial for ensuring the long-term stability and safety of the Yukon's major transportation corridors.

Methodology

This project consists of two spatial datasets: the geohazard inventory and the hazardous landform database. The geohazard inventory is a point layer that identifies segments of the road that are at risk of being impacted by a geohazard. The hazardous landform database is a series of polygons that are within 250 m of either side of the road. Each polygon delineates the extent of a landform, many of which are associated with a geohazard point (Table 1).

The spatial datasets are maintained in a GIS-based relational database, which enables integration with existing highway asset management systems and facilitates visualization of geohazard locations, and potential impacts to the road. Mapping of roads is prioritized based on traffic usage, and social and economic functions.

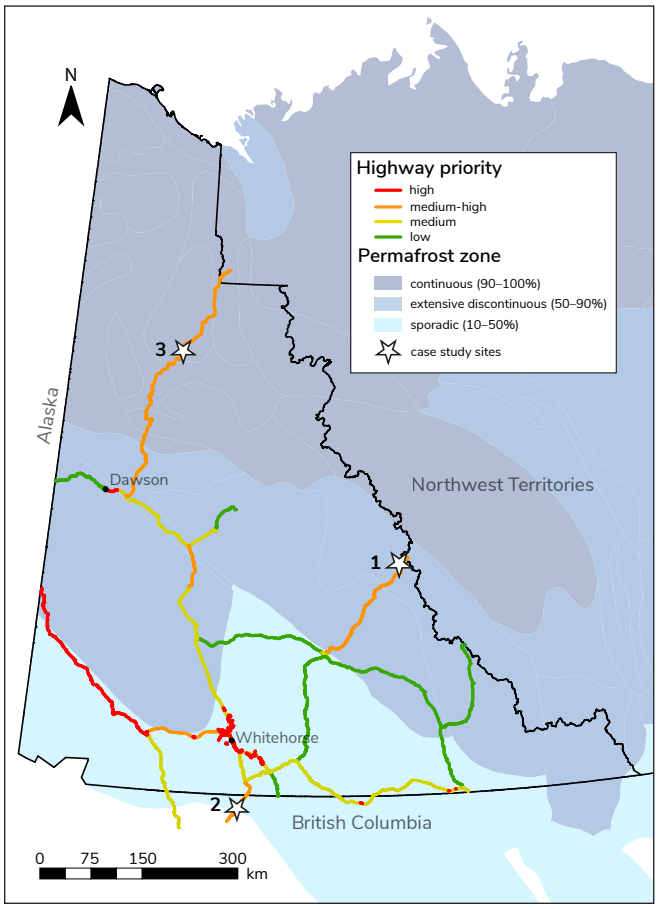


Figure 1. *Permafrost zones, case study locations, and priority of road network within the Yukon. Case studies: 1 – North Canol Road rock glacier; 2 – South Klondike Highway debris flow; 3 – Dempster Highway embankment failure.*

The geohazard inventory identifies ten primary geohazard types: fast and slow-moving landslides, rockfalls, snow avalanches, erosion, subsidence, washouts, flooding, icing, and encroachment (Table 2). Each geohazard is recorded as a geolocated point along the road network and linked to a detailed attribute table describing its type, location, affected road length, activity state, and associated risk variables.

The hazardous landform database identifies seven types of landforms: fast and slow-moving landslides, avalanche paths, gullies, ice-wedge polygons, permafrost mounds, and thermokarsts (Table 1). Each landform is mapped as a polygon and assigned a landform type, location, imagery type and date, surficial material, and activity state. The landforms are tied to polygons and are assigned a date so they can be re-mapped once new imagery or lidar becomes available. This allows for tracking the change in extent over time. In the database, geohazard points are linked to the mapped landforms that they are associated with.

There are three main steps in creating the geohazard inventory: (1) identifying geohazards, (2) inspecting geohazards, and (3) assessing geohazard risk.

Identifying geohazards

Geohazards are identified using multiple information sources, including academic and consultant reports, highway maintenance staff observations, field inspections, satellite imagery, and lidar datasets. Data collection focuses on both historical and active geohazard sites, ensuring that the inventory captures long-term hazard activity as well as recent events.

Many geohazard points are also linked to polygons in the hazardous landform database that delineate the spatial extent of the underlying process and track its evolution over time. These landforms are delineated using lidar, high-resolution satellite imagery, and field-based mapping. Polygons representing active processes, such as subsidence due to ice-wedge thaw, are linked to a geohazard point if they pose a threat to the road. These polygons are temporally variable and allow for monitoring of spatial change, thereby improving understanding of hazard evolution.

Inspecting geohazards

Targeted field inspections were conducted in the summer of 2025 on high, medium-high, and medium priority roads to verify remote-sensing interpretations, update activity states, and record field measurements such as slope geometry and surface displacement. Sites will be revisited on a regular monitoring cycle, and updates will be recorded directly in the database. This iterative process ensures that the geohazard inventory reflects current field conditions and provides a foundation for ongoing risk assessment.

Assessing geohazard risks

Risk matrices are being developed for each of the ten geohazard types (Table 3). The risk matrices include two components: hazard and consequence. Hazard is the product of another two components: magnitude and frequency. Magnitude is the size of

Table 1. Landform types with their definitions and associated geohazard.

Landform	Definition	Associated geohazard
fast-moving landslide	Scar from rapid sliding or flowing of material (disintegrating or cohesive soil, debris, mud, rocks, etc.) downslope.	fast-moving landslide
slow-moving landslide	Ground that is slowly deforming or creeping downslope (e.g., rock glacier, solifluction).	slow-moving landslide
avalanche path	Path where snow and ice, as well as entrained debris, move rapidly downslope by flowing or sliding.	avalanche
gully	Narrow ravines that are parallel and sub-parallel produced by shaping of consolidated and unconsolidated materials by various processes (Resource Inventory Branch, Ministry of Environment, Lands and Parks, 1997). Can be a thermokarst gully.	erosion
ice-wedge polygons	A polygon on the ground surface outlined by connected ice wedges (massive ice feature) beneath its borders (Lewkowicz et al., 2024; Lewkowicz et al., 2025).	subsidence
permafrost mound	Any mound-shaped landform produced in periglacial environments by frost action. Includes palsas, lithalsas, pingos and peat plateaus.	subsidence
thermokarst	Landforms resulting from ice-rich permafrost thaw (Lewkowicz et al., 2025). Includes depressions, ponds and beaded streams.	subsidence

a potential event, and frequency is the known or estimated rate of event occurrence over a length of time. In the case of rockfall, magnitude would consider the potential size of blocks that could fall based on joint configuration and the size of historical rockfall. Frequency would be estimated based on highway maintenance records, the recency of rock debris in the ditches, and the condition of the rock mass.

Consequence is assigned a number from one to six which describes the potential impact of an event to the condition of the road. For example, permafrost subsidence that affects an asset such as a culvert will be assigned a higher consequence rating than subsidence where no major asset is present.

Magnitude, frequency and consequence are estimated based on variables measured in the field, collected through conversations with highway maintenance staff, and determined from remote sensing data. These variables change with the type of geohazard. As such, a risk assessment will be completed for each geohazard separately. This basic risk assessment will highlight high-risk geohazards, and inform prioritization of monitoring and mitigation projects, allowing for improved risk management.

Preliminary results

As of November 2025, 1670 km of the 4828 km of highway, community roads and resources roads maintained by the Government of Yukon have been mapped for geohazards. This includes the South and North Klondike, Alaska and Dempster highways, and the North Canol Road. The geohazard inventory includes a total of 934 recorded geohazard points (Fig. 2).

The most prevalent geohazard is subsidence, with 446 mapped occurrences, followed by icing (144) and encroachment (97). Other notable categories include fast-moving landslides (71), rockfalls (50), snow avalanches (51), washouts (50), slow-moving landslides (15), and erosion (10; Fig. 3).

Additionally, 3093 hazardous landforms have been delineated along 2257 km of road. The roads that have been mapped are the Alaska Highway, the North and South Klondike highways, the Dempster

Table 2. Geohazard types in the inventory and their definitions.

Geohazard	Definition
fast-moving landslide	Rapid sliding, flowing or descent of material (disintegrating or cohesive soil, debris, mud, rocks, etc.) downslope.
slow-moving landslide	The slow deformation or creep of ground downslope (e.g., rock glacier, solifluction).
rockfall	The detachment and subsequent falling, rolling or bouncing of individual rock fragments or clusters.
avalanche	Snow and ice, as well as entrained debris, moving rapidly downslope by flowing or sliding (Resource Inventory Branch, Ministry of Environment, Lands and Parks, 1997).
erosion	The shaping of consolidated and unconsolidated materials by various processes, producing long narrow parallel and sub-parallel ravines (Resource Inventory Branch, Ministry of Environment, Lands and Parks, 1997). Can be a thermokarst process.
subsidence	Sinking of the ground surface due to the thaw of underlying ice-rich permafrost.
encroachment	Progressive erosion of riverbanks caused by meander migration or rapid erosion caused by abrupt channel diversion.
washout	Rapid erosion of a road embankment from a creek or river in flood, or from a beaver dam failure.
flooding	When the water level in a river of lake rises above its banks and floods the surrounding land, or when the groundwater table rises resulting in standing water.
icing	Groundwater that freezes at the ground surface, or river water that freezes above the ice cover as it is forced up by pressure, causing thick sheets of ice to form.

Table 3. Evaluation matrix used for assessing risk of geohazards along roadways. Consequence and hazard levels are determined based on set variables that are observed in the field, measured from remote sensing data, or noted during conversations with highway maintenance staff.

Hazard	Very high - 6	Low (6)	Significant (12)	High (18)	Very high (24)	Very high (30)
	High - 5	Low (5)	Moderate (10)	Significant (15)	High (20)	Very high (25)
	Significant - 4	Low (4)	Moderate (8)	Significant (12)	High (16)	High (20)
	Moderate - 3	Very low (3)	Low (6)	Moderate (9)	Significant (12)	Significant (15)
	Low - 2	Very low (2)	Low (4)	Low (6)	Moderate (8)	Moderate (10)
	Very low - 1	Very low (1)	Very low (2)	Very low (3)	Low (4)	Low (5)
		Minor - 1	Moderate - 2	Significant - 3	Major - 4	Catastrophic - 5
		Consequence				

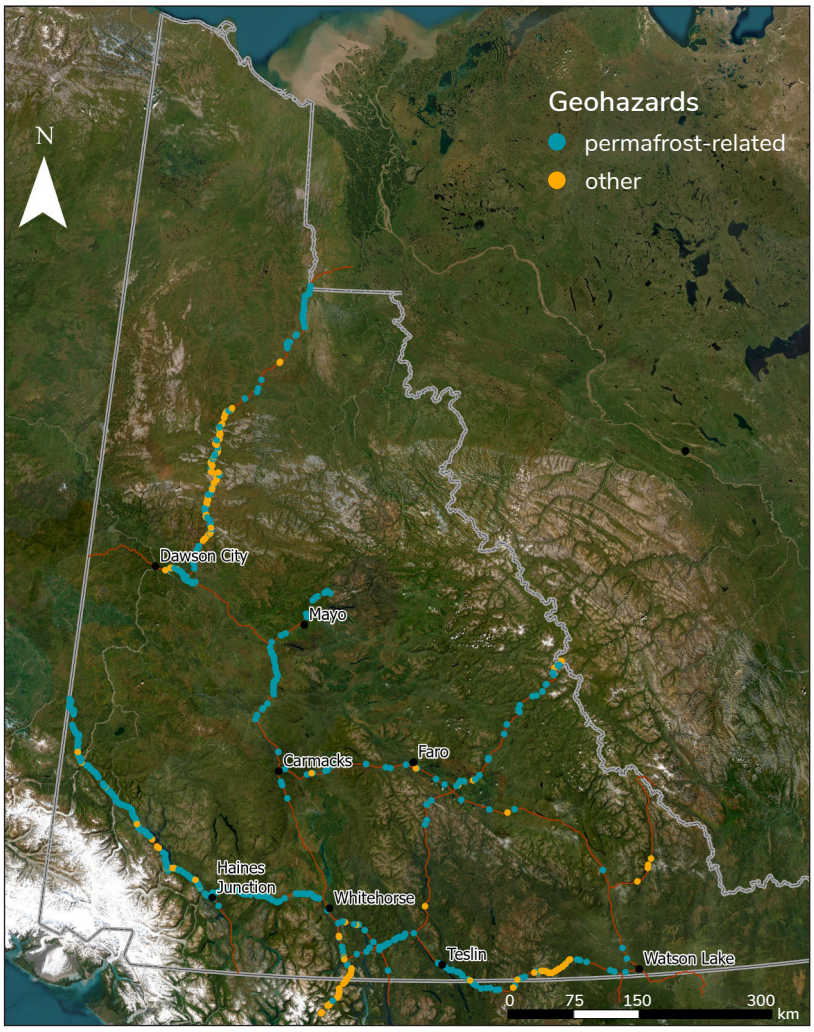


Figure 2. *Map of Yukon highways and resource roads with permafrost-related geohazards noted in blue and other geohazards noted in orange.*

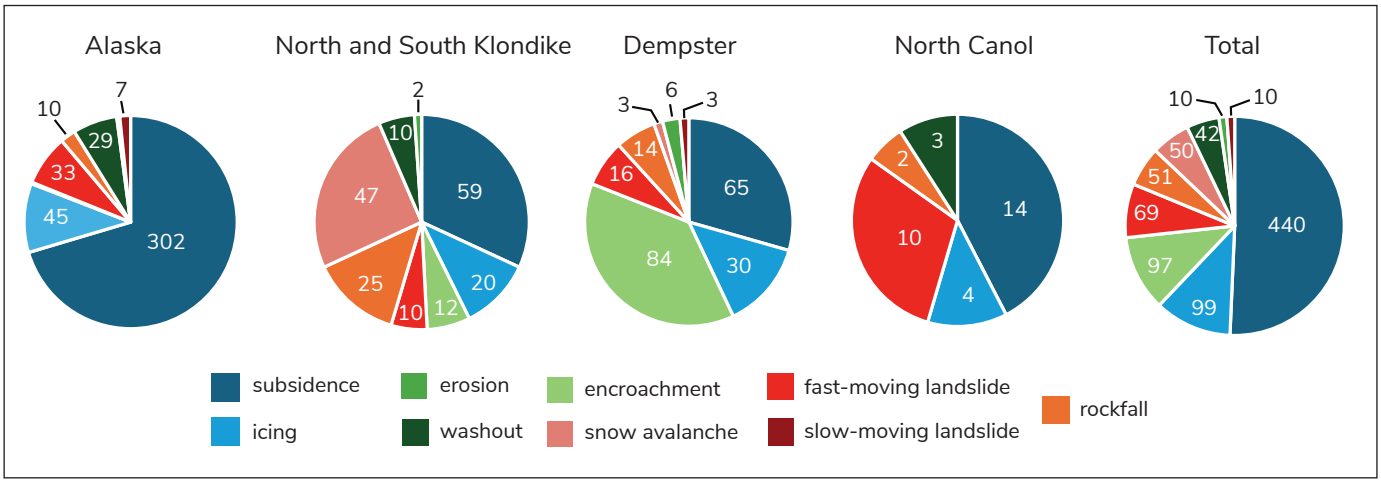


Figure 3. *Number of occurrences of each geohazard type by highway/road. Geohazard types not listed did not have enough mapped occurrences to be visible in the chart.*

Highway, and the North Canol Road. To date, the landform with the most mapped occurrences is thermokarst, which has been identified 1529 times. Following thermokarst is fast-moving landslides (572), permafrost mounds (335), ice-wedge polygons (253), gullying (88), avalanches (85), and slow-moving landslides (59; Fig. 3).

Case studies

North Canol Road rock glacier encroachment

Macmillan Pass is a mountainous region located at the border between the Yukon and Northwest Territories (NWT). There is a high density of rock glaciers in this area, many visible from the North Canol Road. A rock glacier is a tongue-shaped mass of ice-rich debris that creeps downslope through internal deformation. Rock glaciers are mapped in the geohazard database as slow-moving landslides. A rock glacier was identified very close to the road at KM 455 of the North Canol Road, approximately 5.6 km southwest of the NWT border (Figs. 1 and 4). This feature is located between Fireweed Metals' Macpass and Mactung projects, so there is frequent vehicle traffic along this section of the road.

The toe of the rock glacier on the North Canol Road has encroached onto the road, and regular debris clearing is required by maintenance crews to ensure the road is passable (Fig. 5). The toe of the rock glacier is up to 18 m thick on the road surface. Old tension cracks were visible in the 1949 and 1974 air photos near the top of the rock glacier; however, more recent tension cracks were captured in 2013 satellite imagery and formed sometime between 1974 and 2013; these are shown in lidar imagery from 2019 (Fig. 6).

Average displacement rates can be tracked using available lidar, satellite imagery and historic air photos. Two historic air photos of this area were available for 1949 and 1974, lidar was flown for 2012 and 2019, and high-resolution satellite imagery was available for 2013 and 2024. Using these we were able to calculate mean movement rates for each period bracketed by the imagery. From 1949 to 2024 the toe of the rock glacier advanced toward the road by a total of 13.8 m, on average. Advance is not uniform across the front of the rock glacier. In recent years there is greater advance on the western side of the toe, while there is little or no movement on the eastern side. Total displacement from 1949 to 1974 of the centre of the toe of the rock glacier was 19 m. From 1949 to 1974, the displacement across the toe of the rock glacier was 2.15 m, or an average of 0.09 m/year. Between 1974 and 2012, the toe of the rock glacier moved 6.47 m, or an average of 0.17 m/year. From 2012 to 2019, the advance

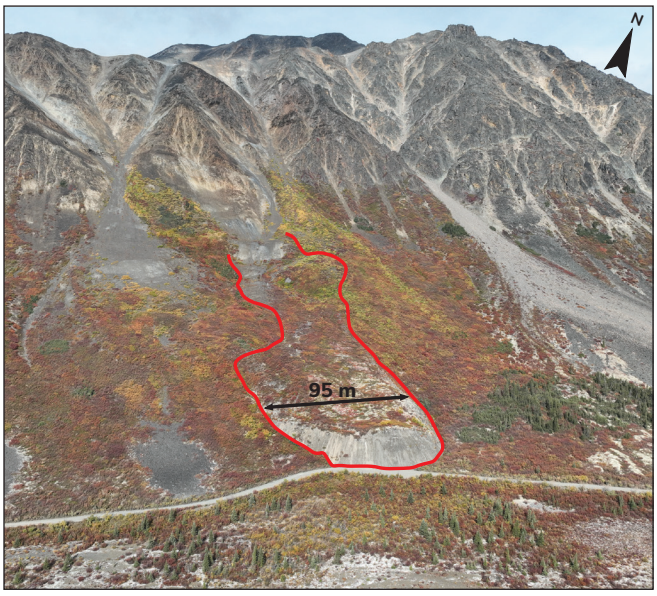


Figure 4. *North Canol Road rock glacier, outlined in red.*

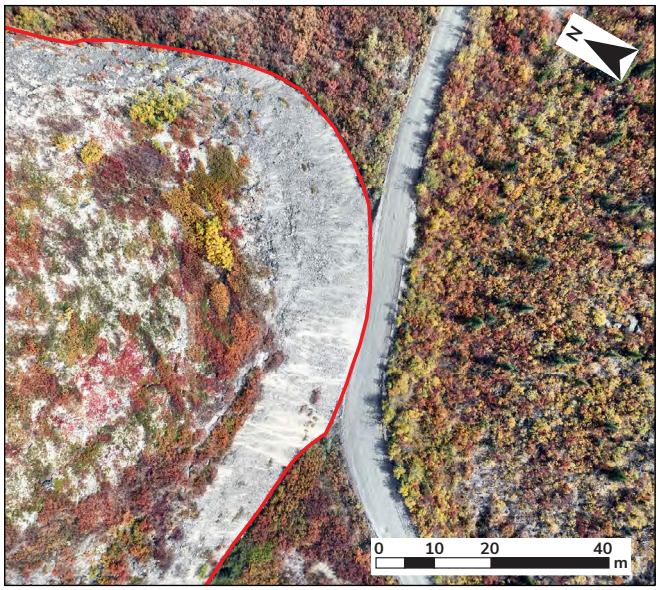


Figure 5. *Birdseye view of the toe of the rock glacier (outlined in red) and its relative position to the North Canol road in September 2025.*

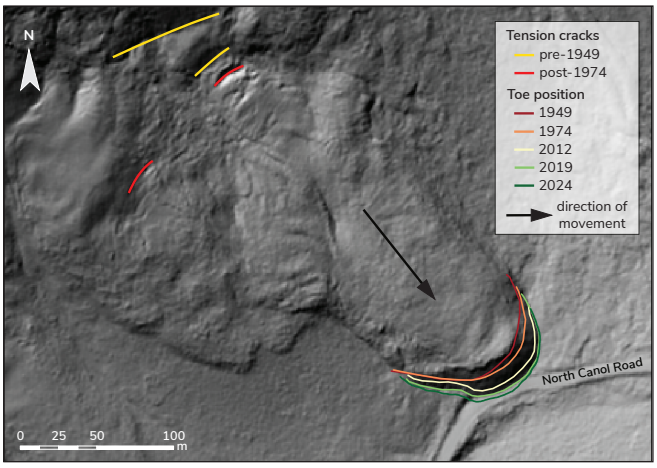


Figure 6. *Lidar image from 2019 of the North Canol rock glacier outlining the maximum toe positions from 1949 to 2024; tension crack locations are also delineated.*

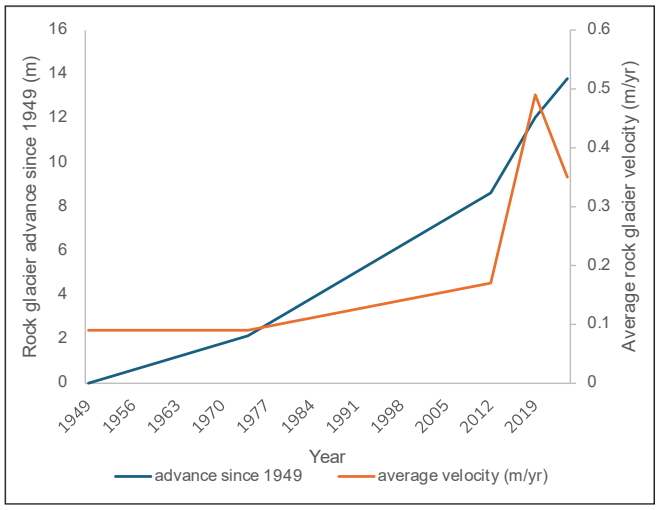


Figure 7. *Average velocity and maximum advance of the toe of the North Canol Road rock glacier since 1949.*

of the rock glacier accelerated to an average of 0.49 m/year, and then dropped to an average of 0.35 m/year from 2019 to 2024 (Fig. 7).

The acceleration of the rock glacier in the last decade is likely related to increasing air temperatures in the Yukon, having a total mean annual air temperature increase of 2.5°C between 1948 and 2021, including notable increases beginning in the mid-1970s (Perrin and Jolkowski, 2022). The relationship between increasing air temperatures and accelerating rock glacier velocities has been observed for rock glaciers globally (Hu et al., 2025), suggesting that, with increasing air temperatures, this rock glacier may continue to accelerate and further encroach onto the road.

South Klondike Highway debris flow

Large sections of the South Klondike highway are built at the base of steep mountain slopes and are therefore prone to avalanches, rockfalls and landslides. A segment of the South Klondike Highway is within British Columbia, but the entirety of the Canadian side of the highway is managed by the Government of Yukon. As the only land route to the port city of Skagway, Alaska, this highway plays a crucial role in transporting fuel and other goods in and out of the Yukon.

In July of 2024, a heavy rainfall event of approximately 50 mm of precipitation over 24 hours triggered a debris flow that covered a 200 m section of the South Klondike Highway at KM 58 (Figs. 1 and 8a). Similar rainfall across the region caused widespread flooding, debris flows and rockslides, and at least one of these events closed the White Pass rail line. At KM 58, the road was closed for less than a day; however, it took seven weeks to fully remove debris, requiring a pilot car to shuttle traffic during this time. Most material originated from the lower part of a pre-existing drainage and its channel deposits (Fig. 8b), resulting in an estimated 63 000 m³ of debris deposited across the road and colluvial fan (Fig. 9).

This is the second major debris flow at this site in a decade. A smaller event occurred in July 2014 after heavy rainfall triggered a debris flow and resulted in a 2-day road closure (Fig. 8c). For another event of this magnitude to occur at this site, a build-up of material in the channel will be required, suggesting that large events in consecutive years are unlikely.

This site is also a common avalanche path in the winter (Fig. 8d), and 52 avalanches were recorded between 1991 and 2020, resulting in two road closures (Tse and Adams, 2024). Recent work has estimated the frequency of size 3 avalanches (large enough to bury and destroy a car or break a few trees) to be every year, and the frequency of size 4 avalanches (large enough to destroy a large truck or several buildings) to occur every 10 years (Sharp, 2025).

With the expected increase of extreme weather events in the Yukon (Perrin and Jolkowski, 2022), debris flows remain a hazard at this site and may become a greater risk elsewhere on the Yukon's road network.

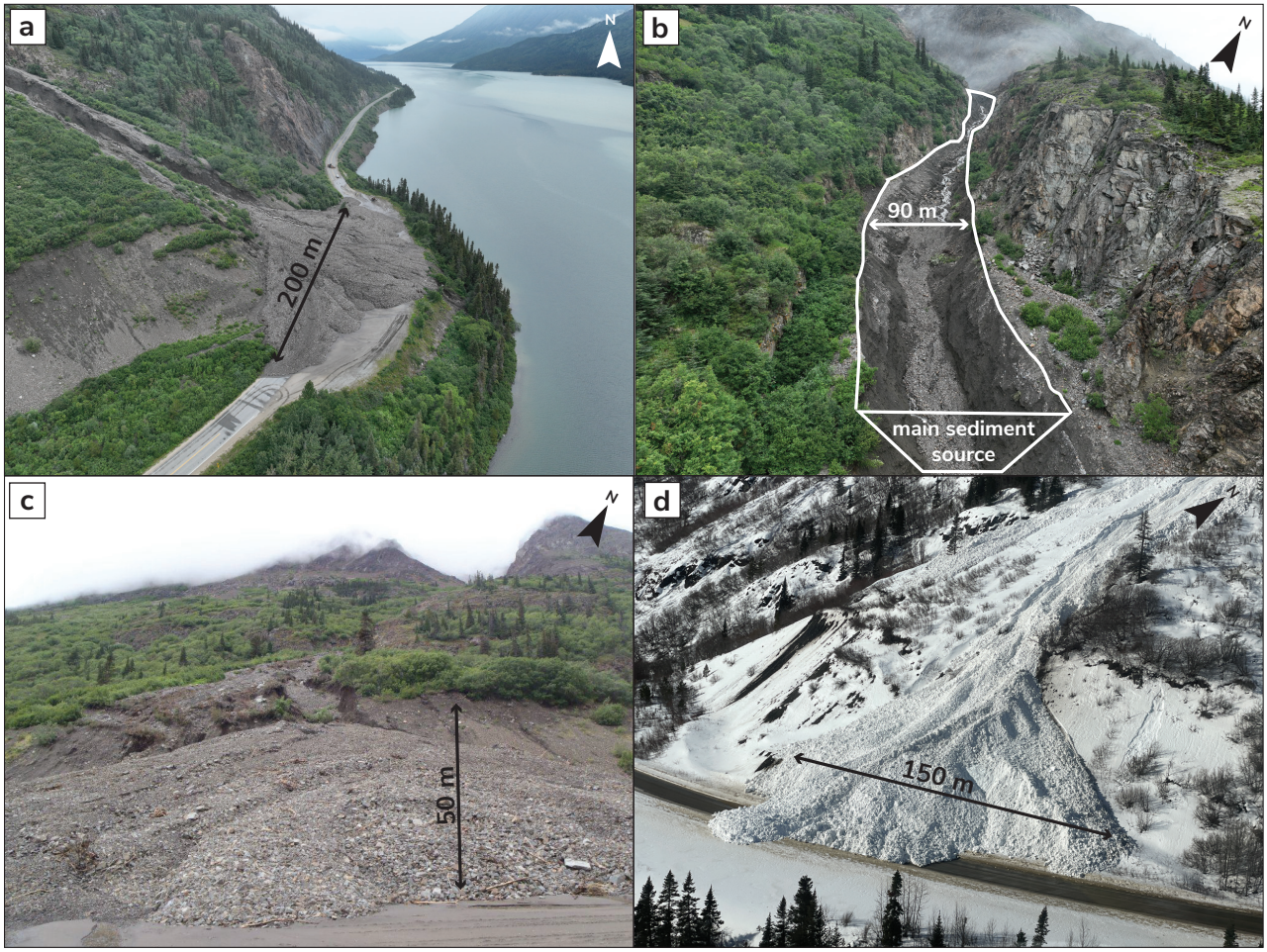


Figure 8. *Photos of the South Klondike Highway KM 58 debris flow site.* ***(a)*** *A photo from July 2024 of the debris flow fan covering the entire width and affecting a 200 m stretch of the highway (photo: Derek Cronmiller).* ***(b)*** *A photo from July 2024 of the scoured drainage resulting from the debris flow; the photo was taken above the road and near the apex of the debris flow fan (photo: Derek Cronmiller).* ***(c)*** *A photo of the toe of the debris flow fan taken from the road in July 2014 (photo: Paul Murchison).* ***(d)*** *A photo of an avalanche triggered by explosives taken in the spring of 2024; the avalanche followed the same path as the debris flow (photo: Colin MacKenzie, Snowshoot Productions).*

Dempster Highway embankment failure, KM 312

A road embankment failed at KM 312 of the Dempster Highway in August 2023 (Figs. 1 and 10a). A large crack initiated along the shoulder of the road, resulting in a vertical displacement of at least 1 m at one end. The embankment failure occurred on the downslope side of the road. At this location, the road intersects a small drainage where the embankment ranges in height from 2 to 4 m.

Material was added to the road in the fall of 2023 to stabilize the embankment before winter. The embankment remained stable (Fig. 10b) until September 2024, when it failed again. That fall, material was added to the toe to stabilize the slope; however, the embankment continued to fail with vertical displacement reaching up to 0.5 m (Fig. 10c). Repairs were not done until the following spring, resulting in a single lane closure at this location throughout the winter months. As of July 2025, there has been no significant movement observed at this site (Fig. 10d).

Prior to 2023, this embankment was stable. This section of the Dempster Highway is within the continuous permafrost zone and has historically shown little permafrost-related instability (Burn, 2015). The failure of the embankment at the end of summer (both in August 2023 and September 2024) suggests that the cause of failure is likely permafrost

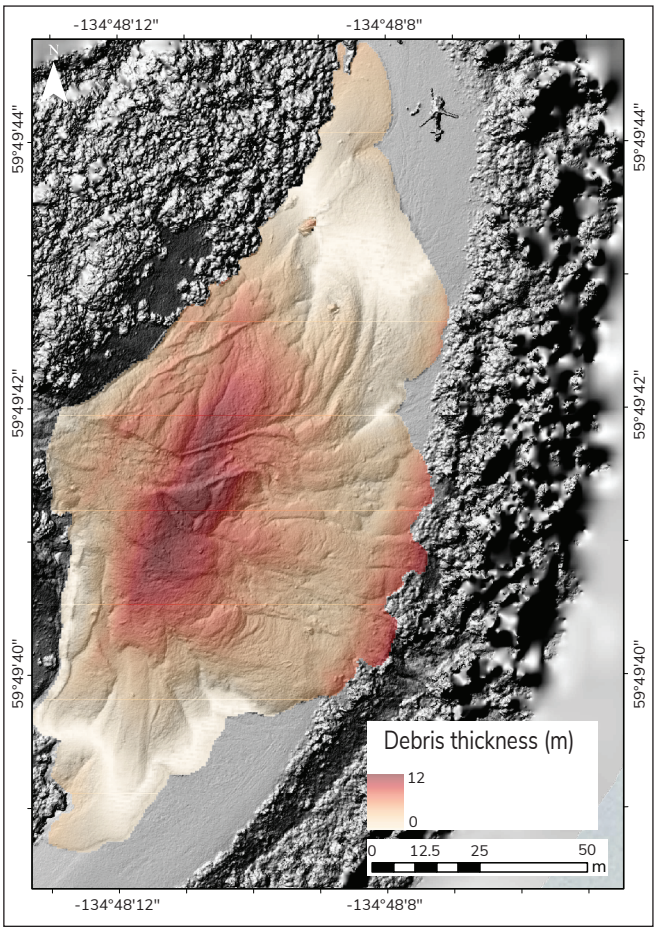


Figure 9. *Lidar imagery of change detection illustrating the thickness of the 2024 debris flow fan on the South Klondike Highway.*

related, as the depth of thaw is greatest in the fall. A possible contributing factor to this failure is the installation of a fibre optic line at the toe of the embankment in July 2022. Stripping of vegetation and the subsequent compression of the organic mat in permafrost terrain accelerates thaw and can lead to visible surface disturbance where ice is present (Brown and Grave, 1979; Fig. 11).

A geotechnical investigation was carried out at this site in the spring of 2025 (Singh and Ismail, 2025). The purpose of the work was to characterize soil, permafrost and geological conditions at the site to identify potential stabilization or mitigation options. Fieldwork included drilling four boreholes, three within the failure zone and one outside; depths ranged from 5.3 to 15.5 m (Figs. 12 and 13).

Subsurface conditions generally consisted of road fill overlying silt and clay (Fig. 13). The road fill in the failure zone varied in thickness from 2.7 to 4.4 m. Visible ice was identified in several boreholes, particularly between 3 and 6 m depth, indicating ice-rich and potentially thaw-sensitive materials. Boreholes 2 and 3, both located within the failure zone, contained the most visible ice. Although total ground ice content is difficult to determine due to the disturbance of ice during drilling, an estimated excess ice measurement was taken from a sample from both boreholes. The sample from borehole 2 taken at a depth of 4.2 m had a volumetric ice content of 58%, whereas the sample from borehole 3 taken at a depth of 4.9 m had a volumetric ice content of 55%.

Three factors are believed to have contributed to the embankment failure at this location:

1. High ground ice content, as was evidenced by greater ice content in the failure zone compared to outside of the failure zone.

2. Disturbance of vegetation and the ground surface during the installation of the fibre optic line, which likely caused ground ice melting and subsidence of the embankment toe.

3. A thick, steep embankment on a slope, which would have exacerbated the effects of the reduced soil strength at the toe as ground ice melted.

Conclusions

This geohazard inventory and hazardous landform database represents a key step toward understanding and managing the growing risks facing the Yukon's road network in a changing climate. The combined mapping of geohazard points and hazardous landforms has demonstrated that extensive sections of the territory's highways are affected by permafrost degradation, slope movement, and hydrological hazards, and have clear implications for maintenance costs and long-term infrastructure resilience. Case studies demonstrate how geohazards can significantly disrupt transportation corridors. With climate change, gradual processes such as creeping rock glaciers are undergoing significant accelerations, resulting in substantial impacts to the roadways. Extreme weather events can increase the frequency of large landslides such as the South Klondike Highway KM 58 debris flow. Surface disturbance can have significant effects on road stability, as seen at KM 312 of the

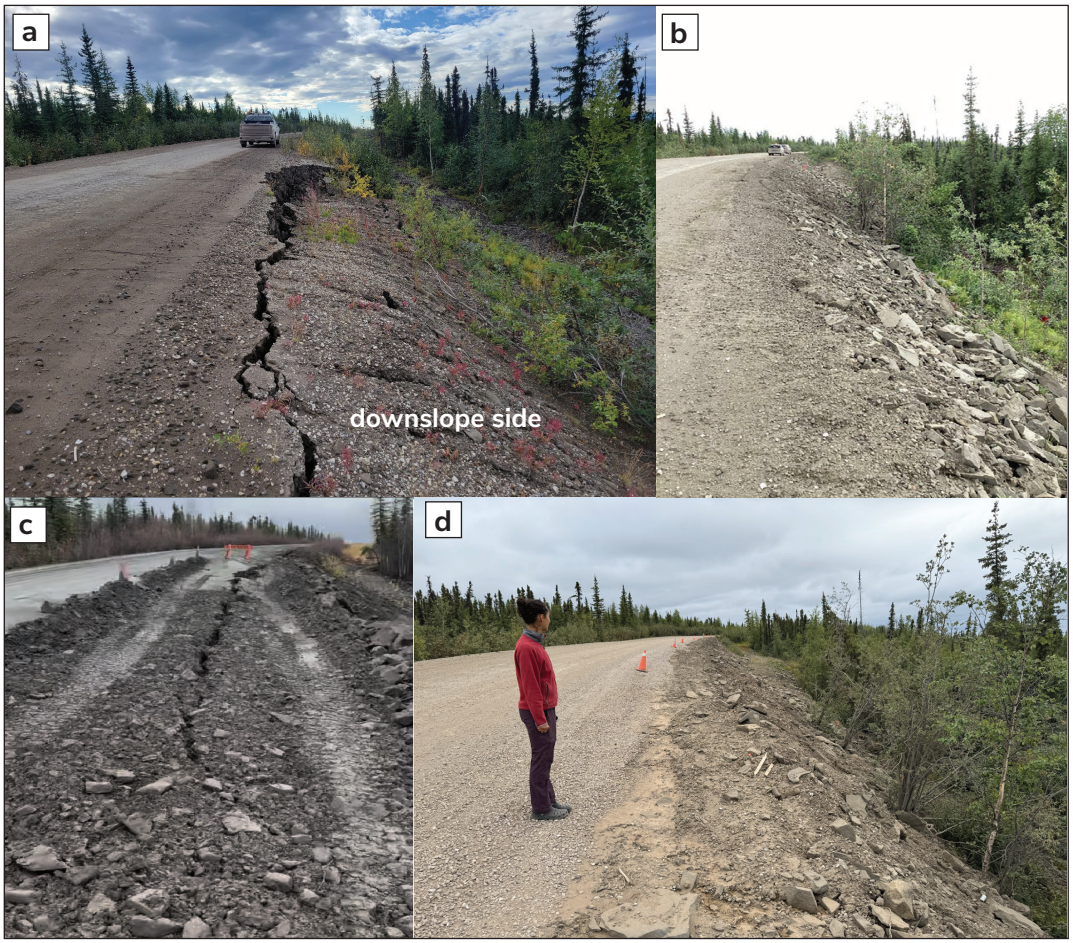


Figure 10. *The evolution of the embankment failure at KM 312 of the Dempster Highway:* ***(a)*** *the initial failure in August 22, 2023;* ***(b)*** *the repaired embankment in July 22, 2024 and minimal cracking;* ***(c)*** *the failed embankment in October 2024; and* ***(d)*** *the stabilized embankment in July 2025. Photo by Stephan Gruber.*



Figure 11. *An example of the installed fibre optic line in 2022 at KM 311.6 of the Dempster Highway. The photo was taken 100 m from the embankment failure, and the removal of vegetation is evident.*

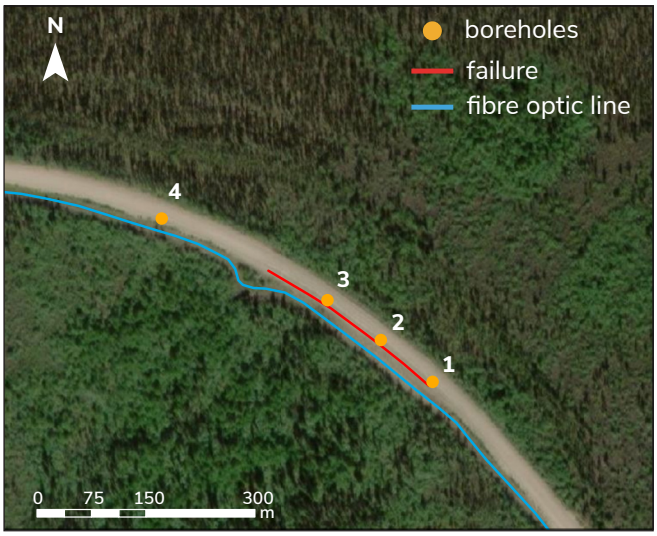


Figure 12. *Aerial photo of the embankment failure at KM 312 of the Dempster Highway and the location of the four boreholes drilled during the investigation.*

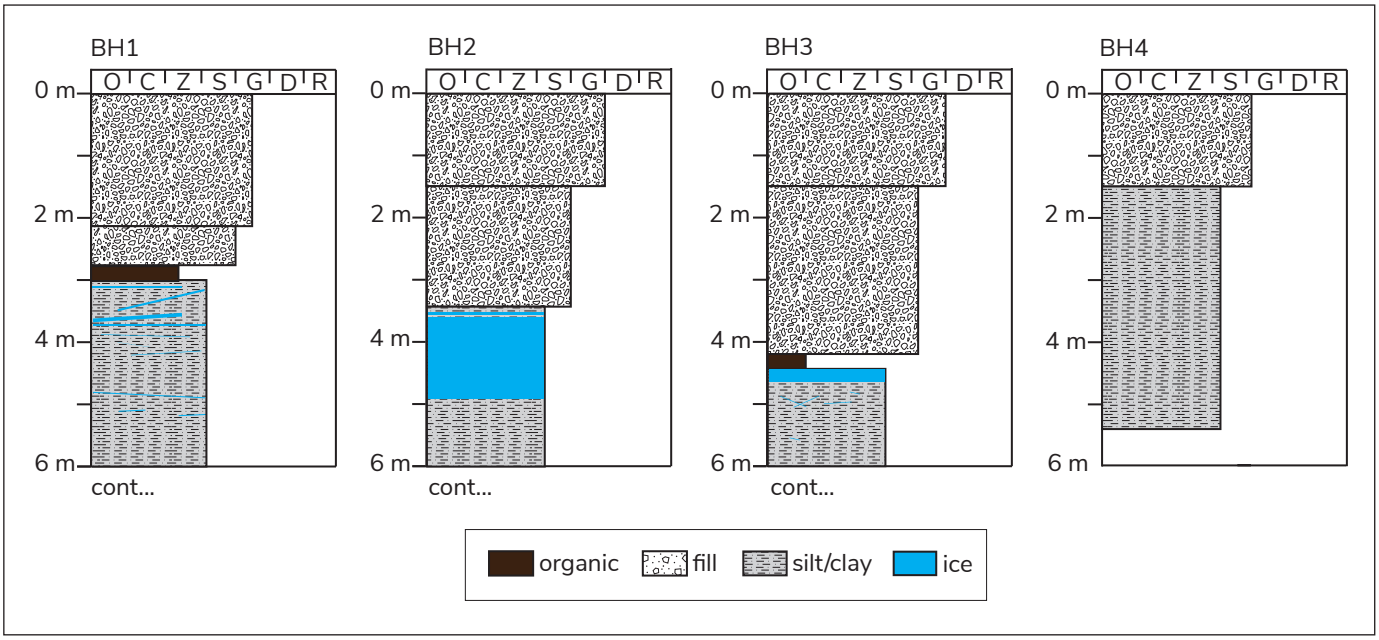


Figure 13. *Stratigraphic logs of the uppermost 6 m for the four boreholes drilled at KM 312 of the Dempster Highway. Borehole logs from Singh and Ismail (2025).*

Dempster Highway. Ongoing monitoring, regular field verification, and updated imagery will continue to refine the dataset and improve risk assessments. As the inventory expands to remaining highway sections, it will provide a foundation for prioritizing maintenance work, planning mitigation efforts, and supporting safe and reliable travel across the Yukon.

References

Burn, C.R., Moore, J.L., O'Neill, H.B., Hayley, D.W., Trimble, J.R., Calmels, F., Orban, S.N. and Idrees, M., 2015. Permafrost characterization of the Dempster Highway, Yukon and Northwest Territories. *In:* Conference proceedings of the 68th Canadian geotechnical conference – GEOQuebec 2015, Canadian Geotechnical Society, Québec City, QC, September 20–23, 2015, https://members.cgs.ca/documents/conference2015/GeoQuebec/prof11.html.

Brown, J. and Grave, G.W., 1979. Physical and thermal disturbance and protection of permafrost. United States Army Corps of Engineers, Cold Regions Research and Engineering Laboratory, Hanover, New Hamshire, USA, Special Report 79-5, 42 p.

Grenier, M., Boudreault, J., Raymond, S. and Boudreault, M., 2024. Projected seasonal flooding in Canada under climate change with statistical and machine learning. Journal of Hydrology: Regional Studies, vol. 53, 101754, 16 p., https://doi.org/10.1016/j.ejrh.2024.101754.

Howes, D.E. and Kenk, E. (eds.), 1997. Terrain classification system for British Columbia (Version 2). Recreational Fisheries Branch, Ministry of Environment, and Surveys and Resource Mapping Branch, Ministry of Crown Lands, Province of British Columbia, 102 p.

Hu, Y., Arenson, L. U., Barboux, C., Bodin, X., Cicoira, A., Delaloye, R., Gärtner-Roer, I., Kääb, A., Kellerer-Pirklbauer, A., Lambiel, C., Liu, L., Pellet, C., Rouyet, L., Schoeneich, P., Seier, G. and Strozzi, T., 2025. Rock glacier velocity: An essential climate variable quantity for permafrost. Reviews of Geophysics, vol. 63, issue 1, 28 p., e2024RG000847, https://doi.org/10.1029/2024RG000847.

Huscroft, C.A., Lipovsky, P. and Bond, J.D., 2004. Permafrost and landslide activity: Case studies from southwestern Yukon Territory. *In:* Yukon Exploration and Geology 2003, D.S. Emond and L.L. Lewis (eds.), Yukon Geological Survey, p. 107–119.

Lantuit, H. and Pollard, W.H., 2008. Fifty years of coastal erosion and retrogressive thaw slump activity in Herschel Island, southern Beaufort Sea, Yukon Territory, Canada. Geomorphology, vol. 95, p. 84–102.

Lewkowicz, A.G., Wolfe, S.A., Roujanski V., Hoeve, E., O'Neill, H.B., Gruber, S., Roy-Léveillée, P., Brown, N., Koenig, C.E.M., Brooks, H., Rudy, A.C.A., Bonnaventure, P.P. and Paquette, M., 2024. An Illustrated Permafrost Dictionary. Canadian Permafrost Association, DOI: 10.52381/CPA.permafrostdictionary.1.

Lewkowicz, A.G., O'Neill, H.B., Wolfe, S.A., Roy-Léveillée, P., Roujanski, V.E., Hoeve, E., Gruber, S., Brooks, H., Rudy, A.C.A., Koenig, C.E.M., Brown, N. and Bonnaventure, P.P., 2025. Glossary of Permafrost Science and Engineering. Canadian Permafrost Association, http://doi.org/10.3138/cpa-gpse.

O'Neill, H.B., Wolfe, S.A. and Duchesne, C., 2019. New ground ice maps for Canada using a paleogeographic modelling approach. The Cryosphere, vol. 13, p. 753–773.

Perrin, A. and Jolkowski, D., 2022. Yukon climate change indicators and key findings 2022. YukonU Research Centre, Yukon University, 126 p.

Schetselaar, A.B. and Burn, C.R., 2024. Increases in highway maintenance costs in a permafrost environment undergoing climate change, Yukon, Canada. *In:* 12th International Conference on Permafrost Proceedings, International Permafrost Association, p. 373–381, ICOP2024_82_Schetselaar_8A.pdf.

Sharp, E., 2025. Avalanche risk assessment. Unpublished consultant report, Alpine Solutions Avalanche Services, 40 p.

Singh, S. and Ismail, S., 2025. Geotechnical investigation report – Dempster Highway km312. Unpublished geotechnical report, AtkinsRéalis, 89 p.

Smith, C.A.S., Meikle, J.C. and Roots, C.F. (eds.), 2004. Ecoregions of the Yukon Territory: Biophysical properties of Yukon landscapes. Agriculture and Agri-Food Canada, PARC Technical Bulletin No. 04-01, Summerland, British Columbia, 313 p.

Tse, D. and Adams, R., 2024. South Klondike Highway Avalanche Program Review. Unpublished consultant report, Dynamic Avalanche Consulting Ltd., 33 p.

Vincent, L.A., Zhang, X., Brown, R.D., Feng, Y., Mekis, E.J., Milewska, E.J., Wan, H. and Wang, X.L., 2015. Observed trends in Canada's climate and influence of low-frequency variability modes. Journal of Climate, vol. 28, p. 4545–4560.

Assessing Miles Ridge landslide activity using an integrated ground-RPAS-satellite approach

John Stix and Justin Roman*
Department of Earth and Planetary Sciences, McGill University

Margaret Kalacska and Oliver Lucanus
Applied Remote Sensing Laboratory (ARSL), Department of Geography, McGill University

Panya S. Lipovsky
Yukon Geological Survey

Pablo Arroyo-Mora
National Research Council of Canada, Flight Research Laboratory

Stix, J., Roman, J., Kalacska, M., Lucanus, O., Lipovsky, P.S. and Arroyo-Mora, P., 2026. Assessing Miles Ridge landslide activity using an integrated ground-RPAS-satellite approach. *In:* Yukon Exploration and Geology 2025, A. Stuart, L.H. Weston and S.K. Schultz (eds.), Yukon Geological Survey, Government of Yukon, p. 221–237.

Abstract

The Miles Ridge landslide in southwest Yukon presents a potential hazard to the nearby White River bridge along the Alaska Highway. To assess the current behaviour and stability of this landslide, we integrated ground-based GNSS surveying, Drone-In-a-Box (DIAB) 3D modelling, and Sentinel-1 InSAR analysis. A ground survey in 2025 identified active tension cracks and widespread loss of the original 2007 GNSS markers, indicating continued deformation at the ridge crest. Five DIAB-derived surface models captured localized but substantial erosion and deposition within the central amphitheatre and lower channel system of the landslide, resulting in measurable volumetric change over a two-month interval (July–September). Over a one-month period (July–August), the DIAB models showed an apparent loss of debris from much of the landslide surface. Differential InSAR (DInSAR) analysis from 2017 to 2024 may indicate long-term subsidence across the landslide. Together, these datasets reveal an actively, but slowly evolving slope characterized by geomorphic change and persistent instability, underscoring the importance of continued monitoring to evaluate future movement and potential impacts to the Alaska Highway.

Plain language summary

The Miles Ridge landslide is an area of active ground movement in the Nutzotin Mountains, a small mountain range at the northern extent of the St. Elias Mountains. Located only a few kilometres from the Alaska Highway and the White River bridge, the landslide poses a potential threat to this critical infrastructure. To better understand the behaviour and current activity of the landslide, we conducted a series of ground-based, RPAS-based (drone), and satellite-based studies in the summer of 2025. We installed a new series of markers near the crest of Miles Ridge and surveyed them during one day of fieldwork. The markers are located in a zone of actively forming tension cracks and will be resurveyed in the future at periodic intervals. Using RPAS and satellite imagery, we mapped out different zones in the landslide's upper and lower parts. The upper part is dominated by a large talus apron which appears to supply material into the lower reaches of the landslide. The lower part is divided

* john.stix@mcgill.ca

into a series of lobes separated by erosional gullies. During the two-month survey, the lower zone experienced both localized debris erosion and accumulation. We also imaged the fan area where debris from the landslide drainage enters the White River several hundred metres upstream from the bridge. Our satellite measurements suggest that the Miles Ridge landslide appears to be moving over time, highlighting the need for further work to evaluate impacts to the Alaska Highway.

Introduction

Natural hazards are an increasing concern for local communities and for territorial, provincial and state governments. They also pose challenges at both national and global scales. From 1980 to 2000, annual global losses from natural disasters never exceeded US$200 billion on an inflation-adjusted basis. Since 2000, this level of loss has frequently been surpassed (Munich RE, 2025). The key issue is twofold: first, residential and commercial structures continue to be constructed in vulnerable areas with insufficient regard to hazard evaluations or hazard maps; and second, the changing global climate is increasing both the frequency and severity of naturally hazardous weather-related events, such as hurricanes (e.g., Holland and Bruyère, 2014), floods (e.g., Hirabayashi et al., 2013), and landslides (e.g., Gariano and Guzzetti, 2016). The problem is accentuated at high latitudes where the rate of warming is greater than at low and mid-latitudes. In northern Canadian environments, such as the Yukon and Northwest Territories, these changes are most evident in the cryosphere, manifesting as increased coastal erosion (e.g., Irrgang et al., 2018), permafrost melting (e.g., Burn and Zhang, 2009), and glacier surges and ice dam formation (e.g., Kochtitzky et al., 2020).

In the Yukon, natural hazards can have a profound impact on critical infrastructure, including highways and railways. An example of such critical infrastructure is the Alaska Highway, which extends 892 km across the Yukon from Watson Lake in the south, to north of Beaver Creek and the Alaska border. This highway is the most heavily used transportation route in the Yukon, and it is also the principal road linking Alaska with the contiguous United States. As such, it serves as one of North America's most important transportation links.

The Alaska Highway is subject to a variety of hazards that can disturb its road surface, including earthquakes, flooding, permafrost melting and wildfires. At kilometre 1818.5, near Koidern, the highway crosses the White River, a major tributary draining the St. Elias Mountains, by means of the White River bridge. An active zone of mass movement, named the Miles Ridge landslide, is located at the head of an unnamed drainage that flows into the White River about 500 m upstream of this bridge (Fig. 1). Since the early 1990s, relatively small-scale rockfall, slumping, and debris flow activity near the crest of Miles Ridge has caused unconsolidated material to accumulate in the upper part of the drainage over 500 vertical metres above the river (Bond et al., 2008). The toe of the landslide is located ~1.4 km from the bridge. Should this debris or any underlying unstable rock masses become mobilized in a larger-scale event, there is potential for it to deflect the White River and cause undermining of the bridge structure or impact the bridge directly. Any damage to the highway or bridge could have significant repercussions for the Yukon and beyond, including Alaska, the contiguous United States and the provinces of British Columbia and Alberta.

The purpose of this contribution is to present new results from ground-based, remotely piloted aircraft system (RPAS or drone), and satellite data of the Miles Ridge landslide and surrounding area, in order to better understand its current behaviour and to gain new insight into potential future movements of the landslide. We first present results from ground-based, RPAS and satellite data, and then discuss their significance and implications to provide an integrated view of the Miles Ridge landslide system at a variety of spatial scales.

Study area

Miles Ridge is located approximately 6 km west of Koidern, Yukon, in the Nutzotin Mountains, a small mountain range at the northern extent of the St. Elias Mountains. The ridge crest is at an elevation of ~1480 m above sea level (ASL) and forms a ~400 m-wide headscarp in the landslide source zone. The landslide covers an area of ~13 ha, extends ~580 m horizontally, and drops ~370 m vertically on a steep (~34°) northeast-facing slope. The White River floodplain is at an elevation of ~700 m at the White River bridge (Fig. 1).



Figure 1. *Location map of the Miles Ridge landslide and surrounding area. The study area is outlined in red.*

The region is geologically very active, owing to steep rugged slopes, permafrost degradation, weak local lithologies, and high regional seismicity (Han et al., 2024). This elevated level of seismicity is exemplified by the M7.0 earthquake and subsequent aftershocks that occurred in December 2025 along the strike-slip Connector fault, 188 km south of Miles Ridge. The Denali fault is another crustal-scale, strike-slip fault which extends in a northwest-southeast direction at the foot of Miles Ridge to the north (Bender and Haeussler, 2017). Although a M7.9 earthquake on the Denali fault occurred in 2002, approximately 400 km to the northwest, the part of the fault at Miles Ridge is located along what is referred to as the Eastern Denali fault (EDF), which has experienced lower seismicity and slip rates than other parts of the fault farther to the west (Haeussler et al., 2017; Marechal et al., 2018). No earthquakes large enough to generate surface ruptures have occurred along the EDF for at least 500 years (Clague, 1979), but Blais-Stevens et al. (2020) determined that up to four >M6 earthquakes have occurred along the EDF in the last 6000 years (Finley et al., 2022).

The landslide source zone is controlled by complex fault-bounded structural geology. Relatively resistant volcanic rocks of the Station Creek Formation buttress extremely incompetent overlying units, including highly altered, clay-rich Kluane ultramafic rocks and Nikolai formation basalts (Bond et al., 2008). Ongoing deformation of these overlying rocks has likely been triggered by partial collapse of the supporting Station Creek Formation rocks.

As further erosion and accumulation of debris occur in the landslide initiation zone, the supporting volcanic rocks are becoming increasingly loaded. This, in combination with the fact that the landslide is located within a region of high seismicity, suggests that the southeast side of the basin will eventually collapse. The consequences of such a failure would vary depending on the seasonal timing, event magnitude, and runout distance of the debris (Bond et al., 2008).

Methodology

Ground measurements

In 2007, forty-eight wooden stakes and rebar monuments were installed and surveyed on the Miles Ridge landslide (Bond et al., 2008), extending along the headscarp and across three transects on the middle and lower sections of the slide. These were installed to facilitate potential future ground deformation monitoring efforts, although no subsequent survey results were ever reported. The site was visited by helicopter on July 9, 2025, to locate and resurvey any remaining stakes and document current ground conditions. Due to safety concerns, the middle and lower sections of the slide could not be accessed by foot; consequently none of the 2007 stakes on the lower three transects could be located on the ground, nor were any visible from the helicopter.

On the crest of Miles Ridge, along the landslide headscarp, only one of the original wooden stakes from the 2007 survey could be located (L102). Only a fragment of this stake remained, so it was replaced with rebar and resurveyed. Twelve new stakes for a GPS-GNSS survey were then installed along a ~110 m transect on an unstable slope encompassing several tension cracks at the northwestern end of the headscarp (Fig. 2). This new transect, termed the MR transect (see below), was oriented in a northwest-southeast line, and the stakes were placed approximately 12 m apart. The new stakes included both wooden stakes and rebar to ensure long-term durability and accessibility.

A two-part GNSS receiver and base station setup was used for this survey. The base station (D-RTK 3 Multifunctional Station; DJI, Shenzhen, China) was temporarily set up on the northern side of the airstrip at Discovery Yukon Lodgings on July 9, 2025. It logged



Figure 2. *Photograph facing southeast illustrating the new MR line of wood and rebar markers installed on July 9, 2025. The markers are spaced approximately 12 m apart. Note person for scale in upper part of image.*

raw GNSS observations continuously throughout the survey on Miles Ridge, which was approximately 2.5 km west of the base station. An Emlid Reach RS2 (Emlid Tech Kft, Budapest, Hungary) receiver was used as the rover to survey all points. The Emlid Flow application on an iPhone 14 Pro Max was used to operate the RS2. The RS2 was set to log GNSS observations continuously from 1255 to 1613 hours local time (1955 to 2313 hours UTC). At each stake, the rover was held stationary for one minute and the locations were recorded through a Survey Project. This method of collection, called stop-and-go, allows for the positions where the rover was stationary to be extracted from the raw logs in post processing. For the naming convention, the resurveyed 2007 Yukon Geological Survey (YGS) point was labeled using its original ID with the suffix '-new' (i.e., L102–new), whereas the newly installed markers were assigned the prefix 'MR' for Miles Ridge, followed by sequential numbers (e.g., MR-01, MR-02, etc.).

After the data collection on the ridge was completed, the base station's raw GNSS observations were converted to standard RINEX files with Emlid Studio v.1.9 (Emlid Tech Kft, Budapest, Hungary) and uploaded to Natural Resources Canada's (NRCAN) Precise Point Positioning (PPP) service (Government of Canada, 2025) to obtain its accurate position. A single-point GNSS solution would only provide metre-level accuracy, whereas PPP applies satellite orbit, clock, and bias corrections to achieve centimetre-level accuracy.

To calculate the positions of the stakes, a post-processed kinematic (PPK) methodology was used. To do so, Emlid Studio v.1.9 was used with the RS2 rover's raw logs and the exported survey positions. The base station's position determined through the PPP processing was also input. This PPK workflow allows for corrections of the rover's GNSS data to improve position accuracy. The outputs from the workflow were latitude, longitude and ellipsoidal height of each location where the RS2 rover was stationary for one minute (also where the survey points were recorded in the Emlid Flow application). Coordinates reported in 2007 for the L102 stake were compared to its position acquired in 2025.

RPAS measurements

The DJI Dock 2 is a compact (~34 kg), fully integrated drone-in-a-box (DIAB) system designed to enable routine, automated RPAS operations with minimal on-site human involvement. The system pairs a weather-resistant docking station equipped with environmental monitoring, automated battery charging, and internal thermal regulation with the DJI Matrice 3D/3TD aircraft, allowing remotely scheduled missions (Fig. 3). For this deployment, the Dock 2 was mounted onto a reinforced wooden base installed on top of a shipping container, providing a secure, elevated platform with stable AC power and hard-wired Ethernet connectivity from a Starlink (a low-orbit satellite-based internet system operated by SpaceX). The installation was located 2.55 km from the ridge crest, the farthest point of the area being monitored. The DJI Mavic 3TD (M3TD) aircraft used here with the Dock 2 integrates three onboard imaging sensors, including a 48 MP wide-angle RGB camera (1/1.32-inch CMOS) that served as the primary mapping instrument due to its RTK-precision geotagging. It also includes a 12 MP telephoto RGB camera and a calibrated thermal infrared sensor with ≤50 mK sensitivity, enabling multi-modal imaging and enhanced situational awareness. The aircraft features six-direction obstacle sensing, ADS-B AirSense capability, a maximum operating range of 10 km, and a maximum flight speed of 15 m/s.

Flight planning was carried out using DJI FlightHub 2, where a custom waypoint-based mission design kept the aircraft within the Canadian legal altitude limits by following terrain-constrained paths across the



Figure 3. *Installation of the DJI Dock 2 on the top of the shipping container; Miles Ridge is in the distance. The inset illustrates the M3TD during take-off. The Dock 2 weighs 34 kg and is 57 × 58.3 × 46.5 cm (L×W×H) with the doors closed.*

landslide surface and transit between the Dock 2 and the survey area. FlightHub 2's information security management system is ISO/IEC 27001 certified ensuring confidentiality, information integrity, and data availability. The installation and flight planning are detailed in Kalacska et al. (2026).

A total of five 3D models of the Miles Ridge landslide were generated between July 13 and September 7, 2025 using the online processing option within FlightHub 2. The last two flights were conducted with the pilot-in-command operating the system remotely from eastern Canada, approximately 4000 km from the installation location (with a local visual observer). Given the distance of the landslide from the installation, the performance of the Dock 2 RTK system, and the accuracy of the Dock 2 calibration at the time of installation (estimated from Natural Resources Canada's Precise Point Positioning service), the combined expected uncertainty of the real-world positioning of the models is approximately 3.56-4.56 cm horizontally and 5.06 cm vertically at the farthest point. Multi-temporal cross-section and volume change analyses were carried out in FlightHub 2 with the Analyzer module.

Because this was the first deployment of the system, and because wind conditions at higher elevations in mountainous terrain can differ substantially from those measured in the valley, a conservative flight plan was adopted. The complexity of the terrain, manned helicopter activity, and regulatory constraints made this an unusually difficult flight-planning exercise and far more involved than what is typically required for DIAB operations.

Satellite data

To determine whether Differential InSAR (DInSAR) products could offer regional scale insight into long-term topographical changes, we examined the Canada-wide InSAR vertical deformation map from Samsonov and Feng (2023), which was produced using a fully automated high-performance computing workflow that processed more than 220 000 Sentinel-1 SAR images acquired between 2017 and 2023. As detailed in Samsonov and Feng (2023), the system generated differential interferograms with GAMMA software (Gamma Remote Sensing, Gümligen, Switzerland), removed the topographic phase using the 30 m ASTER DEM, and combined ascending and descending orbit interferograms to derive horizontal and vertical deformation time series across Canada using the multidimensional small baseline subset (MSBAS) technique (Samsonov and d'Oreye, 2012). Uplift from postglacial rebound and tectonic motion signals were filtered from these data to specifically highlight local-scale ground deformation from processes such as landslides (Samsonov and Feng, 2023).

As part of the field campaign, we also tasked SkySat imagery (optical imagery, 30 cm resolution) to capture a recent high-resolution scene of the landslide, offering an updated landscape context to complement our ground and RPAS observations. We also queried the historical archive of RapidEye optical imagery (5 m spatial resolution) spanning from 2009 to 2015 to determine when the landscape changes currently observable at the base of the landslide first emerged. This temporal comparison allowed us to trace the emergence and growth of features such as the debris fan entering the White River, providing valuable long-term context on the evolution of the landslide.

Results

Ground measurements

Fourteen of fifteen wooden stakes, and one metal rebar, originally positioned along the crest of Miles Ridge in 2007 were no longer present in 2025, potentially due to erosion and retreat of the headscarp, snow avalanches, and/or strong winds. Coordinates and horizontal and vertical differences between the 2025 and the original 2007 positions of the one remaining stake (L102 – restaked as L102-new) are shown in Table 1. Table 2 provides the positions of all newly installed MR-series stakes. When the uncertainty of the base station's position is combined with the survey point uncertainties, the resulting uncertainties for the 2025 stake positions are ± 1.8 cm (north), ± 1.6 cm (east) and ± 3.3 cm (vertical).

During the MR-series survey, fresh tension cracks were noted on a vegetated slope near the top of the ridge. Uneven ground surfaces and local subsidence were also visible along the ridge. These features provide evidence of active mass movement and support the interpretation of ongoing instability at the site. Figure 4 illustrates large tension cracks up to approximately 50 cm wide and between 20 and 30 cm deep with relatively fresh roots stretched across the cracks. These observations highlight the importance of integrating GNSS measurements with visual observations to characterize the slope activity at Miles Ridge.

Table 1. Coordinates of stake L102-new as recorded in 2007 and 2025. Horizontal and vertical differences between the coordinates are also shown. HAE is Height Above Ellipsoid. Coordinates displayed in UTM 7N (WGS84).

Stake ID	Material	2007 coordinates (UTM)	2025 coordinates (UTM)	2007 HAE (m)	2025 HAE (m)	Horizontal displacement (m)	HAE difference (m)
L102-new	wooden stake	521937.87E 6871526.56N	521936.57E 6871526.73N	1487.06	1486.97	1.30	-0.090

Table 2. Positions of newly installed MR-series stakes. HAE is Height Above Ellipsoid. Coordinates displayed in UTM 7N (WGS84).

ID	Material	Easting (m)	Northing (m)	HAE (m)
MR - 01	rebar	521686.09	6871731.50	1470.95
MR - 02	wooden stake	521692.43	6871717.19	1469.01
MR - 03	wooden stake	521699.11	6871707.07	1468.64
MR - 04	wooden stake	521704.48	6871698.29	1468.89
MR - 05	wooden stake	521710.20	6871687.22	1470.47
MR - 06	wooden stake	521716.08	6871676.87	1472.46
MR - 07	wooden stake	521721.52	6871666.45	1474.47
MR - 08	wooden stake	521727.67	6871656.06	1477.61
MR - 09	wooden stake	521732.43	6871647.63	1481.50
MR - 10	rebar	521738.62	6871637.14	1483.66
MR - 11	wooden stake	521700.00	6871687.27	1477.79
MR - 12	rebar	521807.06	6871598.86	1480.42

RPAS observations

The imagery collected by the various RPAS flights reveals a variety of surface characteristics and geomorphological zones across various parts of the landslide (Fig. 5). Most of the landslide lacks vegetation, attesting to its high level of ongoing activity, but a vegetated zone does occur in the upper western sector of the landslide (Fig. 5, zone C). In this area, fresh tension cracks were observed, both by RPAS (Fig. 6) and during our ground survey on July 9 (Fig. 4). One set of cracks are located close to the ridge, and a second set occur approximately 40 m downslope where the topography steepens (Fig. 6). The cracks run parallel to the ridge and to the general strike of the rocks which outcrop along the ridge crest.

The upper part of the slide can be divided into three sectors: eastern, centre and northern. In the eastern sector (Fig. 5, zone A), the slide is dominated by rock outcrops which are grey (Kluane ultramafics; Fig. 5, zone A1) to orange brown (Station Creek Formation; Fig. 5, zone A2) in colour. In the centre (Fig. 5, zone B), a broad apron of dark brown talus can be seen, fed by ongoing rockfall from the basalt cliffs above. The western sector (Fig. 5, zone C) comprises the vegetated zone mentioned above. A horizontal view of this upper part of the slide, captured by RPAS, is shown in Figure 7.

The landslide toe comprises a steep light-coloured colluvial apron that is gullied from ongoing seepage and debris flow activity that has mobilized saturated and weathered ultramafic rock from above. On the



Figure 4. *Large tension crack observed just below Miles Ridge. Note the fresh-appearing nature of the debris and the angular rock fragments. Shovel for scale is 100 cm long x 20 cm wide (blade).*

eastern side of the toe, below the craggy outcrops of the Station Creek Formation, fine-grained debris has accumulated in a steep apron with a relatively smooth surface dissected by a nearly straight small gully (Fig. 5, zone D). A larger gully separates this area from a slightly rougher section of the landslide toe to the west (Fig. 5, zone E). Zone E is dissected by a second gully that roughly parallels the larger gully separating zones D and E.

In the central part of the landslide, below the base of the brown basalt talus apron, these two prominent gullies drain from an amphitheatre-shaped scar ~50 m wide that is the source zone for secondary debris flows (hereafter referred to as the 'amphitheatre'; Fig. 5, zone F; Figs. 7 and 8). A dark-coloured lobe (Fig. 5, zone G) is also observed on the northwestern margin of the landslide. This material is assumed to comprise basalt talus which extends further because there are no crags of Station Creek Formation rocks underlying this area of the slide to retain colluvial material mobilized from the headscarp above. Five large angular blocks of dark brown rock several metres in diameter are scattered across this lobe (Fig. 8). These are assumed to be associated with a larger magnitude collapse of a section of the headscarp.

Two drone images of this area captured on July 14 and August 12, 2025 illustrate ongoing erosional processes that occur in the prominent gullies and their associated source zones (Fig. 9). In the July 14 image, a significant volume of brown-coloured debris appears to be filling and possibly clogging the two main gullies, as well as their amphitheatre source zones. By contrast, in the August 12 image, this debris appears to be largely absent from both the channels and the amphitheatres. We speculate that a precipitation event, or events, mobilized this debris and carried it to lower elevations, possibly into the White River.

Figures 10 and 11 illustrate a temporal comparison of the 3D RPAS-derived models collected on July 14 and September 7. The cross-sections in Figure 10a and 10b show approximately 2 m of erosion along a ~13 m section of the eastern margin of the amphitheatre. In contrast, the lower cross-sections in Figure 10c and 10d reveal material deposition within the channel immediately downslope of the amphitheatre, with gains of roughly 2.3 m in depth across the ~11 m wide channel. Additional transects, extracted in both vertical and horizontal orientations across the broader landslide, showed no measurable change over this interval. Figure 11 provides a relative spatial map of the detected surface change at both the slope and amphitheatre scales, highlighting the localized distribution of erosion and deposition. Overall, the amphitheatre exhibits a net gain of 174.4 m³, derived from an estimated 2076.7 m³ of material lost upslope and 2251.2 m³ deposited downslope within the channel.

Satellite measurements

Apparent subsidence of the Miles Ridge landslide area is observed from the Canada-wide active ground deformation DInSAR map data (Fig. 12). These data clearly show negative vertical displacement (i.e., subsidence) rates of up to 2–3 cm/year for most of the landslide area for the 2017–2024 period (Samsonov and Feng, 2023). Confidence in the absolute magnitudes of these data remains tentative as many areas of positive vertical displacement (red [or warm tones] in Fig. 12) are also observed in surrounding areas. While zones of positive vertical displacement

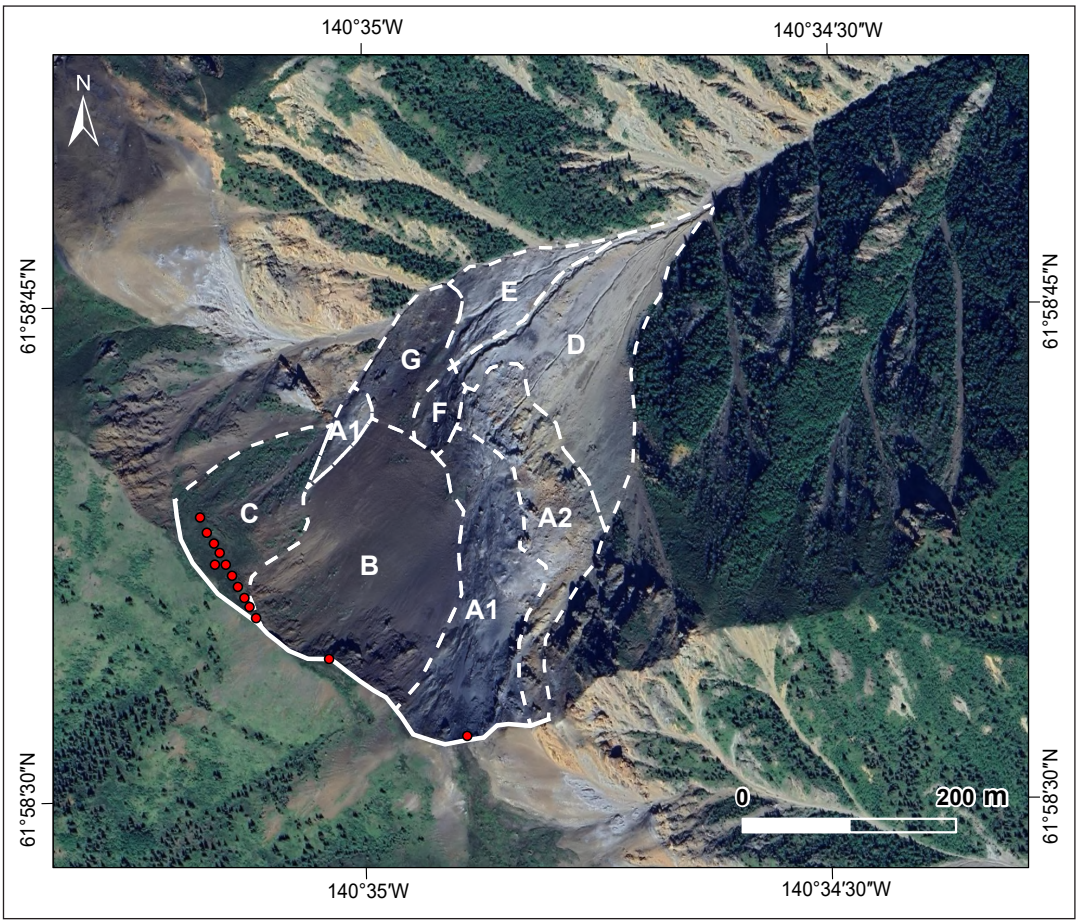


Figure 5. *Geomorphic zones of the Miles Ridge landslide described in the text. Solid white line represents a landslide headscarp located on the ridge crest. Dashed white lines delineate zones. Red points are new stakes that were installed and surveyed on July 9, 2025. The Google Earth background image was acquired on July 4, 2023.*

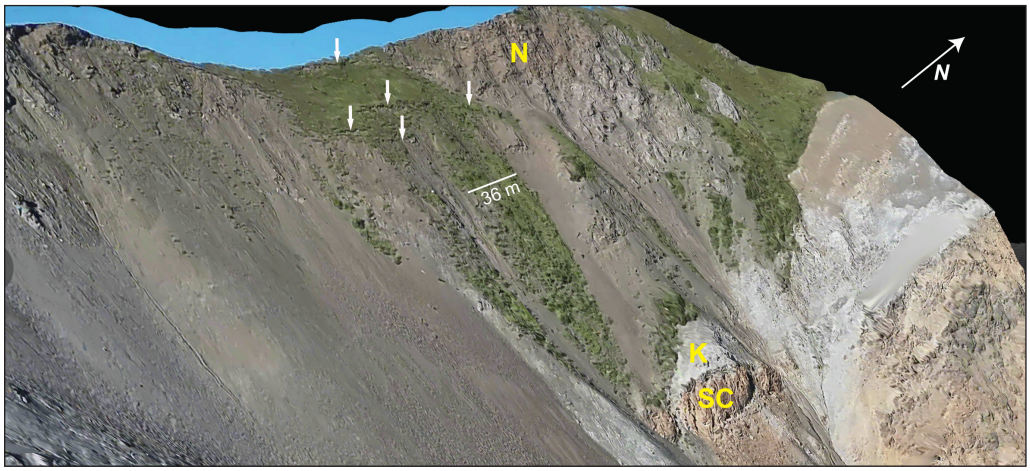


Figure 6. *A 3D RPAS model view displaying tension cracks (white arrows) in the upper vegetated zone of the Miles Ridge landslide. Given the three-dimensional nature of the terrain, the scale bar should be interpreted only for areas lying within the same plane, as distances can be distorted across varying elevations. The main bedrock units are shown as N – Nikolai formation, K – Kluane ultramafics, SC – Station Creek Formation.*



Figure 7. *An RPAS photograph of the landslide.* ***(a)*** *apron of brown talus,* ***(b)*** *smooth lobe,* ***(c)*** *tension cracks,* ***(d)*** *vegetated zones,* ***(e)*** *erosional amphitheatre,* ***(f)*** *highly incised channel,* ***(g)*** *large boulder,* ***(h)*** *dark-coloured lobe,* ***(i)*** *topographically rough lobe.*

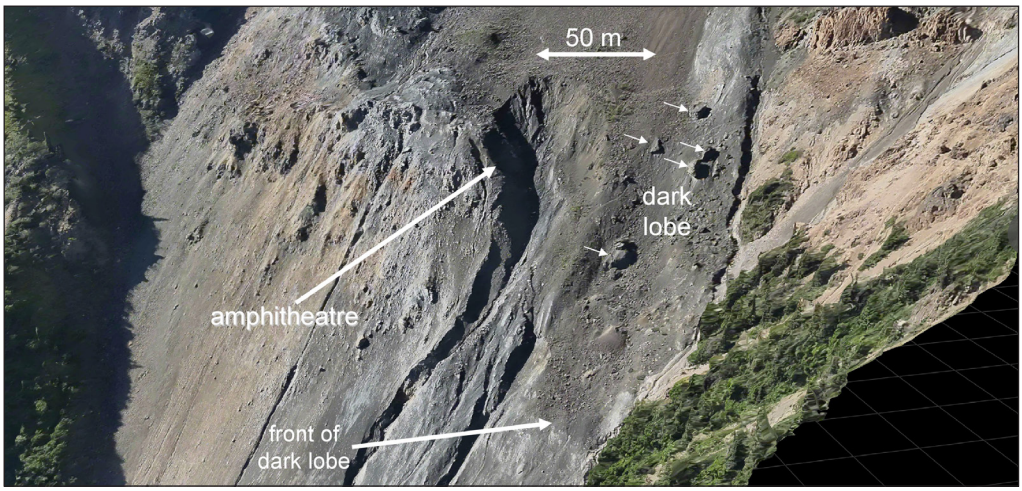


Figure 8. *Detailed view from the August 12, 2025 3D model of the dark-coloured lobe and adjacent amphitheatre. Small white arrows indicate metre-sized rock boulders (largest are 4–6 m in diameter). Given the three-dimensional nature of the terrain, the scale bar should be interpreted only for areas lying within the same plane, as distances can be distorted across varying elevations.*

of up to 3 cm/yr in adjacent areas may be explained by rock glacier movement and floodplain aggradation, we speculate that other, more subtle areas of positive vertical displacement may result from data artefacts. Where holes in the data occur, it is assumed there was either a lack of coherence in ground conditions, or gaps that were not filled by the MSBAS algorithm. Considering that this product has known artefacts and has not yet been formally validated, these findings must be interpreted with appropriate caution.

Finally, based on a Skysat satellite image acquired July 10, 2025, and an orthomosaic of RPAS photographs from July 12, 2025 (Fig. 13), we note that the junction

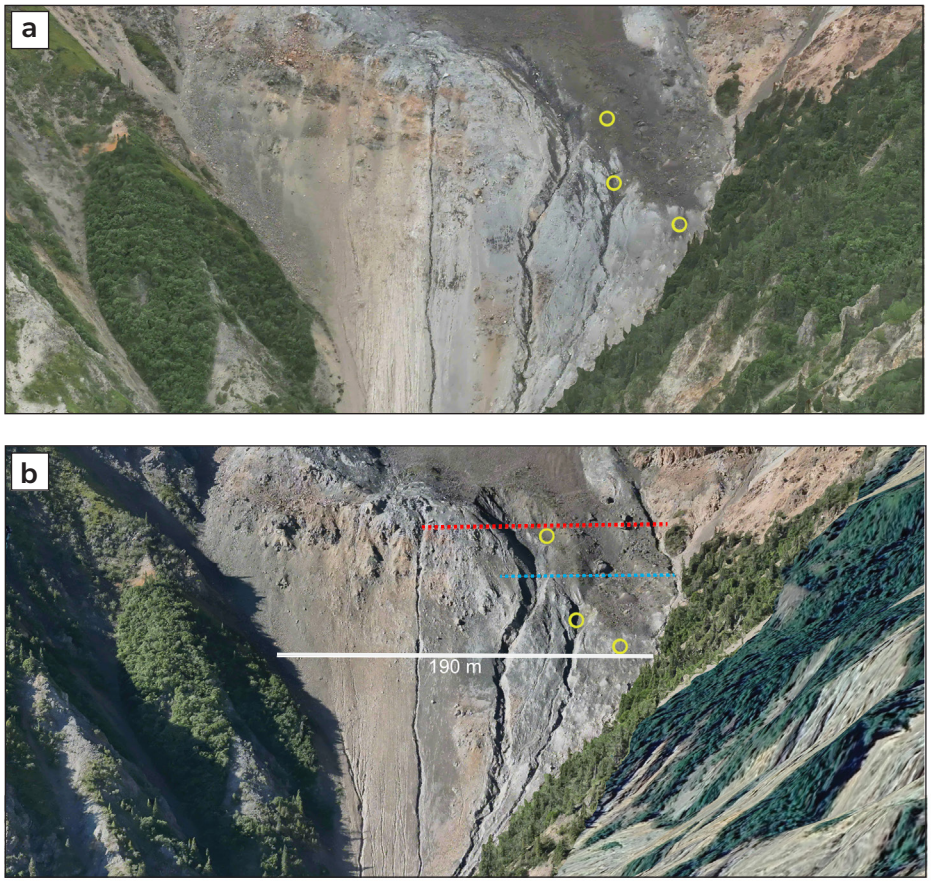


Figure 9. *Two 3D RPAS models showing potential loss of debris from the dark lobe and surrounding erosional features between* ***(a)*** *July 14 and* ***(b)*** *August 12, 2025. Given the three-dimensional nature of the terrain, the scale bar should be interpreted only for areas lying within the same plane, as distances can be distorted across varying elevations. The red and blue dashed lines correspond to the approximate locations of the cross-sections shown in Figure 10. The yellow circles indicate areas where sediment has been lost between the two dates.*

of the landslide drainage channel and the White River, immediately upstream from the bridge, reveals significant debris deposition beyond the immediate margins of the channel. In this area, the forest appears to be partly buried by the large volume of debris. The historical RapidEye imagery acquired between 2009 and 2015 indicates that the debris fan was smaller prior to 2013. The earliest snow-free image, obtained May 15, 2014, reveals further expansion of the fan to approximately its present-day extent (Fig. 13).

Discussion

All but one of the markers installed during the 2007 GPS–GNSS survey on Miles Ridge disappeared or could not be located, likely due to erosion of the ridge crest, snow avalanches, and/or persistent high winds. During the 2025 field campaign, we installed and surveyed a new line of markers just below the ridge (Figs. 2 and 5), providing a modern baseline against which future surveys can assess ground movement in this upper sector of the landslide.

Both our ground survey and our RPAS data revealed a zone of active tension cracks in this upper sector (Figs. 4 and 6). Fresh, vegetation-free soil within the depressions and the presence of fresh roots and angular clasts indicate that these cracks are actively deforming. Future surveys could include repeated measurements of crack width and length, with high-resolution RPAS imagery supporting change detection and aiding in identifying new or expanding fractures.

The upper reaches of the landslide consist of three geomorphic zones. From the southeast to the northwest they are: a sector of rock outcrops, a central talus apron, and a vegetated area containing active tension cracks noted above (Figs. 5 and 7). The central talus zone may be supplying material to the landslide downslope. Mapping moisture patterns in this upper area, using nighttime thermal infrared RPAS surveys, could help identify sections prone to enhanced instability.

The lower reaches of the landslide comprise two main lobes, one relatively smooth on its surface and one relatively rough (Fig. 7). The lobes are incised by several large erosional gullies which originate from

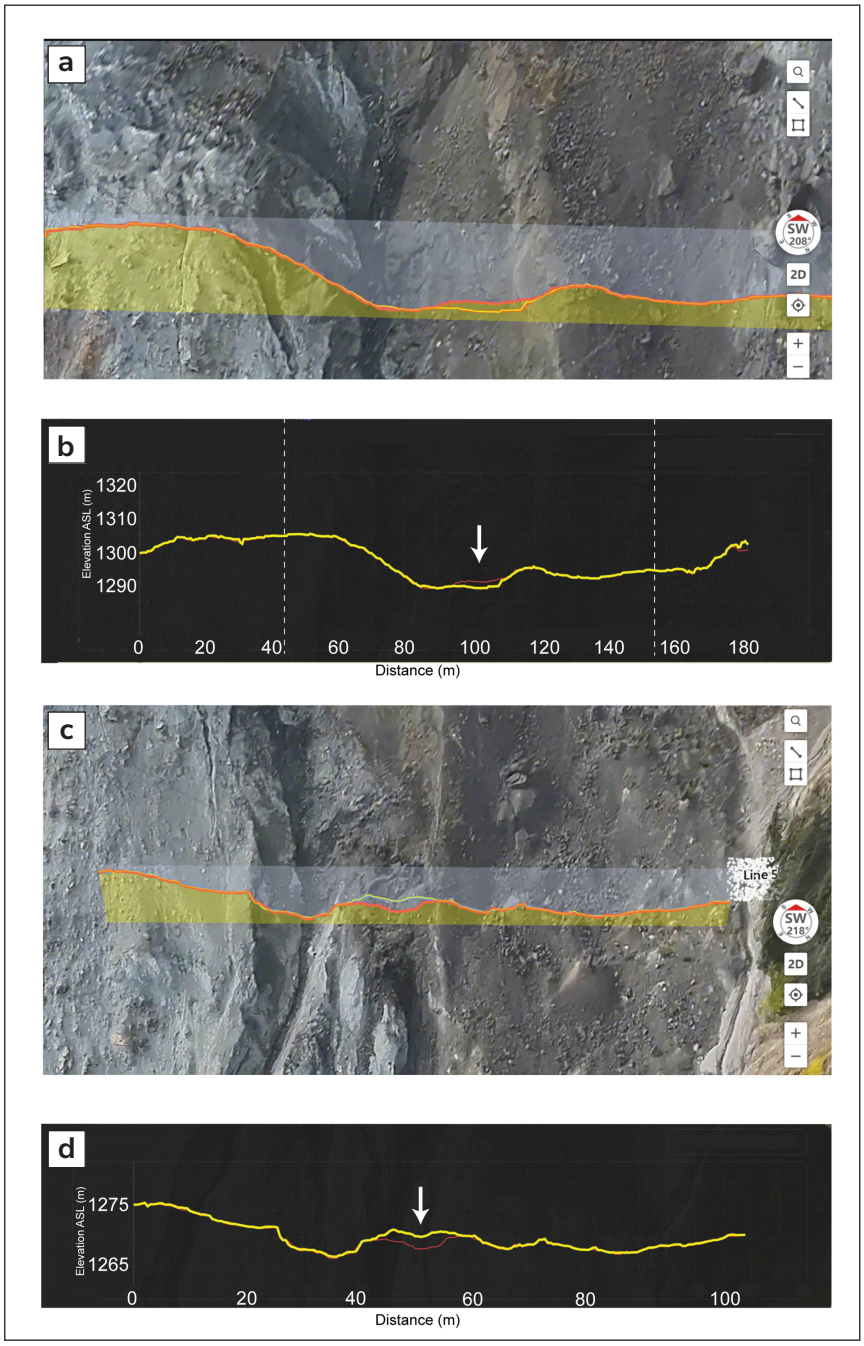


Figure 10. *Comparison of cross-sections across the amphitheatre illustrating areas of material erosion and deposition.* ***(a)*** *Cross-section extracted from the FlightHub 2 3D models showing a zone of erosion between July 14 (red line) and August 12 (yellow line).* ***(b)*** *Elevation-change profile for the same cross-section; the segment between the vertical dashed lines corresponds to the close-up area shown in (a). Arrow indicates area of erosion.* ***(c)*** *Cross-section from the 3D models illustrating a zone of deposition immediately downslope of the amphitheatre over the same time interval.* ***(d)*** *Elevation-change profile for the cross-section shown in (c). Arrow indicates area of deposition.*

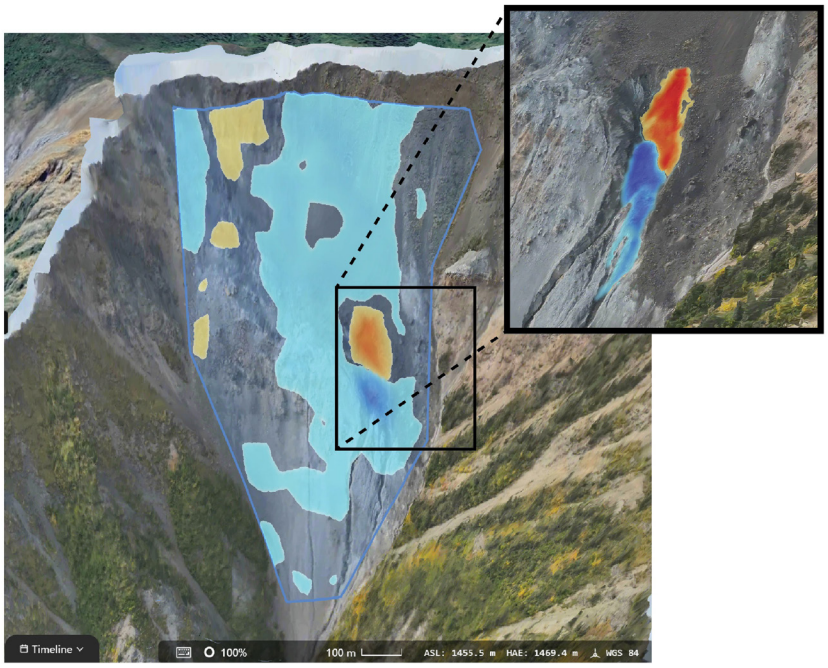


Figure 11. *Relative volume-change map models between July 14 and September 7, 2025, derived from FlightHub 2, where red shading indicates erosion and blue shading indicates deposition. The inset highlights, at higher spatial detail, the two dominant patches exhibiting erosion and deposition, which are associated with the amphitheatre. As of the version released in September 2025 online, volumetric change analyses only provide the total volume change while the spatial map is qualitative only.*

a prominent amphitheatre located in the middle of the landslide. A third prominent dark-coloured lobe is observed on the northern margin of the landslide, adjacent to the amphitheatre and upper gullies (Figs. 7 and 8), and likely receives material from the headscarp above. The amphitheatre and associated region appear to be an area of enhanced erosion, as revealed by our volumetric gain/loss maps (Fig. 11). This can also be seen by the contrasting RPAS imagery of July 14 and August 12, 2025, which suggest erosion of debris, likely during precipitation events (Fig. 9).

To increase spatial detail of the tension cracks near the ridge in future RPAS operations, whether using the Dock 2 or manual flights, two primary approaches can be used. The first is to use the zoom camera, which yields enhanced detail in individual images but cannot support 3D modelling due to the lack of sufficiently accurate geotags. The second is to design flight paths that bring the aircraft closer to the ridge crest, thereby improving the ground-sampling distance. However, this approach increases the likelihood of encountering wind shear or strong local winds associated with daytime anabatic (upslope) and nighttime katabatic (downslope) flows. Conducting RPAS surveys immediately after snowmelt and again prior to snowfall each year would not only provide ground validation for DInSAR deformation estimates but would also supply high-resolution information on the evolution of dynamic geomorphic features such as widening tension cracks and shifting zones of erosion and deposition.

The DInSAR satellite vertical deformation map indicates ongoing localized subsidence across most of the landslide. With continued acquisitions, it may be possible to quantify subsidence rates in different sectors of the landslide, helping to identify zones of acceleration or deceleration and thus assess evolving stability conditions. RapidEye imagery from 2009 to 2015 shows that a major landscape change occurred between 2012 and 2013, during which the debris fan draining into the White River expanded markedly. Notably, the Burwash Landing meteorological station (50 km away) recorded the second-highest annual rainfall on record of 284 mm in 2012 (Kochtitzky et al., 2020), suggesting that unusually wet conditions may have contributed to increased sediment transport during this period. The first cloud-free image from May 15, 2014 reveals that the debris fan had grown further, reaching approximately its present extent (Fig. 13). This expanded fan, characterized by numerous dead and fallen trees, remains evident today in both the SkySat imagery and the RPAS photographs acquired in July 2025. Future analyses could also include digital surface models that can be produced from SkySat stereo pairs or triplets (a single image from a triplet acquired on July 9, 2025 is shown in Figure 13a). Although the resolution is coarser than the RPAS models (metres vs. centimetres), in absence of the Dock 2, these images can be tasked year-round and can provide rapid remote assessments of potential large-scale events or surface changes on the landslide.

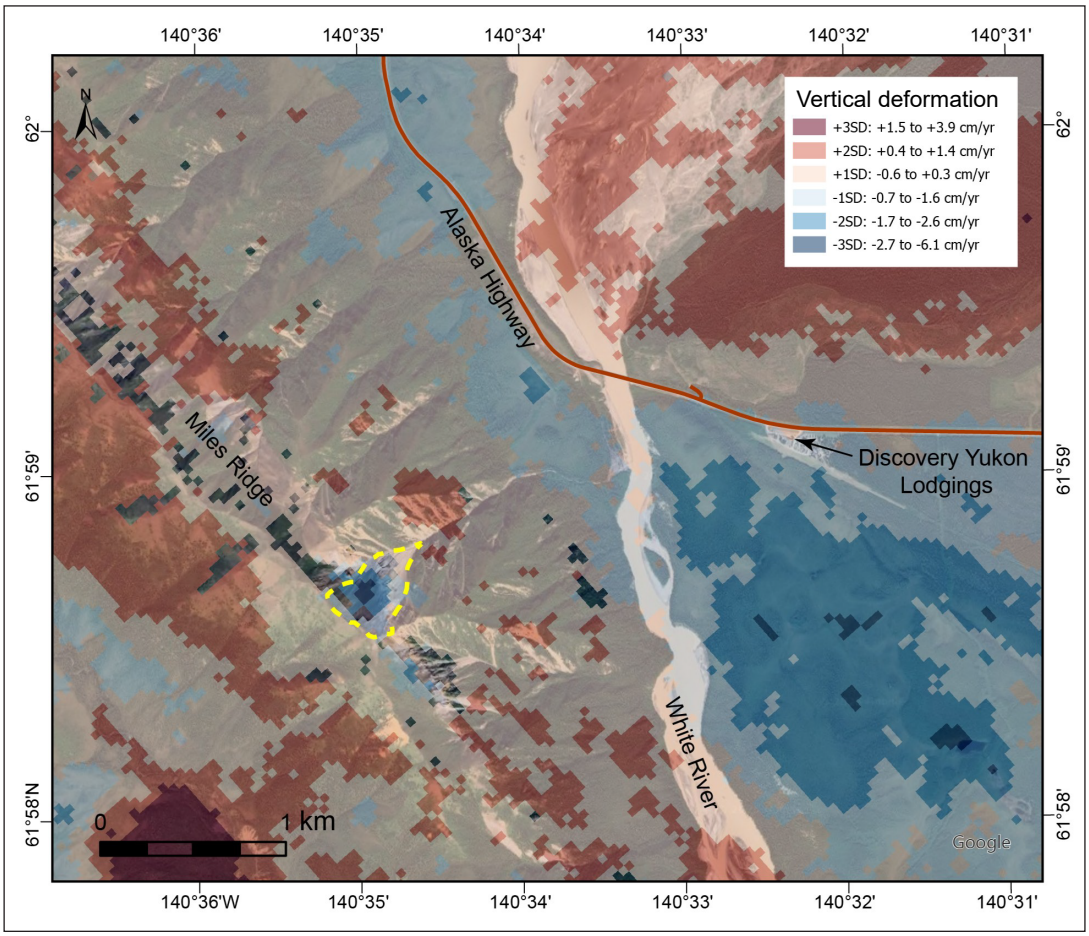


Figure 12. *Annual vertical ground deformation rates measured from InSAR analysis of 2017–2024 Sentinal-1 data (Samsonov and Feng, 2023; Canada Centre for Mapping and Earth Observation, 2024). The Miles Ridge landslide is outlined by the yellow dashed line. The darker blue area south of the Discovery Yukon Lodgings airstrip is interpreted to be subsidence due to the thaw of ice-rich permafrost in glacial drift. The dark red area in the southwest corner is interpreted to be from bulging at the toe of a rock glacier. Google Earth imagery of July 4, 2023 is displayed in the background. Standard deviation classes were generated from a histogram of values observed within a ~25 x 25 km area centred on the White River bridge.*

Concluding remarks

Our integrated ground–RPAS–satellite assessment shows that the Miles Ridge landslide remains a gradually deforming and geomorphically complex system, with localized erosion and deposition in the amphitheatre and continued instability along the ridge crest. Our ground survey documented fresh tension cracks and measurable geomorphic shifts since 2007, while repeated RPAS-derived 3D models revealed focused zones of material loss and accumulation that coincide with the dominant erosional pathways. A vertical deformation map from DInSAR also offers potential for investigating longer-term subsidence patterns across the landslide. Mapping conducted with RPAS offers a promising method for independently validating these DInSAR-derived deformations over multi-year timescales, particularly for small-scale deformation features such as the Miles Ridge landslide, which the national deformation map was originally designed to help monitor.

Given the rapid evolution of DIAB systems, the Dock 2 performed very well during this deployment, demonstrating that semi-autonomous RPAS systems can reliably operate in complex mountainous environments. Newer dock platforms now incorporate built-in battery systems, reducing the need for hard-wired electrical infrastructure and enabling truly mobile deployments from vehicles or semi-permanent field sites. This is an important advance for monitoring remote locations where grid power is unavailable.

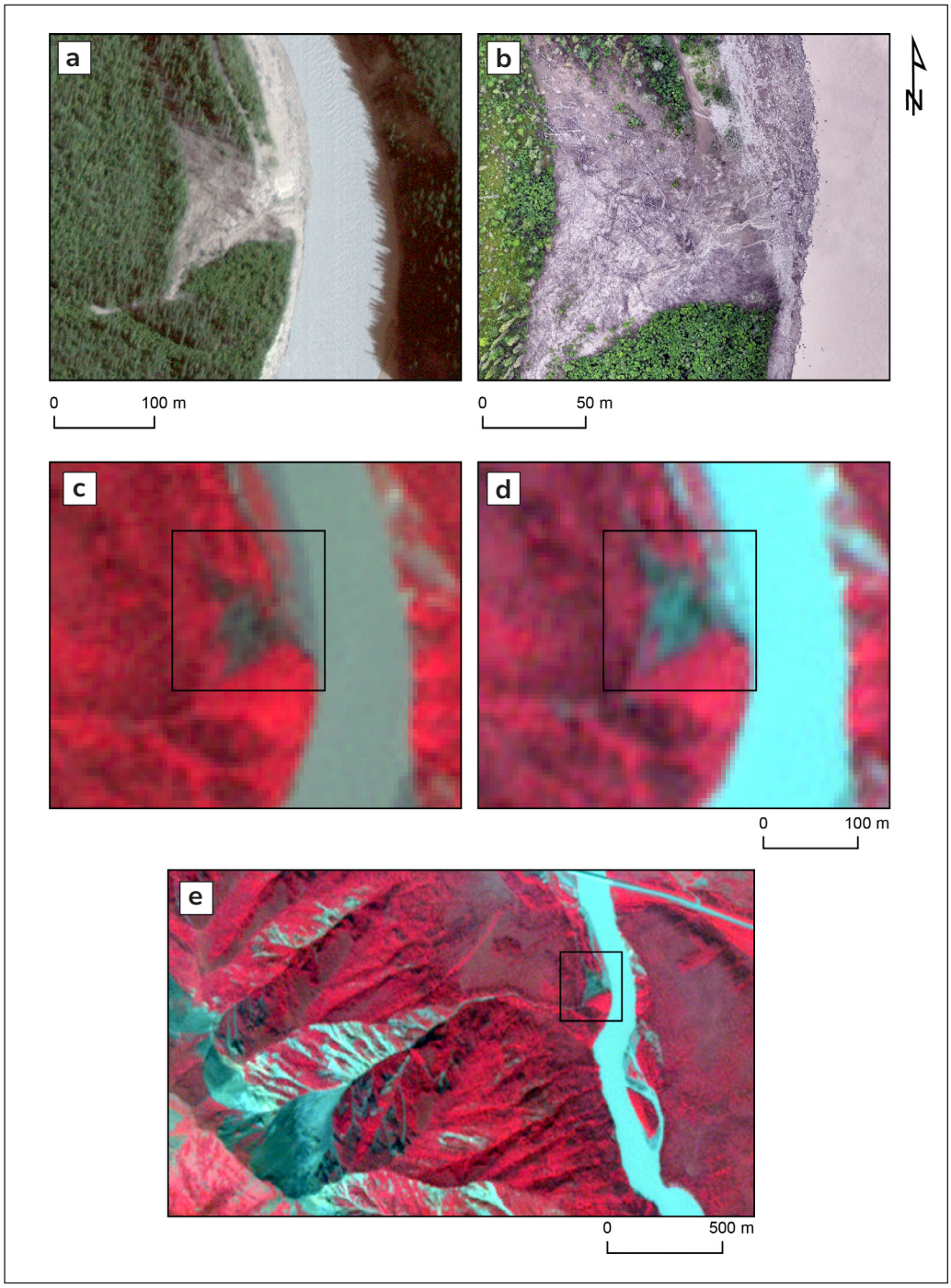


Figure 13. *Change in the extent of the debris fan extending into the White River over time.* ***(a)*** *SkySat satellite image (30 cm pixels) acquired on July 9, 2025, showing the present-day extent.* ***(b)*** *RPAS-derived orthomosaic from July 11, 2025, with a ground sampling distance of 6 cm.* ***(c)*** *RapidEye image acquired on June 28, 2012 (5 m pixels).* ***(d)*** *RapidEye image acquired on July 1, 2013, shown at the same scale as in (c).* ***(e)*** *RapidEye image from June 25, 2015. Panels (a) and (b) are displayed as true-colour RGB composites, whereas panels (c)-(e) use a false-colour NIR–R–G composite to enhance the distinction between vegetation (red tones) and rock/debris (grey tones). Black squares in panels (c)-(e) delineate the location of the debris fan.*

Together, our multiscale observations presented here highlight the ongoing evolution of the Miles Ridge landslide and emphasize the importance of establishing routine monitoring to better evaluate future movement potential and associated risks to the Alaska Highway.

Acknowledgments

This research was funded by the Natural Sciences and Engineering Research Council of Canada (NSERC) Alliance Program grant (grant ALLRP 586350-2), an NSERC Discovery grant (RGPIN-2022-05288) and the Yukon Geological Survey. We thank the Department of Geography, McGill University for access to the RapidEye imagery.

We thank Amanda Harris of Yukon Discovery Lodgings for her enthusiastic and steadfast support of this study, which made this research possible. We also acknowledge the assistance of her staff, in particular Greg Roberts who provided invaluable assistance with the electrical work for the Dock 2 system. We thank Yukon Metals and Capital Helicopters for coordinating flights with us. We also acknowledge Stephen Scheunert and Paul Mondor for access and logistical assistance at a test site in Rigaud, Québec, prior to our Yukon fieldwork. We further acknowledge Kyle Miller formerly from DJI Enterprise and Jason Rule from Transport Canada for help with flight planning. We thank Derek Cronmiller of the Yukon Geological Survey for a helpful review of the manuscript. This work was conducted under the auspices of a Yukon Scientists and Explorers Licence.

References

Bender, A.M. and Haeussler, P.J., 2017. Eastern Denali fault surface trace map, Eastern Alaska and Yukon, Canada. U.S. Geological Survey Open-File Report 2017–1049, 10 p., https://pubs.usgs.gov/of/2017/1049/ofr20171049.pdf.

Blais-Stevens, A., Clague, J.J., Brahney, J., Lipovsky, P., Haeussler, P.J. and Menounos, B., 2020. Evidence for large Holocene earthquakes along the Denali fault in southwest Yukon, Canada. Environmental and Engineering Geoscience, vol. 26, no. 2, p. 149–166, https://doi.org/10.2113/EEG-2263.

Bond, J.D., Lipovsky, P.S. and von Gaza, P., 2008. Surficial geology investigations in Wellesley basin and Nisling Range, southwest Yukon. *In:* Yukon Exploration and Geology 2007, D.S. Emond, L.R. Blackburn, R.P. Hill and L.H. Weston (eds.), Yukon Geological Survey, p. 125–138.

Burn, C.R. and Zhang, Y., 2009. Permafrost and climate change at Herschel Island (Qikiqtaruq), Yukon Territory, Canada. Journal of Geophysical Research Earth Surface, vol. 114, https://agupubs.onlinelibrary.wiley.com/doi/pdf/10.1029/2008JF001087.

Canada Centre for Mapping and Earth Observation, 2024. Pilot national scale maps of active deformation processes in Canada. Natural Resources Canada, Government of Canada, https://app.geo.ca/en-ca/map-browser/record/1da588c1-0dc6-45e4-9e63-9acf2fdc353a [accessed 24/11/2025].

Clague, J.J., 1979. The Denali fault system in southwest Yukon Territory - a geologic hazard? Geological Survey of Canada, Paper No. 79-1A, p. 169–178, https://doi.org/10.4095/104844.

Finley, T., Salomon, G., Stephen, R., Nissen, E., Cassidy, J. and Menounos, B., 2022. Preliminary results and structural interpretations from drone lidar surveys over the Eastern Denali fault, Yukon. *In:* Yukon Exploration and Geology 2021, K.E. MacFarlane (ed.), Yukon Geological Survey, p. 83–105.

Gariano, S.L. and Guzzetti, F., 2016. Landslides in a changing climate. Earth-Science Reviews, vol. 162, p. 227–252, https://doi.org/10.1016/j.earscirev.2016.08.011.

Government of Canada, 2025. Precise point positioning, http://webapp.csrs-scrs.nrcan-rncan.gc.ca/geod/tools-outils/ppp.php [accessed 19/11/2025].

Haeussler, P.J., Matmon, A., Schwartz, D.P. and Seitz, G.G., 2017. Neotectonics of interior Alaska and the late Quaternary slip rate along the Denali fault system. Geosphere, vol. 13, no. 5, p. 1445–1463, https://doi.org/10.1130/GES01447.1.

Han, J., Dettmer, J., Gosselin, J.M., Gilbert, H., Biegel, K. and Kim, S., 2024. Seismicity near the eastern Denali fault from temporary and long-term seismic recordings. *In:* Yukon Exploration and Geology Technical Papers 2023, L.H. Weston and Purple Rock Inc. (eds.), Yukon Geological Survey, p. 37–50.

Hirabayashi, Y., Mahendran, R., Koirala, S., Konoshima, L., Yamazaki, D., Watanabe, S., Kim, H. and Kanae, S., 2013. Global flood risk under climate change. Nature Climate Change, vol. 3, no. 9, p. 816–821, https://doi.org/10.1038/nclimate1911.

Holland, G. and Bruyère, C.L., 2014. Recent intense hurricane response to global climate change. Climate Dynamics, vol. 42, no. 3, p. 617–627, https://doi.org/10.1007/s00382-013-1713-0.

Irrgang, A.M., Lantuit, H., Manson, G.K., Günther, F., Grosse, G. and Overduin, P.P., 2018. Variability in rates of coastal change along the Yukon coast, 1951 to 2015. Journal of Geophysical Research Earth Surface, vol. 123, no. 4, p. 779–800, https://doi.org/10.1002/2017JF004326.

Kalacska, M., Lucanus, O., Arroyo-Mora, J.P., Stix, J., Lipovsky, P. and Roman, J., 2026. Assessing a semi-autonomous drone-in-a-box system for landslide monitoring: A case study from the Yukon Territory, Canada. Sustainability, vol. 18, no. 2, https://doi.org/10.3390/su18020693.

Kochtitzky, W., Winski, D., McConnell, E., Kreutz, K., Campbell, S., Enderlin, E.M., Copland, L., Williamson, S., Main, B. and Jiskoot, H., 2020. Climate and surging of Donjek glacier, Yukon, Canada. Arctic, Antarctic, and Alpine Research, vol. 52, no. 1, p. 264–280, https://doi.org/10.1080/15230430.2020.1744397.

Marechal, A., Ritz, J.-F., Ferry, M., Mazzotti, S., Blard, P.-H., Braucher, R. and Saint-Carlier, D., 2018. Active tectonics around the Yakutat indentor: New geomorphological constraints on the eastern Denali, Totschunda and Duke River faults. Earth and Planetary Science Letters, vol. 482, p. 71–80, https://doi.org/10.1016/j.epsl.2017.10.051.

Munich RE, 2025. Natural disasters worldwide: losses are on the rise as climate change strikes, https://www.munichre.com/en/risks/natural-disasters.html [accessed 23/11/2025].

Samsonov, S. and d'Oreye, N., 2012. Multidimensional time-series analysis of ground deformation from multiple InSAR data sets applied to Virunga Volcanic Province. Geophysical Journal International, vol. 191, no. 3, p. 1095–1108, https://doi.org/10.1111/j.1365-246X.2012.05669.x.

Samsonov, S.V. and Feng, W., 2023. Deformation retrievals for North America and Eurasia from Sentinel-1 DInSAR: Big data approach, processing methodology and challenges. Canadian Journal of Remote Sensing, vol. 49, no. 1, https://doi.org/10.1080/07038992.2023.2247095.

In-situ monazite geochronological constraints on the timing of vein formation and gold mineralization in the Klondike gold district, western Yukon

*Brodie A. Stroh**
Cameco Corporation
Mineral Deposit Research Unit, University of British Columbia

Tyler K. Ambrose
Yukon Geological Survey
Mineral Deposit Research Unit, University of British Columbia

Murray M. Allan
Teck Resources Limited
Mineral Deposit Research Unit, University of British Columbia

Matthijs A. Smit
Department of Earth, Ocean & Atmospheric Sciences, University of British Columbia

Stroh, B.A., Ambrose, T.K., Allan, M.A. and Smit, M.A., 2026. In-situ monazite geochronological constraints on the timing of vein formation and gold mineralization in the Klondike gold district, western Yukon. *In*: Yukon Exploration and Geology 2025, A. Stuart, L.H. Weston and S.K. Schultz (eds.), Yukon Geological Survey, Government of Yukon, p. 239–266, plus digital appendices.

Abstract

Orogenic gold deposits form some of the world's largest gold sources; however, the timing of mineralization is commonly difficult to constrain due to a lack of suitable geochronometers. Most studies rely on $^{40}Ar/^{39}Ar$ dating of mica, which is susceptible to thermal resetting and can be difficult to genetically link to gold deposition. Uranium-thorium-lead (U-Th-Pb) dating of monazite, which crystallizes in metamorphic and in some cases hydrothermal settings, provides an alternative that is not commonly applied to mineral deposits. Approximately 20 Moz of placer gold mined in the Klondike gold district was derived from orogenic, gold-bearing quartz veins of unknown age. In this study, we integrate monazite dates and geochemical analyses with petrographic observations to constrain the age of metamorphic and hydrothermal monazite growth. Our results reveal metamorphic monazite growth between 190 and 150 Ma, overlapping with burial and subsequent regional exhumation of the Yukon-Tanana terrane. Metamorphic monazite occurs with other metamorphic minerals regardless of proximity to veins, and has variable ThO_2 concentrations that depend on the composition of the host rock and metamorphic grade. Hydrothermal monazite dates ranging from 180 to 120 Ma record the duration of vein formation and bracket the timing of gold mineralization. Hydrothermal monazite occurs in, or adjacent to, veins with other hydrothermal minerals and has distinctly low ThO_2 concentrations (<2 wt%). Our findings underpin the complexity and longevity of vein formation in orogenic gold deposits, and demonstrate the utility of monazite in obtaining time-resolved information on this economically relevant process.

* brodie.stroh20@gmail.com

Plain language summary

Most gold in the Klondike goldfields occurs as loose grains and nuggets in river gravel—known as placer gold—deposited over the past several million years. The gold grains likely came from nearby quartz veins in bedrock. Although the age of the placer deposits is fairly well understood, the timing of the quartz veins and especially the gold within them is poorly constrained. To determine the age of the quartz veins and gold mineralization we combined fieldwork and sample collection with laboratory analyses. We focused on monazite, a mineral whose chemical composition can be used to date geological processes. Our results indicate that the rocks exposed in the Klondike region were metamorphosed (i.e., buried, deformed and heated) between approximately 190 and 150 million years ago, and that the veins formed from 180 to 120 million years ago. Our work highlights the utility of monazite and provides insight into the timescale of vein formation and gold mineralization in the Klondike.

Introduction

Orogenic gold deposits typically form at convergent plate margins along structures that act as conduits for hydrothermal fluids generated during metamorphism (e.g., Groves et al., 1998; Bierlein and Crowe, 2000; Goldfarb et al., 2001; Groves et al., 2003; Goldfarb et al., 2005; Goldfarb and Groves, 2015; Mortensen et al., 2023). In contrast to most other gold-bearing deposit types, orogenic gold deposits are not genetically linked with magmatism (Goldfarb and Pitcairn, 2022). Instead, the mineralizing fluid is inferred to be produced by devolatilization reactions during regional metamorphism at pressures and temperatures corresponding to the greenschist-amphibolite transition zone (e.g., Henley et al., 1976; Goldfarb et al., 1991; Stuwe, 1998; Pitcairn et al., 2006). The fluid is channeled through permeable structures and driven upwards before precipitating gold-bearing quartz veins at 3–15 km depth (Groves et al., 1998; Goldfarb and Groves, 2015; White et al., 2015). Orogenic gold deposits form some of Earth's largest gold deposits (e.g., Ashanti, Ghana, 3169 t at 2–7 g/t Au; Golden Mile, Australia, 2079 t at 2 g/t Au; Frimmel, 2008). Still, several components of their generation are highly debated (e.g., Goldfarb and Groves, 2015), including the source of the gold, controls on deposition, and the absolute timing of mineralization.

The formation of orogenic gold deposits typically occurs during or after peak metamorphism of the host rocks (Groves et al., 1998). The timing of orogenic gold formation can be constrained by various methods: $^{40}Ar/^{39}Ar$ dating of muscovite, sericite and biotite (e.g., Bierlein et al., 2001; Mortensen et al., 2010); $^{187}Re/^{187}Os$ dating of arsenopyrite and molybdenite (e.g., Arne et al., 2001; Selby et al., 2002); and U-Pb dating of zircon, titanite and rutile (e.g., Kerrich and King, 1993; Lin and Corfu, 2002). However, determining the precise timing of mineralization is typically non-trivial; geochronometric minerals are often too small to analyze or may have been reset by later hydrothermal events. The latter applies particularly to white mica. Although this phase is common in quartz veins and is the most commonly used geochronometer, its low closure temperature (e.g., ~380°C for muscovite; Reiners and Brandon, 2006) means that it is vulnerable to resetting by later thermal events and fluids. Another issue is that chronometric minerals often lack a clear paragenetic relationship with gold, which leaves uncertainty as to whether the age data represent the timing of vein emplacement or specific vein phases that are associated with gold formation (e.g., Grimshaw, 2018).

Monazite and xenotime U-Th-Pb geochronology are less commonly applied techniques for dating orogenic gold mineralization. These approaches nevertheless have several advantages over $^{40}Ar/^{39}Ar$ white mica dating (e.g., Brown et al., 2002; Vielreicher et al., 2003; Salier et al., 2005; Sarma et al., 2008; Taylor et al., 2015). Monazite is less susceptible to thermal resetting due to its high closure temperature of >800°C (Cherniak et al., 2004), but can be modified by fluid-rock interaction, which can be exploited to date hydrothermal events (Williams et al., 2011). Monazite composition is indicative of petrological processes such as the growth or breakdown of other minerals during crystallization, thus enabling links between age data and mineral reactions (e.g., Pyle and Spear, 1999; Kylander-Clark et al., 2013). These features make monazite very useful in obtaining temporal constraints on geological events and processes. Though such studies have mostly focused on metamorphic rocks, the concepts can also be applied to ore deposits. For example, Schandl and Gorton (2004) used ThO_2 concentrations to distinguish between hydrothermal and igneous monazite, and Taylor et al. (2015) used

europium (Eu) anomalies to identify hydrothermal monazite in the Grass Valley orogenic gold district of California. Linking monazite growth or recrystallization to orogenic gold formation is the next frontier and requires establishing a paragenetic relationship with gold, particularly because monazite can grow through metamorphic or hydrothermal processes. In this study, we explore this for the Klondike gold district in the northwestern Canadian Cordillera.

The Klondike gold district hosts both orogenic gold occurrences and placer gold deposits. An estimated 20 Moz of placer gold were recovered from gold-bearing creeks in the Klondike from an area of ~1200 km^2 (Burke et al., 2005). Microchemical and grain shape analysis of placer grains indicates that the gold is sourced from orogenic quartz veins (e.g., Knight et al., 1999a,b; Mortensen et al., 2004, 2006; Crawford, 2007; Crawford et al., 2007; Chapman et al., 2010a,b, 2011). A regionally widespread, orogenic gold mineralization event in the Late Jurassic has been proposed for the Klondike, Sixtymile and White Gold metallogenic belts of western Yukon (Allan et al., 2013; Bailey, 2013); however, the timing of mineralization in the Klondike itself remains poorly constrained. Gold-bearing quartz veins in the Klondike have yielded $^{40}K/^{40}Ar$ and $^{40}Ar/^{39}Ar$ dates from 183 to 134 Ma (Hunt and Roddick, 1992; Breitsprecher and Mortensen, 2004; Joyce et al., 2015). The only direct age constraint for gold mineralization in the Klondike is an unpublished U-Pb date of 156 ± 8 Ma (Late Jurassic) from hydrothermal rutile in a gold-bearing quartz vein (Mortensen unpublished data, 2012, in Allan et al. 2013).

To constrain the timing of quartz vein emplacement and gold mineralization in the Klondike, we integrated field observations, petrography, whole-rock major and trace-element analysis, mineral major-element analysis, and monazite geochronology. We established a paragenetic framework for veins and alteration through petrographic analysis, quartz vein cathodoluminescence, and whole-rock composition. Our results provide a means to distinguish between metamorphic and hydrothermal monazite. Though we are unable to precisely date the timing of gold mineralization, our results constrain the timing of metamorphism and vein formation. The methods we establish can be applied to other orogenic gold deposits and metamorphic terranes in general.

Monazite growth mechanisms

Monazite is a light rare earth element (LREE) phosphate (PO_4) mineral and is a common accessory mineral in a wide variety of igneous, sedimentary, metamorphic and hydrothermal rocks (Overstreet, 1967). In orogenic gold settings, monazite can grow through both metamorphic and hydrothermal processes. Metamorphic monazite grows by the breakdown of other LREE- or phosphorus (P)-bearing minerals such as allanite, apatite and pre-existing monazite. It commonly forms in metamorphic rocks at amphibolite-facies conditions, but may also grow under greenschist-facies pressures and temperatures (Rasmussen et al., 2007; Williams et al., 2007; Allan et al., 2013; Grand'Homme, 2016). Intergranular fluids that facilitate metamorphic monazite growth through local dissolution and precipitation are typically locally generated and in thermodynamic equilibrium with the host rock. In contrast, hydrothermal monazite precipitates from externally derived hydrothermal fluid that has traveled through interconnected open spaces (i.e., flowed from metre to kilometre scales along permeable structures) and may be out of thermodynamic equilibrium with the host rock. Thus, hydrothermal monazite is only expected to form in and adjacent to veins (Fig. 1). Monazite can also grow by a mixture of local and external fluids, such as the growth of metamorphic monazite adjacent to a vein. Understanding the mechanism(s) by which monazite grows is essential when interpreting dates. To distinguish between metamorphic and hydrothermal monazite, we developed a framework based on petrographic associations, chemical zoning, and thorium (Th) and REE concentrations (Table 1 and Fig. 1).

Regional and local geology

The Klondike gold district is underlain by metaigneous and metasedimentary rocks of the northern Yukon-Tanana terrane (Fig. 2; Nelson et al., 2013). In the Yukon, the Yukon-Tanana terrane consists of three metamorphosed Devonian to Permian magmatic arc successions (Finlayson, Klinkit and Klondike assemblages) built upon metasedimentary rocks of the Neoproterozoic–Devonian Snowcap assemblage (Colpron et al., 2006).

The Klondike assemblage (commonly known as the Klondike schist; 269–253 Ma; Colpron et al., 2006) occurs throughout much of the district and is divided into five units by Mortensen et al. (2019): 1) a felsic package comprising quartz-muscovite-feldspar schist interpreted to be derived from a felsic volcanic or volcaniclastic rock; 2) a quartz-augen schist derived from a felsic quartz ± feldspar-phyric porphyry; 3) a mafic package comprising feldspar-chlorite-quartz ±

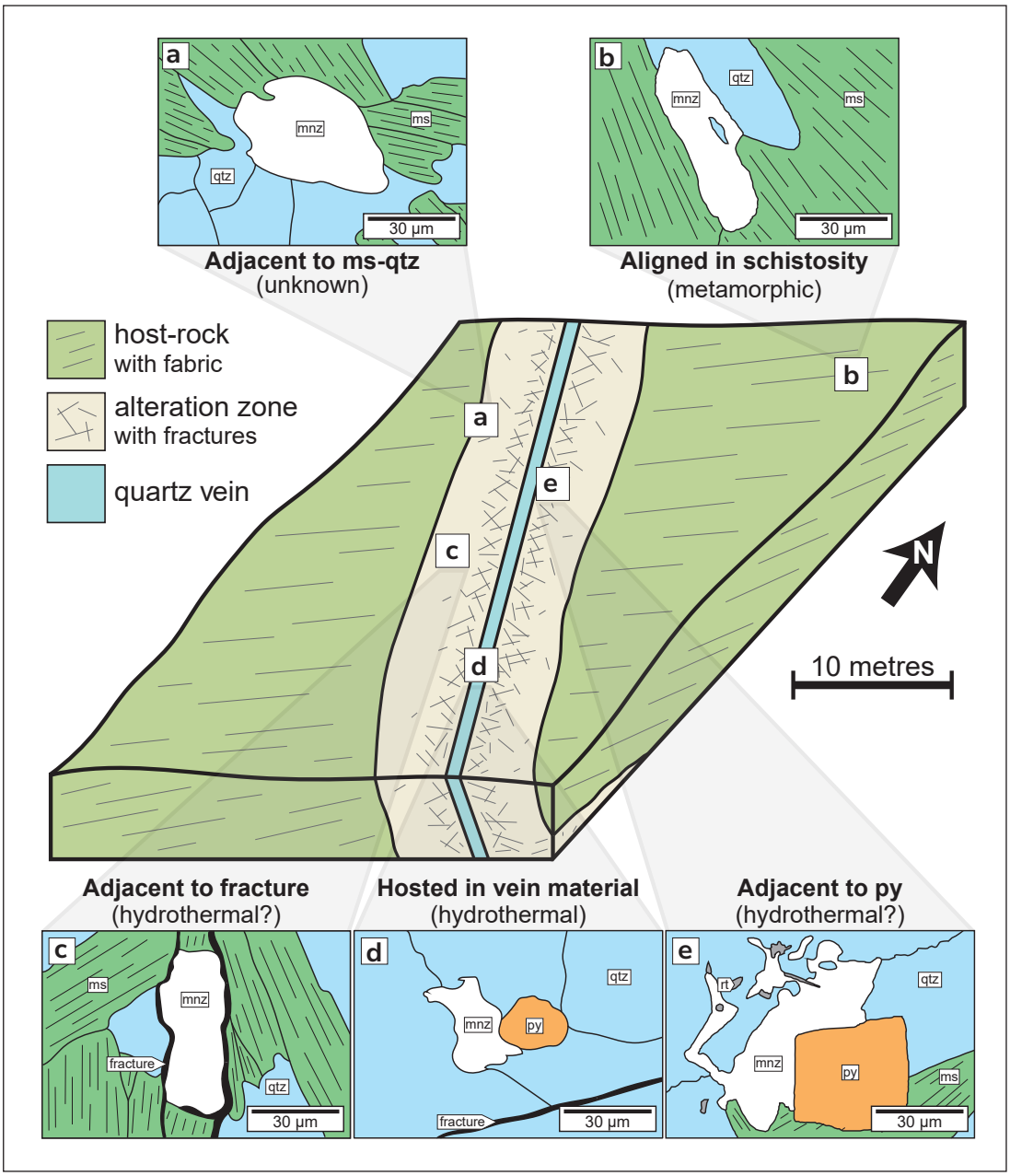


Figure 1. *Schematic diagram illustrating different petrographic contexts of monazite in orogenic gold settings (qtz – quartz; mnz – monazite; ms – muscovite; py – pyrite). The block diagram shows a quartz vein and alteration zone cutting through unaltered metamorphic rock. Schematics* **(a)–(e)** *each represent the expected monazite relationships for different geological settings and textures at each location. Next to each image are the petrographic associations in bold and interpretation in brackets. Only (b) and (d) can be confidently unambiguously interpreted because of their locations in the unaltered host rock and vein.*

epidote ± amphibole ± carbonate schist derived from intermediate or mafic volcanic or volcaniclastic rocks; 4) a metaclastic unit derived from quartz-rich clastic sedimentary rocks; and 5) an undifferentiated package that consists of intimately interlayered components of the felsic, mafic and metaclastic units. Most rocks in the Klondike assemblage are metavolcanic, though plutonic equivalents occur throughout the district (e.g., felsic metaporphyry and metagabbro of Mortensen, 1990).

Gold mineralization occurs in steeply to moderately dipping quartz-sulphide ± carbonate veins that cut the

Table 1. Indicators used to distinguish between different monazite growth mechanisms. The reliability of each indicator decreases towards the bottom. Mineral abbreviations: ab – albite; bt – biotite; fsp – feldspar; qtz – quartz.

Indicator	Igneous	Metamorphic	Hydrothermal	Reference(s)
Petrographic associations	• intergrown with igneous minerals and textures (e.g., qtz, fsp, bt)	• intergrown with metamorphic minerals and textures (e.g., bt)	• intergrown with hydrothermal minerals and textures (e.g., sulphides, oxides, micas, ab, qtz)	• Schandl and Gorton, 2004 • this study
ThO_2 concentration	• 3 to 13 wt% • lower in carbonatites	• 0 to >20 wt% • generally increases with metamorphic grade • dependent on protolith composition	• typically <2 wt%	• Schandl and Gorton, 2004 • Williams et al., 2007 • Cuney and Kyser, 2015 • Taylor et al., 2015 • Kohn and Malloy, 2004 • this study
REE geochemistry	• variable to significant europium (Eu) anomaly	• negative Eu anomaly (smaller after plagioclase breakdown)	• variable to no negative Eu anomaly	• Schandl and Gorton, 2004 • Williams et al., 2007 • Taylor et al., 2015
Other element concentrations	• high uranium (U)	• U and, to a lesser extent, thorium (Th) and yttrium (Y) increase with grade	• high U/Th	• Taylor et al., 2015 • Grand'Homme, 2016
Element zonation	• concentric • sector	• patchy • mottled • intergrowth-like • concentric • strongest Th zonation	• none • mottled • patchy	• Zhu and O'Nions, 1999 • Spear and Pyle, 2002 • Schandl and Gorton, 2004 • Williams et al., 2007 • Didier, 2013
Grain distribution	• sparse and homogeneous	• sparse and homogeneous	• commonly occurs in clusters	• Schandl and Gorton, 2004 • Williams et al., 2007 • this study
Grain size	• unknown	• <10 to >200 µm • increases with grade	• commonly <20 µm	• Schandl and Gorton, 2004 • Rasmussen et al., 2006

dominant foliation (Mortensen et al., 1992; Rushton et al., 1993). The veins are tabular to irregular, typically occur in anastomosing swarms with northeast or northwest trends, and are locally up to three metres wide (MacKenzie et al., 2008a). Texturally, they appear massive and only rarely display syntaxial growth textures typical of multiple crack-seal events (Allan et al., 2013). The veins consist almost entirely of milky white quartz (~98%) with minor pyrite and lesser carbonate, feldspar, muscovite, barite, scheelite, chalcopyrite, galena, sphalerite, rutile and sulfosalts (Hoymann and Friedrich, 1990). Gold typically occurs with pyrite along the vein margins and as free grains (Rushton et al., 1993). Hydrothermal alteration is relatively subtle and is expressed through assemblages comprising pyrite-sericite ± Fe-carbonate (e.g., mafic-hosted Mitchell-Sheba occurrences), kaolinite-silica (quartz-K-feldspar; e.g., metaporphyry-hosted Virgin occurrence), and minor silica (quartz)-pyrite (e.g., felsic-hosted Lone Star occurrence). Fluid inclusions in vein quartz exhibit low salinity (<6 wt% NaCl equivalent), heterogeneous CO_2 content, and reflect trapping conditions between 200 and 350°C and 300 to 2300 bar (Rushton et al., 1993). Rushton et al. (1993) interpreted the range in trapping conditions to reflect rapid exhumation during vein formation. All veins in the Klondike are broadly similar in terms of structural style, mineralogy, texture and fluid chemistry. It is therefore assumed that they

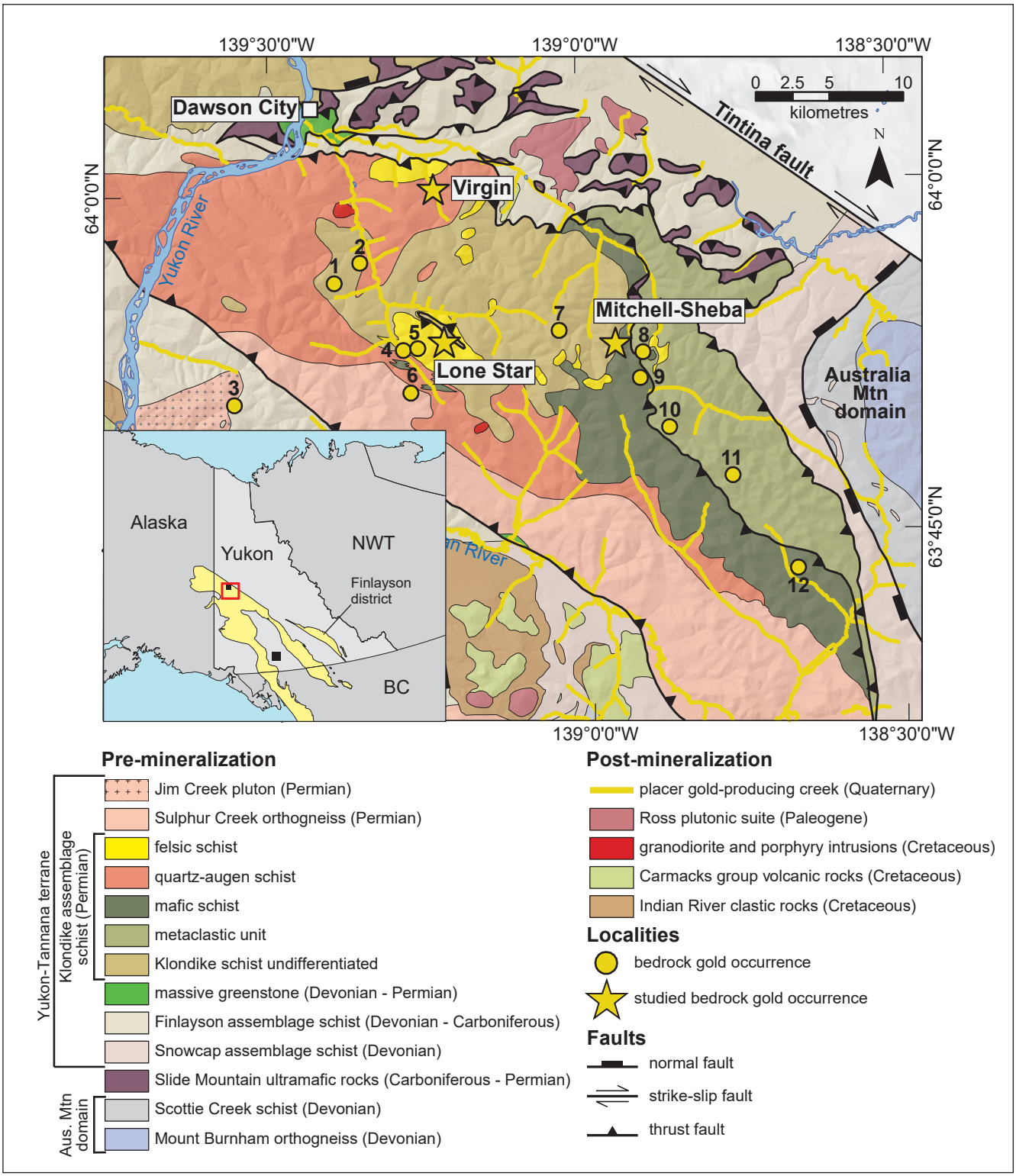


Figure 2. *Simplified geological map of the Klondike gold district (modified from Mortensen, 1996; Gordey and Ryan, 2005; Mortensen et al., 2019). Inset: Yukon-Tannana terrane is yellow; Whitehorse is the large black square; Dawson City is the small black square; map location is the red box. Studied localities are starred and labelled on the map. Other localities are labelled as numbered yellow dots: 1) Plinc; 2) Orofino; 3) IND; 4) Dysle; 5) Nugget; 6) Violet; 7) Boxcar; 8) MacKay; 9) Dome Lode/Hunker Dome; 10) Lloyd; 11) Gold Run; and 12) Aime/Payne.*

represent a single, albeit possibly protracted orogenic gold-forming event (Rushton et al., 1993; Mackenzie et al., 2008a; Allan et al., 2013).

In this study we investigated four bedrock gold occurrences: Virgin, Mitchell, Sheba and Lone Star. The Virgin gold occurrence (Yukon MINFILE 116B 007; Yukon Geological Survey, 2010) is hosted in a quartz-augen, quartz-albite-muscovite ± K-feldspar schist of the quartz-augen subunit (Mortensen, 1996; Mortensen et al., 2019). Quartz ± pyrite veins are associated with a kaolinite-quartz-K-feldspar-pyrite alteration halo. The Mitchell and Sheba gold occurrences (collectively known as Mitchell-Sheba; Yukon MINFILE 115O 068; Yukon Geological Survey, 2010) occur approximately 850 m apart along the same north-south trending vein system. The host rock at Mitchell-Sheba is an albite-chlorite-epidote-muscovite ± carbonate ± quartz ± amphibole schist of the mafic schist subunit (Mortensen, 1996; Mortensen et al., 2019). Quartz ± pyrite ± galena veins occur at Mitchell-Sheba with a muscovite-carbonate-pyrite alteration halo that is locally gold-bearing (Mortensen et al., 1992; Rushton et al., 1993; Chapman et al., 2010b). The Lone Star gold occurrence (Yukon MINFILE 115O 072; Yukon Geological Survey, 2010) is hosted in a quartz-muscovite-albite-chlorite schist of the felsic schist subunit (Mortensen, 1996; Mortensen et al., 2019). Quartz ± pyrite ± galena veins at Lone Star locally have a quartz-pyrite alteration halo. The Lone Star and Virgin occurrences are the only localities in the Klondike that have been mined for bedrock gold, albeit with negligible production (Allan et al., 2013). Modern exploration has focused in the Lone Star area, recently culminating in a 2022 NI-43-101 compliant resource of 469 Koz Au at 0.68 g/t Au (Indicated) and 112 Koz Au at 0.54 g/t Au (Inferred) by Klondike Gold Corporation between Lone Star and the newly discovered Stander zone (Jutras and Kenwood, 2022).

Methods

Below is a summary of our methodology that is described in full in Stroh (2019).

Sampling strategy

Unaltered, altered and vein samples were collected at the Virgin, Mitchel-Sheba and Lone Star occurrences (see Appendix A for a full list of samples). Systematic sampling began with fresh, unaltered host rock collected 5–20 m away from veins. Sampling continued toward the veins, and lightly, moderately and heavily altered samples were collected. Lastly, vein material with adjacent wall rock was sampled. Metamorphic rocks are named with porphyroblastic minerals listed first, followed by major rock-forming minerals (≥5%) in decreasing abundance. Mineral abbreviations are from Kretz (1983).

Whole-rock compositions

Whole-rock chemical analysis was conducted by Bureau Veritas Mineral Laboratories in Vancouver. X-ray fluorescence was used to analyze major elements and inductively coupled plasma mass spectrometry (ICP-MS) was used to analyze lithophile and rare earth elements. A 4-acid digestion with ICP-MS finish was used to analyze other trace elements.

Scanning electron microscope and electron probe micro-analyzer analysis

Scanning electron microscope (SEM) analysis was done at the Electron Microbeam and X-Ray Diffraction Facility at the University of British Columbia. A Philips XL-30 SEM with a Bruker Quantax 200 energy-dispersion X-ray microanalysis system, XFlash 6010 SDD detector, and Robinson cathodoluminescence detector was used to investigate micro-textures, identify unknown minerals, locate monazite, and reveal different generations of quartz veins. Silicon (Si), calcium (Ca), yttrium (Y), Th and U elemental maps of individual monazite grains were produced at the Fipke Laboratory for Trace Element Research at the University of British Columbia Okanagan with a Cameca SXFive Field Emission electron probe micro-analyzer (EPMA) at 15 Kv and 200 nA with a fixed beam, 100 ms dwell time, and 0.5 to 0.1 µm step size.

Monazite U-Th-Pb and trace-element analyses

The complete monazite geochronology dataset, including quantitative concentrations, common Pb-corrected isotope ratios, and calculated dates can be found in Appendix C. Monazite U-Th-Pb and trace-element analyses were conducted in situ by laser ablation (LA)-ICP-MS at the Pacific Centre for Isotopic and Geochemical Research at the University of British Columbia. Ablation spots were selected to avoid grain edges and neighbouring ablation sites. If possible, spots were placed in chemical zones. Two separate analytical procedures, with different laser ablation systems, ablation spot locations, and mass spectrometers, were used to collect U-Th-Pb isotopes and trace element

isotopes (Table 2). Analyses that hit inclusions or where the age uncertainty was >8% (>10% was used at Mitchell-Sheba as monazite grains there are smaller and have higher uncertainty) were omitted.

The U-Th-Pb analyses of monazite were performed using an ArF excimer laser ablation system (ESI-New Wave Research NWR193^{UC}) coupled to a high-resolution ICP-MS instrument (ThermoFinnigan Element2). The grains were analyzed for mass/charge corresponding to isotopes of lead (^{204}Pb, ^{206}Pb, ^{207}Pb, and ^{208}Pb), uranium (^{235}U and ^{238}U), and thorium (^{232}Th), as well as mercury (^{202}Hg) to constrain the isobaric interference of ^{204}Hg on ^{204}Pb. External standardization included bracketing groups of ten unknown monazite analyses with two analyses of the Manangotry monazite (555 ± 1 Ma; Paquette et al., 1994; Horstwood et al., 2003; Paquette and Tiepolo, 2007). The Moacyr monazite (504.3 ± 0.2 Ma; Seydoux-Guillaume et al., 2002a,b; Gasquet et al., 2010) was used as a secondary monitor to ensure the accuracy of the age analyses. Data reduction in Iolite was performed using the VisualAge data reduction scheme (Petrus and Kamber, 2012). After common lead contamination was confirmed by plotting Wetherill (Wetherill, 1956) and Tera-Wasserburg (Tera and Wasserburg, 1972) concordia diagrams, a common lead correction was performed using the method of Andersen (2002). Low ^{204}Pb counts led to this method being used over a conventional ^{204}Pb correction. We only use the ^{208}Pb/^{232}Th dates because of the significant uncertainty in the ^{207}Pb/^{235}U and ^{206}Pb/^{238}U dates of relatively young monazite (Grand'Homme et al., 2016; Scharer, 1984; further discussed in Stroh, 2019).

The trace element analyses of monazite were performed using an ArF excimer laser ablation system (Resonetics RESOlution M-50-LR, ASI Australia) coupled to a quadrupole ICP-MS instrument (Agilent 7700x). The grains were analyzed for mass/charge corresponding to thirty-three isotopes that include the full suite of rare earth elements. External standardization was done by bracketing groups of five unknown monazite analyses with one analysis of the BCR2G glass reference material (Jochum et al., 2005), whereas NIST610 and NIST612 glasses were used as secondary monitors. Because these reference materials are not appropriately matrix-matched to monazite, no internal standardization was used, and data from this procedure are considered to be semi-quantitative.

Table 2. Laser ablation parameters for monazite analysis.

	U-Th-Pb analysis	Trace element analysis
Wavelength	193 nm	193 nm
Spot diameter	10 µm	19 µm
Energy density	3 J/cm^2	2 J/cm^2
Repetition rate	8 Hz	8 Hz
Ablation time	25 s	40 s
Gas blank time	30 s	20 s

Monazite characterization

We used several petrographic and trace element parameters to help determine whether monazite dates record hydrothermal or metamorphic crystallization (Table 1). First, each sample was classified according to its relationship to a vein and assigned an alteration intensity, as summarized in Figure 1. Each grain was also assigned one of four petrographic associations (Fig. 1): 1) adjacent to muscovite-quartz, which is the typical petrographic setting of monazite grains with ambiguous origins; 2) aligned in the schistosity, which indicates the monazite grain may have grown during metamorphism or hydrothermally precipitated along the planar features; 3) adjacent to a fracture, which may indicate the monazite grain precipitated hydrothermally along the fracture; and 4) adjacent to pyrite, which may indicate the monazite grain precipitated hydrothermally, given that pyrite is typically a hydrothermal mineral in the Klondike (aside from the pre-existing pyrite phase in the disseminated Au zone at Lone Star [MacKenzie et al., 2008b]). Additionally, we considered the grain shape (from anhedral to euhedral); grain form factor (4π[area]/√[perimeter]), which is a proxy for grain irregularity where values approaching 1 indicate more equant shapes; the grain cross-sectional area; the grain aspect ratio (major axis/minor axis); the grain compactness (√[4area/π]/major axis); and the grain roundness (4area/π√[major axis]). We integrated the petrographic data with monazite ^{208}Pb/^{232}Th dates, ThO_2 concentration, U/Th, Eu anomaly ($Eu/Eu^* = Eu_N/\sqrt{[Sm_N \times Gd_N]}$; used as a proxy for equilibration with plagioclase and apatite), Gd/Yb (used as proxy for equilibration with garnet and apatite), and Ca concentration (used as a proxy for the component of Ca-rich monazite varieties brabantite and cheralite).

Results

Petrography and vein textures

The Klondike schist comprises a spectrum of felsic (Figs. 3a and 5a) to mafic (Fig. 4a) rock types. The host rock mineralogy for the Virgin, Mitchell-Sheba, and Lone Star occurrences are summarized in Table 3. The rocks exhibit a penetrative schistosity defined by the alignment of micas and alternating mica-rich and quartz-feldspar-rich layers (Fig. 3b). An overprinting crenulation cleavage is locally observed where micas are abundant (Fig. 3b).

Gold mineralization occurs in all subunits of the Klondike schist (Fig. 2). Gold-bearing quartz veins in the Klondike schist consist almost entirely of quartz (>98%) with minor pyrite (<2%) and trace galena (Table 3). Trace vein phases vary by occurrence and include carbonate, muscovite, chlorite, barite, rutile and chalcopyrite. Gold typically occurs with pyrite along vein margins. The alteration is typically quartz-muscovite-pyrite, and accessory phases including chlorite, carbonate, monazite, rutile, gold, barite, galena and chalcopyrite. There are minor to significant variations of this alteration assemblage that depend

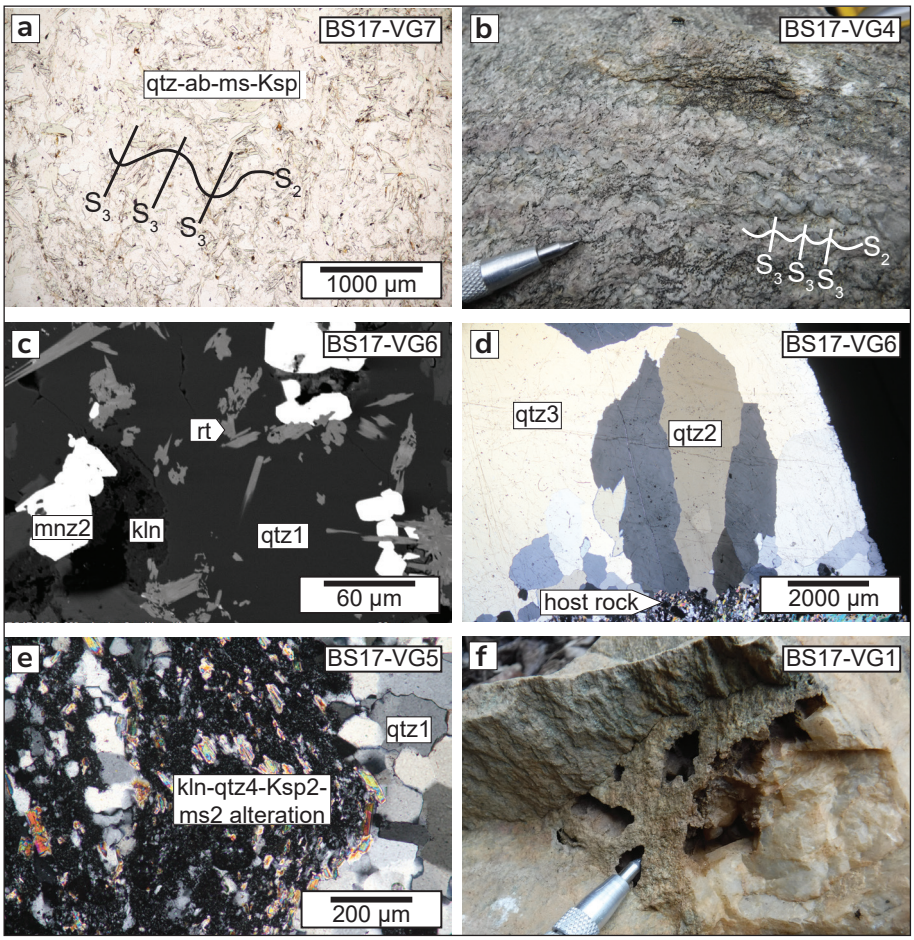


Figure 3. *Hand sample, microscope, and backscattered electron (BSE) images displaying petrographic relationships of the Virgin gold occurrence. Figures (a), (b) and (e) are from the host rock, whereas (c), (d) and (f) are from vein material. Mineral generation numbers are linked to those in Figure 10.* ***(a)*** *Unaltered quartz ± albite-augen quartz-albite-muscovite ± K-feldspar schist with overprinting ductile deformation fabrics (plane polarized light [PPL]; S2 - schistosity, S3 - crenulation).* ***(b)*** *Overprinting ductile deformation fabrics (hand sample).* ***(c)*** *Alteration showing monazite2, rutile and kaolinite (BSE).* ***(d)*** *Syntaxial quartz2 growth from the wall rock, and blocky quartz3 (cross-polarized light [XPL]).* ***(e)*** *Pervasive kaolinite-quartz4-Kfeldspar2-muscovite2 alteration of the wall rock (XPL).* ***(f)*** *Vugs along a vein boundary indicating weathered out pyrite and carbonate (hand sample). Mineral abbreviations: ab – albite; kln – kaolinite; Ksp – K-feldspar; mnz – monazite; ms – muscovite; qtz – quartz; rt – rutile.*

on the local host rocks (Table 3). Gold-bearing quartz vein orientations range from sub-concordant to perpendicular to the wall-rock schistosity. Two different vein textures are observed petrographically (Fig. 3d): 1) elongate, euhedral quartz that grew syntaxially from the wall rock, and 2) blocky quartz that comprises the majority of vein material (Stroh, 2019). These earlier quartz textures were later deformed and partially recrystallized (Fig. 5b). Post-vein deformation features range from subtle kinks of wall-rock fabric to incipiently boudinaged veins (Fig. 6), to boudinaged veins with extensively sheared alteration halos. Microstructures such as undulose extinction, deformation bands, grain boundary migration, and sub-grain rotation in vein-forming quartz also indicate varying degrees of post-vein deformation. Vein quartz has dark, nearly homogeneous cathodoluminescence responses that yield little additional textural information (Stroh, 2019). Brittle fractures, locally filled with carbonate and sparse galena, cross-cut the veins but only rarely propagate into the wall rock (Fig. 4b). Vugs indicate weathering out of carbonate and pyrite in the veins and adjacent wall rock (Fig. 3f).

Virgin

Quartz veins at Virgin are hosted in quartz ± albite-augen, quartz-albite-muscovite ± K-feldspar schist (Fig. 3a). Mortensen (1996) and Mortensen et al. (2019) included these rocks in the quartz-augen schist subunit

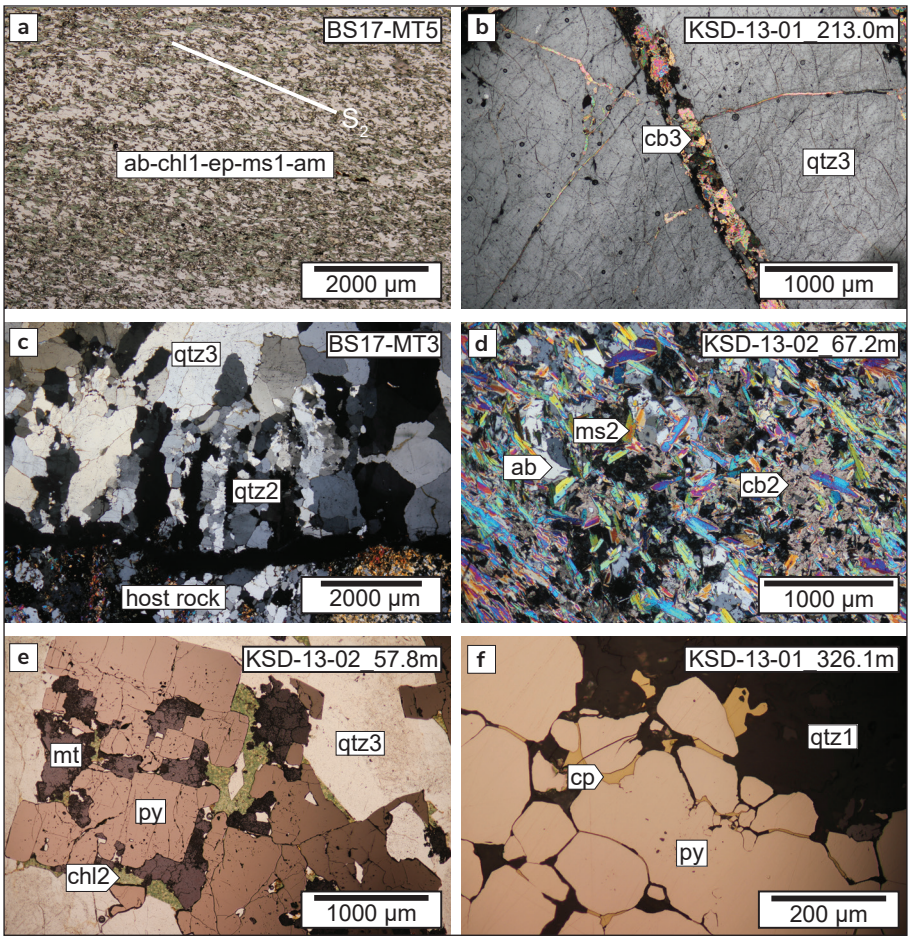


Figure 4. *Microscope images displaying petrographic relationships of the Mitchell-Sheba gold occurrence. Figures (a) and (d) are from the host rock, whereas (b), (c), (e) and (f) are from vein material. Mineral generation numbers are linked to those in Figure 10.* ***(a)*** *Unaltered albite-chlorite-epidote-muscovite ± carbonate ± quartz ± amphibole schist (PPL; S2 - schistosity).* ***(b)*** *Carbonate3 infilling late brittle fractures within a quartz3 vein (XPL).* ***(c)*** *Stretched quartz2 indicating ataxial vein growth and later blocky quartz3 (XPL).* ***(d)*** *Pervasive muscovite2 and carbonate2 alteration (XPL).* ***(e)*** *Pyrite replacing magnetite (reflected light [RL]).* ***(f)*** *Chalcopyrite infilling brittle fractures in pyrite (RL). Mineral abbreviations as in Figure 3; am – amphibole; cb – carbonate mineral; chl – chlorite; cp – chalcopyrite; mt – magnetite; and py – pyrite.*

of the Klondike schist (Fig. 2), which is interpreted to be a hypabyssal equivalent of the metamorphosed felsic volcanic rocks. Quartz ± albite-augen makes up 5–10% of the rock and are surrounded by a finer-grained groundmass of quartz (40%), albite (20%) and muscovite (20%; Table 3). Minor phases (<5%) include K-feldspar, kaolinite and carbonate, whereas trace phases (<<1%) include monazite, zircon and xenotime. The veins at Virgin consist almost entirely of quartz with minor to trace pyrite, muscovite, galena and barite (Table 3). Wall-rock alteration adjacent to the veins is dominated by very fine-grained kaolinite, quartz and K-feldspar with other minor to trace phases, including pyrite, rutile, barite, monazite, and muscovite (Fig. 3e).

Mitchell-Sheba

Quartz veins at Mitchell-Sheba are hosted in fine-grained, albite-chlorite-epidote-muscovite ± carbonate ± quartz ± amphibole schist (Fig. 4a). Mortensen (1996) and Mortensen et al. (2019) included these rocks in the mafic schist subunit of the Klondike schist (Fig. 2). Albite is abundant in the rock (up to 50%), with lesser chlorite (~25%), epidote (~10%) and muscovite (~5%; Table 3). Minor phases include carbonate, quartz, pale-green amphibole and magnetite, whereas trace phases include biotite, K-feldspar, apatite, titanite and zircon. The veins consist almost entirely of quartz, with minor to trace pyrite, muscovite, carbonate, chlorite, rutile and galena (Table 3). Syntaxial quartz growth is not apparent in veins at Mitchell-Sheba. Instead, quartz grains are elongated perpendicular to the vein and do not show growth competition, consistent with ataxial growth (Fig. 4c). Alteration adjacent to the veins is muscovite-carbonate dominated, including chlorite, pyrite and iron alteration of pre-existing chlorite, muscovite and amphibole (Fig. 4d). Pyrite occurs as replacement rims around magnetite (Fig. 4e) and as finely disseminated grains throughout altered wall rock. Trace alteration phases include rutile, galena, chalcopyrite, monazite, arsenopyrite, sphalerite, xenotime and ilmenite. Rutile, arsenopyrite and galena occur as inclusions in pyrite, whereas chalcopyrite and galena occur within fractures in pyrite and quartz (Fig. 4f).

Lone Star

Quartz veins at Lone Star are hosted in quartz-muscovite-albite-chlorite schist (Fig. 5a). Mortensen (1996) and Mortensen et al. (2019) included these rocks in the felsic schist subunit of the Klondike schist (Fig. 2). Quartz dominates the host rock (~50%), and lesser amounts of muscovite (~25%), albite (~15%) and chlorite (~10%) make up the remaining bulk (Table 3). Chlorite is dominantly aligned in the schistosity but locally forms porphyroblasts that have been partially to entirely replaced by carbonate (Fig. 5c). Unlike in the rest of the Klondike, pyrite occurs in relatively high abundance (~1%) and is aligned in the schistosity and crenulation (Fig. 5d; the disseminated Au zone of Mackenzie et al., 2008b). Trace host-rock phases include barite, apatite, monazite and rutile. The veins at Lone Star consist almost entirely of quartz with minor to trace pyrite, carbonate, barite, galena and

Table 3. Summary of petrographic investigations. Minerals are divided into rock-forming minerals, accessory minerals, as well as sulphides and gold. Minerals for each category are listed from most abundant (left) to least abundant (right). Mineral abundances are shown for the unaltered host rock, altered host rock, and vein material of the Virgin, Mitchell-Sheba, and Lone Star gold occurrences. Symbols: * = trace; ** = trace to <2%; *** = ≥2% to <5%; X = ≥5% to <10%; XX = ≥10% to <30%; XXX = ≥30% to <50%; XXXX = ≥50%. Mineral abbreviations: Ab – albite; Am – amphibole; Ap – apatite; Apy – arsenopyrite; Bt – biotite; Brt – barite; Cb – carbonate mineral; Cp – chalcopyrite; Chl – chlorite; Ep – epidote; Gn – galena; Ilm – ilmenite; Kfs – K-feldspar; Kln – kaolinite; Mt – magnetite; Ms – muscovite; Mnz – monazite; Py – pyrite; Qtz – quartz; Rt – rutile; Ser – sericite; Sp – shalerite; Ttn – titanite; Xtm – xenotime; and Zrn – zircon.

Rock type	Rock-forming minerals									Accessory minerals											Sulphides and gold					
	Qtz	Ab	Ms	Chl	Cb	Ep	Kfs	Am	Bt	Kln	Brt	Ser	Rt	Ap	Mt	Mnz	Zrn	Xtm	Ttn	Ilm	Py	Gn	Cp	Sp	Au	Apy
Virgin																										
host rock	XXX	XX	XX		***		X			***		**				*	*	*								
altered host rock	XXX		*				X			XXXX	**		**			*					***				*	
vein	XXXX		**								*										**	*				
Mitchell-Sheba																										
host rock	***	XXX	X	XX	***	XX	**	***	**			**		**	**		*		*							
altered host rock			XXXX	X	XXX								**			*		*		*	***	**	**	*	*	*
vein	XXXX		**	*	**								*								**	*				
Lone Star																										
host rock	XXX	XX	XX	X	X						**	**	*	*		*					**					
altered host rock	XXXX			**	X						**		**			*					***	*	*	*	*	
vein	XXXX				**						**										**	*	*			

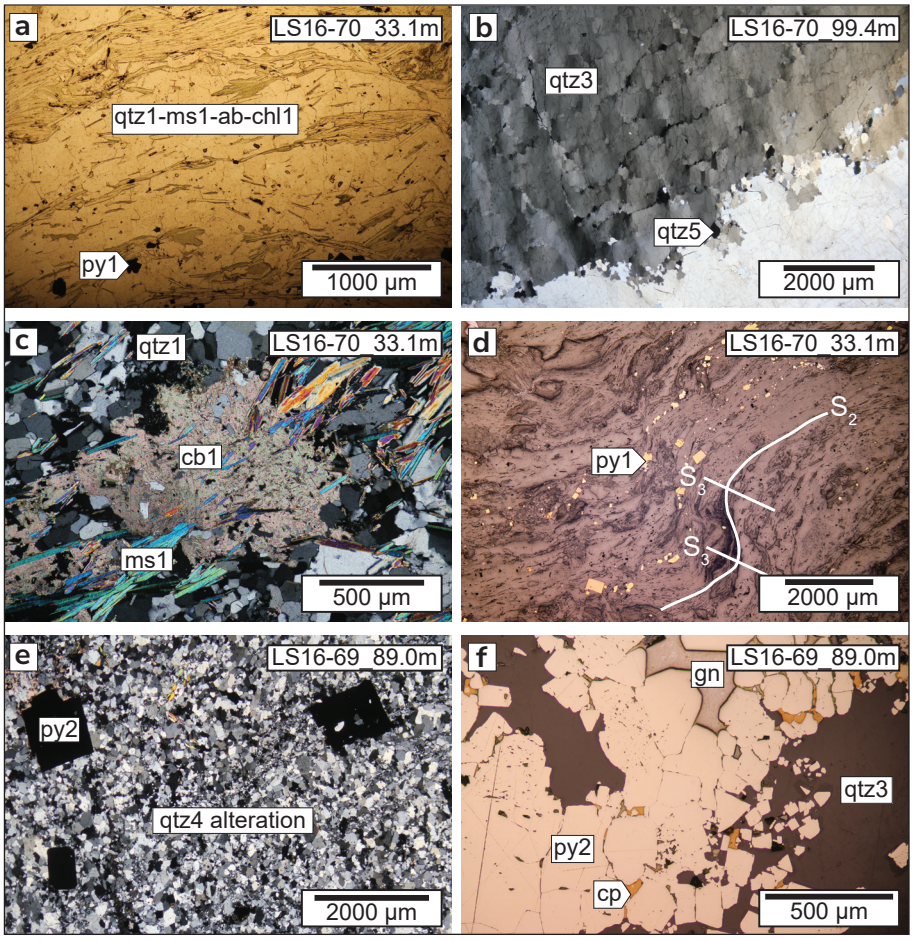


Figure 5. *Microscope images displaying petrographic relationships of the Lone Star gold occurrence. Figures (a), (c), (d) and (f) are from the host rock, whereas (b) and (f) are from vein material. Mineral generation numbers are linked to those in Figure 10.* ***(a)*** *Unaltered quartz-muscovite-albite-chlorite schist (PPL).* ***(b)*** *Blocky vein quartz3 showing ductile deformation in the form of undulose extinction and subgrain rotation (XPL); subgrains rotate to recrystallize and form quartz5.* ***(c)*** *Chlorite porphyroblast replaced by carbonate1 (XPL).* ***(d)*** *Pyrite1 aligned with the schistosity (RL; S2 – schistosity, S3 – crenulation).* ***(e)*** *Pervasive quartz4-pyrite2 alteration (XPL)* ***(f)*** *Galena and chalcopyrite infilling brittle fractures in pyrite indicating they are late in the hydrothermal sequence (RL). Mineral abbreviations as in Figures 3 and 4; gn – galena.*

chalcopyrite (Table 3). Syntaxial quartz vein growth is absent at Lone Star but may have been overprinted by later ductile deformation (Fig. 5b). Wall-rock alteration from the veins is relatively weak and consists mainly of quartz and pyrite (Fig. 5e). Minor to trace alteration phases include carbonate, chlorite, barite, rutile, monazite, galena, chalcopyrite and sphalerite. Galena and chalcopyrite occur within fractures in pyrite and quartz (Fig. 5f). Sub-concordant veins at Lone Star generally have the same vein and alteration assemblage as discordant veins, but locally have more carbonate and chlorite along vein margins, as well as weaker alteration.

Whole-rock lithogeochemistry

On the modified Zr/Ti versus Nb/Y diagram of Pearce (1996; after Winchester and Floyd, 1977), Virgin samples plot in the rhyolite field, Lone Star samples plot across the boundary of the rhyodacite/dacite and andesite fields, and Mitchell-Sheba samples plot in the andesite/basalt field (Fig. 7). No distinct differences exist between unaltered and altered rocks of the same lithology. The complete whole-rock lithogeochemistry dataset can be found in Appendix B.

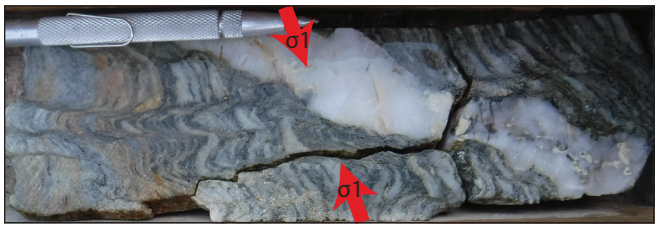


Figure 6. *Locally well-developed crenulation in a mica-rich alteration halo adjacent to an incipiently boudinaged vein. The principal stress direction is indicated by the crenulation and vein deformation (σ1).*

Monazite petrography and characterization

Monazite is a typical trace phase in the unaltered rocks investigated at Virgin and Lone Star (Table 3). The grains are anhedral, equant to elongate, and average ~25 µm in length and have rare grains larger than ~60 µm. They are typically adjacent to muscovite and quartz and are locally aligned with the schistosity. Monazite occurs adjacent to pyrite in unaltered rocks at Lone Star. No monazite was observed in the unaltered rocks at Mitchell-Sheba.

Monazite is rare in vein material and occurs in the altered wall rock at each occurrence (Table 3; Fig. 3c). The size and shape of monazite grains is similar in altered and unaltered rock. Grains in altered rock are also adjacent to muscovite and quartz, and are locally aligned with the schistosity. Thus, it can be difficult with petrography alone to determine whether a monazite crystallized during metamorphism or during a later hydrothermal overprint. A hydrothermal origin was more evident where monazite occurs adjacent to fractures, pyrite, or other hydrothermal minerals such as kaolinite at Virgin.

Monazite element mapping

Electron probe micro-analyzer element maps of Th, Y, U, Ca, and Si in monazite reveal subtle to clear zonation patterns that are dominantly patchy or mottled (Fig. 8; Stroh, 2019). The zonation style is consistent across localities, alteration intensities and petrographic settings. The zoned domains are typically smaller than 10 µm. Thorium is the most prominently zoned element, with domains of relatively high and low concentration in most grains. Yttrium zonation is typically more subdued but generally follows the same pattern as Th. The Y maps also show instances where xenotime is grown adjacent to monazite. Uranium is typically homogeneous. Few monazite grains are entirely free of zonation, and even fewer grains display a core and rim with a high Th and Y core. The Ca and Si maps were used to check for apatite and silicate micro-inclusions.

Monazite geochronology

Monazite U-Th-Pb analyses (n=272) yielded $^{208}Pb/^{232}Th$ dates from 189 ± 14 to 116 ± 4 Ma and indicated ThO_2 concentrations from 0.13 ± 0.01 to 7.38 ± 0.13 wt% (Fig. 9; Appendix C). Different spot analyses of zoned grains typically yielded identical dates, the only exception being monazite LS16-69 89.4m-M11 (Stroh, 2019). Monazite dates and ThO_2 concentrations differ between occurrence and petrographic association (Fig. 9). The ThO_2 concentrations and dates show no systematic relationship with other parameters, including sample, grain form, grain form factor, grain area, grain aspect ratio, grain compactness, grain roundness, U/Th ratio and trace element composition.

The analyses from Virgin yielded dates from 185 ± 14 to 117 ± 4 Ma and ThO_2 concentrations from 0.32 ± 0.02 to 7.38 ± 0.13 wt% (Fig. 9). Our results reveal two distinct populations: a relatively old and ThO_2-rich (>2.00 wt%) population (n = 16) in dominantly unaltered samples, and a relatively young ThO_2-poor (<2.00 wt%) population (n = 32) in altered

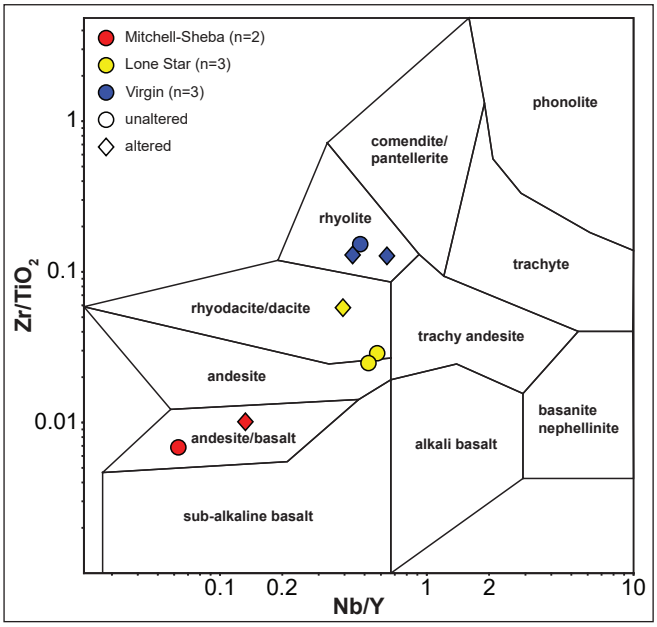


Figure 7. *Modified Winchester and Floyd (1997) diagram of Pearce (1996). Whole-rock lithogeochemistry samples from the Klondike are plotted and coloured based on locality. Lone Star samples are from Nugget but represent the host rock at Lone Star, 1.8 km away. Mitchell-Sheba samples are from Mitchell but represent the same host rock at Sheba, 850 m away. Mitchell-Sheba: mafic protolith; Lone Star: intermediate protolith; Virgin: felsic protolith.*

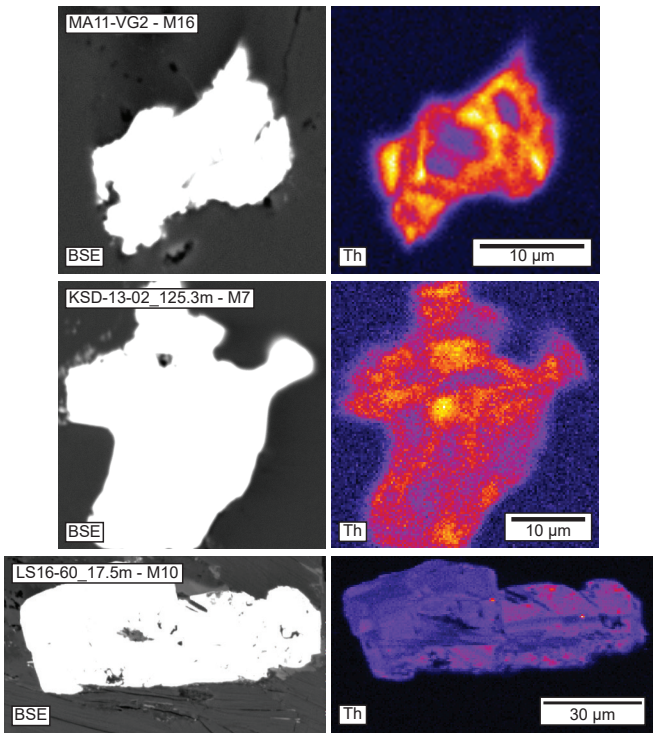


Figure 8. *Representative monazite backscattered electron and element maps. Thorium maps are displayed because they show the most visible zonation.* ***Top:*** *Monazite MA11-VG2-M16 from a vein/wall-rock sample at Virgin displays mottled zonation. The grain is surrounded by vein quartz and interpreted as hydrothermal.* ***Middle:*** *Monazite KSD-13-02 125.3m-M7 from a heavily altered sample at Mitchell-Sheba displays mottled zonation. The grain is adjacent to quartz and is interpreted as hydrothermal.* ***Bottom:*** *Monazite LS16-69 17.5m-M10 from a vein/wall-rock sample at Lone Star displays patchy/mottled zonation. The grain is aligned in the schistosity and may have been reset by hydrothermal fluids.*

samples and grains adjacent to pyrite. Monazite that is adjacent to pyrite (n = 12) yielded dates from 178 ± 6 to 122 ± 7 Ma and ThO_2 concentrations ≤1.80 wt%. The analyses from Mitchell-Sheba yielded dates from 175 ± 13 to 126 ± 8 Ma and ThO_2 concentrations from 0.16 ± 0.01 to 1.57 ± 0.15 wt% (Fig. 9). Monazites adjacent to pyrite (n = 6) yielded dates from 171 ± 14 to 140 ± 13 Ma and ThO_2 concentrations ≤1.57 wt%. The analyses from Lone Star yielded dates from 189 ± 14 to 116 ± 4 Ma and ThO_2 concentrations from 0.13 ± 0.01 to 5.33 ± 0.16 wt% (Fig. 9). There are no clear relationships between date, ThO_2 concentration, grain form, and sample alteration intensity. Grains that are aligned in the schistosity are generally older, whereas the grains adjacent to pyrite are younger, though significant overlap exists. Monazites that are aligned in the schistosity (n = 74) yielded dates from 189 ± 8 to 144 ± 8 Ma and ThO_2 concentrations ≤4.31 wt%. Monazites that are adjacent to pyrite (n = 50) yielded dates from 178 ± 8 to 116 ± 4 Ma and ThO_2 concentrations ≤3.97 wt%.

Monazite trace-element analyses

A total of 90 analyses yielded Gd/Yb values of 21 to 315 and Eu/Eu* of 0.31 to 1.09 (Stroh, 2019). The values for Gd/Yb and Eu/Eu* exhibit a (arguably) weak inverse relationship at Lone Star, whereas no relationship is observed in the relatively small dataset for Virgin. Neither Gd/Yb nor Eu/Eu* correlate with grain form, grain form factor, grain area, grain aspect ratio, grain compactness, grain roundness, date, or ThO_2 concentration. Trace-element analyses were not conducted at Mitchell-Sheba as grains were too small for the required 19 µm spot size. The Ca content of analyzed monazite is uniform and does not reveal distinct populations or trends.

Discussion

Vein formation and overprinting deformation

Quartz veins in the Klondike were previously interpreted to form in two distinct generations: early, barren metamorphic segregation veins, and late, gold-bearing discordant veins that were purely brittle (MacKenzie et al., 2008a). Based on our observations, we developed a paragenetic summary (Fig. 10) with evidence of protracted vein formation in the brittle-ductile transition zone, and ongoing ductile deformation after vein emplacement. Quartz vein textures indicate at least two stages of formation. The first is indicated by epitaxial quartz growth near vein boundaries that suggest multiple crack-seal events (Qtz2; Figs. 3d and 4c). The second stage of vein formation is indicated by blocky quartz grains that compose most of the veins (Qtz3; Figs. 3d and 4c). The blocky texture suggests at least one additional crack-seal event, where the dilation rate exceeded crystal growth, allowing quartz growth into free space (Hilgers et al., 2001). Although Klondike veins were previously thought to have formed in a single stage (MacKenzie et al., 2008a), vein textures here display evidence of multiple crack-seal events, in agreement with Wolff (2012). The early vein formation as narrow epitaxial growths before wider open space filling suggests increasing strain rates over time.

Different degrees of overprinting deformation presented above suggests that veins formed during progressive to brittle-ductile deformation. Vein

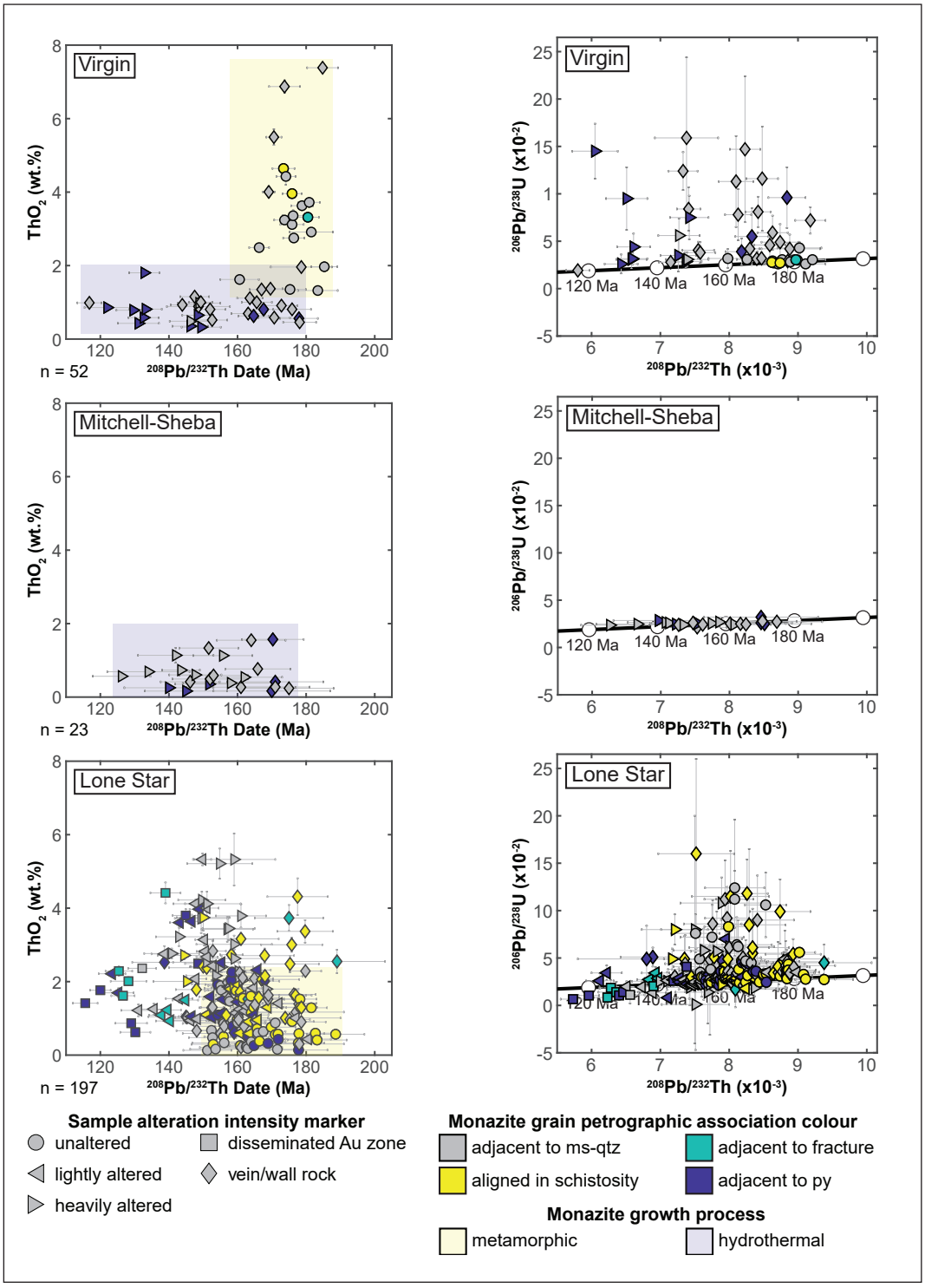


Figure 9. *Monazite geochronology results and growth process interpretations. Each data point represents one LA-ICP-MS analysis. Thin grey lines represent uncertainty in 2σ. Where no uncertainty line is visible, the uncertainty is less than the size of the marker. Multiple samples are shown on the same diagram, and thus the marker shape is dictated by the sample alteration intensity. Marker colour is based on the monazite grain petrographic association.* ***Left:*** *ThO_2 vs. date plots.* ***Right:*** *U-Th-Pb concordia diagrams.* ***Top:*** *Results from Virgin.* ***Middle:*** *Results from Mitchell-Sheba.* ***Bottom:*** *Results from Lone Star. Ms-qtz – muscovite-quartz; py – pyrite.*

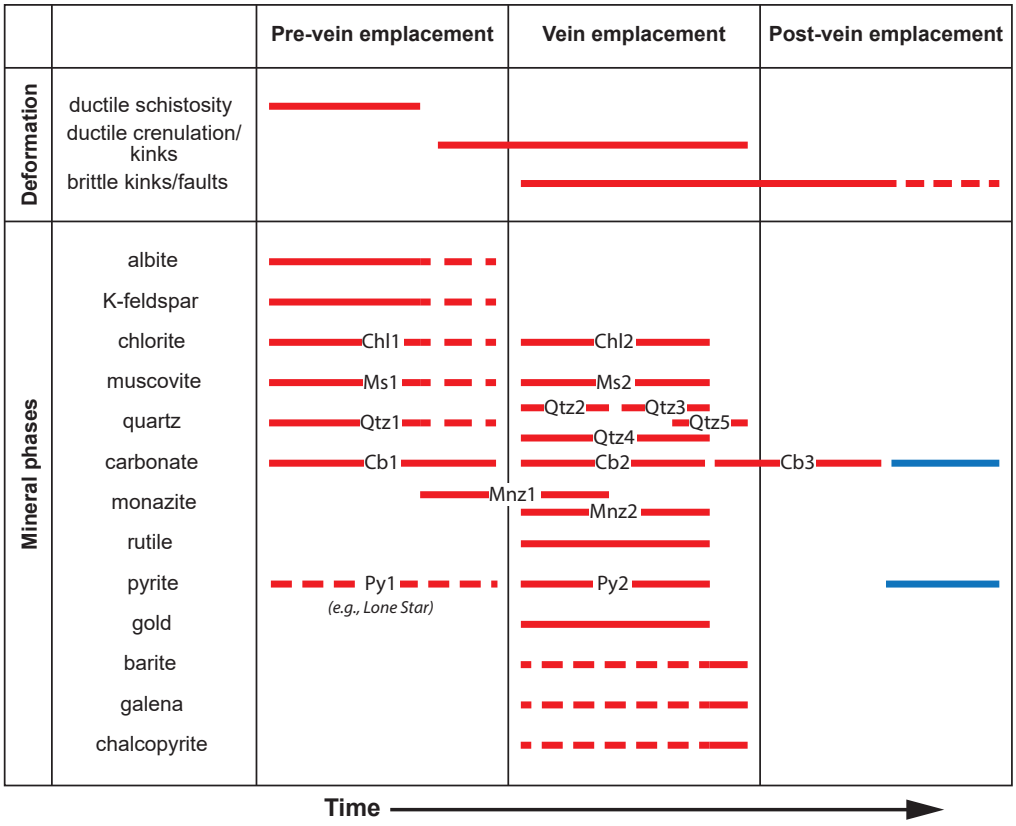


Figure 10. *Simplified paragenesis chart for the Klondike gold occurrences based on petrographic and cathodoluminescence analysis of 37 polished thin sections from the Virgin, Mitchell-Sheba and Lone Star gold occurrences. Red represents phase formation, whereas blue indicates break down by oxidation or weathering. Chl1: metamorphic/recrystallized; Chl2: host alteration; Ms1: metamorphic/recrystallized; Ms2: host alteration; Qtz1: metamorphic/recrystallized; Qtz2: syntaxial vein filling; Qtz3: blocky vein filling; Qtz4: host alteration; Qtz5: dynamic recrystallization of pre-existing vein quartz; Cb1: metamorphic/recrystallized; Cb2: infrequent vein filling/host alteration; Cb3: fracture filling; Mnz1: metamorphic/recrystallized; Mnz2: host alteration. Metamorphic minerals are solid then dashed because most of the mineral growth is interpreted to occur during schistosity formation, but some may be related to the crenulation forming event. Metamorphic carbonate (Cb1) is not dashed because it locally replaces pre-existing, metamorphic chlorite (Chl1; Figure 5c). Barite, galena and chalcopyrite begin dashed because they can be included in quartz and pyrite but are typically late in brittle fractures. Brittle fracturing likely continued during exhumation and weathering and is dashed.*

orientations ranging from sub-concordant to discordant to the wall-rock schistosity as well as macro and micro-structural evidence suggest at least some level of ductile deformational overprinting and local dynamic recrystallization of all vein generations (e.g., Figs. 3d and 4c). Deformation fabrics are locally strong within micaceous vein alteration haloes, suggesting a relative timing whereby vein emplacement and host-rock alteration occurred prior to deformation (Fig. 6). Late in the deformation sequence, carbonate veinlets filled brittle fractures in quartz veins (Fig. 4b) but rarely propagated into the host rock, indicating that the more competent vein-filling quartz behaved brittlely, whereas micaceous wall rock accommodated strain in a ductile manner. Vein quartz investigation by cathodoluminescence indicates dark, nearly homogeneous responses (Stroh, 2019), which agrees with Rusk's (2012) description of recrystallized quartz in orogenic settings.

The exact timing of gold precipitation relative to vein formation and deformation remains ambiguous as gold-bearing veins are overprinted by various amounts of deformation. Limonitic selvages along folded vein margins commonly host gold (Rushton et al., 1993) and suggests that mineralization occurred prior to ductile

deformation. However, Grimshaw (2018) describes a late, brittle deformation stage of gold precipitation at Lone Star, implying that gold was locally introduced or remobilized late in the deformation sequence. This evidence suggests that the timing of gold precipitation in the Klondike may span the timing of vein formation or vary locally by occurrence.

Linking monazite dates with petrographic associations and geochemistry

Our results reveal monazite crystallization from ca. 190 to 120 Ma, a time span of ~70 m.y. (Fig. 9). These dates are considerably younger than the 269 to 253 Ma age of the Klondike assemblage protolith (Colpron et al., 2006) and also coincide with a regional magmatic gap from 179 to 115 Ma (Allan et al., 2013). Thus, we rule out the presence of igneous grains in our dataset and interpret all the dates as either metamorphic or hydrothermal. To discriminate between hydrothermal and metamorphic crystallization we integrated the dates with the petrographic and geochemical parameters summarized in Table 1. We interpret that monazite from unaltered samples is metamorphic, as they are apparently beyond the influence of hydrothermal alteration. Monazite aligned in the schistosity is commonly but not always metamorphic; hydrothermal monazite may have preferentially formed along these planar features.

Petrographic relationships and ThO_2 concentrations of monazite were the most useful parameters for differentiating hydrothermal and metamorphic crystallization. The monazite trace-element data generally lacks discernable relationships to help distinguish growth mechanisms and is interpreted in greater detail in Stroh (2019). The REE composition may help to distinguish hydrothermal (no Eu anomaly; precipitated without plagioclase) from metamorphic (negative Eu anomaly; grew in contact with plagioclase) monazite grains, but petrographic support for this is absent. Similarly, the relationship between Gd/Yb and Eu/Eu* suggests local monazite growth with or without coeval apatite and plagioclase, but this relationship does not reliably differentiate between a hydrothermal and metamorphic origin.

Virgin

Our analyses reveal two populations of monazite dates at the Virgin occurrence: an older (185–161 Ma) population with up to 7.38 wt% ThO_2, and a mostly younger (178–117 Ma) population with ≤1.80 wt% ThO_2 (Fig. 9). Although ThO_2 concentrations are variable in metamorphic monazite, concentrations are typically <2 wt% in hydrothermal monazite (Schandl and Gorton, 2004; Kohn and Malloy, 2004; Catlos, 2013). Collectively, the broad range in ThO_2 concentrations and dominance of monazite in unaltered samples suggest the older monazite at Virgin is metamorphic. A hydrothermal origin is supported for the younger population by the alteration extent of the samples, abundance of grains adjacent to pyrite, and the low ThO_2 concentrations. Grains that are adjacent to pyrite, which overprints the schistosity, all have <2 wt% ThO_2. Although metamorphic monazite can have ThO_2 concentrations <2 wt%, we interpret all monazite with >2 wt% ThO_2 as metamorphic.

Mitchell-Sheba

At Mitchell-Sheba, monazite occurs exclusively in the alteration zone surrounding the vein, commonly occurring adjacent to pyrite. All monazite contains <2 wt% ThO_2, consistent with hydrothermal crystallization. We interpret this group to record the same younger population at Virgin, further bracketing hydrothermal monazite growth between 175 and 126 Ma. The lack of metamorphic monazite is unsurprising given the mafic composition of the host rock (Fig. 7). Whole-rock compositional data from the three occurrences are shown in Figure 11. Higher Zr/TiO_2 ratios indicate more felsic host rocks. The felsic host rock at Virgin is the most enriched in incompatible elements, including Th, thus allowing more Th to be available to metamorphic monazite. The intermediate rock at Lone Star is lower in incompatible elements, including Th, which limits both the growth of metamorphic monazite and its Th concentration. The mafic host rock at Mitchell-Sheba has the lowest Th and cerium (Ce) concentrations, which explains the lack of metamorphic monazite. The felsic host rocks were also more likely to have abundant primary apatite, a precursor to metamorphic monazite, whereas apatite would likely have been absent in the mafic host rocks (Overstreet, 1967). Therefore, not only does the variable ThO_2 concentration of metamorphic monazite increase with increasing grade (Schandl and Gorton, 2004), but it also depends on the composition of the protolith. Under the greenschist metamorphic conditions of the Klondike, monazite develops with 0.13 to 7.38 wt% ThO_2, but is typically <5 wt%. Rocks with a mafic protolith produce no monazite under these conditions, whereas rocks with an intermediate protolith produce monazite with 0.13 to 2.26 wt% ThO_2, and rocks with a felsic protolith produce monazite with 1.32 to 7.38 wt% ThO_2.

Lone Star

The relationship between ThO_2 concentration and age in the Lone Star data is more complex than the other two occurrences (Fig. 9). Monazite from unaltered samples yielded dates from 189 to 151 Ma, which bracket the range of metamorphic dates (185–161 Ma) we infer from the Virgin occurrence. However, these monazite grains are characterized by low ThO_2 concentrations (<2 wt%) and commonly occur adjacent to pyrite, indicative of hydrothermal crystallization. Although characteristic of hydrothermal monazite, low thorium concentrations are also common in metamorphic monazite (Schandl and Gorton, 2004), and, as mentioned above, at least some of the pyrite at Lone Star predates vein formation (Fig. 10). Thus, we interpret older monazite grains from unaltered samples at Lone Star as metamorphic (yellow box in Fig. 9). Analyses at Lone Star with relatively young dates (<151 Ma) have highly variable ThO_2 concentrations that include values up to ~5 wt%, consistent with metamorphic crystallization. However, post ca. 160 Ma, metamorphic growth is inconsistent with our data from Virgin. Our preferred interpretation is that the younger, high-Th monazite is metamorphic monazite in which U-Th-Pb systematics were re-equilibrated. This interpretation requires that a hydrothermal fluid reset the dates, while preserving the ThO_2 concentrations of pre-existing metamorphic monazite. Williams et al. (2011) have previously documented this process. The sparse population of grains with older dates (>151 Ma) and high ThO_2 concentrations (>2 wt%) may be metamorphic monazite that retained its primary age signature. The population of young (<151 Ma), ThO_2-poor (<2 wt%) monazite could be a combination of hydrothermal and partially reset metamorphic monazite.

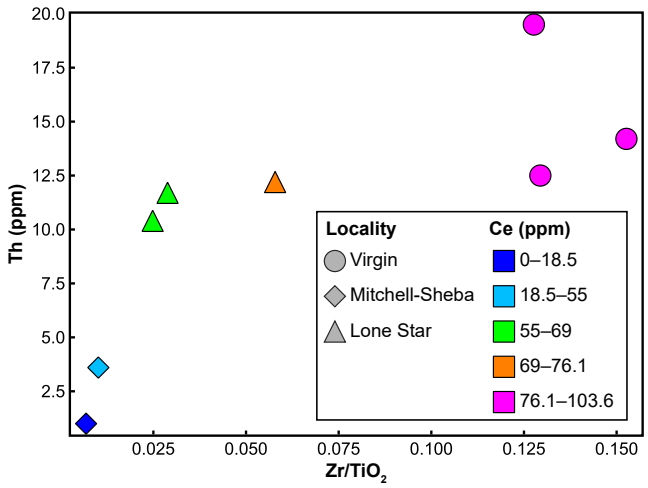


Figure 11. *Whole-rock lithogeochemical data suggesting the host rock composition controls the metamorphic monazite composition. The ratio of Zr/TiO_2 is treated as a measurement from mafic (low) to felsic (high). More felsic host rocks have increasing thorium (Th) and cerium (Ce) concentrations, which translates to metamorphic monazite growth with higher ThO_2 concentration. Mafic rocks do not have metamorphic monazite. Thus, the host-rock composition controls the ThO_2 concentration in metamorphic monazite.*

Linking monazite growth and regional tectonics

Figure 12 presents a compilation of all the monazite dates with their interpreted growth mechanism, as discussed in the previous section. Our results bracket an early (ca. 190–150 Ma) generation of metamorphic monazite followed by a later (ca. 180–120 Ma) population of hydrothermal monazite. Our metamorphic monazite dates align with previously documented evidence for Early–Middle Jurassic deformation and metamorphism of Yukon-Tanana terrane associated with the accretion of the intermontane terranes to North America (Berman et al., 2007; Gaidies et al., 2021; Colpron et al., 2025). The spread of metamorphic dates also coincides with Jurassic cooling ages that record the exhumation of Yukon-Tanana to upper crustal levels (Fig. 13; Joyce et al., 2015; Yukon Geological Survey, 2023), suggesting that monazite growth occurred during prograde and retrograde metamorphism. During exhumation, infiltrating fluids may have facilitated monazite formation through the breakdown of allanite, apatite, or pre-existing monazite (Ayers et al., 2002; Bollinger and Janots, 2006; Finger and Krenn, 2007; Johnson et al., 2015). The dates obtained for hydrothermal monazite (ca. 180–120 Ma) coincide with those obtained for hydrothermal mica, suggesting that vein formation began shortly after the onset of exhumation (Fig. 13; Breitsprecher and Mortensen, 2004; Joyce et al., 2015). The monazite dates indicate that vein formation persisted until after the country rock had cooled through the closure temperature of mica (e.g., ~380°C for muscovite; Reiners and Brandon, 2006), consistent with vein-forming fluid inclusion trapping temperatures of 200 to 350°C (Rushton et al., 1993). We were unable to directly date gold mineralization. The timing of vein formation nevertheless overlaps with an unpublished U-Pb date of 156 ± 8 Ma obtained from hydrothermal rutile in a gold-bearing quartz vein (Mortensen, 2012, in Allan et al., 2013).

In addition to the lengthy timespan of each growth mechanism, our results suggest that hydrothermal and metamorphic monazite growth temporally overlapped for a period of ca. 30 m.y. The large range of monazite dates may in part be due to disturbances of the isotopic U-Th-Pb systematics, highlighted by the evidence of partially reset metamorphic monazite at Lone Star (Fig. 9). Regardless, our data demonstrate that Jurassic regional metamorphism was subsequently followed by Jurassic to Early Cretaceous vein formation and hydrothermal alteration, most likely due to progressive deformation. Evidence of protracted orogenic gold mineralization under similar tectonic circumstances has also been documented in the Cariboo gold district of east-central British Columbia, where vein formation spanned from 155 to 134 Ma during progressive ductile to brittle deformation (Rhys et al., 2009; Mortensen et al., 2011; Allan et al., 2017). Veins that formed early in the deformation sequence are only weakly mineralized and overprinted by ductile deformation, whereas veins that formed later have ore-grade gold values and are only weakly strained to unstrained (Allan et al., 2017). Although the veins formed over 21 m.y., mineralization is interpreted to have lasted 15 m.y., from 149 to 134 Ma (Rhys et al., 2009; Mortensen et al., 2011; Allan et al., 2017). Like the Klondike, veins in the Cariboo district exhibit varying levels of deformation that indicate vein formation progressed as deformation became increasingly brittle.

The protracted time span of vein formation in the Klondike may reflect input from multiple sources. Staples et al. (2016) suggested that amphibolite-facies metamorphism of the Finlayson Lake domain between 169 and 142 Ma led to the release of metamorphic fluids, which travelled into the Klondike assemblage—an assemblage they interpret to have been adjacent the Finlayson Lake domain prior to post Cretaceous dextral displacement along the Tintina fault. The subsequent burial and devolatilization of the Australia Mountain domain from 146 to 118 Ma (Staples et al., 2013) could have provided additional fluids. Finally, vein-forming fluids may have been sourced from the Klondike assemblage itself, through decompression-driven metamorphic devolatilization reactions during regional Jurassic exhumation (Fig. 13; Vry et al., 2010; White et al., 2015). At Lone Star, Grimshaw (2018) demonstrated that most quartz generations are barren and that gold is introduced in a volumetrically minor, late-stage vein filling. Thus, while the different tectono-metamorphic events recorded in the Klondike region had the potential to generate siliceous fluids, gold endowment may have been restricted to one in particular.

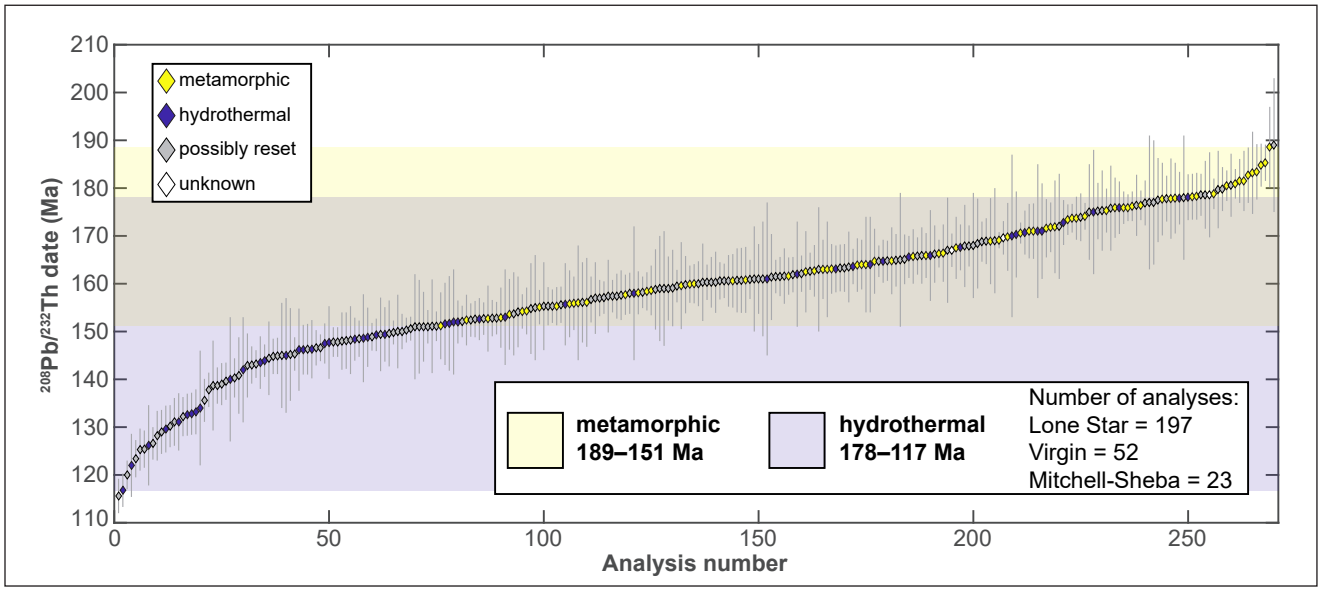


Figure 12. *Summary of all monazite dates in the Klondike and overlain metamorphic and hydrothermal age ranges; grey is overlap. Thin grey lines represent uncertainty in 2σ. Each data point represents one LA-ICP-MS analysis. The marker colour is based on the interpreted growth mechanism that we assigned based on petrographic associations and geochemical (primarily ThO_2 concentration) parameters discussed in the text.*

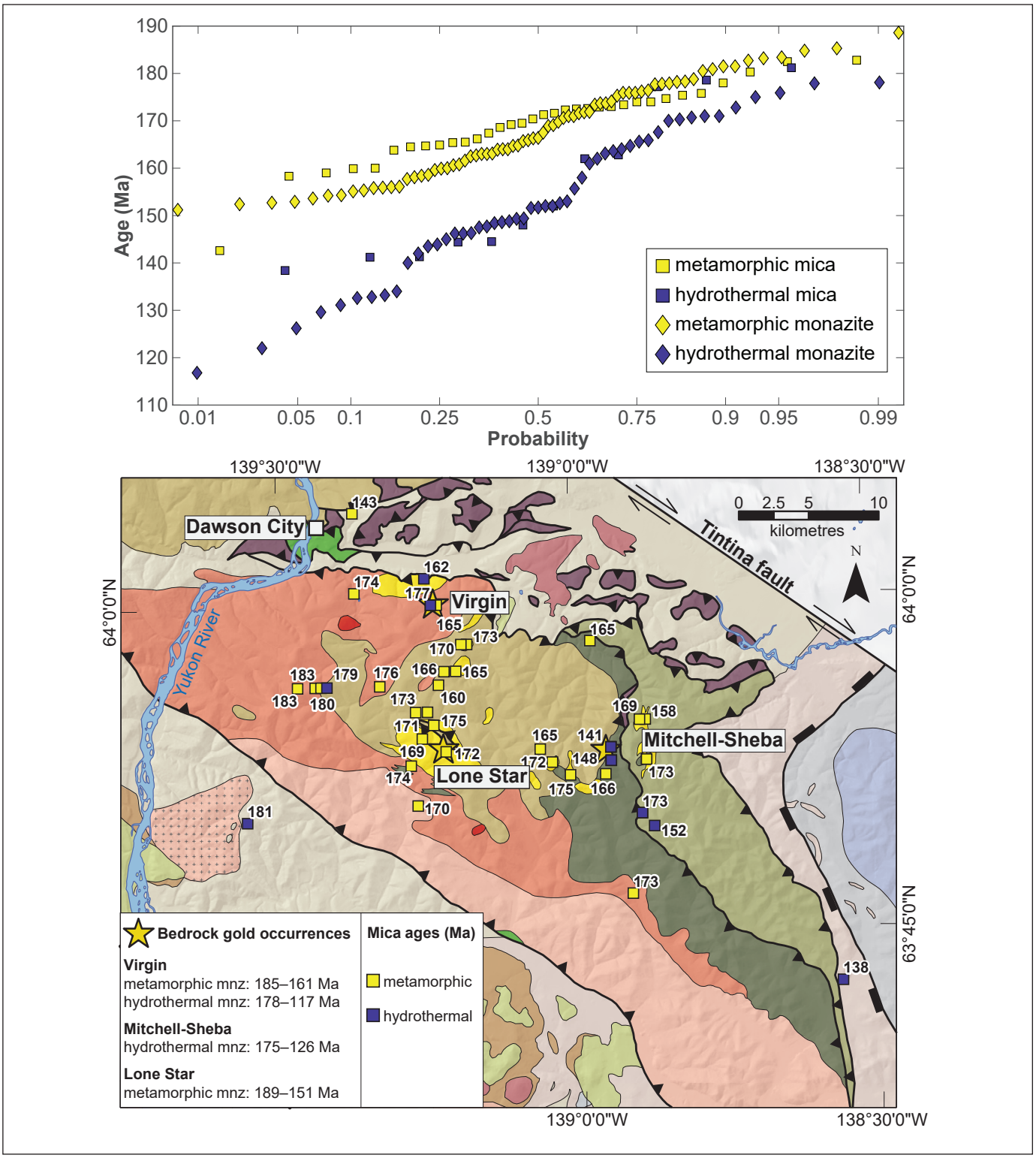


Figure 13. *Comparison of Klondike metamorphic and hydrothermal monazite and mica ages.* ***Top:*** *Split probability plot summarizing the previously published and new metamorphic and hydrothermal ages in the Klondike. The* $^{208}Pb/^{232}Th$ *monazite ages presented herein overlap with previously published* $^{40}Ar/^{39}Ar$ *mica ages. No uncertainty in age is shown for simplicity. Mica ages are from Breitsprecher and Mortensen (2004); Joyce et al. (2015); and unpublished Mineral Deposit Research Unit data. All monazite ages are from this study.* ***Bottom:*** *Geological map of the Klondike summarizing the locations of the ages from the top figure. Monazite age ranges are summarized in the legend. Some mica ages mask others. Legend for geology corresponds to Figure 2.*

Conclusions

The timing of gold mineralization in the Klondike district is constrained by Th-Pb ages of paragenetically related hydrothermal monazite at ca. 180–120 Ma, overlapping with, but generally younger than, an earlier metamorphic monazite population dated at 190–150 Ma. Metamorphic monazite exhibits variable ThO_2 concentrations (0–8 wt% ThO_2) and is prevalent in unaltered rocks distal to orogenic quartz veins. Metamorphic crystallization spanned the burial and subsequent exhumation of the Yukon-Tanana terrane during collision of the Intermontane terranes with North America. In contrast, hydrothermal monazite exhibits low ThO_2 concentrations (<2 wt% ThO_2) and is largely restricted to alteration halos of veins. We were unable to directly link monazite dates to gold mineralization; our inferred timing of vein formation nevertheless overlaps with a previously reported U-Pb date of ca. 156 Ma from hydrothermal rutile in a gold-bearing quartz vein (Mortensen unpublished data, 2012, in Allan et al 2013). Vein-forming fluids likely formed during multiple prograde and retrograde metamorphic events, including regional exhumation (185–140 Ma; Yukon Geological Survey, 2023), Finlayson Lake domain metamorphism (169–142 Ma; Staples, 2014), and Australia Mountain domain metamorphism (146–118 Ma; Staples et al., 2013). Although hydrothermal activity persisted for tens of millions of years, gold mineralization was likely restricted to a significantly shorter time interval. Our monazite dates provide insight into the timing of gold mineralization and reveal the extensive duration and complexity of vein formation in orogenic gold systems.

Acknowledgments

This research was part of the Yukon-Alaska Metallogeny Project based at the Mineral Deposit Research Unit of the University of British Columbia, which was funded by a Natural Sciences and Engineering Research Council of Canada Collaborative Research Development grant, Goldcorp Incorporated (now Newmont Corporation), and Sumac Mines Limited. Additional funds were provided through awards and scholarships, including the Society of Economic Geologists Canada Foundation Graduate Student Fellowship, Northwest Territories and Nunavut Association of Professional Engineers and Geoscientists Finnigan Award for Northern Research, Yukon Foundation Bradshaw Memorial Scholarship, and Plains Midstream Canada Higher Education Award. The authors would like to thank Klondike Gold Corporation, Kestrel Gold Incorporated, and the Yukon Geological Survey for providing access to field sites and drill core. Comments by Patrick Sack and Jim Mortensen on an earlier version of this manuscript led to significant improvements.

References

Allan, M.M., Mortensen, J.K., Hart, C.J.R., Bailey, L.A., Sanchez, M.G., Ciolkiewicz, W., McKenzie, G.G. and Creaser, R.A., 2013. Magmatic and Metallogenic Framework of West-Central Yukon and Eastern Alaska. *In:* Tectonics, Metallogeny and Discovery: The North American Cordillera and Similar Accretionary Settings. M. Colpron, T. Bissig, B.G. Rusk and J.F.H. Thompson (eds.), Society of Economic Geologists Special Publication, vol. 17, p. 111–168.

Allan, M.M., Rhys, D.A. and Hart, C.J.R., 2017. Orogenic gold mineralization of the eastern Cordilleran gold belt, British Columbia: Structural ore controls in the Cariboo (093A/H), Cassiar (104P) and Sheep Creek (082F) mining districts. Geoscience BC Report 2017-15, 108 p.

Andersen, T., 2002. Correction of common lead in U-Pb analyses that do not report 204Pb. Chemical Geology, vol. 192, p. 59–79.

Arne, D., Bierlin, F., Morgan, J. and Stein, H. 2001. Re-Os dating of sulfides associated with gold mineralization in central Victoria, Australia. Economic Geology, vol. 96, no. 6, p. 1455–1459.

Ayers, J., Dunkle, S., Gao, S. and Miller, C., 2002. Constraints on timing of peak and retrograde metamorphism in the Dabie Shan Ultrahigh-Pressure Metamorphic Belt, east-central China, using U-Th-Pb dating of zircon and monazite. Chemical Geology, vol. 186, p. 315–331.

Bailey, L.A., 2013. Late Jurassic fault-hosted gold mineralization of the Golden Saddle deposit, White Gold district, Yukon Territory. MSc thesis, University of British Columbia, Vancouver, BC, Canada, 170 p.

Berman, R.G., Ryan, J.J., Gordey, S.P. and Villeneuve, M., 2007. Permian to Cretaceous polymetamorphic evolution of the Stewart River region, Yukon-Tanana terrane, Yukon, Canada: P-T evolution linked with in-situ SHRIMP monazite geochronology. Journal of Metamorphic Geology, vol. 25, no. 7, p. 803–827.

Bierlein, F.P., Arne, D.C., Foster, D.A. and Reynolds, P., 2001. A geochronological framework for orogenic gold mineralisation in central Victoria, Australia. Mineralium Deposita, vol. 36, no. 8, p. 741–767.

Bierlein, F.P. and Crowe, D.E., 2000. Phanerozoic orogenic lode gold deposits. SEG Reviews, vol. 13, p. 103–139.

Bollinger, L. and Janots, E., 2006. Evidence for Mio-Pliocene retrograde monazite in the Lesser Himalaya, far western Nepal. European Journal of Mineralogy, vol. 18, no. 3, p. 289–297.

Brown, S., Fletcher, I., Stein, H., Snee, L. and Groves, D.I., 2002. Geochronological constraints on pre-, syn-, and postmineralization events at the world-class Cleo gold deposit, eastern goldfields province, Western Australia. Economic Geology, vol. 97, p. 541–559.

Breitsprecher, K. and Mortensen, J., 2004. YukonAge 2004: A database of isotopic age determinations for rock units from Yukon Territory. Yukon Geological Survey (CD-ROM).

Burke, M., Hart, C.J.R. and Lewis, L.L., 2005. Models for epigenetic gold exploration in the northern Cordilleran orogen, Yukon, Canada. *In:* Mineral deposit research: Meeting the global challenge, J. Mao and F.P. Bierlein (eds.), Proceedings of the Eighth Biennial SGA Meeting, Beijing, China, p. 525–528.

Catlos, E.J., 2013. Review: Versatile monazite: resolving geological records and solving challenges in materials science. Generalizations about monazite: Implications for geochronologic studies. American Mineralogist, vol. 98, no. 5–6, p. 819–832, doi:10.2138/am.2013.4336.

Chapman, R.J., Mortensen, J.K., Crawford, E.C. and LeBarge, W.P., 2010a. Microchemical studies of placer and lode gold in the Klondike district, Yukon, Canada: 1. Evidence for a small, gold-rich, orogenic hydrothermal system in the Bonanza and Eldorado Creek area. Economic Geology, vol. 105, no. 8, p. 1369–1392.

Chapman, R.J., Mortensen, J.K., Crawford, E.C. and Lebarge, W.P., 2010b. Microchemical studies of placer and Lode Gold in the Klondike district, Yukon, Canada: 2. Constraints on the nature and location of regional lode sources. Economic Geology, vol. 105, no. 8, p. 1393–1410.

Chapman, R.J., Mortensen, J.K. and LeBarge, W.P., 2011. Styles of lode gold mineralization contributing to the placers of the Indian River and Black Hills Creek, Yukon Territory, Canada as deduced from microchemical characterization of placer gold grains. Mineralium Deposita, vol. 46, no. 8, p. 881–903.

Cherniak, D.J., Watson, E.B., Grove, M. and Harrison, T.M., 2004. Pb diffusion in monazite: a combined RBS/SIMS study. Geochimica et Cosmochimica Acta, vol. 68, no. 4, p. 829–840.

Colpron, M., Nelson, J.L. and Murphy, D.C., 2006. A tectonostratigraphic framework for the pericratonic terranes of the northern Canadian Cordillera. Paleozoic Evolution and Metallogeny of Pericratonic Terranes at the Ancient Pacific Margin of North America, Canadian and Alaskan Cordillera, M. Colpron and J.L. Nelson (eds.), Geological Association of Canada, Special Paper, vol. 45, p. 1–23.

Colpron, M., McClelland, W.C., Piercey, S.J., Kroeger, E.D.L., Crowley, J.L. and Gehrels, G.E., 2025. Revisiting the “Klondike Orogeny”: Permian to Jurassic development of the Yukon-Tanana terrane, northern Canadian Cordillera. Tectonics, vol. 44, no. 6, e2024TC008748, doi:10.1029/2024TC008748.

Crawford, E.C., 2007. Klondike placer gold: New tools for examining morphology, composition and crystallinity. MSc thesis, University of British Columbia, Vancouver, BC, Canada, 151 p.

Crawford, E.C., Chapman, R.J., LeBarge, W.P. and Mortensen, J.K., 2007. Developing a new method to identify previously unrecognized geochemical and morphological complexity in placer gold deposits in western Yukon. In: Yukon Exploration and Geology 2006, D.S. Emond, L. Lewis and L.H. Weston (eds.), Yukon Geological Survey, p. 139–148.

Cuney, M. and Kyser, K., 2015. The geology and geochemistry of uranium and thorium deposits. Mineralogical Association of Canada Short Course Series, vol. 46, 362 p.

Didier, A., 2013. Compartment geochimique du chronometre U-Th-Pb dans la monazite: approche par analyses in-situ au LA-ICP_MS. PhD thesis, University Blaise Pascal, Clermont-Ferrand, France, 346 p.

Finger, F. and Krenn, E., 2007. Three metamorphic monazite generations in a high-pressure rock from the Bohemian Massif and the potentially important role of apatite in stimulating polyphase monazite growth along a PT loop. Lithos, vol. 95, no. 1-2, p. 103–115.

Frimmel, H.E., 2008. Earth's continental crustal gold endowment. Earth and Planetary Science Letters, vol. 267, no. 1-2, p. 45–55.

Gaidies, F., Morneau, Y.E., Petts, D.C., Jackson, S.E., Zagorevski, A. and Ryan, J.J., 2021. Major and trace element mapping of garnet: Unravelling the conditions, timing and rates of metamorphism of the Snowcap assemblage, west-central Yukon. Journal of Metamorphic Geology, vol. 39, no. 2, p. 133–164.

Gasquet, D., Bertrand, J.M., Paquette, J.L., Lehmann, J., Ratzov, G., De Ascencao Guedes, R., Tiepolo, M., Boullier, A.M., Scaillet, S. and Nomade, S., 2010. Miocene to Messinian deformation and hydrothermal activity in a pre-Alpine basement massif of the French western Alps: new U-Th-Pb and argon ages from the Lauziere massif. Bulletin de la Societe Geologique de France, vol. 181, p. 227–241.

Goldfarb, R.J., Baker, T., Dube, B., Groves, D.I., Hart, C.J.R. and Gosselin, P., 2005. Distribution, character, and genesis of gold deposits in metamorphic terranes. Economic Geology 100th Anniversary Volume, p. 407–450.

Goldfarb, R.J. and Groves, D.I., 2015. Orogenic gold: Common or evolving fluid and metal sources through time. Lithos, vol. 233, p. 2–26.

Goldfarb, R.J., Groves, D.I. and Gardoll, S., 2001. Orogenic gold and geologic time: a global synthesis. Ore Geology Reviews, vol. 18, p. 1–75.

Goldfarb, R.J., Newberry, R., Pickthorn, W. and Gent, C., 1991. Oxygen, hydrogen, and sulfur isotope studies in the Juneau gold belt, southeastern Alaska: Constraints on the origin of hydrothermal fluids. Economic Geology, vol. 86, p. 66–80.

Goldfarb, R.J. and Pitcairn, I., 2022. Orogenic gold: is a genetic association with magmatism realistic? Mineralium Deposita, vol. 58, p. 5–35.

Gordey, S.P. and Ryan, J. 2005. Geology, Stewart River Area (115N, 115-O and part of 115-J), Yukon Territory. Geological Survey of Canada, Open File 4970, scale 1:250 000.

Grand'Homme, A., 2016. Hydrothermal monazite: the unavoidable accessory. PhD thesis, Université Grenoble Alpes, Grenoble, France, 253 p.

Grand'Homme, A., Janots, E., Bosse, V., Seydoux-Guillaume, A.M. and De Ascencao Guedes, R., 2016. Interpretation of U-Th-Pb in-situ ages of hydrothermal monazite-(Ce) and xenotime-(Y): evidence from a large-scale regional study in clefts from the western Alps. Mineralogy and Petrology, vol. 110, no. 6, p. 787–807.

Grimshaw, M.R., 2018. Gold Mineralisation in the Lone Star area of the Klondike Gold District, Yukon, Canada. PhD thesis, University of Leeds, Leeds, England, 354 p.

Groves, D.I., Goldfarb, R.J., Gebre-Mariam, M., Hagemann, S.G. and Robert, F., 1998. Orogenic gold deposits: A proposed classification in the context of their crustal distribution and relationship to other gold deposit types. Ore Geology Reviews, vol. 13, p. 7–27.

Groves, D.I., Goldfarb, R.J., Robert, F. and Hart, C.J.R., 2003. Gold deposits in metamorphic belts: overview of current understanding, outstanding problems, future research, and exploration significance. Economic Geology, vol. 98, p. 1–29.

Henley, R., Norris, R. and Paterson, C., 1976. Multistage ore genesis in the New Zealand geosyncline: A history of post-metamorphic lode emplacement. Mineralium Deposita, vol. 11, p. 180–196.

Hilgers, C., Koehn, D., Bons, P.D. and Urai, J., 2001. Development of crystal morphology during unitaxial growth in a progressively widening vein: II. Numerical simulations of the evolution of antitaxial fibrous veins. Journal of Structural Geology, vol. 23, p. 873–885.

Horstwood, M.S.A., Foster, G.L., Parrish, R.R., Noble, S.R. and Nowell, G.M., 2003. Common-Pb corrected in situ U–Pb accessory mineral geochronology by LA-MC-ICP-MS. Journal of Analytical Atomic Spectrometry, vol. 18, no. 8, p. 837–846.

Hoymann, K.H. and Friedrich, G., 1990. Gold and sulphide mineralization in the Hunker Creek area, Yukon Territory, Canada. Yukon Geology, vol. 3, p. 312–326.

Hunt, P.A. and Roddick, J.C., 1992. A compilation of K-Ar ages, report 21. Geological Survey of Canada, Radiogenic age and isotopic studies, Report 5, Paper 91-2, p. 207–252.

Jochum, K., Willbold, M., Raczek, I., Stoll, B. and Herwig, K., 2005. Chemical Characterisation of the USGS Reference Glasses GSA-1G, GSC-1G, GSD-1G, GSE-1G, BCR-2G, BHVO-2G, and BIR-1G Using EPMA, ID-TIMS, ID-ICP-MS, and LA-ICP-MS. Geostandards and Geoanalytical Research, vol. 29, no. 3, p. 285–302.

Johnson, T.E., Clark, C., Taylor, R.J.M., Santosh, M. and Collins, A.S., 2015. Prograde and retrograde growth of monazite in migmatites: An example from the Nagercoil Block, southern India. Geoscience Frontiers, vol. 6, no. 3, p. 373–387.

Joyce, N.L., Ryan, J.J., Colpron, M., Hart, C.J.R. and Murphy, D.C., 2015. A compilation of $^{40}Ar/^{39}Ar$ age determinations for igneous and metamorphic rocks, and mineral occurrences from central and southeast Yukon. Geological Survey of Canada, Open File 7924, 229 p.

Jutras, M. and Kenwood, S., 2022. NI 43-101 technical report on the Klondike district gold project, Yukon Territory, Canada. Prepared for Klondike Gold Corp., issued December 16, 2022, 315 p.

Kerrich, R. and King, R., 1993. Hydrothermal zircon and baddeleyite in Val d'Or Archaean mesothermal gold deposits: characteristics, composition and fluid inclusion properties with implication for timing of primary gold mineralization. Canadian Journal of Earth Sciences, vol. 30, p. 2334–2351.

Knight, J.B., Morison, S.R. and Mortensen, J., 1999a. The relationship between placer gold particle shape, rimming and distance of fluvial transport; as exemplified by gold from the Klondike district, Yukon Territory, Canada. Economic Geology, vol. 94, p. 635–648.

Knight, J.B., Mortensen, J.K. and Morison, S.R., 1999b. Lode and placer gold composition in the Klondike district, Yukon Territory, Canada: Implications for the nature and genesis of Klondike placer and lode gold deposits. Economic Geology, vol. 94, p. 649–664.

Kohn, M.J. and Malloy, M.A., 2004. Formation of monazite via prograde metamorphic reactions among common silicates: implications for age determinations. Geochimica et Cosmochimica Acta, vol. 68, p. 101–113, doi:10.1016/S0016-7037(03)00258-8.

Kretz, R., 1983. Symbols for rock-forming minerals. American Mineralogist, vol. 68, p. 277–279.

Kylander-Clark, A.R.C., Hacker, B.R. and Cottle, J.M., 2013. Laser-ablation split-stream ICP petrochronology. Chemical Geology, vol. 345, p. 99–112.

Lin, S. and Corfu, F., 2002. Structural setting and geochronology of auriferous quartz veins at the High Rock Island gold deposit, northwestern Superior Province, Manitoba, Canada. Economic Geology, vol. 97, p. 43–57.

MacKenzie, D.J., Craw, D. and Mortensen, J.K., 2008a. Structural controls on orogenic gold mineralisation in the Klondike goldfield, Canada. Mineralium Deposita, vol. 43., no. 4, p. 435–448.

MacKenzie, D., Craw, D., Mortensen, J.K. and Liverton, T., 2008b. Disseminated gold mineralization associated with orogenic veins in the Klondike Schist, Yukon. *In:* Yukon Exploration and Geology 2007, D.S. Emond, L.R. Blackburn, R.P. Hill and L.H. Weston (eds.), Yukon Geological Survey, p. 215–224.

Mortensen, J.K., 1990. Geology and U–Pb geochronology of the Klondike district, west-central Yukon Territory. Canadian Journal of Earth Sciences, vol. 27, no. 7, p. 903–914.

Mortensen, J.K., 1996. Geological compilation maps of the northern Stewart River map area, Klondike and Sixtymile Districts (115N/15, 16; 1150/13, 14; and parts of 1150/15, 16). Exploration and Geological Services Division, Yukon Region, Indian and Northern Affairs Canada, Open File 1996-1(G), six 1:50 000-scale maps.

Mortensen, J.K., Chapman, R., LeBarge, W. and Jackson, L., 2004. Application of placer and lode gold geochemistry to gold exploration in western Yukon. *In:* Yukon Exploration and Geology 2004, D.S. Emond, L.L. Lewis and G.D. Bradshaw (eds.), Yukon Geological Survey, p. 205–212.

Mortensen, J.K., Chapman, R.J., LeBarge, W. and Crawford, E.C., 2006. Compositional studies of placer and lode gold from western Yukon: Implications for lode sources. *In:* Yukon Exploration and Geology 2005, D.S. Emond, G.D. Bradshaw, L.L. Lewis and L.H. Weston (eds.), Yukon Geological Survey, p. 247–255.

Mortensen, J.K., Craw, D., MacKenzie, D.J., Gabites, J.E. and Ullrich, T., 2010. Age and origin of orogenic gold mineralization in the Otago Schist Belt, South Island, New Zealand: constraints from lead isotope and 40Ar/39Ar dating studies. Economic Geology, vol. 105, no. 4, p. 777–793.

Mortensen, J.K., Liverton, T. and Dodd, K., 2019. Chemostratigraphic constraints on the nature and origin of felsic schist units hosting stratabound and orogenic vein gold on Lone Star ridge, Klondike gold district, Yukon. Journal of Geochemical Exploration, vol. 204, p. 112–130.

Mortensen, J.K., Nesbitt, B.E. and Rushton, R.W., 1992. Preliminary observations on the geology and geochemistry of quartz veins in the Klondike district, West-Central Yukon. Yukon Geology, vol. 3, p. 260–270.

Mortensen, J.K., Rhys, D.A. and Ross, K.V., 2011. Investigations of orogenic gold deposits in the Cariboo gold district, east-central British Columbia: final report. Summary of Activities 2010, Geoscience BC, Report 2011-1, p. 65–76.

Mortensen, J.K., Craw, D. and MacKenzie, D.J., 2023. Concepts and revised models for Phanerozoic orogenic gold deposits. *In:* Recent Advances in Understanding Gold Deposits: from Orogeny to Alluvium, T. Torvela, J.S. Lambert-Smith and R.J. Chapman (eds.), Geological Society of London Special Publication, vol. 516, p. 15–46, doi:10.1144/SP516-2021-39.

Nelson, J.L., Colpron, M. and Israel, S., 2013. The Cordillera of British Columbia, Yukon, and Alaska: Tectonics and metallogeny. *In:* Metallogeny and Discovery: The North American Cordillera and Similar Accretionary Settings, M. Colpron, T. Bissig, B.G. Rusk and J.F.H. Thompson (eds.), Society of Economic Geologists Special Publication, vol. 17, p. 53–109.

Overstreet, W., 1967. The geologic occurrence of monazite. United States Geological Survey Professional Paper, vol. 530, p. 327.

Paquette, J.-L., N´ed´elec, A., Moine, B. and Rakotondrazafy, M., 1994. U-Pb, single zircon Pb-evaporation, and Sm-Nd isotopic study of a granulite domain in SE Madagascar. The Journal of Geology, vol. 102, no. 5, p. 523–538.

Paquette, J.L. and Tiepolo, M., 2007. High resolution (5 micron) U-Th-Pb isotope dating of monazite with excimer laser ablation (ELA)-ICPMS. Chemical Geology, vol. 240, no. 3-4, p. 222–237.

Pearce, J.A., 1996. A user's guide to basalt discrimination diagrams. In: Trace element geochemistry of volcanic rocks: applications for massive sulphide exploration, Wyman, D. A. (eds.), Geological Association of Canada, short course notes, v. 12, p. 79–113.

Petrus, J.A. and Kamber, B.S., 2012. VizualAge: A novel approach to Laser Ablation ICP-MS U-Pb geochronology data reduction. Geostandards and Geoanalytical Research, vol. 36, no. 3, p. 247–270.

Pitcairn, I., Teagle, D., Craw, D., Olivo, G., Kerrich, R. and Brewer, T., 2006. Sources of metals and fluids in orogenic gold deposits: Insights from the Otago and Alpine schists, New Zealand. Economic Geology, vol. 101, p. 1525–1546.

Pyle, J.M. and Spear, F.S., 1999. Yttrium zoning in garnet: Coupling of major and accessory phases during metamorphic reactions. Geological Materials Research, vol. 1, no. 6, p. 1–49.

Rasmussen, B., Fletcher, I.R. and Muhling, J.R., 2007. In situ U–Pb dating and element mapping of three generations of monazite: Unravelling cryptic tectonothermal events in low-grade terranes. Geochimica et Cosmochimica Acta, vol. 71, no. 3, p. 670–690.

Rasmussen, B., Sheppard, S. and Fletcher, I.R., 2006. Testing ore deposit models using in situ U-Pb geochronology of hydrothermal monazite: Paleoproterozoic gold mineralization in northern Australia. Geology, vol. 34, no. 2, p. 77–80.

Reiners, P.W. and Brandon, M.T., 2006. Using thermochronology to understand orogenic erosion. Annual Review of Earth and Planetary Sciences, vol. 34, no. 1, p. 419–466.

Rhys, D.A., Mortensen, J. and Ross, K.V., 2009. Investigations of orogenic gold deposits in the Cariboo gold district, east-central British Columbia (Parts of NTS 093A, H): Progress Report. Geoscience BC Summary of Activities 2008, Geoscience BC, Report 2009-1, p. 49–74.

Rushton, R.W., Nesbitt, B.E., Muehlenbachs, K. and Mortensen, J.K., 1993. A fluid inclusion and stable isotope study of Au quartz veins in the Klondike district, Yukon Territory, Canada: A section through a mesothermal vein system. Economic Geology, vol. 88, no. 3, p. 647–678.

Rusk, B., 2012. Cathodoluminescent Textures and Trace Elements in Hydrothermal Quartz. *In:* Quartz: Deposits, Mineralogy and Analytics, J. Götze and R. Möckel (eds.), Springer Geology, Springer, Berlin, Heidelberg, p. 307–329, https://doi.org/10.1007/978-3-642-22161-3_14.

Salier, B., Groves, D.I., McNaughton, N.J. and Fletcher, I., 2005. Geochronological and stable isotope evidence for widespread orogenic gold mineralization from a deep-seated fluid source at ca 2.65 Ga in Laverton gold province, Western Australia. Economic Geology, vol. 100, p. 1363–1388.

Sarma, D.S., McNaughton, N.J., Fletcher, I., Groves, D.I., Mohan, M.R. and Balaram, V., 2008. Timing of gold mineralization in the Hutti gold deposit, Dharwar Craton, South India. Economic Geology, vol. 103, p. 1715–1727.

Schandl, E.S. and Gorton, M.P., 2004. A textural and geochemical guide to the identification of hydrothermal monazite: Criteria for selection of samples for dating epigenetic hydrothermal ore deposits. Economic Geology, vol. 99, p. 1027–1035.

Scharer, U., 1984. The effect of initial ^{230}Th disequilibrium on young U-Pb ages: the Makalu case, Himalaya. Earth and Planetary Science Letters, vol. 67, p. 191–204.

Selby, D., Creaser, R.A., Hart, C.J.R., Romback, C.S., Thompson, J.F.H., Smith, M.T., Bakke, A.A. and Goldfarb, R.J., 2002. Absolute timing of sulfide and gold mineralization: A comparison of Re-Os molybdenite and Ar-Ar mica methods from the Tintina gold belt, Alaska. Geology, vol. 30, no. 9, p. 791–794.

Seydoux-Guillaume, A.-M., Paquette, J.-L., Wiedenbeck, M., Montel, J.-M. and Heinrich, W., 2002a. Experimental resetting of the U–Th–Pb systems in monazite. Chemical geology, vol. 191, no. 1, p. 165–181.

Seydoux-Guillaume, A.-M., Wirth, R., Nasdala, L., Gottschalk, M., Montel, J.M. and Heinrich, W., 2002b. An XRD, TEM and Raman study of experimentally annealed natural monazite. Physics and Chemistry of Minerals, vol. 29, no. 4, p. 240–253.

Spear, F.S. and Pyle, J.M., 2002. Apatite, monazite, and xenotime in metamorphic rocks. Reviews in Mineralogy and Geochemistry, vol. 48, no. 1, p. 293–335.

Staples, R.D., 2014. Diachronous Deformation, Metamorphism and Exhumation in the Northern Canadian Cordillera: Revealed from Pressure-Temperature-Time-Deformation Paths of Former Mid-Crustal Rocks. PhD thesis, Simon Fraser University, Vancouver, BC, Canada, 243 p.

Staples, R.D., Gibson, H.D., Berman, R.G., Ryan, J.J. and Colpron, M., 2013. A window into the Early to mid-Cretaceous infrastructure of the Yukon-Tanana terrane recorded in multi-stage garnet of west-central Yukon, Canada. Journal of Metamorphic Geology, vol. 31, no. 7, p. 729–753.

Staples, R.D., Gibson, H.D., Colpron, M. and Ryan, J.J., 2016. An orogenic wedge model for diachronous deformation, metamorphism, and exhumation in the hinterland of the northern Canadian Cordillera. Lithosphere, vol. 8, no. 2, p. 165–184.

Stroh, B., 2019. Resolving Monazite Growth Mechanisms in Orogenic Gold Settings: A Study from the Klondike Gold District, Western Yukon. MSc thesis, University of British Columbia, Vancouver, BC, Canada, 451 p.

Stuwe, K., 1998. Tectonic constraints on the timing relationships of metamorphism, fluid production and gold-bearing quartz vein emplacement. Ore Geology Reviews, vol. 13, p. 219–228.

Taylor, R.D., Goldfarb, R.J., Monecke, T., Fletcher, I.R., Cosca, M.A. and Kelly, N.M., 2015. Application of U-Th-Pb phosphate geochronology to young orogenic gold deposits: New age constraints on the formation of the Grass Valley gold district, Sierra Nevada foothills province, California. Economic Geology, vol. 110, no. 5, p. 1313–1337.

Tera, F. and Wasserburg, G.J., 1972. U-Th-Pb systematics in three apollo 14 basalts and the problem of initial Pb in lunar rocks. Earth and Planetary Science Letters, vol. 14, p. 281–304.

Van Emden, B., Thornber, M., Graham, J. and Lincoln, F., 1997. The incorporation of actinides in monazite and xenotime from placer deposits in Western Australia. The Canadian Mineralogist, vol. 35, p. 95–104.

Vielreicher, N.M., Groves, D.I., Fletcher, I.R., McNaughton, N.J. and Rasmussen, B., 2003. Hydrothermal monazite and xenotime geochronology: A new direction for precise dating of orogenic gold mineralization. Society of Economic Geologists Newsletter, vol. 53, p. 1–16.

Vry, J., Powell, R., Golden, K.M. and Petersen, K., 2010. The role of exhumation in metamorphic dehydration and fluid production. Nature Geoscience, vol. 3, no. 1, p. 31–35.

Wetherill, G.W., 1956. Discordant uranium-lead ages, I. Transactions, American Geophysical Union, vol. 37, no. 3, p. 320–326.

White, A.J.R., Waters, D.J. and Robb, L.J., 2015. Exhumation-driven devolatilization as a fluid source for orogenic gold mineralization at the Damang deposit, Ghana. Economic Geology, vol. 110, no. 4, p. 1009–1025.

Williams, M.L., Jercinovic, M.J., Harlov, D.E., Budzyń, B. and Hetherington, C.J., 2011. Resetting monazite ages during fluid-related alteration. Chemical Geology, vol. 283, no. 3-4, p. 218–225.

Williams, M.L., Jercinovic, M.J. and Hetherington, C.J., 2007. Microprobe monazite geochronology: Understanding geologic processes by integrating composition and chronology. Annual Review of Earth and Planetary Sciences, vol. 35, no. 1, p. 137–175.

Winchester, J. and Floyd, P., 1977. Geochemical discrimination of different magma series and their differentiation products using immobile elements. Chemical Geology, vol. 20, p. 325–343.

Wolff, W.R.G., 2012. Microstructures and Trace Element Signatures of Orogenic Quartz Veins in the Klondike District, Yukon Territory, Canada. BSc thesis, University of British Columbia, Vancouver, BC, Canada, 76 p.

Yukon Geological Survey, 2010. Yukon MINFILE - A database of mineral occurrences. Yukon Geological Survey, https://data.geology.gov.yk.ca/Occurrences/ [accessed 24/05/2017].

Yukon Geolocial Survey, 2023. Yukon Geochronology – A database of Yukon isotopic age determinations. Yukon Geological Survey, https://data.geology.gov.yk.ca/Compilation/22 [accessed 18/09/2025].

Zhu, X.K. and O'Nions, E.K., 1999. Zonation of monazite in metamorphic rocks and its implications for high temperature thermochronology: A case study from the Lewisian terrain. Earth and Planetary Science Letters, vol. 171, p. 209–220.

Yukon Geological Survey list of publications and data releases for 2025

The YGS released 13 publications in 2025: 10 Open Files and 3 Annual Reports.

Open files

Cobbett, R.N., Beranek, L.P., Colpron, M., Piercey, S.J., Crowley, J.L., Strauss, J.V. and Taylor, J.F., 2025. Geochemistry and geochronology of Cambrian and Upper Ordovician mafic igneous rocks along the Dawson fault zone, Yukon. Yukon Geological Survey, Government of Yukon, Open File 2025-1, 42 p. plus appendices.

Ackerson, C.M., Ward, B. and Kennedy, K., 2023. Surficial geology of the central Kluane Ranges (parts of NTS 115B/15, 16 and 115G /1, 2, 3, 6 and 7). Yukon Geological Survey, Government of Yukon, Open File Map 2025-2, scale 1:50 000, 2 sheets.

Ellis, S.H.M., 2025. Preliminary observations from four reduced intrusion-related gold deposits, Selwyn basin, Yukon. Yukon Geological Survey, Government of Yukon, Open File 2025-3, 46 p. plus appendices.

Colpron, M., McClelland, W.C., Piercey, S.J., Kroeger, E.D.L., Crowley, J.L. and Gehrels, G.E., 2025. New geochronological and geochemical data for Permian rocks of the western Yukon-Tanana terrane, Klondike district, Yukon. Yukon Geological Survey, Government of Yukon, Open File 2025-4, 35 p. plus appendices.

Kitchen, J.G., Essman, J.E., Brubacher, A.D. and Johansson, P., 2025. Bedrock geology map of the Coffee Project, Dawson Range, Yukon (parts of NTS 115J/13, 14 and 15). Yukon Geological Survey, Government of Yukon, Open File 2025-5, scale 1:50 000.

Kitchen, J.G., Brubacher, A.D., Essman, J., Valli, F., Johansson, P., Kocay, B., Crowley, J.L. and Larson, K.P., 2025. Geology and bedrock mapping updates at the Coffee Project gold deposit: implications for deposit classification. Yukon Geological Survey, Government of Yukon, Open File 2025-6, 50 p. plus appendices.

Sternbergh, S. and Colpron, M., 2025. Summary of geothermal indicators in the Yukon. Yukon Geological Survey, Government of Yukon, Open File 2025-7, 92 p. plus appendices.

Witter, J.B., 2025. Analysis of geoscience data for the geothermal exploration in the Whitehorse area, Yukon. Yukon Geological Survey, Government of Yukon, Open File 2025-8, 53 p.

Israel, S., Murphy, D., Sack, P.J. and Crowley, J.L., 2025. U-Pb zircon geochronological data for Paleocene to Eocene magmatic rocks in southwest Yukon. Yukon Geological Survey, Government of Yukon, Open File 2025-9, 36 p. plus digital appendices.

Colpron, M., Ambrose, T., Cobbett, R. and Moynihan, D. (compilers), 2025. Yukon Bedrock Geology Map. Yukon Geological Survey, Government of Yukon, Open File 2025-10, 1:1 000 000 scale map and legend.

Annual reports

van Loon, S., 2025. Yukon Placer Mining Industry 2021 to 2023. Yukon Geological Survey, Government of Yukon, 269 p.

Yukon Geological Survey, 2025. Yukon Exploration and Geology Overview 2024. L.H. Weston, A. Stuart, S.K. Schultz, A.D. Brubacher and D.C. Cronmiller (eds.), Yukon Geological Survey, 95 p.

Yukon Geological Survey, 2025. Yukon Exploration and Geology Technical Papers 2024. L.H. Weston A. Stuart, S.K. Schultz, A.D. Brubacher and D.C. Cronmiller (eds.), Yukon Geological Survey, 95 p.

Annual overview papers
(YEG overviews 2024)

Relf, C., 2025. Yukon Geological Survey 2024 overview. *In:* Yukon Exploration and Geology Overview 2024, L.H. Weston, A. Stuart, S.K. Schultz, A.D. Brubacher and D.C. Cronmiller (eds.), Yukon Geological Survey, p. 1–20.

van Loon, S., 2025. Yukon placer mining 2024 development and exploration overview. *In:* Yukon Exploration and Geology Overview 2024, L.H. Weston, A. Stuart, S.K. Schultz, A.D. Brubacher and D.C. Cronmiller (eds.), Yukon Geological Survey, p. 21–35.

Naber, T.V. and Sack, P.J., 2025. Yukon hardrock mining, development and exploration overview 2024. *In:* Yukon Exploration and Geology Overview 2024, L.H. Weston, A. Stuart, S.K. Schultz, A.D. Brubacher and D.C. Cronmiller (eds.), Yukon Geological Survey, p. 37–76.

O'Connor, A. and Weston, L.H., 2025. Yukon Geological Survey's outreach program: 2024 highlights. *In:* Yukon Exploration and Geology Overview 2024, L.H. Weston, A. Stuart, S.K. Schultz, A.D. Brubacher and D.C. Cronmiller (eds.), Yukon Geological Survey, p. 77–83.

Annual report papers
(YEG technical papers 2024)

Gamonal, S., Branson, T., Turner, A., Couper, H. and Yao, S., 2025. Valley deposit: A geological introduction and overview. *In:* Yukon Exploration and Geology Technical Papers 2024, L.H. Weston, A. Stuart, S.K. Schultz, A.D. Brubacher and D.C. Cronmiller (eds.), Yukon Geological Survey, p. 1–18.

Parry, R.K., Lecumberri-Sanchez, P. and Sack, P., 2025. Geology and mineralization of the AurMac metasediment-hosted gold deposits, central Yukon (NTS 105M/13). *In:* Yukon Exploration and Geology Technical Papers 2024, L.H. Weston, A. Stuart, S.K. Schultz, A.D. Brubacher and D.C. Cronmiller (eds.), Yukon Geological Survey, p. 19–39.

Roman, J., Stix, J., Kalacska, M., Lucanus, O., Arroyo-Mora, P. and Lipovsky, P.S., 2025. Thermal imaging and lidar monitoring of ground instability on the Alaska Highway, southwestern Yukon. *In:* Yukon Exploration and Geology Technical Papers 2024, L.H. Weston, A. Stuart, S.K. Schultz, A.D. Brubacher and D.C. Cronmiller (eds.), Yukon Geological Survey, p. 41–50.

Schaeffer, A.J., Gosselin, J.M., Audet, P., Colpron, M., Cairns, S. and Elliott, B., 2025. Western Arctic Regional Network of Seismographs (WARNS): History, challenges and improvements in continuous broadband seismic data recordings in northwestern Canada. *In:* Yukon Exploration and Geology Technical Papers 2024, L.H. Weston, A. Stuart, S.K. Schultz, A.D. Brubacher and D.C. Cronmiller (eds.), Yukon Geological Survey, p. 51–73.

Spruzen, C., Maloney, K.M., Greenman W.J., Lechte, M.A. and Halverson, G.P., 2025. Stratigraphic context for reef-building microbialites in the Tonian Reefal assemblage (Fifteenmile Group) of the Yukon. *In:* Yukon Exploration and Geology Technical Papers 2024, L.H. Weston, A. Stuart, S.K. Schultz, A.D. Brubacher and D.C. Cronmiller (eds.), Yukon Geological Survey, p. 75–95.

Contributions to external publications

Mueller, J.M., **Bond, J.D.**, Farley, K.A. and Ward, B.C., 2025. Cosmogenic ^{3}He dating of olivine with tightly retained mantel ^{3}He, Volcano Mountain, Yukon. Geochronology, vol. 7, no. 3, p. 255–263, https://doi.org/10.5194/gchron-7-255-2025. **YGS Contribution 066**.

Gosselin, J.M., Biegel, K.M., **Dettmer, J.**, Gilbert, H., **Colpron, M.** and Enkelmann, E., 2025. Crustal stress near the Yakutat microplate collision from probabilistic earthquake focal mechanisms. Canadian Journal of Earth Sciences, vol. 62, no. 4, https://doi.org/10.1139/cjes-2024-0095. **YGS Contribution 069**.

Lee, W.-S., Kontak, D.J., **Sack, P.J.**, Crowley, J.L. and Creaser, R.A., 2025. Geology, petrology and geochronology of the Late Cretaceous Klaza epithermal deposit: A window into the petrogenesis of an emerging porphyry belt in the Dawson Range, Yukon, Canada. Minerals, vol. 15, no. 1, https://doi.org/10.3390/min15010038. **YGS Contribution 070**.

Padgett, J., Enkelmanm, E., Kellett, D.A., **Moynihan, D.P.** and Stephan, T., 2025. Cenozoic faulting in the Upper Hyland River Valley, Southeastern Yukon: A thermochronological perspective. Canadian Journal of Earth Sciences, March 31, 2025, https://doi.org/10.1139/cjes-2024-0147. **YGS Contribution 071.**

Cobbett, R.N., Beranek, L.P., **Colpron, M.**, Piercey, S., Crowley, J.L., Strauss, J.V. and Taylor, J.F., 2025. Late Cambrian and Ordovician alkalic magmatism along the Dawson Fault, Yukon: Evidence for multiple reactivations of a rift-transfer fault in the Northern Canadian Cordillera. Tectonics, vol. 44, no. 2, https://doi.org/10.1029/2024TC008645. **YGS Contribution 072.**

Tollefson, K.T., Larson, K.P., **Moynihan, D.P.** and Cleven, N.R., 2025. In situ mica Rb-Sr geochronology and microstructural analysis to evaluate the timing and sense of shear zone movement: Shannon and d'Abbadie Faults, Yukon, Canada. Canadian Journal of Earth Sciences, vol. 62, no. 7, p. 1320–1341, https://doi.org/10.1139/cjes-2024-0144. **YGS Contribution 073.**

Chapman, F.M., Miranda, M.M., **Sternbergh, S.**, Soucy La Roche, R. and Raymond, J., 2025. Geothermal favourability in data-scarce regions: Incorporating physical and socio-economic factors into a modified Play fairway approach, southwestern Yukon, Canada. Geothermal Energy, vol. 13, no. 24, https://doi.org/10.1186/s40517-025-00345-6. **YGS Contribution 074.**

McKenzie, W.F., Gibson, H.D., Colpron, M., Dyck, B., Davies, J.H.F.L. and Perrot, M.G., 2025. New detrital zircon U-Pb and Hf isotope constraints for the Kluane Schist, southwestern Yukon, Canada, and their implications for Cretaceous Insular terrane accretion. Geosphere, vol. 21, no. 6, p. 962–990, https://doi.org/10.1130/GES02845.1. **YGS Contribution 075.**

Faehnrich, K., McClelland, W.C., Webb, L.E., Rasbury, E.T., **Colpron, M.** and Strauss, J.V., 2025. Cretaceous strike–slip displacement along the Porcupine fault system and potential links to the opening of the Canada Basin. Canadian Journal of Earth Sciences, vol. 62, no. 10, p. 1498–1514, https://doi.org/10.1139/cjes-2025-0013. **YGS Contribution 076.**

Colpron, M., McClelland, W.C., Piercey, S.J., Kroeger, E.D.L., Crowley, J.L. and Gehrels, G.E., 2025. Revisiting the "Klondike Orogeny": Permian to Jurassic development of the Yukon-Tanana terrane, northern Canadian Cordillera. Tectonics, vol. 44, no. 6, e2024TC008748, https://doi.org/10.1029/2024TC008748. **YGS Contribution 077.**

Makopoulou, E., Karjalainen, O., **Lipovsky, P.**, Blais-Stevens, A. and Hjort, J., 2025. Susceptibility of active-layer detachment failures and vulnerability of infrastructure in Alaska and northwestern Canada. Landslides, 14 August 2025, https://doi.org/10.1007/s10346-025-02603-x. **YGS Contribution 078.**

Cronmiller, D., 2025. The 17 December 2024 Takhini River landslide and river-ice tsunami, Whitehorse, Yukon, Canada. Landslides, 25 September 2025, https://doi.org/10.1007/s10346-025-02622-8. **YGS Contribution 079**.

Cronmiller, D.C., Ward, B.C., Bond, J.D., Jensen, B.J.L., Lamothe, M., Gosse, J.C., Zazula, G.D., Reyes, A.V. and Telka, A.M., 2025. Timing and interaction of Pleistocene alpine glaciers at the northern margin of the Cordilleran Ice Sheet, Southwest Yukon. Quaternary Science Reviews, vol. 39, https://doi.org/10.1016/j.quascirev.2025.109664. **YGS Contribution 081**.

Gosselin, J.M., **Dettmer, J., Lipovsky, P.** and **Cronmiller, D.,** 2025. Seismic site amplification assessment in the Dakwäkäda (Haines Junction) area of Yukon, Canada, from probabilistic inference of passive seismic measurements. Canadian Geotechnical Journal, https://doi.org/10.1139/cgj-2025-0357. **YGS Contribution 082.**

Articles of interest

Bellamy, D., King, J., and Nadeau, D.F., 2025. Mineral dust emissions from proglacial valleys of western Canada: Historical and future dynamics. Earth Surface Processes and Landforms, vol. 50, no. 5, 18 p., https://onlinelibrary.wiley.com/doi/pdf/10.1002/esp.70069.

Bellamy, D., Nadeau, D.F. and King, J., 2025. Forcing mechanisms of strong surface winds in a dust storm-prone, high latitude proglacial valley. Journal of Applied Meteorology and Climatology, vol. 64, no. 1, p.77–97, https://doi.org/10.1175/JAMC-D-24-0044.1.

Biasi, J.A. and Strauss, J.V., 2025. A review of paleomagnetic studies from Northern Alaska and Yukon: Implications for terrane reconstructions. Canadian Journal of Earth Sciences, vol. 62, no. 4, https://doi.org/10.1139/cjes-2024-0125.

Bogatu, A., Labrousse, L., Martin, C., Zagorevski, A., Bédard, J.H. and Tremblay, A., 2025. Boron isotopic characterization of ophiolitic serpentinites from Atlin terrane, Canadian Cordillera. Lithos, February 2025, vols. 494–495, https://doi.org/10.1016/j.lithos.2024.107922.

Cao, Z. and Furuya, M., 2025. Decades-long evolution of post-fire permafrost deformation detected by InSAR: Insights from chronosequence in North Yukon. AGU Advances, vol. 6, no. 4, https://doi.org/10.1029/2025AV001849.

Carrière, E., Frappier, R., Bjornson, J. and Lacelle, D., 2025. Hydrochemistry of hillslope permafrost catchments with degrading and stable ice wedge polygons, Ogilvie Mountains, Yukon, Canada. Arctic Science, 14 October 2025, https://doi.org/10.1139/as-2025-0029.

Charonnat, B., Baraer, M., Valence, E., Masse-Dufresne, J., Monty, C., Wang, K., Devoie, E. and McKenzie, J.M., 2025. The influence of a rock glacier on the riverbed hydrological system. EGUsphere, vol. 29, no. 22, p. 6479–6498, https://doi.org/10.5194/hess-29-6479-2025.

Charrier, L., Dehecq, A., Guo, L., Brun, F., Millan, R., Lioret, N., Copland, L., Maier, N., Dow, C. and Halas, P., 2025. TICOI: an operational Python package to generate regular glacier velocity time series. EGUsphere, vol. 19, no. 10, p. 4555–4583, https://doi.org/10.5194/tc-19-4555-2025.

Clark, A., Moorman, B., Whalen, D. and Vieira, G., 2025. Segmentation and classification of Pléiades satellite imagery for complex shoreline proxy delineation in the western Canadian Arctic. Journal of Coastal Research, vol. 41, no. 3, p. 391–408, https://doi.org/10.2112/JCOASTRES-D-24-00036.1.

Doumbia, C., Rousseau, A.N., Başağaoğlu, H., Baraer, M. and Chakraborty, D., 2025. Interpretation of glacier mass change within the Upper Yukon Watershed from GRACE using explainable automated machine learning algorithms. Journal of Hydrology, April 2025, vol. 651, https://doi.org/10.1016/j.jhydrol.2024.132519.

Essa, K.S., Elhussein, M., Gomaa, O.A. and Diab, Z.E., 2025. Reliable and efficient magnetic data inversion for resource detection using a hybrid bat algorithm. Scientific Reports, vol. 15, https://doi.org/10.1038/s41598-025-10138-3.

Finley, T., Nissen, E., Cassidy, J.F., Salomon, G., Leonard, L.J. and Froese, D., 2025. Large surface-rupturing earthquakes and a >12 kyr, open interseismic interval on the Tintina fault, Yukon. Geophysical Research Letters, vol. 52, no. 14, https://doi.org/10.1029/2025GL116050.

Gimsa, J., Fritz, M. and Lantuit, H., 2025. Nearshore hydrodynamics and sediment dispersal along eroding permafrost coasts—Insights from acoustic doppler current profiler measurements around Herschel Island-Qikiqtaruk (Yukon, Canada). Permafrost and Periglacial Processes, vol. 36, no. 2, p. 205–216, https://doi.org/10.1002/ppp.2258.

Grewal, A.S., Harman, C.J. and Carey, S.K., 2025. Water storage and release in permafrost catchments: Insights from hydrometrics, end-member mixing, and water age characterization. Water Resources Research, vol. 61, no. 9, https://doi.org/10.1029/2024WR038957.

Grewal, A., Nicholls, E.M. and Carey, S.K., 2025. The role of catchment characteristics, discharge, and active layer thaw on seasonal stream chemistry across ten permafrost catchments. EGUsphere, vol. 29, no. 11, p. 2467–2483, https://doi.org/10.5194/egusphere-2024-2645.

Kim, J., Jung, H.S. and Lu, Z., 2025. Ground surface displacement measurement from SAR imagery using deep learning. Remote Sensing of Environment, vol. 318, https://doi.org/10.1016/j.rse.2024.114577.

Laby, D.A., Sungkono, S. and Biswas, A., 2025. Regularized ensemble Kalman inversion for robust and efficient gravity data modeling to identify mineral and ore deposits. Scientific Reports, vol. 15, no. 43410, https://doi.org/10.1038/s41598-025-30141-y.

Liao, C., Engwirda, D., Cooper, M.G., Li, M. and Fang, Y., 2025. Discrete global grid system flow routing datasets in the Amazon and Yukon basins. Earth System Science Data, vol. 17, no. 5, p. 2035–2062, https://doi.org/10.5194/essd-17-2035-2025.

Macquistan, M.G., Groat, L.A., Peterson, R.C. and Breasley, C.M., 2025. Paragenesis of barium silicate mineralization in Devonian strata at the Gun occurrence, the Yukon, Canada. The Canadian Journal of Mineralogy and Petrology, vol. 63, no. 5, p. 467–489, https://doi.org/10.3749/2400051.

Makopoulou, E. and Varnajot, A., 2025. Permafrost degradation-induced risks for nature-based tourism in the Arctic—case from the Yukon. Climatic Change, vol. 178, no. 93, https://doi.org/10.1007/s10584-025-03942-3.

Muir, M. and Ielpi, A., 2025. Floodplain-age distribution interrogated via photogrammetry and dendrochronology: A case study from the Tsā̃lnjik Chú (Nordenskiold River) of Yukon, Canada. Catena, vol. 259, https://doi.org/10.1016/j.catena.2025.109328.

Partington, G., Copland, L., Lauzon, B., Medrzycka, D., Main, B., Kochtitzky, W. and Dow, C., 2025. Surge history and dynamics of Fisher Glacier, Yukon, 1948–2022. Journal of Glaciology, vol. 71, https://doi.org/10.1017/jog.2025.10084.

Pozsgay, V. and Gruber, S., 2025. Modelling the temporal dynamics of subarctic surface temperature inversions from atmospheric reanalysis for producing point-scale multi-decade meteorological time series in mountains. Arctic Science, vol. 11, https://doi.org/10.1139/as-2025-0027.

Steiner, A.P., Hickey, K.A., Weis, D. and Amini, M., 2025. U-Pb calcite geochronology indicates episodic amagmatic free-convection over tens of millions of years in Carlin-type gold deposits. Miner Deposita, 30 June 2025, https://doi.org/10.1007/s00126-025-01375-7.

Stephan, T. and Enkelmann, E., 2025. All aligned on the western front of North America? Analyzing the stress field in the Northern Cordillera. Tectonics, vol. 44, no. 9, https://doi.org/10.1029/2025TC009014.

Tardif, Y., Richard, L., Bellamy, D., Ahabchane, H.E., Tharaud, M., Schlatt, L., Dourlent, A., Trieu, N., King, J., Wilkinson, K.J. and Hayes, P.L., 2025. Contrasting the elemental composition of fine particulate matter in urban and remote samples using single particle inductively coupled plasma time-of-flight mass spectrometry (SP ICP-ToF-MS). Aerosol Science and Technology, vol. 59, no. 9, p. 1065–1081, https://doi.org/10.1080/02786826.2025.2519091.

Valence, E., Charonnat, B., Baraer, M., Wang, K. and McKenzie, J.M., 2025. Investigating emerging boulder impacts on snowpack ablation. Cold Regions Science and Technology, vol. 237, https://doi.org/10.1016/j.coldregions.2025.104534.

Valisuo, I. and Tietsche, S., 2025. Forecasting Arctic sea ice drift: insights from two case studies. Annals of Glaciology, vol. 66, p. 1–28, https://www.cambridge.org/core/services/aop-cambridge-core/content/view/179BFB7721CFE6E034BFE700FF35A021/S026030552400048Xa.pdf/forecasting-arctic-sea-ice-drift-insights-from-two-case-studies.pdf.

Yang, Y., Rodenhizer, H., Rogers, B.M., Dean, J., Singh, R., Windholz, T., Poston, A., Potter, S., Zolkos, S., Fiske, G., Watts, J., Huang, L., Witharana, C., Nitze, I., Nesterova, N., Barth, S., Grosse, G., Lantz, T., Runge, A., Lombardo, L., Nicu, I.C., Rubensdotter, L., Makopoulou, E. and Natali, S., 2025. A collaborative and scalable geospatial data set for Arctic retrogressive thaw slumps with data standards. Scientific Data, vol. 12, no. 18, https://doi.org/10.1038/s41597-025-04372-7.

Yuan, Q., Zhong, W., Yang, Q., Peng, Y., Bolch, T., Wang, Y., Yue, L., Shen, H. and Zhang, L., 2025. Duration of frozen days show a strong decline in the Northern Hemisphere mainly driven by autumn temperature increase. The Innovation Geoscience, vol. 3, no. 1, https://doi.org/10.59717/j.xinn-geo.2024.100118.

Zhang, Q., Chen, Y., Currie, C.A. and Audet, P., 2025. Factors controlling high elevations in the Canadian Cordillera: isostatic analysis and thermal contributions. Canadian Journal of Earth Sciences, vol. 62, no. 4, p. 865–874, https://doi.org/10.1139/cjes-2024-0134.

Theses

Finley, T., 2025. Neotectonics of major faults in the Canadian Cordillera. PhD thesis, University of Victoria, 151 p. https://hdl.handle.net/1828/22102.

Lord-May, C., 2025. Turbulent heat fluxes and katabatic flow at glacier surfaces: insights from measurements and modelling. PhD thesis, University of British Columbia, 212 p., http://hdl.handle.net/2429/91688.

Nicholson, R.E., 2025. Examining permafrost detection and validation techniques in thermally complex mountainous terrain: a case study in the Ogilvie Mountains, Yukon, Canada. MSc thesis, University of Lethbridge, p. 119, https://hdl.handle.net/10133/7047.

Datasets

Yukon Geological Survey, 2025. Yukon digital bedrock geology. Yukon Geological Survey, https://data.geology.gov.yk.ca/Compilation/3.

Yukon Geological Survey, 2025. Yukon rock physical properties, https://data.geology.gov.yk.ca/Compilation/44.

Yukon Geological Survey
Energy, Mines and Resources
Government of Yukon